

$$F_{opM} = 3.5 \times 10^{-4} \times \frac{F_3}{F_1} \times \frac{F_2}{F_1} \times \frac{F_4}{F_1} \times \frac{F_5}{F_1} \times \frac{F_6}{F_1} \times \frac{F_7}{F_1} \times \frac{F_8}{F_1} \times \frac{F_9}{F_1} \times \frac{F_{10}}{F_1} \times \frac{F_{11}}{F_1} \times \frac{F_{12}}{F_1} \times \frac{F_{13}}{F_1} \times \frac{F_{14}}{F_1} \times \frac{F_{15}}{F_1} \times \frac{F_{16}}{F_1} \times \frac{F_{17}}{F_1} \times \frac{F_{18}}{F_1} \times \frac{F_{19}}{F_1} \times \frac{F_{20}}{F_1} \times \frac{F_{21}}{F_1} \times \frac{F_{22}}{F_1} \times \frac{F_{23}}{F_1} \times \frac{F_{24}}{F_1} \times \frac{F_{25}}{F_1} \times \frac{F_{26}}{F_1} \times \frac{F_{27}}{F_1} \times \frac{F_{28}}{F_1} \times \frac{F_{29}}{F_1} \times \frac{F_{30}}{F_1} \times \frac{F_{31}}{F_1} \times \frac{F_{32}}{F_1} \times \frac{F_{33}}{F_1} \times \frac{F_{34}}{F_1} \times \frac{F_{35}}{F_1} \times \frac{F_{36}}{F_1} \times \frac{F_{37}}{F_1} \times \frac{F_{38}}{F_1} \times \frac{F_{39}}{F_1} \times \frac{F_{40}}{F_1} \times \frac{F_{41}}{F_1} \times \frac{F_{42}}{F_1} \times \frac{F_{43}}{F_1} \times \frac{F_{44}}{F_1} \times \frac{F_{45}}{F_1} \times \frac{F_{46}}{F_1} \times \frac{F_{47}}{F_1} \times \frac{F_{48}}{F_1} \times \frac{F_{49}}{F_1} \times \frac{F_{50}}{F_1} \times \frac{F_{51}}{F_1} \times \frac{F_{52}}{F_1} \times \frac{F_{53}}{F_1} \times \frac{F_{54}}{F_1} \times \frac{F_{55}}{F_1} \times \frac{F_{56}}{F_1} \times \frac{F_{57}}{F_1} \times \frac{F_{58}}{F_1} \times \frac{F_{59}}{F_1} \times \frac{F_{60}}{F_1} \times \frac{F_{61}}{F_1} \times \frac{F_{62}}{F_1} \times \frac{F_{63}}{F_1} \times \frac{F_{64}}{F_1} \times \frac{F_{65}}{F_1} \times \frac{F_{66}}{F_1} \times \frac{F_{67}}{F_1} \times \frac{F_{68}}{F_1} \times \frac{F_{69}}{F_1} \times \frac{F_{70}}{F_1} \times \frac{F_{71}}{F_1} \times \frac{F_{72}}{F_1} \times \frac{F_{73}}{F_1} \times \frac{F_{74}}{F_1} \times \frac{F_{75}}{F_1} \times \frac{F_{76}}{F_1} \times \frac{F_{77}}{F_1} \times \frac{F_{78}}{F_1} \times \frac{F_{79}}{F_1} \times \frac{F_{80}}{F_1} \times \frac{F_{81}}{F_1} \times \frac{F_{82}}{F_1} \times \frac{F_{83}}{F_1} \times \frac{F_{84}}{F_1} \times \frac{F_{85}}{F_1} \times \frac{F_{86}}{F_1} \times \frac{F_{87}}{F_1} \times \frac{F_{88}}{F_1} \times \frac{F_{89}}{F_1} \times \frac{F_{90}}{F_1} \times \frac{F_{91}}{F_1} \times \frac{F_{92}}{F_1} \times \frac{F_{93}}{F_1} \times \frac{F_{94}}{F_1} \times \frac{F_{95}}{F_1} \times \frac{F_{96}}{F_1} \times \frac{F_{97}}{F_1} \times \frac{F_{98}}{F_1} \times \frac{F_{99}}{F_1} \times \frac{F_{100}}{F_1}$$

Diamond Light Source Ltd

2011/12



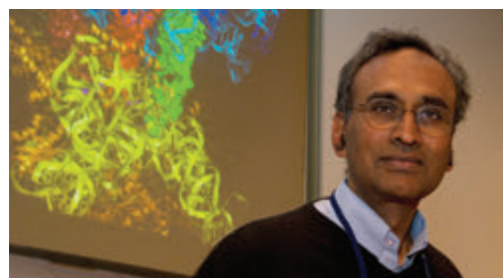
Contents

2	Foreword
4	Introduction
6	Beamline development and technical summary
8	Spectroscopy Village
22	Soft Condensed Matter Village
44	Engineering and Environment Village
66	Surfaces and Interfaces Village
78	Materials Village
98	Macromolecular Crystallography Village
138	Machine Operations
140	Optics and Metrology Group
142	Detector Group
144	Data Acquisition and Scientific Computing
146	Key Facts and Figures
148	The Industrial Diamond
150	Public Engagement
152	Governance and Management
153	Staffing and Financial Information
154	Committee Membership



Venki Ramakrishnan

Nobel Prize Winner 2009



Modern structural biology would essentially be unthinkable without synchrotron radiation. In particular, the large macromolecular complexes and machines that are part of the cell can currently only be visualized at the atomic level by synchrotron based X-ray crystallography.

It allows us to obtain information from very small crystals that would otherwise be impossible to do. Finally, outside my own field there are a host of applications in physics and chemistry that require these powerful sources of X-rays. Given this increasing and crucial need, it has been extremely useful to have the Diamond Light Source, a state-of-the-art facility that is easily accessible to users in the UK. I also think that having allied institutions nearby for structural biology and other fields will have a synergistic effect by improving both the user facilities and the science that will be done at Diamond. This will benefit both the pursuit of applied knowledge and applied research.

Lord Broers

Chairman of the Board of Diamond



This has been another year in which the performance and scientific and technological output of Diamond has strongly advanced.

The facility now rivals the most advanced and successful synchrotron facilities in the world in terms of reliability and output. Close links have also been established with industry to ensure that we capitalise on the contributions that Diamond can make to product development and enhancement. If academic research in collaboration with industry is included then more than 20% of beamtime is now directly connected with industry.

In addition to the growth in the use of the facility we have been pressing ahead with the completion of the Phase II beamlines and ramping up our work on Phase III. The final set of ten Phase III beamlines was determined through a process of detailed engagement with the user community. The first of these beamlines will commence operation in 2014 and the final beamline in 2018. As in the past we are being fortunate in being able to attract outstanding scientists and engineers to work on this final phase of the project so we are confident that Diamond will continue to meet and exceed expectations.



Introduction

Gerhard Materlik, Chief Executive Officer

This year Diamond Light Source Ltd is celebrating its 10th Anniversary. The company was officially formed on the 27th March 2002 by the signing of the Joint Venture Agreement between the UK Government and the Wellcome Trust.

This milestone provides an opportunity to reflect on the challenges and achievements this anniversary celebrates. We built Diamond during the initial five years and have in the following five years established a very successful operation programme, while still building the new beamlines of Phases II and III. There are many facets to this success – the commitment and dedication of our staff and contractors, the continued support of our user community and the ongoing financial backing of our shareholders. These ingredients are each filled with their many challenges, and in overcoming those, there lies success!

The confirmation in 2010 that Phase III funding was granted allows for 10 additional beamlines to be constructed and will bring the total number of beamlines to 32 by 2018. This maximises the initial capital investment made in the facility. The selection of these beamlines required the initial proposal from the science community, the evaluation by the Scientific and Industrial Advisory Committees (SAC and DISCo), the inclusion of the funders through the Large Facilities Steering Group (LFSG) and the final approval by Diamond's Board of Directors and the Shareholders, namely the Science and Technology Facilities Council (STFC) and the Wellcome Trust. I would like to thank the members of these various groups and committees for their active and positive engagement, making sure that Diamond is well positioned to provide the most sought-after and leading edge instruments for the UK and international communities.

With 20 beamlines now operational, there has been an increase in science delivered by the facility. Over the past financial year, a total of 4851 user visits were serviced by Diamond, with 398 from outside the UK, conducting experiments over a broad range of scientific fields. This means that 6349 shifts were allocated enabling users to follow their scientific goals formulated in 475 successful proposals. Users from 281 academic institutes have visited Diamond for beamtime with 142 coming from outside the UK.

By April 2012, Diamond's activities had led to over 1700 scientific publications with more than 420 reported so far in 2011/12. In 2011 just over 200 protein structures from Diamond were deposited in the World Protein Databank, reaching 825 since our start of operations.

Diamond supports the delivery of the research portfolio of the UK Research Councils but has also a major role to play with Industry. We close the financial year with our 50th industrial customer and we have increased our support of industrial research, with overall 6% proprietary access across 17 beamlines, rising to 19% on a single beamline. In addition 15% of non-MX (Macromolecular Crystallography) academic proposals were also directly related to industrial partners and 32% of the MX BAGs (Block Allocation Groups) reported direct industrial involvement.

This user success has only become possible through the excellent reliability and stability of the accelerators which is reflected in 98% uptime and an increase of the mean time between failures by a factor of two, bringing it to now 56 hours.

Our vision for Diamond remains bold: "Throughout its lifetime, Diamond endeavours to be a leading edge facility for scientific research, supporting a wide range of users from both academia and industry, thereby delivering benefits to the UK society and economy. Diamond will strive to respond to the 21st century scientific challenges through the successful management of the facility, the high quality science it delivers and encourage its wide dissemination".

Diamond will continue to play a major role in the UK scientific landscape for decades to come. Being part of the Diamond team has been a very rewarding experience for me. I have been grateful for my staff's commitment and support and I thank them for their continued efforts and hard work to make Diamond a true user facility.

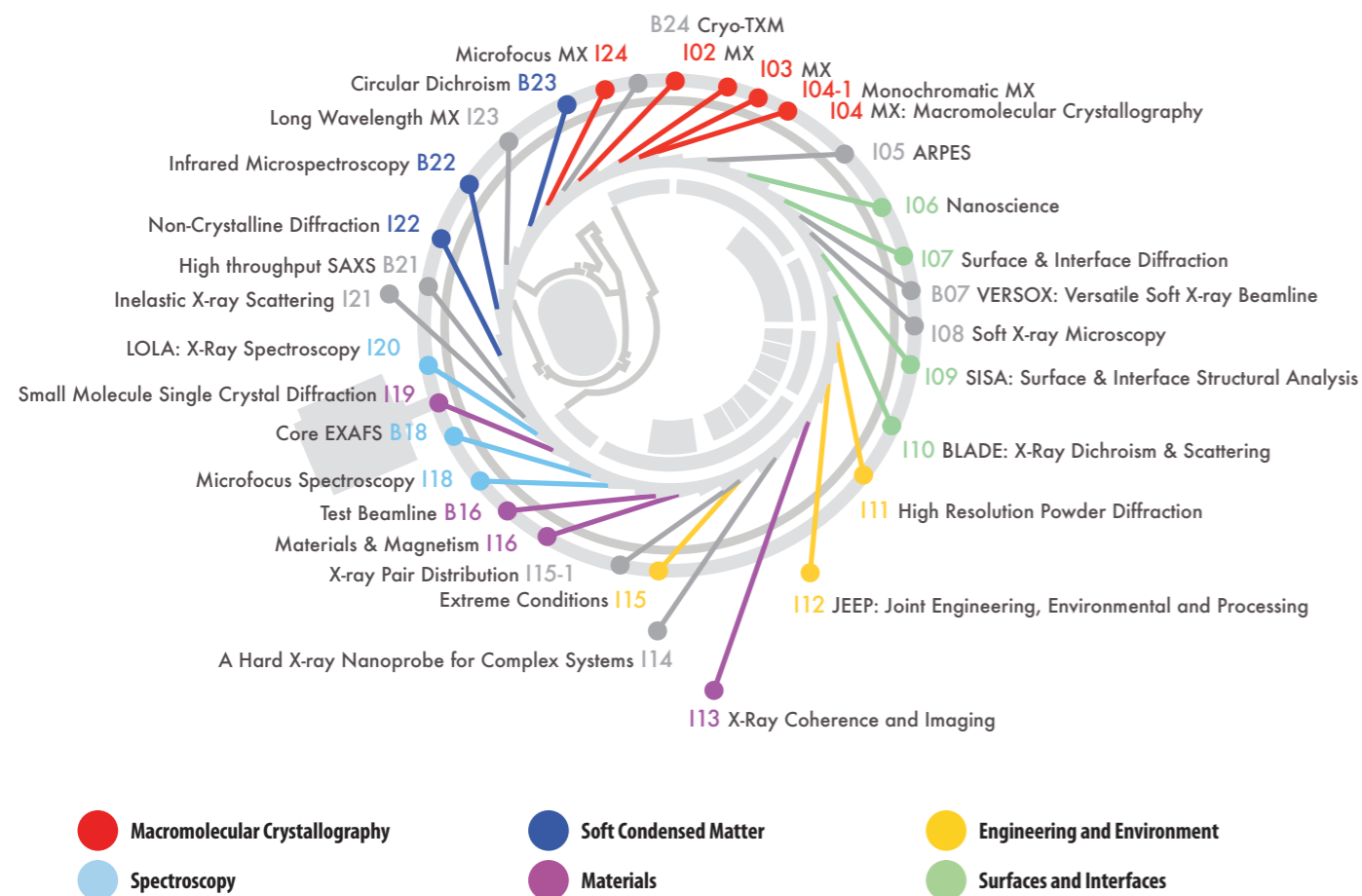
I would finally like to thank our shareholders, once again, together with the UK Research Councils and all our partners and stakeholders for their outstanding support over the past ten years. I am sure that the team will remain focused on delivering science of the highest quality with a strong impact.



Beamline development and technical summary

Diamond now has 20 operational beamlines, with the final Phase II beamlines in optimisation mode within 2012. The first six approved Phase III beamlines are underway. The last four beamlines have now been selected by the Science Advisory Committee and taken forward.

The beamlines are organised into six villages as described below. Phase III beamlines are shown in grey.



With Phase II almost completed and funding confirmation for Phase III, in October 2010, Diamond Light Source issued a call for ideas for new beamlines as part of the final prioritisation procedure for Phase III.

Outline Proposals were considered by the SAC and DISCo in June 2011, and full proposals considered at an Open Meeting of the SAC on 11th October 2011. The final recommendations from SAC and DISCo to complete the Diamond Phase III beamline portfolio were considered and approved by the Diamond Board of Directors in December 2011. This will now give Diamond 32 operational beamlines by 2018.

Diamond's beamlines: current operation status April 2012

Beamline Name and Number	Main Techniques	Energy / Wavelength Range	Status
I02 - Macromolecular Crystallography	Macromolecular Crystallography, Multiwavelength Anomalous Diffraction (MAD)	5 - 25 keV	Operational
I02/I02-1 VMX	Versatile Macromolecular Crystallography (VMX)		Phase III approved
I03 - Macromolecular Crystallography	Macromolecular Crystallography, MAD	5 - 25 keV	Operational
I04 - Macromolecular Crystallography	Macromolecular Crystallography, MAD	5 - 25 keV	Operational
I04-1 - Monochromatic MX	Macromolecular Crystallography	13.53 keV (0.9163 Å – fixed wavelength)	Operational
I05 - ARPES	Angle-resolved PhotoEmission Spectroscopy (ARPES)	18 - 240 eV	Phase III under construction
I06 - Nanoscience	X-ray absorption spectroscopy, X-ray photoemission microscopy and X-Ray Magnetic Circular and Linear Dichroism	First harmonic circular: 106 - 1300 eV; Linear Horizontal: 80 - 2100 eV; Linear Vertical: 130 - 1500 eV	Operational
I07 - Surface and Interface Diffraction	Surface X-ray diffraction, Grazing Incidence X-ray Diffraction (GIXD), Grazing Incidence Small Angle X-ray Scattering (GISAXS), X-ray Reflectivity (XRR)	6 - 25 (30) keV	Operational
B07 - VERSOX: Versatile Soft X-ray beamline	Spectroscopic and scanned-probe imaging	50 - 2000 eV	Phase III approved
I08 - Soft X-ray Microscopy	X-ray scanning microscopy	250 eV - 4 keV	Phase III under construction
I09 - SISA: Surface and Interface Structural Analysis	Photoelectron Spectroscopy, X-ray Standing Waves, X-ray Absorption Spectroscopy, X-ray Photoelectron Diffraction, X-ray Reflectivity	Hard X-rays: 2.1 keV - 20 keV+ Soft X-rays: 150 eV - 2.1 keV	Completion date: Oct 2012
I10 - BLADE: Beamline for Advanced Dichroism Experiments	soft X-ray resonant scattering, X-ray absorption spectroscopy and X-ray magnetic circular and linear dichroism	400 - 2000 eV	Operational
I11 - High resolution powder diffraction	X-ray powder diffraction	5 - 30 keV (0.4 - 2.5 Å)	Operational
I12 - JEEP: Joint Engineering, Environmental and Processing	Imaging and tomography, X-ray diffraction, Small Angle X-ray Scattering (SAXS), Single Crystal Diffraction, Powder diffraction	50 - 150 keV	Operational
I13L - X-ray Imaging and Coherence	Phase contrast imaging, Tomography	Imaging branch: 8 - 35 keV Coherence: 2 - 20 keV	Operational in optimisation mode
I14 - A Hard X-ray Nanoprobe for Complex Systems	Scanning X-ray Fluorescence, X-ray spectroscopy and diffraction, small and wide angle X-ray scanning	3.5 - 30 keV	PHASE III under construction
I15 - Extreme Conditions	Powder diffraction, single crystal diffraction	20 - 70 keV mono mode. Beam size conditions apply for high energies > 30 KeV. 20 - 50 µm pinholes available.	Operational
I15-1 - XPDF	X-ray Pair Scattering Distribution Function (XPDF)		Phase III approved
I16 - Materials and Magnetism	Diffraction/Scattering, Spectroscopy	3.5 - 25 keV	Operational
B16 - Test beamline	Diffraction, imaging, reflectometry	4 - 20 keV monochromatic focused 4 - 20 keV monochromatic unfocused White beam	Operational
I18 - Microfocus Spectroscopy	X-ray absorption spectroscopy (XAS), Extended X-ray Absorption Fine Structure (EXAFS), Fluorescence tomography	2 - 20 keV	Operational
B18 - Core EXAFS	X-ray absorption spectroscopy	2.05 - 35 keV	Operational
I19 - Small molecule single crystal diffraction	Small Molecule Single Crystal Diffraction	5 to 25 keV / 0.5 to 2.5 Å	Operational
I20 - LOLA: X-ray spectroscopy	X-ray Absorption Spectroscopy (XAS), Energy Dispersive EXAFS (EDE), X-ray Emission Spectroscopy	Dispersive branch: 6 - 26 keV; Scanning branch: 4 - 34 keV	Commissioning
B21 - High throughput SAXS	Small Angle X-ray Scattering & Diffraction	6 - 23 keV	Phase III under construction
I21 - Inelastic X-ray Scattering	Inelastic X-ray Scattering (IXS)		Phase III under construction
I22 - Non-crystalline diffraction	Non-Crystalline diffraction: SAXS, WAXS, ASAXS, USAXS	3.7 - 20 keV	Operational
B22 - Infrared Microspectroscopy	Infrared Microspectroscopy	1.2 eV - 2.4 meV	Operational
I23 - Long Wavelength MX	Long wavelength MX	1 - 4 Å but optimised for 1.5 and 3.1 Å Operational Module A: 125 - 500nm	PHASE III under construction
B23 - Circular dichroism	Circular Dichroism	Operational Module B: 160 - 650nm	Operational
B24 - Cryo-TXM	Full field X-ray imaging	Up to 2.5keV	Phase III under construction
I24 - Microfocus MX	Macromolecular Crystallography, MAD	6.5 - 25.0 keV	Operational

Spectroscopy Village

Fred Mosselmanns, Village Coordinator

It is an exciting time in the Spectroscopy Village as two of the new Phase III beamlines currently being designed will provide nanofocus spectroscopic imaging on dedicated beamlines in the soft and hard X-ray regimes. The two first XAS beamlines, I18 microfocuss spectroscopy and B18 core EXAFS, continue to progress with both now running reliably in the new style generic data acquisition (GDA) software. I20 LOLA is beginning to see light at the end of the beampipe as solutions have been developed for its difficult technical challenges.

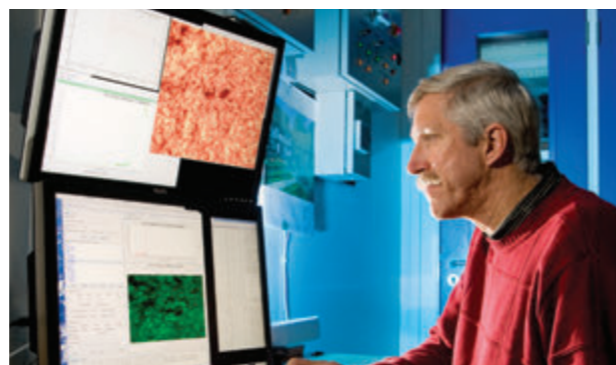
Furthermore, the new radionuclide laboratory facility has had its first users: the BIGRAD (biogeochemical gradients and radionuclide transport) consortium, which is funded by NERC, the Natural Environment Research Council. This facility enables some low level radionuclides to be handled onsite before they are sealed securely, allowing the possibility for delicate radionuclide species to be examined at Diamond.

The range of science on spectroscopy beamlines is diverse, with much biological imaging continuing on I18 such as: Jon Dobson and his colleagues' work investigating Alzheimer's Disease; the University of Kent's invaluable Mary Rose research informing the strategy for the conservation of archaeological marine wood; and Rob Dryfe and collaborators looking at the formation of gold nanoparticles at the interface between organic and aqueous phases with a microfocuss beam. On B18, users are often chemists and include the catalysis studies by Moniek Tromp's team, where they are trying to capture information on short lived intermediates; and Serena Corr and associates' work in understanding lithium batteries. Environmental scientists are frequent visitors to the beamlines, Giannantonio Cibi and co-workers have studied airborne mineral dust from ice cores, which can inform the climate change debate.

B18 has now been open for nearly two years in March 2012. The number of user groups using the beamline has continued to grow, and many positive comments about the quality of data have been received. Commissioning time was mainly spent improving the QEXAFS capability of the beamline and the software. After the replacement of the stepper motor Bragg axis with a servo motor in August 2011, the reliability of QEXAFS improved dramatically and it is now the default mode of operation providing a factor of two improvement in throughput. Whilst the beamline was not intended for ultra dilute EXAFS, it has been possible to measure 1 mM Cu protein and few hundred ppm absorbed species on a mineral in typically 6-8 hours.

On I18, the optical table of the end station was replaced with two large granite blocks in November 2011, at the same time the opportunity was taken to optimise the table top layout. This now gives more space for additional optics, such as zone plates, and in October a zone plate trial in collaboration with the Optics group produced the first sub 100 nm hard X-ray beam measured on Diamond. The granite blocks should provide better stability as we aim to open a sub-micron XRF mapping option on I18 for 2013. We are also beginning to develop XANES mapping on the beamline and performed the first trial experiment in February 2012. The new GDA gui combined with sample stage rastering has substantially increased the mapping speeds feasible on the beamline. We are looking to reduce the time per point still further in summer 2012 when we aim for 100 Hz sampling frequency.

After solving the vacuum problems and the thermal management issues of the I20 four bounce monochromator in 2010-2011, further commissioning brought to light time and energy dependent intensity fluctuations in its operation. These effects prevented the collection of good quality EXAFS spectra and were tracked down to factors related with the mechanical flexibility of the monochromator crystal cages. To solve these issues a complete re-design of



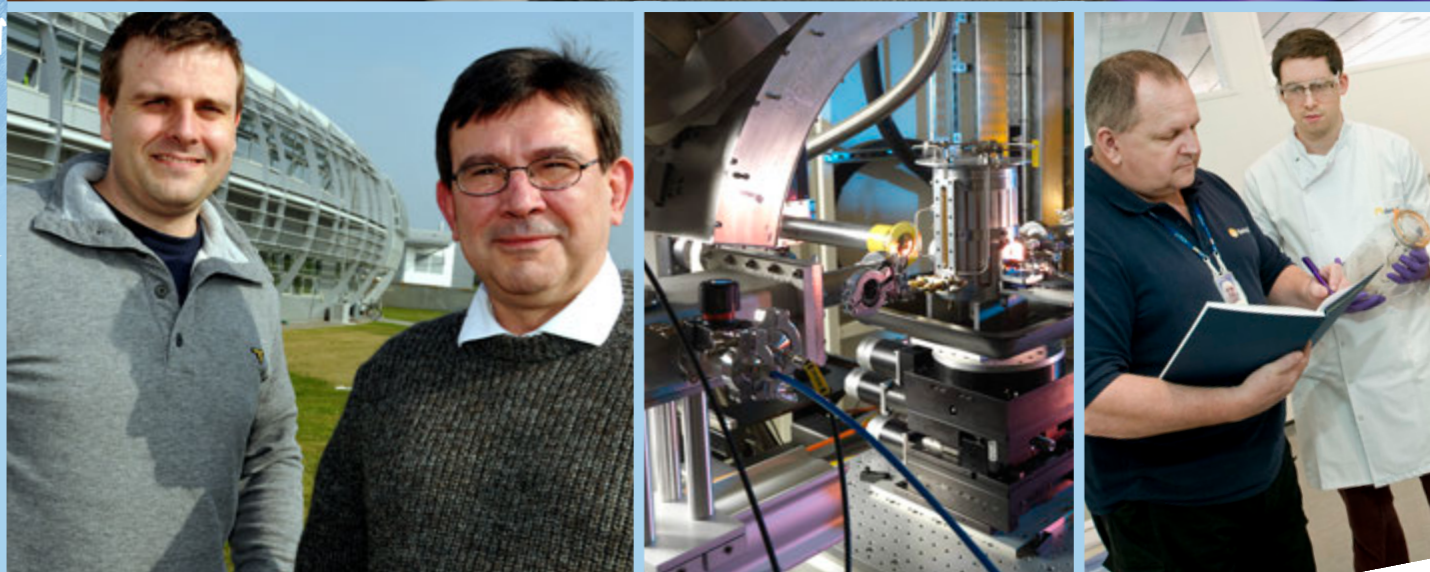
the crystal cages of the two monochromator axes was required. This project began in June 2011 and the installation of the newly designed components is scheduled for the June 2012 shutdown. The rest of the beamline components have now been commissioned, taking advantage of the time needed to solve the monochromator problems. The emission spectrometer assembly has been completed and is now ready to take X-ray beam.

Over the past year, significant progress in building of the dispersive branch of the beamline has been achieved. First light in the Optics Hutch was seen in early 2012. The polychromator, a Diamond in-house design, is scheduled for installation in May 2012, and this will complete the installation of components in the Polychromator Hutch. Furthermore the assembly of the spectrometer in the Experimental Hutch is also very advanced and we expect to be ready for X-ray commissioning of this branch at I20 in the summer of 2012.

I08-SXM will be filling the gap on international level by providing unique capabilities in its energy range for a scanning X-ray microscope (SXM). The instrument covers a 250-4200 eV photon energy range from soft to X-rays providing access to major K- and L- absorption edges for elemental and chemical analysis with lateral resolutions better than 20 nm. This is complemented by versatile X-ray transmission contrasts and exploring new imaging techniques, including new 3D imaging by depth profiling approaches, for example by structured illumination. The central objective of the I08-SXM beamline is the ability to obtain morphological and chemically-specific information on a broad range of organic and inorganic matter under in-situ conditions, mimicking real environments. The technical design review for I08 took place in October 2011 and it is on track to open for users in 2014.

I14-Hard X-ray nanoprobe will be an instrument to provide X-ray beam sizes from 1µm to 25nm and beyond. The beamline will be over 185m long and will consist of two endstations. The first will provide beam sizes from 1µm to 100nm and will target on SAXS/WAXS and elemental analysis with ample space for a wide range of sample environments. The second endstation is a nanoprobe dedicated to delivering the smallest possible beam size for elemental, spectroscopic and diffraction studies, with beam sizes down to 25nm. The ability to study elemental and structural variations on such a wide scale has attracted a broad user community with a wide range of applications in biological, environmental and material science. The beamline had its conceptual design review in February 2012 and is scheduled to open in 2016.

5.0x10⁵
4.0x10⁵
3.0x10⁵
2.0x10⁵
1.0x10⁵
0.0
-1.0x10⁵
-2.0x10⁵
-3.0x10⁵
-4.0x10⁵



Application of microfocus X-ray beams from synchrotrons in heritage conservation

Schofield, E.J., Sarangi, R., Mehta, A., Jones, A.M., Mosselmans, F. J. W., Chadwick A. V. Nanoparticle de-acidification of the *Mary Rose*, *Materials Today*, **14**, 354-358 (2011)

A major cause of the degradation of heritage and museum objects is attack by acid, including the attack by acids caused by atmospheric pollution or acidic species generated from within the artefact. In the case of the *Mary Rose*, the warship of Henry VIII that was raised in 1982 and is currently being prepared for exhibition in a new museum in Portsmouth Harbour, the acid is sulfuric acid which originates from the oxidation of sulfur compounds deposited in the wood by bacteria on the seabed. Treatment of objects with mild alkali is one method of neutralising the acids in artefacts; however this can lead to the growth of salt deposits which can disrupt the structure due to the pressures that are generated. A relatively recent approach to the problem is to impregnate the object with nanoparticles of an insoluble alkaline earth oxide, hydroxide or carbonate which will only form small particles with acids and act as a de-acidification reservoir. We have been using nanoparticles of strontium carbonate to treat *Mary Rose* timbers and using X-ray absorption spectroscopy to monitor the effectiveness of the treatment, to understand the chemistry involved and to measure the penetration in the wood.

The *Mary Rose* was a favourite warship of King Henry VIII of England. It sank in July 1545 whilst en route to confront ships of the French fleet outside Portsmouth harbour. It remained on the seabed for over 400 years before it was uncovered and then raised in 1982. Approximately half of the ship survived as a consequence of being buried by silt, and thereby protected from the currents and from the organisms that eroded away the exposed timbers. However, the surviving timbers now exhibit potentially damaging sulfur salt precipitates. The problem was first identified in 2000 in the conserved Swedish warship, *Vasa*^{1,2}. The origin of the precipitates is the formation of H_2S in the polluted sea of the harbour by sulfur reducing bacteria which diffuses into the wood and reacts to form a range of reduced

sulfur compounds. In the anoxic conditions of the sea-bed these materials are not a problem, but in the raised timbers air causes oxidation, the formation of sulfuric acid with degradation of the cellulose and formation of the mineral deposits. The growth of these deposits causes further disruption of the timber. The problems are further exacerbated by the presence of iron species in the wood (from original fittings, bolts and nails) which catalyse the formation of sulfuric acid. The effect is illustrated in Fig. 1, which shows sulfate mineral aggregates on a knife handle.

At Diamond Light Source we have been using X-ray absorption spectroscopy (XAS) to monitor the iron and sulfur speciation in the *Mary Rose*



Figure 1: A recovered Tudor knife handle from the *Mary Rose*. Note the deposits where it was attached to the iron-based blade.

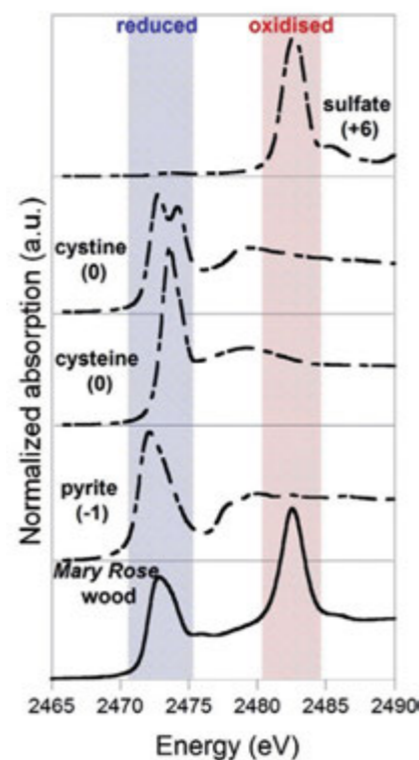


Figure 2: The sulfur K-edge XANES of *Mary Rose* timber and compound known to be present in the timber.

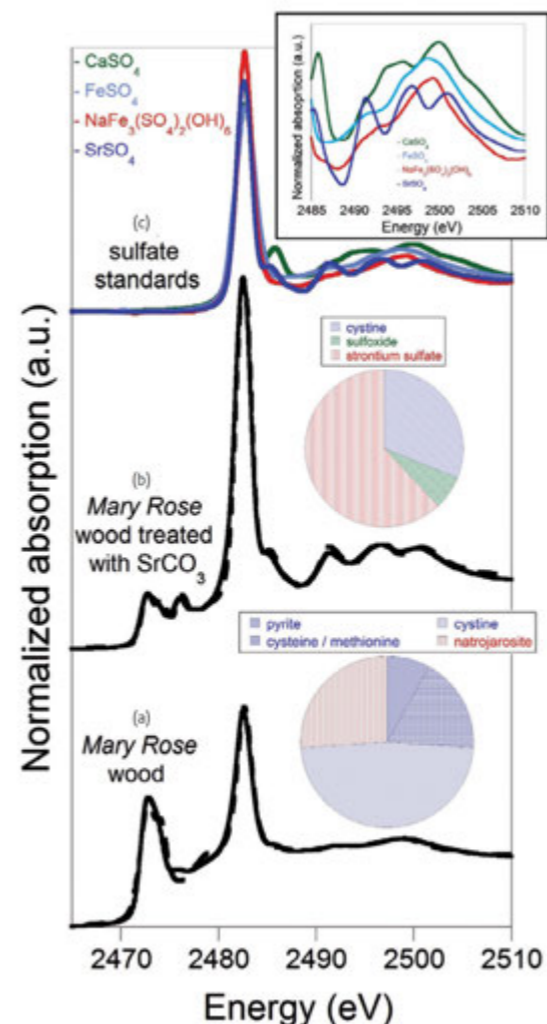


Figure 3: Speciation change of sulfur compounds after reaction with $SrCO_3$ nanoparticles. Sulfur K-edge XANES spectra and pie charts from least-squares fitting with model compounds of (a) *Mary Rose* timbers before treatment, (b) *Mary Rose* timbers after treatment with $SrCO_3$, and (c) sulfate model compounds; (inset) illustrating the post absorption edge variation.

timber and artefacts to measure the effectiveness of various preservation techniques. In the case of sulfur XAS is particularly powerful as the shift in the K-edge absorption edge in the X-ray absorption near edge structure (XANES) can distinguish all the sulfur oxidation states³, i.e. from -1 to +6. This is illustrated in Fig.2, which shows the sulfur K-edge XANES of a *Mary Rose* timber and compounds known to be present in the timber.

We have used the microfocus XAS station, I18, to characterise the composition of the *Mary Rose* timbers and artefacts⁴ and used bulk XAS measurements to monitor the effectiveness of a number of standard iron-chelating agents (EDTA, DTPA, ammonium citrate) in the removal of iron compounds. In addition, we have examined the effect of chelating agents on timbers which have been impregnated with polyethylene glycol (PEG), a polymer used to 'fill' the holes in degraded water-logged wood and give them mechanical stability. This blocks the entrance of the chelating agents.

It has been estimated that the *Mary Rose* timbers contain some 2 tonnes of sulfur² in various chemical forms, both inorganic (pyrites and other salts) and organic (cysteine, cysteine, methionine and thiols) and many of them can potentially oxidise to sulfuric acid. Therefore treatments that provide a long-term protection from acid attack are desirable. In a series of sulfur K-edge XAS experiments undertaken at beamline 4-3, S.S.R.L. and Diamond

beamline I18, we have explored treatment with alkaline nanoparticles to provide de-acidification reservoirs, a method that has been used in other heritage artefacts⁵. Timbers and artefacts were impregnated with 20-50 nm diameter particles of strontium carbonate ($SrCO_3$) prepared by high energy ball-milling. We have impregnated timbers and artefacts with 20-50 nm diameter particles of strontium carbonate, $SrCO_3$, prepared by high energy ball-milling. $SrCO_3$ was chosen as other alkaline earths (magnesium and calcium) are present in the *Mary Rose* and could unnecessarily complicate the analysis. Wood samples were sonicated in 2-propanol dispersions of the nanoparticles for various periods of time and then examined by XAS. The sulfur K-edge results for *Mary Rose* wood treated for three days are shown in Fig. 3. The treatment leads to dramatic changes in the spectra, most notably being the growth of sulfate after the treatment. Further analysis was possible by simulating the wood spectra as the linear combination of components of sulfur compounds known to be in the wood. This not only shows the formation of strontium sulfate but also a reduction in the concentration of the organic sulfur compounds. Thus there is an added advantage of using the nanoparticles.

Recently we have studied simulated *Mary Rose* timbers prepared from fresh oak and impregnated with iron sulfate. These were treated with $SrCO_3$ nanoparticles and the iron and strontium K-edge XAS collected on B18. These measurements confirmed the removal of sulfate to form inactive strontium sulfate. In addition, they provided information on the penetration of the nanoparticles into the wood. This work showed that water dispersions gave a greater penetration depth for the nanoparticles, compared to 2-propanol dispersions and that the penetration is hindered in PEG treated samples. This information, along with the sulfur K-edge results now allows us to design the optimum nanoparticle treatment regimes for timber and artefacts.

References

1. Sandström, M., Jalilehvand, F., Persson, I., Gelius, U., Frank, P. & Hall-Roth, I. Deterioration of the seventeenth-century warship *Vasa* by internal formation of sulphuric acid. *Nature*, **415**, 893-897 (2002).
2. Sandström, M., Jalilehvand, F., Damian, E., Fors, Y., Gelius, U., Jones, A.M. & Salome, M., Sulfur accumulation in the timbers of King Henry VIII's warship *Mary Rose*: A pathway in the sulfur cycle of conservation concern. *Proc. Natl. Acad. Sci USA*, **102**, 14165-14170 (2005).
3. Wetherall, K.M., Moss, R.M., Jones, A.M., Smith, A.D., Skinner, T., Pickup, D.M., Goatham, S.W., Chadwick, A.V. & Newport, R.J., Sulfur and iron speciation in recently recovered timbers of the *Mary Rose* revealed via X-ray absorption spectroscopy. *J. Arch. Sci.*, **35**, 1317-1328 (2008).
4. Chadwick, A.V., Berko, A., Schofield, E.J., Jones, A.M., Mosselmans, J.F.W. and Smith, A.D., *Int. J. Arch. Heritage*, **6**, 228-258 (2012).
5. Baglioni, P., & Giorgi, R., Soft and hard nanomaterials for restoration and conservation of cultural heritage. *Soft Matter*, **2**, 293-303 (2006).

Funding Acknowledgements

We thank the Heritage Lottery Fund for continued support of the conservation of the *Mary Rose* and the grant which funded this project. AVC would like to thank the Leverhulme Trust for an Emeritus Grant to support this research.

Research carried out at Diamond Light Source on beamline I18 and at the SSRL on beamline 4.3.

DOI 10.1016/S1369-7021(11)70166-3

Nucleation and growth processes of gold nanoparticles at the liquid-liquid interface

Gründer, Y., Ho, H.L.T., Mosselmans, J.F.W., Schroeder S.L.M. & Dryfe, R.A.W. Inhibited and Enhanced Nucleation of Au Nanoparticles at the Water/1,2-Dichloroethane Interface. *Phys. Chem. Chem. Phys.* **13**, 15681-15689 (2011)

Nanoparticles have attracted enormous interest recently because of their unique optical, electrical, and chemical properties. The properties of these particles, which have dimensions in the range 1 to 100 nm, are very promising for medical applications in biotechnology and catalysis. However their performance depends on their size, structure and composition, hence much effort has been invested to develop methods to control the properties of nanoparticles. One promising way to make nanoparticles is using the 'two-phase' methods, where a metal ion (gold, in this case) is dissolved in an 'oil' phase and the agent, that reduces the ion to form the metal particles, is dissolved in water. We have combined this two-phase method with in situ X-ray absorption spectroscopy on beamline I18 which allows us to examine the local environment of the Au ion, and gain insight in this important particle formation process.

Wet-chemical routes to the formation of metallic nanoparticles are currently among the most intensely studied chemical processes. Gold nanoparticles (Au NPs), because of their myriad applications, have attracted particular attention. One of the most popular routes to Au NPs is the two-phase Brust-Schiffrin method¹, in which the tetrachloroaurate ion is phase transferred to an organic phase (e.g. toluene), and undergoes interfacial reduction using aqueous phase borohydride in the presence of thiol agents, the latter are believed to 'cap' the growing particle, see Fig.1. An electrochemical variant of this process was subsequently reported by Schiffrin and Cheng², where the tetrachloroaurate ion undergoes reduction with ferrocyanide under electrochemical control (polarisation of the liquid-liquid interface).

The mechanistic aspects of both of these reduction processes are somewhat ambiguous, which motivated us to revisit the latter (electrochemical) system, in combination with X-ray absorption spectroscopy of the Au ion on either side of the water/organic interface, to shed light on this reaction and

the wider class of two-phase routes to Au NPs. We note there is considerable interest at present in the hitherto unclear mechanism of the Brust-Schiffrin process^{3,4}. Two-phase deposition under electrochemical control is an interesting way to follow the interfacial nucleation/growth process, however there has been some debate⁵ about the reproducibility of such experiments. Our preliminary work suggested that this variability can be traced to the presence of metallic residues from previous experiments, presumably acting as sites for nucleation in subsequent experiments. Consistent results for the two-phase Au reduction process were seen when cells were thoroughly cleaned using Aqua regia and Piranha solution with caution. Importantly, the tetrachloroaurate ion (Au(III)) was found to transfer reversibly across the liquid-liquid interface in the absence of the reducing agent (Fig.2.), but on addition of ferrocyanide an homogeneous reduction of the ion to Au(I) took place.

XANES was used to show that the tetrachloroaurate ion retained its structure in both phases (in the absence of ferrocyanide, see Fig. 3). Significantly, in the presence of ferrocyanide, reduction to form metallic gold was not seen. Metallic gold formation, which had been described in the earlier report by Schiffrin and Cheng², occurred only in the presence of (added) metallic nuclei, see Fig. 4. This indicates that there is a high

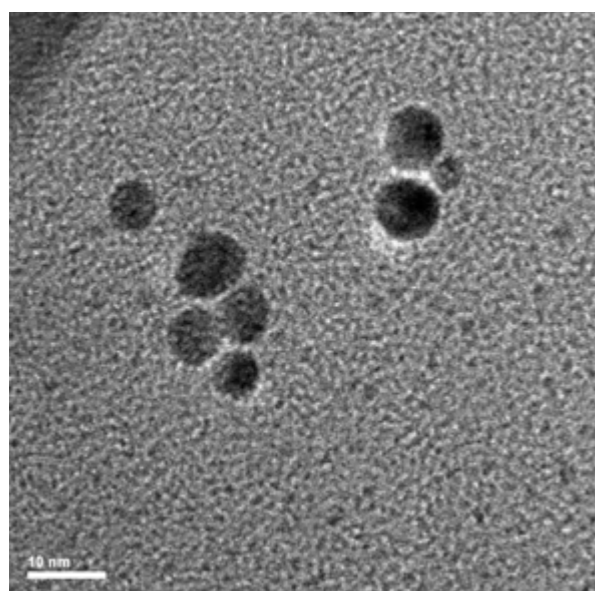


Figure 1: Transmission electron micrograph showing tetraoctylammonium capped Au nanoparticles formed in 1,2-dichloroethane via the reduction of Au(III) using aqueous phase sodium borohydride. XANES spectrum of the tetrachloroaurate ion in 1,2-dichloroethane.

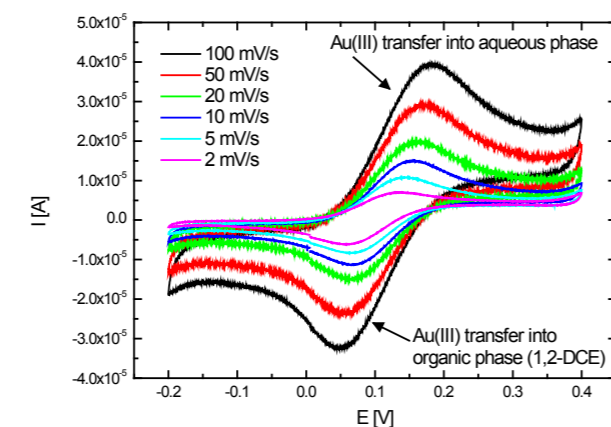


Figure 2: Reversible transfer of the tetrachloroaurate ion across the water/1,2-dichloroethane interface.

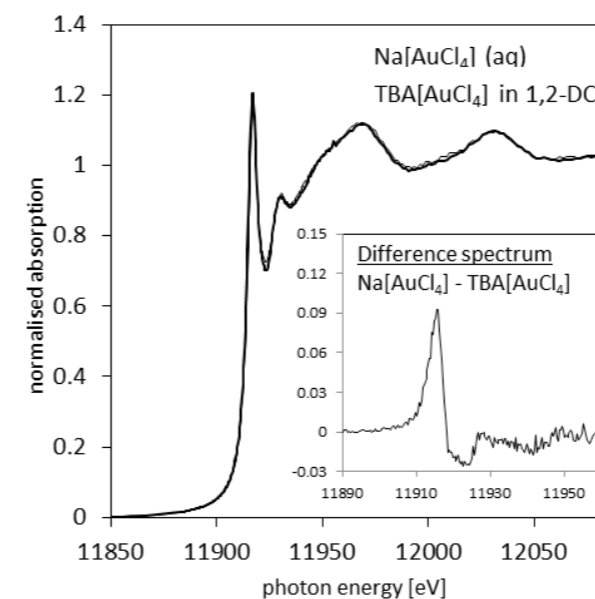
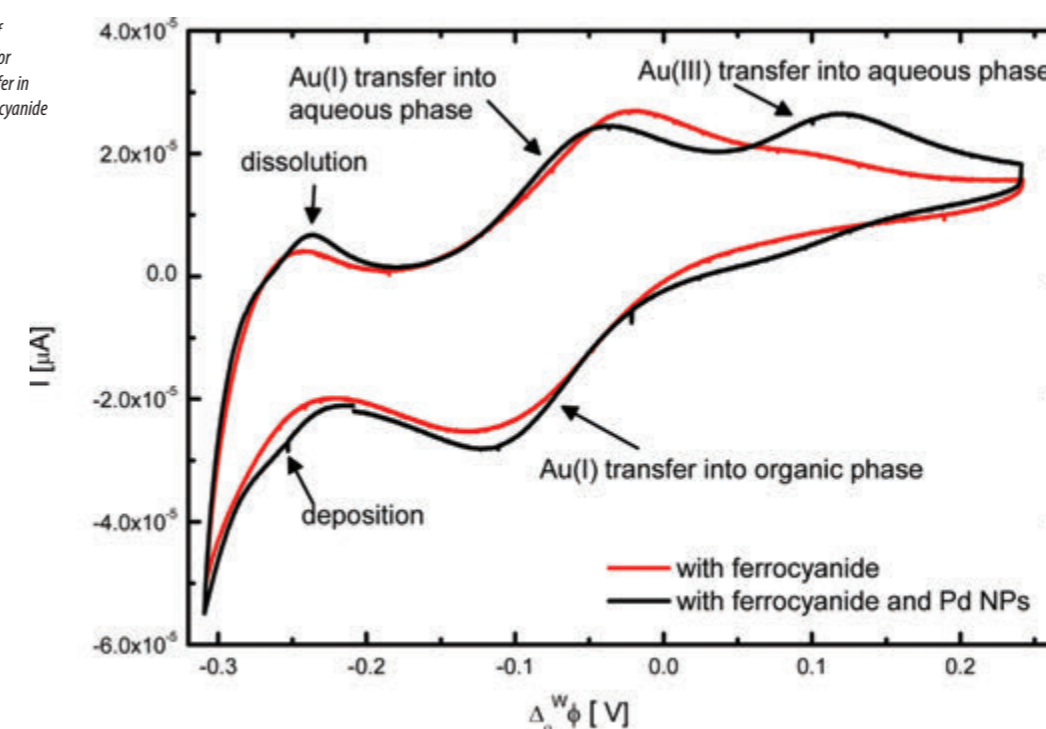


Figure 3: XANES spectrum of the tetrachloroaurate ion in 1,2-dichloroethane.

activation barrier to particle formation at the liquid-liquid interface, which could be attributed to the energetics of phase formation.

We aim to improve the time and spatial resolution of these processes to obtain more information on the intermediates involved in the deposition process. We also seek to modify our chemical system to probe a reaction closer to the spontaneous chemical processes used to form Au NPs using, via the Brust-Schiffrin approach.

Figure 4: Modification of the cyclic voltammetry for tetrachloroaurate transfer in the presence of the ferrocyanide and Pd NPs.



References

1. Brust, M., Walker, M., Bethell, D., Schiffrin, D. J. & Whyman, R. Synthesis of thiol-derivatized gold nanoparticles in a two-phase liquid-liquid system. *J. Chem. Soc., Chem. Commun.* **7**, 801-802 (1994).
2. Cheng Y.F. & Schiffrin, D.J. Electrodeposition of metallic gold clusters at the water/1,2-dichloroethane interface. *J. Chem. Soc. Farad. Trans.* **92**, 3865-3871 (1996).
3. Goulet, P.J.G. & Lennox, R.B. New insights into Brust-Schiffrin metal nanoparticle synthesis. *J. Amer. Chem. Soc.* **132**, 9582-9584 (2010)
4. Li, Y., Zaluzhna, O., Xu, B., Gao, Y., Modest, J.M. & Tong, Y.J. Mechanistic insights into the Brust-Schiffrin two-phase synthesis of organochalcogenate-protected metal nanoparticles. *J. Amer. Chem. Soc.* **133**, 2092-2095 (2011).
5. Trojaneck, A., Langmaier, A. & Samec, Z. Random nucleation and growth of Pt nanoparticles at the polarised interface between two immiscible electrolyte solutions. *J. Electroanal. Chem.* **599**, 160-166 (2007).

Funding Acknowledgements

Work supported by EPSRC via grant reference EP/H047786/1 (EPSRC/NSF 'Materials World' collaborative programme).

DOI 10.1039/C1CP21536A

High field magnetic resonance microscopy of the human hippocampus in Alzheimer's disease: Quantitative imaging and correlation with iron

Antharam, V., Collingwood, J.F., Bullivant, J.P., Davidson, M., Chandra, S., Mikhaylova, A., Finnegan, M., Batich, C., Forder, J. & Dobson, J. High field magnetic resonance microscopy of the human hippocampus in Alzheimer's disease: Quantitative imaging and correlation with iron. *Neuroimage*. **59**, 1249-1260 (2011)

The accumulation of iron compounds in the brain has been known to be associated with Alzheimer's disease (AD) since the early 1950's. Only recently, however, have we begun to develop and refine techniques that enable us to map and characterise these iron compounds. By mapping the distribution of these iron compounds in AD tissue and by characterising their chemical nature - which significantly impacts their magnetic properties - we hope to build a better understanding of iron's potential role in AD pathology as well as exploit the effects of magnetic iron compounds on Magnetic Resonance image signal parameters. At beamline I18 we have used X-ray fluorescence (XRF) techniques to examine human brain tissue and characterise the nature and spatial distribution of anomalous iron compounds associated with Alzheimer's disease. By analysing adjacent tissue sections with XRF and magnetic resonance imaging (MRI), we have been able to identify specific iron compounds in a region of the brain, the hippocampus, that is critical to AD pathology. We have correlated, for the first time, brain iron distribution in hippocampal sub-regions with quantifiable effects of MRI signal intensity and identified image parameters that enable us to distinguish between AD and control tissue samples. The goal of this work is to use iron as a biomarker to develop a new, MRI-based diagnostic technique for this disease.

The association between iron and Alzheimer's disease was first reported nearly 60 years ago¹; however, until recently, very little was known about the form of iron, its distribution and whether it plays a role in the disease or is simply a by-product, perhaps a potential biomarker. While the last question has proven more difficult to unravel, we have been able to shed some light on the form and distribution of iron in the affected brain using synchrotron X-ray techniques. Regardless of the role it plays in the disease, as iron compounds are generally strongly magnetic, understanding the form and spatial distribution has implications for the development of MRI-based diagnostic techniques due to iron's effect on proton spin relaxation rates in nearby tissue.

Our initial studies of brain iron using microfocus X-ray fluorescence (μ XRF) mapping and X-ray absorption near-edge spectroscopy (μ XANES) started in 1999. We developed techniques for tissue handling and processing that enabled us to examine human brain tissue and produce the first maps of iron in regions of the AD brain, complete with characterisation of the iron compounds detected² (Fig. 1). The objective of this work was to map and characterise iron compounds in tissue sections in order to better understand the potential role of iron in neurodegenerative diseases but also to determine the appropriateness of iron as a biomarker that could be used in Alzheimer's diagnosis.

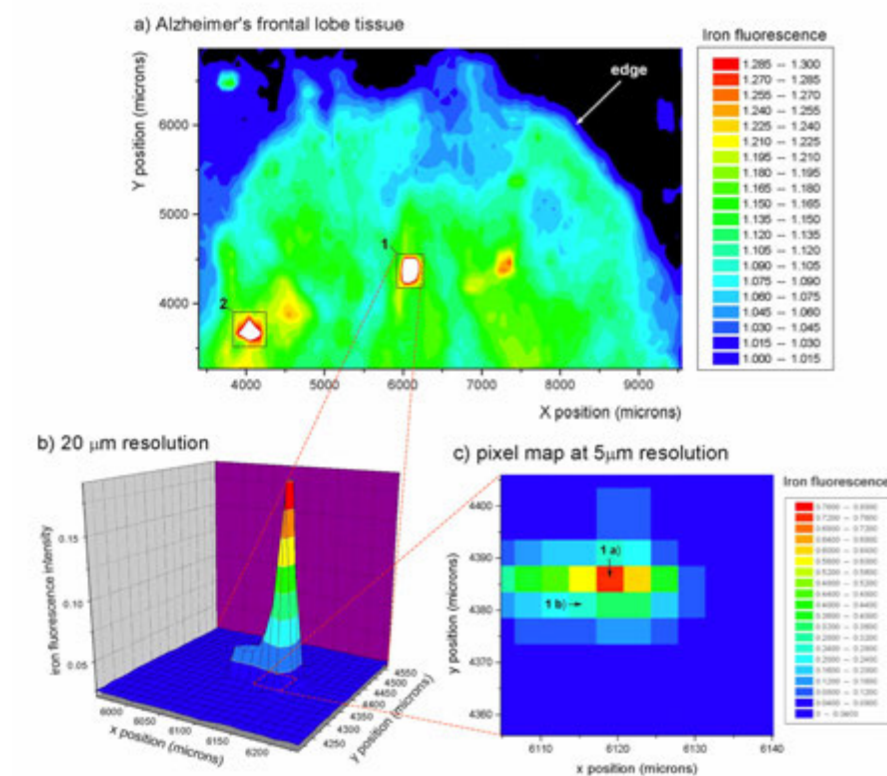


Figure 1: The process of locating anomalous iron concentrations by mapping iron fluorescence intensity over the tissue section, and then microfocusing in regions of interest, is illustrated. a) Initial low-resolution ($\sim 100 \mu\text{m}$) contour map of the tissue section. b) Medium-resolution scan of area 1, revealing that the source of the bright spot in a) is located within a $20 \mu\text{m}$ pixel. c) High-resolution scan within b), locating the source of the high intensity spot to a $5 \mu\text{m}$ pixel. XANES scans of the absorption edge are performed at area 1a), at a point slightly offset from the highest intensity, area 1b), and at the highest intensity $5 \mu\text{m}$ pixel in area 2 which is located in an identical fashion. (From Ref. 2).

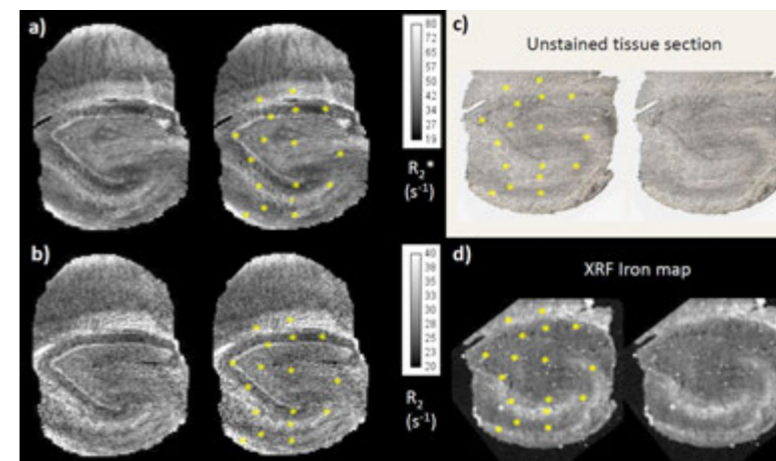


Figure 2: Guide to the segmentation process adopted for the cross sections through the blocks of hippocampal tissue. a) Where image resolution permitted, regions of interest were selected from within the boundaries shown for the following subfields: Cornu Ammonis regions (CA1-CA3); Cornu Ammonis region 4 and dentate gyrus (CA4-DG); alveus (ALV); polymorphic layer (PL); stratum granulosum (SG); stratum moleculare (SM); stratum pyramidale (SP); stratum radiatum (SR); subiculum (sub, not evident in this particular slice). Some layers could not be segmented reliably at this resolution (e.g. stratum lacunosum), the position of the divisions between CA1, CA2, and CA3 cannot be determined in these MRI sections, and the stratum moleculare for the CA and DG was also treated as one region. For histogram and R_2 analysis, the primary subfields CA1-CA3 and CA4-DG were selected as shown in b). (From Ref. 6).

There is a critical need for an early diagnostic tool for the disease. At present, Alzheimer's can only be definitively diagnosed after death. As most new pharmaceutical therapies being evaluated for treatment of AD are aimed at slowing the disease's progression - or at best, halting it - it is important to be able to determine when a patient's symptoms are due to AD and when they are the result of another form of neurological disorder. This is also very important when choosing patient cohorts for clinical trials. It is difficult to evaluate a drug's effect on a patient population if a considerable number of participants are found at some later stage not to have the disease the trial drug is trying to treat.

Iron compounds have the potential to act as a natural contrast agent in MRI, as they affect quantifiable parameters including the proton transverse relaxation rate (R_2) and the susceptibility-related parameter R_2^* . Characterising the iron compounds - particularly iron oxides - present in AD tissue is important as some, such as magnetite (Fe_3O_4) are about 100 times more 'magnetic' than the normal form of stored iron in the body, ferrihydrite ($5\text{Fe}_2\text{O}_3 \cdot 9\text{H}_2\text{O}$). The outstanding sensitivity and specificity of synchrotron μ XRF is used to obtain maps of iron distribution in brain tissue sections. μ XANES traces are then obtained from localised iron concentrations revealed in the maps, and by performing linear combination fits with standards, we are able to identify the various iron compounds present and their distribution in relation to tissue structure, pathological inclusions, and brain region. This information permits direct investigation of the influence of iron on MRI at the microscopic scale, to establish the source of iron-related contrast in healthy and diseased brain tissue.

The relationship between iron distribution in AD and MRI contrast is not a straightforward one. Current clinical studies of brain iron as a potential biomarker of neurodegeneration rely on assumptions that signal changes in MRI are due to iron, where interpretation of data is often based on post-mortem measures of iron in tissues^{3,4}. As Alzheimer's is simultaneously associated with increased iron deposition (via disrupted iron homeostasis) and tissue atrophy (the loss of tissue replaced by water) these two phenomena have competing and opposite effects on MR signal intensity⁵. In addition, our studies have shown that the distribution of iron compounds is highly inhomogeneous. These factors have contributed to the difficulty of developing efficient MRI algorithms that are able to track iron in AD.

In our recent study at beamline I18 we mapped the iron distribution in tissue sections cut from blocks in which the R_2 and R_2^* parameters had already been measured using magnetic resonance microscopy with a similar in-plane spatial resolution of $60 \mu\text{m}$. The region investigated was the hippocampus, a critical region for AD pathology. The hippocampus contains distinct subfields which are differently affected in AD, and contain different baseline concentrations of iron as revealed in the synchrotron μ XRF maps. Analysis of the individual sections provided direct evidence of the predicted positive correlation between iron and the R_2 and R_2^* parameters, and

statistically significant differences in iron concentration were observed as a function of hippocampus sub-field⁶ (Fig. 2). While significant differences in iron concentration were not observed between AD and controls in the small number of cases studied here, we did observe that the variance in the susceptibility-related MRI parameter, R_2^* , is significantly different between affected and control groups ($p < 0.001$). This difference was clearly revealed in histogram plots of the signal, and may provide a useful measure of altered iron distribution within the tissue, allowing differences in tissue iron between AD and healthy brains to be observed even though the absolute concentration may not vary significantly in the hippocampus. The application of μ XRF to enable direct quantification of the relationship between iron distribution and MRI contrast has confirmed the link between iron and specific MRI parameters at high spatial resolution, and provided a potential starting point in our search for an iron-based, clinically relevant Alzheimer's disease biomarker.

References

1. Goodman, L. Alzheimer's disease: A clinic-pathologic analysis of 23 cases with a theory on pathogenesis. *J. Nervous System & Mental Disease* **118**, 97-130 (1953).
2. Collingwood, J.F., Mikhaylova, A., Davidson, M., Batich, C., Streit, W.J., Terry, J. & Dobson, J. In situ characterization and mapping of iron compounds in Alzheimer's disease tissue. *J. Alz. Dis.* **7**, 267-272 (2005).
3. Bartzokis, G., Sultzer, D., Cummings, J., Holt, L.E., Hance, D.B., Henderson, V.W., Minz, J. In vivo evaluation of brain iron in Alzheimer's disease using magnetic resonance imaging. *Arch. Gen. Psychiatry* **57**, 47-53 (2010).
4. Sesack, S.R. & Grace, A.A. Cortico-basal ganglia reward network: microcircuitry. *Neuropsychopharmacology* **35**, 27-47 (2010).
5. House, M.J., St. Pierre, T.G., Foster, J.K., Martins, R.N. & Clarnette, R. Quantitative MR imaging R-2 relaxometry in elderly participants reporting memory loss. *Amer. J. Neuroradiol.* **27**, 430-439 (2006).
6. Antharam, V., Collingwood, J.F., Bullivant, J.P., Davidson, M., Chandra, S., Mikhaylova, A., Finnegan, M., Batich, C., Forder, J. & Dobson, J. Relaxation properties of human hippocampus in Alzheimer's Disease using high field MRI microscopy. *Neuroimage*. **59**, 1249-1260 (2012).

Funding Acknowledgements

This work is supported by NIH grants 1R21NS060304-01 and 1UL1RR029890, a grant from the US National High Magnetic Field Laboratory's Advanced Magnetic Resonance Imaging and Spectroscopy Center, the EPSRC (LSI Postdoctoral Fellowship EP/D066654/1), and RCUK (Fellowship).

DOI 10.1016/j.neuroimage.2011.08.019

Insights in the Mechanism of Selective Olefin Oligomerisation Catalysis using Stopped-Flow Techniques: a Mo K edge (Q) EXAFS Study

Bartlett, S. A., Wells, P. P., Nachtegaal, M., Dent, A. J., Cibir, G., Reid, G., Evans, J., Tromp, M. Insights in the Mechanism of Selective Olefin Oligomerisation Catalysis using Stopped-Flow Freeze-Quench Techniques: a Mo K edge QEXAFS Study. *J. Catal.* **284**, 247-258(2011)

Polyethylene (PE) is the most widely used plastic, with its primary use in packaging. The polymer is classified into several different categories based mostly on its density and branching, properties which govern its mechanical properties. Linear low density PE (LLDPE) is an overall linear polymer, with significant numbers of short branches, and therefore has a narrower molecular weight distribution and different melt flow properties from other PEs. It is less shear-sensitive and has a low viscosity at all strain rates. In contrast to other PEs, very thin LLDPE films can therefore be produced easily, while maintaining high strength and toughness, making it perfect for applications in flexible tubing as well as plastic bags, sheets, films and membranes. The selective trimerisation and tetramerisation of ethene to produce the linear alpha-olefins (LAOs) 1-hexene and 1-octene respectively are of major significance due to the importance of these co-monomers in the production of (LLDPE), which accounts for around 50% of the LAO co-monomers produced industrially.¹ A variety of transition metal catalysts, most of which are based on early transition metals, can facilitate this type of selective oligomerisation. By using a Cr(III) pre-catalyst with ethene in the presence of methylaluminoxane (MAO) as co-catalyst, an extremely high selectivity can be obtained.¹ This process is thought to occur by the formation of a metallocyclic intermediate, originating from the Cr(III) pre-catalyst. In the research presented here, we have devised methods to probe Molybdenum analogues of catalytic systems *in situ*, to obtain insights in the structural and electronic changes of the catalysts and thereby the reaction mechanism.

A variety of transition metal catalysts facilitate the selective trimerisation of ethene, most importantly chromium, which forms the basis of several key industrial catalysts, including the Phillips pyrrolide system, the Sasol mixed heteroatom systems and the BP diphosphine systems. The extremely high selectivity for 1-hexene is thought to occur via a mechanism based upon a metallocyclic intermediate formed through reaction of Cr(III) pre-catalysts with ethene in the presence of methylaluminoxane co-catalyst. The pursuit of higher performance catalysts requires a detailed understanding of the individual stages of the catalytic cycle, the dependence upon metal, promoter and/or co-catalyst. However, developing such catalyst systems is hindered by characterisation difficulties due to the paramagnetism of the majority of the Cr complexes.

Stopped flow systems have recently been developed to probe homogeneous catalysis *in situ* and time-resolved (down to milliseconds) using X-ray Absorption Spectroscopy (XAS) (in energy dispersive or quick EXAFS mode).² However, while the method has been proven for homogeneous Ni and Cu systems, the Cr K-edge is at a lower energy at which solvent, reactant and even a few cm of air are highly absorbing and severely hamper the transmission experiment.

We have pursued two methods to allow characterisation of these catalytic systems: (i) substituting Mo(III) for the Cr(III) to allow the use of time-resolved XAS to model the early stages of the activation, and (ii) modification of the stopped flow system in order to maintain the time resolution advantages, but trap the intermediates to allow for long XAS data acquisition for low X-ray energy systems.

We have prepared the analogous Mo(III) trichloro complexes, $[\text{MoCl}_3(\text{L})]$ (here data on $\text{L} = \text{SNS} = \text{RS}(\text{CH}_2)_2\text{NH}(\text{CH}_2)_2\text{SR}$ and $\text{SBz} = \text{S}(\text{CH}_2\text{CH}_2\text{SCH}_2\text{-C}_6\text{H}_4\text{-p-C}(\text{CH}_3)_3)_2$ are presented) and investigated their utility as stoichiometric model systems for the Cr catalysts by determining their reactivities with AlMe_3 . Although the complexes show little catalytic activity towards ethene oligomerisation, it is reasonable that the Mo systems undergo similar chemistry in the initial stages of activation, whereby the slower kinetics at Mo will aid identification of individual species in

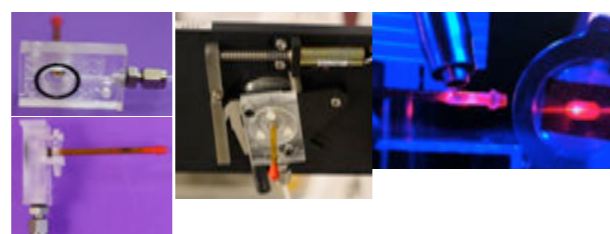


Figure 1: Stopped-flow Freeze-Quench accessory: A Perspex box is constructed to be mounted to the standard spray outlet of the stopped-flow quench accessory and to hold the Kapton® tube. A gas inlet and outlet provide an argon gas atmosphere from the spray exit to the tube inlet. The right picture shows the Kapton® tube, containing frozen Mo intermediate, positioned in the X-ray beam using a red laser whilst in the cryostream.

the reaction. The Mo(III) tribromide analogues were prepared to allow distinction between first shell ligand (S) and halide in EXAFS.

The set-up as developed here is based on a commercially available stopped-flow system (SFM400/QS, Biologic, France) with a proven performance for combined EDE/UV-Vis experimentation. Due to the air and moisture sensitive nature of the chemistry, the entire stopped flow is connected to a Schlenk line under an argon atmosphere. We have developed a freeze-quench XAS measurement cell to be attached to the stopped flow, Fig. 1. A Kapton® capillary is mounted into a custom holder attached to the Biologic freeze-quench accessory and allows direct injection into the Kapton® tube, while an argon gas flow prevents ingress of air (or moisture) into the sample. The tube is sealed at one end with a plug, and immersed into liquid nitrogen (before and during injection), directly freezing the mixture at 77 K. The injection and freezing time was estimated <1 second. Different delays in the stopped flow allow the accurate timing of reaction intermediates. The tube with frozen sample is subsequently placed into a holder in the X-ray beam, with simultaneous cooling using a Cryostream (100 K).

Time-resolved QEXAFS/UV-Vis reactions were performed using the stopped-flow instrument. No changes in the time-resolved UV/Vis spectra

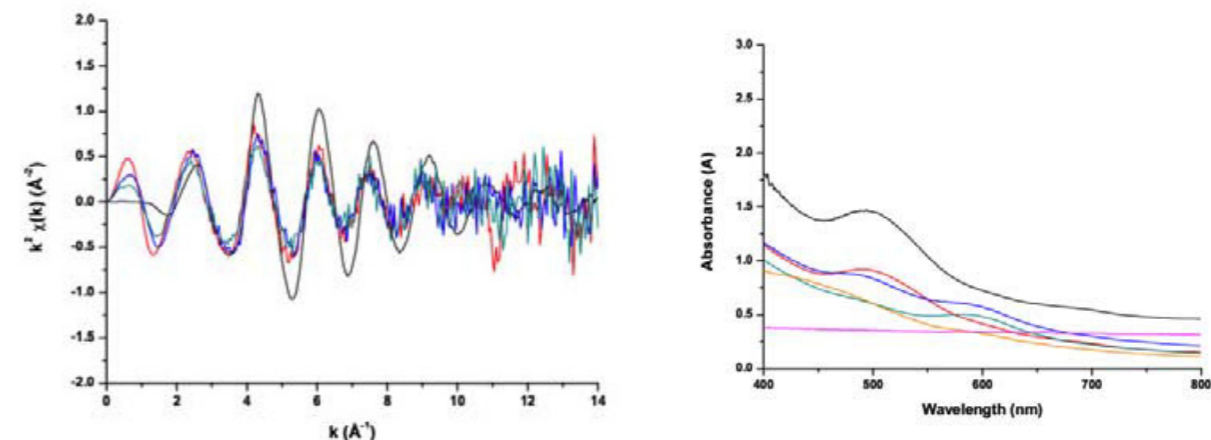


Figure 2: Combined time resolved UV-Vis and QEXAFS data on the reaction of $[\text{MoCl}_3(\text{SNS})]$ (25 mM in toluene) with 20 equivalents of AlMe_3 at $t = 0$ (black), $t = 1$ min (red), $t = 2.5$ min (blue), $t = 7$ min (green), $t = 18$ min (orange), $t = 19$ min (pink).

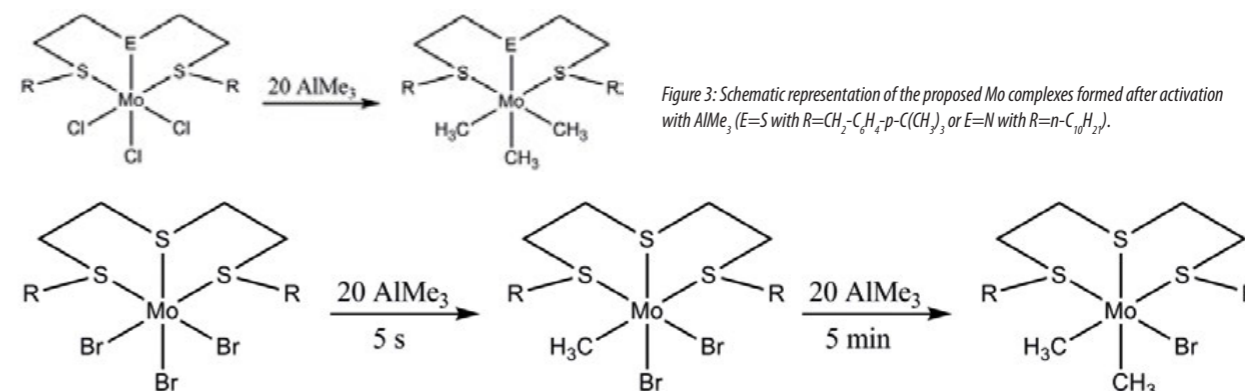


Figure 3: Schematic representation of the proposed Mo complexes formed after activation with AlMe_3 ($\text{E}=\text{S}$ with $\text{R}=\text{CH}_2\text{-C}_6\text{H}_4\text{-p-C}(\text{CH}_3)_3$ or $\text{E}=\text{N}$ with $\text{R}=\text{n-C}_{10}\text{H}_7$).

were observed upon performing the reactions in the X-ray beam, suggesting we are genuinely observing the chemical reaction taking place. The combined time-resolved data (20 seconds data acquisition time per spectrum) from the reaction of $[\text{MoCl}_3(\text{SNS})]$ (25 mM in toluene) with 20 equivalents of AlMe_3 are displayed in Fig. 2.

The EXAFS clearly shows an overall loss in intensity, indicating loss of chloride, which is confirmed by analysis in which chlorine is replaced by carbon, i.e. methyl groups, while the SNS-ligand remains intact (Fig. 3). After 18 minutes of reaction in the stopped-flow, the Mo K-edge XAS signal, as well as the UV/Vis signal, are lost completely, indicating the precipitation of Mo (not X-ray beam induced).

To validate the freeze-quench approach we have investigated the reaction of $[\text{MoBr}_3(\text{SBz})]$ with 20 equivalents of AlMe_3 . The reaction was freeze-quenched after 5 seconds and 5 minutes of reaction. EXAFS analyses show the partial removal of Br, without dissociation of the SBz ligand (Fig. 3). In addition, the freeze-quench set-up now gives access to good quality EXAFS data 5 seconds after mixing, something which could not be obtained using QEXAFS as performed (QEXAFS time-resolution at our beamtimes: 20-30 s/spectrum, or 1-3 minutes/spectrum).

The results demonstrate that treatment of the Mo complex solution with excess AlMe_3 leads to halide loss, forming $[\text{Mo}(\text{CH}_3)_2(\text{L})]$, and provides strong evidence that dinuclear species with direct Mo-Mo bonds or halide-bridged dimers³ are not present under the conditions examined (1:20 Mo:Al). At the high AlMe_3 ratios used, with the complexes investigated, the activation reaction is in competition with the deactivation reaction, especially for the trichloride complexes, providing insights in the low overall catalytic activity and deactivation as has been reported for these systems under real catalytic conditions.⁴ The new freeze-quench attachment allows reactive, short-lived intermediate species to be trapped (in <1s), and enables EXAFS data collections to be conducted on these over long time-scales and in fluorescence mode, which is essential for studying systems with low energy absorption edges (e.g. Cr, Sc etc). In fact, the methodology increases the XAS

time resolution for these systems with a factor of 4 000 to 10 000 (1 second compared to 1-4 hours as before). Not only reactions can be quenched and measured, also in case of samples easily affected by beam damage, beam damage can be prevented or decreased by keeping the samples at low temperature.

References

- McGuinness D.S. Olefin oligomerization via metallacycles: dimerization, trimerization, tetramerization, and beyond. *Chemical Reviews* **111**, 2321-2341 (2011) and references therein.
- Tromp M., van Strijdonck G.P.F., van Berkel S.S., van den Hoogenband A., Feiters M.C., de Bruin B., Fiddy S.G., van der Eerden A.M.J., van Bokhoven J.A., van Leeuwen P.W.N.M. & Koningsberger D.C. Multitechnique approach to reveal the mechanism of copper(II)-catalyzed arylation reactions. *Organometallics* **29**, 3085-3097 (2010).
- Liu S., Pattacini R. & Braunstein P. Reactions between an ethylene oligomerization chromium(III) precatalyst and aluminum-based activators: alkyl and cationic complexes with a tridentate NPN ligand *Organometallics* **30**, 3549-3558 (2011).
- Downing S.P., M. J. Hanton M.J., Slawin A.M.Z. & Tooze R.P. Bis(alkylthioethyl)amine complexes of molybdenum *Organometallics* **28**, 2417-2422 (2009).

Funding Acknowledgements

EU funding under EU project FP7 ELISA. MT gratefully acknowledges the EPSRC (EP/E060404/1), SAB and PPW acknowledge the EPSRC (EP/F032463/1).

Research carried out at Diamond Light Source on beamline B18, at the ESRF on beamline BM26A and at the SLS on beamline SuperXAS.

DOI 10.1016/j.jcat.2011.10.015

An XRF-XANES characterization of deep ice core dust

Marcelli, A., Hampai, D., Giannone, F., Sala, M., Maggi, V., Marino, F., Pignotti S. and Cibin, G. XRF-XANES characterization of deep ice core insoluble dust. *J. Anal. At. Spectrom.* **27**, 33-37(2012).

Ice formed in old glaciers is among the most important sources of paleo-proxy data. Ice cores contain information on ancient variations of Earth's climate, some reaching back almost a million years. The knowledge of the mineralogy of the airborne dust in particular, allows the reconstruction of the aerosol trajectories and consequently the patterns of transport in the last climatic cycles. In this research, we have used TXRF and XANES to analyse the composition of the insoluble fraction extracted from deep ice cores from Antarctica, on samples dating across the last glacial transition, and compared these with samples from a glacier in the Italian Alps. We were able to detect and follow the variations in the composition patterns with time. The results show that such synchrotron radiation-based combined analysis complements XRD and traditional aerosol analysis techniques. They give clear element-specific insights into the local structure of specific fractions of the analyte, adding invaluable information on the dust composition and aerosol transport mechanisms that can lead to the recognition of the dust source areas.

Climate changes, natural or anthropogenic, may have a large impact on the Earth in the next decades. As a consequence, paleoclimatology is a new emerging research area. While meteorological instruments may show trends

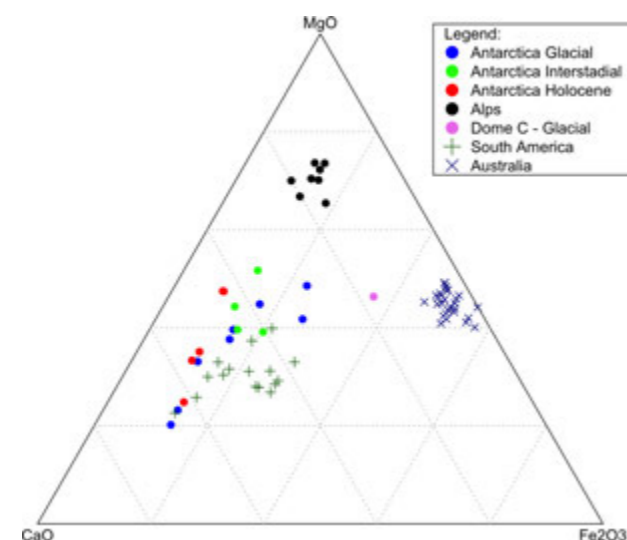


Figure 1: Chemical Index of Alteration ternary diagram of Antarctic and Alpine dust compared to reference rock compositions from possible source areas.

over the past century, paleo-proxy data provide information on climatic variability regarding thousands and even millions of years. However, proxy records are not direct measurements and information has to be extracted and calibrated to have reliable estimates.

A vertical timeline of the past climate is stored in ice sheets and mountain glaciers, as in marine sediments and other proxies. Deep ice cores cover relatively short periods, but with a high temporal resolution. As an example, the longest chronological record from ice cores comes from the EPICA perforation in Antarctica, and covers the last 820,000 years, providing information about the temperature, precipitation levels, the atmospheric composition and volcanic activity. Aeolian mineral dust archived in polar and mid-latitude ice cores represents a particularly precious proxy for assessing environmental and atmospheric circulation variability, with special emphasis on the regional-to-global climate changes at different time scales. Results

from drilling sites around the world help distinguish the local climate (i.e. the Alps, Andes, and Himalayas) from global climate trends (i.e. in Antarctica and Greenland).

One of the major challenges of this research is the extremely small amount (in the μg range) of the available ice core insoluble fraction, containing small crystallites, poorly crystalline and often including glass and tephra

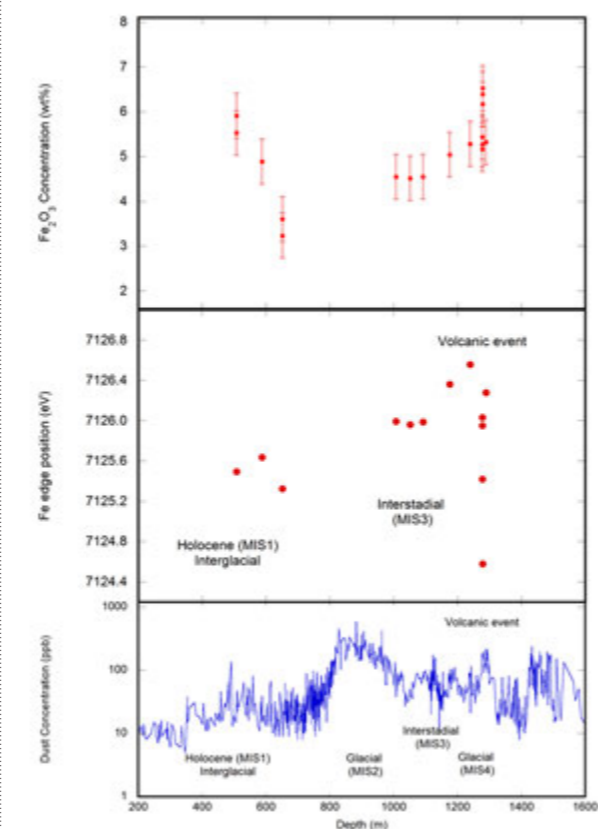


Figure 2: Dust concentration (ppb) of the TALOS Dome ice core (bottom, previous experiment), XANES absorption edge position (middle) and Fe_2O_3 concentration (top) vs. depth (i.e. vs. time). Our data cover the last warm period (Interglacial, MIS1) and the last interstadial period, just before the last glaciation. While the Fe_2O_3 concentration is relatively insensitive to the temperature (there is a clear descending trend towards the glacial period), the Fe K edge position moves up with lower temperatures and quickly descend to a sharp minimum in correspondence of a strong volcanic event (on the right side).

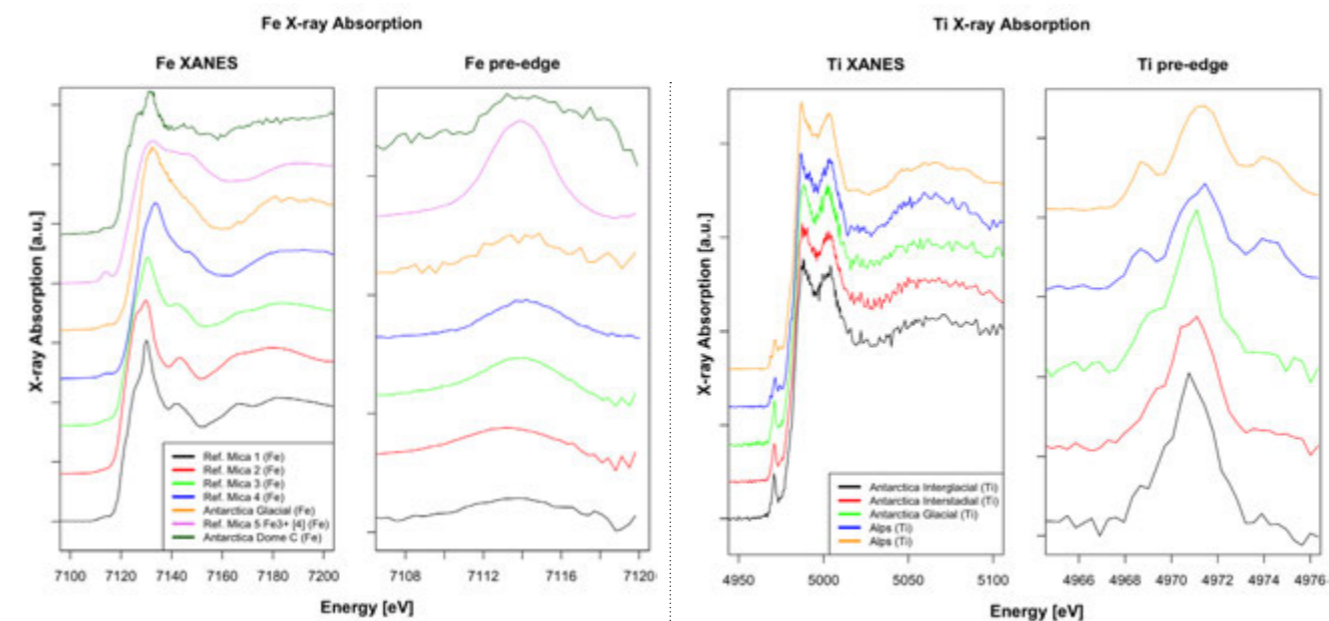


Figure 3: Comparison among Fe K-edge XANES spectra of a sample belonging to a glacial period (corresponding to a volcanic event), reference phyllosilicate samples (i.e. micas having Fe in different local environments) and a sample from a recent period (top).

Figure 4: Comparison of Ti K-edge XANES (left, pre-edge) spectra among samples belonging to the different glacial periods collected in Antarctica and in an Alps glacier.

contributions from volcanic events. In our case, the low amount of dust available required clean procedures to collect, prepare and store samples. In our experiments, after filtration, part of the insoluble fraction was deposited on thin membranes and the remaining aliquot was suspended in water evaporated on high purity Si wafer substrates.

We applied the spectroscopic techniques Total-Reflection X-Ray Fluorescence (TXRF) and XANES to the mineralogical analysis of such challenging samples. We combined elemental and spectroscopic information with data obtained by other techniques such as XRD, transmission electron microscopy and Particle Induced X-ray and Gamma-ray Emission, to achieve a clear element-specific insight into the local structure of specific fractions of the analyte.

Some of the experiments were performed at the Stanford Synchrotron Radiation Lightsource (SSRL) at beamline 10-2, using a dedicated TXRF set-up, while a custom clean sample chamber was used at the Core XAS beamline (B18) at Diamond. Silicon Drift Detectors were used allowing detection of low Z elements, down to Al. XAS spectra have been collected at the Fe and the Ti K edges.

Dust from Antarctic and Alpine samples is qualitatively composed of a mixture of silicates: clays, quartz, and feldspars, with minor contributions of pyroxenes, amphiboles, metal oxides, and volcanic glasses. XRF and XANES results are compared with rock and soil geochemical data, as possible dust source areas, from the available literature. In Fig. 1 we show a comparison between our samples with reference rocks and minerals from the possible dust source areas (Australia, South America). Alpine samples in particular are a close group separate from the other datasets.

Moreover, the distribution of the Antarctic samples lies closely in the region of the Patagonian samples. Fig. 2 shows the iron oxide concentration in mineral dust vs. time for samples collected in Talos Dome, Antarctica. It represents a partial time evolution of the iron oxide concentration in mineral dust from Holocene to the 4th Marine isotope stage (MIS4) period and its trend evidences the minimum typically observed in the interglacial periods. Characteristic Fe K edge XANES spectra of Antarctic samples shown in Fig. 3 indicate the presence of clay minerals in the dust. The spectra show that

iron is octahedrally coordinated, with variable oxidation state. The observed absorption edge shift (middle panel in Fig. 2) demonstrates that the amounts of Fe^{3+} changes with time (i.e. vs. depth). The highest Fe^{2+} concentration point demonstrates the occurrence of a volcanic event.

Combining XANES information from spectra at different edges improves the mineralogical characterisation of dust. As an example, significant differences among Antarctic and Alpine samples appear in the XANES (left) and in the pre-edge (right) regions at Ti K-edge (Fig. 4). So the composition differences highlighted in the ternary plot of Fig. 1 are also related to different concentrations of Ti-bearing minerals. Continental and oceanic materials are characterised by having different Fe/Ti ratios. In our case, comparing Fe and Ti allows identification of samples containing mineral fractions coming from the nearby Antarctic coast.

In conclusion, our research, although still limited in terms of samples analysed, has demonstrated that the combined use of synchrotron radiation-based techniques to obtain both elemental and species-selective information on the dust mineralogy, can be a valuable resource for the analysis of the aerosol transport mechanisms and of the climatic variability during the last climatic cycles.

Funding Acknowledgements

Research was carried out in the framework of Proposals 90U5 and 3082M at SSRL, a national user facility operated by Stanford University on behalf of the U.S. Department of Energy, Office of Basic Energy Sciences.

This work was partly supported by Museo Nazionale dell'Antartide, Ente Italiano della Montagna and Istituto Nazionale di Fisica Nucleare and carried out in the framework of the Project on Glaciology of the Programma Nazionale di Ricerche in Antartide -MIUR, financially supported through collaboration with ENEA Roma.

Research carried out at Diamond Light Source on beamline B18 and at the SSRL on beamline BL10-2.

DOI: 10.1039/c1ja10169b

Investigation of the lithium ion-battery cycling mechanism in a 3.90 V iron-based fluorosulphate cathode material

Barpanda, P., Ati, M., Melot, B. C., Rouse, G., Chotard, J.-N., Doublet, M.-L., Sougrati, M. T., Corr, S. A., Jumas, J.-C., & Tarascon, J.-M. A 3.90 V iron-based fluorosulphate material for lithium-ion batteries crystallizing in the triplite structure. *Nature Mater.* **10**, 772-779 (2011)

The diminishing supply of fossil fuels, together with a desire to reduce greenhouse gas emissions, has propelled electrochemical storage to the forefront of modern research. In particular, lithium ion batteries, which possess high power capabilities, have been identified for future use in hybrid electric vehicles, where high power densities become essential.¹ To understand the intimate relationship between structure, property, and function in materials for applications as positive insertion electrodes, we have employed a broad range of characterisation methods including local structure studies performed at the B18 Core EXAFS beamline at the Diamond Light Source. Of particular interest is the mechanism through which the insertion and deinsertion of lithium ions occurs. In the present study, we have investigated the triplite-phase of LiFeSO_4F which exhibits the highest $\text{Fe}^{2+}/\text{Fe}^{3+}$ redox voltage of any inorganic compound to date.

The search for new positive cathodes with enhanced electrochemical performance continues, with a focus on the role of the polyanion as a way to manipulate the position of the transition metal redox couple.² An example of this is the tavorite-phase of LiFeSO_4F , where the potential of the $\text{Fe}^{2+}/\text{Fe}^{3+}$ redox couple is 150 mV higher than that of LiFePO_4 due to the increased electronegativity of the SO_4 groups compared to PO_4 .³ Interestingly, the manganese-based homologue, LiMnSO_4F , does not adopt the tavorite structure but instead is found to crystallize in the triplite structure and shows no discernible electrochemical activity. The triplite structure is characterized by edge-sharing chains of MO_2 octahedra, which exhibit a significant degree of site-mixing between manganese and lithium and can be contrasted against the tavorite phase, which displays corner-sharing chains that are well-ordered (Fig. 1). These structural differences led us to postulate that substitution of iron into the structure may introduce some electrochemical activity and therefore we investigated a solid-solution series of $\text{Li}(\text{Fe}_{1-x}\text{Mn}_x)\text{SO}_4\text{F}$ in an attempt to establish a link between the atomic structure and the electrochemical performance. Central to our work has been the use of synchrotron facilities such as the Diamond Light Source, where we have employed *in-situ* local structure studies to probe changes that occur in materials while undergoing electrochemical cycling.

The solid solution $\text{Li}(\text{Fe}_{1-x}\text{Mn}_x)\text{SO}_4\text{F}$ was prepared by reacting stoichiometric amounts of a mixed-metal sulphate monohydrate precursor $(\text{Fe}_{1-x}\text{Mn}_x)\text{SO}_4 \cdot \text{H}_2\text{O}$ with LiF at 295 °C using a traditional solid state synthesis for 2 to 3 days.⁴ The triplite phase was found for samples with as little as 5 atomic per cent of manganese substituting for iron. These materials were characterised by a broad range of techniques, including synchrotron X-ray diffraction, Mössbauer spectroscopy, synchrotron X-ray absorption spectroscopy and electrochemical cycling.

We observe a linear increase in the unit cell volume of triplite with increasing substitution of manganese for iron, as should be expected given that the ionic radius of Mn^{2+} is larger than that of the Fe^{2+} . Mössbauer spectroscopy, which provides a direct probe of the local iron environment, revealed significant differences between the tavorite and triplite phases. The tavorite phase, which has two distinct crystallographic sites for iron, displays a corresponding two sharp sets of peaks. In contrast, the triplite phase gives non-resolved, broad peaks, indicating multiple iron environments and an increase in disorder in the triplite phase. This inherent disorder may be the reason for the absence of electrochemical activity in this phase; without a coherent pathway to follow, lithium ion diffusion would prove difficult in such a phase.

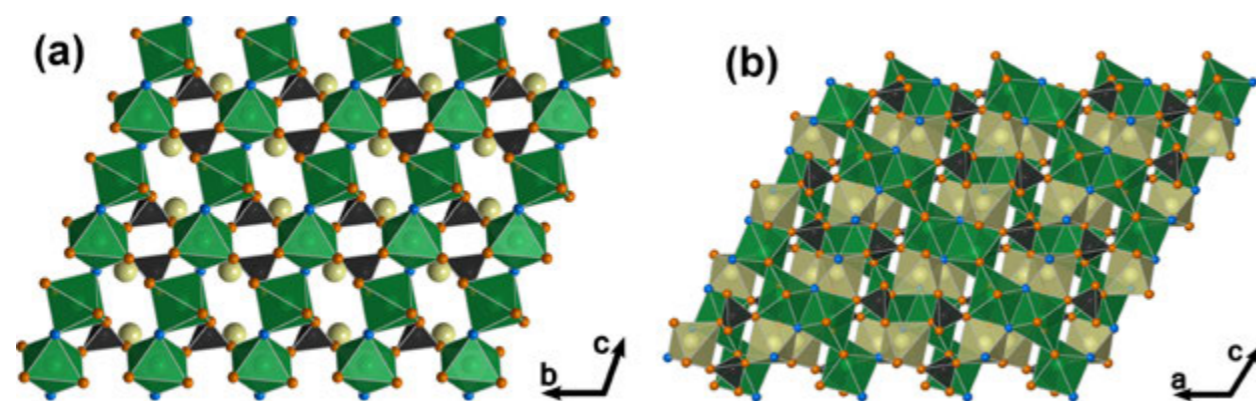


Figure 1: Crystal structure of (a) tavorite characterized by chains of corner-sharing octahedra and (b) triplite, which consists of chains of edge-sharing octahedra.

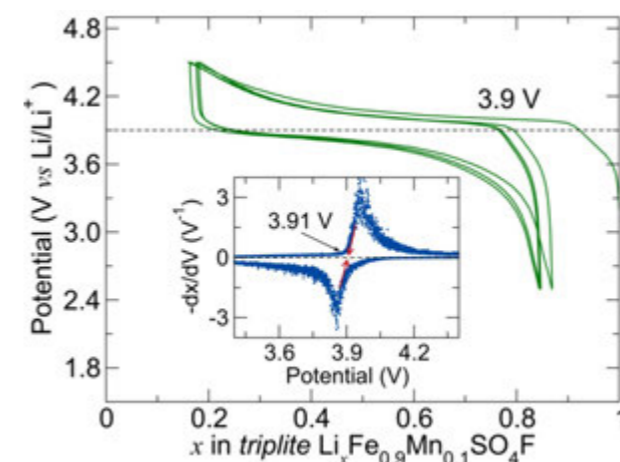


Figure 2: Voltage-composition curve for the triplite phase, $\text{Li}_x\text{Fe}_{0.9}\text{Mn}_{0.1}\text{SO}_4\text{F}$, showing a 3.9 V redox potential, the highest recorded for the $\text{Fe}^{2+}/\text{Fe}^{3+}$ couple to date for an inorganic compound.

Of particular note in this study has been the electrochemical performance of the triplite phase $\text{Li}(\text{Fe}_{0.9}\text{Mn}_{0.1})\text{SO}_4\text{F}$, which, at 3.90 V, displays the highest $\text{Fe}^{2+}/\text{Fe}^{3+}$ redox voltage reported to date for an inorganic compound (Fig. 2). Powder X-ray diffraction patterns and Mössbauer measurements were collected *in-situ* on a sample during electrochemical cycling to monitor

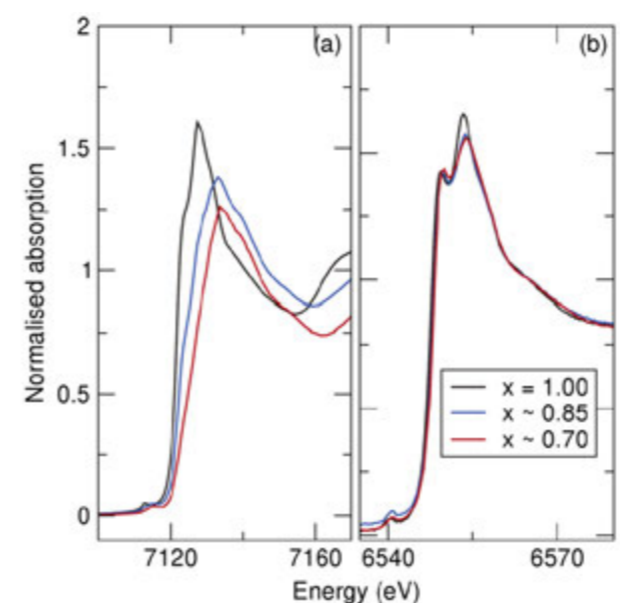


Figure 3: Normalised XANES spectra recorded at the (a) Fe K-edge and (b) Mn K-edge during electrochemical cycling using the triplite phase, $\text{Li}_{0.8}\text{Fe}_{0.2}\text{SO}_4\text{F}$ as positive cathode. Black lines show the first data collection, blue line for data collected after 15% Li removal and red line after 30% Li removal. These *in-situ* measurements show that the iron undergoes a change from Fe^{2+} to Fe^{3+} upon delithiation, while there is no discernible change in the oxidation state of manganese.

the changes occurring and both confirmed the reversibility of the lithium insertion/extraction process in the samples which contained iron. Also of interest has been the observation that the total volume change between the

lithiated and delithiated species is a mere 0.6%. This is in contrast to what is seen for the tavorite phase, where a volume change of 10.4% is observed. This is an important observation for commercial applications, where large volume changes on extended cycling give rise to mechanical stresses which can cause dewetting from current collectors and thereby result in device failures.⁵

Given the practical importance of this material and the unprecedentedly high redox potential, we wanted to study more closely the roles of iron and manganese during cycling. Vital to this exploration and in an effort to elucidate the lithium insertion in the triplite phase $\text{LiFe}_{0.8}\text{Mn}_{0.2}\text{SO}_4\text{F}$, we made use of the B18 Core EXAFS beamline to conduct *in-situ* studies to monitor the changes in the X-ray absorption spectra as lithium is inserted and deinserted from the triplite phase. X-Ray Absorption Spectroscopy (XAS) is an innovative method for following *in-situ* the changes occurring in materials upon cycling since, by collecting data on a particular edge of interest, oxidation state changes and changes in nearest neighbour environment of a particular element may be isolated and tracked during electrochemical cycling. Normalized XANES (X-ray absorption near structure) spectra recorded at the iron and manganese K-edges during lithium deinsertion in an operating battery cell revealed that the iron undergoes a change from Fe^{2+} to Fe^{3+} upon delithiation, while there is no discernible change in the oxidation state of manganese (Fig. 3). From these XANES measurements at the B18 beamline, it is clear that the role of the manganese ion is that of a spectator – complicit in the structural transformation to the triplite structure, but itself electrochemically inactive.

It is clear that these kinds of local structure studies shed light on reactions occurring in battery materials and could be useful in determining the mechanisms these compounds undergo during the intercalation process.

References

1. Tarascon, J.-M. & Armand, M. *Nature*, **414**, 359–367 (2001)
2. Padhi, A.K., Nanjundaswamy, K. S. & Goodenough, J. B. *J. Electrochem. Soc.* **145**, 1518–1520 (1998)
3. Recham, N., Chotard, J.-N., Dupont, L., Delacourt, C., Walker, W., Armand, M. & Tarascon, J.-M. *Nature Mater.* **9**, 68–74 (2010)
4. Barpanda, P., Recham, N., Chotard, J.-N., Djellab, K., Walker, W., Armand, M. & Tarascon, J.-M. *J. Mater. Chem.* **20**, 1659–1669 (2010)
5. Ati, M., Melot, B. C., Chotard, J.-N., Rouse, G., Reynaud, M. & Tarascon, J.-M. *Electrochem. Comm.* **13**, 1280 – 1283 (2011)

Funding Acknowledgements

The authors thank the ALISTORE-ERI for sponsoring this research.

Research carried out at Diamond Light Source on B18, at ESRF on BM10A (Swiss–Norwegian beamline) and at Argonne National Laboratory on 11-BM.

DOI 10.1038/nmat3093

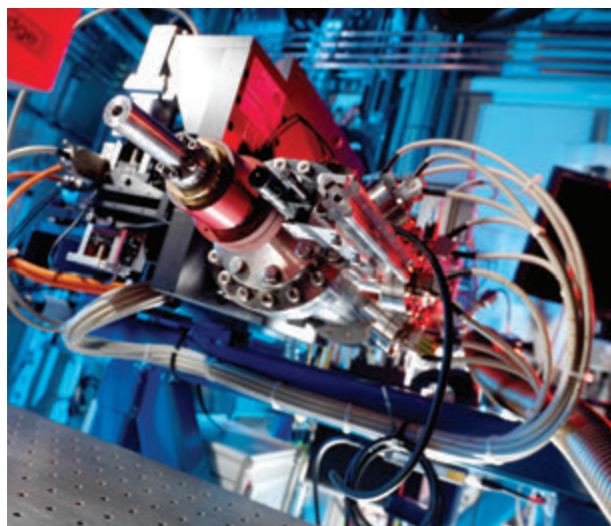
Soft Condensed Matter Village

Nick Terrill, Village Coordinator

The scientific output of the Soft Condensed Matter village covers a very diverse range of scientific communities; from cultural heritage and archaeology, through biology and chemistry to energy and engineering, and it is also reflected in the range of scientific papers that have been published this year and represented by the articles that appear in this section.

With its final name of MIRIAM (Multimode InfraRed Imaging And Microspectroscopy), the IR beamline B22 completed its optimisation period this year and now joins I22 and B23 in full user operations. Using the Infrared generated by the synchrotron, B22 offers two complete Fourier Transform interferometers (FTIR) coupled to IR microscopes as end stations enabling molecular analysis at microscopic scale. Meanwhile installation and commissioning for B21, HATSAXS (Highly Automated Throughput Small Angle X-ray Scattering) the second SAXS beamline for Diamond, is progressing well. The beamline team expects to take first light later in 2012 leading up to first user experiments in the first half of 2013.

Mid-IR 'fingerprint' analysis on the B22 MIRIAM beamline has been successfully utilised by more than 20 research groups from the UK and EU in a wide range of fields including mainly the life sciences and biomedical communities, some cultural heritage and archaeology as well as environmental research and materials science.



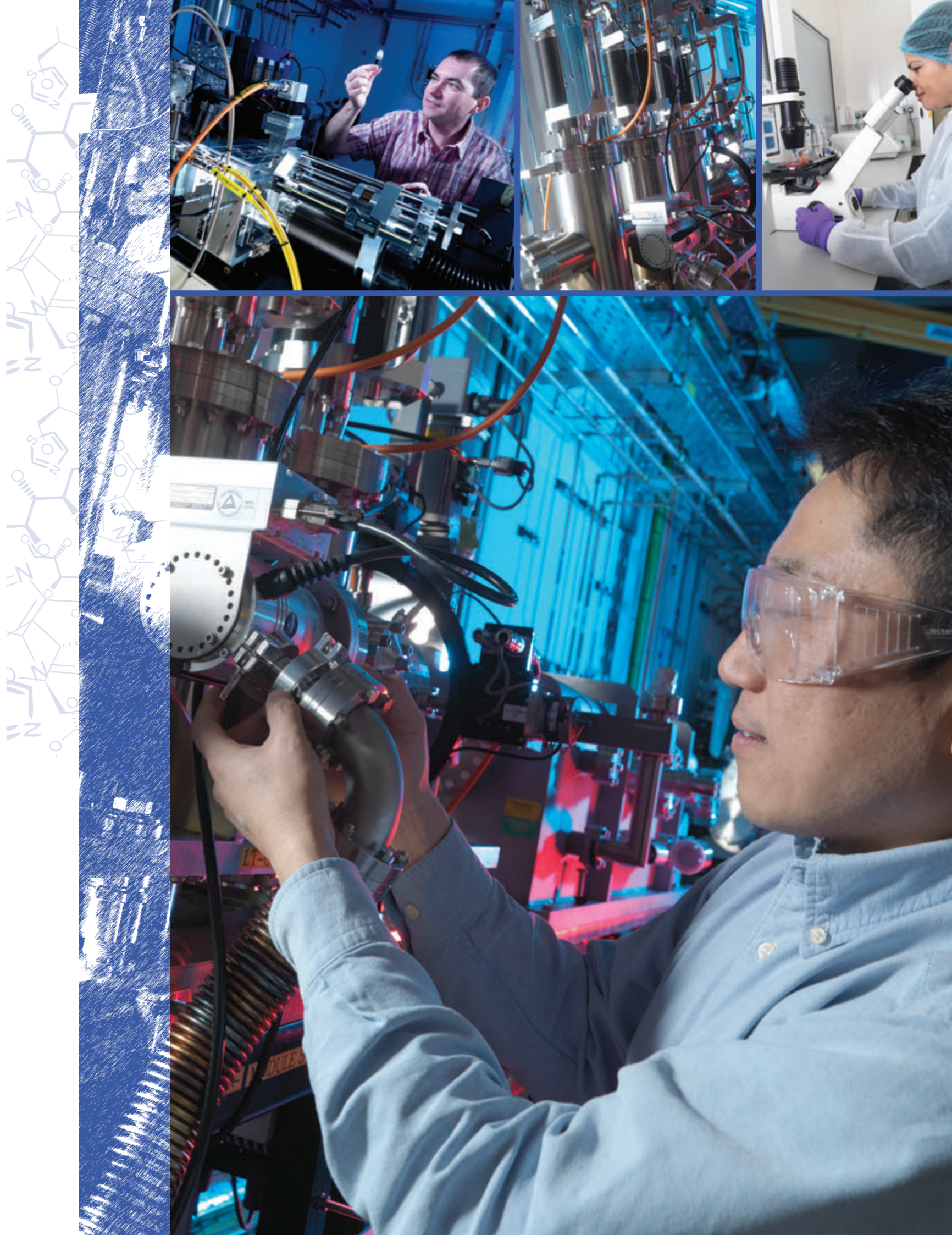
With particular focus on cancer, histological tissue analysis and microbiology at the single cell level, the IR microprobe on B22 is extremely bright and non-destructive which makes it ideal for the fingerprint analysis of biological systems. In the case of ex vivo cells, spectromicroscopy on B22 allowed researchers to monitor via FTIR the biochemical events within spatially different compartments of an individual living cell at the micron scale without the need for fixing, staining, or labelling. A collaboration between Diamond and Manchester University has led to the development of a microfluidic device for an in vivo study of single cells in an aqueous environment.

Even before MIRIAM began operation, its user working group considered the surrounding facilities and recognised the need for a cell culture lab close to the IR facility to enable live cell work. During 2011, the cell culture lab has been made operational under Containment Level II and it is now available for users and in-house research. Diamond joins the rank of a handful of Light Sources with a dedicated cell culture laboratory. Conveniently located close to the beamline, this will minimise the risk of sample damage and contamination while transporting from the laboratory to the IR beamline.

B23, the Circular Dichroism (CD) beamline, which produces high intensity collimated UV beams, enables the measurement of small volumes of sample solutions with high signal-to-noise ratios. B23 had an extremely busy and exciting 2011. It has been used by researchers from biological, biochemical, chemical, pharmaceutical, and crystallographic sciences to examine a range of biological macromolecules and drug complexes. In July, more than 130 delegates from around the world, including leading experts in the field of CD spectroscopy, gathered in Oxford for the 13th International Conference on Chiroptical Spectroscopy (CD2011). Delegates at the conference presented new theoretical and practical advances in the field including: the fundamental forces influencing chiral transitions, the origins of homochirality in the universe, nano and meta-materials and single particle spectroscopy, as well as emerging techniques such as vibrational CD and Raman Optical Activity. The conference was organised by Prof Giuliano Siligardi and Dr Rohanah Hussain from Diamond, together with Dr George Tranter (Chiralab) and Prof Laurence Barron (University of Glasgow). Prof Siligardi was appointed onto the International Scientific Advisory Committee during the meeting, thus ensuring that Diamond continues to be a very active contributor to this important international conference. The B23 team also achieved a major technical milestone in 2011 by delivering a collimated microbeam allowing the detection of protein structures with low concentration of proteins (from 0.5-1ppm) with low volume requirement. This development is now available for research into nanoparticles and particularly understanding nanotoxicology.

I22 continues to develop its science portfolio exemplified by the science contributions presented later in this section. The Moggridge group from Cambridge examined potential alternatives to mechanical or bioprosthetic heart valves on the beamline. Both former types have their associated problems, whereas polymeric heart valves have the potential to overcome these limitations and be a useful alternative in surgery. The examination of the mechanical properties of these polymer artificial heart valves exemplifies what is possible with the RAPID detector system, uniquely available on I22. While the data described was collected on the millisecond timescale, proof of principle measurements were carried out on the tens of microsecond timescales and provided evidence that this would also be feasible for experiments that could be cycled. Continuing the medical theme; researchers from Cardiff have been looking at the collagen structure contained in the cornea and have some cautionary advice to offer on the use of a hypo-osmolar riboflavin/UVA cross-linking for the treatment of very thin keratoconus corneas.

Biological solution scattering is playing an ever-increasing role on all SAXS beamlines. The article by the Brady group from Bristol shows how I22 is being used to provide valuable additional information to structural biology on complicated multi domain macromolecules. At Diamond, we are developing a range of sample delivery systems to meet the needs of this ever growing community; including a BioSAXS robot for automated sample delivery and an online HPLC for aggregating samples. These are described in greater detail later in the technical developments section. Other upgrades to I22 sees a Pilatus 2M now performing routinely as the default SAXS detector.



Polymeric materials for application in a novel prosthetic heart valve

Stasiak, J., Zaffora, A., Costantino, M. L. & Moggridge, G.D. A real time SAXS study of oriented block copolymers during fast cyclical deformation, with potential application for prosthetic heart valves. *Soft Matter*. **7**, 11475 – 11482 (2011)

Although artificial heart valves have been used for over half a century and some improvements have been made, no significant change in their clinical outcome has been achieved. At present, commercially available heart valves are either mechanical or biological. The main complication of the mechanical valves is thrombogenicity, which is a tendency to coagulation of the blood caused by artificial material. Bioprosthetic valves, usually made from porcine tissue, have limited durability and are prone to calcification. Polymeric heart valves could be an alternative for heart valve replacement, overcoming the limitations of mechanical and bioprosthetic valves. Among other desired characteristics, a potential polymeric material should have good mechanical properties such as tensile strength and durability. These, as we have demonstrated, can be enhanced by ordering the microstructure of phase separated block copolymers such as styrenic elastomers¹. Long term stability of these properties depends on how the microstructure responds to fast cyclical mechanical stress. The facilities available at the I22 beamline at Diamond Light Source allowed monitoring of microstructural evolution in real time while applying deformation mimicking valve opening and closing in a real heart beat cycle. X-ray measurements in millisecond timescales have been performed to track microstructural changes. The dynamic measurements were used to evaluate the response of materials to mechanical stress and the reversibility of the response over 10,000 cycles.

The cardiac valves consist of thin flaps of flexible, tough, fibrous tissue firmly attached at the base to the valve rings. The orientation of the cardiac valves is responsible for unidirectional flow of blood by opening and closing during the contractions of the heart. Beside the biomorphic shape (shown in Fig. 1.) and hemocompatibility, a good prosthetic heart valve should demonstrate extended durability². Therefore an important step in the use of new materials for the design of such biomedical devices is the acquisition of basic understanding of their short and long term mechanical and fatigue properties, as well as their performance under realistic conditions of cyclic loading and unloading. These tests aim to identify any hysteresis present in the behaviour of the material while loading and unloading is applied, as well as the minimum number of preconditioning cycles required to obtain steady state properties.

Block copolymers with cylindrical morphology allow molecules to arrange in evenly dispersed fibrous composite materials at the nanometre scale. A flexible matrix, reinforced with the rigid one, allows combination of flexibility with strength. Moreover, long range alignment of the cylindrical microstructure results in orthotropic mechanical properties of the material. Such a fibrous structure is present in natural heart valve, where collagen fibres, arranged in a specific orientation, add strength to elastic tissue.

For advanced polymeric nano-composites, which mimic the natural fibrous structure, microstructural arrangement has a significant impact on mechanical performance^{1,2}. Hence dynamic microstructural studies of the materials in real time during deformation are of great importance.

Three cylinder-forming block copolymers were examined: polystyrene-*block*-polyisoprene-*block*-polystyrene, containing 30% wt styrene (SIS30); polystyrene-*block*-polyisoprene-*block*-polystyrene containing 18% wt styrene (SIS18) and polystyrene-*block*-polyisobutylene-*block*-polystyrene having 30% wt styrene (SIBS30). Samples of oriented microstructure were prepared by compression moulding in a die. Stretching of samples with cylinders oriented both parallel and perpendicular to the direction of loading was carried out for each material.

One heartbeat lasts about 800 ms, valve opening and closure each occurring in ten milliseconds. To mimic the natural loading cycle, the materials were stretched and relaxed in a cycle based on a nominal rate of 67 beats per minute. To achieve such fast loading and unloading, a deformation



Figure 1: A prototype of polymeric heart valve.

rate of 200 mm s⁻¹ was applied. Under load, the polymer morphology undergoes continuous change during constant strain-rate deformation (Fig. 2). The higher the time resolution of the X-ray pattern recorded, the more accurate can be the information about transitory microstructural responses. On beamline I22 of Diamond Light Source, we were able to collect good quality SAXS pattern, in real time during mechanical deformation, in only 10 ms. This was possible by using the RAPID detector system on I22, which offered unique capabilities for the experiment, such as short time frames at very high rates, therefore eliminating stroboscopic effects³. Thus each diffraction pattern represented an average of an evolving structure over the 10 ms time step. Each material was followed over 10,000 stretching cycles, each cycle designed to mimic the maximum distortion which can occur during the natural heart beat. The aim was firstly to determine whether

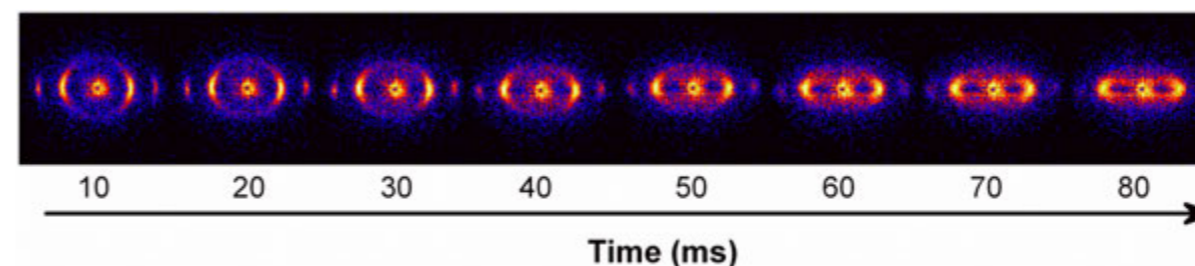


Figure 2: Microstructural changes during stretching of SIS30. Each X-ray pattern was acquired in 10 milliseconds.

the materials' microstructure was able to deform at the same rate as the stretching, and secondly whether there was any long term degradation of the materials over 10,000 cycles of stretching.

It was essential to find a simple method of data reduction, since for each sample, up to 10,000 SAXS patterns were available. We found that the peak intensity variation, as well as total scattered intensity, can be good markers of molecular scale dynamics. Analysis of integrated intensity of X-ray patterns

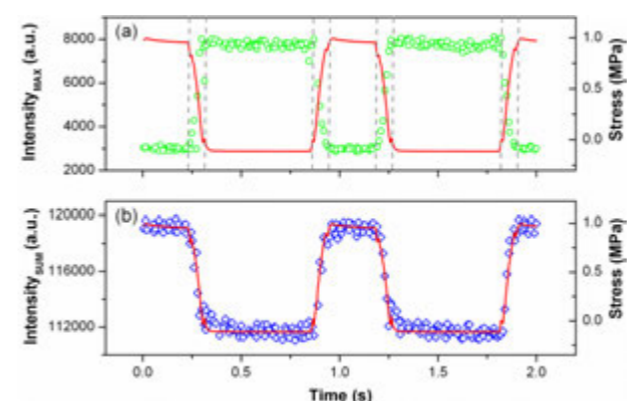


Figure 3: Maximum intensity of the first order peak (a) and total integrated intensity (b) for SIS18 stretched parallel to the orientation direction, as a function of stress. Stress is represented by the red line.

allowed tracking of microstructural changes as the deformation proceeded. Fig. 3. shows a representative set of reduced SAXS data for one sample, over one stretching cycle. The microstructural changes exactly followed the macroscopic deformation; the dynamics of macro and micro changes were indistinguishable.

Long term stretching tests provided an effective comparison between polymers, while also representing the scenario of conditions that would be experienced by the polymers in applications such as a heart valve leaflet. Mechanical properties of these polymers are governed first by the direction

of stretching with respect to microstructural orientation, and second by the hard and soft segment composition. Microstructural stability over an extended time (10,000 cycles) was evaluated by tracking the amplitude of intensity changes observed between the loaded and unloaded conditions. The inherent stability has also been confirmed by monitoring domain spacing, which in this case is the distance between cylinders. Within the range investigated, the increase of domain spacing was proportional to the deformation of the sample, consistent with affine deformation. Cyclic stretching over a long period of time does not significantly affect the degree of deformation during each cycle. As shown in Fig.4. both at the early stage of cyclic deformation, and later after 9800 cycles, the distance between cylinders changed proportionally to the stress.

This study links orientation to mechanical properties, tracking the evolution of the morphology from the initial state as the deformation proceeded, unravelling the nanoscale influences on the long term cyclical strain behaviour. All materials showed good long term stability over 10 000 cycles, the best performance being exhibited by SIBS30 (followed by SIS18), with no discernible structural changes per cycle. This is an encouraging result for potential applications such as a prosthetic heart valve, where great structural stability over very long periods of use is of paramount importance.

References

1. Stasiak, J., Zaffora, A., Costantino, M. L., Pandolfi, A. & Moggridge, G.D. *Funct Mater Lett.* **3**(4), 249-252 (2010).
2. El Fray, M., Prowans, P., Puskas, J.E. & Altstädt, V., *Biomacromolecules*. **7**, 844-850 (2006).
3. Berry, A., Helsby, W.I., Parker, B.T., Hall, C.J., Buksh, P.A., Hill, A., Clague, N., Hilton, M., Corbett, G., Clifford, P., Tidbury, A., Lewis, R.A., Cernik, B.J. & Barnes, P. G.E. *Derbyshire, Nucl. Instr. and Meth.* **A513**, 260 (2003).

DOI 10.1039/C1SM06503C

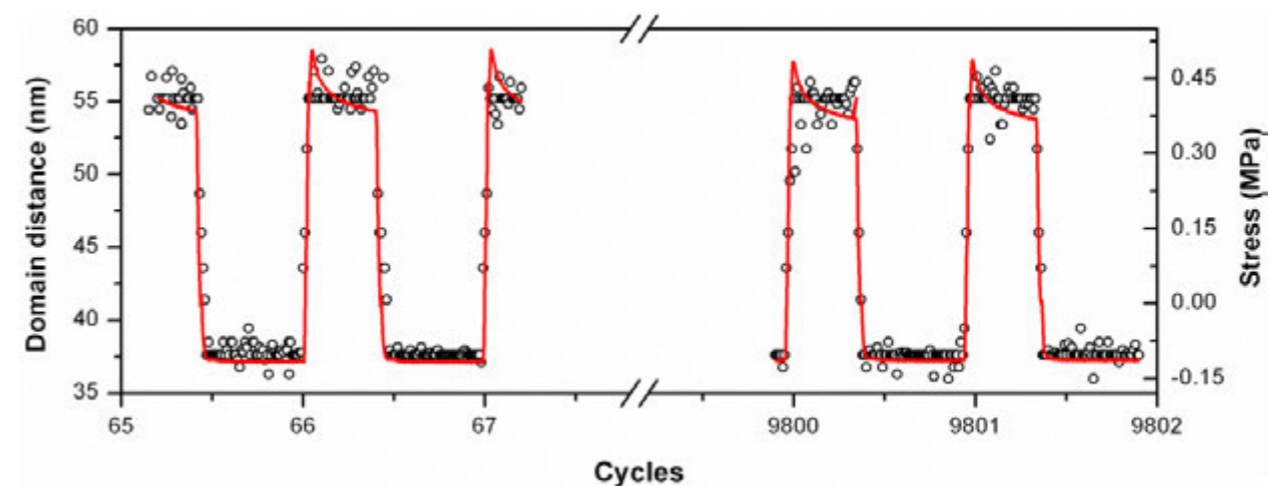


Figure 4: Domain distance for SIBS30 as a function of stress and cycle number.

Structural implications of a new therapy for corneal disease

Hayes, S., Boote, C., Kamma-Lorger, C.S., Rajan, M.S., Harris, J., Dooley, E., Hawskworth, N., Hiller, J., Terill, N.J., Hafezi, F., Brahma, A., Quantock, A.J. and Meek, K.M. Riboflavin/UVA collagen cross-linking-induced changes in normal and keratoconus corneal stroma. *PLoS One*. **6**, e22405 (2011)

The cornea is the precisely curved, transparent window at the front of the eye. It is responsible for over two-thirds of the eye's refractive power and variations in its shape are detrimental to the quality of the image formed on the retina. As its essential properties are largely governed by a unique arrangement of collagen, abnormalities in the structural organisation of collagen have been implicated in keratoconus (Fig. 1)¹, a condition characterised by progressive corneal thinning and steepening and severe, irregular astigmatism. Keratoconus is an area of great scientific and economic importance as it affects up to 200 people per 100,000 and is a leading cause of corneal transplant surgery.

Collagen cross-linking therapy, an *in vivo* technique for increasing corneal stiffness, has recently been deemed an effective therapy for keratoconus². In this treatment, the cornea is exposed to UVA light for 30-minutes, in the presence of riboflavin. The riboflavin acts as a photosensitiser to encourage the production of collagen cross-links. Furthermore, as an absorber of UVA irradiation, it has the added benefit of helping to prevent damage to the sensitive endothelial cells lining the back of the cornea, as well as deeper ocular structures such as the lens and the retina. Despite the clinical success of the technique, little is known about the specific nature of the cross-links that are formed during cross-linking, or about their location (either within collagen fibrils or in the interfibrillar matrix) and, although guidelines exist regarding the safe use of crosslinking, variations of the technique are being continually developed. One such variation is the substitution of the standard iso-osmolar riboflavin solution (containing the dehydrating agent dextran) with a hypo-osmolar riboflavin solution which allows the cornea to swell. This facilitates the treatment of very thin corneas (<400 µm) which were previously regarded as unsuitable for cross-linking due to the potential for damage to deeper ocular structures³. The safety of this modification, which increases the thickness of thin corneas by up to 30% to reach the safe threshold for riboflavin/UVA cross-linking, has caused much controversy amongst ophthalmologists and vision scientists, largely because the effect of this treatment on corneal structure is unknown.

In order to investigate the effect of hypo-osmolar and iso-osmolar cross-linking on collagen organisation within the corneal stroma, small-angle X-ray scattering data was collected on beamline I22 from nine post-mortem donor corneas and two keratoconus corneas (donated following corneal transplantation) before and after cross-linking with either an iso-osmolar or hypo-osmolar riboflavin solution. As collagen interfibrillar spacing is sensitive to changes in corneal hydration, the water content of the tissue was calculated before and after treatment and the corneas classified as 'swollen'

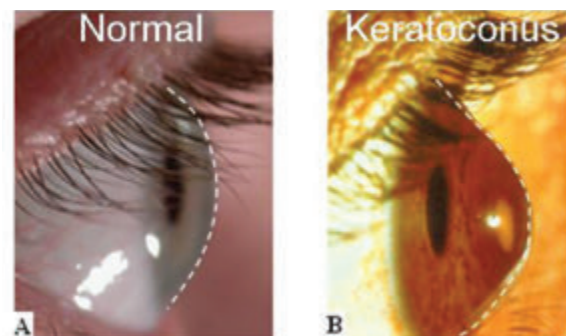


Figure 1: The normal curvature of the cornea (highlighted by a broken white line) (A) is gradually lost in keratoconus (B) resulting in the development of severe, irregular astigmatism.

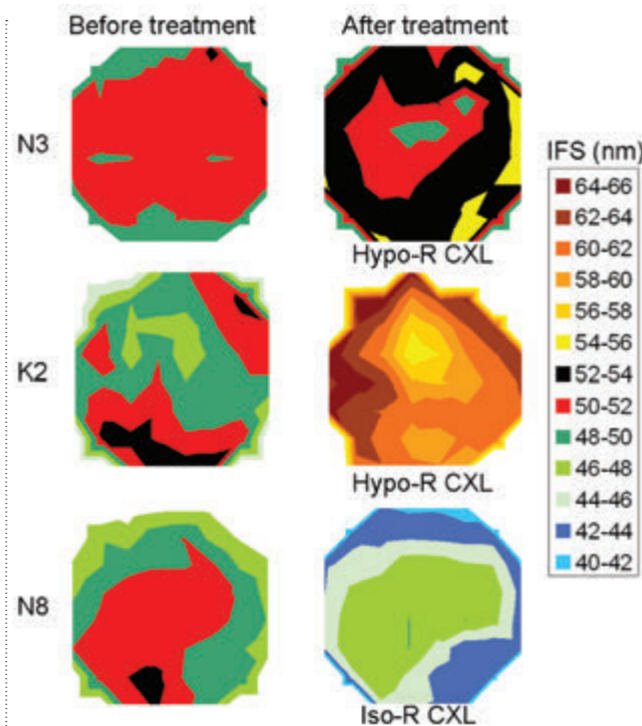


Figure 2: Changes in collagen interfibrillar spacing (IFS) following riboflavin/UVA cross-linking. The contour maps show collagen interfibrillar spacing (IFS) in an unswollen normal cornea (N3) and a slightly swollen keratoconus cornea (K2) before and after hypo-osmolar riboflavin/UVA cross-linking (Hypo-R CXL) and a normal unswollen cornea (N8) before and after iso-osmolar riboflavin/UVA cross-linking (Iso-R CXL). The centre of each corneal button corresponds approximately with the centre of each map.

(above a physiological water content of 76%) or 'unswollen' (water content ≤76%) (Table 1).

The corneas were wrapped in low density polyethylene to prevent tissue dehydration and mounted in a sealed Perspex chamber with Mylar windows. X-ray scatter patterns, resulting from a 10s exposure to a 0.1 nm wavelength X-ray beam focussed to measure 0.2x0.2 mm at the specimen were collected at 1 mm intervals (in a grid) over each cornea before and after crosslinking and recorded on a RAPID detector system⁴ positioned 5m behind the specimen. Measurements of collagen axial D-period, inter-fibrillar Bragg spacing and fibril diameter (Table 1) were determined from the calibrated positions of the sharp meridional, the intense equatorial reflection and the fainter and broader subsidiary equatorial maxima, respectively⁵.

The study revealed no direct structural changes attributable to cross-linkage; fibril diameters increased only when hypo-osmolar conditions were used and only when the cornea was at or slightly below physiological hydration (Table 1). The post-treatment increase in fibril diameter is therefore

Sample	Water content (%)		Fibril Diameter (nm)		Interfibrillar Spacing (nm)		D-period (nm)	
	CXL-	CXL+	CXL-	CXL+	CXL-	CXL+	CXL-	CXL+
Hypo-osmolar riboflavin/UVA cross-linking: Keratoconus								
K1 (unswollen)	69	80	31.1 (0.1)	32.8 (0.1)	38.3 (0.3)	47.3 (0.2)	65.4 (0.1)	65.5 (0.1)
K2 (swollen)	79	86	31.6 (0.1)	32.0 (0.2)	49.7 (0.3)	61.2 (0.4)	65.5 (0.1)	65.4 (0.1)
Hypo-osmolar riboflavin/UVA cross-linking: Normal								
N1 (unswollen)	70	78	34.5 (0.1)	34.8 (0.1)	48.1 (0.1)	51.1 (0.2)	65.2 (0.1)	65.2 (0.1)
N2 (unswollen)	71	80	32.9 (0.3)	32.7 (0.2)	48.2 (0.2)	52.6 (0.2)	66.1 (0.1)	66.1 (0.1)
N3 (unswollen)	68	74	34.3 (0.1)	34.6 (0.1)	50.5 (0.1)	52.6 (0.2)	65.2 (0.1)	65.2 (0.1)
N4 (unswollen)	71	77	33.4 (0.1)	33.8 (0.1)	50.7 (0.3)	54.2 (0.3)	66.1 (0.1)	66.1 (0.1)
N5 (swollen)	87	87	33.8 (0.2)	33.5 (0.1)	58.6 (0.4)	60.2 (0.3)	64.7 (0.1)	64.5 (0.1)
N6 (swollen)	87	87	33.2 (0.2)	33.8 (0.4)	57.9 (0.3)	57.2 (0.3)	63.7 (0.1)	63.5 (0.1)
Iso-osmolar riboflavin/UVA cross-linking: Normal								
N7 (unswollen)	67	69	33.6 (0.1)	31.0 (0.1)	50.0 (0.1)	39.2 (0.1)	66.1 (0.1)	66.1 (0.1)
N8 (unswollen)	66	64	33.5 (0.1)	32.4 (0.1)	49.2 (0.3)	44.9 (0.3)	65.2 (0.1)	65.2 (0.1)
N9 (unswollen)	71	73	34.0 (0.1)	31.9 (0.1)	49.1 (0.2)	41.6 (0.3)	65.2 (0.1)	65.2 (0.1)

Table 1: Tissue hydration and collagen parameters measured before (CXL-) and after (CXL+) riboflavin/UVA collagen cross-linking. Average values (+/- SEM) of collagen parameters for all normal (N) and keratoconus (K) corneas were calculated using >50 measurements recorded from the central 8mm region of the cornea before (CXL-) and after crosslinking (CXL+). Bold type is used to indicate pre and post treatment differences in collagen parameters at p<0.001.

more likely due to tissue swelling than to molecules being pushed further apart by newly formed inter-molecular cross-links.

Inter-fibrillar spacing was found to decrease in human corneas following iso-osmolar riboflavin/UVA treatment (Table 1 and Figure 2), due to the dehydrating effect of the dextran within the riboflavin solution. One would expect the ordering to increase as fibrils approach each other and this is consistent with the reported rise in transparency of hen corneas following iso-osmolar riboflavin/UVA collagen crosslinking⁶. In the keratoconus corneas and the unswollen normal corneas, inter-fibrillar spacing increased significantly after hypo-osmolar riboflavin/UVA treatment (Table 1 and Figure 2).

Measurements of collagen D-period (Table 1) have shown that riboflavin/UVA induced cross-linking does not have any measurable effect on the axial stagger or the tilt of the collagen molecules within the fibrils, but this is not surprising since it seems that D-period is rather insensitive to cross-linking even with a strong fixative such as glutaraldehyde.

The use of a hypo-osmolar riboflavin/UVA cross-linking for the treatment of very thin keratoconus corneas remains controversial and on the basis of our scientific studies we offer some words of caution. As we have shown that the majority of the tissue swelling occurs between fibrils it is foreseeable that this will reduce the effective thickness of the protective riboflavin film. Since the hypo-osmolar solution also has a lower viscosity and lower UVA absorption coefficient than that of the iso-osmolar solution and becomes unstable after only 90 seconds, we suggest that this therapy is used with caution in a clinical setting and that this procedure warrants further scientific investigation.

References

- Hayes, S., Boote, C., Tuft, S., Quantock, A. and Meek, K.M. A study of corneal thickness, shape and collagen organisation in keratoconus

using videokeratography and x-ray scattering techniques. *Experimental Eye Research*. **84**, 423-434 (2007).

- Spoerl, E., Mrochen, M., Sliney, D., Trokel, S., Seiler, T. Safety of UVA-Riboflavin Cross-Linking of the Cornea. *Cornea*. **26**, 385-389 (2007).
- Hafezi, F., Mrochen, M., Iseli, H.P., Seiler, T.J. Collagen crosslinking with ultraviolet-A and hypoosmolar riboflavin solution in thin corneas. *Journal of Cataract and Refractive Surgery*. **35**, 621-624 (2009).
- Berry, A., Helsby, W.I., Parker, B.T., Hall, C.J., Buksh, P.A., Hill, A., Clague, N., Hilton, M., Corbett, G., Clifford, P., Tidbury, A., Lewis, R.A., Cernik, B.J. & Barnes, P.G.E. *Derbyshire, Nucl. Instr. and Meth.* **A513**, 260 (2003).
- Boote, C., Dennis, S., Newton, R.H., Puri, H., Meek, K.M. Collagen fibrils appear more closely packed in the prepupillary cornea: optical and biomechanical implications. *Investigative Ophthalmology and Vision Science*. **44**, 2941-8 (2003).
- Blanco, T., Merayo-Llodes, J., Fabiani, L., Del Olmo Aguado, S., Mar-Sardana, S., et al. Corneal Collagen Cross-Linking With Riboflavin and UVA Improves Transparency in Hen Corneas. *ARVO Meeting Abstracts*. **49**, 3911 (2008).

Funding Acknowledgements

This work was supported by a UK Medical Research Council Programme Grant (Grant G0600755) and a STFC Beam-time Programme Grant. Prof. Meek is a Royal Society-Wolfson Research Merit Award Holder. We would like to thank the Bristol Eye Bank for the provision of specimens.

DOI 0.1371/journal.pone.0022405

Mechanosensitive responses of a bacterial adhesin at the cell surface

Agnew, C., Borodina, E., Zaccari, N.R., Conners, R., Burton, N.M., Vicary, J.A., Cole, D.K., Antognozzi, M., Virji, M. & Brady, R.L. Correlation of *in situ* mechanosensitive responses of the *Moraxella catarrhalis* adhesin UspA1 with fibronectin and receptor CEACAM1 binding. *PNAS (USA)* **108(37)**, 15174-15178 (2011)

Bacteria are the source of countless human diseases. Understanding how bacteria infect humans is crucial to preventing such diseases. Traditional approaches to understanding infection have concentrated on either studies of whole bacteria and their host organisms, or dissection of the molecules present within these cells. In this study a novel method has been developed for bridging these, until now, separate approaches. The target of these studies is the common bacterium, *Moraxella catarrhalis*, which causes middle ear infections in young children, exacerbates common obstructive pulmonary disease and is frequently a major cause of morbidity in those with heart disease. The *Moraxella* cell surface is decorated with a forest-like layer formed from multiple copies of a large adhesin protein, termed UspA1. Dominating the bacterial surface, these proteins are the first point of contact with host organisms (humans) and infection proceeds via UspA1 binding specifically to a range of receptors. However, the functioning of the UspA1 protein is also affected by its dense packing within the cell surface layer, and hence its study has therefore required a unique combination of techniques to probe its workings both as isolated molecules and *in situ* at the cell surface. This has required the development of new technologies. Diamond Light Source has been central to several of these approaches.

Firstly, electron microscopy was used¹ to show UspA1 proteins (homotrimers of 3 x ~1,000 amino acids) form a densely packed annular layer at the *Moraxella* surface. At about 800 Å in length, UspA1 provides an extended surface along which a range of receptor binding regions are strewn: extracellular proteins such as fibronectin and laminin bind towards the head, whereas the specific receptor CEACAM1 has been shown^{1,2} to bind some 400 Å distant down the coiled-coil stalk of UspA1. At least the latter of these sites is inaccessible in the densely packed arrangements of UspA1 at the cell surface. We hypothesised that large-scale physical deformations of UspA1 may therefore regulate the processes by which it interacts with its range of receptors.

To understand the molecular arrangement of UspA1, due to its large size we initially had to truncate UspA1 into bite-sized segments that were more amenable to crystallographic techniques. As there was very limited

discrete domain structure, this initial phase was greatly accelerated by the application of high-throughput cloning and expression techniques accessed through the Oxford Protein Production Facility (OPPF, now in the Research Complex at Harwell (RCaH)). Many constructs of varying stabilities were derived: three of these were successfully crystallized and their structures determined from diffraction data collected on the MX beamlines I02 and I04 (Fig. 1). Combining these structures enabled us to assemble an overall model for UspA1, although in isolation this told us little of its actual function in infection.

To progress our understanding, mutagenesis was used to identify both the CEACAM1 and fibronectin binding sites. Truncated forms of UspA1 containing each of these regions were produced and complexed with soluble portions of each receptor. As usable crystals of neither complex could be obtained, we instead determined their structures via SAXS studies

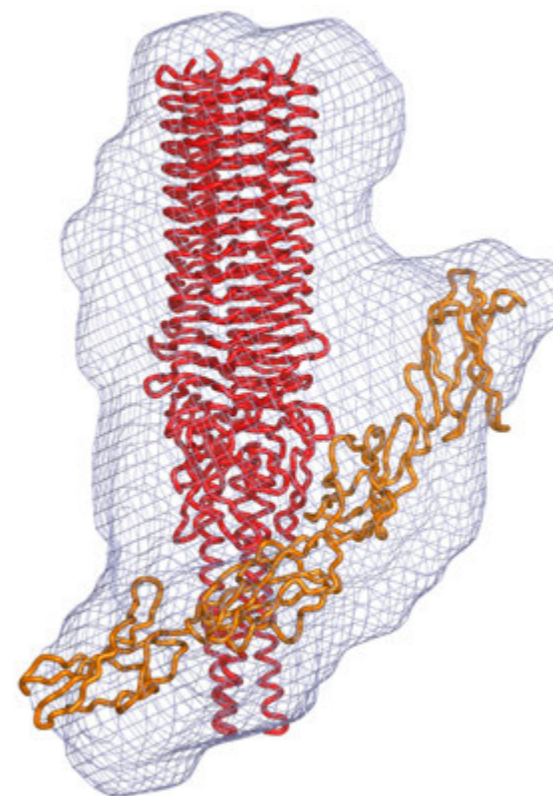


Figure 2: Molecular envelope for the UspA1 head domain-fibronectin (domains 12-15) complex as determined by SAXS.

using the I22 beamline at Diamond Light Source. Distinctive molecular envelopes for each complex were calculated from the scattering data, and models of the complexes could be reliably assembled from the crystal structures of each component (Fig. 2). What was evident in both cases was that the fully extended and tightly packed UspA1 structures observed at the bacteria surface did not seem compatible with the angular receptor-ligand pair associations we observed using the isolated molecular fragments. This therefore stressed the importance of measuring UspA1 mechanics directly at the cell surface, and how this might change on exposure to its various receptors.

To achieve this, we exploited the recent development³ of a specialised AFM with a transverse cantilever combined with Total Internal Reflection Fluorescence (TIRF) detection (Fig. 3). The Lateral Molecular Force Microscope (LMFM) differs from more conventional atomic force microscopes in laterally tapping samples (in this case, individual cells) against an extremely fine oscillating lever, rather than fluctuating the lever vertically across the surface of a fixed sample as is more usually the case. Fabrication of extremely thin but stiff cantilevers, together with exceptionally fine motor movements and a specialised visualisation system, have all been combined in the device to tremendous effect. The result has been a machine that can measure exquisitely fine molecular changes and forces in individual molecules directly on a living cell surface without deforming the bacterial membrane. This has permitted measurement of adhesion forces and detection of changes in the thickness of the annular UspA1 layer, and hence the degree of bending of extended molecular structures. Once the technology was perfected, AFM data was obtained that indicated, at the *Moraxella* cell surface, the adhesion properties and thickness of the UspA1 annular layer decrease significantly in the presence of either the fibronectin or CEACAM1 receptors, but not with a control protein. Adhesion events also decreased after saturation with either receptor, and individual single-molecule binding events could be observed. The decrease in thickness of the adhesin layer could be measured with sufficient accuracy to correlate these *in situ* changes with the expected dimensions produced by discrete bending of UspA1 molecules. This receptor-induced

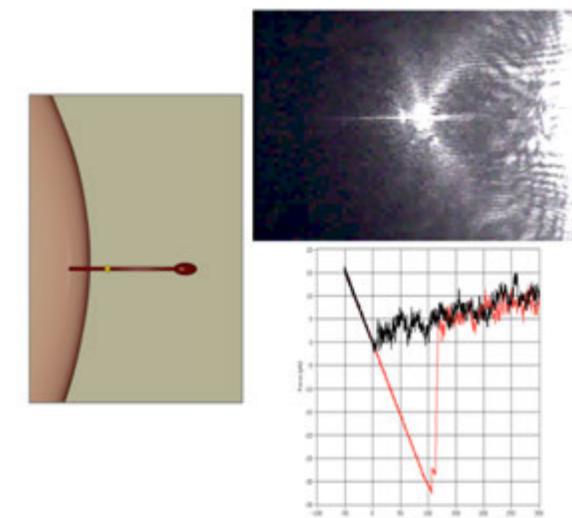


Figure 3: Bending of a single UspA1 molecule (left) as detected with TIRF (top right) which measures displacement of the stylus (bottom right, red line deflection corresponds to a single molecular event).

distortion of the extended UspA1 molecules could be correlated with the UspA1 model derived from both the crystallographic and SAXS studies.

This study therefore provides a rare demonstration of substantial conformational changes in proteins directly at the cell surface, and correlates this with the instigating molecular structures. These molecular changes lead to significant changes in the physical properties of the bacterial cell surface and are believed to relate to its permissiveness for receptor binding. They are therefore integral to the infection process. To date conformational changes in proteins have usually only been observed in isolated structures, not *in situ* within their native cellular environment. This study demonstrates the feasibility of visualising such changes and may prove equally useful for the study of many other biological processes directly within their natural environment, something that has long been needed in molecular medicine.

References

1. Conners, R., Hill, D.J., Borodina, E. *et al.* The *Moraxella* adhesin UspA1 binds to its human CEACAM1 receptor by a deformable trimeric coiled-coil. *EMBO J.* **27**, 1779-1789 (2008).
2. Hill, D.J., Edwards, A.M., Rowe, H.A. & Virji, M. Carcinoembryonic antigen-related cell adhesion molecule (CEACAM)-binding recombinant polypeptide confers protection against infection by respiratory and urogenital pathogens. *Mol. Microbiol.* **55**, 1515-1527 (2005).
3. Scholz, T., Vicary, J.A., Jeppesen, G.M., Ulcinas, A., Hörber, J.K.H. & Antognozzi, M. Processive behaviour of kinesin observed using micro-fabricated cantilevers. *Nanotechnology.* **22**, 095707 (2011).

Funding Acknowledgements

These studies were supported by grants from the Wellcome Trust (07746) and UK Biological and Biotechnology Research Council (BBSRC) (BB/F007256). C. Agnew was supported by a studentship provided by the BBSRC.

DOI 10.1073/pnas.1106341108

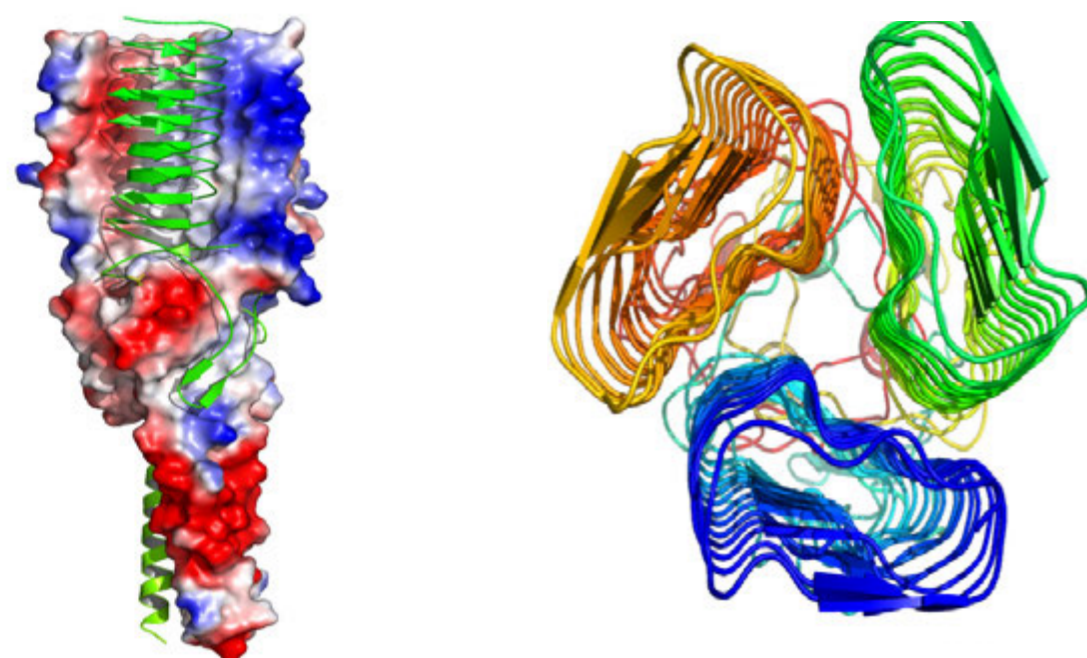


Figure 1: Surface diagram (left) and top view (right) of the UspA1 trimer, compiled from crystal structures of two fragments. The trimer is intertwined and assembled with high charge complementarity.

A step towards true quantitative analysis in infrared microscopy: from models to real samples

Filik, J., Frogley, M. D., Pijanka, J. K., Wehbe, K., and Cinque, G. Electric field standing wave artefacts in FTIR micro-spectroscopy of biological materials, *Analyst*. **137**(4), 853 (2012)

Accurate detection and classification of materials, such as diseased tissues or illicit substances, is critical and misclassification can sometimes have life threatening consequences. Infrared (IR) absorption spectroscopy has been widely adopted as a simple but powerful characterisation tool, effectively producing a fingerprint of the samples' molecular composition and aiding classification. IR absorption spectroscopy is quantitative and highly sensitive, but some measurement configurations, particularly in microspectroscopy¹, can suffer from optical artefacts^{2,3}. Misleading results can be obtained if changes in the IR absorption spectrum are not directly associated with chemical changes in the sample. Whether caused by the optical arrangement of the measurement or something intrinsic to the sample morphology itself, it is important to understand, and ideally correct for, any source of variance in the spectrum which is not due to the molecular composition. In this work a severe artefact is addressed which is present for samples on IR reflective slides due to the drop in IR intensity near a metallic surface.

There is a linear relationship between the IR light absorbed and the amount of absorbing material or chemical concentration in the sampled volume, which is expressed in the well known Beer-Lambert law. Molecular composition can, for example, help determine whether a histological tissue sample is healthy or diseased. In order to correctly and consistently classify samples it is crucial that the quantitative accuracy of the IR absorption spectra is maintained in all measurement configurations, especially as there is no standard measurement protocol.

The most common modes of measuring IR absorption spectra with a microscope are transmission and transfection. In transmission, the quantitative nature of IR spectroscopy is maintained, samples are mounted on a transparent window and the amount of light that passes through the sample and window is measured. In the transfection geometry, samples are mounted on reflective substrates, the IR light passes through the sample, is reflected off the substrate and passes back out through the sample, doubling the absorption path length. This configuration is popular in the biomedical sciences because it produces the strongest absorption signal for thin transparent samples such as cytology or histology specimens, it works over a broad spectral range and the substrates are relatively inexpensive.

In this work, it is shown that despite its advantages, the transfection measurement geometry induces complex optical effects which destroy the quantitative linear relationship between IR absorption and sample composition in a way which varies strongly with the IR wavelength.

The first investigation used a standard, homogenous material, (Bovine Serum Albumin, BSA) with a well characterised IR absorption spectrum, to determine the relationship between absorbance and sample thickness. Measurement of several samples of BSA gel with different thicknesses in

transmission showed the material was indeed homogeneous and that the transmission configuration maintains the Beer-Lambert relationship. In the transfection geometry, however, clear non-linear behaviour is observed. Typical transfection spectra for BSA gels of thickness 200–1200 nm are shown in Fig. 1(a) with absorbance normalised to the N-H stretching peak at 3300 cm⁻¹. If the absorbance was linear with thickness in transfection these spectra would all be identical. The non-linearity is illustrated by integrating two spectral regions: the C-H stretching band (Fig. 1 (b), 2830–3010 cm⁻¹); and the amide I+II bands (Fig. 1 (c), 1480–1760 cm⁻¹), and plotting them against the sample thickness determined by atomic force microscopy (AFM). The non-linearity of absorbance with thickness is caused by heterogeneity in the IR intensity at the reflective surface. When light is reflected from a perfect conductor, the reflected wave undergoes a phase shift of ~180°, causing the incident and reflected light to interfere with each other. This interference creates a sinusoidal standing-wave in the light intensity which drops close to zero at the reflective surface⁴. The spacing between intensity maxima and minima depends on the refractive index of the sample and the wavelength of the light. The dashed lines in Fig. 1 (b) and (c) show the predicted variation of the absorbance with sample thickness based on a new phenomenological model of the optical electric-field standing wave (EFSW):

$$(1) \quad A(\lambda) = a_0(\lambda) \int_{z=0}^l \sin^2\left(\frac{2\pi n z}{g\lambda}\right) dz \times \left[1 + R(\lambda)\sin^2\left(\frac{2\pi n l}{g\lambda}\right)\right]$$

where A is the absorbance of light of wavelength λ by a sample of thickness l and refractive index n in the presence of the EFSW, g is a scaling parameter for the optical geometry, a_0 is a spectrum of scaling coefficients for the absorbance - proportional to the true absorption coefficients, z is the distance from the reflective surface and R is a positive valued

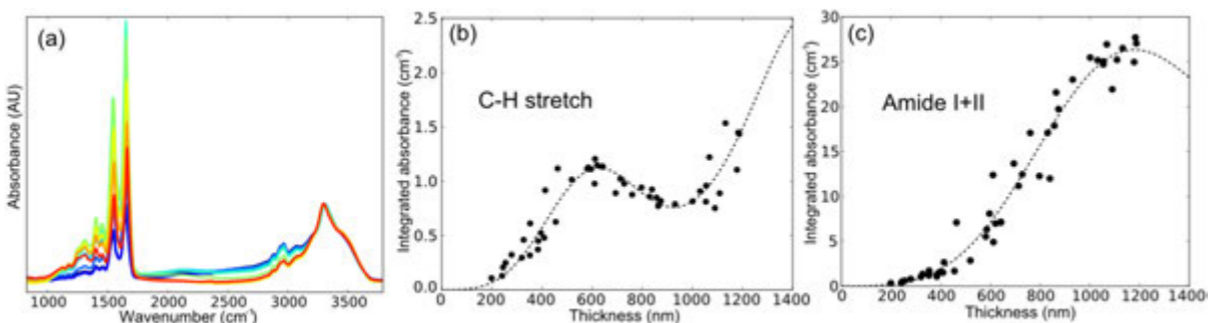


Figure 1: Deviation of transfection IR absorbance data from the Beer-Lambert law, (a) Spectra of different thickness BSA films normalised to the N-H stretching band at 3300 cm⁻¹, (b) Integrated C-H stretch absorbance vs. thickness, (c) Integrated amide I+II absorbance vs. thickness. The dashed lines are the predictions of the model described in the text (equation (1)).

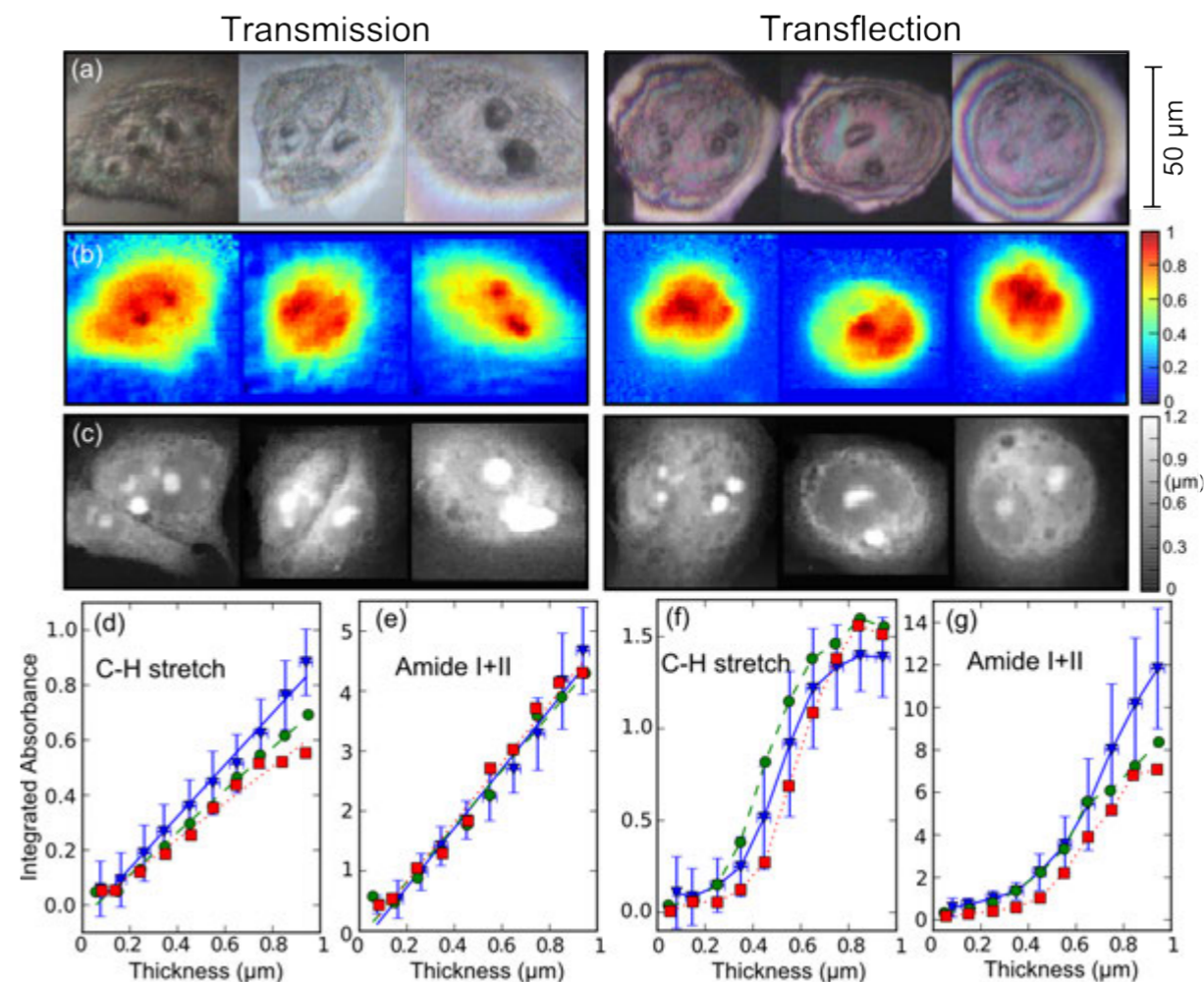


Figure 2: Comparison of IR images of six MCF-7 cells, three measured in transmission and three in transfection, (a) Visible microscope images, (b) IR absorption images, (c) AFM topography images, (d,e) Integrated C-H stretch and Amide I+II absorbance vs. thickness in transmission, (f,g) Integrated C-H stretch and Amide I+II absorbance vs. thickness in transfection. The symbols in (d)-(g) represent different cells.

interference coefficient at each wavelength which is strongly dependent on the reflectivity of the sample/air interface. The integral term describes how much of the sinusoidal EFSW interacts with the sample and the term in the square brackets describes optical interference effects due to internal reflections.

Having used the BSA standard material to quantify the relationship between absorbance and thickness for a homogenous sample, the results were compared with a heterogeneous biological material, of the kind commonly studied by IR microscopy.

Breast adenocarcinoma cells, MCF-7, were grown on IR transmission and transfection substrates (Fig. 2 (a)) and analysed using an IR microscope equipped with a Focal Plane Array (FPA) imaging detector. The FPA has 64×64 pixels for simultaneous collection of 4096 IR spectra. The IR absorbance image of six cells was measured, three in transmission and three in transfection (Fig. 2 (b)). AFM topography images (Fig. 2 (c)) were measured to determine the thickness of the cells at each point in the FPA images. The C-H stretch and amide I+II bands of the IR spectra were again integrated and plotted against the sample thickness (Fig. 2(d-g)). The integrated absorbance values were segregated into 100 nm thickness bins and averaged for plotting. Sample regions over 1 μm thick were rejected from the analysis because the spectra were few in number and corresponded to small, localised regions below the spatial resolution of the IR measurement. Integrated absorbance vs. thickness plots for the cells are shown at the bottom of Fig. 2. The transmission data (Fig. 2(d) and (e)), shows a linear relationship between the sample thickness and absorbance, i.e. it obeys the Beer-Lambert law, demonstrating also that there is a negligible change in component concentration in different cell regions. The cell transfection data (Fig. 2(f) and (g)) shows a very similar trend to the BSA standard transfection

data (Fig. 1 (b) and (c)), especially the almost quadratic relationship between the absorbance and thickness below 600 nm.

The results of the full analysis of these six cells confirm that the EFSW artefact has a profound effect on the transfection spectra of such materials, and that the main spectral variations can be related to the sample thickness rather than any chemical differences. Understanding to what extent the EFSW artefact has affected the conclusions of previous investigations using the transfection geometry (of which there are many) and whether it can be corrected is the focus of ongoing work.

References

1. Cinque, G. *et al.* Multimode InfraRed Imaging and Microspectroscopy (MIRIAM) beamline at Diamond. *Synchrotron Radiation News* **24**, 24–33 (2011).
2. Bassan, P. *et al.* Reflection contributions to the dispersion artefact in FTIR spectra of single biological cells. *Analyst* **134**, 1171–1175, (2009).
3. Bassan, P. *et al.* Resonant Mie scattering in infrared spectroscopy of biological materials - understanding the 'dispersion artefact'. *Analyst*, **134**, 1586–1593 (2009).
4. Brook, H. *et al.* A Study of Electric Field Standing Waves on Reflection Microspectroscopy of Polystyrene Particles. *Appl. Spectrosc.* **63**, 1293–1302, (2009).

DOI 10.1039/C2AN15995C

Tools for cancer research and diagnosis: infrared spectroscopy and microscopy

Bellisola, G. and Sorio, C. Infrared spectroscopy and microscopy in cancer research and diagnosis. *Am J Cancer Res.* 2(1), 1–21 (2012)

Since the middle of the 20th century, infrared (IR) spectroscopy coupled to microscopy has been used as a non destructive, label free, highly sensitive and specific analytical method to reveal molecular structure. Nowadays, synchrotron based IR microspectroscopy offers a signal-to-noise spectral quality unreachable by other broadband sources, and achieves the highest optically attainable IR spatial resolution on microscopic scale samples. This is particularly relevant in Life Sciences, with a significant progression of applications in biomedical research and in particular cancer studies. In view of the validation of the IR fingerprint region as a spectral marker of cancer and anticancer therapy follow up, we have recently performed a set of key experiments on leukemic blasts at the IR beamline B22 'MIRIAM'. The results on identification and cross-validation of IR markers of drug actions in the spectra of K562 leukemic blasts are in the following report.

The underlining principle of IR spectroscopy is that the molecular structure can be revealed by exciting the vibrational modes in materials. The absorption bands in an IR spectrum are thus a fingerprint of the molecular composition. Within the linear range of Lambert-Beer law, the absorbance is a quantitative measure of the molecular species concentration.

Modern IR spectrometers are based on Fourier Transform (FT) interferometer and they are commonly coupled to all-reflective IR microscopes enabling the acquisition of spatially resolved IR information, for instance, in an individual cell¹. When the microscope aperture defining the IR imaging spot at the sample is reduced to 20 μm or less, the photon throughput towards the detector significantly reduces while the detector noise remains constant, thus the signal to noise ratio (S/N) is strongly decreased. Moreover, when working with microbeams approaching in size the wavelength of mid-IR radiation (above 2.5 to 25 μm wavelength), the diffraction limit becomes dominant in the IR spectral interpretation.

By exploiting Synchrotron Radiation (SR) as an IR source, the brightness of the photon flux density reaching the sample is no more a limitation in the illumination of microscopic sample features. High quality spectra of individual cells with a diameter around 15 μm , which is the average diameter of a granulocyte, were obtained at beamline B22. For reference, samples composed of very homogeneous cell populations were measured and usable spectra with acceptable S/R values were achieved with conventional source from larger areas (e.g. 50 μm), which demonstrated the complementarity of microFT-IR with conventional lab instruments.

The IR spectrum of a cell usually contains a large number of absorption bands, many of them can be confidently assigned to the molecular vibrations of a particular group, in particular analysing the 'fingerprint region'. The unequivocal interpretation of pre-assigned vibrational mode is not straightforward because the common modes of different molecular components within a cell may overlap and the spectrum may reflect only the average biochemical composition. The development of the so-called molecular medicine requires the identification of biomarkers that can be associated to disease-specific molecular pathways. In an attempt to extend the biomedical applications of microFT-IR, we applied mid-IR analysis to search for specific vibrational components with the equivalent significance of a traditional cancer biomarker. That is: a specific gene, or a more or less expressed protein, or protein activity, or as some '...omics' signatures. Specific protein components, for instance BCR/ABL oncoprotein, cannot be directly measured in the spectrum of leukemic cells without some labelling and/or other forms of pre-treatment in samples, and in the absence of a

calibration method. Nevertheless, in perturbing cells, with drugs specifically targeting BCR/ABL-associated tyrosine kinase, we were able to identify some spectral components with the potential significance of IR biomarkers exhibiting the downstream effects of specific oncogene activity.

Cells interacting with their environment receive signals that are transduced to the nucleus through a complex array of biochemical signals known as signal transduction processes. These signaling events are specific for the agonist/s but can have some common features, like the activation of phosphorylation/dephosphorylation processes on a specific set of macromolecules. Biochemical, functional, structural and dynamical changes occurring also in complex systems subjected to specific perturbations can be identified by difference spectroscopy². For instance, during typical time-course or dose-response experiments with drugs, the spectral features from groups that do not change during the stimulation annihilated one another, and only the changes occurring as a consequence of the activation/inhibition become evident in the difference spectrum.

In the attempt to move microFTIR from spectroscopy labs to Hospitals', we have recently demonstrated with a set of experiments performed at the IR beamline B22 'MIRIAM', that a specific region of mid-IR absorbance spectrum is associated to the reduction in tyrosine phosphorylation levels in human leukemic cell models following treatment with the tyrosine kinase inhibitor (TKI) imatinib-mesylate, the founder of a class of highly effective BCR/ABL inhibitors of clinical efficacy³. Moreover, we have also identified and cross-validated some typical IR signatures of drug action in cells⁴ as shown in Fig. 1.

To this scope we acquired SR-based microFT-IR spectra of individual leukemic cells exposed to the pro-apoptotic drug imatinib-mesylate (IMA). Typical IR signatures of cell apoptosis were identified by supervised data analysis in the spectra (Fig. 1 (A & B)). Unsupervised cluster analysis was applied to the dataset allowing the classification of the spectra of cells with apoptotic (drug-sensitive) and viable (drug-resistant) IR patterns (Fig. 1 (C)). This application may suggest that a rapid and economic screening platform based on microFT-IR could be implemented for drug screening of compounds targeting phosphorylation processes or to monitor ex vivo in future, with minimal sample treatment, the efficacy of TKI treatment in the individual patient as hypothesised. These qualitative measurements point to a possible application of the technique in clinical trial with patients, where the procedure could be used as a diagnostic tool influencing thereby the treatment of the patients. This could be a step forward for a more efficient and targeted personalised medicine.

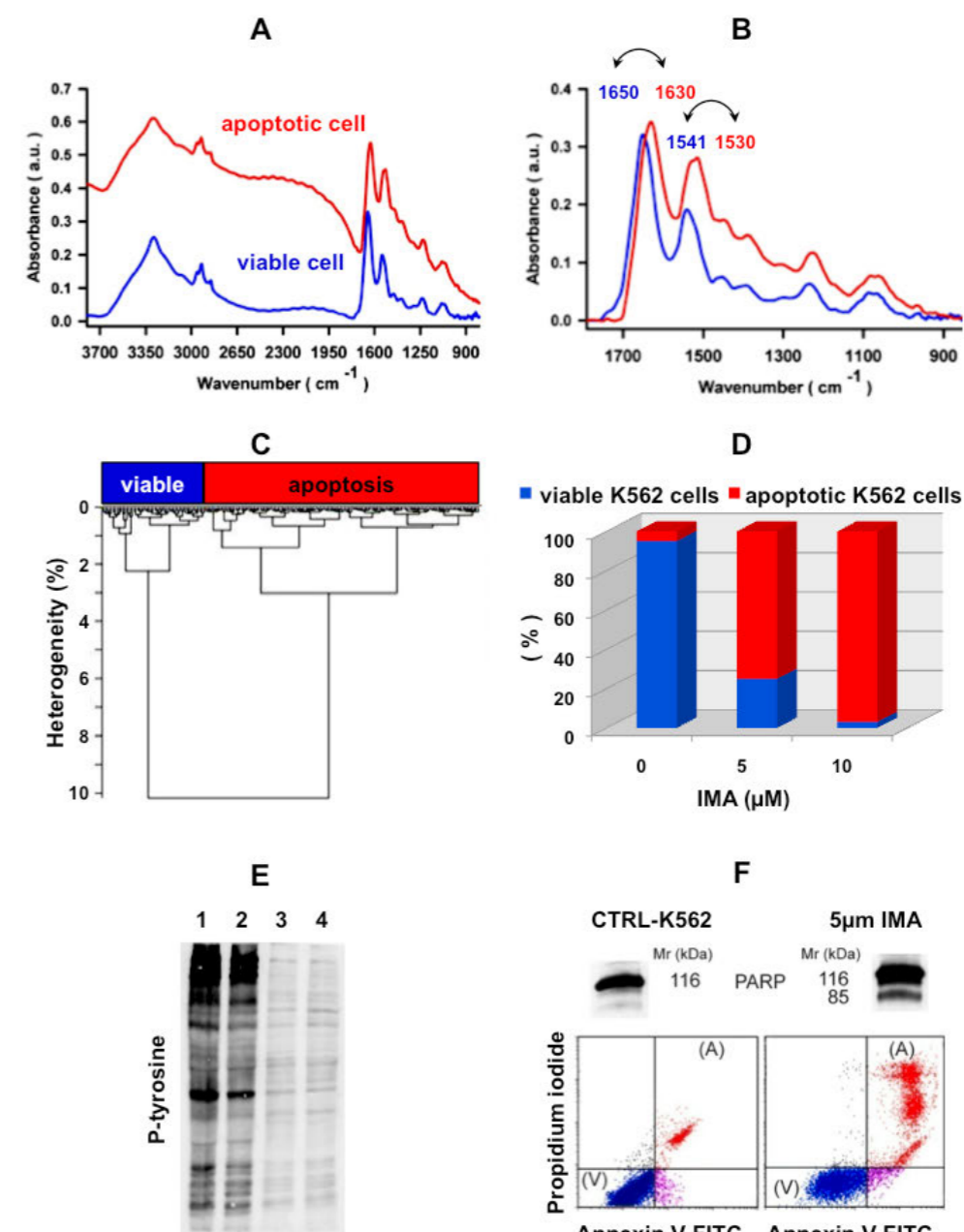


Figure 1: The identification and cross-validation of IR markers of drug actions in the spectra of K562 leukemic blasts. (A) The representative SR FT-IR absorbance spectra of viable (blue trace) and apoptotic (red trace) K562 blast cells exposed for 24 hours to 5 μM imatinib mesylate (IMA) in the interval of wavenumbers between 3800 and 850 cm^{-1} . (B) The same base-line corrected spectra within the interval of wavenumbers 1800 and 850 cm^{-1} showing the significant shift of amide I and amide II towards (double-edged arrows) in the absorbance spectrum of the cell undergoing apoptosis (red line). (C) The unsupervised recognition of the IR patterns of viable (drug-resistant) and apoptotic (drug-sensitive) K562 cells in samples, respectively. (D) The cumulative fractions of K562 blast cells with viable (blue) and apoptotic (red) IR patterns resulting from a typical dose-response experiment with IMA, respectively. (E) and (F) cross-validation of IR analysis by immunoblotting analysis of phosphorylated proteins. (E) Cell lysates of untreated CTRL (lanes 1 and 2) and of K562 cells exposed to 5 μM IMA for 24 hours (lanes 3 and 4) were probed with anti-phosphotyrosine antibodies PY99 and 4G10. (F) The cleaved 85 kDa band of poly(ADP-ribose) polymerase (PARP) is a molecular marker of cell apoptosis. (F) The relative percentages of dead cells determined by flow cytometric analysis in parallel untreated CTRL and IMA-treated K562 samples. (E) and (F) were taken from ref. 4.

References

- Chalmers, J. M. & Griffiths, P. R. Handbook of vibrational spectroscopy. J. Wiley (2002).
- Kotting, C., Suveyzdis, Y., Bojja, R. S., Metzler-Nolte, N. & Gerwert, K. Label-free screening of drug-protein interactions by time-resolved Fourier transform infrared spectroscopic assays exemplified by Ras interactions. *Appl Spectrosc.* 64, 967-972, (2010).
- Deininger, M. W. & Druker, B. J. Specific targeted therapy of chronic myelogenous leukemia with imatinib. *Pharmacol Rev.* 55, 401-423, (2003).
- Bellisola, G. et al. Tracking infrared signatures of drugs in cancer cells by Fourier transform microspectroscopy. *Analyst.* 135, 3077-3086, (2010).

PMCID: PMC3236568

Analysing functional DNA nanomaterials with SRCD spectroscopy

Brewer, A., Siligardi, G., Neylon, C., Stulz, E. Introducing structural flexibility into porphyrin–DNA zipper arrays, *Org. Biomol. Chem.* **9**, 777–782, (2011)

DNA is, besides displaying its central biological role as bearer of the genetic material, an extremely versatile construction material. DNA has become very attractive for the creation of novel nanosized objects. We are studying the influence of modifications of DNA with the aim to create functional DNA based nano-materials. Our modifications generally consist of large chromophores, which show specific light-induced activity such as energy or electron transfer. We are using modifications which are derived from naturally occurring molecules, such as porphyrins. Both DNA and the porphyrins show specific response when measured using circular dichroism (CD) spectroscopy, where the UV part gives insight into the structure of the DNA, and the visible part displays important electronic information on the porphyrin. By making use of the sensitivity of the beamline B23 SRCD spectroscopy station, we have analysed a number of different DNA strands. The CD spectra are also extremely valuable in determining the presence of different metals within the porphyrins; metallation of porphyrins can be used to change their optoelectronic properties. In addition to the porphyrins, we are also investigating other metal-binding substituents which can be used to cross-link DNA strands together to create extended structures held with complementary interactions.

The synthesis of electronically active organic molecules on the macromolecular scale is of major interest due to their promising applications in light harvesting devices, photovoltaics, logic gates and molecular wires. The limiting factor in the development and refinement of these systems is often the speed of fabrication, since the introduction of a minor change to the final compound may dictate a completely different synthetic pathway. One solution to this is the development of modular building blocks, whereby the system as a whole can be tweaked and optimised through the relatively facile substitution of a different building block during the synthesis. Nature provides us with an abundant, easily modified scaffold upon which to base our building blocks, namely DNA. A great deal of research has been conducted on modified DNA, with many different electronically active molecules being covalently bound¹. Our focus is on the multiple attachments of porphyrins and metal complexes to the DNA scaffold. Porphyrins are an ideal choice for this purpose due to the facile tunability of their electronic properties through modification of the attached substituents or through metallation of the porphyrin macrocycle and they can easily be attached to a variety of scaffolds. The same properties are true for terpyridine based metal complexes, hence provide a second very interesting modification unit.

Previous research in our group has focused on tetraphenyl porphyrins connected *via* a rigid acetylene linker (Fig. 1). We are still holding the record

for attaching the largest number (11) of such a large and hydrophobic substituent onto DNA.² Positioning all modifications on one strand leads to a destabilisation of the duplex, whereas when positioned on alternate strands (creating a zipper system) the modifications provide a significant degree of stabilisation to the system^{3,4}. The rationale for an enormous stabilisation effect of > 40 °C in the zipper system is in the π - π -stacking of the hydrophobic aromatic porphyrin molecules, leading to a positive interaction and outweighing the structurally unfavourable changes in the DNA duplex, which are inherently induced by such a large substituent. We have extended the concept to introduce a more flexible and longer propargyl-amide base connection. Molecular modelling shows an even distribution of the porphyrins along the major groove of the DNA (Fig. 1); CD spectroscopy has proven an invaluable tool to determine the structural influence of the new linkers on the DNA. Of particular importance was, in this case, the large electronic difference in the visible range, which arises from both different attachment and different metallation states. These features are not easily detectable using standard UV-vis spectroscopy.

Alongside the porphyrins, transition metal complexes based on terpyridine (terpy, Fig. 2) ligands are inherently interesting to study due to their large diversity in both electrochemistry and photophysics. We have recently synthesised the corresponding nucleoside-terpy building block and

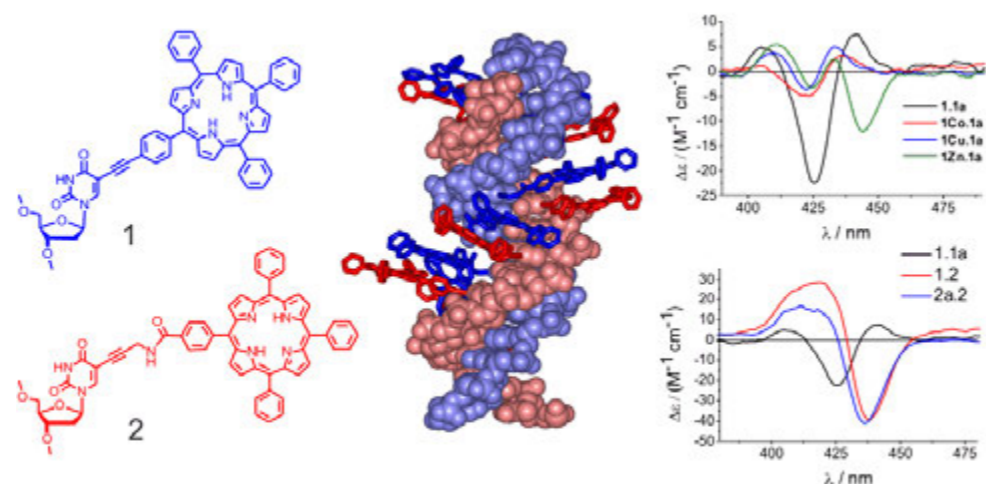
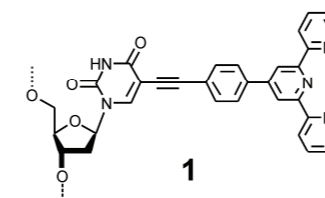


Figure 1: Left: structure of the porphyrin modifications with either rigid (1) or flexible (2) attachment; middle: modelled structure of the modified rigid-flexible hybrid-DNA (1.2) showing the even distribution of the porphyrins along the DNA major groove; right: CD spectra of metallated rigid-rigid DNA (without metal 1.1a, and with metal Co, Cu or Zn; only one of the complementary strands is metallated) (top) and CD spectra of the rigid-rigid (1.1a), rigid-flexible (1.2) and flexible-flexible (2a.2) porphyrin-DNA (bottom).



2 5'-CA \times TGTGAGGCA \times ACGTATCCA \times TGTGAGGCA \times ACGTATCCA \times TGTGAGGCA \times ACGTATC-3'
 3 5'-CC \times CAC AAT GGA \times AC GTA TG-3'
 2, 3: \times =T; 2t, 3t: \times =1

5'-CA \times TGTGAGGCA \times ACGTATCCA \times TGTGAGGCA \times ACGTATCCA \times TGTGAGGCA \times ACGTATC-3'
 3'-GTATGCA \times AGGTAACAC \times CCGTATGCA \times AGGTAACAC \times CCGTATGCA \times AGGTAACAC \times CC-5'

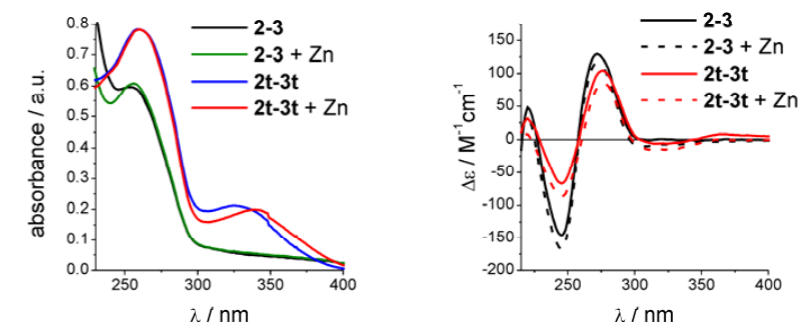


Figure 2: Terpyridine-DNA building block with DNA sequences (top). UV-vis and CD spectra are displayed at the bottom, showing the spectral differences between the modified and natural DNA in the presence and absence of metal (zinc).

incorporated it site specifically into DNA. To probe their efficiency as metal chelators, we have designed a supramolecular system which makes use of orthogonal binding modes to assemble nano-sized DNA structures (Fig. 3)⁵. First, the DNA strands were designed to be in part self-complementary with overhanging 'sticky ends'. Those sticky ends, which are again complementary to each other, will selectively anneal to form the DNA duplex according to the highly selective and specific base pairing. The result is that the strands, once mixed, will spontaneously form an almost infinitely long DNA strand. Or so we thought: AFM pictures revealed that the linear terpy-DNA actually folds into well-defined nano-rings of 50 to 100 nm diameter. By strategically placing terpy units into the strands, the metal binding units can now be used to connect different strands, and with it form an extended array of DNA. Again, CD spectroscopy has proven very valuable to follow the metal binding event. Furthermore, since the optical window of the chelator is outside that of the DNA, and seems very sensitive to the environment of the structure, it will provide a structural handle for further exploration. However, the combination of the base pairing and selective metal binding leads to the formation of nano-tubes, which are 50–200 nm wide and 2–50 nm high, and

have a length of several micrometers. This result can, to a certain extent, be explained by the fact that the terpy units are not positioned at exactly 180° in the DNA duplex, but rather form an angle of about 130°, thus facilitating the formation of tubular structures rather than flat sheets. Nevertheless, the directed formation of DNA nano-arrays through orthogonal self-assembly is still a very promising approach to obtain new functional materials.

The modifications, which we attach to the DNA and successfully characterise using the excellent facilities available at Diamond Light Source, are now under further investigation as optical handles to analyse DNA in more biological environments. As an example, we have designed molecular rulers based on porphyrin-DNA, which allows the analysis of DNA on a nanometer resolution; this ruler is now being applied to the study of DNA protein interactions.

References

1. Stulz, E., Clever, G., Shionoya, M. & Mao, C. DNA in a modern world. *Chem. Soc. Rev.* **40**, 5633–5635 (2011).
2. Fendt, L. A., Bouamaied, I., Thöni, S., Amiot, N. & Stulz, E. DNA as supramolecular scaffold for porphyrin arrays on the nanometer scale. *J. Am. Chem. Soc.* **129**, 15319–15329 (2007).
3. Brewer, A., Siligardi, G., Neylon, C. & Stulz, E. Introducing Structural Flexibility Into Porphyrin-DNA Zipper Arrays. *Org. Biomol. Chem.* **9**, 777–782 (2011).
4. Nguyen, T., Brewer, A. & Stulz, E. Duplex Stabilization and Energy Transfer in Zipper Porphyrin-DNA. *Angew. Chem. Int. Ed.* **48**, 1974–1977 (2009).
5. Burns, J. R., Zekonyte, J., Siligardi, G., Hussain, R. & Stulz, E. Directed Formation of DNA Nanoarrays through Orthogonal Self-Assembly. *Molecules*. **16**, 4912–4922 (2011).

Funding Acknowledgements

Funding by the EPSRC (EP/E045693/1, EP/F34296/1), BBSRC (DTA) and ATDbio Southampton is acknowledged.

DOI 10.1039/c0ob00535e

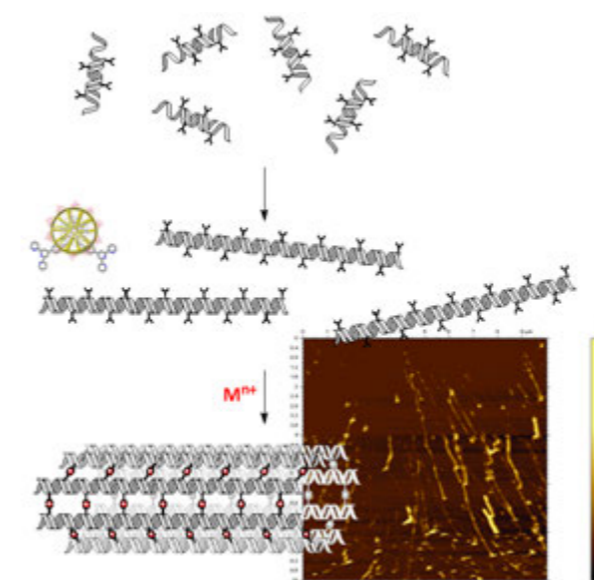


Figure 3: Putative representation of the annealing of long DNA strands through sticky-end recognition and formation of tubular assemblies by metal complexation (including AFM picture).

Effect of side chains on the conformational preference of cyclic α,β -peptoids

De Santis, E., Hjelmgard, T., Faure, S., Roy, O., Didierjean, C., Alexander, B. D., Siligardi, G., Hussain, R., Javorfi, T., Edwards, A. A. & Taillefumier, C. Cyclic α,β -peptoid octamers with differing side chain patterns: synthesis and conformational investigation. *Amino Acids*. **41** (3), 663-672 (2011)

The three dimensional structure (i.e. conformation) of natural proteins and peptides plays an important role in their biological activity and has led to the development of non-natural backbones which mimic such conformations and offers therapeutic advantages. Peptoids are peptidomimetics where the chemical modification is responsible for desirable chemical, physical and biological properties. The presence of tertiary amides in the peptoid backbone results in complex NMR spectra due to *cis/trans* isomerism of the amide bond. As a result, chiroptical techniques become essential tools for conformational investigation. Our study focuses on the conformational investigation of novel alternating α,β -peptoids to develop improved peptidomimetic scaffolds.

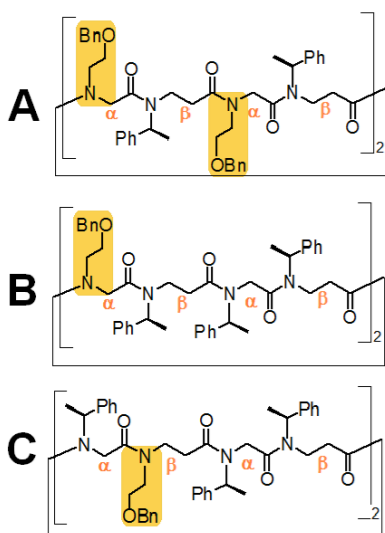


Figure 1: Cyclic peptoid octamers **A**, **B** and **C** with different side chain patterns. (Bn: benzyl; Ph: phenyl).

Peptoids are peptidomimetics, where the side chain is moved from the α -carbon to the adjacent amide nitrogen, generating a tertiary amide. This chemical modification is responsible for desirable chemical, physical and biological properties, e.g. different interactions along the backbone, flexibility, resistance to proteases and higher cell permeability. The presence of the tertiary amide is also responsible for the low energy barrier for the *cis/trans* isomerism of the amide bond, thus complicating NMR spectra. As a result, chiroptical techniques become essential tools for conformational investigation.

Our study focuses on the conformational investigation of novel alternating α,β -peptoids to develop improved peptidomimetic scaffolds for the display of carbohydrate antigens. The use of circular dichroism was essential for the conformational analysis of these novel compounds as the far UV below 200 nm was the most characteristic region and the high signal/noise ratio in this spectral region was essential for the understanding of the data.

Peptoids are structurally related to natural α -peptides, where the side chain is moved along the backbone from the α -carbon to the adjacent amide nitrogen.¹ Compared to peptides, they have key advantages; such as resistance to enzymatic hydrolysis¹ and improved cell permeability.² In addition, peptoids are not immunogenic³ and this is essential for the development of peptoid-based therapeutics. Due to these properties, peptoids have a vast potential for therapeutic application, some of which have already been considered to date and include mimicry of antimicrobial peptides and lung surfactant protein⁴ C.

The biological activity of natural peptides and proteins is related to

their sequence composition as well as to their three dimensional structure. Therefore, when generating synthetic peptidomimetics, their ability to fold into a three dimensional structure (i.e. conformation) needs to be considered and their conformational preference investigated. However, the conformational investigation of peptoids is complicated by their inherent flexibility due to the presence of tertiary amide bonds which are devoid of H-bonding donors. Thus the H-bonding potential of the peptoid backbone is significantly reduced. Also, the energy barrier for *cis/trans* isomerism of the tertiary amide is decreased relative to the secondary amide in peptides.⁵ As a result, interpretation of NMR spectra is generally complicated, and chiroptical techniques, such as circular dichroism, become essential tools for the conformational investigation of peptoids.

The use of SRCD was essential for the conformational analysis of these novel compounds as the far UV below 200 nm was the most characteristic region and the high signal/noise ratio in this spectral region was essential for the understanding of the data.

Our research has focused on investigation of the conformational preference of novel α,β -peptoids, which are composed of alternating α - and β -peptoid residues. In our previous work we have shown that, despite the decreased hydrogen-bonding potential of the peptoid backbone, linear and cyclic α,β -peptoids can adopt more than one ordered conformation⁶ and these can be perturbed by different solvent environments and temperatures.

In this study, we investigated the effect of different side chain patterns on the spectral features and conformational preference of α,β -peptoids.⁷ Three cyclic peptoids with different side chain compositions were selected for the study (Fig. 1).

Preliminary ¹H NMR studies were undertaken in CDCl₃, CD₃CN and CD₃OD but NMR signals could not be assigned due to the complexity deriving from the presence of *cis* and *trans* isomers of the tertiary amide in the NMR time scale. Despite this, octamer **C** had the greatest resolution in the ¹H NMR spectra and particularly in CD₃OD and CDCl₃. This was indicative of a smaller area of conformational space being sampled by **C**, i.e. a reduced conformational heterogeneity thus an increased population of some conformers. Notably, **C** also crystallised from methanol. To further investigate these observations, synchrotron radiation circular dichroism (SRCD) studies were undertaken. The use of SRCD was essential for the conformational analysis of these novel compounds as the far UV below 200 nm was the most characteristic region and the high signal/noise ratio in this spectral region was essential for the understanding of the data.

SRCD studies of **A-C** in MeCN showed similar spectral features (data not shown). By contrast, the SRCD spectra in MeOH showed that **C** had the

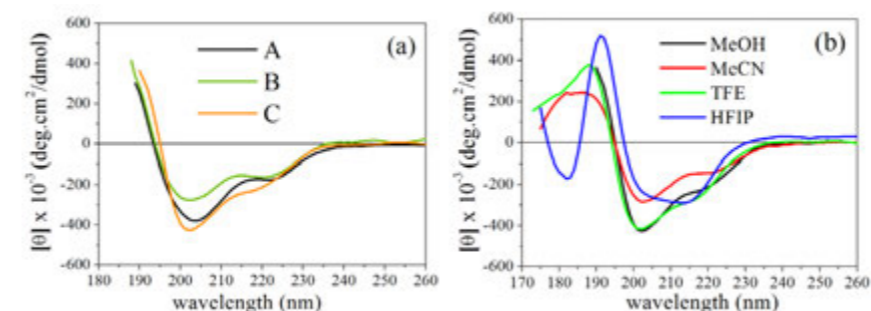


Figure 2: SRCD spectra of (a) cyclic octamers (A-C) with differing side chain sequences in MeOH and (b) octamer **C** in different solvents. All spectra were recorded at 20 °C at known concentrations in the range 205 - 255 μ M using a cylindrical cell of 0.01 cm pathlength.

greatest intensity of the molar ellipticity compared to other cyclic peptoids with different sequence patterns (Fig. 2a). This indicated that the side chain pattern promoted adoption of a preferred conformation or an ensemble of closely related conformations in MeOH. The same trend was also observed in 2,2,2-trifluoroethanol (TFE), whilst different spectral features were observed in 1,1,1,3,3,3-hexafluoro-2-propanol (HFIP) (Fig. 2b).

Octamers **B** and **C**, which have the same percentage of chiral side chains and only differ by the position of the *N*-2-(benzyloxy)ethyl side chain respectively on the α - or β -residue (Fig. 1), were studied at variable temperatures (data not shown) to give further insight into the effect of the side chain composition. Temperature studies in MeOH showed a greater change in molar ellipticity upon heating for **C** by contrast to **B**. A similar result was obtained in the other protic solvents investigated (TFE and HFIP). By contrast, the degree of change in MeCN (aprotic) was similar for **B** and **C**. This confirmed that the sequence pattern of **C** (with the *N*-2-(benzyloxy)ethyl on the β -residue) determined the adoption of a more ordered conformation.

To further explore the greater conformational order demonstrated for **C** in MeOH by contrast to MeCN, a solvent titration from MeCN to MeOH was undertaken. Interestingly, rather than the anticipated gradual increase of ellipticity with increasing MeOH, the most intense ellipticity was observed in 1:1 and 1:3 mixtures of MeCN : MeOH, and not in neat MeOH (Fig. 3). This indicated that the greatest conformational stabilisation occurred in the presence of a mixture of protic/aprotic solvents and can be explained by an intricate balance of inter- (i.e. solvent-peptoid) and intra-molecular interactions determining a favourable 'ordered solvation' where the conformational stabilisation is enhanced in a mixture of MeOH and MeCN rather than for each solvent in isolation.

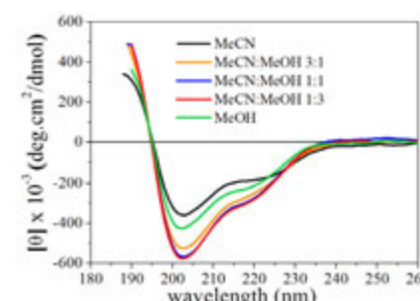


Figure 3: Titration of compound **C** in MeOH with increasing percentage of MeCN. All spectra were recorded at 20 °C in the solvent stated at the concentration of 229 μ M using a cylindrical cell of 0.01 cm pathlength.

Solvent titrations with MeCN and HFIP were also undertaken for both **B** and **C** (Fig. 4). It was found that in both cases the spectral features in MeCN were largely maintained until 100% HFIP where a conformational change was then observed, most clearly for **C** (Fig. 4b). However, a slight increase of ellipticity was observed for the 1:1 and 1:3 mixtures of MeCN : HFIP, suggesting that a combination of protic/aprotic solvents can increase conformational order but that a small amount of HFIP was not sufficient to induce the significant conformational change observed in neat HFIP.

The results of this study clearly demonstrated that the side chain patterns can affect the conformational preference of the α,β -peptoid backbone.

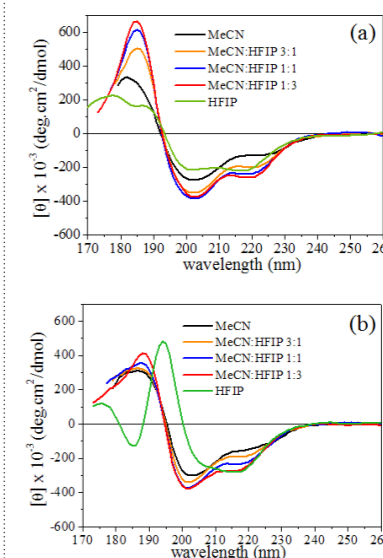


Figure 4: Titration of compound (a) **B** and (b) **C** in MeCN with increasing percentage of HFIP. All spectra were recorded at 20 °C in the solvent stated at 214 μ M for **B** and 208 μ M for **C** using a cylindrical cell of 0.01 cm pathlength.

In particular, positioning of the *N*-2-(benzyloxy)ethyl side chain on the β -residue was found to increase conformational order in protic solvents. This observation is vital for understanding the conformational preference of these novel systems and how this can be directed by the chemical structure. This work has significantly furthered efforts towards the engineering of compact ordered secondary structures of α,β -peptoids.

References

- Simon, R. J. *et al.* Peptoids: a modular approach to drug discovery. *Proceedings of the National Academy of Sciences of the United States of America*. **89**, 9367-9371 (1992).
- Kwon, Y.-U. & Kodadek, T. Quantitative evaluation of the relative cell permeability of peptoids and peptides. *Journal of the American Chemical Society*. **129**, 1508-1509 (2007).
- Astle, J. M. *et al.* A VEGFR2 antagonist and other peptoids evade immune recognition. *International Journal of Peptide Research and Therapeutics*. **14**, 223-227(2008).
- Patch, JA, *et al.* Versatile oligo(N-substituted) glycines: The many roles of peptoids in drug discovery. *Pseudopeptides in Drug Discovery*, ed. PE Nielsen, Wiley-VCH Weinheim, Germany, 1-31 (2004).
- Moehle, K. & Hofmann, H. J. Peptides and peptoids - A quantum chemical structure comparison. *Biopolymers*. **38**, 781-790 (1996).
- Hjelmgard, T. *et al.* Convenient solution-phase synthesis and conformational studies of novel linear and cyclic α,β -alternating peptoids. *Organic Letters*. **11**, 4100 - 4103 (2009).
- De Santis, E. *et al.* Cyclic α,β -peptoid octamers with differing side chain patterns: synthesis and conformational investigation. *Amino Acids*. **41**, 663-672 (2011).

Funding Acknowledgements

The authors acknowledge the Medway School of Pharmacy for the PhD scholarship for Ms De Santis.

DOI 10.1007/s00726-011-0887-1

Innovative methods for protein-nanoparticles interactions using synchrotron radiation circular dichroism

Laera, S., Ceccone, G., Rossi, F., Gilliland, D., Hussain, R., Siligardi, G. & Calzolari, L. Measuring protein structure and stability of protein-nanoparticle systems with synchrotron radiation circular dichroism. *Nano Lett.* **11**, 4480-4 (2011)

Nanoparticles (NP) are used in different applications such as cosmetics and medicine. To assess potential toxic effects and to design NP-based drug delivery systems it is critical to understand what happens to proteins upon interaction with these special particles. This information is difficult to obtain, but for the first time we have shown that using the B23 beamline, it is possible to detect and analyze structural changes of proteins in protein-metallic nanoparticle complexes¹. By using synchrotron radiation circular dichroism (SRCD) we have measured the structure and stability changes of proteins upon their interaction with nanoparticles at nanomolar concentration. In particular, we measured a decrease of 6°C in the thermal unfolding of human serum albumin upon interaction with silver nanoparticles. This effect does not emerge with gold nanoparticles. SRCD allows the measurement of critical parameters for protein-nanoparticle interactions by using only a few micrograms of proteins, providing the relative stability of key proteins. This information will help understanding and predicting the potential toxicity of nanomaterials. In addition it may contribute to the design of the next generation of non toxic nanoparticle-based drug delivery systems.

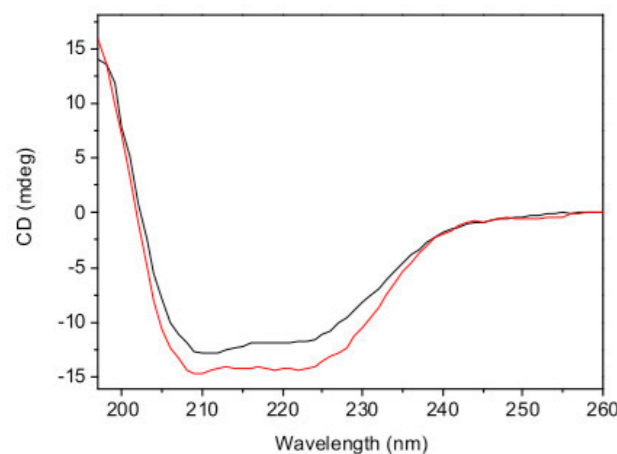


Figure 1: CD spectra of HSA 20nM (black line) and HSA 20nM+AgNP (red line).

Nanotechnology is gaining more and more interest in many industrial activity fields. Nanoparticles are already extensively used in widely different applications such as cosmetic sunscreens, in diagnostics and in medicine as drug delivery systems². When nanoparticles enter a biological system, they become coated with a complex mixture of proteins (the so-called protein corona³) and this interaction can both alter the properties of the nanoparticles and of the interacting proteins. In particular it has been

shown that this interaction can change enzymatic activity, alter protein conformation, expose previously hidden epitopes⁴, and all these alterations can induce unexpected biological reactions and lead to toxicity⁵. In order to investigate possible toxic effects of nanoparticles and to design the next generation of drug delivery systems, it is essential to understand what happens to the structure and stability of relevant proteins upon interaction with it. Unfortunately this kind of information is very difficult to obtain due to the very complex nature of the system (solid/liquid interface) and the experimental constraints, usually the amount of protein-NP is very low.

Circular dichroism (CD) is an excellent and sensitive method for rapidly evaluating the secondary structure, folding and binding properties of proteins, and recently has also been used to detect structural changes of proteins interacting with nanoparticles⁶. The use of synchrotron radiation to perform CD experiments presents several advantages with respect to the conventional CD technique. The major advantage is the high flux provided by synchrotron radiation that allows CD data to be measured both with very low amounts of proteins and in the presence of highly absorbing chemicals such as suspensions of gold and silver nanoparticles. It enables the detection of the secondary structure of proteins with only a few hundred nanograms in the spectral range of 195-250 nm.

Using beamline B23 at Diamond Light Source we have shown that, using a 10 cm cell with total volume under 0.8 ml, it is possible to detect and

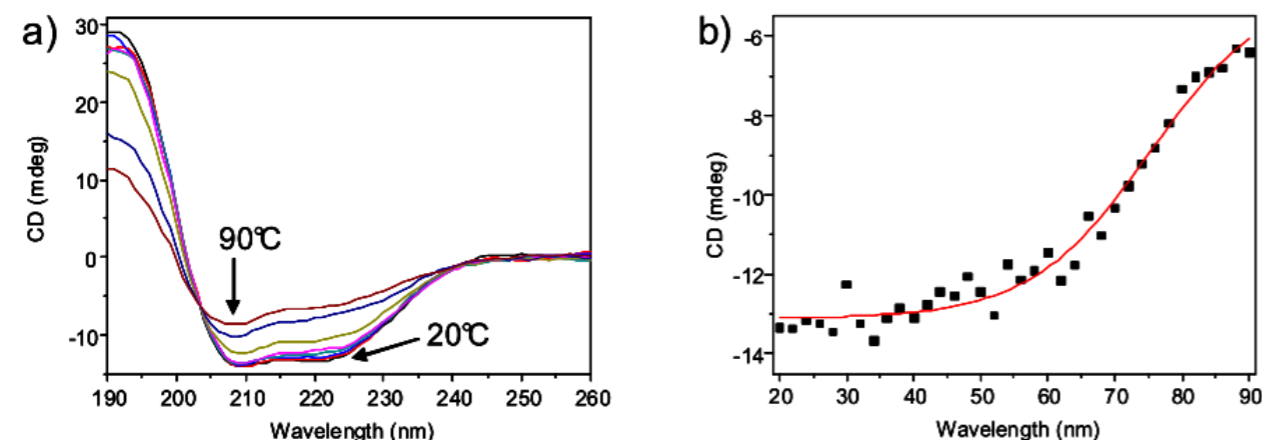


Figure 2: Thermal unfolding of free HSA 80nM. (a) CD spectra at selected temperatures. (b) Complete temperature unfolding profile at 222nm with sigmoidal fit (red line) to calculate melting temperature.

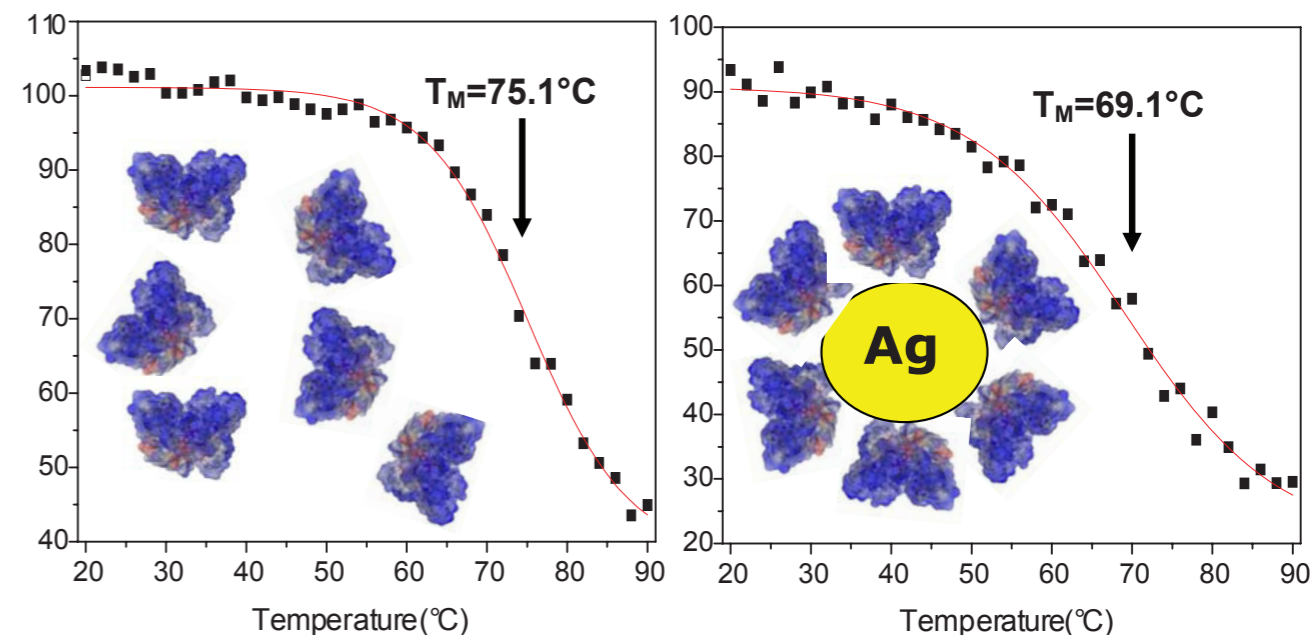


Figure 3: Thermal unfolding of free HSA and HSA-AgNP complex.

analyse structural changes of proteins in the low nanomolar concentration range when forming stable non-covalent protein-metallic nanoparticle complexes. In particular, we measured the secondary structure of human serum albumin (HSA) in a well-defined stoichiometric complex with silver (AgNP) and gold (AuNP) nanoparticles at nanomolar concentrations. An example of these studies is illustrated in Fig.1, where the SRCD data of the HSA/AgNP system are reported.

In addition we have been also able to follow the changes in the thermal stability of human serum albumin when complexed to metallic nanoparticles. Fig. 2 shows the thermal unfolding of free HSA and the fitting of the data used to calculate the melting temperature (T_m) of the protein. By collecting the CD spectra of the protein at variable temperatures between 20°C and 90°C and fitting the data of the protein unfolding with a sigmoid equation (indicative of a cooperative unfolding process) we calculated a melting temperature of 75.1°C for the free HSA protein.

By repeating this experiment with HSA-AuNP and HSA-AgNP we could calculate the melting temperature of the human serum albumin protein when interacting with AuNP ($T_m = 74.8^\circ\text{C}$) and with AgNP ($T_m = 69.1^\circ\text{C}$). The comparison of the unfolding of HSA in the three conditions (alone, -AgNP, -AuNP), partially shown in Fig.3, indicates that upon interaction with silver nanoparticles the protein changes its melting temperature from 75.1°C to 69.1°C. This decrease of 6°C in the melting temperature indicates that upon interaction with AgNP the serum albumin significantly reduces its thermal stability. On the other hand a similar destabilisation is not observed in the case of HSA-AuNP complexes, which have a melting temperature of 74.8°C, experimentally indistinguishable from the T_m value for the protein alone.

Our work shows that by using synchrotron radiation circular dichroism it is possible to analyse the secondary structure and stability of proteins in the low nanomolar concentration range, thus providing a unique method for detecting the relative stability of key biological proteins interacting with nanoparticles. In particular, this extreme sensitivity has allowed us to show

that human serum albumin is significantly destabilised when interacting with silver nanoparticles, while its stability is not affected when interacting with gold nanoparticles. The high sensitivity provides structural information on protein-nanoparticles complexes at near equimolar ratios and allows access to detailed information that has been very difficult to obtain until now.

References

- Laera, S. *et al.* Measuring protein structure and stability of protein-nanoparticle systems with synchrotron radiation circular dichroism. *Nano Lett.* **11**, 4480-4 (2011).
- Petros, R. A. & DeSimone, J. M. Strategies in the design of nanoparticles for therapeutic applications. *Nat Rev Drug Discov.* **9**, 615-627 (2011).
- Cedervall, T. *et al.* Understanding the nanoparticle-protein corona using methods to quantify exchange rates and affinities of proteins for nanoparticles. *Proceedings of the National Academy of Sciences.* **104**, 2050-2055 (2007).
- Deng, Z. J., Liang, M., Monteiro, M., Toth, I. & Minchin, R. F. Nanoparticle-induced unfolding of fibrinogen promotes Mac-1 receptor activation and inflammation. *Nat Nanotechnol.* **6**, 39-44 (2011).
- Nel, A. E. *et al.* Understanding biophysicochemical interactions at the nano-bio interface. *Nat Mater.* **8**, 543-57 (2009).
- Shang, W. *et al.* Cytochrome C on silica nanoparticles: influence of nanoparticle size on protein structure, stability, and activity. *Small.* **5**, 470-6 (2009).

DOI 10.1021/nl202909s

Technical Developments

G. Cinque, G. Siligardi, K. Inoue, M. Malfois and N.J. Terrill

BioSAXS at Diamond

BioSAXS, solution scattering from proteins and other macromolecules, is an important and growing aspect of Small Angle X-ray Scattering (SAXS) worldwide. Based on the needs of the user community, Diamond has invested in state of the art delivery systems. The technologies described in this article are either available at Diamond on I22 now or will be available from October 2012 onwards.

Development of a micro-droplet flow system for BioSAXS

The development of a micro-droplet flow system for BioSAXS has been the subject of a collaboration between Diamond Scattering Group and University of Reading started in 2009. Essentially, the micro flow system uses a capillary cell which is connected to a syringe pump via fluorinated tubing and is capable of delivering microlitre volume droplets. Full automation of droplet flow and data collection has been achieved by exploiting the significant change in transmission between air and water-based sample droplets. It was shown that a minimum sample volume of 1 µl was sufficient to measure a useful scattering pattern (Fig.1). Another advantage of this system is its simplicity of setting up and therefore this system would also suit the high throughput concept. After commissioning with a range of standard proteins, this system was successfully used to study a range of challenging biological systems. One of the most successful experiments was carried out in collaboration with Dr. Watson (University of Reading) to investigate a scarce transmembrane protein.

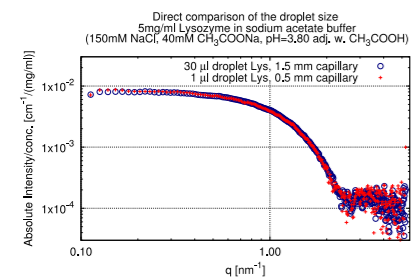


Figure 1: Direct comparison of a 1 and 30 micro litre droplet of the very same lysozyme sample.

Beamline I22 - First Stop flow BioSAXS experiments

A stopped-flow instrument is a rapid mixing device used to study the kinetics of reactions in a solution system. After two or more solutions containing the reagents are mixed, SAXS measurements can be collected with millisecond time resolution. A 4-syringe-type stopped-flow apparatus has been installed on I22 for the dynamical study of protein function, molecular motion, and molecular assembly processes etc. The first experiment with a protein solution was carried out on the flavoprotein NADPH-cytochrome P450 reductase (CPR) system. It is well known that CPR supplies electrons to cytochromes P450 which play a central role in drug metabolism. There is evidence showing a domain movement in CPR plays an important role in electron transfer from NADPH to P450 and such the domain motion may contribute to the rate-limiting step. The kinetics of the domain movement, relating to the interflavin electron transfer, was studied

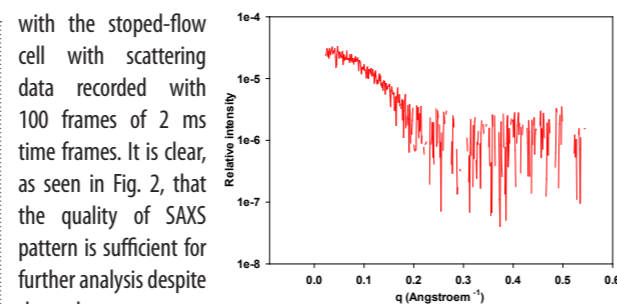


Figure 2: Scattering from cytochrome C, which was measured with the stop flow system.

Solution SAXS experiments with inline HPLC system

High-performance liquid chromatography (HPLC) is a chromatographic technique used to separate a mixture of compounds in analytical chemistry and biochemistry with the purpose of identifying, quantifying and purifying the individual components of the mixture. A specialised online sample environment for solution SAXS experiments, combining a commercially available HPLC system (Agilent 1200 Series) with a specially designed capillary sample cell has been built and commissioned for I22. Between the separating column and the end fraction collector, the separated components of the solution pass through a capillary cell, allowing SAXS measurements to be made. During commissioning a range of cells were tested. Developed



Figure 3: The flow cell for HPLC/SAXS system.

through the collaboration between Reading University and Diamond, a shared design for the HPLC and micro-droplet cell has been established with appropriate adaptors for each sample environment (Fig. 3). The flow cell consists of a 2 mm-thick capillary, consequently giving a higher signal to noise ratio for BioSAXS samples.

Test experiments with standard protein samples, such as lysozyme, bovine serum albumin and ovalbumin, have confirmed that the HPLC system works well. Moreover, a trial experiment with the size exclusion column was carried out on E. coli chaperonin, GroEL, successfully obtaining SAXS data (Fig. 4). It has been established that approximately 100 µl of 10 mg/ml will be needed to get optimal data for further analysis from this system. It should be noted that a whole concentration series SAXS data can be obtained from just one injection with these conditions. This principle will allow reduced total quantities of protein to be used and as a result will fit the high throughput concept for the systems. We expect to offer the HPLC system for users after some final commissioning experiments on the *in situ* separation of protein mixture samples in April 2011.

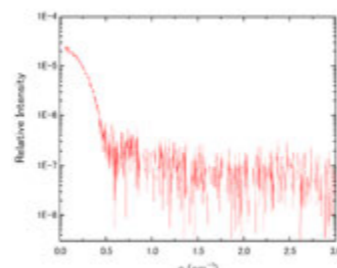


Figure 4: SAXS curve from GroEL recorded with HPLC system.

BioSAXS robot

The EMBL-Grenoble designed BIOSAXS robot, now used at both the ESRF and PETRA III (DESY), was purchased to promote high-throughput studies in the BioSAXS field and is now in final manufacture by MAATEL. The basic concept of this BioSAXS robot is the same as the micro-drop equipment described above, but additionally comprises a temperature-controlled auto-sampler connecting with the high performance pump system (Fig. 5). Protein samples which are located on a 96-well plate in the auto-sampler

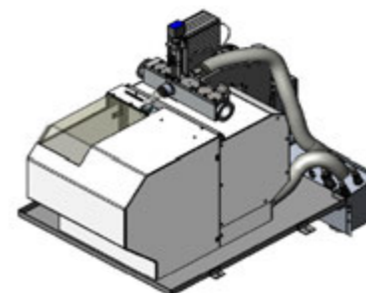


Figure 5: The main component of BioSAXS robot (schematic drawing).

SAXS studies can be carried out in a fully automated manner. The robot has a capability to perform with a minimum sample volume of 5 µl at a maximum rate of 20 measurements an hour. The robot will be delivered to Diamond in mid June 2012 and is planned to be commissioned on I22 before its ultimate home, B21, is available. We aim to ensure all sample environments described are compatible across the two SAXS beamlines at Diamond.

Further Developments

Beamline B22 – Overview of the IR beamline

The design of IR beamline B22 (MIRIAM) allows the two separate end stations to be operational from the same beamline mirror optics and front end by using, respectively, the bending and edge synchrotron radiation available from the B22 bending magnet source. A unique feature of B22, with respect to other synchrotron IR beamlines worldwide, is its in-vacuum environment along the complete length of the beam path. The two end stations can be operated independently and, by a detector upgrade also implemented in 2011, they are both capable of point-by-point IR microspectroscopy and mapping via single detector (scanning mode), and IR imaging by a pixellated Focal Plane Array detectors (full field mode). This last mode is still a novelty among the set up found routinely at other facilities, especially in combination with the 74x magnification objective/condenser at the microscope.

Preliminary tests are in progress on a microfluidic device for *in vivo* experiments of single cell in aqueous environment in collaboration between B22 staff and Manchester University.

The beamline B22 was conceived as a research tool to perform IR absorption microscopy and spectroscopy at the maximum spatial resolution, highest sensitivity and signal to noise ratio attainable.

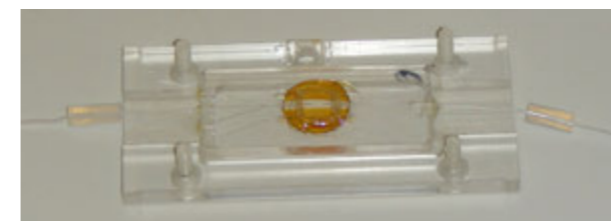


Figure 6: Close up of prototype microfluidic device for B22.



Figure 7: Experimental hut of the IR beamline B22.

The IR beamline at Diamond offers an extremely bright microbeam with optimal optical performance exceeding the signal-to-noise specifications in the mid-IR range at the microscopes, and allows spectroscopic analysis via Fourier Transform IR interferometry over a wider spectral range up to the far-IR/THz regime. Running with the latest introduction, the machine in low-alpha mode, this enables spectroscopy to be done using coherent synchrotron radiation up to 2 millimetre wavelength.

Beamline B23 - High Throughput

The 96-well multiplate attachment (Fig. 8) for B23 was successfully commissioned. Preliminary testing with reference protein samples

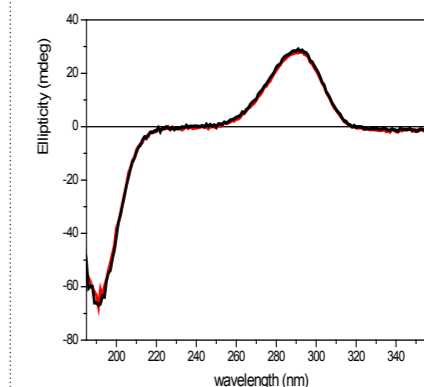
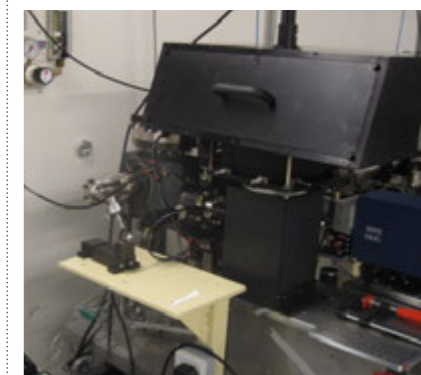


Figure 8: Left - Assembled multiplate chamber operated using B23 module A. Right - Proof of concept of CD spectra of camphor sulphonic acid (CSA) measured successfully in two different cell wells (red and black lines).

and standard reference material was successfully carried out. The sample unit of this high throughput attachment will be optimised. Further rigorous testing of the unit will be implemented before release to the users. This will greatly enhance the capability of the circular dichroism (CD) beamline for the characterisation of biological molecules as a function of solvent polarity/concentration, ligand interaction, pH, UV-stability, and perturbing agents such as denaturants and detergents. In addition, the wavelength capability of Module A has been extended down to 125 nm. This will benefit users who measure solid films. Special cuvette cells of small volume capacity that exploit the B23 microbeam have been designed and are now available for users to carry experiments that cannot be achieved with commercial bench-top CD instruments.

References

1. Seddon, A.M. *et al.* A highly oriented cubic phase formed by lipids under shear. *JACS*. 7,133(35), 13860-3 (2011).

The broadband far-IR coherent synchrotron radiation from beamline B22 in low α -mode: a new scientific tool for experiments in the THz gap at Diamond

Cinque, G., Frogley, M. and Bartolini, R. Far-IR/THz spectral characterization of the coherent synchrotron radiation emission at Diamond IR beamline B22, *Rendiconti Lincei* **22**, 33-47, (2011)

The beamline B22 at Diamond is a Multimode Infrared (IR) Imaging And Microspectroscopy beamline known as MIRIAM. This beamline has been operational since late 2009 for diffraction limited microscopy and imaging in the mid-IR range. Since its design, the broadest IR regime was also foreseen for general Fourier Transform IR (FTIR) spectroscopy. Diamond introduced a new mode of operation for Synchrotron Radiation (SR) called low alpha, which generates significantly shorter electron bunches for time resolved studies across a broad range of science activities from solid state physics to Life Sciences ranging from hydrogen bond formation to collective modes in organic complexes.

The scientific driver for using far-IR radiation in the millimeter wavelength range, also known as the 'TeraHertz gap', has grown with the technical availability of tunable or broadband intense THz sources. For example in Life Sciences, access to the TeraHertz gap allows the study of folding/twisting of large molecules or biological complexes, DNA inter- and intra-molecular modes enzyme activity, conformational changes as well as hydrogen tunneling. In condensed matter physics straightforward applications concern far-IR optoelectronic/photonics devices, including new IR detector materials, superconductor characterization, inter-/intra-band e-transitions in structured semiconductors, phonon band observation in solid phase transitions and vibronic modes in molecular crystals.

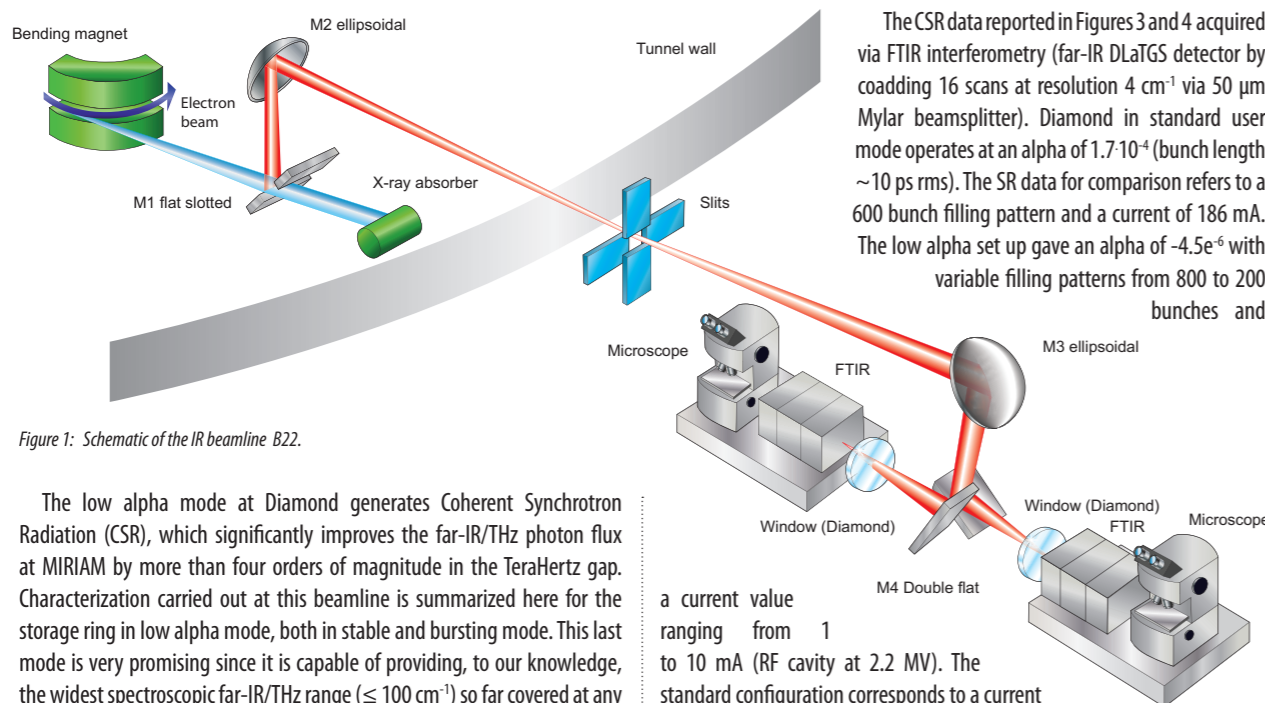


Figure 1: Schematic of the IR beamline B22.

The low alpha mode at Diamond generates Coherent Synchrotron Radiation (CSR), which significantly improves the far-IR/THz photon flux at MIRIAM by more than four orders of magnitude in the TeraHertz gap. Characterization carried out at this beamline is summarized here for the storage ring in low alpha mode, both in stable and bursting mode. This last mode is very promising since it is capable of providing, to our knowledge, the widest spectroscopic far-IR/THz range ($\leq 100 \text{ cm}^{-1}$) so far covered at any SR facility worldwide.

Generating significant intensity and broadband electromagnetic radiation in the THz region, which lies between wavelengths from 3 mm to 30 μm , (0.1 to 10 THz, respectively), is not straightforward. Storage rings at modern SR facilities already cover broad IR emission, with high stability and afford considerable advantage in microspectroscopy in terms of excellent signal-to-noise ratio and microbeam. Long wavelength SR emission can be enhanced using intra-bunch electron coherence. Shortening an e- bunch to millimeter length allows comparable electromagnetic wavelengths to positively interfere. Minimization of the momentum compaction factor or

low-alpha lattice is implemented at a number of light sources (MLS, BESSY, Elettra, and ANKA in Europe, NSLS in USA, or Australian Synchrotron) mostly in stable conditions² with some noticeable recent exceptions³.

The low-alpha mode for Diamond has been in development since 2005 by Martin *et al.*⁴ and the CSR performance was recently studied at MIRIAM for the far-IR range⁵.

Figure 1 gives an overview of how MIRIAM exploits the radiation emitted by the bending magnet⁶. The IR emission from B22's bending magnet is plotted in Figure 2 as an intensity map at 1 THz. The image shows that the far-IR radiation is fully gathered at the longest IR wavelength.

The CSR data reported in Figures 3 and 4 acquired via FTIR interferometry (far-IR DLaTGS detector by coadding 16 scans at resolution 4 cm^{-1} via 50 μm Mylar beamsplitter). Diamond in standard user mode operates at an alpha of $1.7 \cdot 10^{-4}$ (bunch length $\sim 10 \text{ ps}$ rms). The SR data for comparison refers to a 600 bunch filling pattern and a current of 186 mA. The low alpha set up gave an alpha of $4.5 \cdot 10^{-6}$ with variable filling patterns from 800 to 200 bunches and

a current value ranging from 1 to 10 mA (RF cavity at 2.2 MV). The standard configuration corresponds to a current equivalent per bunch between 1 and 6 μA (bunch length $\sim 2 \text{ psec}$), whereas these values are between 10 and 50 μA current per bunch (bunch length $\sim 4 \text{ psec}$) in the special low alpha mode.

The first set of data in Figure 3 refers to CSR IR spectra in stable low alpha mode over 800 bunches. The prominent feature is a well defined coherent emission peak centered around 11 cm^{-1} and FWHM 8 cm^{-1} . This is the clear fingerprint of CSR emission corresponding to an e- bunch length of 0.9 mm (3 psec) FWHM. The second most important feature is the superlinear behavior of the total intensity of the emission as a function of the current, which is a signature of the electron coherence effect. With respect to normal

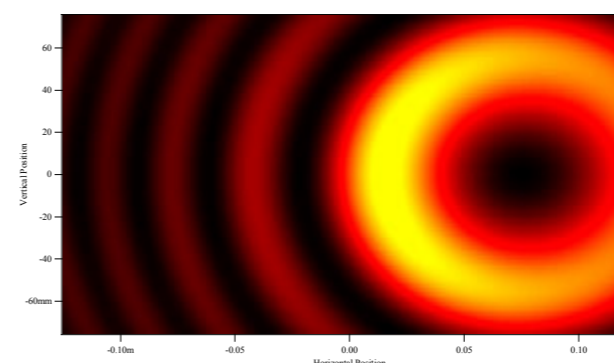


Figure 2: SR IR emission at 1 THz (map in false color) from B22 bending magnet source.

user mode, the gain in CSR photon flux is evident below 30 cm^{-1} and reaches 1000 times above normal mode SR.

The second set of data in Figure 4 concern the bursting mode low alpha over 200 bunches. The logarithmic plots reveal the wider far-IR range up to 100 cm^{-1} . The intensity of the photon flux is more than quadratic with the current and the gain in the region below 70 cm^{-1} reaches 10000 times normal mode SR.

The experimental findings summarised here for low alpha mode support the conclusion that CSR operation at MIRIAM is feasible, that far-IR/THz absorption spectroscopy can be performed, and that a uniquely wide spectral range is accessible in bursting mode. This is very promising since this special mode is capable of providing a unique facility for a wide range of science applications.

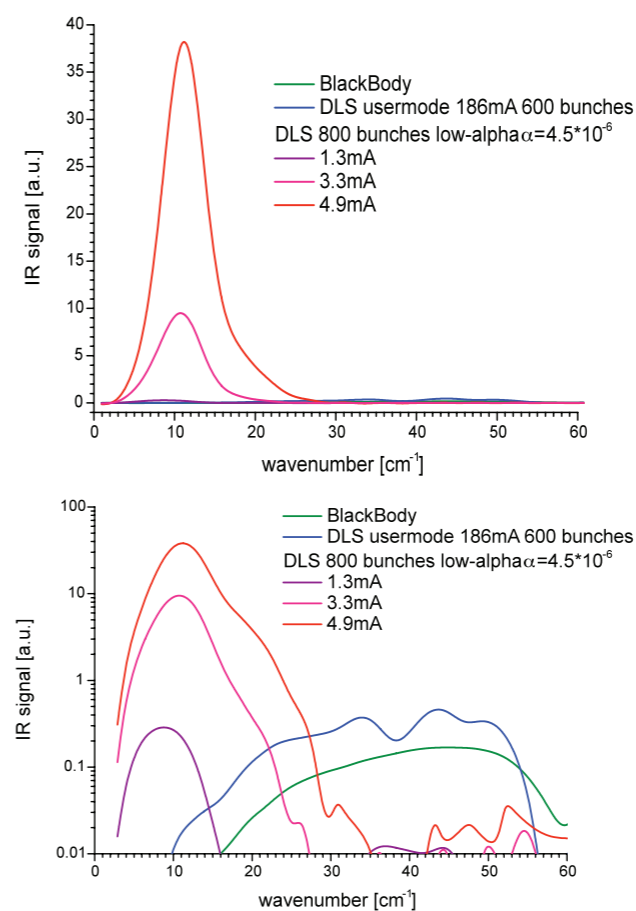


Figure 3: IR spectra in linear (left) and logarithmic (right) scales acquired in stable low alpha mode at B22.

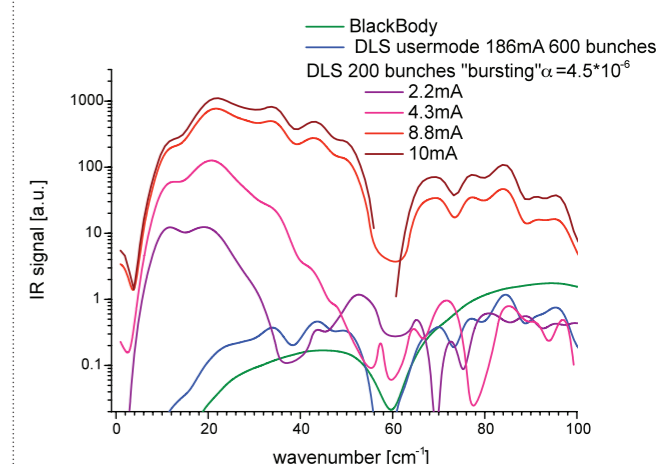
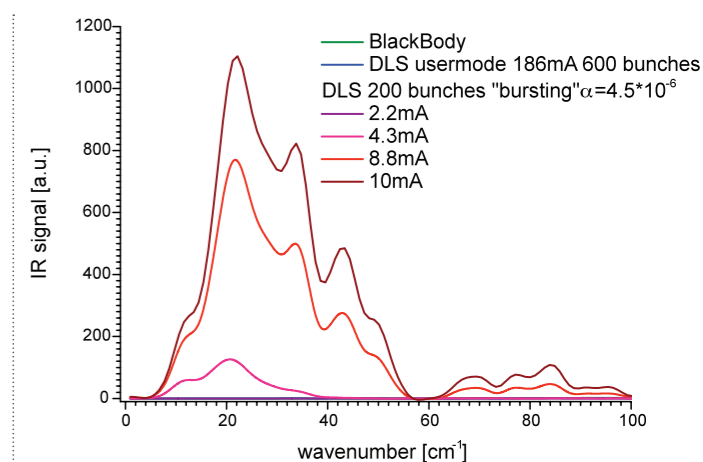


Figure 4: IR spectra in linear (left) and logarithmic (right) scales acquired in bursting low alpha mode at Diamond IR beamline.

References

- Williams, G.P. Filling the THz gap - high power sources and applications. *Rep Prog Phys.* **69**, 301-326, (2006).
- Abo-Bakr, M., Feikes, J., Holldack, K., Wüstefeld, G., Hübers, H.-W. Steady-State Far-Infrared Coherent Synchrotron Radiation detected at BESSY II. *Phys. Rev. Lett.* **88**, 254801 (2002).
- Karantzoulis, E., Penco, G., Perucchi, A., Lupi, S. Characterization of coherent THz radiation bursting regime at Elettra. *Infrared Phys and Tech.* **53**, 300 (2010).
- Martin, I.P.S., Rehm, G., Thomas, C. and Bartolini, R. Experience with low-alpha lattices at the Diamond Light Source. *Phys. Rev. Spec. Topics-Acc. and Beams*, **14**, 040705 (2011).
- Cinque, G., Frogley, M.D., Bartolini, R. Far-IR/THz spectral characterization of the coherent synchrotron radiation emission at diamond IR beamline B22. *Rendiconti Lincei* **22**, 33-47, (2011).
- Cinque, G., Frogley, M., Wehbe, K., Filik, J., Pijanka, J. Multimode InfraRed Imaging and Microspectroscopy (MIRIAM) Beamline at Diamond. **24**, 24-33 (2011).

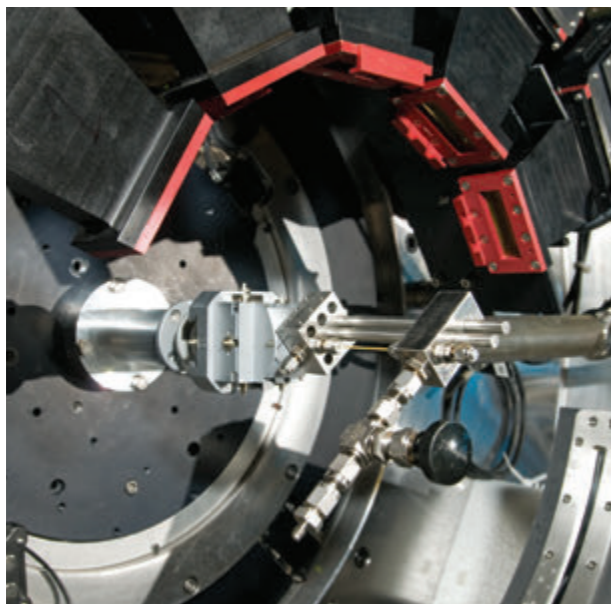
DOI 10.1007/s12210-0

Engineering and Environment Village

Chiu Tang, Village Coordinator

In the Engineering and Environment Village, we now have three operational beamlines: I15 Extreme Conditions, I11 High Resolution Powder Diffraction and I12 Joint Engineering, Environmental and Processing, JEEP. The first two beamlines have maintained their operational effectiveness, supporting thousands of user hours and performing many routine experiments, as well as challenging experiments. The operational time (user beamtime) of our newest beamline, I12 has increased in the reporting year, offering multiple X-ray techniques such as imaging, tomography, single crystal and powder diffraction and small angle scattering (SAXS). The new second experimental hutch in the external building is now fully operational, supporting sample environments up to 2 tonnes in weight, using similar techniques to those already available in the first experimental hutch. With this additional facility, high energy SAXS experiments with a sample-detector distance of 30 m are now possible. As all the beamlines' hardware and software have been improved, their performance and reliability have also increased. In addition, new instrumental developments or upgrades have further enhanced their capabilities. As a consequence, our users, together with beamline staff, have continued to publish many papers from the results using these facilities. The articles here are representative contributions reflecting the interesting work performed in this village. We also have contributions describing the commissioning of recent upgrades.

The high pressure capability of I15 using high-energy angular-dispersive diffraction has continued to produce interesting new science. The common theme of the user contributions is structural changes under strong compression, achieved using small volume diamond anvil cells. The high pressure (HP) structural behaviour of mineral barite (BaSO_4) was studied by David Santanaría-Pérez and co-workers. Although the mineral is of great interest for Earth and material sciences, the behaviour under compression was poorly understood before this study. The research group have therefore accurately measured the structural sequence and compressibility of the mineral from ambient to high pressure. The effect of pressure on Bismuth atomic displacement in pyrochlore structured materials at non-ambient

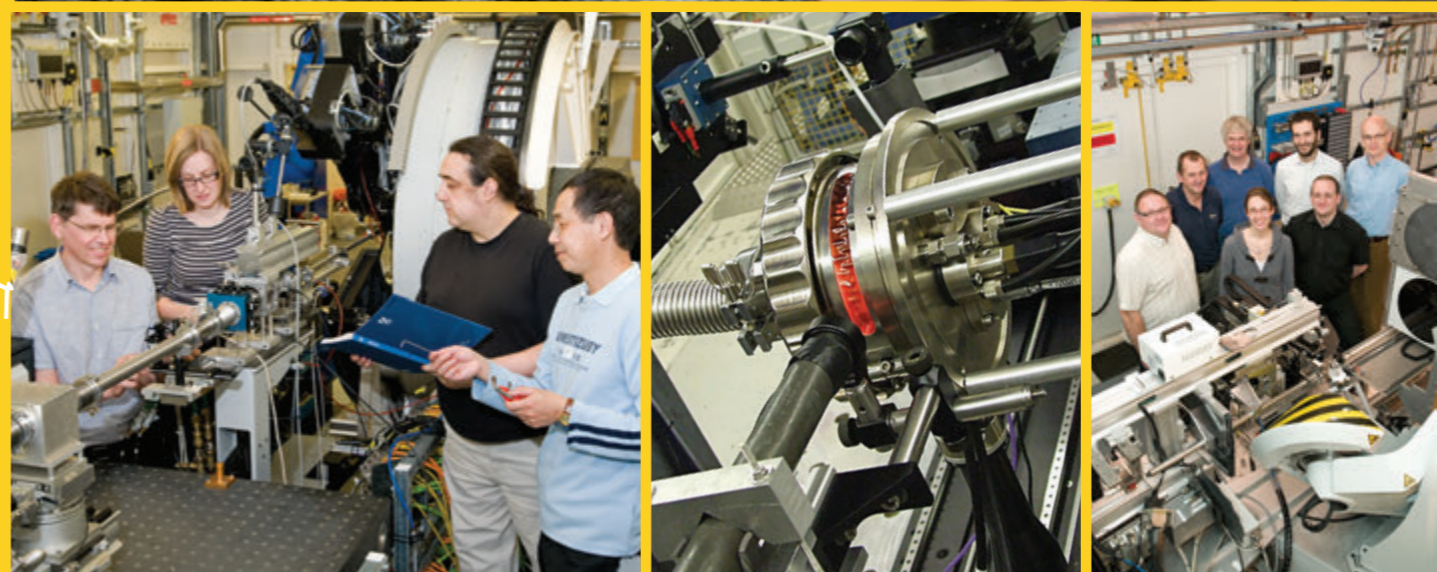


temperatures has been investigated by Andrew Hector and his colleagues. They examined the interaction between Bi atoms that are responsible for structural changes in the crystal lattices of Bi-Ti and Bi-Sn oxide pyrochlores. Complex melting behaviours under compression are commonly observed in alkali metals. Considering the similarities in HP behaviour of potassium with that of the other alkali metals, its apparent simple or normal melting curve reported in the literature is surprising. Olga Narygina et al. have recently re-measured the melting curve of K using I15 and the results presented are very different from previously reported. They conclude that the complex

behaviour closely resembles that of Na, and is related to structural and electronic changes in the solid/liquid phase.

The high resolution (HR) mode of beamline I11 using multi-analysing crystals (MAC) detectors has continued to work reliably and produced the bulk of the publications by our users. Andrew Cooper and his research group contributed the latest research on microporous crystalline cages, which are promising framework materials for gas storage, carbon capture and sequestration. The new porous crystals they have synthesised show exceptionally high gas uptakes for this class of material. Another research group (Alvaro Mayoral et al.) also studied a microporous solid (Ag-zeolite A) using the I11 HR capability. Complementary results were obtained from atomic resolution electron microscopy, and the detailed crystalline structure of the zeolite was described, including the locations of catalytic Ag atoms in the framework. With high quality powder diffraction data obtained from multiferroic fluorides at non-ambient temperatures, Philip Lightfoot describes how his team have observed unexpected and complex phase behaviour in these materials. The new results could help with the interpretation of the electrical and magnetic behaviour reported in the literature.

The contributions from the JEEP beamline I12 show the versatility of this instrument, which uses high energy X-rays (50-150 keV). Firstly, the mapping of the orientation of crystalline grains and strain in thick (several mm) engineering samples were performed using transmission Laue micro-beam diffraction. Felix Hofmann, his colleagues and beamline staff have developed two novel setups for the mapping of microstructure, lattice orientation and elastic strain in individual grains of polycrystalline engineering materials. The other two contributions used *in situ* energy dispersive powder diffraction with two different sample environments. Using a specifically designed electro-winning cell and furnace, Matthew Rowles and co-workers studied the structural and chemical changes of an inert electrolysis anode at a high temperature. As molten-salt electrolysis is used extensively in the production of light metals, an inert probe, if operated reliably, is more cost effective and has a much lower environmental impact compared with a conventional reactive carbon anode. The final research group (Gareth Williams et al.) studied the intercalation chemistry of the layered double hydroxide, $\text{Al}(\text{OH})_2$, using an in-situ reaction cell. The results obtained have revealed the interesting insights into the reaction mechanisms.



Atomic resolution analysis of silver ion-exchanged zeolite A

Mayoral, A., Carey, T., Anderson, P. A., Lubk, A. & Diaz, I. Atomic Resolution Analysis of Silver Ion-Exchanged Zeolite A. *Angew. Chem. Int. Ed.* **50**, 11230–11233(2011)

Electron microscopy is currently one of the most powerful techniques for the characterisation of inorganic solids, which unfortunately presents some difficulties with respect to zeolites due to their strong beam sensitivity. By controlling the beam current, we have successfully managed to image the most beam sensitive zeolite: zeolite A (LTA structure type; Si/Al = 1) and capture the distribution of silver within the cages, observing directly for the first time silver octahedra composed of 6 atoms. These results were compared to those obtained through Rietveld refinement of the structure against powder synchrotron X-ray diffraction data collected on I11, corroborating the formation of such species.

Zeolites are microporous inorganic solids first noted by a Swedish mineralogist, Baron Axel Fredrik Cronstedt, in 1756, who discovered examples in Iceland and in a mine in the north of Sweden. The first zeolite synthesis was carried out in 1948 with Barrer's synthesis of mordenite¹. Industrial applications became apparent in the 1950's with zeolites finding usage as dryers for gases and as molecular sieves. In 1962, zeolite X was introduced as a cracking catalyst. About ten years later, zeolite A started to replace phosphates in detergents.

Zeolites have a pore size below 20 Å and their structure is based on infinitely extending three-dimensional, four-connected frameworks of AlO₄ and SiO₄ tetrahedra, linked to each other by sharing oxygens. The combination of these tetrahedra can lead to at least 176 different zeolitic types². As a result they can

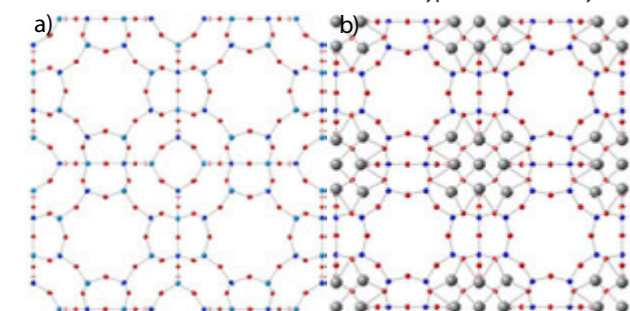


Figure 1: Models derived from Rietveld refinement against powder synchrotron XRD data for the zeolite A structure (the oxygen atoms are in red and the blue atoms correspond to Si and Al): a) with no silver in the structure and b) with silver atoms displayed in grey.

be employed as desiccants, molecular sieves (water/air treatment) and more importantly as detergents and catalysts in petrochemical companies. They are used either on their own or as bifunctional catalysts carrying a catalytically active metal, such as Pt, Pd, Ag or Cu. In order to fully characterize the zeolitic framework, together with the guest elements, a combination of diffraction techniques and conventional transmission electron microscopy (TEM) has been commonly employed.

In the present work we report a detailed study, performed on silver ion-exchanged zeolite A (LTA structure type) with Si/Al = 1. The characterisation was done by means of aberration (Cs) corrected scanning transmission electron microscopy (STEM) in combination with high resolution powder XRD.

Sodium zeolite A (NaA) was prepared using a verified standard synthesis for zeolite A, followed by silver ion exchange and complete dehydration³. Powder synchrotron X-ray diffraction profiles were collected on beamline I11 ($\lambda=0.825035$ Å). All samples were loaded into borosilicate glass capillaries of 0.5 mm diameter and sealed using a small blowtorch flame. The scattered radiation was detected as a function of 2θ (scattering angle) by the multi-analyzing crystals (MAC) detector with a step size of 0.005°. Aberration-corrected STEM-HAADF data were acquired using a XFEI TITAN 60–300 kV microscope, equipped with a high-brightness field emission gun (XFEG), a monochromator, and a CEOS hexapole aberration corrector for the electron probe. A beam convergence of 24.8 mrad half-angle was used, yielding a calculated probe size of 0.7 Å.

The crystallographic positions of all atoms were determined through Rietveld refinement against high-resolution XRD data (Fig. 1 [space group $Fm\bar{3}c$, $a = 24.66358(7)$ Å, $X^2 = 1.14$, $R_{wp} = 8.89 = R_p 6.99$]). The framework is shown both with and without silver and the refined atomic positions are given in table 1. The powder synchrotron XRD profile with its corresponding Rietveld fit is shown in Fig. 2.

Fig. 3 shows the Cs corrected EM analysis of the dehydrated AgA. In STEM mode using a HAADF detector the contrast observed is directly related to the atomic number of the elements, and therefore heavy elements are more easily observed in lighter support materials³. In the current case, the zeolitic framework is virtually invisible due to the high difference between Ag and Si/Al and only 4 or 9 atomic columns corresponding to Ag are observed (Fig. 3a). Figs. 3b and 3c show a closer observation of the framework where 9 atomic columns are easily identified showing a similar pattern to that depicted in Fig. 1b. The experimentally measured distances between Ag are in good

Atom	Wyckoff position	X	Y	Z	Occupancy	B
Si (1)	96i	0	0.0939 (3)	0.1841 (3)	1	0.70 (4)
Al (1)	96i	0	0.1853 (3)	0.0914 (3)	1	0.70 (4)
O (1)	96i	0	0.1109 (2)	0.2479 (7)	1	1.38 (9)
O (2)	96i	0	0.1476 (6)	0.1515 (6)	1	1.38 (9)
O (3)	192j	0.0526 (3)	0.0568 (3)	0.1714 (2)	1	1.38 (9)
Ag (1)	64g	0.0964 (3)	0.0964 (3)	0.0964 (3)	0.9706	2.90 (4)
Ag (2)	96i	0	0.2227 (2)	0.2089 (3)	0.1942	2.90 (4)
Ag (3)	48e	0	0	0.0806 (3)	0.1692	2.90 (4)

Table 1: Refined atomic parameters obtained from Rietveld analysis of dehydrated silver zeolite.

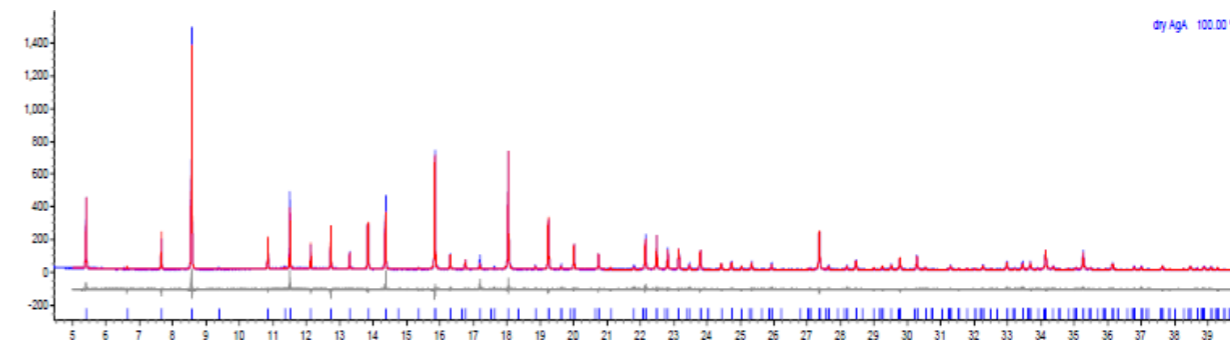


Figure 2: Powder XRD profile with the corresponding Rietveld fit for dehydrated silver zeolite A. Note: an Ag position was also refined at (0.25, 0.07(8), 0.07(8)) but was removed as it had a very low occupancy and did not improve the fit significantly. The refinement was carried out using the computer program TOPAS².

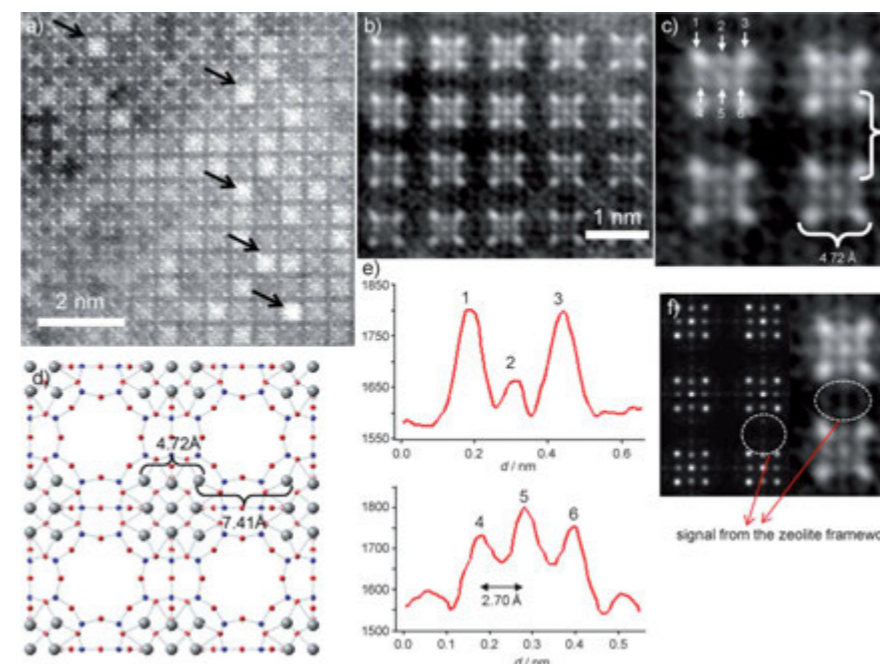


Figure 3: (a) Aberration-corrected STEM-HAADF image of dehydrated silver zeolite A (AgA) along the [001] direction, where the white spots are single atomic columns and the black arrows point to Ag clusters in the alpha cages, formed during manipulation of the sample before inserting it in the microscope. (b, c) Fourier-filtered images of the atomic distribution where the four columns of Ag at the corners of the sodalite cage are separated by 4.72 Å and each sodalite cage is separated by 7.41 Å; the Ag₆ cluster is also observed in these cages. (d) Proposed model with the Ag atoms in grey. (e) Intensity profiles performed on the atoms marked as 1, 2, and 3 in (c) and 4, 5, and 6, with the interatomic distance between these atoms being 2.70 Å. (f) Multislice STEM simulation along the [001] direction using 300 kV, Cs=0 mm, a defocus value of 0, a probe convergence semiangle of 24 mrad, and a collection angle of 70–200 mrad. The experimental image is shown alongside, and in both cases the zeolite framework signal is indicated by a white circle.

agreement with the values obtained by powder XRD refinement, respectively, 4.72 Å and 4.76 Å between the corners of the cages and 7.41 Å and 7.57 Å between two adjacent cages (Fig. 3c and 3d). With the aim of corroborating the nature of the species observed in the sodalite cages, intensity profile analyses were performed over the atomic columns marked 1 to 6. The intensity profile observed was, in this case, consistent with an octahedron surrounded by 8 Ag⁺ cations⁴. The atomic positions obtained from the Rietveld refinement were used for theoretical simulations (Fig. 3f), which also showed good agreement, with respect to atomic positions and intensities, with the experimental data.

In conclusion, the present results demonstrate the ability of aberration-corrected STEM-HAADF to characterise, at atomic resolution, zeolite frameworks with different metal cations incorporated in the structure. With these results, we have been able to image for the first time the silver arrangement in dehydrated silver-exchanged zeolite A, which was first described by Kim and Seff in 1977⁵. We have been able to confirm the formation of silver octahedra inside the sodalite cages, surrounded by eight cations, each located in the centre of a 6-ring. Many important bifunctional catalysts consist of noble metals incorporated into the zeolite structure, and this work, represents a considerable step forward in the characterisation of these and other solids, as we have demonstrated the feasibility of imaging even the most beam-sensitive materials at a resolution as high as one single atom.

References

1. C. Baerlocher, L. B. McCusker, Data Base of zeolite structures, www.iza-structure.org/databases/books/Atlas_6ed.pdf, (2011).
2. A. Coelho, Topas Academic, Version 4.1, Coelho Software, Brisbane (2007).
3. Mayoral, A., Blom, D. A., Mariscal, M. M., Guiterrez-Wing, C., Aspiaz, J. and Jose-Yacaman, M. Gold clusters showing pentagonal atomic arrays revealed by aberration-corrected scanning transmission electron microscopy. *Chem. Commun.* **46**, 8758–8760 (2010).
4. Mayoral, A., Carey, T., Anderson, P. A., Lubk, A. & Diaz, I. Atomic Resolution Analysis of Silver Ion-Exchanged Zeolite A. *Angew. Chem. Int. Ed.* **50**, 11230–11233 (2011).
5. Kim, Y. & Seff, K. Structure of a very small piece of silver metal. The octahedral silver (Ag₆) molecule. Two crystal structures of partially decomposed vacuum-dehydrated fully silver(1⁺) ion-exchanged zeolite A. *J. Am. Chem. Soc.* **99**, 7055–7057 (1977).

DOI 10.1002/anie.201105450

Using high-resolution powder diffraction to unravel the unexpected phase behaviour of multiferroic fluorides

Reisinger, S. A., Leblanc, M., Mercier, A.-M., Tang, C. C., Parker, J. E., Morrison, F. D. and Lightfoot, P. Phase separation and phase transitions in multiferroic $K_{0.58}FeF_3$ with the tetragonal tungsten bronze structure, *Chem. Mater.* **23**, 5440-5445 (2011)

Multiferroic materials display two or more 'ferroic' properties simultaneously, usually ferroelectric and ferromagnetic ordering. Such materials may form the basis for future information storage devices. However they are rare, since the two ordering phenomena are often intrinsically mutually exclusive. Understanding of these materials relies on detailed knowledge of crystal structure and its relationship to the two physical properties. In this experiment, the high resolution available on beamline I11 has been used to reveal an unexpected and complex phase separation phenomenon in the multiferroic fluoride $K_{0.58}FeF_3$. At ambient temperature, the as-made material is shown to consist of a mixture of two very similar phases, one tetragonal and one orthorhombic. Heating above 340 K causes the phase separation to disappear, but this returns on cooling and persists below room temperature, whence the tetragonal phase transforms to a second, distinct orthorhombic phase. The two orthorhombic phases continue to co-exist down to at least 125 K. This previously unobserved behaviour will help in interpretation of the structural, electrical and magnetic properties reported by other workers.

During the recent resurgence of interest in this field, the vast majority of multiferroics studied have been oxides¹. Amongst the non-oxides which have been studied, the mixed metal fluorides based on the 'tetragonal tungsten bronze' (TTB) structure (Fig. 1) have been some of the most promising. Compositions of the type $K_{0.6-x}FeF_3$ have been well studied, but there have been conflicting reports of their crystallographic nature, as well as their electrical and magnetic behaviour. Previous structural studies have generally been carried out on either single crystals or by electron microscopy^{2,3}, both of which may suffer from seeing only an unrepresentative portion of a bulk, ceramic sample. The aim of our study was therefore to exploit the advantages of powder diffraction in this respect, to look at the whole sample, and also to ensure that key crystallographic subtleties could be seen by obtaining the highest resolution possible, on beamline I11.

The beamline was used in high-resolution mode (MAC detectors) and data were collected at 34 temperatures between 100 and 500 K, each data collection lasting 30 minutes. At ambient temperature a good Rietveld fit

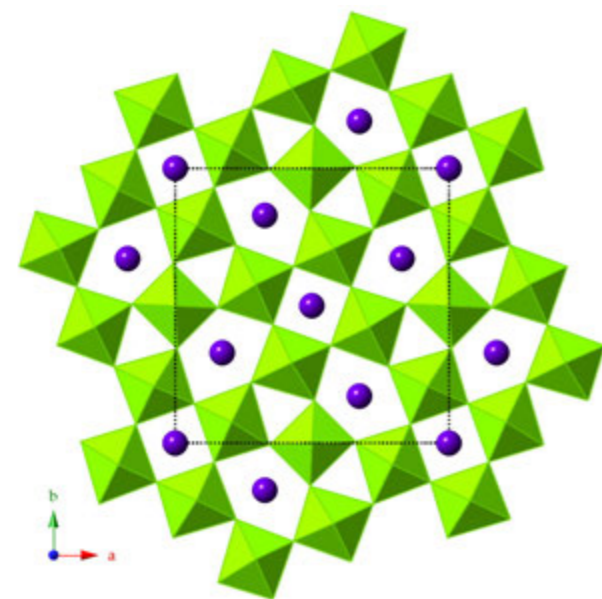


Figure 1: The aristotype TTB structure.

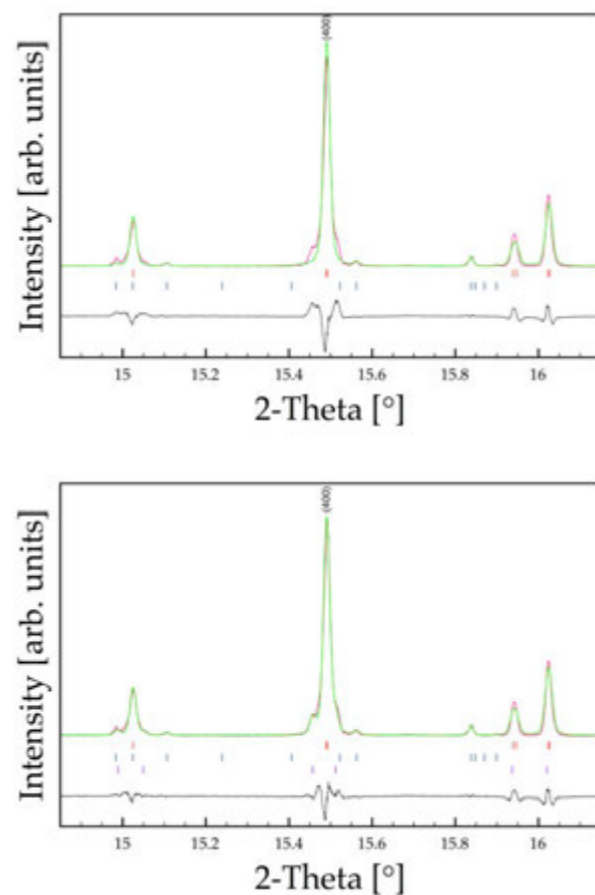


Figure 2: Comparative portion of the Rietveld refinements at ambient temperature, showing the inadequate fit using a single tetragonal phase model (top) versus a two-phase model (bottom): note in particular the shoulders on the peak at 15.5°.

could be obtained using the standard tetragonal TTB aristotype model (P4/mbm, $a \sim 12.68 \text{ \AA}$, $c \sim 3.98 \text{ \AA}$). However, on closer inspection, this model can be seen to be inadequate (Fig. 2). Subtle shoulders on certain peaks cannot be explained by a simple symmetry-lowering of the tetragonal phase, and are in fact best modelled by invoking a phase separation, with ca. 10% of a second, very similar but orthorhombic phase with a ~ 12.66

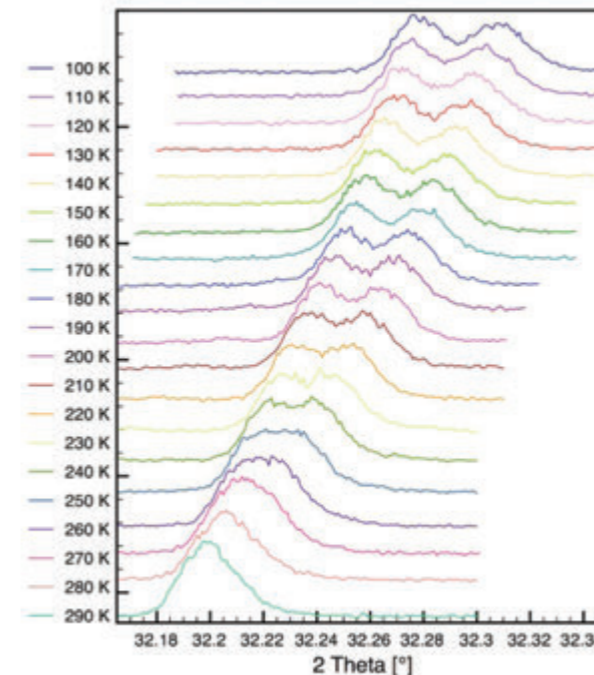


Figure 3: Splitting of key Bragg peaks below ambient, revealing a further subtle phase transition.

\AA , $b \sim 12.70 \text{ \AA}$ co-existing with the parent phase. On further cooling below 300 K the tetragonal phase transforms to a second type of orthorhombic phase (this one having an enlarged unit cell, at least $\sqrt{2} \times \sqrt{2}$ bigger than the aristotype). This is evidenced by splitting of a different set of Bragg peaks, as shown in Fig. 3. These two distinct orthorhombic phases continue to co-exist down to the lowest temperatures studied, as summarised by the lattice parameter trends presented in Fig 4. Such subtle features cannot be seen on a conventional lab-based powder diffractometer.

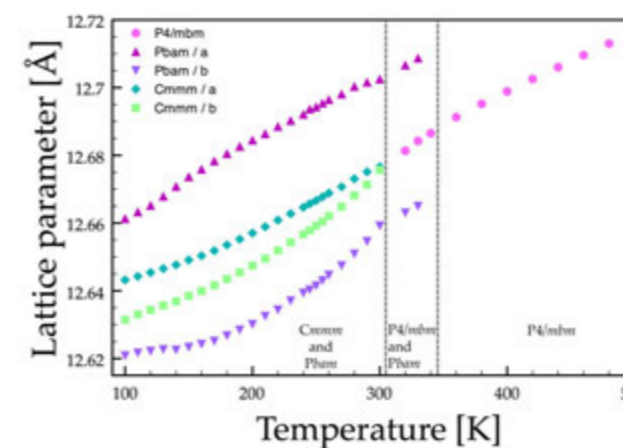


Figure 4: Summary of the evolution of lattice parameters within the three distinct phase fields.

The previously reported ferroelectric T_c for this composition is around 490 K, whereas the ferromagnetic ordering temperature is $\sim 120 \text{ K}$. The significance of our work lies especially, therefore, in the interpretation of previous magnetic data, where single phase behaviour has previously been assumed, despite more than one 'magnetic' event apparently occurring below 125 K, in some studies⁴.

We also carried out a follow-up experiment on a closely-related composition with somewhat lower potassium content; again we find a systematic and reproducible phase separation phenomenon, this time of a slightly different nature. It seems that competing instabilities in these systems lead to intrinsic phase separation. From this study it is not possible to pinpoint the precise difference between the two co-existing phases, or indeed the reasons behind the phase separation, so subtle are the details we observe. Only approximate structural models can be used, due to the severe overlap of inequivalent Bragg peaks, although the differences in unit cell metrics can be clearly seen, and refined robustly. The phase separation may be due, inter alia, to a miscibility gap in potassium content, competing Fe^{2+}/Fe^{3+} charge-ordering preferences, or competing 'octahedral tilt' instabilities. These possibilities require further study using neutron diffraction and other techniques; nevertheless, this study provides a clear new insight into the structural behaviour of these materials, which may have important repercussions in the interpretation of their electrical and magnetic properties.

References

1. Fiebig, M. Revival of the magnetoelectric effect *J. Phys. D Appl. Phys.* **38** (8), R123 (2005).
2. Fabbri S., Montanari E., Righi L., Calestani G., Migliori A. *Chem. Mater.*, **16** (16), 3007-3019 (2004).
3. Ishihara S. Rivera J., Kita D., Ye Z., Kubela F., Schmid H., Studies of single crystalline tetragonal tungsten bronze type $K_3Fe_5F_{15}$, a potential magnetoelectric material *Ferroelectrics*. **162**, 399-409 (1994).
4. Potočník A., Zorko A., Arčon D., Goresnik E., Žemva B., Blinc R., Cevc P., Trontelj Z., Jagličić Z., Scott J., Muon spin relaxation in some multiferroic fluorides *Phys. Rev. B*. **81**, 214420 (2010).

Funding Acknowledgements

We thank the University of St Andrews for partial support of a studentship to S.A. Reisinger.

DOI 10.1021/cm202713n

Porous organic cages: gas trapping in modular crystals

Bojdys, M. J., Briggs, M. E., Jones, J. T. A., Adams, D. J., Chong, S. Y., Schmidtman, M., Cooper, A. I. Supramolecular Engineering of Intrinsic and Extrinsic Porosity in Covalent Organic Cages. *J. Am. Chem. Soc.* **133**, 16566–16571 (2011)

Porous materials are useful for catalysis and separations, and have gained recent prominence in technologies such as hydrogen storage and carbon capture and storage (CCS). Beside the well-known inorganic examples, such as zeolites or metal oxides, new materials comprised entirely of light, abundant atoms offer to extend the range of properties and applications. Organic polymer networks, in particular, allow broad control over composition because of the wide range of chemistry that is available. However, porous polymer networks have some limitations: for example, they cannot dissolve and are hence not solution processable. It is therefore desirable to synthesise porous functional materials which combine inherent porosity with the processability and modularity associated with single molecules. In this contribution, we present functional porous materials and the underlying design-principles for their assembly from inherently porous organic cages, along with the potential advantages of these self-assembled, extended solids. The synthetic strategies for organic cages and their assembly into crystalline porous materials are relevant to several challenges in research, such as the generation of free volume in solids via 'badly packing' molecular building blocks, and this gives rise to new tools for the chemist to rationally design adsorptive surfaces.

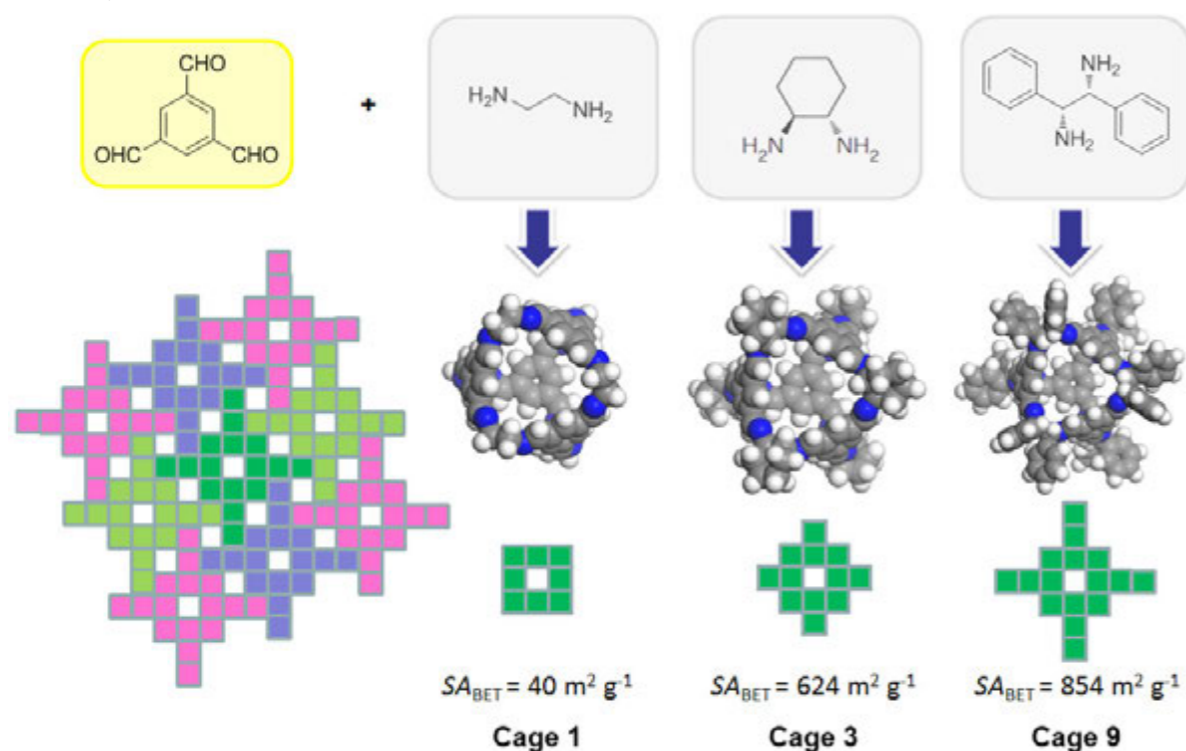


Figure 1: Building blocks for porous organic crystals. Porous organic cages **1**, **3**, and **9** are obtained via [4+6] Schiff-base condensation of 1,3,5-triformylbenzene (yellow box) with 1,2-ethylenediamine, (R,R)-1,2-diaminocyclohexane and (R,R)-1,2-diphenylethylenediamine (all grey boxes), respectively. Accessible surface areas (as seen by N₂ BET sorption) vary according to packing mode and bulkiness of cage vertex functionalities.

Recently, microporous and mesoporous organic polymers¹ and covalent organic frameworks (COFs),² in particular, have extended the range of possible properties and applications of functional materials because their constituent building blocks can be readily diversified using organic synthesis. The surface area in such networks is generated typically via templating or scaffolding approaches: as such, the porosity is a consequence of the solid-state packing, or enforced by the binding-motif of the respective building blocks, and is 'extrinsic' in nature – that is, between the building blocks. Other organic materials exhibit 'intrinsic' porosity that results from the shape of the isolated molecules themselves, for example in the form of synthetically prefabricated pores, cavities, or windows. Examples of such 'porous molecules' include calixarenes and a range of other small organic molecules with shape-persistent covalent cavities. In this context, cage-like molecules might be desirable as porous solids. Recently, a family of porous organic cage compounds was shown to demonstrate either extrinsic or

intrinsic porosity, depending on the packing mode of the cages.³ The cavities and windows in these molecules are created by a reversible [4+6] Schiff-base condensation of amine and aldehyde components. The materials have permanent micropore structures and exhibit Brunauer–Emmett–Teller surface areas (SA_{BET}) of up to 854 m² g⁻¹. Notably, packing of these cages – and hence the porosity and connectivity of accessible voids in the resulting crystalline solids – is influenced by the bulkiness of the cage vertices (Fig. 1).

To achieve programmed assembly in porous molecular crystals, it is desirable to use the established tools of crystal engineering and supramolecular chemistry to direct molecular assembly. For example, to generate additional porosity it may be necessary to engineer both intrinsic and extrinsic porosity within the same molecular solid – that is, pores which run both through and between the cage units. This requires the development of cage tectons that assemble in predictable ways

which necessitates, in turn, the chemical incorporation of structure-directing functionality within the cage modules. Starting with this simple design premise—that bulky directing groups might frustrate molecular packing and create additional extrinsic porosity between the cage units, thus enhancing the pore volume—two cages, cage **9** and cage **10**, were synthesised by cycloimination of 1,3,5-triformylbenzene with (R,R)-1,2-diphenylethylenediamine and (R,R)-1,2-bis(4-fluorophenyl)ethane-1,2-diamine, respectively, in dichloromethane using trifluoroacetic acid as a catalyst. Two different polymorphs are observed for the resulting desolvated cage **9** (space groups R3 and P3), while cage **10** forms an R32 polymorph only (Fig. 2). These crystallographic differences have an immediate impact on the quantities of gas that the desolvated molecular solids can physisorb. The Langmuir surface areas calculated from the Type I nitrogen sorption isotherms were 952 m² g⁻¹ (SA_{BET} = 854 m² g⁻¹) for cage **9** (P3), 575 m² g⁻¹ (SA_{BET} = 501 m² g⁻¹) for cage **9** (R3), and 533 m² g⁻¹ (SA_{BET} = 460 m² g⁻¹) for cage **10**.

The apparent drop-off in accessible surface area for cage **10** can be rationalised by closer inspection of the crystal structure in this molecular solid. Unlike the 1-D gas transport channels in the cage **9** polymorphs, the extrinsic pore channels in cage **10** vary by the presence of hydrogen bonds.

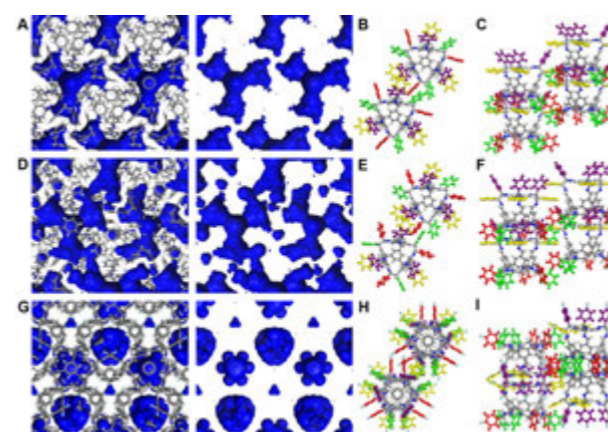


Figure 2: Connolly surface plots for cage **9** (R3) (A), cage **9** (P3) (D), and cage **10** (G) with probe radii of 1.82 Å (blue) based on the crystal structures for the desolvated materials shown along the c-axis with (left) and without (right) the cage framework. Schematic of cage-cage packing in the molecular solid as determined by X-ray crystallography for desolvated cage **9** (R3), cage **9** (P3), and cage **10** shown top-down (B, E, and H) and across (C, F, and I), respectively. Carbon, nitrogen, hydrogen and fluorine atoms are coloured grey, blue, white and teal, respectively. Vicinal aryl groups with the same orientation with respect to the cage-core are marked in the same colours with red and green, and purple and yellow each forming a set of neighbouring aryl groups on the same vertex.

For one of these extrinsic pore channels, aryl groups (colored green and yellow in Figure 3) from three neighboring cage stacks engage in a pattern of cooperative C-H...F bonds (Fig. 3. E and F). This pattern has been observed previously – and exclusively – for small organo-fluorines, and has been defined as a rare supramolecular synthon of fluorobenzene. The other set of 1-D channels in cage **10**, by contrast, shows no sign of the influence of anisotropic electrostatic interactions. Here, the aryl units (marked red in Fig. 3. G and H) are sufficiently far apart to give rise to a helical 1-D pore channel. Interestingly, both the hydrogen bonded and the π-π stacked aryls (marked red and green in Fig. 3. B and C) assume orientations close to or identical to the most favourable packing observed for smaller, 'free' molecular entities,^{4,5} despite the fact that the vertex arenes in cage **10** are locked into place relative to one another by the cage core. The research was carried out on beamline I11.

To conclude, the vertex functionality in these new cages was chosen to enhance porosity with respect to our previous materials by creating additional, extrinsic porosity to augment the intrinsic porosity inside the cages. We have therefore demonstrated a step towards rational, synthetic

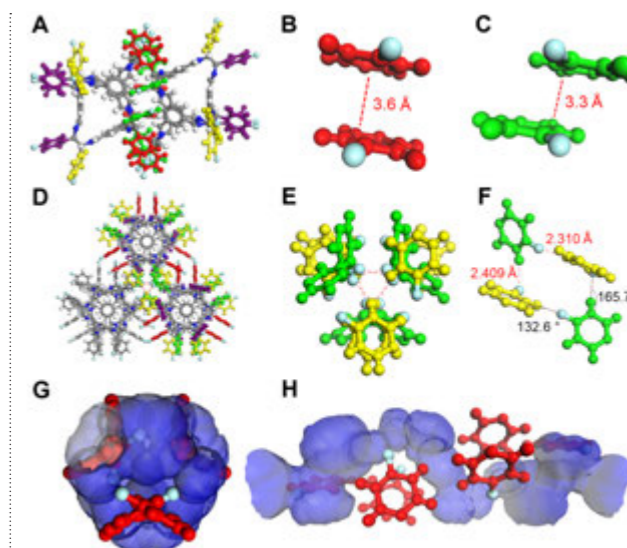


Figure 3: Scheme illustrating solid-state packing for cage **10**. Arenes with the same orientation with respect to the cage-core are colour-coded to guide the eye, as in Figure 2. In dimer shown (A), the red and green arenes interdigitate to form a mutual cage-cage void, connected by a window-to-window interaction but formally disconnected from the extrinsic, between-cage porosity and other cage-cage voids. C-H...F bonds are marked as dashed, red lines. Top-down (G) and perspective (H) view of the helical, 1-D extrinsic pore channel in cage **10**, spanned by vicinal aryl groups.

design of additional extrinsic porosity within this class of intrinsically porous organic cage molecules. The vertex groups were chosen to direct molecular assembly in ways that are familiar in the fields of crystal engineering and supramolecular chemistry. The porous molecular crystals obtained show exceptionally high gas uptakes within this class of material resulting from a combination of intrinsic and extrinsic pore volume. These observations suggest that enhancing porosity further in such materials could conceivably be achieved by the design of tectons that form porous solids comprising, as near as possible, 'point contacts' between molecules such that the guest-accessible surface is maximized. In this respect, hydrogen bonding at 'sticky' functionalized vertices is a promising tool.

References

- Jiang, J. X. *et al.* Conjugated microporous poly (aryleneethynylene) networks. *Angew Chem Int Ed.* **46**, 8574–8578 (2007).
- Cote, A. P. *et al.* Porous, crystalline, covalent organic frameworks. *Science*. **310**, 1166–1170, (2005).
- Tozawa, T. *et al.* Porous organic cages. *Nat. Mater.* **8**, 973–978 (2009).
- Merz, K. & Vasylyeva, V. Development and boundaries in the field of supramolecular synthons. *CrystEngComm*. **12**, 3989–4002 (2010).
- D'Oria, E. & Novoa, J. J. On the hydrogen bond nature of the C-HF interactions in molecular crystals. An exhaustive investigation combining a crystallographic database search and ab initio theoretical calculations. *CrystEngComm*. **10**, 423–436 (2008).

Funding Acknowledgements

The authors thank EPSRC for funding (EP/F057865/1 & EP/H000925), in particular via the Programme Grant scheme. A. I. C. is a Royal Society Wolfson Merit Award holder.

In parts reprinted with permission from Bojdys, M. J. *et al.* Supramolecular Engineering of Intrinsic and Extrinsic Porosity in Covalent Organic Cages. *J. Am. Chem. Soc.* **133**, 16566–16571. Copyright 2011 American Chemical Society.

DOI 10.1021/ja2056374

New insights into the intercalation chemistry of Al(OH)₃

Williams, G.R., Moorhouse, S.J., Prior, T.J., Fogg, A.M., Rees, N.H. & O'Hare, D. New insights into the intercalation chemistry of Al(OH)₃. *Dalton Trans.* **40**(22):6012-22 (2011)

Aluminium hydroxide, Al(OH)₃, is a lamellar material with octahedral vacancies in its layers. It has long been known that it can 'imbibe' LiX salts to form layered double hydroxides (LDHs) of the form [LiAl₂(OH)₆]_x·xH₂O, where X is a generic anion. LDHs are important ion-exchangers, with applications in catalysis, biomedicine, and polymer science. Although size considerations should not be problematic, the incorporation of other metal ions into the octahedral vacancies in Al(OH)₃ is challenging, and was not reported until 2004 when Zn^{II}, Cu^{II}, Ni^{II} and Co^{II} nitrates were successfully intercalated to give novel [MAI₄(OH)₁₂](NO₃)₂·yH₂O LDHs.¹ In this work, we report recent developments in the intercalation chemistry of Al(OH)₃. These include a detailed structural study, the synthesis of new LDHs containing mixtures of M^{II} cations, and a comprehensive *in situ* study of their intercalation reactions. Through use of the high-quality energy-dispersive diffraction capabilities of beamline I12, we were able to continuously record diffraction patterns in real time as reactions proceeded, and from these data deduce information on the reaction mechanisms. These results are crucially important in our quest to understand more about how solid state and heterogeneous solid/liquid reactions proceed.

Layered double hydroxides are a widely studied class of materials comprising positively charged layers, with charge-balancing anions located in the interlayer space. They have the generic formula [M^{II}_{1-x}M^{III}_x(OH)₂]^{q+}Xⁿ⁻_{q/n}·yH₂O. LDHs have a range of potential applications, including in catalysis, biomedicine, and polymer science.^{2,3} They display a diverse ion-exchange intercalation chemistry, in which the initial interlayer anion is replaced by another. Generally, LDHs contain M^{II} and M^{III} metal ions, with the M^{II}:M^{III} ratio in the range 2:1 – 4:1. The LDH [LiAl₂(OH)₆]_x·xH₂O (X = Cl⁻, Br⁻, NO₃⁻, 0.5SO₄²⁻, etc) is prepared through the reaction of LiX salts with Al(OH)₃ at around 90 °C, and is the only LDH containing mono- and trivalent metal cations. Although Li⁺ is similar in size to Zn²⁺, Cu²⁺, Ni²⁺, and Co²⁺, it is much harder to intercalate the latter into Al(OH)₃. Successful reaction could only be achieved by first grinding γ-Al(OH)₃ (gibbsite) in a ball mill, and then subjecting it to an extended hydrothermal treatment.¹ The LDHs thereby generated are highly novel synthetic materials with formula [MAI₄(OH)₁₂](NO₃)₂·yH₂O (M = Zn, Cu, Ni, Co; MAI₄-NO₃).

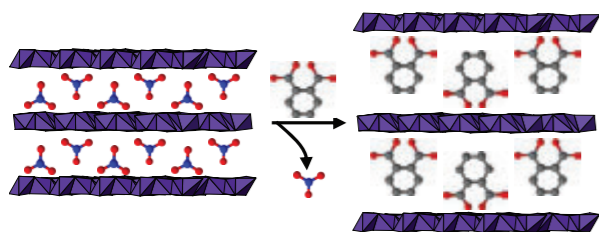


Figure 1: A schematic representation of intercalation into the LDH [CoZnAl₈(OH)₂₄](NO₃)₂·yH₂O, showing the initial nitrate anion (left) being replaced with phthalate to give [CoZnAl₈(OH)₂₄](C₈H₄O₂)₂·yH₂O (right).

The study of reaction mechanisms and kinetics has been neglected for the solid state, largely because there are few non-invasive probes available. A powerful non-invasive probe is *in-situ* energy-dispersive X-ray diffraction (EDXRD). The exceptional EDXRD capabilities of beamline I12 provide an unparalleled opportunity to extend our knowledge in this area, and the present study forms part of work to explore the nanoscopic processes involved in a range of solid state reaction processes.

In this study,⁴ we sought to expand our earlier work in a number of ways. First, we used Rietveld refinement methods to propose a structure for the new MAI₄-NO₃ materials. It was found that M^{II} cations occupy half the octahedral vacancies in the Al(OH)₃ layers, with almost complete ordering of M^{II} cations. Next, we explored the possibility of incorporating salts other than nitrates, and of further reacting the MAI₄-NO₃ materials to fill the remaining octahedral holes. Beyond this, experiments were undertaken to

prepare three-metal LDHs by reacting Al(OH)₃ with mixtures of M^{II} nitrates. The idealised formula of these materials is [MM'Al₄(OH)₁₂](NO₃)₂·yH₂O. However, it was found that Al(OH)₃ exhibits selective intercalation chemistry, imbibing metal cations preferentially in the order Li⁺ >> Ni²⁺ >> Co²⁺ ≈ Zn²⁺. By varying the ratio of metals in the reaction gel, it proved possible to control the stoichiometry of the LDHs produced. For instance, a 1 : 1 mixture of Zn and Co nitrates yields the LDH [CoZnAl₈(OH)₂₄](NO₃)₂·yH₂O.

In order to prove definitively that the new materials prepared are layered double hydroxides, it was necessary to demonstrate that the interlayer nitrate anion could be replaced with other anions, and hence reactions were undertaken using a range of simple organic anions (see Fig. 1). It proved facile to replace the nitrate anions with a range of organic species such as phthalate (C₈H₄O₂²⁻).

These experiments proved that the new materials were indeed LDHs. As they are highly crystalline, with distinct and non-overlapping sets of Bragg reflections for each phase, they were chosen as ideal candidates for the first time-resolved study of a chemical reaction system to be undertaken at Diamond Light Source. The existing Oxford-Daresbury *in situ* reaction cell was refurbished, commissioned onto beamline I12, and detailed alignment with the I12 optics undertaken. Photographic and schematic representations of the reaction cell are given in Fig. 2.

We were pleased that, with very little optimisation, it proved possible to record high-quality diffraction patterns in as little as 5 – 10 s. Unfortunately, the LDH intercalation reactions were observed to be very rapid (< 30s); hence, a syringe pump was used to add a solution of the guest to a suspension of the LDH dropwise. In order to extract all the desired chemical information, it proved necessary to move the 23-element detector system on I12 to an offset position. This required removal of a collimator, introducing extra noise into the diffraction patterns. Nevertheless, very high quality data were obtained. Data for the reaction between [CoZnAl₈(OH)₂₄](NO₃)₂·yH₂O (CoZnAl₈-NO₃) and phthalate to give CoZnAl₈-phthalate are shown in Fig. 3. A plot showing the variation in diffracted intensity with time is depicted in Fig. 3a. This contains only two phases: CoZnAl₈-NO₃ and CoZnAl₈-phthalate. No crystalline intermediates may be observed.

The observed Bragg reflections were integrated and converted into the extent of reaction, α , where $\alpha = I_{hkl}(t) / I_{hkl}(\max)$ [I_{hkl} is the integrated intensity of the hkl reflection]. The extent of reaction vs. time plots given in Fig. 3b show that the host and product curves cross very close to $\alpha = 0.5$, suggesting that loss in diffracted intensity from the host is exactly matched by the increase in intensity from the product, and confirming a one-step

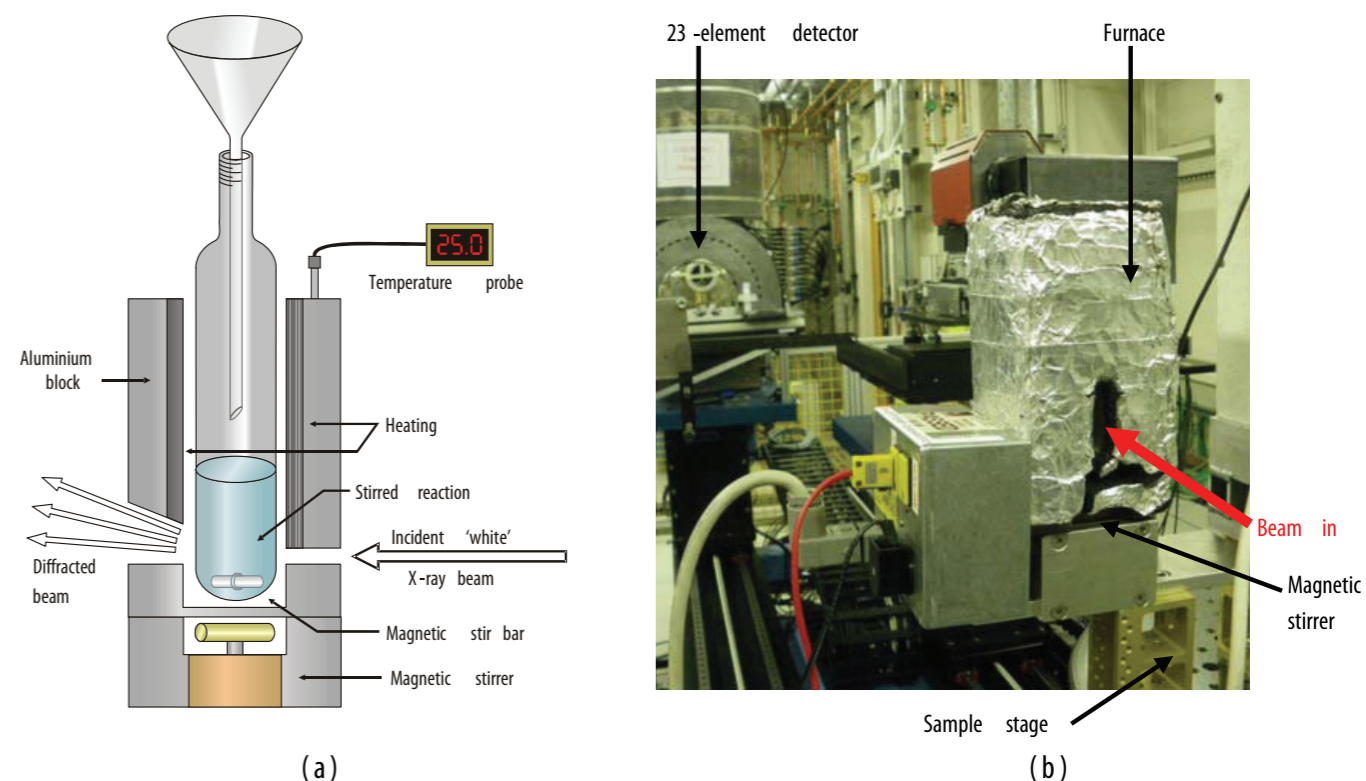


Figure 2: (a) Schematic and (b) photographic representations of the *in situ* chemical reaction monitoring cell used on beamline I12.

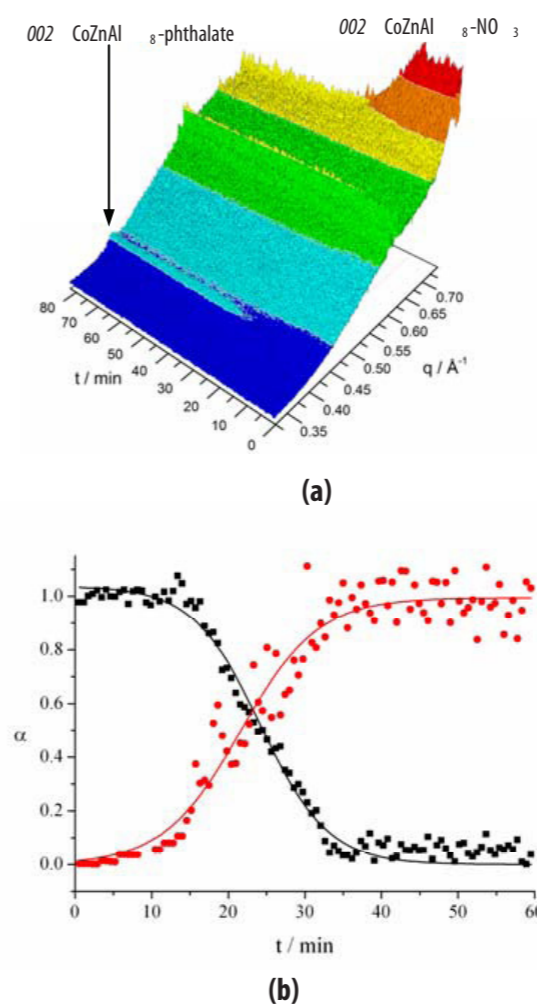
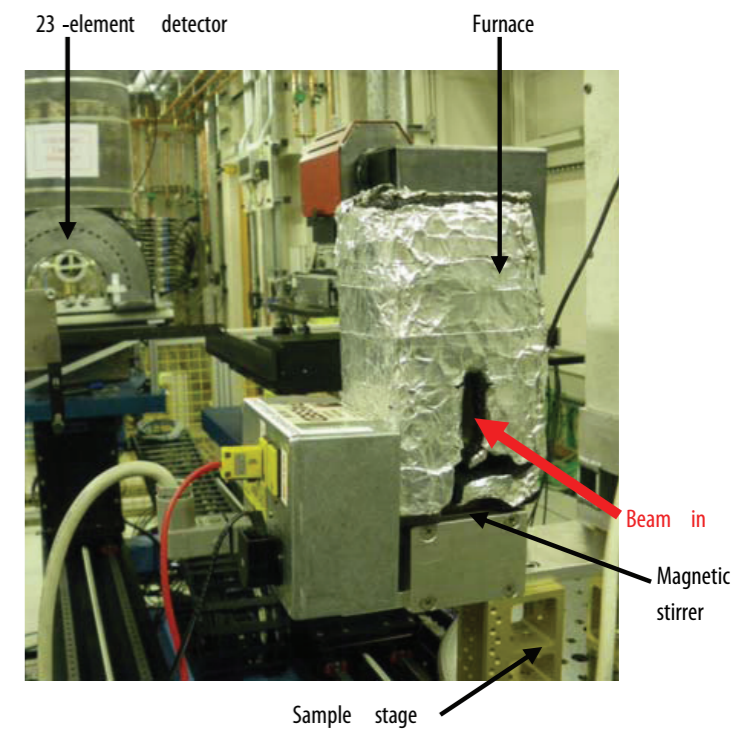


Figure 3: EDXRD data for the conversion of CoZnAl₈-NO₃ to CoZnAl₈-phthalate. (a) 3D stacked plot and (b) a vs. time plots showing the starting material (■) and product (●). Reproduced with permission from ref 2. Copyright Royal Society of Chemistry, 2011.



reaction process (if intermediates were involved, then the curves would cross at a ca. 0). This is in agreement with previously reported results for the MAI₄-NO₃ LDHs.¹

As a result of these preliminary experiments, we have now developed an optimised set-up for the study of chemical reactions on I12, and are actively working with Diamond Light Source to develop a new furnace with improved capabilities, as well as to reduce the noise introduced to the system when the detectors are moved to an offset position to access the high d-spacing region. This research forms part of a programme of investigations seeking to elucidate more detail on the nanoscopic processes involved in solid state reaction mechanisms, and the outstanding capabilities of I12 will be profoundly important in allowing us to drive this work forward.

Funding Acknowledgements

AMF thanks the Royal Society for a University Research Fellowship, and SJM the EPSRC and Diamond Light Source for provision of a research studentship.

References

- Fogg, A. M., Williams, G. R., Chester, R. & O'Hare, D. A novel family of layered double hydroxides-[MAI₄(OH)₁₂](NO₃)₂·xH₂O (M = Co, Ni, Cu, Zn). *J. Mater. Chem.* **14**, 2369-2371 (2004).
- Oh, J.-M., Biswick, T. T. & Choy, J.-H. Layered nanomaterials for green materials. *J. Mater. Chem.* **19**, 2553-2553 (2009).
- Williams, G. & O'Hare, D. Towards understanding, control and application of layered double hydroxide chemistry. *J. Mater. Chem.* **16**, 3065-3074 (2006).
- Williams, G. R. *et al.* New insights into the intercalation chemistry of Al(OH)₃. *Dalton Trans.* **40**, 6012-6022 (2011).

PMID 21556398

Probing inert anodes with high-energy X-rays

Rowles, M. R., Styles, M. J., Madsen, I. C., Scarlett, N. V. Y., McGregor, K., Riley, D. P., Snook, G. A., Urban, A. J., Connolly, T. & Reinhard, C. Quantification of Passivation Layer Growth in Inert Anodes for Molten Salt Electrochemistry by In Situ Energy-Dispersive Diffraction. *J. Appl. Cryst.* **45**(1), 28-37 (2012)

To date, the development of inert anode materials has relied on the characterisation of samples which have been removed from their operational environment at various pre-defined points of interest¹. This *ex situ* approach can be problematic, as conventional analysis techniques typically require some form of sample preparation, ranging from simply allowing the sample to cool, to more invasive procedures such as cutting and polishing. While any material studied outside of its operational environment will be altered to some extent, friable surface layers, crucial to the understanding of reaction mechanism, are at particular risk. Obtaining clear information about how these layers evolve during cell operation, without disrupting their fragile structure, requires a quantitative *in situ* characterisation method.

Molten-salt electrolysis is used extensively in the production of light metals such as aluminium, lithium and magnesium, and is being investigated² as a potential replacement for the Kroll³ process for titanium production. Currently, reactive carbon anodes are used in titanium electro-winning research with many unwanted outcomes, such as the emission of greenhouse gases, reaction of carbon with the electrolyte, and carbon contamination of electro-won metal. Conversely, an ideal inert anode is not consumed during the electrolysis, does not react with the electrolyte and produces only oxygen, therefore having a much lower impact on process control and the environment. However, inert anodes are prone to failure as, in practice, they are attacked by both the electrolyte and the oxygen evolved at the anode. In order to develop these new anode materials further, a detailed understanding of the structural and chemical changes that lead to their failure is needed.

Due to the aggressive sample environment, molten calcium chloride at 950 °C, the *in situ* characterisation of inert anodes employed in molten-salt electrochemistry is difficult. A 'see-through cell', developed by McGregor *et al.*⁴, which uses a transparent quartz crucible for the direct observation of both the anode and cathode, has given many insights into physical aspects of anode behaviour; however, determining chemical and structural changes in an operational anode requires a different approach. In order to study structural changes in materials with respect to time, synchrotron and neutron diffraction techniques are often used. The intensity of such advanced radiation sources allows data to be collected on the time scales necessary to observe reaction changes and investigate their kinetics.

This experiment, performed at beamline I12, aimed to look at the formation of surface layers on the anodes whilst they were operating in

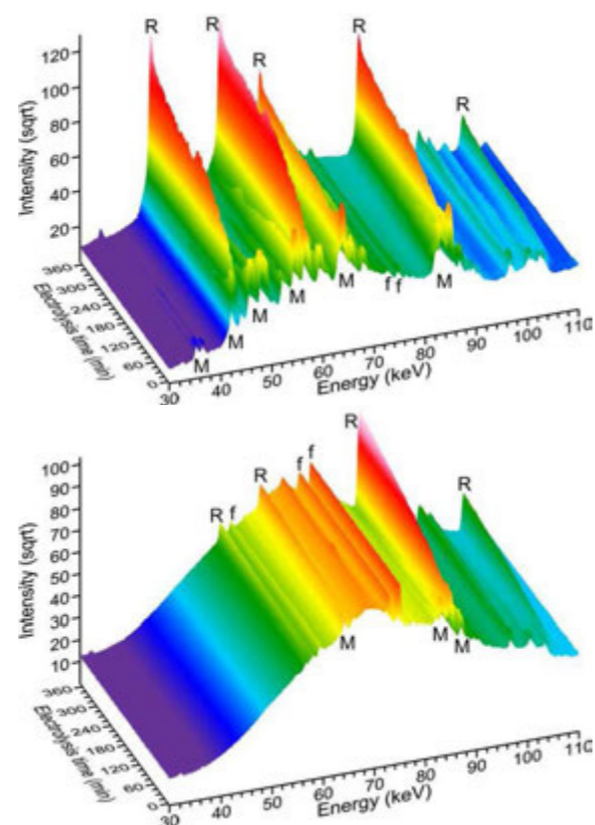


Figure 2: Accumulated EDXRD patterns as a function of time for data collected top and bottom the electrolyte. The transformation of the Magnéli (M) phases into rutile (R) can be seen clearly. (Fluorescence peaks, which are constant throughout the experiment and incidental to the reaction, are designated 'f'.) Differences in the relative intensities between the two datasets is due to the absorption of low energy X-rays in the electrolyte.

molten salt at 950°C, required; (i) highly penetrating radiation in order to pass through the furnace walls and several centimetres of electrolyte, (ii) high spatial resolution in order to selectively study only the anode surface in a complex sample environment and (iii) high temporal resolution in order to study the changes in the anode on a minute by minute basis. Synchrotron-based energy-dispersive X-ray diffraction (EDXRD) is uniquely suited to fulfil these experimental requirements as its characteristics include; (i) penetrating high-energy X-rays, (ii) a fixed detector position, allowing tight collimation of the diffracted beam, providing good spatial resolution, and (iii) a very high intensity beam allowing for short data acquisition times. In order to carry out this work, an electro-winning cell and furnace, Fig. 1 was designed⁵ to allow for the safe operation of a molten-salt electrochemical cell in a beamline environment whilst still allowing for valid diffraction data to be obtained. The guiding principle behind the design of the cell and furnace was to enable *in situ* characterisation of an inert anode using EDXRD, without

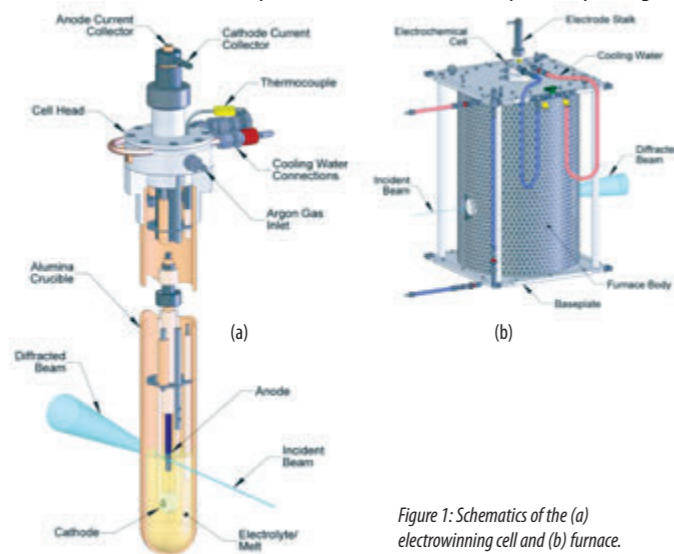


Figure 1: Schematics of the (a) electro-winning cell and (b) furnace.

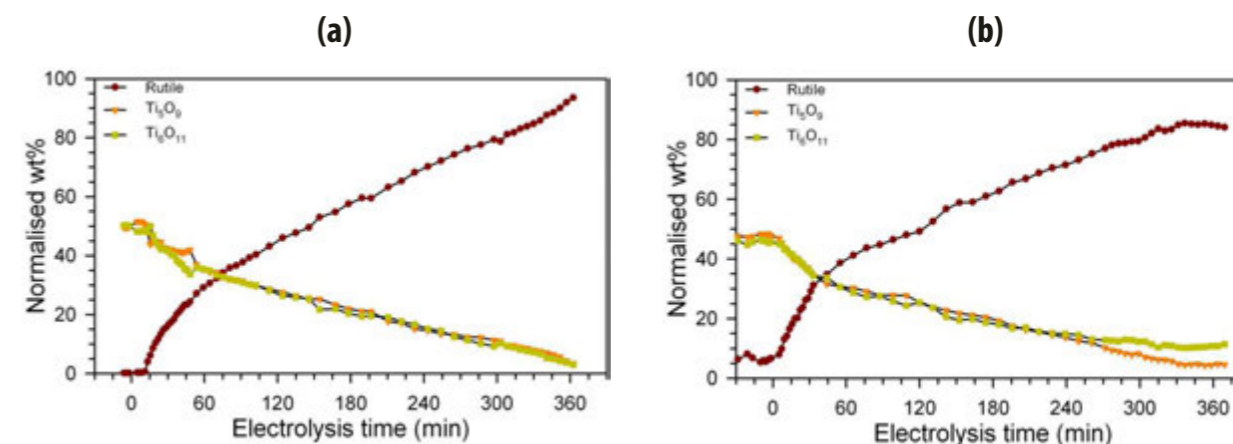


Figure 3: Results of quantitative phase analysis of the EDXRD data collected (a) above and (b) below the surface of the electrolyte.

compromising the electrochemical reactions at either the anode or cathode.

The electro-winning cell was designed to minimise the X-ray beam path through the electrolyte, while still allowing sufficient electrolyte for electrolysis to occur. The furnace was designed to reach a maximum of 1100°C, while only using a standard 240 V, 10 A power supply.

The anodes used in this study were a Magnéli-phase material (Ebonex™, containing Ti_nO_{2n-1} , $n = 4-6$)⁶. This material oxidises to rutile (TiO_2) due to the evolution of oxygen at the anode surface, producing a passivation layer which ultimately causes the anode to fail. Ebonex™ was used as a model anode as; (i) the phase changes that occur in this material during electrolysis have been substantially characterised *ex situ*¹ allowing findings made during *in situ* experimentation to be corroborated by *ex situ* data, (ii) it does not contaminate the electrolyte or cathode, and (iii) it remains dimensionally stable.

In separate experiments, *in situ* EDXRD data were collected above or below the surface of the electrolyte to observe the effect of electrolyte absorption on the diffracted intensities; electrolysis is still possible slightly above the surface of the electrolyte as it creeps up the surface of the anode. Datasets were collected for 60 sec, with a 5 sec delay between consecutive datasets, for the duration of the experiment, typically 6-7 hours. Accumulated diffraction patterns collected centrally on the anode are shown in Fig. 2; top and bottom the surface of the electrolyte. The oxidation of the Magnéli-phases to rutile can be seen clearly. For the data collected above the electrolyte, the diffraction peaks for each phase are clearly visible. For the data collected below, the diffraction peaks for each phase are less visible due to the absorption of lower energy X-rays by the electrolyte.

The data were analysed quantitatively using the Rietveld⁷ method to track the evolution of the various phases present in the anode. Scarlett *et al.*⁸ had previously developed this methodology for the quantitative analysis of EDXRD data which uses the energy spectrum of the incident beam, sample absorption, and the crystal structures of the anode materials in order to calculate a model diffraction pattern. Such a model was then refined against the EDXRD data in order to extract quantitative phase analyses. Fig. 3 shows the results of this quantitative phase analysis. It can be seen that in all systems, rutile forms at the expense of both Magnéli phases equally.

The similarities in the quantitative phase analysis both above and below the electrolyte surface suggest that it is possible to obtain meaningful *in situ* diffraction data with the incident beam just above the electrolyte, mitigating the deleterious effect of X-ray absorption on the resultant diffraction patterns. Initial kinetics modelling suggests that the limiting factor in the

growth of the rutile layer is the rate of solid-state diffusion of oxygen within the anode structure. This continual monitoring of the rutile phase fraction throughout the duration of the experiment revealed the way in which the layer grows, something that would be very difficult to do accurately *via ex situ* experimentation. It also confirms the absence of any intermediate phases which would not be observed using traditional *post mortem* methodologies.

References

- McGregor, K., Frazer, E.J., Urban, A.J., Pownceby, M.L., & Deutscher, R.L. Development of Inert Anode Materials for Electro-winning in Calcium Chloride Melts. *ECS Trans.* **2**, (3), 369380 (2006).
- Fray, D.J. Novel methods for the production of titanium. *Int. Mater. Rev.* **53**, (6), 317-325(2008).
- Kroll, W. The production of ductile titanium. *Trans. Am. Electrochem. Soc.* **78**, 35-47 (1940).
- McGregor, K., Urban, A.J., & Frazer, E.J., presented at the Proceedings of the 11th World Conference on Titanium, Sendai, 2007 (unpublished).
- Styles, M.J. *et al.* A Furnace and Environmental Cell for Studying Molten Salt Electrolysis In situ using High Energy X-ray Diffraction. *J. Synchrotron Radia.* **19**, (1), 39-47 (2012).
- Hayfield, P.C.S., US Patent No. 4422917 (1983).
- Rietveld, H.M. A Profile Refinement Method for Nuclear and Magnetic Structures. *J. Appl. Cryst.* **2**, 65-71 (1969).
- Scarlett, N.V.Y. *et al.* Energy Dispersive Diffraction Studies of Inert Anodes. *J. Appl. Cryst.* **42**, 502-512 (2009).

Funding Acknowledgements

We acknowledge travel funding provided by the International Synchrotron Access Program (ISAP). ISAP is an initiative of the Australian Government being conducted as part of the National Collaborative Research Infrastructure Strategy. M. J. Styles gratefully acknowledges receipt of a full PhD scholarship from the CSIRO Flagship Collaboration Fund, and additional funding from the CSIRO Light Metals Flagship.

DOI 10.1107/S0021889811044104

High-energy transmission Laue (HETL) diffraction: a tool for mapping grain-level orientation and strain in thicker metallic polycrystals

Hofmann, F., Abbey, B., Connor, L., Baimpas, N., Song, X., Keegan, S. & Korsunsky, A.M. Imaging of grain-level orientation and strain in thicker metallic polycrystals by high energy transmission micro-beam Laue (HETL) diffraction techniques. *Int. J. Mat. Res.* **103**, 192-199 (2012)

Hofmann, F., Song, X., Abbey, B., Jun, T.-S., Korsunsky, A. M. High-energy transmission Laue micro-beam X-ray diffraction: a probe for intra-granular lattice orientation and elastic strain in thicker samples, *J. Sync. Rad.* **19**, 3 (2012)

Micro-beam Laue diffraction is a versatile probe for orientation and elastic strain in individual grains of metallic polycrystals. It can help elucidate the dependence of macroscopic material behaviour (deformation response, fatigue, fracture etc.) on microstructure, defect population, macro- to microscopic load redistribution, etc. Furthermore, it can provide quantitative validation for the crystal plasticity models used to study structural engineering alloys. The application of micro-beam Laue diffraction to real-life engineering components is limited by the absorption of the probing beam. To improve penetration into thicker samples we developed a high-energy transmission Laue (HETL) micro-beam diffraction setup on I12. The use of higher photon energies (50 – 150 keV) permits measurements in several-millimetre-thick polycrystalline samples. We established two different approaches to extend this method and allow resolution in three dimensions. The first approach relies on the application of tomographic reconstruction principles to orientation-specific scattered intensity. The second uses wire scans and triangulation to determine the volume of origin of each scattered contribution recorded on the detector.

For safety-critical aerospace applications, the ability to obtain accurate predictions of the grain-level response to deformation of polycrystalline alloys is essential. This is particularly the case since material failure is governed by 'weakest link' type mechanisms such as grain boundary creep and cracking, void nucleation, etc. that strongly depend on local inter- and intra-granular interactions and on the partitioning of macroscopic loading at the micro-scale. Computationally these phenomena can be studied by crystal plasticity simulations that take into account local morphology, evolution of crystal slip, lattice rotation and dislocation density^{1,2}. For model calibration and validation, experimental measurements at the same (micro-) scale are essential. Micro-beam Laue synchrotron X-ray diffraction is ideally suited to this purpose. Conventionally, a polychromatic, micro-focussed X-ray beam probe (5-25 keV) is used to illuminate intra-granular scattering volumes. The resulting diffraction patterns consist of a number of Laue spots and are recorded on an area detector positioned in reflection geometry. By indexing the spots and refining their positions, lattice orientation and elastic strain in the scattering volume can be computed^{3,4}. Orientation spread in the illuminated volume causes streaking of reflections that can be interpreted in terms of the underlying dislocation structure and active slip system(s)⁵.

The shallow penetration of the probing beam (~70 μm in nickel) precludes the application of micro-beam Laue diffraction to the study of deformation in the bulk of real-life engineering components. To increase penetration to several millimetres, we extended the technique to significantly higher photon energies (50 to 150 keV). Transmission geometry is the natural choice since Bragg's law dictates that at higher photon energies, the stronger, lower order reflections are forward scattered⁶. We used this new technique to study the evolution of lattice orientation and strain in individual grains of polycrystalline nickel samples during *in-situ* deformation. The results highlighted that, even for uniform macroscopic loading, significant heterogeneities exist at the grain-scale. Furthermore

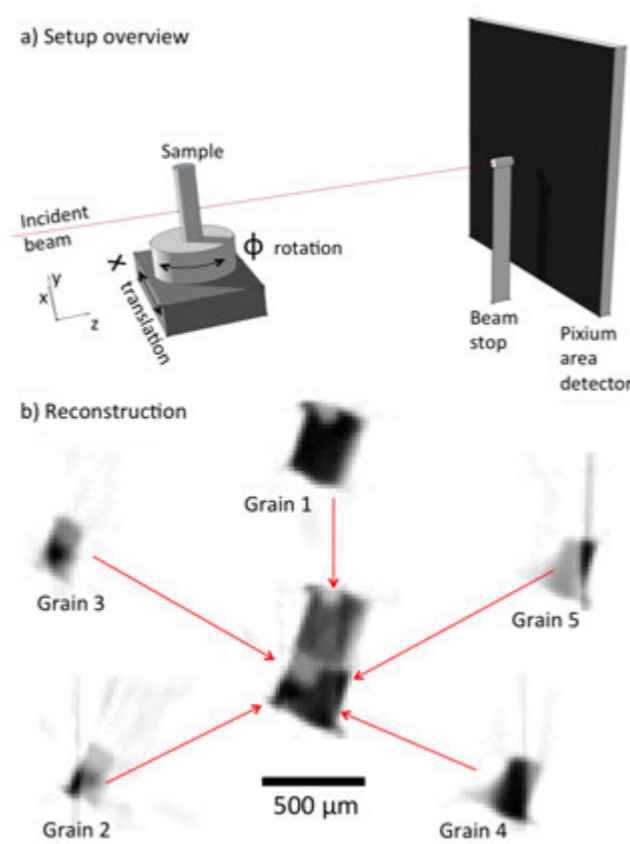


Figure 1: Laue Orientation Tomography (LOT). a) Schematic of the experimental setup. b) Reconstruction of 5 grains in the cross-section of a polycrystalline nickel sample.

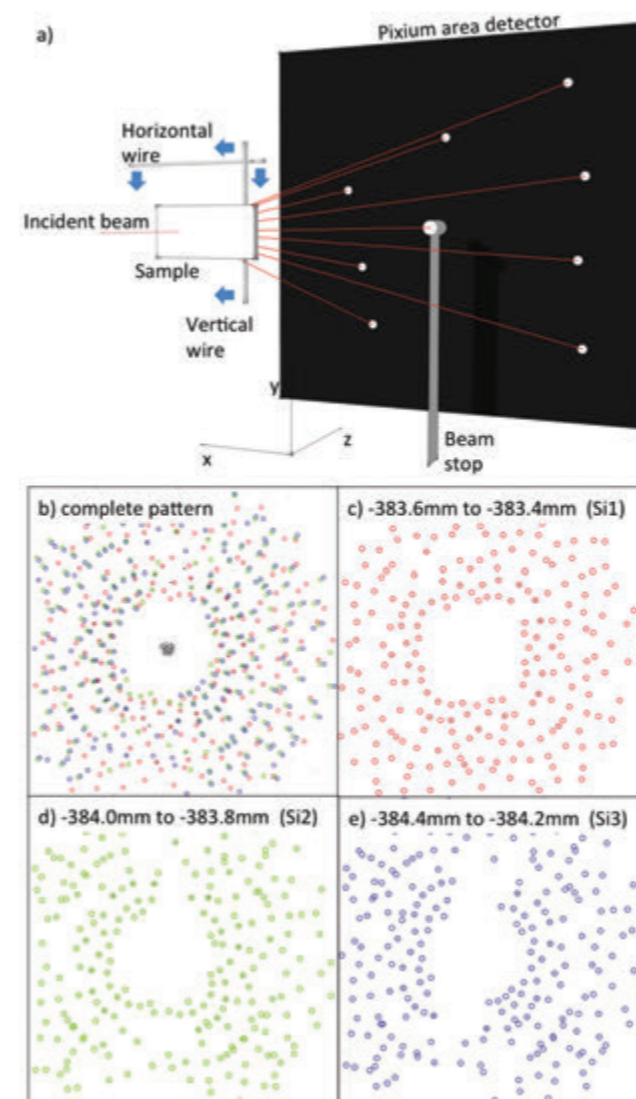


Figure 2: High Energy Differential Aperture X-ray Microscopy (HEDAXM). a) Schematic of the experimental setup. b) Experimental Laue pattern of three-layered silicon wafer sample. c)-e) Reconstructed Laue patterns from each of the three silicon wafer layers.

the local stress state is strongly influenced by the morphology of the grain neighbourhood.

At beamline I12 we developed two novel techniques to extend HETL to 3D grain-level resolution. The first, Laue Orientation Tomography (LOT), relies on the application of tomographic reconstruction principles to orientation-specific scattered intensity. The sample is mounted in transmission geometry (Fig. 1a.). Laue patterns are collected at x -positions covering the entire width of the sample for 91 ϕ -rotations between 0° and 180° . Indexation of the Laue patterns acts as an orientation-sensitive filter. Similar to absorption tomography, lattice-orientation-specific sinograms ('origrams') are then established as functions of x and ϕ , considering only the scattered intensity

that corresponds to a certain orientation. The shapes of individual grains in the illuminated sample slice are reconstructed by inverting these 'origrams' using filtered back projection algorithms. Fig. 1b. shows five grains present in the slice of a polycrystalline nickel sample reconstructed on I12. To map the full 3D microstructure, slices at different heights of the sample are reconstructed. Further work is under way to obtain maps of intra-granular mis-orientation within individual crystallites.

The second technique, High Energy Differential Aperture X-ray Microscopy (HEDAXM), is an extension of the corresponding low energy technique⁷. Tungsten wires are scanned across the scattered beams immediately downstream of the sample (Fig. 2a.). When a given reflection is obscured by a scanning wire we triangulate from the reflection position on the detector, via the wire, to the incident beam. Hence the through-thickness position of the coherently scattering volume that gives rise to the reflection can be determined. On I12 we studied a three-layer silicon wafer sample as a proof of principle. Fig. 2b., shows the complete diffraction pattern arising from this sample. Using HEDAXM we successfully separated this pattern into the individual contribution from each layer (Fig. 2c-e.).

These successful first results demonstrate the promise of LOT and HEDAXM for the 3D mapping of microstructure, lattice orientation and elastic strain in individual grains of polycrystalline engineering samples.

References

1. Busso, E.P., Meissonnier, F.T., O'Dowd, N.P. *J. Mech. Phys. Solids.* **48**, 2333–2361 (2000).
2. Beaudoin, A.J., Acharya, A., Chen, S.R., Korzekwa, D.A. & Stout, M.G. *Acta Mater.* **48**, 3409–3423 (2000).
3. Budai, J.D., Yang, W., Tamura, N., Chung, J.S., Tischler, J.Z., Larson, B.C., Ice, G.E., Park, C. & Norton, D.P. *Nat. Mater.* **2**, 487–492 (2003).
4. Hofmann, F., Song, X., Dolbnya, I., Abbey, B. & Korsunsky, A.M. *Procedia Engineering* **1**, 193–196 (2009).
5. Barabash, R.I., Ice, G.E., Larson, B.C., Pharr, G.M., Chung, K.S. & Yang, W. *Appl. Phys. Lett.* **79**, 749–751 (2001).
6. Hofmann, F., Song, X., Jun, T.S., Abbey, B., Peel, M., Daniels, J., Honkimäki, V. & Korsunsky A.M. *Mater. Lett.* **64**, 1302–1305 (2010).
7. Yang, W., Larson, B.C., Tischler, J.Z., Ice, G.E., Budai, J.D. & Liu, W. *Micron*, **35**, 431–439 (2004).

Funding Acknowledgements

Funding for this project was provided by the EPSRC in the form of a DTA and a PhD+ grant and project grants EP/H003215, EP/G035059 and EP/I020691.

DOI 10.3139/146.110660

DOI 10.1107/S0909049512003044

The effect of pressure on bismuth displacements in pyrochlore materials

Salamat, A., Hector, A. L., McMillan, P. F., Ritter, C. Structure, bonding, and phase relations in $\text{Bi}_2\text{Sn}_2\text{O}_7$ and $\text{Bi}_2\text{Ti}_2\text{O}_7$ pyrochlores: new insights from high pressure and high temperature studies. *Inorg. Chem.* **50(23)**, 11905-11913 (2011)

Pyrochlore-structured materials containing bismuth are useful electroceramics, and they have also been studied for their interesting crystal structures and polymorphic phase transformations. This study applies pressure to two of these materials and used synchrotron X-ray diffraction on beamline I15, combined with further studies at the ESRF and ILL, to observe how the structures change. Examining the way in which the environment around bismuth changes gives insight into the interactions between bismuth atoms that are responsible for structural change, and also the factors that are responsible for the asymmetric environments around bismuth. In the latter case our results suggest that the bismuth sites are underbonded and that this has a more significant effect on the Bi^{3+} cation than the possible active lone pair.

Interest in bismuth-containing pyrochlore materials is derived from their complex structural chemistry in which bismuth ions are displaced from the centre of the coordination site normally occupied in pyrochlores by large cations including group 2 or 3 metals. The displacements have been linked to the high dielectric constants and other desirable electrical properties of pyrochlores including useful materials such as $\text{Bi}_2\text{Ti}_2\text{O}_7$ and $(\text{Bi,Zn})_2(\text{Zn,Nb})_2\text{O}_7$ (BZN).² The latter compound is now being incorporated into capacitors for microwave applications and thin film devices. In $\text{Bi}_2\text{Ti}_2\text{O}_7$, the Bi^{3+} ions are displaced in a disordered manner,³ and so the off-centre displacements do not cause any changes in the overall cubic symmetry of the structure. However, $\text{Bi}_2\text{Sn}_2\text{O}_7$ and $\text{Bi}_2\text{Hf}_2\text{O}_7$ exhibit displacements that are cooperative between the metal centres and the distortion is seen to cause a significant overall change to the lattice, resulting in a monoclinic symmetry with a four-fold increase in unit cell volume. Local environments around the large 'A' cation are shown in Fig. 1.

$\text{Bi}_2\text{Ti}_2\text{O}_7$ is known to remain stable between 2 and 730 K, above which point it starts to decompose into $\text{Bi}_4\text{Ti}_3\text{O}_{12}$ along with other phases. $\text{Bi}_2\text{Sn}_2\text{O}_7$ undergoes phase changes at 412 and 903 K but does not decompose in this T range. Prior to this work the structures of the α - (<470 K) and γ - (>903 K) $\text{Bi}_2\text{Sn}_2\text{O}_7$ phases had been determined, with γ - $\text{Bi}_2\text{Sn}_2\text{O}_7$ isostructural with $\text{Bi}_2\text{Ti}_2\text{O}_7$. Our Diamond Light Source experiment was conceived around the idea that the phase behaviour of these compounds was likely to give some indication of the fundamental causes for the Bi^{3+} displacements. We examined both $\text{Bi}_2\text{Ti}_2\text{O}_7$ and $\text{Bi}_2\text{Sn}_2\text{O}_7$ structures by X-ray diffraction during compression to high pressure in a diamond anvil cell, at ambient and elevated temperatures. Bismuth displacements have been argued previously to be due to an active lone pair on the Bi^{3+} ion, or as a response to underbonding of the Bi^{3+} ions at the centre of the coordination sphere. We considered that the bismuth sites were likely to be more compressible than the tin or titanium sites, and hence that compression would relieve

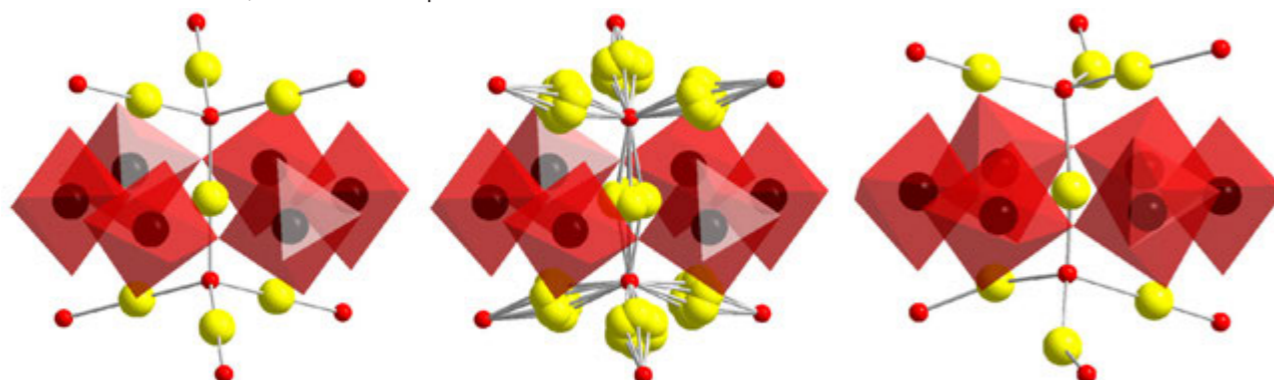


Figure 1: La or Bi environment (yellow) in $\text{La}_2\text{Ti}_2\text{O}_7$ (left) with La at the centre of the coordination sphere, $\text{Bi}_2\text{Ti}_2\text{O}_7$ (middle) with disordered Bi displacements and $\text{Bi}_2\text{Sn}_2\text{O}_7$ (right) with ordered Bi displacements. Red octahedra are the TiO_6 or SnO_6 units, and red spheres are oxygen atoms.

any under bonding characteristics. In contrast, effects due to the lone pair electrons centred on the Bi^{3+} ions should become more significant on compression.

High resolution angle-dispersive diffraction experiments were carried out at beamline I15 using 0.4454 Å X-rays and a MAR image plate. The image plate data were calibrated and integrated using Fit2D and structure refinements were carried out using the GSAS package, often using Le Bail fits to interpret the data due to texturing within the very small samples. Compression of $\text{Bi}_2\text{Ti}_2\text{O}_7$ results in a smooth volume reduction trend observed up to around 33 GPa. From this trend we were able to derive a bulk modulus of $K_0 = 202$ GPa, which is in the range of values typically found for rare earth pyrochlores (185-213 GPa). Above 33 GPa the structure starts to disorder with broad fluorite-like peaks developing (pyrochlore is often described as a site-defective modification of a fluorite lattice), though this process was not complete even at 60 GPa. Compression of $\text{Bi}_2\text{Sn}_2\text{O}_7$ results in a series of structural and phase changes that mimic those seen for this phase with increasing temperature. The α - β phase transition is observed at around 12 GPa, and the β - γ transition occurs at ~20 GPa. Above 34 GPa disordering to a fluorite-like phase is seen, similar to $\text{Bi}_2\text{Ti}_2\text{O}_7$. Heating the $\text{Bi}_2\text{Sn}_2\text{O}_7$ to a temperature at which the β -phase is present at ambient pressure and then applying pressure results in a β - γ transition at ~16 GPa. Examples of the data for the three $\text{Bi}_2\text{Sn}_2\text{O}_7$ phases are given in Fig. 2 and the volume changes with pressurisation in $\text{Bi}_2\text{Sn}_2\text{O}_7$ are shown in Fig. 3. The latter shows clear discontinuities at the phase change pressures and similar slopes in the β - and γ - $\text{Bi}_2\text{Sn}_2\text{O}_7$ V-P relationship at both temperatures.

Pyrochlores are often considered as two interpenetrating lattices, with the oxygen atoms that are not directly bonded to the B cation (Sn in this case) labelled as O' . The bismuth atoms in the Bi_2O_7 sublattice, which locally resembles β -cristobalite, are linked to their nearest bismuth neighbours by

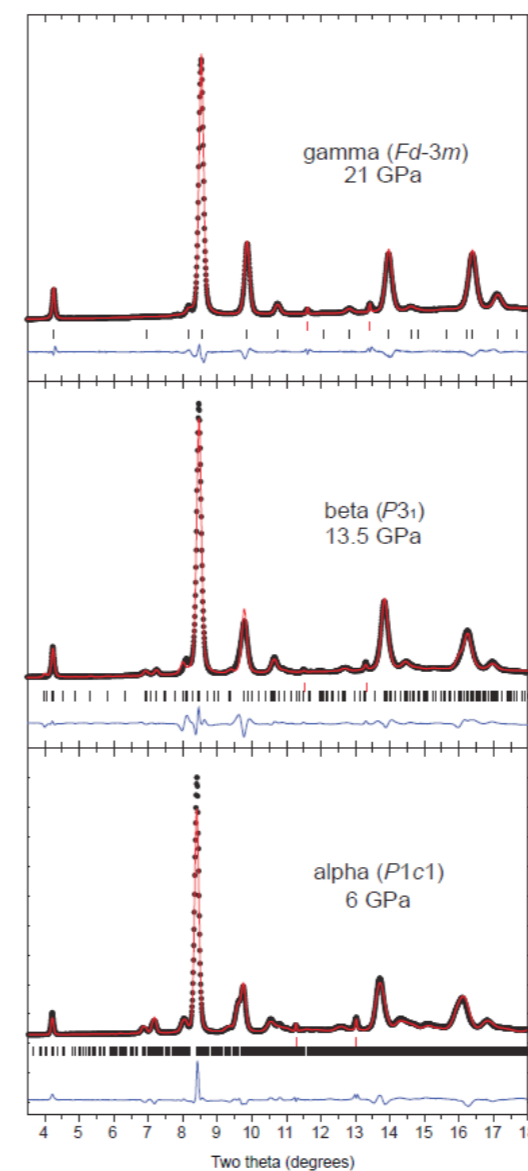


Figure 2: Le Bail fits to XRD patterns of $\text{Bi}_2\text{Sn}_2\text{O}_7$ collected at the pressures shown in a LiF pressure transmitting medium. Data points are shown as black crosses, the fit as the red line and the difference as the blue line. Black tick marks indicate allowed reflection positions for $\text{Bi}_2\text{Sn}_2\text{O}_7$, and red tick marks the LiF peaks.

tetrahedral oxygen sites, and there are further links via other oxygen atoms. α - $\text{Bi}_2\text{Sn}_2\text{O}_7$ has displacements within the ring of 6 O' atoms that coordinate it, and also a further displacement toward one of the O' atoms that results in an overall ice-like network in which every O' atom has two longer and two

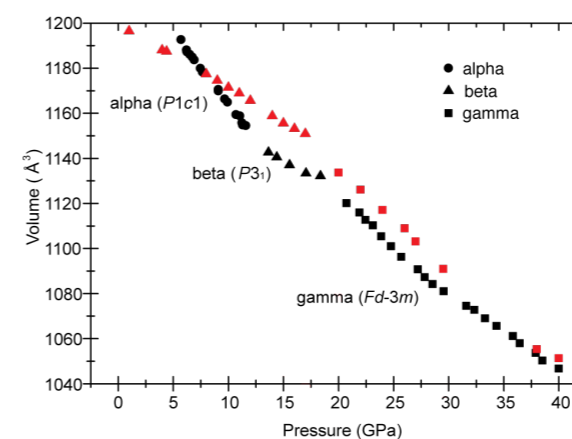


Figure 3: Volume of the $\text{Bi}_2\text{Sn}_2\text{O}_7$ unit cell at various temperatures and pressures – black symbols represent volume at 298 K and red symbols at 623 K. Volumes are normalised to that of γ - $\text{Bi}_2\text{Sn}_2\text{O}_7$, by dividing that of α - $\text{Bi}_2\text{Sn}_2\text{O}_7$ by 4, and that of β - $\text{Bi}_2\text{Sn}_2\text{O}_7$ by 1.5.

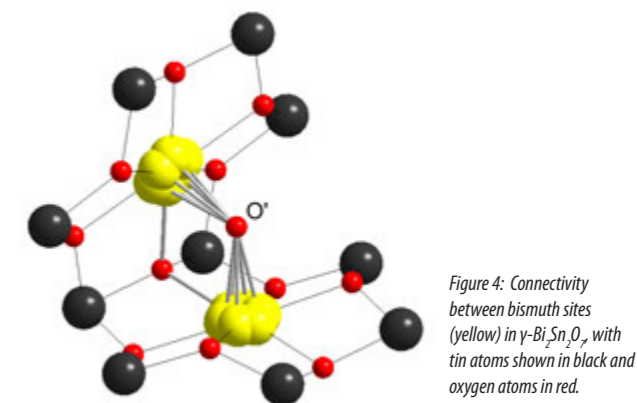


Figure 4: Connectivity between bismuth sites (yellow) in γ - $\text{Bi}_2\text{Sn}_2\text{O}_7$, with tin atoms shown in black and oxygen atoms in red.

shorter Bi- O' bonds. β - $\text{Bi}_2\text{Sn}_2\text{O}_7$ seems to have only the displacements within the ring, and in γ - $\text{Bi}_2\text{Sn}_2\text{O}_7$ these become disordered (Fig. 4). Interactions within the tetrahedral network would be expected to be subject to some degree of frustration, and the phase changes can be understood in reference to the different strengths of the correlations via the O' atom (i.e., out of plane displacement, β - γ transition at higher temperature) and either through-space or via the O' atoms (ordering of in plane displacement, α - β transition at lower temperature).

The differences in observed behaviour between $\text{Bi}_2\text{Ti}_2\text{O}_7$ and $\text{Bi}_2\text{Sn}_2\text{O}_7$, and the α - β $\text{Bi}_2\text{Sn}_2\text{O}_7$ phase transition, present a compelling case for the fundamental cause of Bi^{3+} displacement (i.e., the α -phase exhibits the out-of-plane displacement, whereas the β -phase does not). Compression of the BiO_8 coordination sphere should restrict space for any active lone pair and hence would be expected to increase the distortion at this site. Increasing the pressure, or reducing the B cation size (Sn \rightarrow Ti), reduces this distortion. In contrast, an under bonded Bi site would gain electron density on compression and reduce the need for distortion. Hence the experimental data show that the bond valence sum at the Bi^{3+} ion is more influential in the structural distortions that determine the important materials properties of these compounds than lone pair effects.

References

- Esquivel-Elizondo, J. R., Hinojosa, B. B. & Nino, J. C. $\text{Bi}_2\text{Ti}_2\text{O}_7$: It is not what you have read. *Chem. Mater.* **23(22)**, 4965-4974 (2011).
- Levin, I., Amos, T. G., Nino, J. C., Vanderah, T. A., Randall, C. A. & Lanagan, M. T. Structural study of an unusual cubic pyrochlore $\text{Bi}_{1.5}\text{Zn}_{0.92}\text{Nb}_{1.5}\text{O}_{6.92}$. *J. Solid State Chem.* **168(1)**, 69-75 (2002).
- Hector, A. L., & Wiggin, S. B. Synthesis and structural study of stoichiometric $\text{Bi}_2\text{Ti}_2\text{O}_7$ pyrochlore. *J. Solid State Chem.* **177(1)**, 139-145 (2004).
- Radosavljevic Evans, I., Howard, J. A. K. & Evans, J. S. O. α - $\text{Bi}_2\text{Sn}_2\text{O}_7$ – a 176 atom crystal structure from powder diffraction data. *J. Mater. Chem.* **13(9)**, 2098-2103 (2003).
- Henderson, S. J., Shebanova, O., Hector, A. L., McMillan, P. F. & Weller, M. T. Structural variations in pyrochlore-structured $\text{Bi}_2\text{Hf}_2\text{O}_7$, $\text{Bi}_2\text{Ti}_2\text{O}_7$ and $\text{Bi}_2\text{Hf}_{2-x}\text{Ti}_x\text{O}_7$ solid solutions as a function of composition and temperature by neutron and X-ray diffraction and Raman spectroscopy. *Chem. Mater.* **19(7)**, 1712-1722 (2007).

Funding Acknowledgements

PFM and AS thank EPSRC for support under a senior research fellowship (EP/D07357X/1).

Research carried out at Diamond Light Source on I15, at the ESRF on beamline ID31 and at the ILL on D2B.

DOI 10.1021/ic200841v

Melting curve of potassium to 22 GPa

Narygina, O., McBride, E. E., Stinton G. W. and McMahon, M. I. Melting curve of potassium to 22 GPa, *Phys. Rev. B* **84**, 054111 (2011)

Since the work of Zha and Boehler in 1985, potassium 'K' has been believed to have a 'simple' melting curve, characterised by the continuous increase of the melting temperature with pressure, at least to 14.5 GPa. This 'normal' melting is in contrast to that observed in the other alkali metals Li, Na, Rb and Cs, where one or more maxima in the melting curve are followed by substantial decreases in the melting temperature to minimum values, above which the melting curve recovers a large positive slope. Considering the strong similarities in high-pressure behaviour of K with that of the other alkali metals, its simple melting curve seems to be rather surprising. Using X-ray diffraction facilities of I15 beamline, we have shown that the melting behaviour of K is far more complex than was previously reported. A melting maximum is found in the stability field of the K-I phase at ~ 6 GPa, followed by a decrease in the melting temperature down to a melting minimum at the phase transition from K-II to K-III at ~ 19 GPa. Above 19 GPa, the melting curve recovers a positive slope, increasing rapidly with pressure, changing by some 65(5) K/GPa. The re-measured K melting curve closely resembles that of Na, the complex behaviour of which is believed to be related to structural/electronic changes either in the solid or liquid phase, or both. Similarities between the melting curves of these two alkali metals suggest that the same mechanisms might explain the melting curve of K.

Complex melting behaviour is one of the common features among alkali metals. The appearance of one or more melting-curve maxima has been observed in Li, Na, Rb and Cs, but not, however, in K, at least not up to 14.5 GPa¹. Using optical observations of a sample enclosed in a diamond anvil cell (DAC) Zha & Boehler¹ reported that the melting temperature continuously increases in both the K-I (which has a body-centred cubic (bcc) crystal structure) and K-II (with a face-centred cubic (fcc) crystal structure) phases, reaching a value of 649 K at 14.5 GPa. However, theoretical calculations of the melting temperature of K have suggested the presence of a melting maximum between 4 and 8 GPa². To resolve this apparent discrepancy between experimental and theoretical results, and to extend the measurements of the potassium melting curve into the incommensurate K-III phase (with the *t*/19 host-guest crystal structure) above 19 GPa, we have performed an *in situ* synchrotron X-ray diffraction (XRD) study of the melting curve of K at pressures up to 22 GPa using a DAC. XRD measurements were performed principally on beamline I15 at the Diamond Light Source, and also on beamline ID09a at the ESRF.

A representative set of high-pressure high-temperature 2D XRD images, and their integrated XRD profiles (Fig. 1), demonstrates the sharp melting transition from fcc-K to liquid-K at 18.3(3) GPa, induced by the small increase in temperature of only 4 K. A subsequent pressure increase of about 2 GPa at the same temperature, 408(10) K, brings the sample into the stability field of the incommensurate *t*/19 phase. By varying pressure and temperature conditions we tracked the melting curve of potassium at pressures from ambient to 22 GPa, as shown in Fig. 2.

Our data, combined with all the previous melting curve measurements up to 3 GPa³, suggest the presence of a melting maximum in the bcc phase, the position of which was estimated using the Kechin equation. The obtained value of 530(2) K and 5.8(5) GPa is in good agreement with theoretical calculations². At pressures above this maximum, the melting temperature decreases to 466(10) K at the bcc-fcc-liquid triple point at 13.6(3) GPa, and then remains almost constant up to 15.6(3) GPa, where the melting curve again changes its behaviour, descending to a clear minimum at 390(10) K and 19.0(3) GPa at the fcc-*t*/19-liquid triple point. The fcc-*t*/19 phase boundary is found to be almost vertical. In the *t*/19 phase, the melting temperature increases very rapidly with pressure, changing by some 65(5) K/GPa (Fig. 2).

This behaviour is very similar to that observed in Na, where the melting temperature, after passing through a deep minimum at 300 K and 118 GPa,

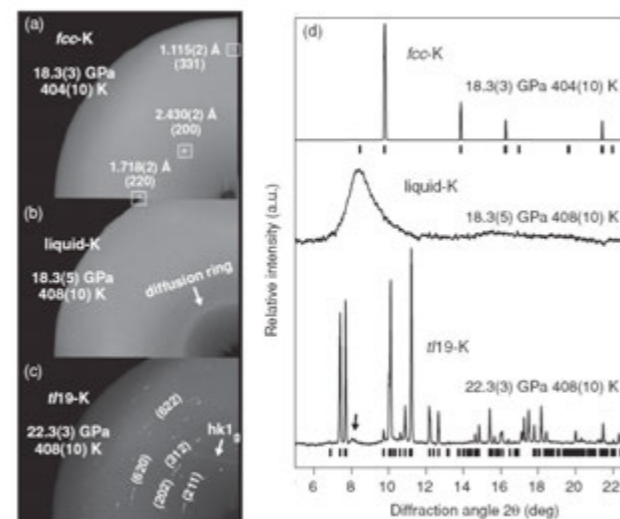


Figure 1: (a-c) Representative quadrants of XRD images from the solid and liquid phases of the alkali metal K. Three *d* spacings of fcc-K, 1st order reflection of liquid-K and Miller indices for some reflections of *t*/19-K are marked in the images (a-c). Please, note that *d* spacings of fcc-K were identified from isolated single-crystal reflections. (d) The corresponding integrated XRD profiles. The crystalline phases are indexed to the fcc and 'host-guest' *t*/19 structures, and vertical bars show fitted position of the diffraction reflections of fcc-K [$a_{fcc} = 4.856(1) \text{ \AA}$] and 'host' phase of *t*/19-K [$a_{host} = 9.769(1) \text{ \AA}$, $c_{host} = 4.730(1) \text{ \AA}$], black arrow shows positions of 'guest' reflections of *t*/19-K. The XRD profile of the liquid-K obtained at 18.3(5) GPa and 408(10) K is plotted with the subtracted background.

increases again after the transition to the *t*/19 phase at 125 GPa. The close resemblance of the melting curves of these two alkalis might suggest that similar physical mechanisms lying behind the melting behaviour of K and Na. Currently there are two theoretical approaches to explain the complex nature of the Na melting curve: (i) softening of the elastic moduli of solid Na above 30 GPa and a consequent decrease of Debye temperature, which, according to the Lindeman criterion, results in a negative slope of a melting curve⁴; (ii) structural and electronic transitions in liquid-Na at about 30 and 80 GPa, which resemble the transitions occurring in solid-Na at higher pressures⁵.

In attempting to explain the melting curve of K (Fig. 2) we have considered both approaches. The theoretical work by Katsnelson *et al.*² did show softening of elastic constants in both bcc- and fcc-K. Using the Lindeman criterion they also predicted a melting-curve maximum at about 5 GPa (in a good agreement with the 5.8 GPa presented here). However,

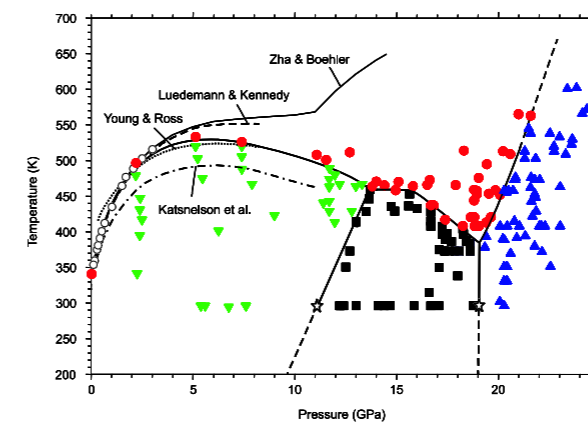


Figure 2: The melting curve of K measured to 22 GPa. Filled symbols represent the data from this study; downward-pointing triangles correspond to bcc-K, squares to fcc-K, upward-pointing triangles to *t*/19-K, and circles to the liquid phase. The melting temperature at ambient pressure was obtained by observation of the K sample sealed in a glass capsule. Solid and dashed lines represent the measured phase boundaries and their extrapolations, respectively. The data points marked with stars show the location of the bcc-fcc and fcc-*t*/19 phase transitions at room temperature. Open circles are data points from Refs. 3. The melting curve in the pressure range from ambient up to the 13.6(8) GPa (the location of the bcc-fcc-liquid triple point) represents the fit of the experimental data using the Kechin equation. Some previously-reported experimental and theoretically-calculated melting curves of K are from Refs. 1-3.

the same calculation underestimates the melting temperature over a large pressure range (dash-dotted line in Fig. 2). The possible softening of elastic moduli in bcc- and fcc-K, and its effect on the melting curve of K, is yet to be investigated.

In the framework of the second approach⁵, the melting maximum at about 6 GPa followed by a decrease of the melting temperature down to the bcc-fcc-liquid triple point, would suggest a transition in liquid-K from a bcc-like to a more dense fcc-like liquid at about 6 GPa. Above the bcc-fcc-liquid triple point, where the solid-K itself assumes the fcc-structure, the melting temperature is almost constant. The following decrease of the melting temperature between 15.6 GPa and 19 GPa would suggest a second transition in liquid-K, from fcc-like to *t*/19-like. To confirm these predictions further, experimental studies, as well as computer simulations of the properties of both solid and liquid dense K, are required. However, our data do indeed show some structural changes in liquid-K (Fig. 3), thus providing evidence in the favour of the approach suggested by Raty *et al.*⁵ Below 5 GPa the position of the first diffraction peak of liquid-K is in a good agreement with the bcc-K equation of state, while between 5 and 14 GPa it closely follows the fcc-K equation of state. This might be related to a bcc-to-fcc-like liquid transition in liquid-K. Above 14 GPa there is another change in the structural behaviour of liquid-K, which again could be related to a structural transition, this time, from fcc-like to *t*/19-like. We hope to use high pressure facilities of I15 beamline again in the near future to investigate these changes further and in more detail.

To conclude, the re-visited melting curve of K appears to be very different from that previously reported. In the stability field of bcc-K there is a melting maximum, like that observed previously in Na, Rb and Cs. The melting behaviour of fcc-K resembles that reported for fcc-Na. Using similar arguments put forward previously to explain the melting curve of Na, we suggest that the behaviour of the K melting curve is likely to be due to structural and electronic changes in liquid-K at ~ 6 and 14 GPa, which mirror those that occur in the solid phase at 13.6 and 19 GPa, respectively. However, the anomalous melting of bcc- and fcc-K may also suggest a softening of elastic moduli of these phases as pressure increases. Further work is required to understand the complex nature of dense K.

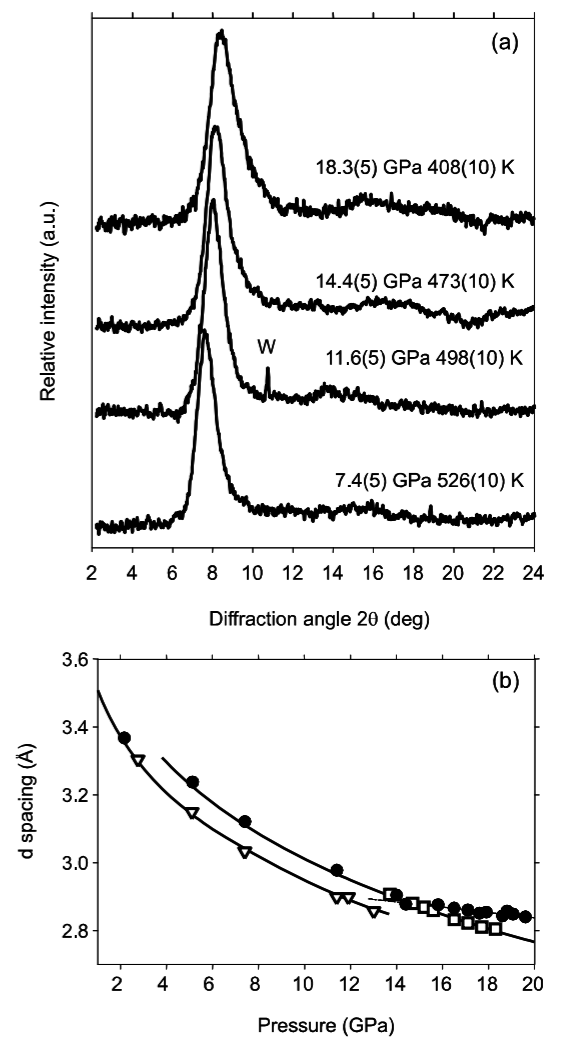


Figure 3: (a) Integrated XRD profiles from liquid-K obtained at different pressures. The background has been subtracted. A weak diffraction peak from the tungsten (W) gasket is marked. (b) The pressure-induced shift of the first diffraction peak from liquid-K (solid circles) and the (110) and (111) diffraction peak from bcc-K (open triangles) and fcc-K (open squares), respectively. The lines through the data points are guides to the eye.

References

- Zha C.-S. & Boehler R. Melting of sodium and potassium in a diamond anvil cell. *Phys. Rev. B* **31**, 3199-3201 (1985).
- Young D.A. & Ross M. Theoretical high-pressure equations of state and phase diagrams of the alkali metals. *Phys. Rev. B* **29**, 682-691 (1984); Katsnelson M.I., Sinko G.V., Smirnov N.A., Trefilov A.V., and Khromov K.Yu. *Phys. Rev. B* **61**, 14420-14424 (2000).
- Boehler R. Melting temperature, adiabats and Grüneisen parameter of lithium, sodium and potassium versus pressure. *Phys. Rev. B* **27**, 6754-6762 (1983) and references therein.
- Martinez-Canales M. & Bergara A. Lindeman criterion and the anomalous melting curve of sodium. *J. Phys. Chem. Solids* **69**, 2151-2154 (2008).
- Raty J.-Y., Schwegler E., and Bonev S.A. Electronic and structural transitions in dense liquid sodium. *Nature* **449**, 448-451 (2007).

Funding Acknowledgments

This work was supported by a research grant from the U.K. Engineering and Physical Sciences Research Council. Research carried out at Diamond Light Source on I15 and at the ESRF on beamline ID09A.

DOI 10.1103/PhysRevB.84.054111

Structural behaviour of mineral barite under strong compression

Santamaría-Pérez, D., Gracia, L., Garbarino, G., Beltrán, A., Chuliá-Jordán, R., Gomis, O., Errandonea, D., Ferrer-Roca, Ch., Martínez-García, D. & Segura, A. High-pressure study of the behavior of mineral barite by X-ray diffraction. *Phys. Rev. B*. **84**, 054102 (2011)

Research on the mineral barite, BaSO_4 , is of great interest for Earth and material sciences. Its unique properties, the high density and chemical inertness, make barite useful for instance for oil and gas drilling. Particularly, this compound has recently been of renewed interest regarding its high-pressure behaviour. Previous reports present some controversial results on the behaviour of this mineral under strong compression. Some authors observed small changes in the X-ray diffraction patterns and they inferred a phase transition below 13 GPa, whereas others did not observe any transition up to 21.5 GPa. In this study, we have made use of the high-energy synchrotron radiation available in the I15 beamline of Diamond Light Source and in the ID27 beamline of the ESRF to accurately determine the structural sequence and compressibility of BaSO_4 .

Mineral barite, BaSO_4 , crystallises at ambient conditions in an orthorhombic structure (space group: $Pnma$, $Z=4$) with lattice parameters: $a=8.8721(4)$ Å, $b=5.4522(2)$ and $c=7.1491(3)$ Å [$V=345.586(7)$ Å³]. Its structure can be easily described in terms of the cation subarray BaS which is of the FeB-type (B27), the structure consisting of triangular prisms of Ba atoms that share faces along the b direction and corners in the other two directions, with the $[\text{SO}_4]$ groups inserted into these metal prisms (see Fig. 1). Barite had been studied under pressure using Raman spectroscopy and energy-dispersive X-ray diffraction. Lee *et al.* observed small changes in the diffraction patterns and a subtle variation of the lattice parameters at about 13 GPa and they inferred a phase transition¹. The high-pressure (HP) phase was tentatively determined to be triclinic. More recently, however, Crichton *et al.* carried out Raman and angle-dispersive X-ray diffraction (XRD) measurements in barite up to 21.5 GPa using He as pressure medium². They did not observe any phase transition in BaSO_4 , the barite-type structure remaining to the highest investigated pressure.

Therefore, in order to better understand the poorly known behavior of this mineral under compression, we performed high pressure XRD measurements using a diamond anvil cell (DAC). Silicone oil and He were used as pressure-transmitting media. The pressure was estimated using the ruby fluorescence technique³.

Fig. 2. shows some XRD patterns at selected pressures using He as pressure medium. In good agreement with Crichton's data², high-pressure

XRD patterns could be indexed in the orthorhombic phase which is stable at room conditions, up to 27 GPa. Above this pressure, new peaks appear in the XRD pattern, indicating the onset of a phase transition in BaSO_4 . At 40.5 GPa, the diffraction peaks of the low-pressure phase have almost disappeared completely. This transition was also observed using silicone oil as pressure medium, but the lack of hydrostaticity led the phase transition to occur at lower pressures, at 19 GPa. These structural changes were found to be reversible.

From the analysis of the XRD patterns, we obtained the pressure evolution of the unit-cell volume and lattice parameters of the low-pressure phase. The contraction of the lattice constants is rather isotropic. The pressure-volume curve was analysed using a third-order Birch-Murnaghan equation of state (EOS). By fixing the zero-pressure volume (V_0) to its measured value, we obtained the bulk modulus, $B_0 = 58.6(2)$ GPa, and its pressure derivative, $B'_0 = 4.8(1)$. The values of these characteristic parameters are in excellent agreement with those theoretically calculated.

We have also proposed a crystalline structure for the high-pressure phase³. As it can be seen in Figs. 2 and 3, the diffraction pattern of the high-pressure phase (40.5 GPa) obtained with He as pressure medium still has very well defined peaks. They could be indexed in an orthorhombic cell with lattice constants: $a=6.55(5)$ Å, $b=5.87(4)$ Å and $c=6.33(4)$ Å [$V=243.3(8)$ Å³, $Z=4$] with a high figure of merit ($M(20) = 21.2$). Therefore, this structure implies a volume change of about 2% at the transition. The systematic

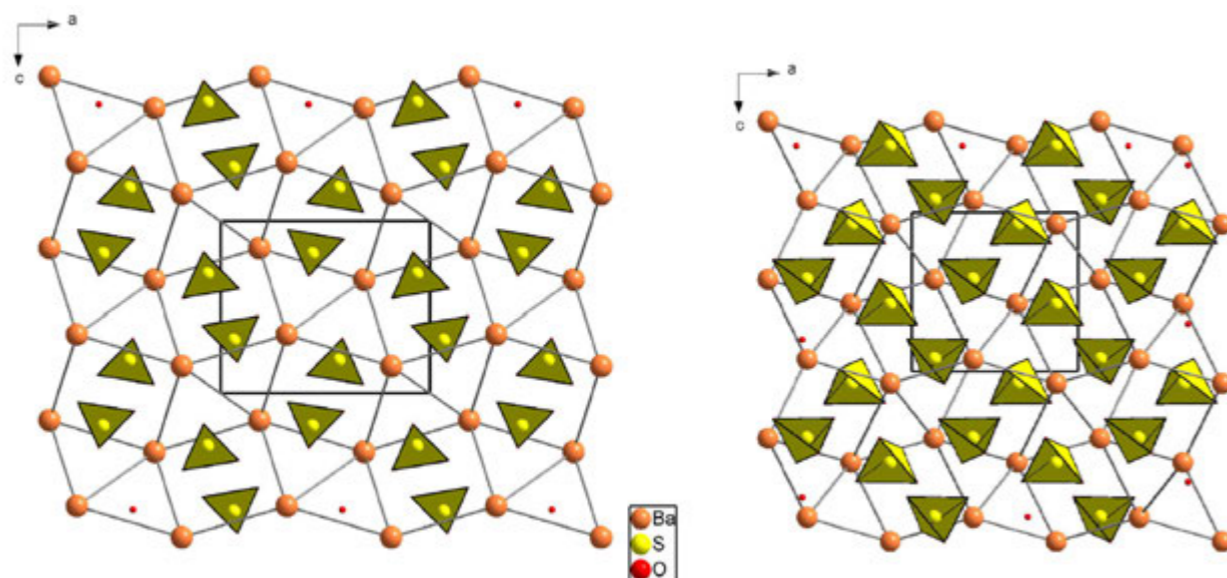


Figure 1: Crystal structures of the low- (left) and high-pressure (right) phases of BaSO_4 .

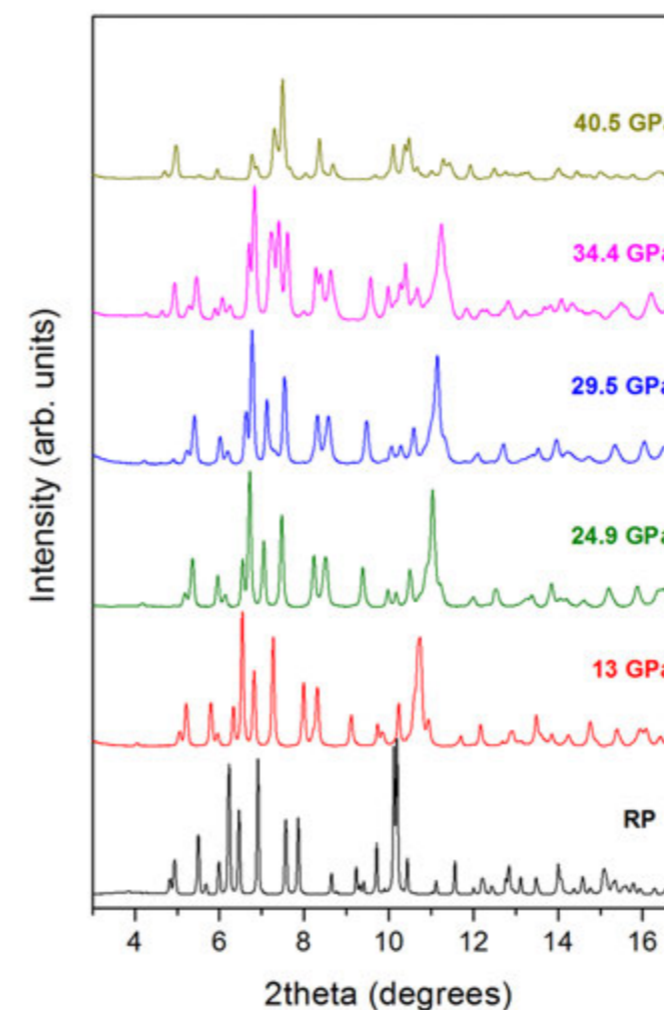


Figure 2: Selected HP XRD patterns: He as pressure transmitting medium. Changes in the diffraction patterns above 30 GPa indicate the occurrence of a phase transition. Pressures are indicated in the plot.

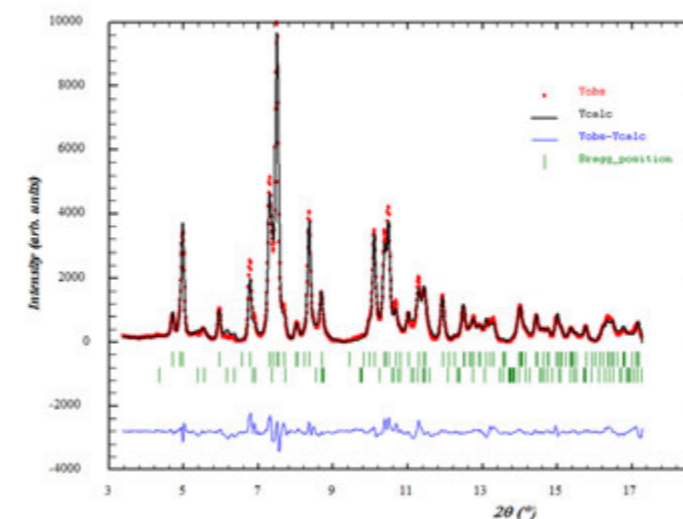


Figure 3: Observed, calculated and difference X-ray diffraction profiles for the high-pressure phase of BaSO_4 at 40.5 GPa. Vertical markers indicate Bragg reflections of the new orthorhombic $P2_12_1$ structure (above) and the initial orthorhombic $Pnma$ structure (below).

absences or extinctions in the indexed lattice planes were consistent with symmetry elements (screw axes) of the space group $P2_12_1$. A distorted barite-type structure model was refined by the Rietveld method (see Fig. 3), leading to the atomic parameters.

The structure of the high-pressure phase is basically a strong distortion of the initial barite phase (see Fig. 1). The a axis contracts approximately 18.3%, the b axis expands approximately 20% and the c axis remains nearly constant at the transition pressure. This lattice transformation entails a small displacement and tilting movement of the $[\text{SO}_4]$ tetrahedra and the elongation of the b axis implies that we can not consider the existence of trigonal prisms anymore.

The variation of the unit cell volumes of the high-pressure phase of BaSO_4 with pressure could be fitted to a third-order Birch-Murnaghan EOS where the values of the bulk modulus (B_0) and cell volume at zero pressure (V_0) are left to vary freely and B'_0 is fixed to 4. The characteristic parameters for the $P2_12_1$ phase are: $V_0 = 325(3)$ Å³ and $B_0 = 78(4)$ GPa.

The HP structural behavior of barite is very interesting regarding the position of this compound on the Bastide's diagram⁴. This diagram has proven useful in classifying and predicting phase transitions in ABX_4 compounds. The location of BaSO_4 in the lower-right quadrant, due to its relationship of cation-to-anion radii ratios (r_A/r_X , r_B/r_X), did not allow for the prediction of a post-barite structure, which was to be described. Thus, the post-barite structure found in this study^{3,5}, the HP- $P2_12_1$ phase, turns out to be one of the missing structural types in the Bastide's diagram and gives, therefore, further insight on the structural sequences of the ABO_4 oxides under compression.

References

- Lee, P.L, Huang, E. & Yu, S. C. High pressure Raman and X-ray studies of Barite, BaSO_4 . *High Pressure Research*. **23**, 439-450 (2003).
- Crichton, W.A., Merlini, M., Hanfland, M. & Muller, H. The crystal structure of barite, BaSO_4 , at high pressure. *Am. Mineral*. **96**, 364-367 (2011).
- Santamaria-Perez, D. *et al.* High-pressure study of the behavior of mineral barite by x-ray diffraction *Phys. Rev. B*. **84**, 054102 (2011).
- Bastide, J.P. Systématique simplifiée des composés ABX_4 ($X = \text{O}^{2-}, \text{F}^-$) et évolution possible de leurs structures cristallines sous pression. *J. Solid State Chem.* **71**, 115 (1987).
- Santamaria-Perez, D. and Chulia-Jordan, R. High Press. Res. (2011) In press. ISSN 0895-7959 print/ISSN 1477-2299 online.

Funding Acknowledgements

Spanish Consolider Ingenio 2010 Program (Project No. CDS2007-00045), Spanish MICCIN Grants CTQ2009-14596-C02-01 and No. MAT2010-21270-C04-01 and Comunidad de Madrid and European Social Fund: S2009/PPQ-1551 4161893.

Research carried out at Diamond Light Source on beamline I15 and at the ESRF on beamline ID27.

DOI 10.1103/PhysRevB.84.054102

Beamline I11 In-situ gas control system and sample cells

Julia Parker and Stephen Thompson

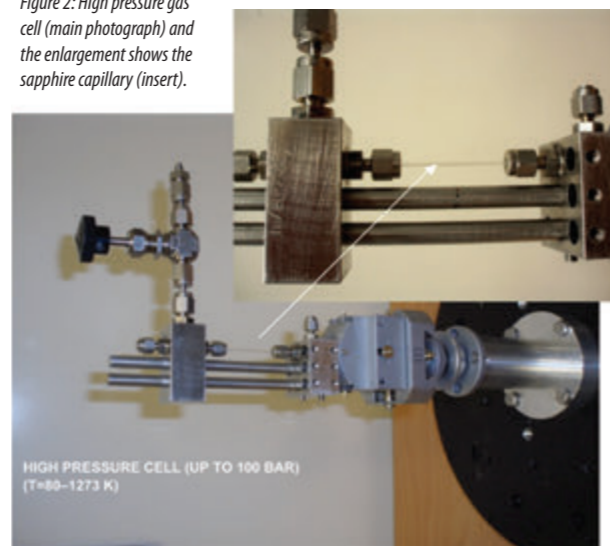
One of the most exciting and rapidly evolving fields in modern materials is the study of how gases interact with solids, particularly under non-ambient conditions of pressure and temperature. Typical areas of interest include the study of catalysts under realistic working conditions, host-guest interactions in gas loaded frameworks and porous materials for gas storage or pollution scrubbing, absorption/desorption kinetics in novel hydrogen storage systems for future energy storage technologies and in the development of materials tailored to CO₂ sequestration for greenhouse gas remediation. In order to allow the user community of beamline I11 to meet these fast moving scientific challenges, a recent addition to the beamline's non-ambient capabilities has been the commissioning of a gas control system to allow the in-situ dosing of powder samples with gases such as hydrogen, methane and carbon dioxide.



Figure 1: The gas control system, in its specially constructed aluminium support frame, is located outside of the experimental hutch.

The gas control system has been designed to handle gases over a wide pressure range (mbar – 100 bar), be simple for user operation, allow in-situ gas dosing and connect easily to both beamline and user sample environments. To compliment this system, low and high pressure capillary sample cells have also been constructed and, together with the gas delivery system, are now in routine use during user experiments. The cells are based on a simple to operate design and have the flexibility to be used with non-contact, non-ambient, sample environments, such as cryostream or hot-air blower, to allow a wide range of temperatures (80 – 1273 K) to be applied to the sample under investigation, while a connection to a turbo pump allows vacuum pressures in the region of 10⁻³-10⁻⁴ mbar to be applied prior to dosing. The gas control system (Fig. 1) is located outside the experimental hutch, allowing sample dosing to be controlled while data collection is underway, and is configured to enable the use of either one low pressure gas, or two high pressure gases, during any one experiment. The outlet from the system is transferred to the sample cells in the experimental hutch via

Figure 2: High pressure gas cell (main photograph) and the enlargement shows the sapphire capillary (insert).



a stainless steel line, which is terminated with a self-sealing 'quick-connect' fitting (Swagelok) for ease of cell mounting and dismantling.

The low and high pressure capillary gas cells can be used with glass, quartz or sapphire capillaries, and mount on a goniometer at the centre of the I11 diffractometer using a custom mounting plate, allowing diffraction data to be collected with either the high resolution multiple analysing crystal (MAC) system for detailed structural investigation, or the position sensitive detector (PSD) for time resolved kinetic studies. During data collection the cells can be oscillated by rocking the θ circle, e.g. by $\pm 10^\circ$, to improve particle statistics. Figure 2 shows one of the gas cells for high pressure experiments. Figure 3 shows the diffraction pattern of a clathrate hydrate which was produced by injecting CO₂ gas at 20 bar of pressure into water ice held at 220 K inside the high pressure cell. The original hexagonal ice structure has been transformed into a cubic hydrate structure, where CO₂ molecules reside within a large H₂O cage structure. The new facility opens up new possibilities for users at beamline I11, in particular for the study of gas adsorption in microporous materials, e.g. zeolites and metal-organic frameworks, where structural investigations using I11 have already produced a number of high profile publications.

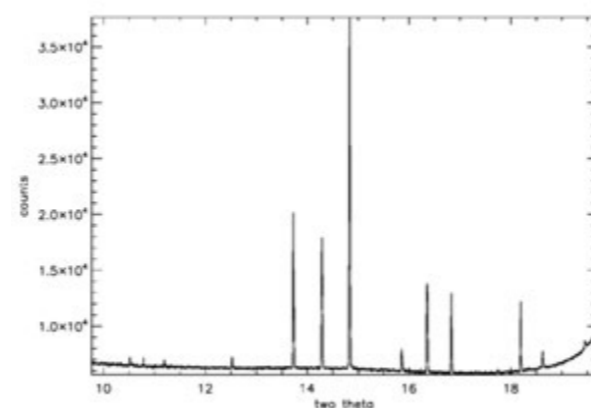
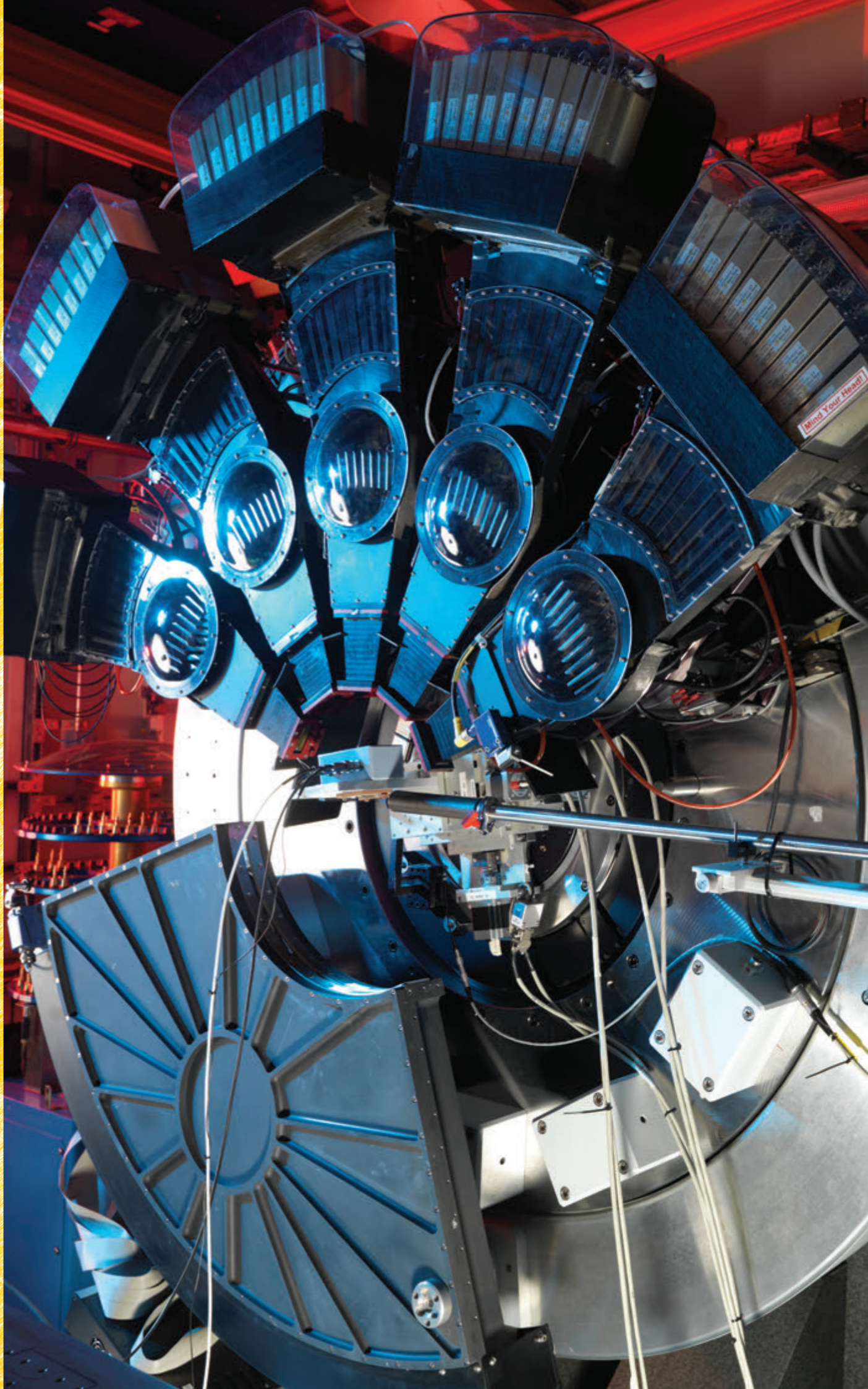


Figure 3: High pressure powder pattern of clathrate hydrate produced by 20 bar CO₂ in ice (T=220 K, E=15 keV).

$$F_{PM} = \frac{Q \cdot E^4}{36 \cdot F_0^4} = \frac{4 \cdot \pi \cdot r_e \cdot E^4}{F_0^3} \cdot \frac{1}{r}$$



Surfaces and Interfaces Village

Sarnjeet Dhesi, Village Coordinator

Over the last year the Surfaces and Interfaces Village beamlines have continued to explore the fundamental properties of a wide range of materials, reveal intriguing hidden properties of matter and develop new methods with which to explore nanostructures. The Village now has three operational beamlines (I06, I07 and I10) with another two (I09, I05) in an advanced stage of construction. Furthermore, a new Phase III beamline (VERSOX) dedicated to photoemission spectroscopy under ambient conditions will start its detailed planning and design phase in the coming year. In this section we have selected some exciting new results covering time-resolved diffraction to X-ray holography to self-organisation in organic overlayers.

Modern devices exploit not only the charge of an electron, but also its intrinsic spin leading to incredible advances in data storage capacity. In recent years new materials have been engineered with novel properties such as perpendicular magnetic anisotropy. Nistor *et al.* (ICN, Barcelona) have taken this a step further and combined perpendicular magnetic anisotropy (PMA) with the Rashba effect in heterostructures lacking inversion symmetry. Angle-dependent X-Ray Magnetic Circular Dichroism (XMCD) was then used on the I06 superconducting vector magnet in order to determine the relationship between the spin and orbital magnetic moments for different thicknesses of ferromagnetic material in the heterostructures. An interfacial orbital moment anisotropy favouring out-of-plane magnetisation for the thinnest films was determined with the size of this anisotropy shown to be directly related to the Rashba effect.

New and versatile probes are crucial to fully understand the magnetism in nanostructures. In this respect, Duckworth *et al.* have developed a new lensless magnetic imaging technique based on polarised soft X-ray holography. The approach allows magnetic domains to be imaged in micron sized nanostructures with 30nm resolution and, crucially, is easily able to image out-of-plane as well as in-plane magnetic domains. The probe also

lends itself neatly to time-resolved studies, which will allow magnetisation dynamics in nanostructures to be probed in the near future.

The recent addition of a dedicated laser system on beamline I06 means that pump-probe based time-resolved experiments are now much more straight-forward. This area of activity was developed by the I06 beamline team in collaboration with the group of Cavalleri (University of Oxford and CFEL, Hamburg) to study the photoinduced melting of electronic ordering in manganites and superconductors. Resonant soft X-ray scattering has been used to understand the orbital and magnetic ordering in many materials in recent years, but on I06 the technique has been extended to the ultrafast timescale to probe the photoinduced melting of orbital and magnetic order in a half doped manganite. The long-lived phase, existing several hundred picoseconds after photoexcitation, was found to retain the lattice distortions, but without any magnetic ordering demonstrating a previously hidden phase of this material. This work was extended to even faster timescale by developing the Diamond synchrotron for a low- α mode of operation which has now also started to benefit other beamlines. However, the fastest timescales were achieved when this work was repeated at the Linac Coherent Light Source (LCLS, Stanford) where femtosecond dynamics were studied for the first time.



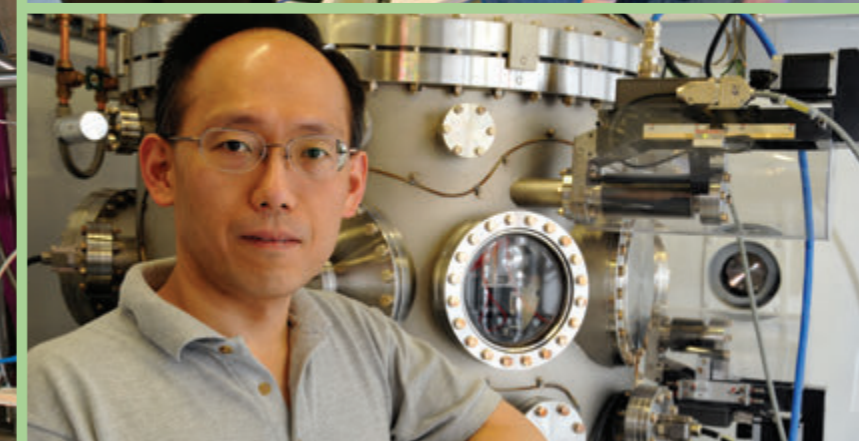
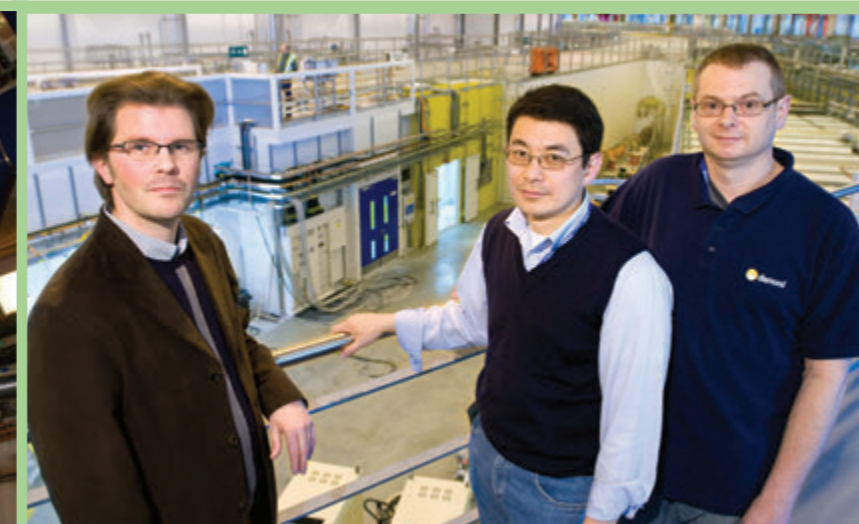
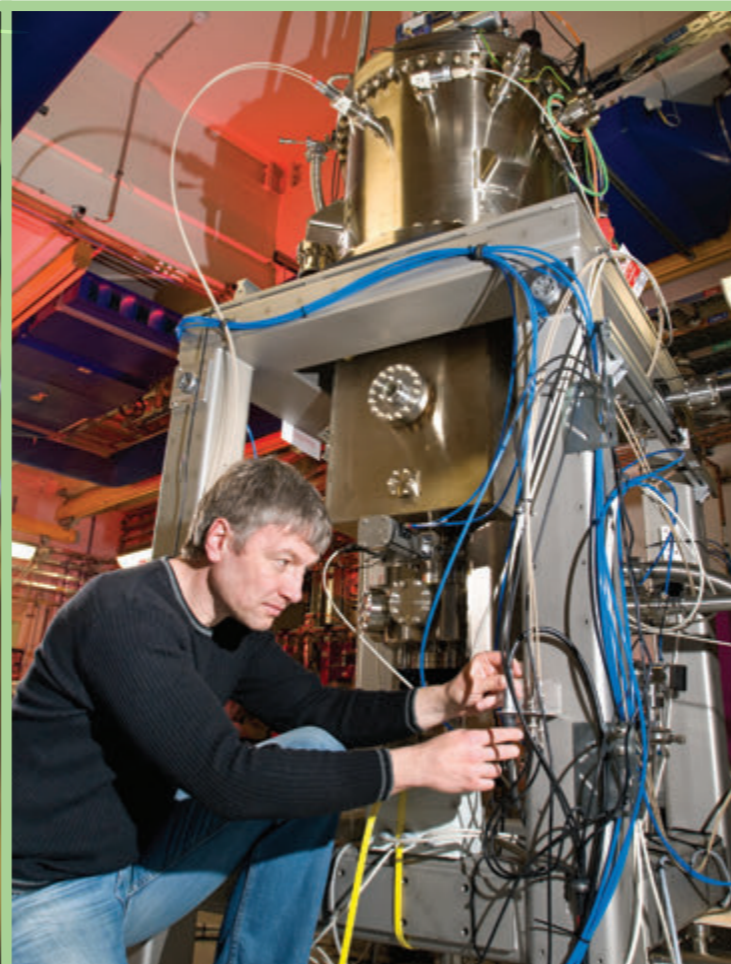
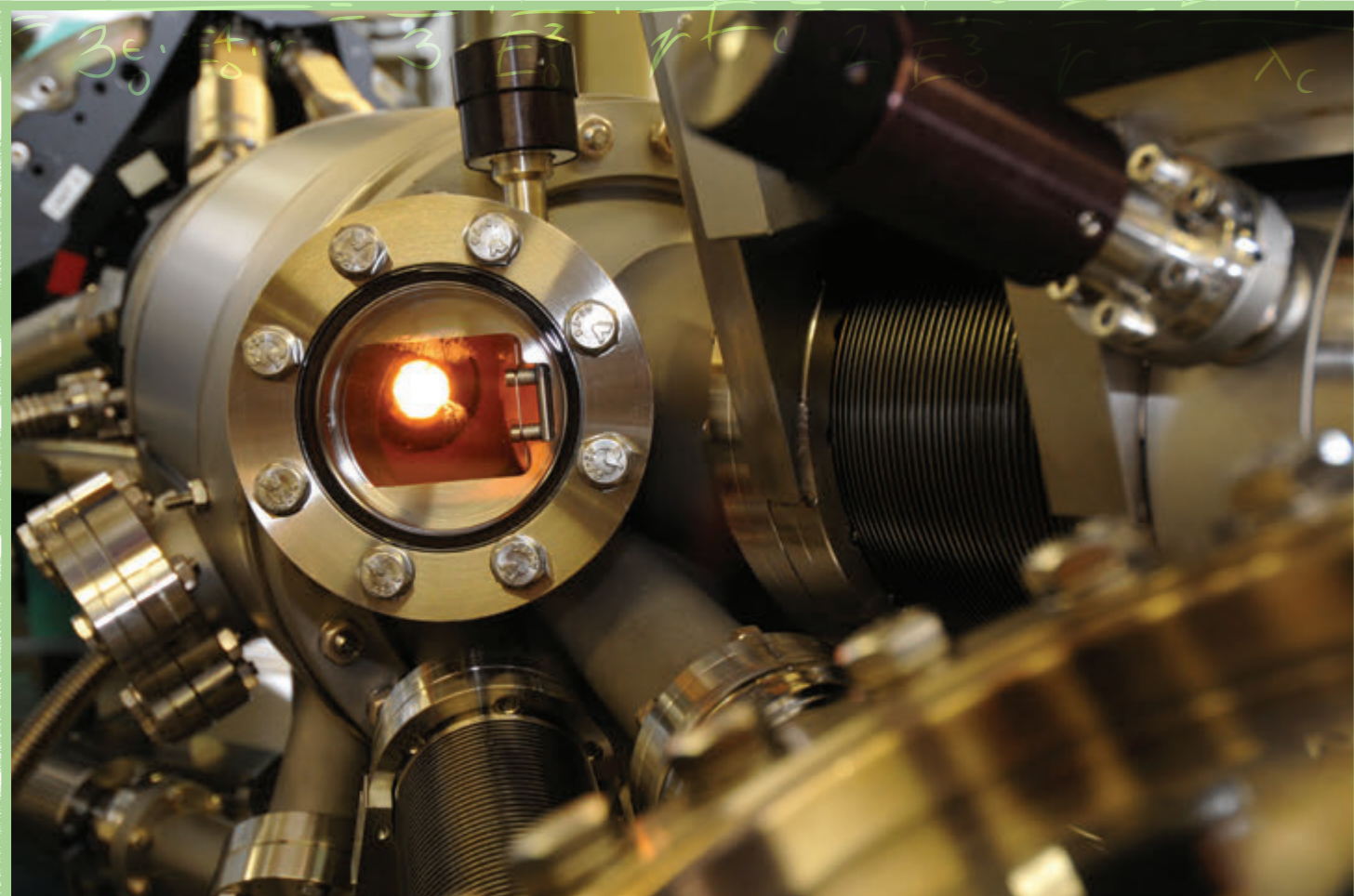
Electrochemistry is a key element in many energy-related applications, such as fuel cells and batteries, making an understanding of the complex interface processes vital. On beamline I07 Lucas *et al.* (University of Liverpool) have used surface X-ray diffraction to study the effects of interacting electrolytes on Ag surfaces. Structural changes of the Ag surface and cation substrate distance were found to change dramatically depending on the electrode potential, which has important implications for the understanding of electrochemical reactions.

Surface X-ray diffraction on beamline I07 has also been used to investigate self-organisation of conducting polymer structures. These intriguing multilayer structures are grown on Si substrates with the exact lamellar morphology determined by acid doping during growth. The surface X-ray diffraction work revealed the effects of the acid doping on the multilayer long range order and helped identify the aniline oligomer with the lowest level of disorder which is important for efficient charge-transport properties.

The village research facilities continue to expand with I10 continuing its commissioning phase with the installation of a 14T superconducting magnet for X-Ray Magnetic Dichroism studies. De Groot and co-workers (University of Southampton) were the first users of the magnet and studied exchange-spring-driven spin flops in DyFe₂/YFe₂ and ErFe₂/YFe₂ multilayers. The I10 insertion devices have also been commissioned to enable the angle of linear polarisation to be varied from 0 to 180° which has now been used successfully by several users groups. In addition, the ability to analyse the scattered polarisation in the soft X-ray diffractometer, enables a complete measurement of the complicated magnetic ordering in many materials. In the coming months I10 will embark on a fast polarisation switching mode of operation that should allow much faster acquisition of dichroism spectra.

Beamline I07 continues to provide accurate surface structure information for a wide range of materials and sample environments. The double crystal deflector, which enables X-ray reflectivity from liquid interfaces, has been used to study nanoparticle formation at liquid-liquid interfaces, incorporation of proteins into lipid bilayers and self-assembled molecular systems. A second experimental end-station for surface X-ray diffraction has been developed allowing *in-situ* sample preparation and characterisation. The surface X-ray diffraction results can be correlated with other structural probes, available on the same system, such as low-energy electron diffraction, X-ray photoelectron spectroscopy and Auger electron spectroscopy to provide a comprehensive set of structural data. Amongst the first to use the system was the group of Bennet (University of Reading), who studied the internal atomic structure of Cr nanocastles grown on W surfaces. In February 2012, beamline I09 received first light and we will continue commissioning the beamline in 2012 with first users planned for the end of the year. In addition, I09 will also proceed with building a separate soft X-ray branchline covering the energy range 150eV to 2100eV. Beamline I05 is ready to start the installation phase of the beamline components and is on course to start user operation next year. In the past year, also I06 and I10 have also benefitted from a high-precision soft X-ray polarimeter developed in collaboration with colleagues from the STFC. The polarisation state of circular and linear light at an arbitrary angle at low (400eV) and high (1500eV) energies has been completely quantified on I06 and I10 with the high-quality results indicating some small and subtle differences in the output of the different undulators. The UHV laboratory has also continued to support the SI Village beamlines. The laboratory allows samples to be grown, characterised using Scanning Tunnelling Microscopy, and easily transferred to the beamlines under UHV conditions for X-ray studies.

$$e^2 \cdot E^4 \quad 4\pi r_e \quad E^4 \quad 3 \hbar \cdot c \quad E^3 \quad 2\pi \cdot \hbar \cdot c$$



Promising candidates for spintronics - vector measurement of the orbital moment anisotropy of Pt/Co/AIO_x heterostructures with a strong Rashba interaction

Nistor, C., Balashov, T., Kavich, J. J., Lodi Rizzini, A., Ballesteros, B., Gaudin, G., Auffret, S., Rodmacq, B., Dhési, S. S. & Gambardella, P. Orbital moment anisotropy of Pt/Co/AIO_x heterostructures with strong Rashba interaction. *Phys. Rev. B.* **84**, 054464 (2011)

Ultrathin magnetic structures with surface-induced perpendicular magnetic anisotropy (PMA) are promising candidates for novel spintronic systems such as non-volatile high-density memory devices and magnetic tunnel junctions with perpendicular magnetisation, which should be much faster than their electronic counterparts. Of particular interest are Pt/Co/AIO_x heterostructures, owing to their PMA and large coercivity, which allows stable encoding of information over long periods of time. Moreover, the strong Rashba spin-orbit interaction exhibited by these trilayers enables perpendicular magnetic switching via in-plane current injection, which is a simple and efficient method for magnetic encoding¹. We present here a study of PMA in Pt/Co/AIO_x heterostructures, which we show to be related to the Rashba interaction. By combining transverse and collinear X-ray magnetic circular dichroism (XMCD) on beamline I06, we achieve a vector measurement of the Co spin and orbital moments. We derive the anisotropy of the Co orbital moment and demonstrate its connection with the macroscopic magnetic anisotropy of the heterostructure, as predicted theoretically.

Following early predictions of interface-induced PMA by Néel, a host of layered systems with surface-induced anisotropy has been proposed and studied. New phenomena were discovered in these systems, such as enhanced spin and orbital moments². It was shown that PMA is a consequence of the orbital moment anisotropy, which couples the crystallographic symmetry axes of the system to the spin magnetic moment^{3,4}. Although the orbital magnetic moment is only a small fraction of the order of 10% of the total magnetisation, it couples simultaneously to the crystal field and to the spin magnetic moment through spin-orbit coupling and consequently mediates an interaction between the spin moment and the lattice.

The coupling between spin and orbital moments is of great interest in structures lacking inversion symmetry, such as Pt/Co/AIO_x trilayers. In such systems, PMA combines with nonequilibrium current-induced spin-orbit torques, which provides effective means to control the magnetisation of high-coercivity ferromagnetic layers¹. However, few studies of systems displaying such effects have been performed, and several outstanding questions remain open. In particular, the magnitude of the orbital moment anisotropy defining the PMA and, likely, the current-induced spin-orbit torques needs to be studied together with its dependence on the thickness of the magnetic layer.

In order to address these points, a set of four Pt (3 nm)/Co (t)/AIO_x (1.6 nm) heterostructures with Co thickness $t = 0.6, 1, 1.5, 2$ nm were prepared by dc magnetron sputtering onto thermally oxidised Si substrates and subsequently exposed to a radiofrequency oxygen plasma (Fig. 1a). The

asymmetric interfaces that sandwich the Co film after oxidation generate a large crystal electric field across the trilayer, resulting in a strong Rashba interaction. Interfacial hybridisation of the electronic states at the two Co interfaces induces an anisotropy in the Co orbital moment, which we investigate in this study. The XMCD technique is uniquely suited for this purpose, allowing for the separation of the spin and orbital contributions to the magnetisation with element-resolved sensitivity. The measurements were performed at the I06 beamline taking advantage of the triple axis superconducting magnet end-station (Fig. 1b).

To achieve a vector measurement of the spin and orbital moments we probed the Co layer magnetisation along three measurement geometries, as shown in Fig. 1 (c-e). The anisotropic part of the orbital moment can be directly probed using the transverse XMCD geometry,⁴ whereas one measurement in geometry (c) and one in geometry (d) are needed to obtain the two Cartesian components of the orbital moment. Three measurements, one in each of the three geometries are necessary to get the magnitude and orientation of the spin moment.⁵ XAS and XMCD spectra taken from the Co (0.6 nm) and Co (2 nm) samples at the Co L_{2,3} edges are shown in Fig. 2. From these spectra, we can extract the Co orbital and spin magnetic moments by application of the XMCD sum rules.

The measured Co orbital and spin magnetic moments in vector representation are shown in Fig. 3 (a) for all four Co film thicknesses. We see that in the thinnest Co film (0.6 nm) the orbital and spin moments are pulled away from the field direction and towards the sample normal. This indicates

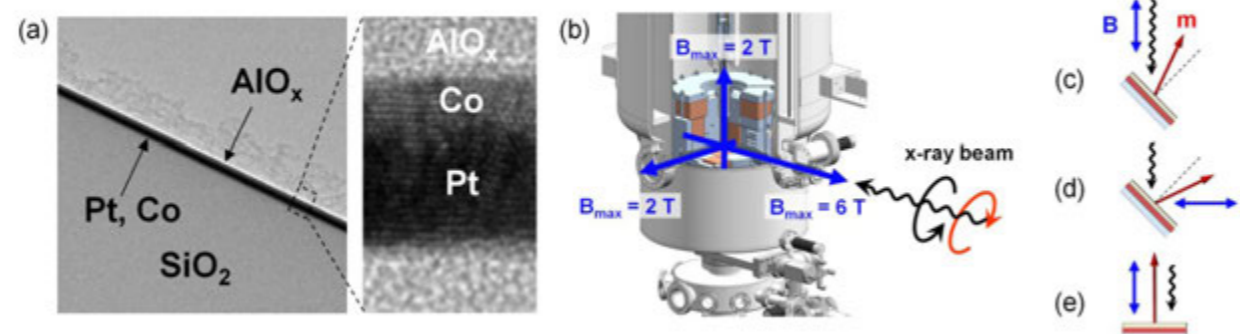


Figure 1: (a) TEM images of a Pt(3nm)/Co(2nm)/AIO_x(2nm) trilayer. (b) Schematic of the triple-axis superconducting magnet on beamline I06. (c-e) XMCD measurement geometries used to derive the orbital and spin magnetic moment vectors. (c) collinear geometry at 45° incidence angle, (d) transverse geometry at 45° incidence angle, (e) collinear geometry at normal incidence.

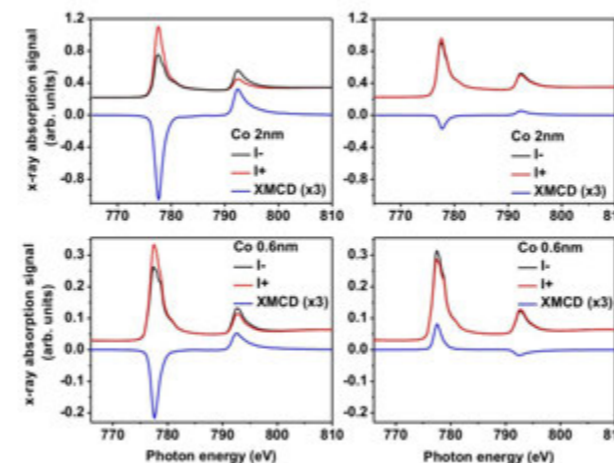


Figure 2: XAS and XMCD spectra recorded at the L_{2,3} edges for Co (2 nm) and Co (0.6 nm) in collinear (left panels) and transverse (right panels) geometries. The applied magnetic field is 1.95 T in both cases. Note that both the magnitude and sign of the transverse XMCD in the thin and thick samples are different, due to the stronger orbital moment anisotropy of the former.

a strong magnetic anisotropy in the out-of-plane direction. As the Co film thickness increases, the spin and orbital moments gradually rotate towards the in-plane direction. This behaviour can be explained as a competition between the out-of-plane anisotropy which pulls the orbital moment out-of-plane and the shape anisotropy which pulls the magnetisation towards the sample plane. We also notice that the orbital and spin Co moments are non-collinear in the thinnest Co (0.6 nm) film, which suggests that the anisotropy of the spin moment is indeed driven by the orbital moment, which ties the Co magnetisation to the out-of-plane direction.

In order to quantify the orbital moment anisotropy, we propose a simple model which assumes that the orbital moment of the Co film is composed of the (anisotropic) orbital moment of the two interface Co monolayers and the orbital moment of the Co monolayers that do not belong to either interface. This simple model gives for the Co (0.6 nm) sample an orbital moment anisotropy ($m_{\text{ORB}}^{\perp} - m_{\text{ORB}}^{\parallel}$) = 0.045 μ_B /atom. A tight-binding model which relates the magnetocrystalline anisotropy (E_{MCA}) to the orbital moment anisotropy yields a value $E_{\text{MCA}} \approx 0.11$ meV for the Co(0.6 nm) sample³. We compare this theoretical value for E_{MCA} with the experimental E_{MCA} that we derive by setting the effective magnetic field parallel to the Co magnetisation. Depending on the degree of oxidation of the top Co monolayer, we obtain for the experimental E_{MCA} of Co (0.6 nm) values in the range [0.7 meV, 0.12 meV], which are reasonably close to the theoretical value of 0.11 meV. This agreement provides further evidence that the spin moment anisotropy is a consequence of orbital moment anisotropy in this class of samples.

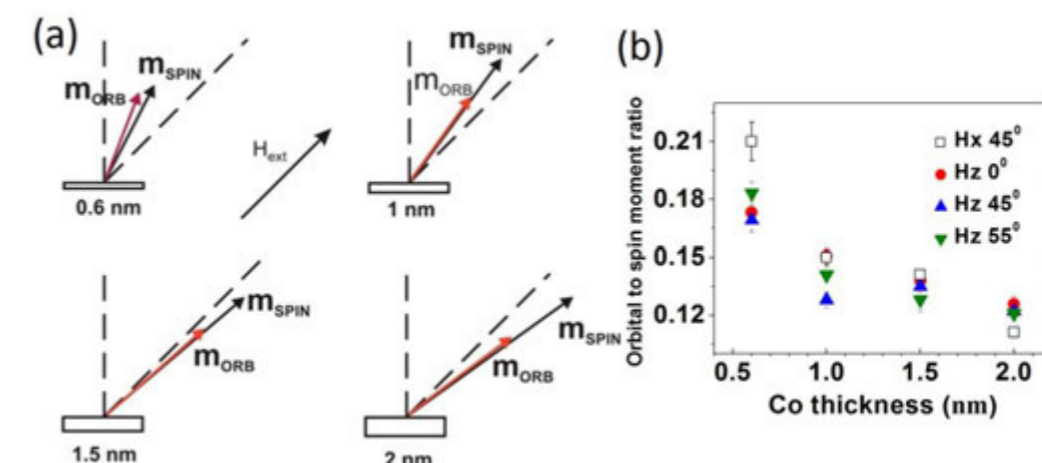


Figure 3: (a) Vectorial representation of the orbital and spin magnetic moments for all four Co layer thicknesses. A 1.95 T field was applied at 45° with respect to the sample normal (dotted lines indicate the field direction). The orbital and spin moment magnitudes are drawn on different scales, for clarity. (b) Orbital-to-spin moment ratio as a function of Co thickness.

Finally, although the absolute values for both spin and orbital magnetic moments increase with Co thickness, we find that the orbital-to-spin ratio of the magnetic moments are considerably larger in the thinnest Co layers, as shown in Fig. 3b. Our data indicate that the interactions responsible for PMA, the Rashba effect, and the generation of spin-orbit torques are stronger in the ultrathin limit ($t < 1$ nm), and provide clues on how to optimise such effects in spintronic devices.

References

- Miron, I.M., Garello, K., Gaudin, G., Zermatten, P. -J., Costache, M. V., Auffret, S., Bandera, S., Rodmacq, B., Schuhl, A. and Gambardella, P. Perpendicular switching of a single ferromagnetic layer induced by in-plane current injection. *Nature.* **476**, 735 (2011).
- Heinrich, B. & Bland, J. A. C. Ultrathin Magnetic Structures, Vol 1, Chap. 2 (Springer-Verlag, Berlin) (2010).
- Bruno, P. Tight-binding approach to the orbital magnetic moment and magnetocrystalline anisotropy of transition-metal monolayers. *Phys. Rev. B.* **39**, 865 (1989).
- Dürr, H. A., Guo, G. Y., van der Laan, G., Lee, J., Lauhoff, G. and Bland, J. A. C. Element-Specific Magnetic Anisotropy Determined by Transverse Magnetic Circular X-ray Dichroism. *Science.* **277**, 213 (1997).
- Van der Laan, G. Relation between the angular dependence of magnetic x-ray dichroism and anisotropic ground-state moments. *Phys. Rev. B.* **57**, 5250 (1998).

Funding Acknowledgements

This work was supported by the European Research Council (StG 203239 NOMAD, Ministerio de Ciencia y Innovación (ERA-Net EUI2008-03884, MAT2010-15659, PTA2008-1108-I), and Agència de Gestió d'Ajuts Universitaris i de Recerca (2009 SGR 695).

DOI 10.1103/PhysRevB.84.054464

Holographic imaging of magnetic nanostructures using extended references

Duckworth, T.A., Ogrin, F., Dhesi, S.S., Langridge, S., Whiteside, A., Moore, T., Beutier, G. and van der Laan, G. Magnetic imaging by x-ray holography using extended references. *Opt. Express*. **19**, 16223-16228 (2011)

Magnetic microscopy forms an important part of today's science because it provides scientists with a powerful tool to study the magnetic structure on a submicron scale. We have used state-of-the-art Fourier transform holography (FTH) techniques to produce high-resolution images of multilayered magnetic samples with different magnetic properties. For this we used a novel imaging method known as 'holography with extended reference by autocorrelation linear differential operator' (HERALDO), which allowed us to investigate magnetic coupling effects in systems which are of tremendous interest for advancing spintronic technologies.

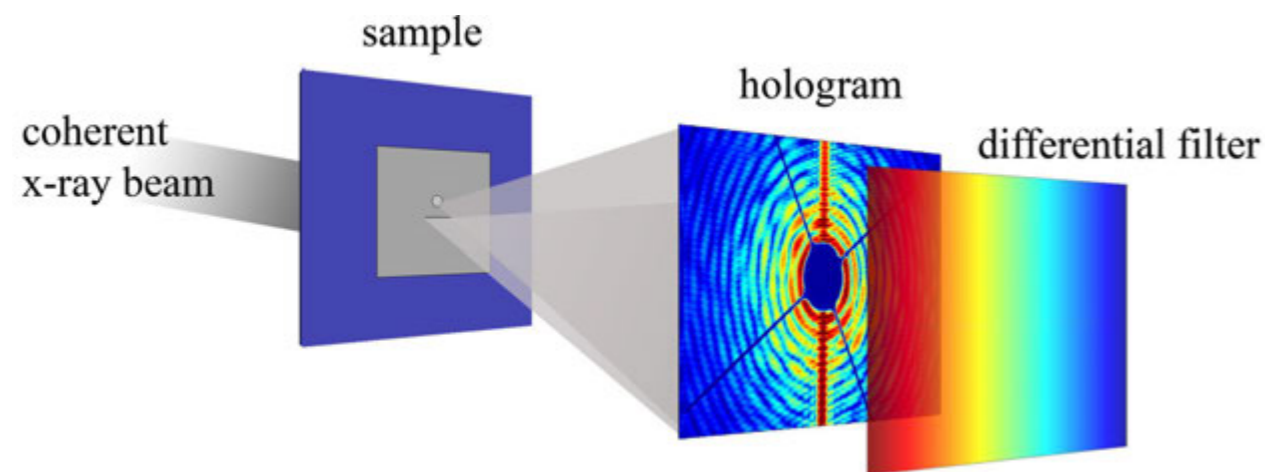


Figure 1: Experimental setup (HERALDO).

We used the Nanoscience beamline I06 to perform a series of soft X-ray HERALDO experiments to study the detailed magnetic structure of thin magnetic films. We found that the HERALDO¹ method significantly reduced the required counting time to record a hologram in comparison with conventional magnetic FTH², which relies upon small-diameter pinholes to provide the holographic reference waves. This is due to the increased photon flux that passes through the extended reference structure.

The sample substrate was an X-ray transparent silicon nitride membrane holding the magnetic film on one side. On the opposite side of the membrane, a thick film of gold was deposited in order to block all incident X-rays from passing through when the sample is exposed to the beam. Focused ion beam milling was then used to pattern a viewing aperture into the gold which was milled down to the membrane substrate and allowed the radiation to transverse through the magnetic layers. Close to the viewing aperture we milled an extended holographic reference slit through the entire gold-sample ensemble. In these experiments magnetic contrast is obtained using X-ray magnetic circular dichroism (XMCD). The circularly polarised X-rays passing through the reference slit interfere with the scattered X-rays from magnetic layers resulting in an interference pattern that was recorded on a charge-coupled device (CCD) camera situated in the far field.

An essential part of HERALDO imaging is for the extended reference structure to contain a sharp feature. In our series of experiments we concentrated on using a slit as an extended reference, which contains sharp discontinuities at either end. Fig. 1 shows the experimental setup that we implemented for the measurements. To retrieve unique isolated reconstructions, which are produced by the sharp features on the extended

reference object, one has to employ a differential filtering step with HERALDO, which is not required with conventional FTH. This is quick and straight forward to apply, and all the information required is readily available from the recorded interference pattern.

We performed the initial experiments on a magnetic film containing a stack of ~30 Co/Pt bilayers with induced perpendicular anisotropy. Fig. 2a shows the resulting hologram after a differential filter was digitally applied to the recorded interference pattern on the CCD. The corresponding Fourier transform of this outcome is shown in Fig. 2b and reveals the reconstructed magnetic domain pattern contained within the viewing aperture (an enlargement of one of the cross correlations is shown in Fig. 2c).

Next, we used this technique to study a similar sample which contained an additional magnetic layer. We were able to image each layer individually and to investigate the magnetic coupling between the two films. The bulk of our sample contained a stack of ~30 Co/Pt bilayers with induced perpendicular anisotropy. On top of the stack, an 8 nm Ta spacer was deposited followed by a 5 nm permalloy (i.e., nickel-iron alloy) layer. From previous magnetization and spectroscopic studies on these systems it was observed that the perpendicular domains in the Co/Pt induce an in-plane structure in the permalloy layer³. The out-of-plane striped domain pattern, which forms in a Co/Pt multilayer, can be recorded with the sample surface perpendicular to the beam direction. However, to access the contrast of the in-plane magnetization the sample has to be rotated so that the surface plane and beam direction are no longer perpendicular to each another. Thus, the coupled in-plane domain configuration in the permalloy layer was imaged by recording holograms at off-normal incidence⁴.

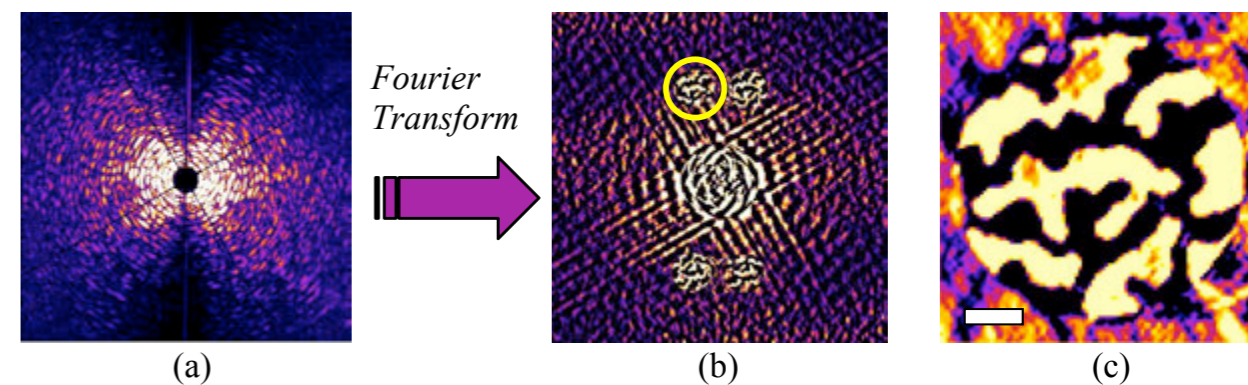


Figure 2: (a) Hologram from a magnetic multilayer of $[\text{Co}(4 \text{ \AA})/\text{Pt}(10 \text{ \AA})]_{\times 30}$, which is the difference between images recorded for the two x-ray helicities, after applying a differential filter. (b) The Fourier transform of the hologram in (a) reveals four object-reference cross-correlations. (c) Enlarged object for the yellow circle in (b). The light and dark areas in the disc represent magnetic domains pointing in and out of the page (white scale bar = 300 nm).

To independently measure the scattering from the different magnetic layers the X-ray energy was tuned to the absorption edges of the specific elements. A reconstruction of the domain structure in the Co/Pt multilayer with the sample normal to the beam direction was recorded (Fig. 3a) before the sample was rotated to an angle of 45°. Here the X-ray energy was tuned to the Co L_3 absorption edge. The domain structure in the Co/Pt was imaged again in the off-normal geometry (Fig. 3b), shortly followed by an image of the permalloy (Fig. 3c) recorded with a beam energy corresponding to the nickel L_3 absorption edge.

We found that the domains in the permalloy layer were closely correlated with the contrast in the Co/Pt multilayer. We also found that applying a magnetic field removed the induced domain structure and that returning to the remanence state did not revive the domain structure in the permalloy (results not shown here). It is speculated that after magnetising with the applied field, the permalloy layer forms larger domains which are not affected by the dipolar field from the Co/Pt due to high exchange coupling within the domains.

References

1. Guizar-Sicairos, M. & Fienup, J.R. Holography with extended reference

by autocorrelation linear differential operation. *Opt. Express*. **15**, 17592-17612 (2007).

2. Eisebitt, S., Luning, J., Schlotter, W. F., Lorgen, M., Hellwig, O., Eberhardt W. & Stohr, J. Lensless imaging of magnetic nanostructures by x-ray spectro-holography. *Nature*. **432**, 885-888 (2004).
3. Kinane, C. J., Suszka, A. K. & Marrows, C. H. *et al.* Soft x-ray resonant magnetic scattering from an imprinted magnetic domain pattern. *Appl. Phys Lett*. **89**, 092507 (2006).
4. Tieg, C., Frömter, R., Stickler, D., Hankemeier, S., Kobs, A., Streit-Nierobisch, S., Gutt, C., Grübel, G. & Oepen, H. P. Imaging the in-plane magnetization in a Co microstructure by Fourier transform holography. *Opt. Express*. **18**, 27251-27256 (2010).

Funding Acknowledgements

The Centre for Material Physics and Chemistry (CMPC) of the Science Technology Facilities Council (STFC), UK and the Engineering and Physical Sciences Research Council (EPSRC), UK.

DOI 1364/OE.19.016223

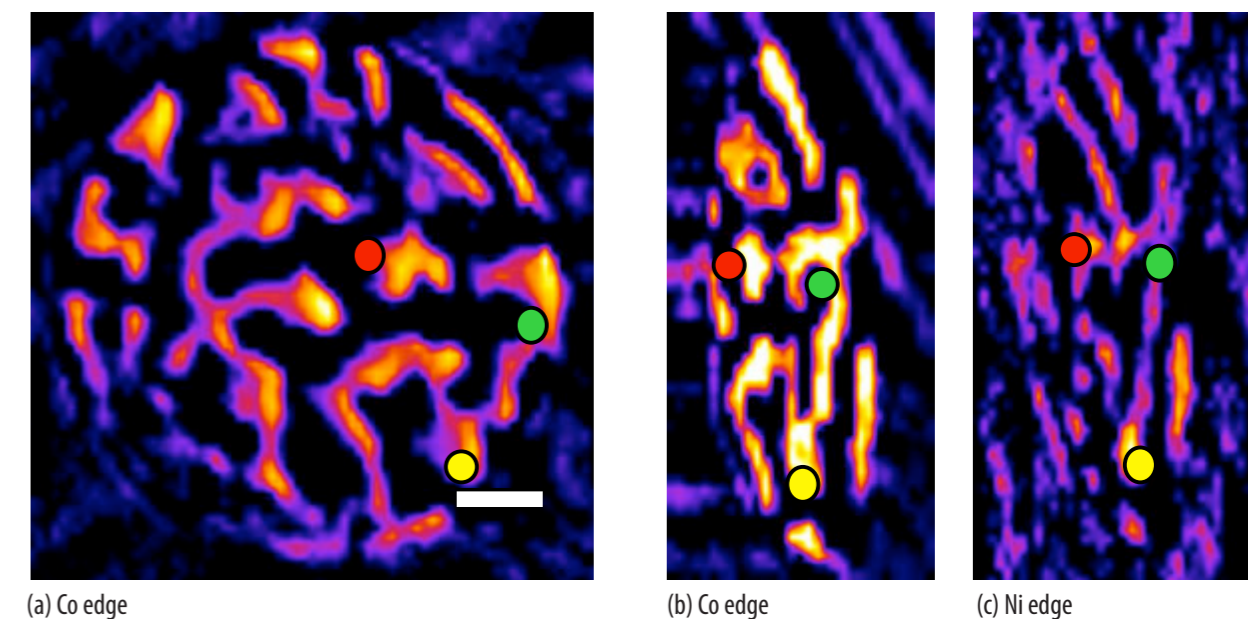


Figure 3: Tuning the energy of the incident X-ray beam to an absorption edge for a specific element allows independent imaging of different magnetic layers within the sample. (a) The sample is perpendicular to the beam (white scale bar = 300 nm). (b), (c) The sample was rotated to 45°. The magnetic structure in the permalloy (c) closely follows that in the Co/Pt multilayer (a), (b). Coloured dots have been added to indicate the same spatial locations in each of the reconstructions.

Light-induced melting of magnetic order in a manganite probed with ultrafast resonant soft X-ray diffraction

Ehrke, H., Tobey, R.I., Wall, S., Cavill, S.A., Först, M., Khanna, V., Garl, Th., Stojanovic, N., Prabhakaran, D., Boothroyd, A.T., Gensch, M., Mirone, A., Reutler, P., Revcolevschi, A., Dhesi, S.S. and Cavalleri A. Photoinduced melting of antiferromagnetic order in $\text{La}_{0.5}\text{Sr}_{1.5}\text{MnO}_4$ measured using ultrafast resonant soft X-ray diffraction. *Physical Review Letters*. **106**, 217401 (2011)

Manganites are a prototype of strongly correlated electron systems. This is a class of solid state materials in which Coulomb interactions between pairs of carriers exceed their kinetic energies to promote a variety of spectacular phenomena beyond the familiar concepts of classical band theory. Examples include insulator-to-metal transitions and the colossal magnetoresistive effect. The understanding of such phenomena are essential for improving magnetic switching processes, which enable processing and storage of information. Electronic order on nanometer length scales is a common feature in these compounds, stabilised by a complex interplay between charge, orbital, spin and lattice degrees of freedom. This interplay provide extreme sensitivity of the quantum states to external stimulations, enabling control with magnetic fields, pressure, electric currents, or light^{1,2}. In this work, we used time-resolved resonant soft X-ray diffraction to probe the picosecond dynamics of spin and orbital order in $\text{La}_{0.5}\text{Sr}_{1.5}\text{MnO}_4$ after optical excitation with femtosecond pulses of 1.5 eV photon energy. Complete melting of antiferromagnetic spin order is evidenced by the disappearance of a $(1/4\ 1/4\ 1/2)$ diffraction peak. On the other hand, the $(1/4\ 1/4\ 0)$ diffraction peak, reflecting orbital order, is only partially reduced. Our results evidence a non-thermal destabilisation in the short-range magnetic interactions with no significant relaxation of the long-range lattice distortions.

Photo-excitation in a manganite at near-infrared or visible wavelengths transfers charges across semicovalent bonds, drastically perturbing spin and orbital order to enable optical control of magnetism. However, a comprehensive understanding of the underlying physics is still missing. This is particularly elusive because charge, spin, and orbital arrangements are interdependent degrees of freedom. They evolve on sub-picosecond time scales and nanometer length scales, and can only be disentangled with ultrafast techniques sensitive to nanometer-scale modulations of charge and spin densities.

In the past, static electronic order in manganites has been probed with resonant soft X-ray diffraction (RSXD)³. This technique is directly sensitive to electronic states close to the Fermi level using photon energies resonant with

the $2p \rightarrow 3d$ dipole transitions (Mn $L_{2,3}$ edges). The energy dependence of the RSXD intensity can be used to understand the competing interactions leading to spin and orbital ordering.

Here, we have extended RSXD to the ultrafast time scale in order to investigate photo-induced dynamics in the single-layer, half-doped manganite $\text{La}_{0.5}\text{Sr}_{1.5}\text{MnO}_4$. Time resolved RSXD was measured in a pump-probe scheme. To this end, trains of 100 fs, 800 nm wavelength (1.5 eV photon energy) laser pulses at a repetition rate of 22 kHz were synchronized to soft X-ray pulses at beamline I06. The time delay τ between laser pump and X-ray probe was set by a mechanical delay stage. Separation of transient spin and orbital order is achieved by detecting changes in the time-dependent intensity at two different diffraction peaks. Single-bunch X-ray

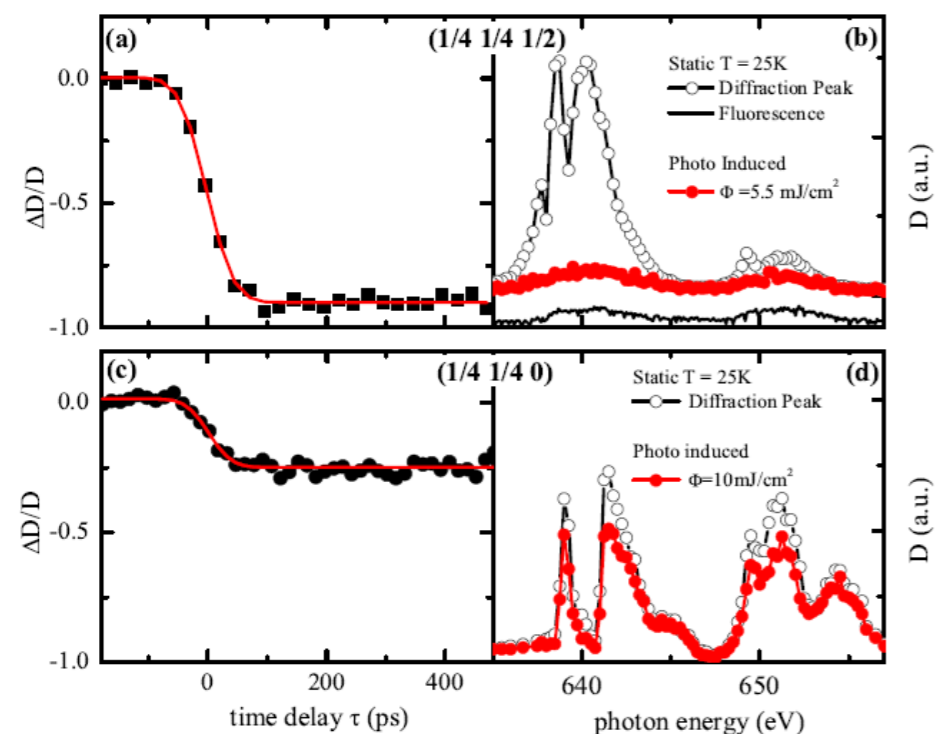


Figure 1: Photo-induced normalized change in the diffraction signal ($\Delta D/D$) for (a) the spin order $(1/4\ 1/4\ 1/2)$ and (c) the orbital order $(1/4\ 1/4\ 0)$ peak. The panels (b) and (d) show the energy dependence of the diffraction signals at a pump-probe delay time of 200 ps (red dots) in comparison to the static diffraction intensities (black circles).

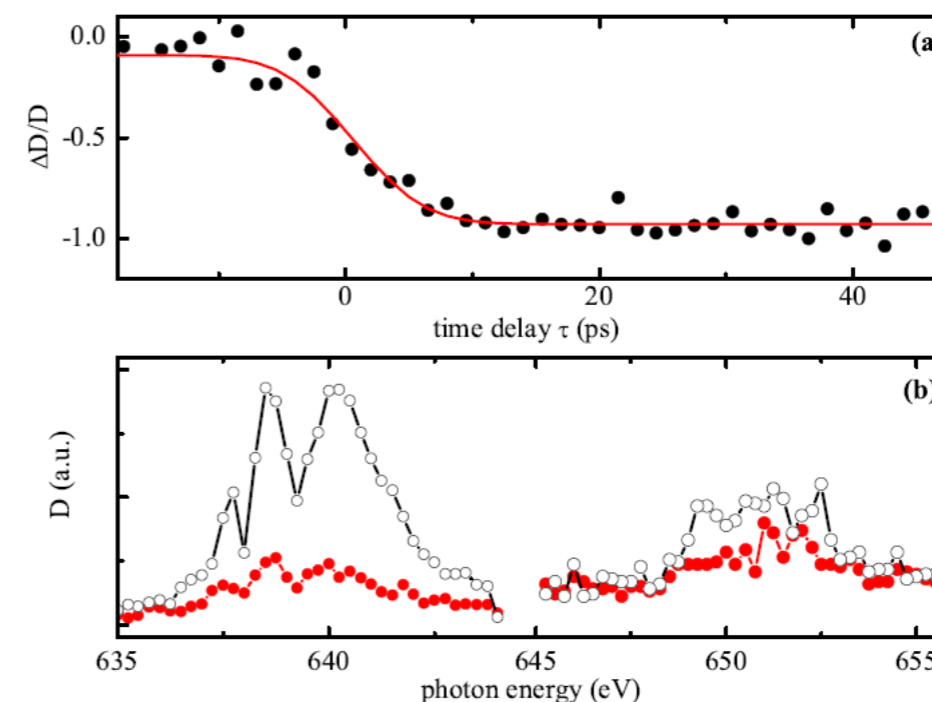


Figure 2: (a) Time dependence of the $(1/4\ 1/4\ 1/2)$ diffraction peak intensity measured at 640.25 eV in low- α mode. The red line shows a fit to the data using an error function with a FWHM of 10 ps. (b) Energy dependence of the $(1/4\ 1/4\ 1/2)$ diffraction peak intensity before (black circles) and 20 ps after photo-excitation (red dots). The low intensity after photoexcitation is due to fluorescence and was removed to calculate $\Delta D/D$.

pulses were resolved using photon counting and gating electronics. The time resolution of this experiment was limited by the X-ray pulse duration to about ~ 50 ps in hybrid mode and ~ 10 ps in low- α mode.

In the low-temperature CE-type antiferromagnetic phase of $\text{La}_{0.5}\text{Sr}_{1.5}\text{MnO}_4$, charge, spins, and orbitals form a characteristic pattern, well visualised as a set of antiferromagnetically coupled ferromagnetic zigzag chains of $3x^2-r^2$ ($3y^2-r^2$) orbitals at the Mn^{3+} sites. Fig. 1a and 1c show the time-resolved photo-induced changes in the diffraction intensity of the $(1/4\ 1/4\ 1/2)$ and the $(1/4\ 1/4\ 0)$ peaks, measured near the Mn L_3 -edge at 641.5 eV and 640.25 eV, respectively. Antiferromagnetic order along the c-axis, proportional to the $(1/4\ 1/4\ 1/2)$ diffraction signal, is completely melted for an excitation fluence of $5.5\ \text{mJ}/\text{cm}^2$, while in-plane orbital order, measured at the $(1/4\ 1/4\ 0)$ peak, is reduced by about 25% only. At 200 ps time delay, the energy-resolved diffraction intensity at the magnetic wave vector leaves a weak, structureless fluorescence signal (see Fig. 1b), while the spectral characteristics of orbital diffraction peak show only minor changes (Fig. 1d).

The temporal resolution of our experiments was improved by operating Diamond Light Source in low- α mode. Here, shorter X-ray pulses (~ 9 ps) were generated by compressing the electron bunches in the ring at the expense of total current and X-ray flux. Already on the sub-10 ps time scale the magnetic $(1/4\ 1/4\ 1/2)$ diffraction peak promptly disappears (see Fig. 2). Finally, we measured the dynamics on longer time scales by electronically controlling the delay between pump and probe pulses. The diffraction intensity of the magnetic peak recovers back to the static value with double-exponential time constants of 10 and 110 ps.

Comparing the time-resolved intensity changes of the different diffraction peaks to static temperature dependence, the optically induced rearrangement of spin and orbital order cannot be explained by laser induced heating effects. This is also confirmed by a calculation of the heat in the sample generated through the laser pulse. Thus, the magnetic and orbital order melting must be strongly influenced by the non-thermal physics occurring immediately after optical excitation.

We interpret our observations along the following lines: Due to strong on-site Hund's coupling, excitation with the linearly polarised 800 nm pulses results in charge transfer along the ferromagnetically aligned zigzag chains. This photo-excitation can be thought of as the injection of sparse defects into these chains, perturbing the orbital occupancy of various orbitals. According

to the Goodenough-Kanamori-Anderson rules⁴, these charge defects effectively couple to the magnetic order, which is stabilised by short-range exchange interactions. Furthermore, this excitation triggers long-range distortions of the lattice by rearranging the Jahn-Teller energy. Obviously, the long-range lattice order is more robust against the optical excitation than the short-range exchange interactions. It is then possible that the long-lived product phase relaxes into a metastable spin-disordered or even ferromagnetic phase or a mixture of the two.

This work was continued using time-resolved soft X-ray diffraction experiments at a 4th generation light source, the free electron X-ray laser LCLS, where optically induced changes in the magnetic ordering were studied on the femtosecond timescale⁵.

References

- Miyano, K., Tanaka, T., Tomioka, Y. & Tokura T., Photoinduced insulator-to-metal transition in a perovskite manganite. *Phys. Rev. Lett.* **78**, 4257-4260 (1997).
- Rini, M., Tobey, R., Dean, N., Itatani, J., Tomioka, Y., Tokura, Y., Schoenlein, R.W. & Cavalleri, A. Control of the electronic phase of a manganite by mode-selective vibrational excitation. *Nature*. **449**, 72-74 (2007).
- Dhesi, S.S., Mirone, A., De Nadai, C., Ohresser, P., Bencok, P., Brookes, N.B., Reutler, P., Revcolevschi, A., Tagliaferri, A., Toulemonde, O. & van der Laan, G. Unraveling Orbital Ordering in $\text{La}_{0.5}\text{Sr}_{1.5}\text{MnO}_4$. *Phys. Rev. Lett.* **92**, 056403 (2003).
- Goodenough, J.B. Theory of the role of covalence in the perovskite-type manganites $[\text{La}, \text{M}(\text{II})]\text{MnO}_3$. *Phys. Rev.* **100**, 564-573 (1955).
- Först, M., Tobey, R.I., Wall, S., Bromberger, H., Khanna, V., Cavalleri, A.L., Chuang, Y.-D., Lee, W.S., Moore, R., Schlotter, W.F., Turner, J.J., Krupin, O., Trigo, M., Zheng, H., Mitchell, J.F., Dhesi, S.S., Hill, J.P. & Cavalleri, A. Driving magnetic order in a manganite by ultrafast lattice excitation. *Phys. Rev. B*. **84**, 241104 (R) (2011).

DOI 10.1103/PhysRevLett.106.217401

Probing the atomic structure of the electrochemical double layer

Lucas, C. A., Thompson, P., Grunder, Y. & Markovic, N. M. The structure of the electrochemical double layer: Ag(111) in alkaline electrolytes. *Electrochemistry Communications*. **13**, 1205 (2011)

Discovering the fundamental principles that govern electrochemical reactivity is the key to the design of new materials for a range of scientific applications, particularly in energy-related technologies. Such information can only be obtained from model systems with well-defined elemental reaction sites using state-of-the-art instrumental probes. In this report we describe the application of *in-situ* surface X-ray scattering (SXS) to study the structure of the electrochemical double layer at the interface between a Ag(111) electrode and alkaline electrolyte. Detailed modelling of the SXS data at negative potential is consistent with the presence of a hydrated K^+ cation layer at a distance of 4.1 Å from the Ag surface and, at positive potential, indicates that the presence of OH_{ad} stabilizes the hydrated K^+ cations through a non-covalent interaction forming a compact double layer structure in which the Ag- K^+ distance is reduced to 3.6 Å. Knowledge of the double layer structure is key to understanding electrochemical reactivity, as solution species must traverse the structure at the interface in order to react.

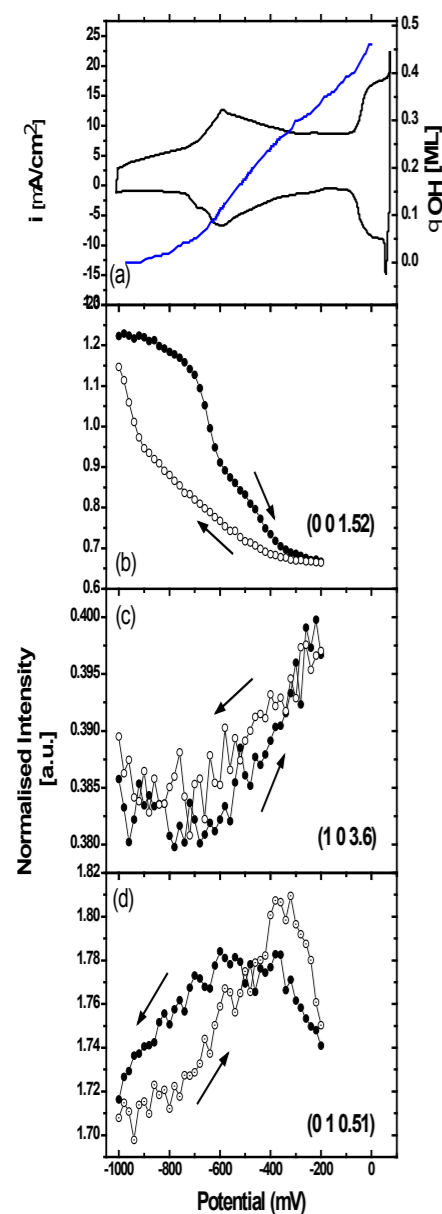


Figure 1: Cyclic voltammetry of Ag(111) in 0.1 M KOH recorded at a sweep rate of 50 mV/s, the potential dependent coverage by OH_{ad} calculated from the CV is shown as a solid blue line. X-ray voltammetry (XRV) measured at (0, 0, 1.52), (1, 0, 3.6) and (0, 1, 0.51). The sweep rate for the XRV measurements was 5 mV/sec.

The design and synthesis of energy efficient and stable electrochemical interfaces (materials and double layer components) for accelerating and directing chemical transformations, is the key to developing new alternative energy systems – fuel cells, electrolyzers and batteries. Two types of interactions have traditionally been considered in aqueous electrolytes, depending on the nature of the reacting species, the supporting electrolyte and the metal electrodes: (i) direct –covalent bond formation between adsorbates and electrodes, involving chemisorption, electron transfer and release of the ion hydration shell; and (ii) relatively weak non-covalent metal-ion forces that may affect the concentration of ions in the vicinity of the electrode but do not involve direct metal-adsorbate bonding. The latter type of interactions are characteristic for the alkaline environment and it has been shown that the interaction of covalently bonded OH and alkali hydrated cations on Pt electrodes, leads to the formation of OH-cation complexes with the locus centered in the compact part of the double layer¹. Although these findings have established the importance of non-covalent interactions in surface chemistry, many important questions from previous studies remain open; a central issue being the determination of the position of hydrated cation clusters in the compact part of the double layer. Surface X-ray scattering (SXS) is an ideal technique for probing the atomic structure at the electrochemical interface. By combining specular crystal truncation rod (CTR) results (where the momentum transfer, Q , is entirely along the surface normal direction) with non-specular CTR results (where Q has an additional in-plane component), it is possible to probe both the termination of the crystal lattice and layer ordering above the interface, i.e. in the electrolyte layer, where the species are incommensurate with the underlying crystal lattice. X-ray voltammetry (XRV) measurements^{2,3}, in which the scattered X-ray intensity at structure-sensitive reciprocal lattice positions is measured as a function of the applied electrode potential, are shown in Fig. 1 (b) an ‘anti-Bragg’ position on the specular CTR sensitive to any layered ordering at the interface, (c) is primarily sensitive to lattice relaxation of the Ag surface, and (d) an ‘anti-Bragg’ position on the non-specular CTR which is sensitive to interfacial atomic positions that are commensurate with the Ag lattice. The fact that the changes at the non-specular CTR positions are very small, ~4%, indicates that there are only subtle changes to the Ag surface. In contrast, the changes at the specular CTR position are relatively large, ~50% change in the scattered intensity. The intensity along the specular CTR is sensitive to ordering normal to the interface, including species that are not necessarily commensurate with the Ag lattice; this implies that there are significant structural changes on the electrolyte side of the interface.

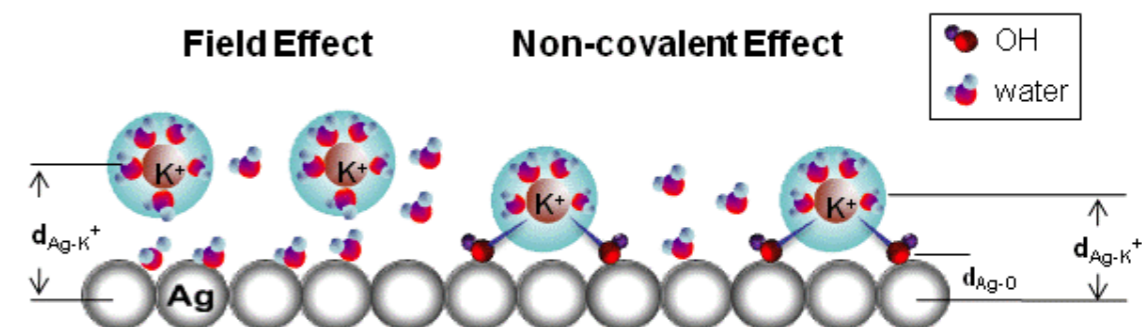


Figure 2: A schematic illustration of the interface structure at the negatively charged (left) and positively charged (right) surface.

In order to derive a structural model for the interface, CTR data at fixed potentials (-1.0 V and -0.2 V) were measured by performing rocking scans around the surface normal at successive L values to obtain background-subtracted integrated intensities⁴. A potential of -1.0 V corresponds to the double layer region and no species are chemically bonded to the surface. At this potential, the best fit to the non-specular CTR data indicated that the surface Ag layer has a slightly reduced occupancy with a small *inward* relaxation of ~0.7 % of the Ag(111) layer spacing ($d_{(111)} = 2.36$ Å). Although this structural model gave a good fit to the (1, 0, L) CTR data, it did not give a good fit to the specular CTR. In order to get a good fit to the specular CTR data it was necessary to include a layer in the electrolyte at a distance of 4.1 Å from the topmost Ag layer. Given that there is no specific adsorption at negative electrode potentials, we assign this layer to hydrated K^+ cations in the outer part of the double layer. The best fit to the data has a cation layer with a surface coverage, $\theta_{K^+} = 0.25 \pm 0.1$ ML at a distance, $d_{Ag-K^+} = 4.1 \pm 0.3$ Å above the Ag surface.

As shown by the XRV data in Fig. 1, scanning the electrode potential from -1.0 V to -0.2 V substantially changes the specular CTR data. CTR data were measured at -0.2 V and a ratio of the 2 CTR data sets ($R = I_{-0.2V} / I_{-1.0V}$) showed clear systematic changes consistent with the potentiodynamic measurements presented in Fig. 1. The non-specular CTR ratio data was modeled by a change of relaxation at the Ag surface and indicated that the inward surface relaxation of the topmost Ag atomic layer has increased to ~1.1% of the Ag(111) lattice spacing. In order to model the specular CTR ratio data set, however, it was necessary to include two layers in the electrolyte, one representing OH_{ad} and the other which we assign to hydrated K^+ cations.

A schematic illustration of the interface structures determined from the CTR measurements is shown in Fig. 2 and summarises the results. At $E = -1.0$ V, where there is no chemisorbed species on the surface, the CTR measurements are consistent with the presence of an hydrated cation adlayer at a distance of 4.1 Å above the Ag surface. At $E = -0.2$ V, however, OH_{ad} stabilises the hydrated K^+ cations, at a distance of 3.6 Å above the Ag surface, through a non-covalent (van der Waal's) interaction. Although the

results presented here are specific to the Ag(111) electrode in alkaline solution, both the methodology and results are important in developing an understanding of the role that the compact electrolyte layer at the interface (and the specific cation in solution) plays in determining the kinetics of electrochemical reactions that occur in this potential range. Recent measurements, performed on beamline I07, have probed the structure of thin metal Ag and Co films electrodeposited onto Au(111) surfaces. These systems have allowed the influence of the double layer structure on sacrificial metal oxidation to be studied in detail.

References

1. Strmcnik, D., Kodama, K., Van der Vliet, D., Greeley, J., Stamenkovic, V. R. & Markovic, N. M. *Nat. Chem.* **1** 466 (2009).
2. Lucas, C. A. & Markovic, N. M. in: R. Alkire, D.M. Kolb, P.N. Ross and J. Lipkowsky (Eds.) 9th Volume of 'Advances in Electrochemical Science and Engineering', Wiley-VCH, 2006, Chapter 1.
3. Lucas, C. A., Thompson, P., Cormack, M., Brownrigg, A., Fowler, B., Strmcnik, D., Stamenkovic, V.R., Greeley, J., Menzel, A., You, H. & Markovic, N. M. *J. Am. Chem. Soc.* **131**, 7654 (2009).
4. Lucas, C. A. Thompson, P. Grunder, Y. Markovic, N. M. *Electrochem. Comm.* **13**, 1205 (2011).

Funding Acknowledgements

EPSRC, 'Combined Atomic Imaging and Diffraction Studies of the Electrooxidation of Supported Metal Multilayers', EP/G068372/1.

DOI 10.1016/j.elecom.2011.08.043

Understanding the nanoscale self-organisation of conducting organic materials

Dane, T.G., Cresswell, P.T., Bikondoa, O., Newby, G.E., Arnold, T., Faul, C.F.J., Briscoe, W.H. Structured oligo(aniline) nanofilms via ionic self-assembly. *Soft Matter*. **8**, 2824-2832 (2012)

Conducting organic materials have long been investigated for application in a range of flexible electronic and optoelectronic devices. A key aspect to realising the potential of such materials is to understand and control the assembly of constituent molecules and resultant supramolecular structures, which are fundamentally related to the conductive properties. In this work we have used synchrotron surface diffraction to understand the self-assembly of drop-cast nanofilms of oligomeric derivatives of the conducting polymer poly(aniline) (PANI) on silicon. We found that by treating oligomeric derivatives with an acid surfactant, we simultaneously generated the conductive species through protonic doping and induced self-assembly into well-ordered lamellar morphologies with a d -spacing ranging between 2.15 nm and 2.35 nm. The exact structural nature of the nanofilm was investigated as a function of the oligomer molecular architecture, the film thickness and the interfacial roughness.

Electroactive organic materials offer tunable functionality afforded through facile synthetic preparation balanced with good charge-transport properties arising from a highly conjugated polymer backbone¹. One well-studied example is PANI, which demonstrates a variety of oxidation states with associated colour changes, in addition to relatively high levels of conductivity. The polymer, however, is by nature poorly soluble, which inhibits solution processing and leads to a range of structural defects, thus limiting the observed conductivity². A solution to these issues is to use short well-defined oligomeric species, which afford tunable architectures and unlock new processing routes. Oligomers also offer enhanced supramolecular self-assembly as a means to overcome the disorder inherent in the polymeric analogue³. This has been shown to be an effective strategy in the bulk, when combining oligomers with an acid-surfactant using the so-called *ionic self-assembly* (ISA) approach. ISA serves both to dope the oligomer to the conducting state and facilitate the self-assembly into well-ordered columnar structures through the secondary π - π and van der Waals interactions⁴.

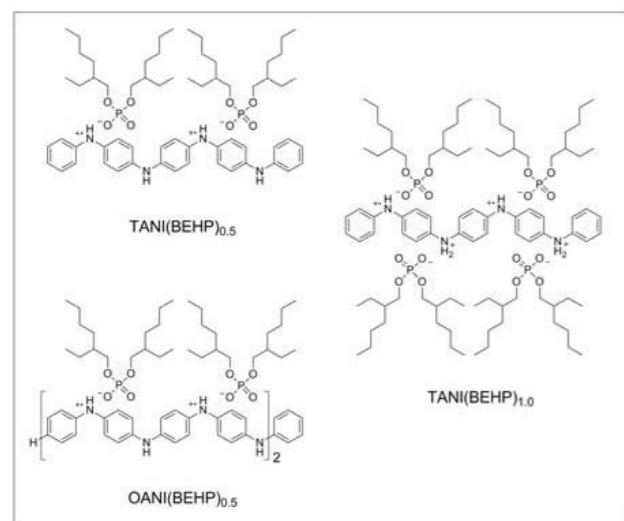
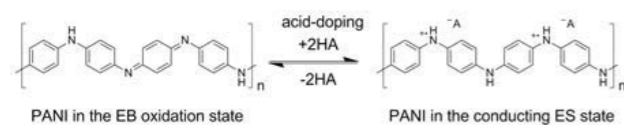


Figure 1: The three oligo(aniline)-surfactant complexes studied in this work. The general mechanism for generating the conducting ES state of PANI through acid-doping where the acid HA can be an acid surfactant is shown in the top inset. Note that the nomenclature used is n ANI(BEHP) $_x$, where BEHP is the surfactant dopant and x is the fraction of nitrogen atoms in the chain backbone that have been protonated by surfactant molecules.

Despite the wide range of research into such materials, very little is known of the thin film properties. Such thin films are important as electronic devices and are often manufactured with an active organic layer of approximately 100 nm. Within this regime, interfacial effects can lead to a range of microstructures and crystalline orientations, thus giving rise to varied and unpredictable behaviour. In this work we have prepared nanofilms of aniline oligomers and oligomer-surfactant complexes by drop casting onto silicon followed by solvent annealing, both steps using tetrahydrofuran (THF) solvent. When dry, the structural details of the films were examined using synchrotron surface diffraction performed in the X-ray reflectivity (XRR) geometry. The effect of oligomer molecular architecture on the self-assembly behaviour was studied by considering two oligomers: four aniline monomers (TANI) and eight monomers (OANI), the structures of which are shown in Fig. 1. Additionally, the thickness of the films was controlled by varying the concentration of the initial solution, allowing two regimes to be examined: thick film samples (~ 350 nm) and thin film samples (~ 35 nm).

Surface diffraction data revealed that in the native EB oxidation state the oligomers did not self-assemble into any long-range structures. When complexed with the acid-surfactant BEHP, however, all thick film samples exhibited Bragg peaks in the reflectivity curves, indicating well-ordered lamellae lying parallel to the underlying substrate (Fig. 2a). In the case of TANI(BEHP)_{0.5} the d -spacing was found to be 2.15 nm. In addition, two higher order Bragg peaks can be seen corresponding to $n = 2$ and 3 reflections, indicating a high degree of long-range order. Using the interpretation of the bulk scattering data from this complex we can infer that the lamellar structure is made up of a bilayer of TANI molecules separated by interdigitated alkyl tails⁴ as shown in Fig. 3. This arrangement allows efficient packing of alkyl tails into a thermodynamically stable structure with optimal van der Waals interactions stabilized by π - π stacking. As XRR measures the electron density profile perpendicular to the substrate it is clear that the lamellae must be aligned approximately parallel to the substrate.

With a greater doping ratio, the multilayer spacing of TANI(BEHP)_{1.0} increased slightly by ~ 0.02 nm to 2.17 nm. This is not a significant departure from the value for TANI(BEHP)_{0.5} and suggests that the similar lamellar structure is retained despite doubling the volume of alkyl tails. There are two possible explanations for this observation: either the TANI(BEHP)_{1.0} complex has not been fully formed, or the crystal structure has expanded along another lattice vector. When the oligomer chain-length is doubled (i.e., in the OANI system) we found that the reflectivity curves retained the Bragg diffraction peaks, however, they were much broader with lower intensity.

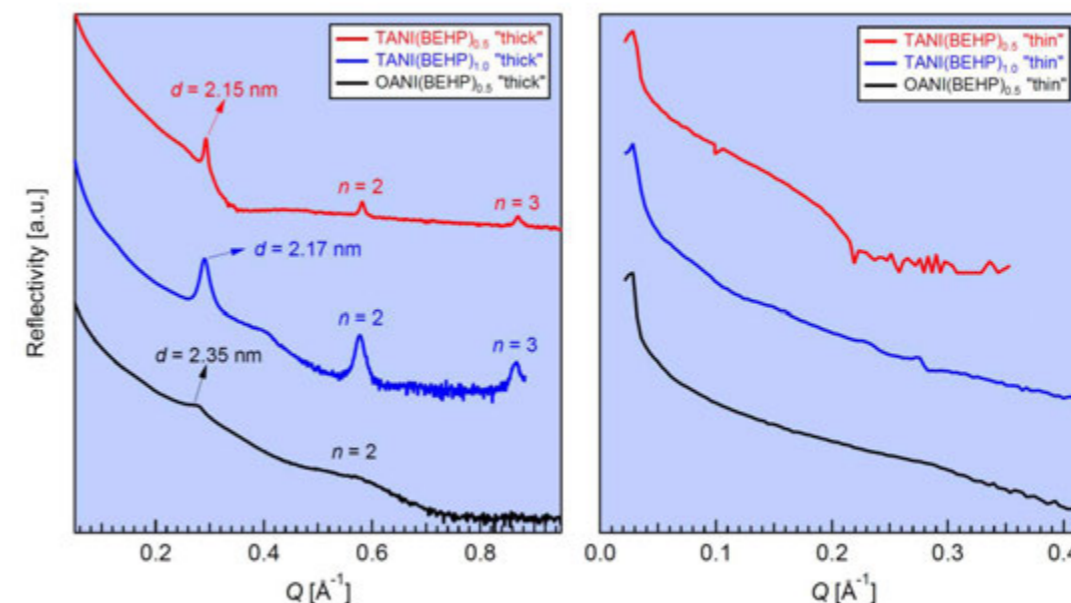


Figure 2: XRR curves for oligo(aniline)-surfactant nanofilms. (a) Thick films show clear Bragg diffraction peaks arising from a long-range lamellar structure; and (b) for thin samples the Bragg diffraction peaks are no longer present due to the overwhelming disorder at interfaces, introduced during film drying.

The d -spacing increased to 2.35 nm but the overall level of order within the system was lower. The shape of Bragg diffraction peaks was considered to further characterise the degree of order in these films. The full-width at half-maximum (FWHM) is inversely proportional to the size of the ordered domain or coherence length (L_c), which for the TANI(BEHP)_{0.5} thick film was extremely large at around 100 nm. This value is especially significant since the thickness of the film was only around 350 nm. This L_c value was roughly halved to 48 nm for the TANI(BEHP)_{1.0} complex, possibly due to the greater volume of surfactant, giving the complex a softer nature and

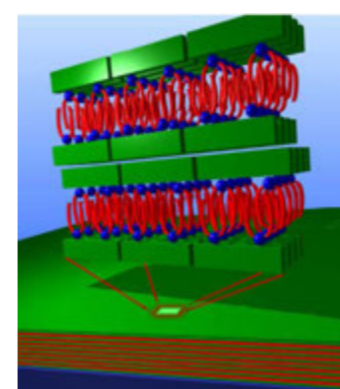


Figure 3: Schematic representation of the TANI(BEHP)_{0.5} multilayer structure. Green layers represent the TANI and red the BEHP. The enlargement atop shows the proposed molecular arrangement in the multilayers structure and the orientation with respect to the underlying substrate.

inducing greater disorder. For OANI(BEHP)_{0.5} L_c was only ~ 7 nm. This result can be explained in light of the different molecular architectures of TANI and OANI. With more monomer units in the chain, OANI is more flexible than TANI owing to the increased number of phenyl-nitrogen-phenyl bonds about which rotation can occur. This results in a greater entropic barrier to ordered structure formation. A summary of structural information is presented in Table 1.

Sample	TANI(BEHP) _{0.5}	TANI(BEHP) _{1.0}	OANI(BEHP) _{0.5}
Structure	Lamellar	Lamellar	Lamellar
d -spacing / nm	2.15	2.17	2.35
Coherence length L_c / nm	102	54	7
Number of layers	48	25	3

Table 1: Summary of structural parameters for oligo(aniline)-surfactant complexes.

For the thick films, this region approaches the substrate and the level of disorder smears through the film, disrupting self-assembly.

These results demonstrate that highly-ordered nanofilms of aniline oligomer-surfactant complexes with well-defined lamellar morphologies can be generated through drop casting and solvent annealing. We have found that, the presence of the surfactant dopant is necessary to induce self-assembly, the nature of organisation within the film depends of the molecular architecture of the constituent components and the formation of structure is dependent on the thickness of the film, a property which is related to the interfacial energy at the air-film interface. These results provide a platform for us to correlate the self-assembled, ordered thin film structures with the enhanced conductive properties that they promise to mediate.

References

- Forrest, S.R. The path to ubiquitous and low-cost organic electronic appliances on plastic. *Nature* **428**, 911-918 (2004).
- Geniès, E.M., Boyle, A., Lapkowski, M. & Tsintavis, C. Polyaniline: A historical survey. *Synthetic Metals* **36**, 139-182 (1990).
- Wei, Z.X. & Faul, C.F.J. Aniline oligomers - Architecture, function and new opportunities for nanostructured materials. *Macromolecular Rapid Communications* **29**, 280-292 (2008).
- Wei, Z.X., Laitinen, T., Smarsly, B., Ikkala, O. & Faul, C.F.J. Self-assembly and electrical conductivity transitions in conjugated oligoaniline - Surfactant complexes. *Angewandte Chemie-International Edition* **44**, 751-756 (2005).

Funding Acknowledgments

The authors would like to thank the EPSRC and ERC for funding.

Research carried out at Diamond Light Source on beamline I07 and at the ESRF on beamline BM28.

DOI 10.1039/C2SM06492H

Materials Village

Steve Collins, Village Coordinator

The Materials Village has continued to thrive, with the established beamlines – I19, I16 and B16 – producing an exciting array of scientific highlights and developments. The most exciting newcomer to the village is the coherence and imaging beamline I13, which will be operated in collaboration with the University of Manchester. It is now available for users and is set to provide a world-leading resource for the future.

The beamline I13 is one of Diamond's long beamlines, dedicated to hard X-ray imaging on the micro and nano length scale and coherence related experiments. It comprises two independent branches: the coherence branch, which welcomed its first users in October; and the imaging branch will followed suit in April 2012.

The funding from the University of Manchester includes capital staff and operational costs towards the I13 imaging branch beamline in return for dedicated access. The staff financed through this collaboration have accelerated the completion of the I13 imaging branch and ensured its operation for the next seven years. The effort is further supported by a team from The University of Manchester, based at the Research Complex at Harwell, to drive forward the research.

Over the last year the construction of the I13 beamline has forged ahead, implementing novel concepts for the optical elements, such as a horizontally deflecting monochromator and mirror; and a robot arm for coherent diffraction X-ray experiments. The 'mini-beta' modification to the storage ring has proved extremely successful in enhancing the undulator brilliance, and has now been adopted for beamline I09.

To complement these advances in electron and X-ray optics, state-of-the-art imaging detector technology is essential. For the short-term, a MaxiPixII photon counting pixel detector has been acquired. The next generation of detectors, based on the MediPixIII chip, is already in an advanced stage of development, with Diamond and STFC working in partnership to ensure that the new X-ray detector EXCALIBUR will be available this summer.

The first I13 users, John Rodenburg (Sheffield University) and Thomas Waigh (Manchester) carried out pilot experiments on a new coherent scattering technique called 'Ptychography' (from the Greek word for fold), which combined scanning microscopy and coherent imaging techniques to provide an image of microscopic polystyrene spheres with high spatial resolution and a wide field of view. The first biologically-oriented experiment was carried out by the team of Ian Robinson (UCL), with a particular interest in chromosomes. Experiments with a world-leading



Figure 1: Robot arm at beamline I13. The device replaces the traditional diffractometer, holding the future EXCALIBUR detector at large distance for coherent X-ray diffraction experiments.

scanning probe are planned for the near future in collaboration with Yong Chu from NSLS-II, who has developed Multilayer Laue Lenses that can provide a focus spot down to 10 nm (less than one thousandth of the width of a human hair) – made possible by the long length of the I13 beamline.

I19, the small-molecule single-crystal diffraction beamline, has just marked its third year of operation and it has hosted approximately 220 user visits in the current period, producing in excess of 80 publications. Over the past year an increasing number of users were supported at beamline I19. The range of sample environment equipment was further developed and can now

be made available to users. The 'Helix' helium gas-jet cooler already has been available for user experiment during the last allocation period, giving temperatures down to 30 K. More recently, an alternative gas-jet system was commissioned for use in Experimental Hutch 2, which is capable of extending the base temperature down to 5 K. For studies requiring additional sample environment cells, a closed-cycle cryostat is available in Experimental Hutch 2, which can also attain 5 K, and this has already been used for studies at simultaneous low-temperature and high-pressure with diamond-anvil cells.

In addition an X-ray chopper and laser system have been successfully commissioned for time-resolved studies and the first successful study of a photo excited species, with a millisecond lifetime, was conducted at the start of the first run in this year.

Considerable progress has been made in the commissioning of the Pilatus 300 K detector on the Newport 4-circle diffractometer in Experimental Hutch 2, and a GDA software development is under test prior to making the detector available to tolerant and experienced users. Experimental Hutch 1 at beamline I19 continues to support the majority of users of the beamline and an increasing number are benefiting from the use of the robotic sample changer. A fluorescence detector for studies probing anomalous scattering effects close to absorption edges has recently been commissioned.

Over the last year the beamline has been used to determine crystal structures that have been included in a number of high-profile publications which are well represented in this report. Highlights include: the structure determination of a molecular pentafoil knot, which was synthesised using self-assembly techniques (Leigh *et al.*); the structure determination of a high-nuclearity metal-organic nanosphere (Champness *et al.*); and the structural pressure dependence of a metal-organic framework system (Moggach *et al.*).

The primary mandate of B16, Diamond's Test beamline, is to facilitate technical developments in optics, detectors and instrumentation. This is complemented by a disparate and varied range of science based experiments. This test beamline facilitates research in many areas, from material science, to radiation physics and biology. In the past year, a range of experiments based on diffraction, reflectivity, imaging and topography have been progressed on B16 by different user groups. Much of this research required extensive technique development and/or optimisation of complex experiment setups, making B16 an ideal platform to progress such experiments.

The radiation physics/biology research led by Fred Currell of Queen's University, included in this section, is a superb example of cross-disciplinary research involving international collaborations and the use of complementary techniques across international facilities to understand the nanoscale mechanisms underpinning a new approach to cancer therapy.

An interesting example of a technique development on B16 applied to an important science area is reported by Kachkanov *et al.* The micro-focused 3D X-ray reciprocal space mapping was established to provide invaluable information about microstructure of the nitride alloy epilayers. Commercial use of nitrides spans a wide field from optoelectronics to microwave technology.

The capability and functionality of B16 is continuously being evolved, and several important developments have been made in the last year. One of which was the establishment of techniques for at-wavelength (i.e. using X-rays) metrology on B16 and employing them to characterise several

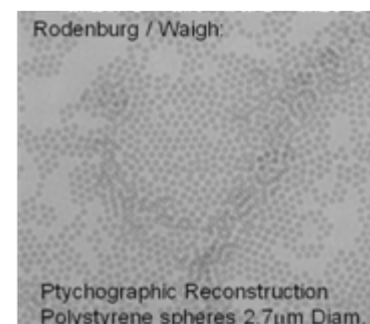


Figure 2: First scientific result on the I13 coherence branch. Ptychographic reconstruction of polystyrene spheres. Experiment with first user group J. Rodenburg (Sheffield) and T. Waigh (Manchester).

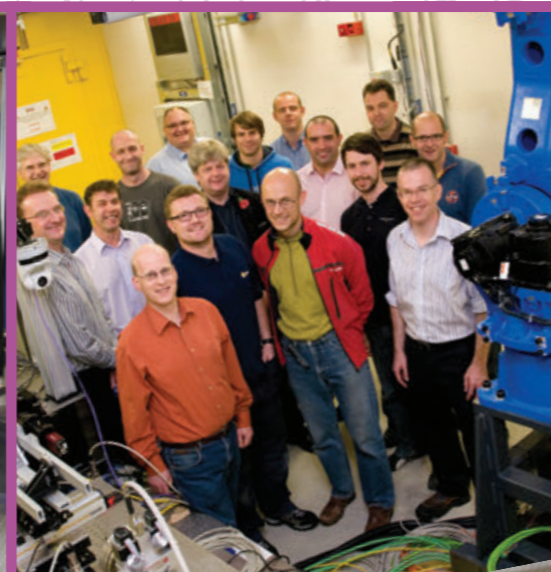
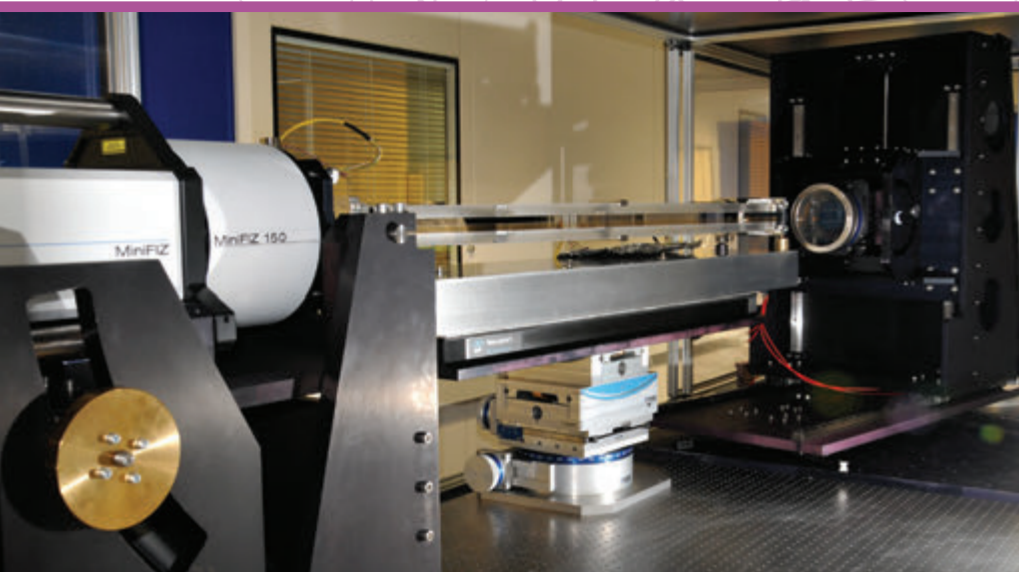
important X-ray optics, as it is demonstrated in the development section.

I16 (Materials & Magnetism), the most mature of the Village beamlines, continues to pursue an active development programme. A cryogen-free 2K cryostat, mounted on the six-circle kappa diffractometer, has recently been tested very

successfully. While scattering is restricted to the horizontal plane, such geometry is proving increasingly popular for studies of thin-film samples, and as a means of obtaining high quality resonant magnetic scattering with enhanced sensitivity to magnetic moment directions.

The move onwards and ever-increasing use of state-of-the-art area detectors continues, with two- and three-dimensional reciprocal space maps finding their way to high quality publications. For example, the work by Gorfman *et al.* on the structure of an important ferroelectric material, $\text{PbZr}_{1-x}\text{Ti}_x\text{O}_3$ – or PZT. The majority of this work has exploited the Pilatus 100K detector, but routine availability of the larger Pilatus 2M, mounted on its dedicated support stage, has prompted considerable activity in software development, with the short-term goal of using the large detector to pre-orient samples on the diffractometer. Continuous scanning has been tested with Pilatus detectors to provide data which is not only collected faster, but also with improved angular accuracy.

The core science output of the beamline remains focused on electronic ordering in novel materials, as you will see from this year's science contributions. Pascut *et al.*, used beamline I16 to investigate a novel symmetry-breaking in AgNiO_2 by resonant X-ray scattering, where it becomes energetically favourable to create a 'charge-honeycomb metal'. Non-resonant magnetic scattering, on the other hand, was found by Johnson *et al.* to be the technique of choice for elucidating the unusual 'helical' magnetic structure of $\text{Cu}_3\text{Nb}_2\text{O}_8$, suggesting an unusual form of magnetic coupling to explain the observed electric polarisation in this multiferroic material.



Direct observation of charge order in triangular metallic AgNiO_2 by single-crystal resonant X-ray scattering

Pascut, G. L., Coldea, R., Radaelli, P. G., Bombardi, A., Beutier, G., Mazin, I. I., Johannes, M. D., and Jansen, M. Direct Observation of Charge Order in Triangular Metallic AgNiO_2 by Single-Crystal Resonant X-Ray Scattering. *Phys. Rev. Lett.* **106**, 157206 (2011)

Single-crystal resonant X-ray scattering was used on beamline I16 to reveal a novel form of spontaneous electronic order in a two-dimensional triangular metal described as a 'charge-ordered honeycomb metal'. This phase occurs in the hexagonal metallic magnet AgNiO_2 , which contains orbitally-degenerate electrons in the cross-over region close to the Mott transition. The electronic ordering in such materials has been intensively investigated, in order to understand related phenomena such as e.g. colossal magnetoresistance, and possibly hightemperature superconductivity. The charge ordered phase occurs as a surprising alternative to the conventional Jahn-Teller orbital order, ubiquitous in more localised systems. This radically different metallic electronic phase, which is charge- but not orbitally-ordered, was predicted theoretically based on indirect structural evidence that observed a small oxygen breathing distortion leading to expanded and contracted octahedra around Ni sites. Here we use resonant single-crystal X-ray scattering to be directly sensitive to changes in the electronic structure at the Ni sites themselves, and observe direct and quantitative evidence for charge order. By tuning close to a Ni resonance, we observe large enhancements of the supercell reflections and a rich spectrum as a function of energy. This we quantitatively explain in terms of interference scattering from Ni sites with energy-shifted atomic form factors, a characteristic signature of charge order.

Orbital ordering whereby orbital degeneracy is lifted either by a spontaneous lattice distortion driven by the cooperative Jahn-Teller (JT) effect¹, or by similar orbital physics², has been considered ubiquitous in both band and Mott insulators containing "JT-active" ions. For this reason, the recent proposal³ of a radically different type of electronic ordering in the weakly metallic hexagonal 2H-AgNiO_2 was surprising. In this scenario, orbital degeneracy at JT-active low-spin Ni^{2+} would be lifted through charge disproportionation and charge ordering (CO) rather than orbital ordering (OO), in sharp contrast with the closely related but insulating nickelate NaNiO_2 , a rather conventional JT system⁴. The first indication for CO in 2H-AgNiO_2 was structural, and relied on an accurate neutron refinement of an oxygen breathing mode around the different Ni sites (Fig. 1b) in the $\sqrt{3}a_0 \times \sqrt{3}a_0 \times c$ supercell structure below 365 K, which suggested a 'honeycomb' CO pattern (Fig. 1a) with electron rich Ni1 sites nested inside a honeycomb of electron-depleted Ni2,3 sites.

Here we present resonant X-ray scattering data to probe directly the electronic order at the Ni sites. In particular, Ni K-edge resonant scattering probes primarily dipole-allowed transitions from the core 1s levels, which shift in response to the amount of charge on the ion, to the empty 4p band, which is strongly sensitive to changes in the coordination environment. From

our data, we extract in an unbiased way the anomalous scattering factors of the different Ni sites. By comparing the experimental results with LDA band-structure calculations, we show that the 4p level shift accounts for just over half of the edge shift, implying a core-level shift of 1 eV that provides direct evidence of CO. We also show that the results are quantitatively consistent with the amount of charge disproportionation predicted by band-structure calculations which propose that in weakly-metallic systems close to the Mott transition, CO can be an energetically more favourable way to lift orbital degeneracy than JT distortions, due to an energy gain in Hund's rule coupling energy, gain in Ni-O covalent energy and a much reduced Hubbard U energy cost for double occupancy due to metallic screening^{3,5}.

Experiments were performed on a small single crystal of 2H-AgNiO_2 (70 μm diameter in ab plane) using the I16 beamline operated with a Si (111) double-crystal monochromator ($\Delta E/E \approx 10^{-4}$ at 8.35 keV). Fig. 2a shows the energy-dependent Bragg peak intensity, after correction for absorption and conversion to absolute units, for three representative supercell reflections. The top panel shows a supercell peak entirely due to anomalous scattering from Ni as it is practically absent off resonance. The middle and bottom panels show supercell peaks with a sizeable oxygen contribution, as evidenced by the pre-edge scattering. The rich structures observed are due to

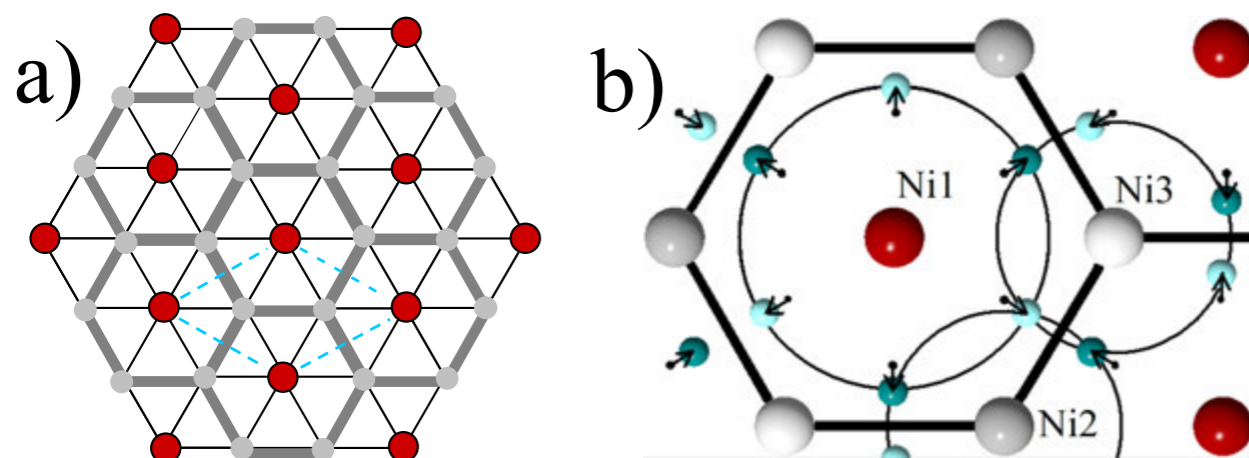


Figure 1: a) Schematic of the honeycomb charge ordering on the triangular lattice: red balls are electron-rich Ni1 sites nested inside a honeycomb (thick contour) of electron-depleted Ni2,3 sites (gray balls). The dashed rhombus is the CO supercell. b) Oxygen breathing mode around electron-rich Ni sites.

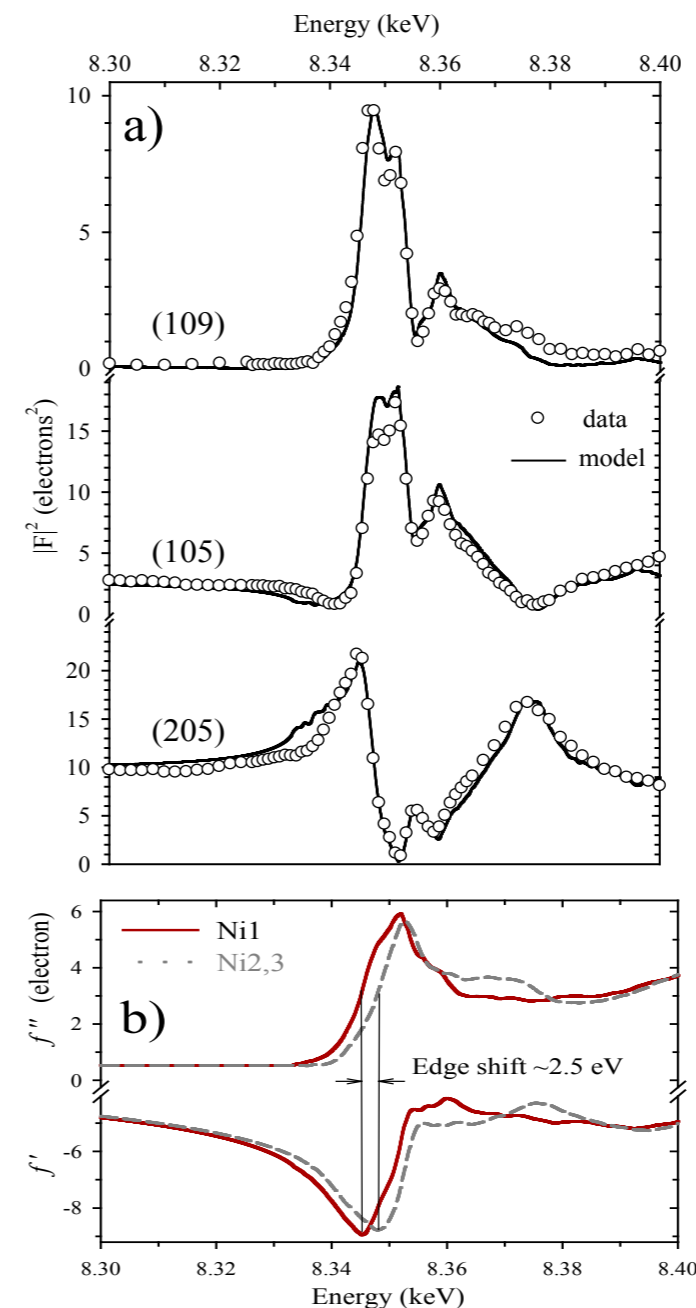


Figure 2: a) Energy-dependent intensity of three supercell reflections at 300 K near the Ni K-edge (solid lines are model calculations using the atomic scattering functions shown in Fig 3). b) Energy-dependence of the empirically-extracted real and imaginary parts of the anomalous atomic scattering factors for Ni1 (solid line) and Ni2,3 (dashed line) obtained from the best fit to the data in a).

the fact that the K-edge absorption energy of the electron-rich Ni1 is slightly different from that of electron-depleted Ni2,3 providing a strong energy-dependent contrast between the two sites. The spectra can be reproduced quantitatively in absolute units by a model (solid lines) based on an unbiased reconstruction of the atomic scattering factors for the Ni1 and Ni2,3 (Fig. 2b), which shows a clear energy shift of the edge of +2.5(3) eV. The sign of the edge shift is consistent with an electron-rich Ni1 site and the absolute scaling of the intensities ensures an accurate and reliable determination of the magnitude of the edge shift.

Edge shifts are often taken as directly proportional to changes in the formal valence of the ion. For octahedral Ni, the proportionality

constant is ~ 0.66 electrons/eV, so an edge shift of 2.5 eV corresponds to a disproportionation of ~ 1.65 electrons, in very good agreement with the expected³ CO scenario of $\text{Ni}^{1.2+}$ and $\text{Ni}_{2,3}^{3.5+}$. However, the initial- and final-states contributions to the edge shift are typically of similar magnitudes, while only the former are directly related to charge ordering. The shift in the final states due to hybridisation with the oxygens, are calculated using LDA to be ~ 1.5 eV, which can account for only half of the total observed shift of 2.5 eV. This implies a shift of the core 1s level of ~ 1 eV between Ni1 and Ni2,3, attributed to the different charge states of the distinct Ni sites. Furthermore, this extracted core level shift of ~ 1 eV is also in quantitative agreement with LDA calculations extended to calculate the core levels of the distinct Ni sites.

In summary, we have reported Ni-K-edge resonant X-ray scattering measurements on a single-crystal of the orbitally-degenerate triangular-lattice metal 2H-AgNiO_2 to investigate the transition to a tripled hexagonal unit cell. We have observed a large resonant effect on the superstructure reflections with a rich energy-dependent structure that can be quantitatively accounted for by interference scattering from the electron-rich and -depleted Ni sites with energy-shifted atomic scattering factors. By considering the various contributions to this edge shift we have determined a core-level shift of ~ 1 eV between Ni sites, in quantitative agreement with first principles electronic structure calculations, thus providing clear, direct and quantitative evidence of charge order in the triangular Ni layers. Charge order as an alternative to orbital ordering in systems with Jahn-Teller active ions was recently brought into the spotlight in connection with 3D perovskite nickelates RNiO_3 , and is likely controlling the essential physics of ferrates CaFeO_3 and $\text{Sr}_3\text{Fe}_2\text{O}_7$, and other orbitally-degenerate systems located in the cross-over region between local Mott insulator and itinerant behaviour⁵.

References

- Jahn, H. & Teller, E. Stability of Polyatomic Molecules in Degenerate Electronic States. I. Orbital Degeneracy. *Proceedings of the Royal Society London A.* **161**, 220-235 (1937).
- Kugel, K.I. & Khomskii, D.I., The Jahn-Teller effect and magnetism: transition metal compounds. *Sov. Phys. Usp.* **25**, 231 (1982).
- Wawrzyńska, E., Coldea, R., Wheeler, E.M., Mazin, I.I., Johannes, M.D., Sörgel, T., Jansen, M., Ibberson, R.M. & Radaelli, P. G. Orbital Degeneracy Removed by Charge Order in Triangular Antiferromagnet AgNiO_2 . *Phys. Rev. Lett.* **99**, 157204 (2007).
- Chappel, E., Núñez-Regueiro, M. D., Chouteau, G., Isnard, O. & Darie, C., Study of the ferrodistorive orbital ordering in NaNiO_2 by neutron diffraction and submillimeter wave ESR. *Eur. Phys. J. B.* **17**, 615 (2000).
- Mazin, I.I., Khomskii, D. I., Lengsdorf, R., Alonso, J. A., Marshall, W. G., Ibberson, R. M., Podlesnyak, A., Martínez-Lope, M. J. & Abd-Elmeguid, M. M. Charge Ordering as Alternative to Jahn-Teller Distortion. *Phys. Rev. Lett.* **98**, 176406 (2007).

Funding Acknowledgements

We acknowledge support from EPSRC UK and a studentship from the University of Bristol and Harold Herbert Potter Fund for G.L. Pascut.

DOI 10.1103/PhysRevLett.106.157206

High-resolution X-ray diffraction study of single crystals of lead zirconate titanate 'PZT'

Gorfman, S., Keeble, D.S., Glazer, A.M., Long, X., Xie, Y., Ye, Z.-G., Collins, S. & Thomas, P.A. High-resolution x-ray diffraction study of single crystals of lead zirconate titanate *Phys. Rev. B* **84**, 020102(R) (2011)

Lead zirconate titanate, $\text{PbZr}_{1-x}\text{Ti}_x\text{O}_3$ (PZT), is a perovskite-based ferroelectric which possesses exceptionally good piezoelectric properties and is currently the most important material in the piezoelectric industry. Although a number of studies of PZT have been performed to date, the reason for the remarkably piezoactivity is not yet understood. The piezoelectric response of PZT is particularly enhanced in the vicinity of the so-called morphotropic phase boundary (MPB), originally defined as a nearly vertical line on the x - T phase diagram, separating the Zr-rich $R3m$ phase, and the titanium rich $P4mm$ phase¹. Since these space groups are not group-subgroup related, either a two phase coexistence region, or an intermediate phase should be present. The symmetry of any intermediate phase is particularly important, predefining such macroscopic properties as the allowed crystallographic direction of the polarisation, the non-zero piezoelectric tensor coefficients, type of domain pattern, etc. In particular the atomic structure, domain distribution and disorder parameters of PZT, especially for the composition ranges around the MPB, are matters of strenuous scientific debate.

As single crystals of PZT were not available until very recently, the most current conclusions regarding the structure and symmetry of this ferroelectric were drawn from powder-diffraction data, where the results are often ambiguous. The so-called monoclinic PZT phase, suggested by Noheda *et al.*² using high-resolution powder diffraction, was highly questioned. Wang *et al.*³ showed that the lamellar structure of rhombohedral/tetragonal nanodomains (so-called adaptive phase) would produce a powder diffraction pattern impossible to discriminate from a monoclinic PZT pattern. Only through diffraction from a single crystal can the true MPB structure of zirconate titanate be elucidated.

The first successful synthesis of PZT single crystals for the composition close to the MPB region was only recently achieved⁴. The aim of the work described here is to perform detailed X-ray diffraction studies of PZT single crystals to obtain the most precise current information about the average structure. Two single crystals of PZT (PZT31 and PZT46) were attached to a specially designed holder to be transferrable between diffractometers⁵ while maintaining the orientation of the crystal. The orientation of the crystal was determined and large areas of reciprocal space were explored using a Gemini R diffractometer (Agilent Technologies). The crystals were then transferred to a high-resolution X'Pert Pro diffractometer (PANalytical) to collect high-resolution reciprocal-space maps around a series of selected Bragg reflections.

Finally, the crystals were taken to beamline I16 to measure representative reciprocal space maps for $\{hhh\}$, $\{0hh\}$ and $\{00h\}$ type reflections at higher temperatures. The wavelength selected was 0.96 Å, corresponding to an X-ray absorption coefficient 3 times lower than for the laboratory X-ray source: the synchrotron measurements therefore provide information more from the bulk of the crystal, rather than from a surface layer.

To elucidate the symmetry of a single domain, we analysed the observed splitting of Bragg reflections in 2θ , corresponding to different values of d . The positions of the peaks in the maps can be used to identify the diffraction effect due to adaptive phases, since a peak produced by the interference between rhombohedral/tetragonal nanodomains, is expected to be located on the line between the two reflections which would be produced by coarse domains of the same symmetry. The analysis was followed by a least-squares fit of all the observed reflections, assuming different models for the symmetry of a single ferroelastic domain, and supposing that the twinning originates from the high-temperature prototypic phase of point group $m\bar{3}m$.

Fig. 1. shows reciprocal space maps of the reflections collected from the twinned PZT46 and PZT31 crystals. The vertical lines show the results of least-square refinement and indicate the simulated 2θ values when all possible twin domains are present. A combination of rhombohedral and monoclinic

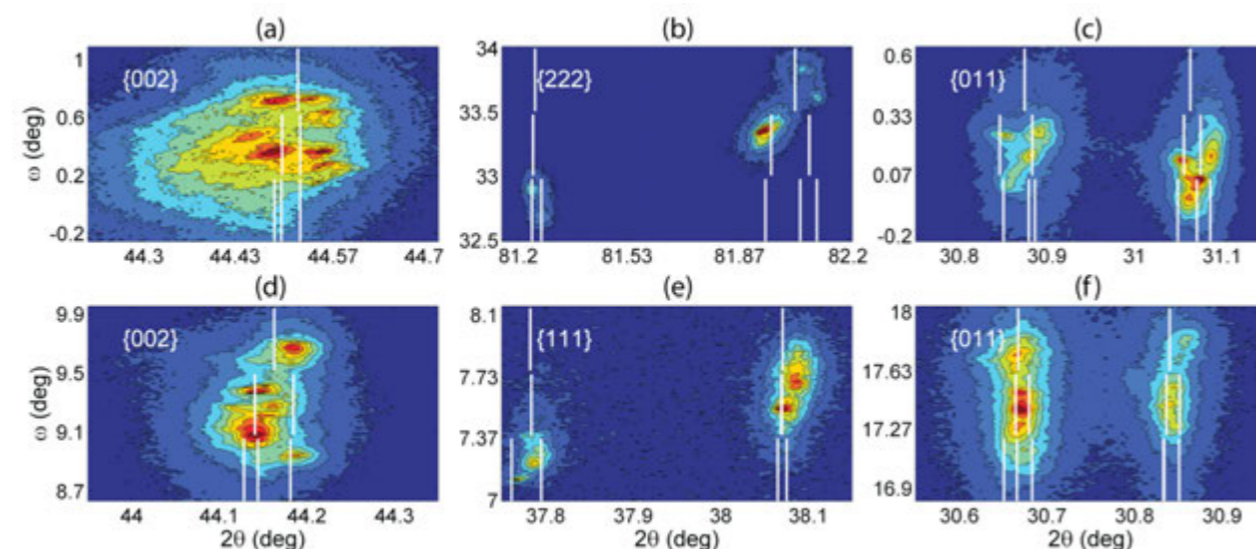


Figure 1: Room-temperature reciprocal space maps for different $\{hkl\}$ reflections collected for PZT46 (a), (b), (c) and PZT31 (d), (e), (f).

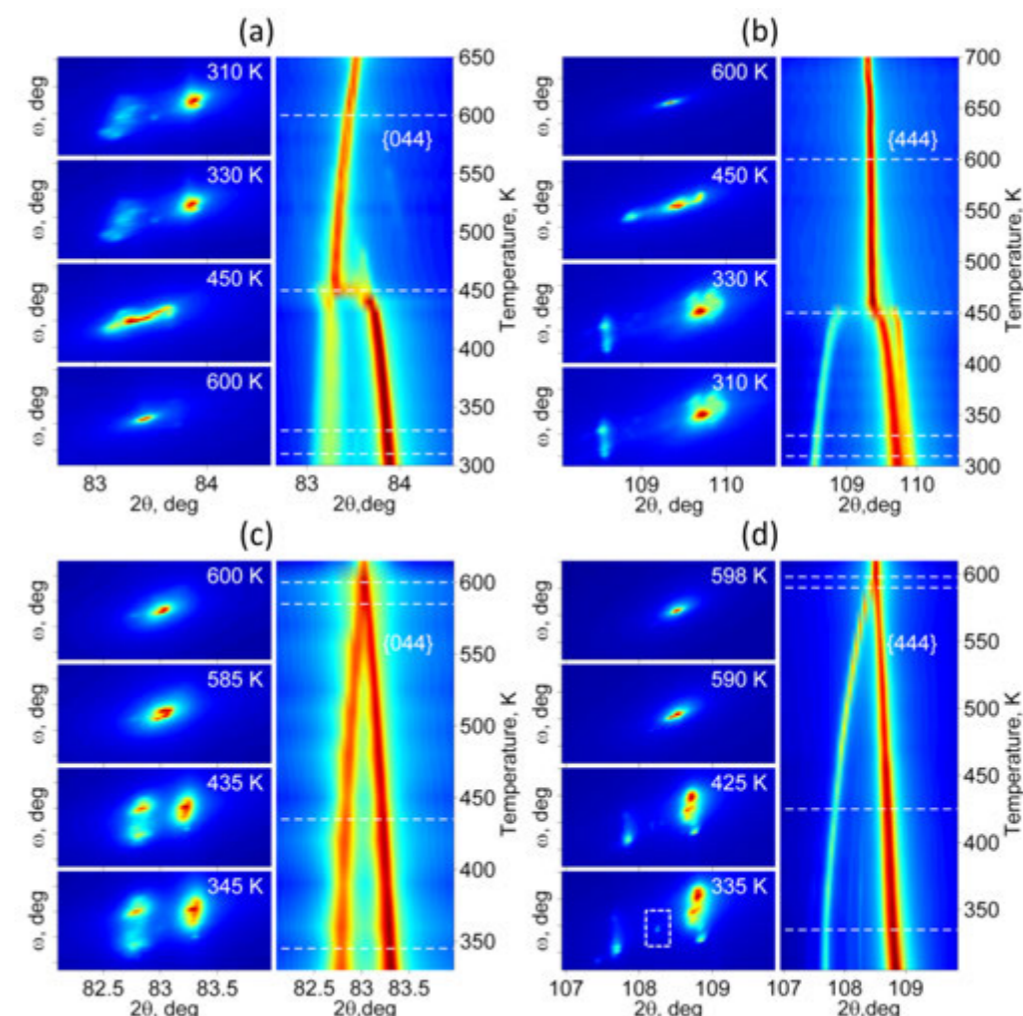


Figure 2: The results of high-temperature measurements, revealing the changes of the symmetry of PZT46 (a,b) and PZT31 (c,d). The distance between ticks on the ω axis corresponds to 0.5°. The rectangle on (d) highlights the weak peak, which can be assigned to the adaptive phase diffraction phenomena.

lattices in PZT46 accounts for the splitting observed in most of the maps. In particular, it reproduces the fine splitting of the {222} and {011} reflections, where single-phase rhombohedral or even single-phase monoclinic models fail to do so. For PZT31, previously believed to be purely rhombohedral, the collected reciprocal-space maps also show the peak-splitting characteristic of a combination of monoclinic and rhombohedral phases. The deviation of the refined monoclinic lattice constants from rhombohedral in PZT31 is much smaller than for the PZT46; this result is reasonable as PZT31 is further away from the MPB than PZT46. However, it shows that contrary to common belief, PZT retains its monoclinic phase over a large compositional range, albeit with reducing monoclinic distortion away from the MPB. Fig. 2 show the results of the synchrotron multi-temperature measurements of the {044} and {444} reflections. For both PZT46 and PZT31, the room-temperature maps, obtained with the shorter wavelength (0.96 Å), show features similar to those observed using the laboratory diffractometer (1.54 Å) confirming that the splitting does not simply result from the structure of the surface, but is relevant to the bulk phase.

Although the nominal Curie point of PZT46 is 670 K (dielectric constant maxima), a pseudocubic symmetry - no splitting - is observed for temperatures down to ≈ 450 K. This unusual phenomenon is in agreement with optical studies of PZT crystals, and can be explained by anomalously small ferroelectric domains below 670 K and transformation to a phase consisting of micrometer-sized domains. In contrast, the splitting in 2θ from PZT31 appears at ≈ 600 K. In addition, the synchrotron data show the presence of very weak peaks in both {044} and {444} maps, located exactly on the line between two stronger Bragg peaks (one such peak is highlighted) in Fig. 2. Note that these peaks could not be observed using the laboratory experiment and could not be accounted for by the proposed model of phase mixtures.

In conclusion, we have performed a series of high-resolution X-ray diffraction studies of twinned PZT crystals of two different compositions (PZT31 and PZT46). Analysing the angular positions of reflections lends credence that the key splittings, important in determining crystal symmetry, do not arise from the presence of adaptive phases. This provides further proof of the existence of the low-symmetry monoclinic phases in PZT. Furthermore, we have shown that the average structures of PZTs of both investigated compositions are best described by a combination of at least rhombohedral and monoclinic symmetries.

References

1. Jaffe, B., Cook, W. R. & Jaffe, H.L.C. in *Piezoelectric Ceramics* (Academic, London (1971).
2. Noheda, B., Cox, D.E., Shirane, G., Gonzalo, J.E., Cross, L.E. & Park, S.-E. *Appl. Phys. Lett.* **74**, 2059, (1999).
3. Bokov, A.A., Long, X. & Ye, Z.-G. *Phys. Rev. Lett.* **84**, 5427 (2010).
4. Wang, Y.U. *Phys. Rev. B* **74**, 104109 (2006).
5. Gorfman, S. & Thomas, P.A. *J. Appl. Cryst.* **43**, 1409 (2010).

Funding Acknowledgements

We are grateful for financial support of the EPSRC (Materials World Network: Nanoscale Structure-Property Relationships in Lead-Free Morphotropic Phase Boundary Piezoelectrics), the US Office of Naval Research (Contract No. N0014-06-1-0166) and the Natural Science and Engineering Research Council of Canada.

DOI 10.1103/PhysRevB.84.020102

A new twist for multiferroics

Johnson, R. D., Nair, S., Chapon, L. C., Bombardi, A., Vecchini, C., Prabhakaran, D., Boothroyd, A. T., and Radaelli, P. G. $\text{Cu}_3\text{Nb}_2\text{O}_8$: A Multiferroic with Chiral Coupling to the Crystal Structure. *Phys. Rev. Lett.* **107**, 137205 (2011)

Multiferroics are materials that are simultaneously magnetic and ferroelectric. The possibility to use them to develop an electrical read-and-write technology for magnetic information storage has stimulated an intense research activity in the past few years. Through electric polarisation and bulk magnetisation measurements, we show that a new complex oxide, $\text{Cu}_3\text{Nb}_2\text{O}_8$, is multiferroic below 24 K, the electric polarisation occurring concomitantly with a magnetically ordered phase. By using neutron powder diffraction and non-resonant X-ray diffraction measurements we demonstrate that the ferroelectric polarisation is induced by a long-range generalised helicoidal magnetic structure. Unusually, the electric polarisation was found to lie perpendicular to the plane of rotation of the magnetic moments. This observation cannot be reconciled with conventional theories developed for cycloidal multiferroics, in which the electric polarisation must strictly lie within the plane of rotation. Our results are consistent with a new multiferroic mechanism of *ferroaxial* coupling between a macroscopic structural rotation allowed in the paramagnetic point group, and magnetically induced structural chirality.

The research in this field has been driven by the discovery of a new class of materials, such as TbMnO_3 . In this material the electrical polarisation is directly induced by magnetic symmetry breaking, and couples very strongly to the magnetism¹. Most materials of this kind possess the so-called cycloidal magnetic structure, where all the spins rotate in a plane containing the propagation vector of the magnetic wave. A comprehensive theory has been developed to account for the magneto-electric coupling in these cycloidal magnets²; a strong prediction of this theory is that the electrical polarisation is constrained to lie in the plane of rotation of the spins. Here, we describe a previously unreported multiferroic compound, $\text{Cu}_3\text{Nb}_2\text{O}_8$, where the electrical polarisation is almost perpendicular to the plane of spin rotation, leading us to postulate a new magneto-elastic coupling mechanism.

High quality single crystals of $\text{Cu}_3\text{Nb}_2\text{O}_8$ were grown in an optical floating-zone furnace, giving samples with approximate dimensions of $2 \times 2 \times 1 \text{ mm}^3$. The room temperature crystal structure was determined through lab-based

X-ray diffraction and was found to adopt the centrosymmetric tridinic spacegroup $P\bar{1}$. As shown in Fig. 1, there are two distinct Cu^{2+} sites in the unit cell, located at Wyckoff positions 1a (Cu_1 , on an inversion centre and in square planar coordination) and 2i (Cu_2 in a general position), which form sawtooth chains parallel to the a -axis. The chains are composed of Cu_2 - Cu_1 - Cu_2 steps linked by Cu_2 - Cu_2 risers, and are separated along the b -axis by a layer of non-magnetic Nb^{5+} ions (Fig. 1).

Heat capacity measurements (Fig. 2a) displayed two anomalies at 26.5 K and 24.2 K. Neutron powder diffraction experiments showed that the first anomaly (T_N) coincided with the onset of long-range antiferromagnetic order, as shown in Fig. 2b. Indexing the powder diffraction data indicated that the magnetic order had the propagation vector $(0.4876, 0.2813, 0.2029)$ - incommensurate in all reciprocal space directions. Given that the RT crystal structure has $P\bar{1}$ symmetry, any low temperature phase transitions were likely to be associated with the breaking of inversion symmetry (the only

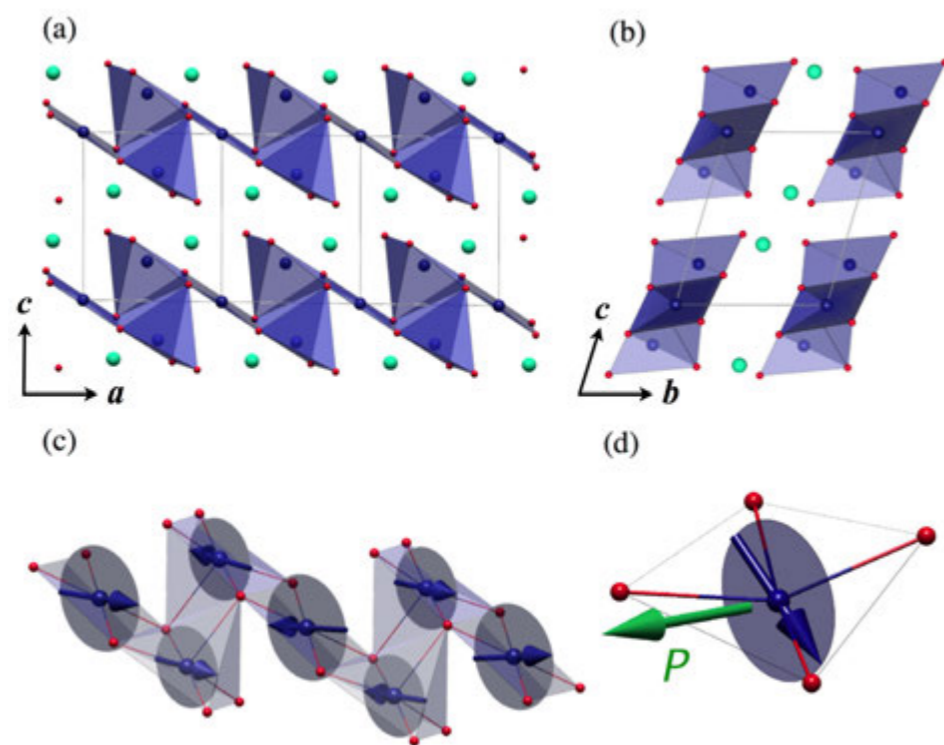


Figure 1: (a),(b) The crystal structure of $\text{Cu}_3\text{Nb}_2\text{O}_8$ in the ac and bc plane, respectively. Copper, niobium and oxygen atoms are shown in blue, green, and red, respectively. (c) The magnetic structure of the copper chains. The envelope of the spin rotation is shown by gray circles. (d) The relationship between the electric polarisation and the spin rotation plane.

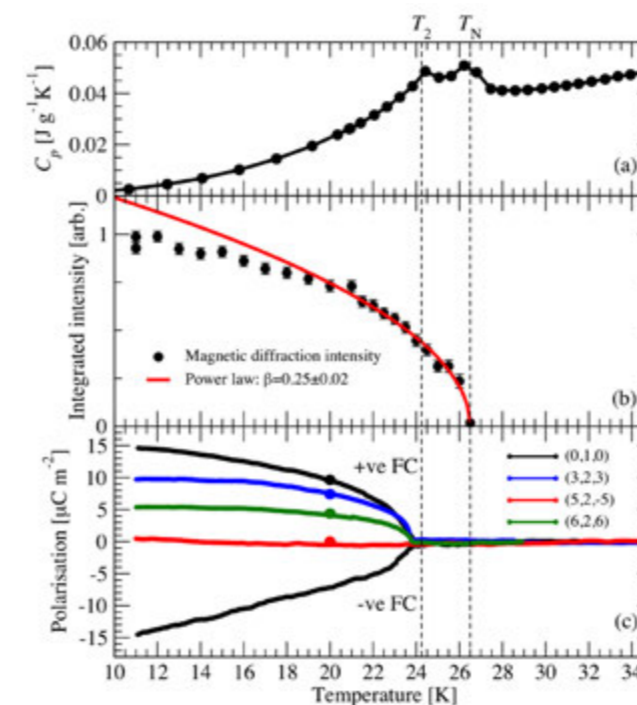


Figure 2: (a) The specific heat of $\text{Cu}_3\text{Nb}_2\text{O}_8$ measured as a function of temperature. (b) The temperature dependence of the neutron magnetic diffraction intensity of the fundamental reflection. The data have been fitted with a power law. (c) The electric polarisation in three approximately orthogonal and the general $(6,2,6)$ directions.

symmetry element except E) and hence result in a polar phase. Indeed, pyroelectric measurements confirmed the development of a ferroelectric polarisation below T_2 . The electric polarisation was measured in four independent directions, as shown in Fig. 2c., in order to determine the direction $[(1, 3, 2)$ in reciprocal lattice units] and magnitude $[17.8 \mu\text{C m}^{-2}$ at 10 K], of the polarisation vector P .

To understand the multiferroic properties of $\text{Cu}_3\text{Nb}_2\text{O}_8$ it was necessary to determine the microscopic magnetic structure that induces the ferroelectric polarisation below T_2 . Initial fits to the neutron powder diffraction data showed that the Cu^{2+} magnetic moments form a rotating spin structure, however, it was not possible to uniquely determine the plane of rotation of the spins, a crucial ingredient in the theoretical interpretation of the multiferroicity. We therefore performed a non-resonant magnetic X-ray diffraction (NRMXD) experiment at 116, in which we exploit the dependence of the NRMXD cross section on the direction of the magnetic moment with respect to the incident and scattered directions of light and the x-ray polarisation. To reduce the fluorescent background the incident beam energy was tuned to 7.835 keV, well below the copper and niobium K absorption edges. Three magnetic diffraction peaks were located, and at each the diffraction intensity (in both $(\sigma-\sigma')$ and $(\sigma-\pi')$ channels) was measured whilst rotating the sample around the scattering vector (azimuthal scan). The data is plotted in Fig. 3. Initial fits to the azimuthal dependences showed that all spins rotated in a common plane within experimental error. The final fits, shown in Fig. 3., were therefore constrained to just four free parameters: the vector normal to the rotation plane (θ and φ) and two scale factors for each copper site, F_1 and F_2 . These were found to be $\theta = 75.5(2)^\circ$, $\varphi = 54.9(2)^\circ$, and $F_2/F_1 = 1.00(3)$. The above parameters were then fed back into the neutron powder diffraction data refinement to quantitatively determine the magnitude of the magnetic moments, $m_{\text{Cu1}} = 0.89(2) \mu_B$ and $m_{\text{Cu2}} = 0.69(1) \mu_B$, and the relative phase of the two Cu_2 ions $(1.03(7)\pi$ and $1.05(7)\pi$).

The magnetic structure comprises an essentially ferromagnetic coupling within the Cu_2 - Cu_1 - Cu_2 steps of the copper chains, with a predominantly

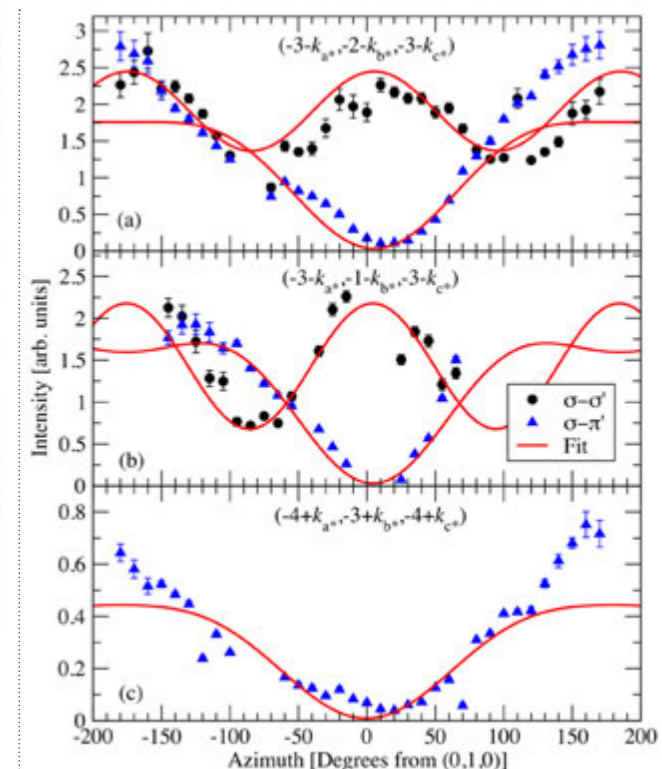


Figure 3: Non-resonant magnetic X-ray diffraction intensity measured as a function of azimuth angle at three separate reflections. The line shape, dependent on the magnetic moment direction, has been fitted (solid red line) to find the spin rotation plane.

antiferromagnetic coupling through the risers, as shown in Fig. 1. The incommensurate propagation vector then gives rise to a slow rotation parallel to the a -axis, and a fast rotation in the b and c directions. The most significant result of this study comes from comparing the direction of the electric polarisation with respect to the plane of rotation of the spins. P was found to be almost perpendicular to the rotation plane (14° from the normal).

These results cannot be explained by the theory developed for cycloidal magnets such as TbMnO_3 , which requires that the electrical polarisation be constrained to lie within the plane of rotation of the spins. We propose an alternative mechanism, which couples the chiral component of the magnetic structure to an axial rotation of the crystal structure that is allowed in the $P\bar{1}$ space group. This 'ferroaxial' coupling is weak in $\text{Cu}_3\text{Nb}_2\text{O}_8$, leading to a small induced polarisation. However, the conceptual framework developed in this study has recently led us to the discovery³ of 'giant' improper ferroelectricity at rather high temperature in the ferroaxial magnet $\text{CaMn}_7\text{O}_{12}$.

References

- Kimura, T., Goto T., Shintani H., Ishizaka K., Arima T. & Tokura Y. Magnetic control of ferroelectric polarization. *Nature*. **426**, 55 (2003).
- Mostovoy M. Ferroelectricity in Spiral Magnets. *Physical Review Letters*. **96**, 067601 (2006).
- Johnson R. D., Chapon L. C., Khalyavin D. D., Manuel P., Radaelli P. G., and Martin C. *Physical Review Letters*. **108**, 067201 (2012).

Funding Acknowledgements

The work done at the University of Oxford was funded by an EPSRC grant, number EP/J003557/1, entitled 'New Concepts in Multiferroics and Magnetoelectrics'.

DOI 10.1103/PhysRevLett.107.137205

Microdiffraction X-Ray reciprocal space mapping of nitride alloy epilayers

Kachkanov, V., Dolbnya, I. P., O'Donnell, K. P., Martin, R. W., Edwards, P. R., Pereira, S. InGaN epilayer characterisation by microfocused x-ray reciprocal space mapping. *Applied Physics Letters*. **99** (18), 181909 (2011)

The III-nitride semiconductors, GaN, InN, AlN and their alloys, have become the subject of intense research in the past fifteen years due to their huge commercial utility and unique physical properties. These include a wide direct bandgap, remarkable mechanical strength and high melting temperatures. The technological breakthrough in the epitaxial growth of InGaN structures¹ has revolutionised the optoelectronic industry, leading recently to robust and compact all-solid state light sources covering the broad spectral range from infra-red to ultraviolet. However, further advances in nitride technology, for example nitride laser diodes emitting in the green, red and ultra-violet spectral regions, require a deeper understanding of the microstructure and nanostructure of $\text{In}_x\text{Ga}_{1-x}\text{N}$ and $\text{In}_x\text{Al}_{1-x}\text{N}$ alloy films. X-ray Reciprocal Space Mapping (RSM) is a powerful tool to explore the structure of materials. However, RSMs are usually measured in two dimensions ignoring the third dimension of diffraction space volume. The idea of full three-dimensional diffraction space mapping to obtain information on the structure of materials was first introduced by Fewster *et al.*². In order to shed light on the structural properties of InGaN and InAlN epilayers we used 3D RSM while probing the material with a microfocused X-ray beam.

The samples studied were two $\text{In}_x\text{Ga}_{1-x}\text{N}$ epilayers, labelled A and B, and one $\text{In}_x\text{Al}_{1-x}\text{N}$ epilayer, grown by Metalorganic Chemical Vapor Deposition (MOCVD) on GaN/Al₂O₃ (0001) substrates. The thickness of the InGaN and InAlN epilayers was 250 nm and 120 nm respectively. The X-ray beam with energy of 12400 eV (1 Å) was focused by Beryllium Compound Refractive Lenses (CRLs) to a spot size with full widths at half maximum (FWHM) of 3.2 μm × 1.6 μm (horizontal x vertical). The measurements of the full 3D shape of the (10 $\bar{1}$ 3) Reciprocal Lattice Point (RLP) were done in skew symmetric geometry by changing the incident angle ω to the diffracting plane and recording the 2D diffraction pattern with a Pilatus100k area detector. The reciprocal space subtended by the detector was converted into scattering vector components in the reference frame of the GaN substrate with Q_x lying along [120], Q_y along [100] and Q_z along [001] directions.

Fig. 1(a) and Fig. 1(b), show the 3D volume of (10 $\bar{1}$ 3) RLP for samples A and B respectively. The presence of 'tails' on either side of Q_x=0 plane is clear. Fig. 2(a) and Fig. 2(b), show projections of the (10 $\bar{1}$ 3) RLP onto the Q_y-Q_z plane for samples A and B. The (10 $\bar{1}$ 3) RLPs corresponding to the InGaN epilayers are broadened due to both composition and strain variation. Reciprocal space coordinates Q_y and Q_z of the InGaN RLP are directly related to the lattice constants *a* and *c* respectively. The InN content *x* was estimated from alloy lattice parameters by solving two dimensional Poisson ratio³. In the sample A, the InN fraction varies from ~12% to ~25%. The strain state of InGaN varies from fully relaxed to pseudomorphic to the substrate. The center of mass (COM) of the (10 $\bar{1}$ 3) RLP corresponds to an InN content of 22% under slight compressive strain. Interestingly, the 'seed' InGaN with

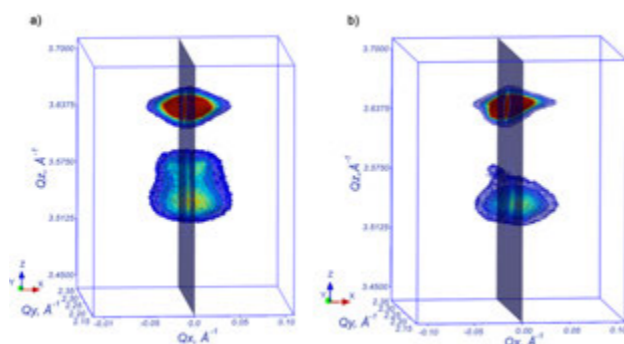


Figure 1: Full 3D view on (10 $\bar{1}$ 3) RLP for sample A (a) and sample B (b). The plane represents a cut along Q_x=0.

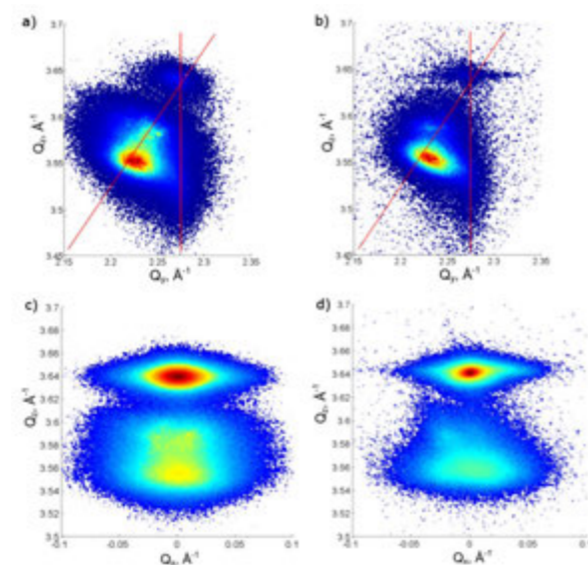


Figure 2: (a) and (b) show projections of the RLP (10 $\bar{1}$ 3) onto the Q_y-Q_z plane for sample A and sample B measured for ω=19.424° and ω=19.357° respectively, (c) and (d) are projections of the (10 $\bar{1}$ 3) RLP on the Q_y-Q_z plane for the same samples. The inclined and vertical red lines in (a) and (b) indicate lattice constants for relaxed InGaN alloys and a lattice constant (3.189 Å) for unstrained GaN. The 'tails' of (10 $\bar{1}$ 3) RLPs correspond to the 'seed' InGaN.

12% of InN is completely relaxed. For sample B, the InN content ranges from ~10% to ~24% and the strain state changes from relaxed to pseudomorphic. Again, the COM of the RLP corresponds to 20% InN under compressive strain and the 'seed', with 10% of InN, is completely relaxed.

A spatial scan across the sample B, monitoring the position of the COM for the (10 $\bar{1}$ 3) RLP and calculating the InN content at each point, revealed the presence of a weak lateral composition gradient as shown in Fig. 3. Note that microfocusing allows us to disentangle lateral and vertical composition gradients on the length scales defined by the effective size of the beam which was ~4×5 μm FWHM for the (10 $\bar{1}$ 3) reflection.

Figs. 2 (c) and (d), show the projection of the (10 $\bar{1}$ 3) RLP on to the Q_y-Q_z plane for samples A and B, respectively. What is observed here is that the 'seeds' of composition gradient in both samples are inclined with respect to the COM of the InGaN RLP. In the case of sample B there is only one sharp 'seed'.

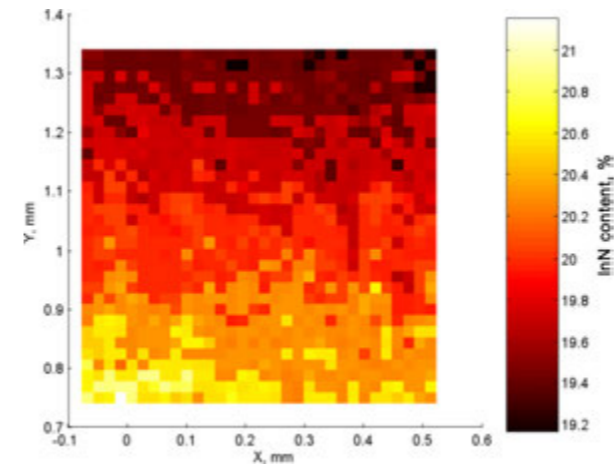


Figure 3: Map of InN content *x* for $\text{In}_x\text{Ga}_{1-x}\text{N}$ sample B measured at ω=19.220°.

Heteroepitaxial films with large lattice mismatch and exhibiting a high density of dislocations are best described as a collection of mosaic crystallites, tilted and twisted with respect to each other. In the geometry of the experiment, a tilt θ along the [120] direction corresponds mainly to a twist φ with respect to the [001] direction through the following relation:

$$(1) \tan \phi = -\frac{1}{\sin \chi} \tan \theta,$$

where χ is the angle between the (10 $\bar{1}$ 3) and (0001) planes.

A speckle pattern of diffracted X-ray intensity is observed for the InGaN 'seeds' in both samples, an example is shown in Fig. 4. The appearance of the speckles is due to partial coherence of the incident X-ray beam. The significance of the speckle pattern is that it indicates that the size of the crystallites in the 'seeds' is less than the transverse coherence length of X-ray beam, which is estimated to be ~250 nm after demagnification by CRLs and change of beam footprint for (10 $\bar{1}$ 3) reflection.

Fig. 5(a) shows the projection of (10 $\bar{1}$ 3) RLP on onto the Q_y-Q_z plane for InAlN epilayer. The COM corresponds to the ~16% of InN. Composition gradient is observed ranging from 20% to 9% of InN. Note that disorder, as indicated by the breadth of RLP, is increasing when going from 20% to 9% of InN. Rutherford Backscattering Spectrometry (RBS) experiments confirmed the existence of composition gradient as shown in Fig. 5(b). Simultaneous fitting of two curves using NDF code⁴ and assuming three layer structure of composition gradient produced following results: 1st layer: 52 nm thick, x=0.085; 2nd layer: 34 nm thick, x=0.129; 3rd layer: 35 nm thick, x=0.167. The order of the layers is from surface to the epilayer/GaN buffer interface.

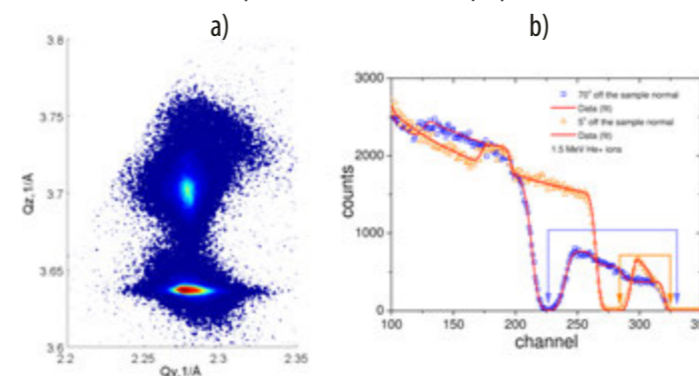


Figure 5: (a) Projection of (10 $\bar{1}$ 3) RLP on onto the Q_y-Q_z plane for InAlN sample measured at ω=20.251°, (b) Simultaneous fitting of experimental RBS spectra using NDF code [4], signal due to Indium atoms is indicated by arrows.

The compositions estimated from RBS are in very good agreement with those estimated from RSM.

In summary, 3D RSM with a microfocused X-ray beam reveals a complex structure of InGaN and InAlN epilayers on the microscale and smaller. Strain-free and twisted InGaN nanocrystallites, less than ~250 nm in lateral size, are observed at the lower end of composition gradient. Formation of strain-free InGaN islands during the initial phases of growth was also observed by *in-situ* 2D RSM⁵. Most importantly it was observed that structural

and compositional disorder increases with growth time, thus supporting suggestion that the islands observed in our *ex-situ* experiments correspond to the beginning of epitaxial growth. The twist of InGaN nanocrystallites is caused by the twist of the underlying GaN mosaic blocks which, in the case of III-nitrides, was found to be related to *a*-type edge dislocations⁶. The lattice mismatch between InGaN and GaN may be relieved by the microstrain associated with *a*-type edge dislocation. Thus, the initial stages of InGaN epitaxial growth correspond to Volmer-Weber growth with the nucleation of 'seed' nanoislands on strain fields generated by the *a*-type edge dislocations. As more of the substrate surface is covered, the structural disorder increases, as indicated by the breadth of the InGaN RLP. In the case of InAlN epilayer, the composition gradient was observed at the beginning of epitaxial growth. The existence and direction of composition gradient was confirmed independently by RBS. Therefore, 3D shape of RLP can provide information about epitaxial growth of semiconductor alloy epilayers.

References

1. Nakamura, S., Senoh, M., Mukai, T. P-GaN/n-InGaN/n-GaN double-heterostructure blue-light-emitting diodes. *Jpn. J. Appl. Phys.* **32**, L8-L11 (1993).
2. Fewster, P.F. & Andrew, N.L. Applications of multiple-crystal diffractometry. *J. Phys. D: Appl. Phys.* **28**, A97-A103 (1995).
3. Pereira, S., Correia, M.R., Pereira, E., O'Donnell, K.P., Alves, E., Sequeira, A.D. & Franco, N. Interpretation of double x-ray diffraction peaks from InGaN layers. *Appl. Phys. Lett.* **79**, 1432-1434 (2001).
4. Barradas, N.P., Jaynes, C., Webb, R.P. Simulated annealing analysis of Rutherford backscattering data. *Appl. Phys. Lett.* **71**, 291-293 (1997).
5. Richard, M.-I., Highland, M. J., Fister, T.T., Munkholm, A., Mei, J., Streiffer, S. K., Thompson, C., Fuoss, P. H. & Stephenson, G. B. In situ synchrotron x-ray studies of strain and composition evolution during metal-organic chemical vapor deposition of InGaN. *Appl. Phys. Lett.* **96**, 051911 (2010).
6. Metzger, T., Hopler, R., Born, E., Ambacher, O., Stutzmann, M., Stommer, R., Schuster, M., Gobel, H., Christiansen, S., Albrecht, M. & Strunk, H.P. Defect structure of epitaxial GaN films determined by transmission electron microscopy and triple-axis X-ray diffractometry. *Philos. Mag.* **A 77**, 1013-1025 (1998).

DOI 10.1063/1.3658619

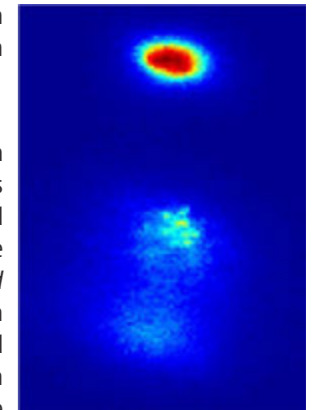


Figure 4: The X-ray diffraction intensity speckle pattern for sample A observed during spatial scan. Note that the image is not transformed to reciprocal space.

Radioenhancement of gold nanoparticle doped biological systems: understanding the nanoscale mechanisms underpinning a new approach to cancer therapy

McMahon, S.J., Hyland, W.B., Brun, E., Butterworth, K.T., Coulter, J.A., Douki, T., Hirst, D.G., Jain, S., Kavanagh, A.P., Mendenhall, M.H., Muir, M.F., Prise, K.P., Requardt, H., Sanche, L., Schettino, G., Currell, F.J. & Sicard-Roselli, C. Energy Dependence of Gold Nanoparticle Radiosensitization in Plasmid DNA. *J. Phys. Chem. C* **115** 20160–20167 (2011)

McMahon, S.J., Hyland, W.B., Muir, M.F., Coulter, J.A., Jain, S., Butterworth, K.T., Schettino, G., Dickson, G.R., Hounsell, A.R., O'Sullivan, J.M., Prise, K.M., Hirst, D.G. & Currell, F.J. Biological consequences of nanoscale energy deposition near irradiated heavy atom nanoparticles. *Nature Scientific Reports*. **1**, 18 (2011)

Effective treatment of cancer is widely recognised as one of the major healthcare challenges of our age. Selectively administering gold nanoparticles to tumours can increase the radiation dose and, more importantly, the biological effect of that dose to the tumour, making them an attractive therapeutic agent. When a gold nanoparticle interacts with radiation, it can act to compress the distance over which the energy is deposited in the neighbouring biological environment from centimetres to 10s of nanometres. Inner-shell ionisation of one of the gold atoms followed by an Auger cascade acts to replace a single long-range photon with several shorter-range electrons, which collectively produce large amounts of localised biological damage. An international collaboration, primarily involving scientists from Queen's University Belfast and Université Paris-Sud, has been using monochromatic synchrotron radiation to investigate the biophysical mechanisms and effects that take place in this situation.

Cancer, the second most common form of death after cardiovascular disease, is a major health concern. In 2006, within Europe alone there were 3.1 million new cases diagnosed, and it caused 1.7 million deaths¹. With the ageing population, current estimates predict that, even with no change in incidence rates, the number of cases will increase by 20% by 2020. Around 50% of patients receive radiotherapy as part of their cancer treatment². However, radiotherapy is limited by the need to minimise the dose delivered to healthy tissue in order to prevent harmful side effects. Approaches that enhance radiosensitivity within tumours relative to normal tissue, therefore,

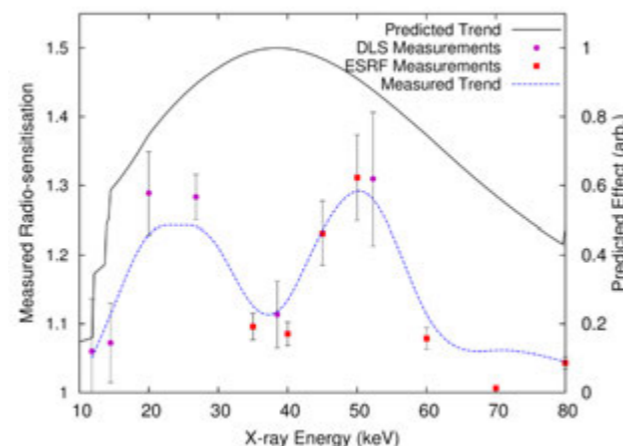


Figure 2: Measured energy dependence of the enhancement of DNA single strand break induction, compared to a model that considers the macroscopic increase in dose due to the absorption of the gold.

have the potential to have a major impact on the delivery of radiotherapy to patients.

Gold nanoparticles can be selectively delivered to tumours as a natural result of the leaky tumour vasculature. Additionally, the gold nanoparticles can have specific biological functionalising groups attached on the outside of the nanoparticles, causing them to be taken up by the cells showing the corresponding disease marker. In either case the tumour selectively takes up the gold. This leads to the interesting idea of administering the gold nanoparticles to patients prior to radiotherapy treatment to increase the effects of the radiation on the tumour whilst leaving the healthy tissue effects unchanged for a given radiation dose.

When a gold nanoparticle interacts with radiation, inner shell ionisation of one of the gold atoms can occur, leading to the creation of an inner-shell vacancy. The vacancy stabilises through a combination of radiative and Auger processes with typically several low energy electrons being emitted. If the ionisation occurs near the nanoparticle's surface then these electrons can escape to interact with the nearby biological environment as is illustrated

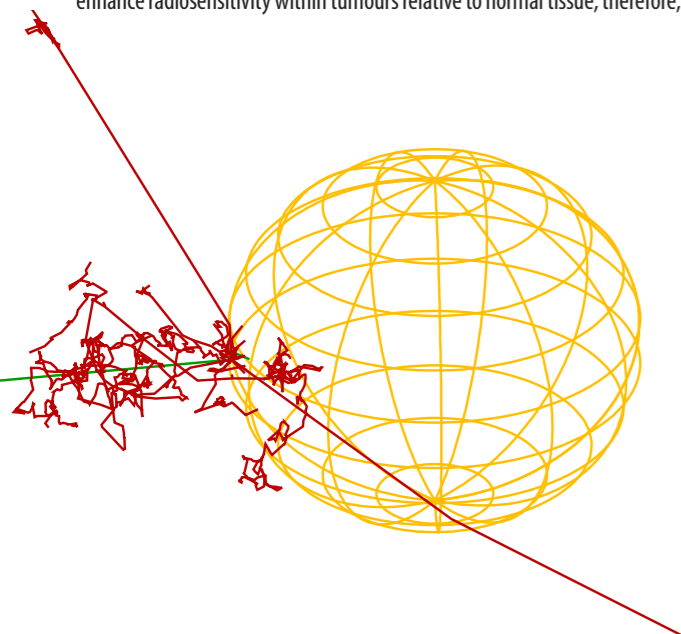


Figure 1: Results of a Monte Carlo radiation transport simulation showing L-shell ionisation by a 50 keV photon near the surface of a 20 nm diameter gold nanoparticle (represented as the wire-mesh sphere). The photon track is shown in green while the electron tracks are shown in red. The photoelectron and the first Auger electron depart with high energy and correspondingly few interactions, producing fairly straight tracks. The lower energy Auger electrons give rise to multiple interactions depositing all of their energy near the nanoparticles as is evidenced by the complex and localised track structure they produce.

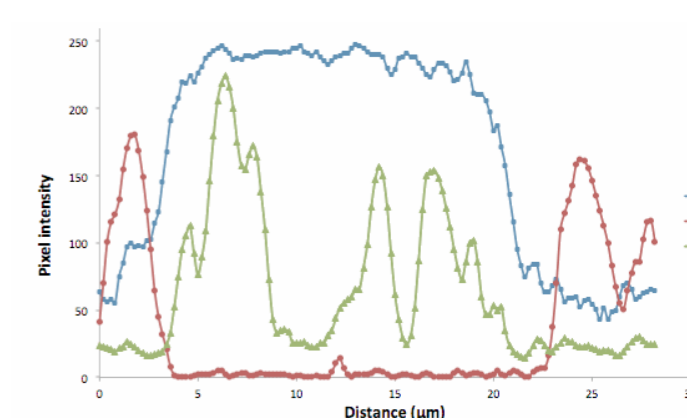
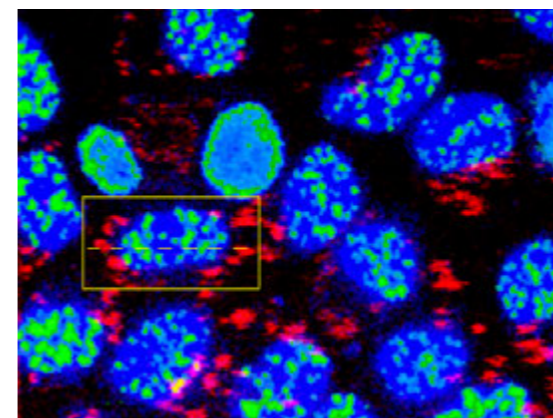


Figure 3 Left: confocal microscope image showing cell nuclei (blue), DNA damage (green) and gold nanoparticles (red) taken using the Octopus facility post irradiation at 11.8 keV using beamline B16. The dotted line through the rectangle shown on this image shows the section indicated in the right panel.

in Fig. 1. Associated with this process is a massive increase in the local dose, e.g. about 100,000 Gy in the vicinity of the nanoparticle, compared to a few Gy usually used in radiotherapy. As the response to radiation is non-linear, this local dose escalation produces a big enhancement to the cell killing for cells that have taken up nanoparticles, even though the average dose over the whole cell is hardly changed. This phenomenon has been modelled by considering the localisation of biological effects in a theoretical framework originally developed to describe biological interactions with heavy ions³, implying that gold nanoparticle dose enhancement might convey the same advantages in treating radioresistant tumours at existing therapy centres and at a fraction of the cost.

The MeV photons used in radiotherapy trigger a cascade of processes that eventually produce lower energy photons and electrons, which have a high probability of causing the inner-shell ionisation, thereby producing the large localised enhancement effects in the clinical situation⁴. Although radiotherapy uses MeV photon beams, the interaction with monoenergetic X-ray beams of lower energy is of great interest in understanding the mechanisms involved. Tuneable monoenergetic X-rays can be used to perform experiments either side of an absorption edge. Crossing from below to above an edge makes ionisation from an additional inner shell possible. Hence, by comparing the effects either side of an edge, one can probe the effects of ionisation from a specific inner shell. In between absorption edges, the Auger electron spectrum is constant to a very good approximation, while the energy of the photoelectrons changes monotonically, meaning that the energy dependence between the edges can be used to deduce the role of photoelectrons.

Nuclear DNA is considered to be the primary target for radiotherapy as it is the only molecule in the cell that acts in a serial rather than parallel fashion (i.e. there is only one DNA molecule per cell, all the others have multiple copies or they can be remade if they are destroyed). Samples of plasmid DNA were suspended in water with gold nanoparticles. These samples were irradiated at various energies and at various dose depositions with all results being compared to similarly irradiated controls that contained no nanoparticles. The results are shown in Fig. 2 along with comparison to a model considering the total dose absorbed by the sample. Not only is there clear discrepancy between the experiment and the model, it is striking that the local minimum in the measurements (about 37 keV) coincides with the maximum in the absorbed dose relative to water. This is something we are currently investigating by looking at the radiolysis products produced when water containing gold nanoparticles is irradiated.

We measured the biological radioenhancement due to doping cells with gold nanoparticles prior to irradiation and we have observed significant radioenhancements in the level of DNA damage and cell killing compared

to undoped cells. Additionally, using the Octopus facility in the Research Complex at Harwell (RCAH), we have imaged both the nanoparticles of gold taken up by the cells and the DNA damage produced after irradiation at beamline B16. An example of the images obtained is shown in Fig. 3. Since these images are collected using confocal microscopy it is possible to build up a three-dimensional representation of the cell, the DNA damage and the gold nanoparticles. Such rich data sets contain lots of information about the relationship between the gold and the DNA damage. We are currently developing data analysis tools to mine this data with a view to extracting this relationship.

References

1. Ferlay, J., Autier, P., Boniol, M., Heanue, M., Colombet, M. & Boyle, P. Estimates of the cancer incidence and mortality in Europe in 2006. *Annals Oncol.* **18**, 581-92 (2007).
2. Delaney, G., Jacob, S., Fetherstone, C. & Barton, M. The role of radiotherapy in cancer treatment. *Cancer*. **104**, 1129-1137 (2005).
3. McMahon, S.J., Hyland, W.B., Muir, M.F., Coulter, J.A., Jain, S., Butterworth, K.T., Schettino, G., Dickson, G.R., Hounsell, A.R., O'Sullivan, J.M., Prise, K.M., Hirst, D.G. & Currell, F.J. Nanodosimetric effects of gold nanoparticles in megavoltage radiation therapy. *Radiotherapy and Oncology*. **100**, 412-6 (2011).
4. McMahon, S.J., Hyland, W.B., Brun, E., Butterworth, K.T., Coulter, J.A., Douki, T., Hirst, D.G., Jain, S., Kavanagh, A.P., Mendenhall, M.H., Muir, M.F., Prise, K.P., Requardt, H., Sanche, L., Schettino, G., Currell, F.J. & Sicard-Roselli, C. Energy Dependence of Gold Nanoparticle Radiosensitization in Plasmid DNA. *J. Phys. Chem. C*. **115**, 20160–20167 (2011).

Funding Acknowledgements

This work was supported by Cancer Research UK grants (Grant C1278/A9901 and C1513/A7047), an EPSRC grant (EP/I017550) and by the Triangle de la Physique.

Research carried out at Diamond Light Source on beamline B16 and at the ESRF on beamline I17.

DOI 10.1021/jp206854s

DOI 10.1038/srep00018

High-nuclearity metal-organic nanospheres

Argent, S.P., Greenaway, A., Gimenez-Lopez, M.C., Lewis, W., Nowell, H., Khlobystov, A.N., Blake, A.J., Champness, N.R., Schröder, M. High-Nuclearity Metal-organic Nanospheres: A Cd_{66} Ball. *J. Am. Chem. Soc.* **134**, 55-58 (2012)

The synthesis of high-nuclearity transition metal co-ordination clusters has been the focus of much research over recent years due to interest in tailoring the properties of nanoscale objects. Such molecules are a target for bottom-up nanotechnology fabrication techniques and, despite many potential applications, large clusters are often most admired for their attractive architectures and topologies that are reminiscent of Platonic and Archimedean solids and even viruses.¹ We report herein the synthesis and full characterisation of a highly unusual Cd_{66} cluster, a high-nuclearity system which comprises a central inorganic Cd-oxo-hydroxy-nitrate cluster core surrounded by an organic shell of ligands. This highly unusual molecular compound has a molecular weight of about 23,800 Daltons, has an external diameter of 3.18 nm, an internal diameter of 1.22 nm, and thus, can be considered a metal-organic nanosphere.

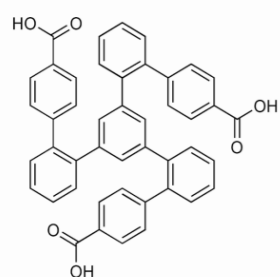


Figure 1: View of ligand H_3L .

As a development of our research into metal-organic frameworks^{2,3} we have initiated a research program to prepare high-nuclearity transition metal clusters. Our strategy employs a carboxylate-based ligand H_3L (Fig. 1) which was designed as an ambivalent non-planar building-block that can bind to metal centres via three carboxylates on the same face to stabilize high-nuclearity clusters, or via carboxylate donors that point in opposing directions to

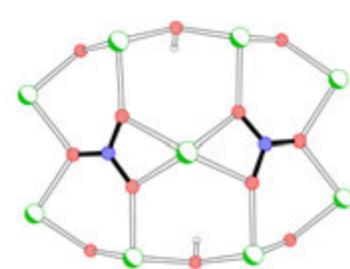


Figure 3: View of the co-ordination environment of nitrate anions in the Cd_{66} nanosphere. Atom colours: nitrogen blue; oxygen red; cadmium green.

generate co-ordination polymers.

Reaction of H_3L and $Cd(NO_3)_2 \cdot 4H_2O$ in dimethylformamide (DMF) solution affords single crystals of a compound as colourless parallelepipeds. Single crystal X-ray analysis on Diamond beamline I19 revealed the resulting compound to be a

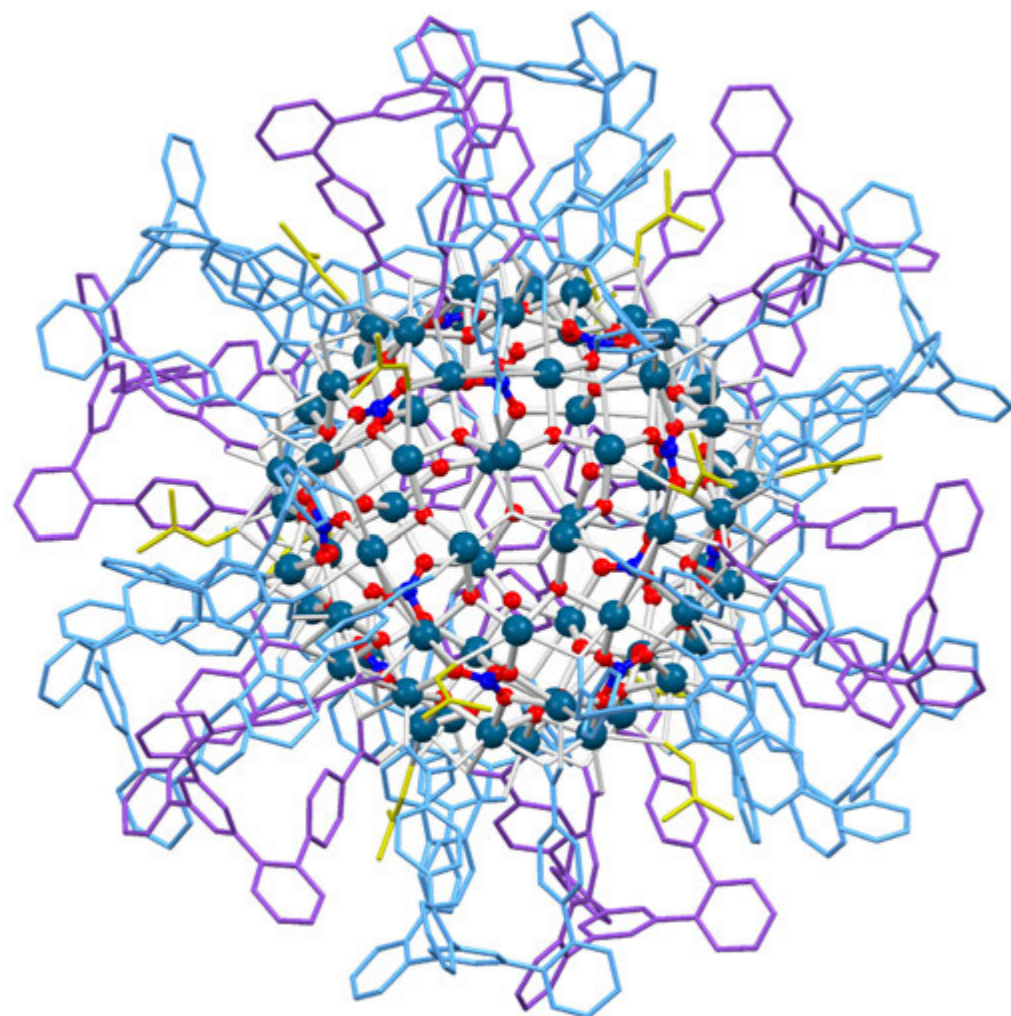


Figure 2: View of the Cd_{66} nanosphere. Atom colours: cadmium dark blue; oxygen red; ligands of different symmetry coloured light blue and purple. Ligand at front of ball removed to aid clarity.

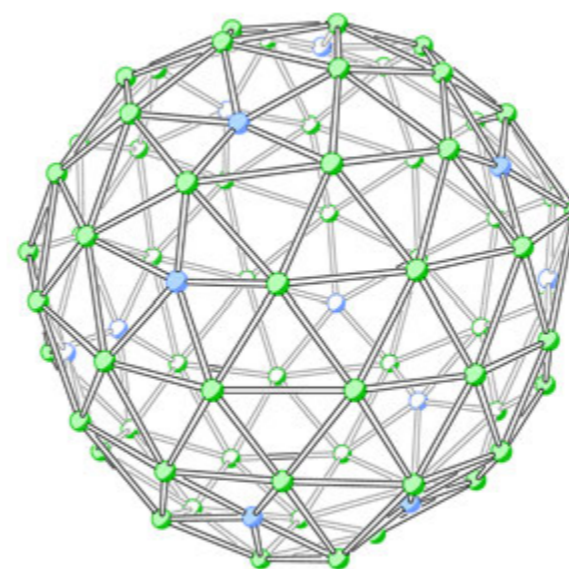


Figure 5: Bright field transmission electron micrographs of the Cd_{66} nanosphere inserted into a carbon nanotube (scale bar is 5 nm). b) Schematic representation of a).

highly complex cluster composed of a spherical shell of 66 Cd(II) cations bridged by 28 μ^3 -hydroxide, 16 μ^3 -oxo and 5 μ^5 - NO_3^- anions surrounded by a shell of 20 tripodal capping ligands (L^{3-}) and 12 DMF ligands, $[Cd_{66}(\mu^3-OH)_{28}(\mu^3-O)_{16}(\mu^5-NO_3-O,O,O';O',O')_{12}(L)_{20}(\mu^2-DMF)_{12}(DMF)_9]$ (Fig. 2). The cluster crystallises in the trigonal space group $R\bar{3}$ with the cluster having C_3 crystallographic symmetry and idealised chiral tetrahedral T symmetry. However, each crystal is a racemate with chiral molecules of both hand found in the unit cell.

A dual-shell structure for the cluster can readily be observed (Fig. 2) in which a central inorganic core is covered by an organic layer of ligands L^{3-} . The 66 Cd(II) cations can be divided into six groups of centres with the same approximate symmetry; five groups of twelve centres show a distorted octahedral co-ordination geometry, and one group of six centres have bis-capped square pyramidal geometry. The NO_3^- anions lie parallel to the surface of the spherical inorganic core with each anion bridging five Cd(II) centres (Fig. 3). Considering the idealized T symmetry of the cluster, there are two ligand environments (Fig. 2): eight ligands sit at the corners of a cubic array on positions of three-fold symmetry, bridging a triangle of three symmetry-related Cd(II) cations; twelve ligands sit along the edges of the cubic array binding to one central Cd(II) *via* their three carboxylate groups. The two types of ligand have opposing twist *i.e.* eight (three-fold symmetric) ligands have a clockwise twist, with the remaining twelve ligands having an anti-clockwise twist.

Some electron density peaks in the centre of the inorganic shell could not be modelled as discrete atomic sites, but this void of 861 \AA^3 is large enough to accommodate up to nine small solvent molecules assigned as DMF.

If the 66 Cd(II) centres and 12 NO_3^- anions are considered as vertices, a polydeltahedron can be constructed (Fig. 4). The Cd vertices are all six-connected with Cd-Cd separations ranging from 3.49 to 3.99 \AA , with the NO_3^- anions five-connected to Cd(II) centres (Cd-N separations range from 2.74 to 3.33 \AA). Importantly, the 12 NO_3^- vertices are the precise number of five-co-ordinate defects necessary to allow the 66 six-co-ordinate vertices to enclose a sphere as stated by Euler's theorem. Thus, the convex polyhedron has 78 vertices (V) [$Cd(II)$ and NO_3^-], 228 edges (E) and 152 triangular faces (F) giving it a closed shell Euler characteristic χ of 2 ($\chi = V + F - E$).

Although the Cd_{66} nanosphere is only sparingly soluble in organic solvents the compound can be characterised by NMR spectroscopy, MALDI mass spectrometry and Dynamic Light Scattering (DLS) measurements, the last indicating a species with a diameter of $2.9(\pm 1.1)$ nm, consistent with the structurally characterised molecule. Due to the large size of the nanosphere we were able to directly visualize it using high resolution transmission electron microscopy (HRTEM). HRTEM images of the nanosphere deposited into multi-walled carbon nanotubes (MWNT) reveal clusters (Fig. 5) of a size consistent with that expected from the single crystal results.

In conclusion, we have successfully demonstrated the synthesis and characterisation of a highly unusual, high-nuclearity Cd_{66} metal-organic nanosphere. Our strategy leads to the formation of a dual-shell cluster defined by an inorganic shell built from Cd(II) cations, O^{2-} , HO^- and NO_3^- anions, capped by an organic shell of tricarboxylate and DMF ligands. The cluster forms a unique polydeltahedron that encompasses a large void space over 1.2 nm in diameter. Future work seeks to develop and investigate new methodologies for the synthesis of complex high-nuclearity metal nanoclusters and aggregates.

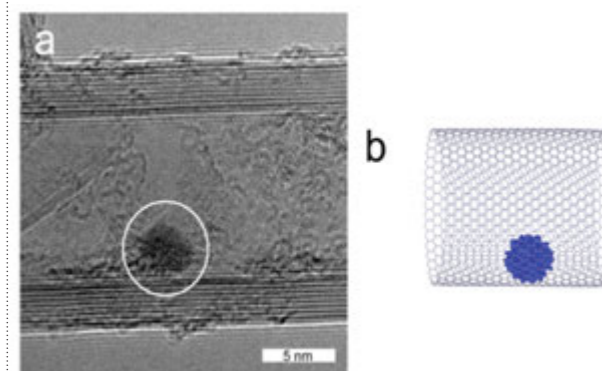


Figure 4: The polydeltahedron formed by the Cd_{66} nanosphere based on 66 Cd(II) centres (green) and 12 NO_3^- anions (blue) as vertices. The object has 78 vertices, 228 edges and 152 triangular faces.

References

1. Ward M.D. Polynuclear coordination cages. *Chem. Commun.* **30**, 4487-4499 (2009).
2. Yang, S., Lin, X., Blake, A.J., Walker, G.S., Hubberstey, P., Champness, N.R., Schröder, M. Cation-induced Kinetic Trapping and Enhanced Hydrogen Adsorption in a Modulated Anionic Metal Organic Framework. *Nature Chem.* **1**, 487-493 (2009).
3. Blake, A.J., Champness, N.R., Easun, T.L., Allan, D.R., Nowell, H., George, M.W., Jia, J., Sun, X-Z. Photoreactivity Examined Through Incorporation In Metal-Organic Frameworks. *Nature Chem.* **2**, 688 - 694 (2010).

Funding Acknowledgements

M. Schröder gratefully acknowledges receipt of an ERC Advanced Grant and EPSRC Programme Grant. N.R. Champness gratefully acknowledges receipt of a Royal Society Wolfson Merit Award.

PMID 22111987

Squeezing porous materials

Graham, A. J., Tan, J.-C., Allan, D. R. & Moggach, S. A. The effect of pressure on Cu-btc: framework compression vs. guest inclusion. *Chem. Commun.* **48**, 1535-1537 (2012)

Porous materials have been used, amongst other applications, for storing gases such as hydrogen to be used as a clean energy source, with one of the most studied materials being metal organic frameworks (MOFs). MOFs are special because we can *chemically* tune their pore size and selectivity, thereby tuning its application for specific target 'guests'. To date, chemical modification has been the primary route to changing pore size, with chemists utilising temperature as the main variable in their manufacture. In our group, we have been using extreme pressures to modify the pores of MOFs. Applying high pressures may seem impractical for pore modification; however e.g. guacamole is already manufactured at 8000 atmospheres in the food processing industry. Here, we apply pressure by loading our sample into a diamond anvil cell. We then surround the sample with a liquid (or medium) to make sure that pressure is applied evenly. In this study, applying pressure to a MOF called Cu-btc caused the medium to be squeezed into the pores. This caused Cu-btc to *expand* on initially increasing pressure. On increasing pressure further, more material was then squeezed into Cu-btc until a gating pressure of 50,000 atmospheres was reached. Above this threshold, the liquid comes out of the pores, driven by a sudden decrease and *increase* in length of the Cu-O bonds. The ability to tune pore content with pressure has numerous applications. Synchrotron radiation allows us to study this behaviour in detail, which is essential if we are to use this technology.

A large body of scientific research is directed towards the design and synthesis of an ever more varied and complex variety of porous metal-organic framework materials. MOFs have been designed for a number of different applications, including molecular sensing^{1,2}, gas separation and storage^{3,4}, drug transport and as high surface area catalysts⁵. Whatever the application, the primary factor that makes MOFs so appealing is the ability to tune their pore size and shape, and therefore selectivity. To date, there is a large body of literature where these properties have been altered via 'chemical' means, modifying the rigid organic unit, metal linker, or both. More recently, the ability to tune the pore size and shape of MOFs, including guest content, has been achieved by applying high pressures (> 10,000 atmospheres)⁶.

In this study, a high-pressure single-crystal X-ray diffraction study was performed on the porous framework Cu-btc ($[\text{Cu}_3(\text{BTC})_2(\text{H}_2\text{O})_3]_n$, BTC = benzene-1,3,5-tricarboxylate (Fig. 1). Prior to our pressure experiment, an ambient pressure and temperature X-ray data set was collected on a crystal of Cu-btc in order to provide data for comparison with the high pressure studies (which were also performed at ambient temperature). The same crystal was then loaded into a Merrill-Bassett Diamond Anvil Cell (DAC) equipped with 600 μm culets and a tungsten gasket using a 16:3:1 mixture of methanol-ethanol-water (MEW) as the hydrostatic liquid. High-pressure data were collected at in approximately 0.5 GPa steps between ambient pressure and 5.0 GPa (Table 1).

Cu-btc crystallises in the cubic space group Fm-3m ($a = 26.434$ (6) \AA ,

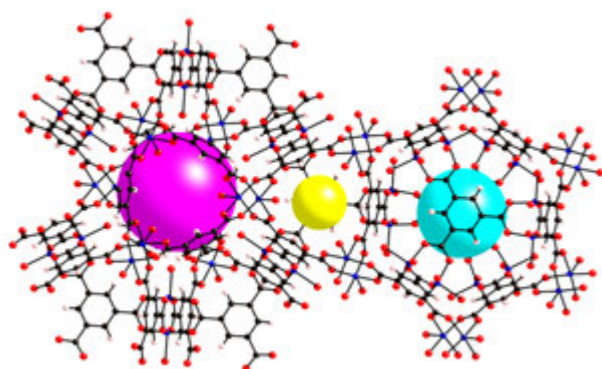


Figure 1: A representation of the three distinct but interconnected pore volumes in Cu-btc. Guest accessible cavities at (0,0,0) (pink), (1/2,1/2,1/2) (yellow) and (1/4,1/4,1/4) (blue) are shown.

Pressure (GPa)	a (\AA)	Cell Volume (\AA^3)	Total Pore Volume (\AA^3)	Electron Count
0.0	26.3015(4)	18194.6(5)	11597	1858
0.5	26.3867(12)	18371.9(14)	11741	2441
1.3	26.3368(12)	18267.9(14)	11656	2689
1.8	26.3081(12)	18208.3(14)	11586	2897
2.2	26.2896(15)	18169.9(18)	11575	3035
3.0	26.2564(15)	18101.1(18)	11519	3337
3.9	26.1823(18)	17948.3(30)	11445	3897
5.0	25.9467(17)	17468.1(20)	10996	3278

Table 1: Crystallographic and pore data for Cu-btc as a function of pressure. Pore volume and electron count are calculated per unit cell.

$\text{Vol.} = 18471(12) \text{\AA}^3$). Pairs of Cu(II) ions, bridged by four carboxylate (μ_2 -OCO) groups on discrete 1,3,5-benzenetricarboxylate (btc) ligands, form Cu(II) dimers (square planar connectivity) which are linked via the trigonal btc molecules to form an extended three-dimensional network. The Cu(II) dimers coordinate to water molecules to form a Jahn-Teller distorted axis creating a distorted octahedral environment around the Cu(II) centres (Fig. 2).

Cu-btc contains three distinct guest accessible pores which are linked together along the body diagonal of the cubic structure (Fig. 1). From our ambient pressure single crystal data, it was clear that there were some residual water molecules in the pores. On initially increasing pressure to 0.5 GPa, a sudden and marked *increase* in pore content was observed, equating to a volume *increase* on increasing pressure. Application of pressure therefore causes Cu-btc to uptake the hydrostatic media within the pores. On increasing pressure further to 3.9 GPa, a gradual and steady increase in pore content was observed, while the volume decreased continuously. The data collected shows that on initial application of pressure, the pores are filled with the MEW medium. On increasing pressure further to 5.0 GPa, a sudden and marked decrease in volume occurs. This region actually represents a pore emptying mechanism. However, although a decrease in pore content is observed on increasing pressure from 3.9 to 5.0 GPa, the pore content is not reduced substantially ($\approx 16\%$ decrease), and equates to approximately the same pore content as observed at 3.0 GPa on increasing pressure. The sudden decrease in volume can therefore not be solely due to the pores emptying above 5.0 GPa.

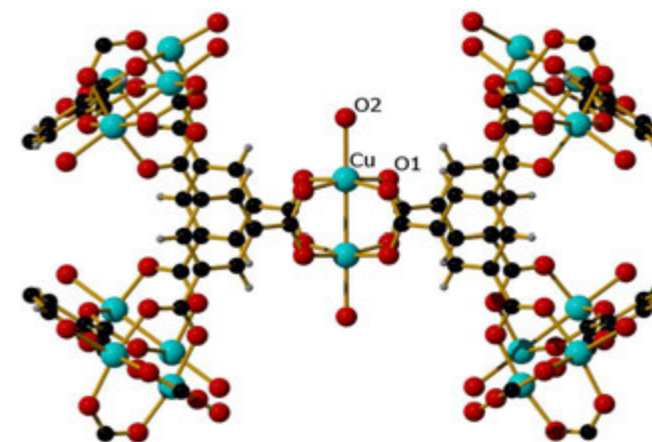


Figure 2: Representation of the Cu paddlewheel units present in Cu-btc showing the equatorial and axial Cu-O bonds, Cu-O1 and Cu-O2 respectively.

In our previous work on amino acids, compression of covalent bond lengths is not expected within this pressure regime, rather the compression of much weaker intermolecular interactions takes place.⁷ By contrast, metal-ligand bond distances are much more flexible and compliant in nature,⁸ for example, pressure induced co-ordination changes have been observed.⁹ The unit cell compression of Cu-btc is therefore likely to be mediated through the Cu-O bonding interactions within the Cu-paddlewheel. In Cu-btc, there are two symmetry independent Cu-O bonding interactions, the axial Cu-O bond (Cu-O2) which points into the pores of the guest-accessible cavities at (0,0,0) and the equatorial Cu-O bond (Cu-O1, Fig. 2). All four Cu-O1 bonds are symmetry equivalent. On initially increasing pressure to 0.5 GPa, no reduction in the equatorial Cu-O1 bonds occurs, while the axial Cu-O2 bond actually *increases* in length (Fig. 3). This coincides nicely with the increase in unit cell volume observed on increasing pressure to 0.5 GPa, which suggests that the swelling phenomena observed here is driven by the elongation of the Cu-O2 bonds. We postulate that increasing the pore content with MEW at 0.5 GPa increases H-bonding interactions with the O2 water ligand that points into the large central pore volume at (0,0,0), weakening the Cu-O2 bond causing it to increase in length. It is striking to see that, upon increasing pressure further to 3.9 GPa, the axial Cu-O2 bond continuously decreases in length, even though the pore content increases, while the equatorial Cu-O1 bonds remain unchanged (Fig. 3). It would therefore appear that after the initial swelling, the overriding drive to smaller volume on applying pressures higher than 0.5 GPa appears to override any energy penalty for compressing the axial Cu-O2 bond.

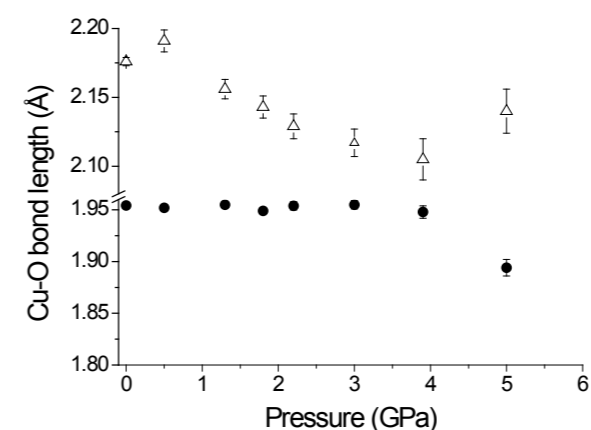


Figure 3: Equatorial Cu-O1 bonds (circles) and axial Cu-O2 bond length as a function of pressure.

On increasing pressure to 5.0 GPa and on entering the pore emptying region, the axial Cu-O2 bond actually *increases* in length again, while the volume and equatorial Cu-O1 bonds, which until now remained relatively unchanged, suddenly decrease (Fig. 3). Interestingly, our results demonstrate that the transition at higher pressure is driven not by a

decrease in pore content, but by the sudden compression of the significantly stiffer equatorial Cu-O1 bonds. We postulate that the sudden shortening of the Cu-O1 bonds causes the axial Cu-O2 bond to increase in length on undergoing the transition, and the transition here is driven by the need to minimise the volume of the system at 5.0 GPa.

In summary, we have shown that by applying pressure to Cu-btc we can force the hydrostatic medium to enter the pore, initially causing the sample to expand. On increasing pressure further to 3.9 GPa, the unit cell volume and the axial Cu-O bond contract, even though more solvent enters the pore. On increasing pressure further to 5.0 GPa, we enter a pore emptying region. The volume decreases quite dramatically here, however we discover that the transition from a pore filling to a pore emptying mechanism is in fact associated with the sudden compressibility of the stiffer equatorial Cu-O1 bonds. The Cu-O1 bonds are actually very resilient to any compression to 3.9 GPa, and only contract on increasing pressure to 5.0 GPa.

References

- Sapchenko, S. A., Samsonenko, D. G., Dybtsev, D. N., Melgunov, M. S. & Fedin, V. P. Microporous sensor: gas sorption, guest exchange and guest-dependant luminescence of metal-organic framework. *Dalton Trans.* **40**, 2196-2203 (2011).
- Lee, T., Liu, Z. X. & Lee, H. L. A Biomimetic Nose by Microcrystals and Oriented Films of Luminescent Porous Metal-Organic Frameworks. *Cryst. Growth Des.* **11**, 4146-4154 (2011).
- Huang, A., Dou, W. & Caro, J. Steam-Stable Zeolitic Imidazolate Framework ZIF-90 Membrane with Hydrogen Selectivity through Covalent Functionalization. *J. Am. Chem. Soc.* **132**, 15562-15564 (2010).
- Lu, G. & Hupp, J. T. Metal-Organic Frameworks as Sensors: A ZIF-8 Based Fabry-Perot Device as a Selective Sensor for Chemical Vapors and Gases. *J. Am. Chem. Soc.* **132**, 7832-7833 (2010).
- Lee, J. Y. *et al.* Metal-organic framework materials as catalysts. *Chem. Soc. Rev.* **38**, 1450-1459 (2009).
- Moggach, S. A., Bennett, T. D. & Cheetham, A. K. The Effect of Pressure on ZIF-8: Increasing Pore Size with Pressure and the Formation of a High-Pressure Phase at 1.47 GPa. *Angew. Chem., Int. Ed.* **48**, 7087-7089 (2009).
- Moggach, S. A., Parsons, S. & Wood, P. A. High-pressure polymorphism in amino acids. *Crystallogr. Rev.* **14**, 143-184 (2008).
- Tan, J. C. & Cheetham, A. K. Mechanical properties of hybrid inorganic-organic framework materials: establishing fundamental structure-property relationships. *Chem. Soc. Rev.* **40**, 1059-1080 (2011).
- Moggach, S. A. *et al.* Polymerization of a Cu(II) dimer into 1D chains using high pressure. *CrystEngComm.* **11**, 2601-2604 (2009).

Funding Acknowledgements

We thank the Royal Society of Edinburgh and the Scottish Government for a fellowship to Dr Stephen A. Moggach. We also thank the STFC for provision of beamtime and the EPSRC for financial support.

DOI 10.1039/C1CC16045A

A synthetic molecular pentafoil knot

Ayme, J.-F., Beves, J. E., Leigh, D. A., McBurney, R. T., Rissanen K. & Schultz, D. A synthetic molecular pentafoil knot. *Nature Chem.* **4**, 15-20 (2012)

Knots are found in DNA and proteins and even in the molecules that make up natural and man-made polymers, where they can play an important role in the substance's properties. For example, up to 85% of the elasticity of natural rubber is thought to be due to knot-like entanglements in the rubber molecules chains. However, deliberately tying molecules into knots so that these effects can be studied is extremely difficult. Up to now only the simplest types of knot, the trefoil knot with three crossing points and the topologically-trivial unknot with no (zero) crossing points, have succumbed to chemical synthesis using non-DNA building blocks. Here we describe the first small-molecule pentafoil knot, which is also known as a cinquefoil knot or a Solomon's seal knot — a knot with five crossing points that looks like a five-pointed star. The structure of the knot was determined using data collected on I19 through the Engineering and Physical Sciences Research Council (EPSRC) National Crystallography Service. Making knotted structures from simple chemical building blocks should make it easier to understand why entanglements and knots have such important effects on material properties and may also help scientists to make new materials with improved properties based on knotted molecular architectures.

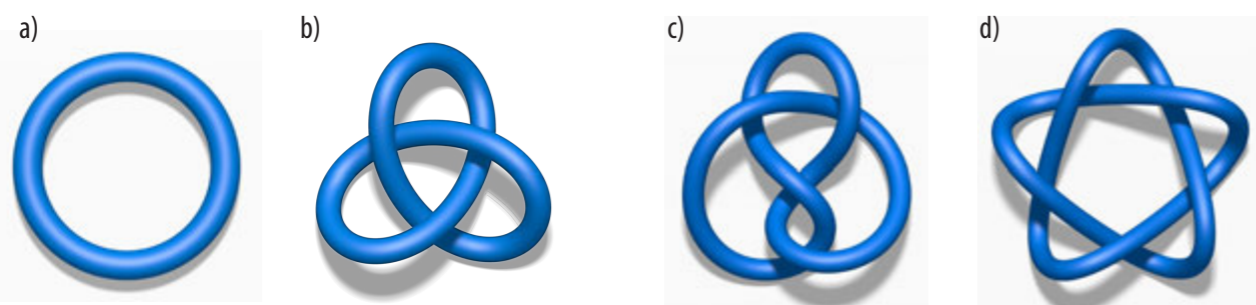


Figure 1: The topologies of the four simplest prime knots: (a) unknot (zero crossing points); (b) trefoil knot (three crossing points); (c) figure-of-eight knot (four crossing points); (d) pentafoil knot (five crossing points).

Knots are important structural features in DNA. They are found in some proteins and play a significant role in the physical properties of both natural and synthetic polymers.¹ Although billions of prime knots are known to mathematics², to date the only ones to have succumbed to chemical

synthesis using building blocks other than DNA, are the topologically-trivial unknot, i.e. a simple closed loop without any crossing points (Fig. 1a) and the next simplest knot, featuring three crossing points, the trefoil knot^{1,2} (Fig. 1b). A pentafoil knot (Fig. 1d) or cinquefoil knot (the 5_1 knot in Alexander-

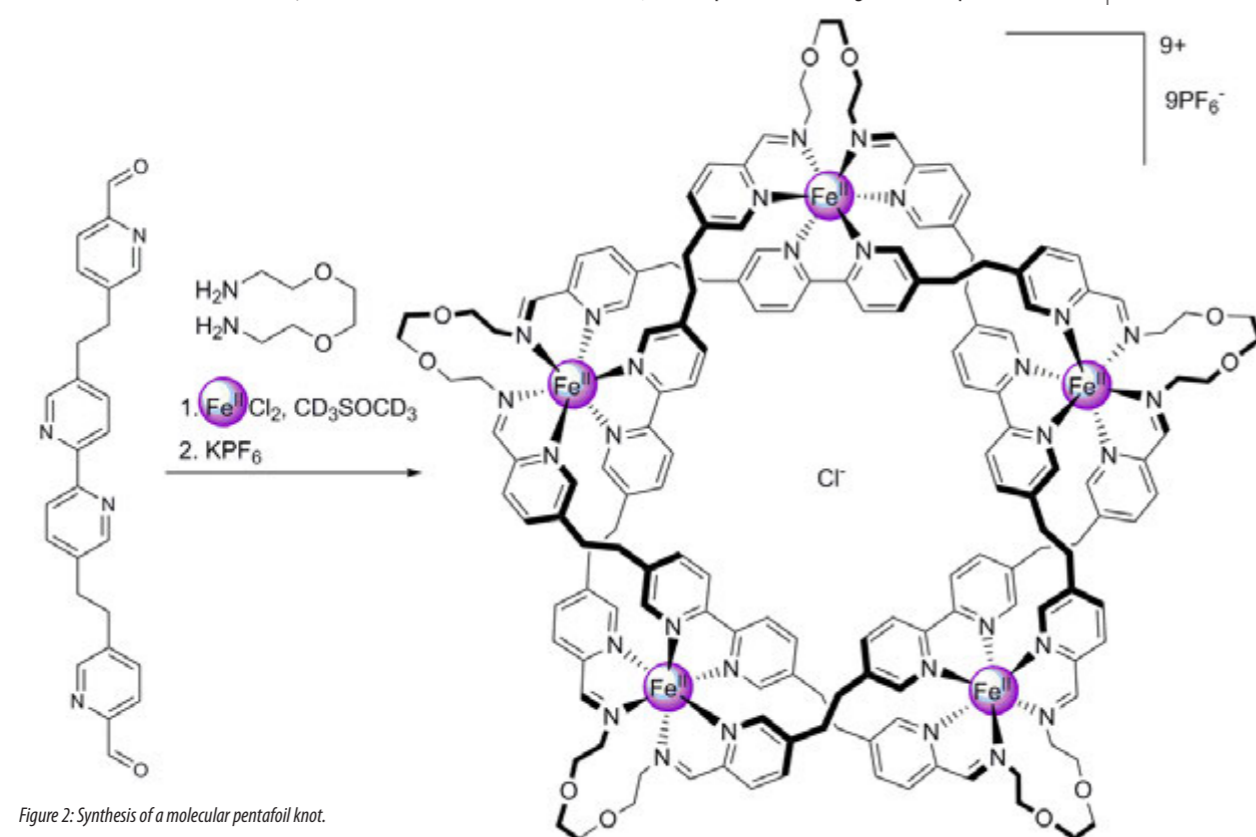


Figure 2: Synthesis of a molecular pentafoil knot.

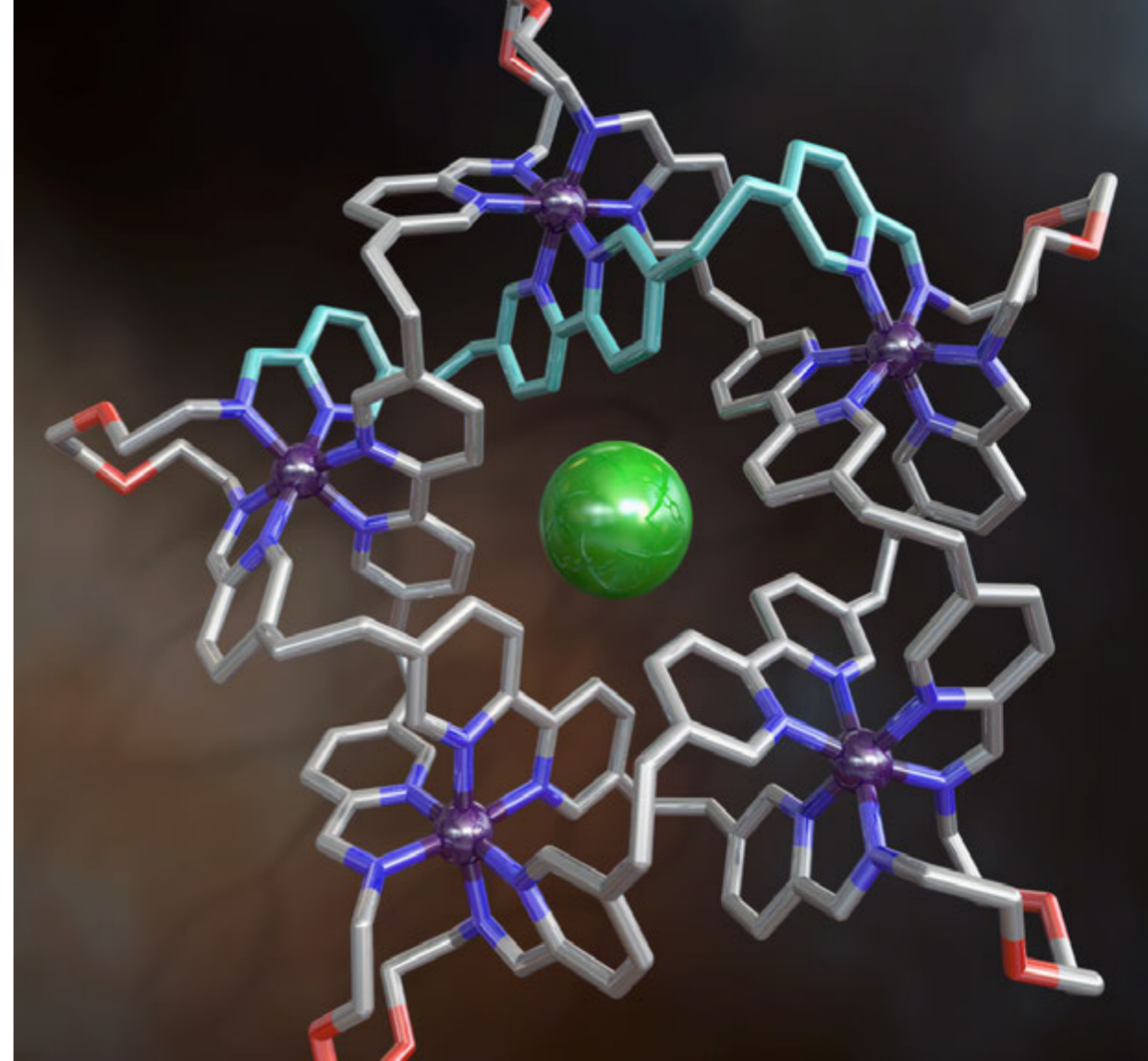


Figure 3: X-ray crystal structure of a molecular pentafoil knot. (Image credit: Robert W. McGregor, www.mcgregorfinart.com).

Briggs notation²) — is a torus knot² with five crossing points, is inherently chiral, and is the fourth prime knot (following the unknot, trefoil knot and figure-of-eight knot (Fig. 1c) in terms of number of crossing points and complexity².

The synthesis of a molecular pentafoil knot was achieved in a one-pot, 16-component self-assembly reaction by combining the use of metal helicates to create crossover points³, anion template assembly to form a cyclic array of the correct size⁴, and the joining of the metal complexes by reversible imine bond formation,⁵ aided by the *gauche* effect to make the continuous 160-atom-long covalent backbone of the molecular knot (Fig. 2).

Single crystals of the molecular pentafoil knot were obtained by slow diffusion of diethyl ether vapour into a solution of the knot in acetonitrile:toluene (3:2) and the solid-state structure determined by X-ray crystallography on station I19. The crystal structure (Fig. 3) confirmed the topology and symmetry of the molecular pentafoil knot. The single organic ligand weaves a continuous path about the five co-planar iron centres, the loop passing over and under itself each time it wraps around a metal ion. At the centre of the structure is a chloride anion, held in place by ten CH...Cl hydrogen bonds.

The pentafoil knot has symbolic significance in many ancient and modern cultures and religions (as does its two-dimensional projection, the pentagram) and features as the central emblem on the present day flags of both Morocco and Ethiopia. The practical significance of its preparation in molecular form includes the lessons learned from the multitude of different structural design features used in its assembly and the potential for the synthesis of higher order structures with precisely defined knotted

architectures that may enable the role of entanglements in molecular materials to be elucidated and exploited.

References

1. Beves, J. E., Blight, B. A., Campbell, C. J., Leigh, D. A. & McBurney, R. T. Strategies and tactics for the metal-directed synthesis of rotaxanes, knots, catenanes, and higher order links. *Angew. Chem. Int. Ed.* **50**, 9260–9327 (2011).
2. Adams, C. C. *The Knot Book* (American Mathematical Society, USA, 2004).
3. Dietrich-Buchecker, C. O. & Sauvage, J.-P. A synthetic molecular trefoil knot. *Angew. Chem., Int. Ed. Engl.* **28**, 189–192 (1989).
4. Hasenknopf, B., Lehn, J.-M., Kneisel, B. O., Baum, G. & Fenske, D. Self-assembly of a circular double helicate. *Angew. Chem. Int. Ed. Engl.* **35**, 1838–1840 (1996).
5. Leigh, D. A., Lusby, P. J., Teat, S. J., Wilson, A. J. & Wong, J. K. Y. Benzylic imine catenates: Readily accessible octahedral analogues of the Sauvage catenates. *Angew. Chem. Int. Ed.* **40**, 1538–1543 (2001).

Funding Acknowledgements

This research was funded by the EPSRC.

DOI 10.1038/nchem.1193

Development of at-wavelength metrology on B16

Hongchang Wang, Sébastien Bérubon and Kawal Sawhney

One challenge of the research with synchrotron radiation is to achieve coherence preserving and diffraction-limited hard X-ray optics. This requires development of precise, accurate and repeatable metrology. In this respect, *in-situ* at-wavelength, i.e. using X-rays, methods are considered a major pathway. Two of these methods have been established and further developed on B16, Diamond's Test beamline. One is based on a grating shearing interferometer whereas the other is based on the X-ray speckle tracking technique. Both at-wavelength metrology methods have opened up new possibilities for an optics characterization.

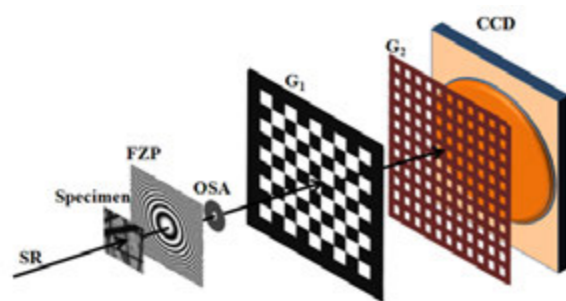


Figure 1: A schematic of the optical layout used for the sub-micron phase contrast imaging with a Fresnel Zone Plate (FZP) and a two dimensional (2D) grating interferometer (SR: synchrotron radiation light from B16 bending magnet, OSA: order sorting aperture; G1: 2D phase grating; G2: 2D absorption grating, CCD: area detector).

Grating interferometer

Grating interferometers are very attractive for performing at-wavelength metrology as they are able to measure wavefront gradients with tens of nanoradian accuracy and with a low sensitivity to mechanical vibrations. Furthermore, they have a low requirement on longitudinal and transverse coherence. The interferometer consists of a one dimensional (1D) phase grating as a beam splitter and an absorption grating as a transmission mask for the detector. The two gratings produce Moiré fringes, and the calculation of their distortion from the straight lines allows one to measure wavefront aberration of the order of the wavelength. Such an interferometer has been established on B16 that works at hard X-ray energies (8 -20 keV). Both the Moiré fringes method and the phase stepping method can be used to determine the wavefront distortions. The method has been enhanced by developing a rotating shearing interferometer technique¹, in which one of the two gratings of the shearing interferometer is rotated to derive the X-ray wavefront radius of curvature and its distortions from a single image. The method has been successfully used to derive the wavefront distortions caused by reflecting mirrors and Be compound refractive lenses.

Recently, a 2D grating interferometer has been introduced into the X-ray

regime which allows, simultaneously, the recovery of both the horizontal and vertical beam phase gradient, eliminating most of the common reconstruction artifacts usually encountered with the 1D interferometer. We have demonstrated that it is also possible to perform sub-micron phase microscopy using a Fresnel zone plate (FZP) and a 2D grating interferometer². The technique provides the spatial resolution of absorption-contrast microscopy, and also provides the wavefront gradient profile of the specimen with a high sensitivity, independent of the orientation of the sample features.

A sketch and a photo of the experiment setup are shown in Fig. 1 and Fig. 2 respectively. A bunch of carbon fibres has been used as a representative specimen. The two reconstructed orthogonal wavefront gradient maps are shown in Fig. 3. It can be seen that the vertical features in the horizontal wavefront gradient map have very low visibility, and vice versa: this demonstrates the advantage of the 2D grating interferometer over the more traditionally used 1D interferometer. When working using a 1D grating interferometer, the gradient map is lost in one direction because of the insensitivity of the device to objects oriented parallel to the lines of the grating. This problem can be solved by using simultaneously the vertical and horizontal gradients, the final reconstructed wavefront is shown in Fig. 4. For comparison, absorption and dark field images are also shown. The sensitivity of our FZP-2D grating microscope is <100 nrad, and this high and quantitative sensitivity thus makes it a promising candidate for sub-micron analysis of complex samples made of light materials and different feature orientations.

X-ray Speckle Tracking Technique

Sébastien Bérubon, who is a joint PhD student of the ESRF and of the Diamond Light Source, has developed a new method to analyse quantitatively the wavefront of a partially coherent X-ray beam using two-dimensional speckle patterns³. The X-ray speckle tracking (XST) technique is based on the use of 2D speckle patterns combined with digital image

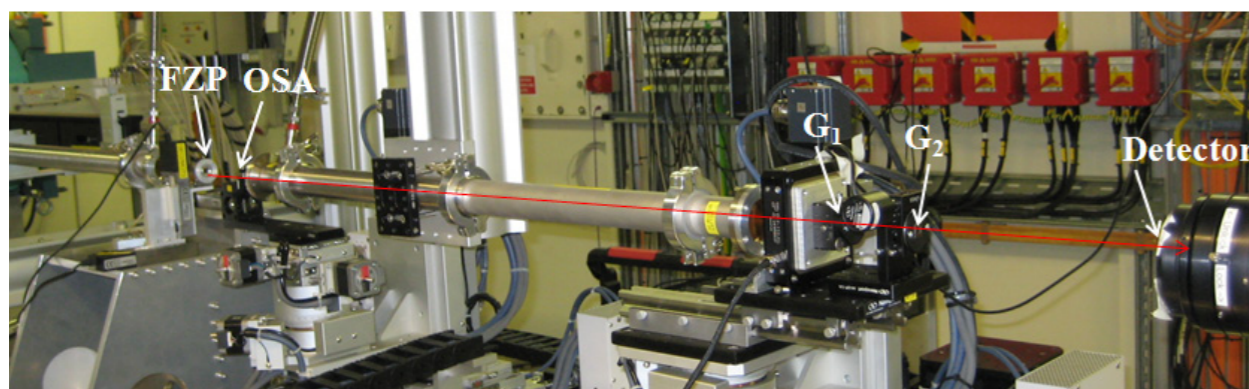


Figure 2: Experiment setup on B16 for the sub-micron phase contrast imaging with a Fresnel Zone Plate and a two dimensional grating interferometer.

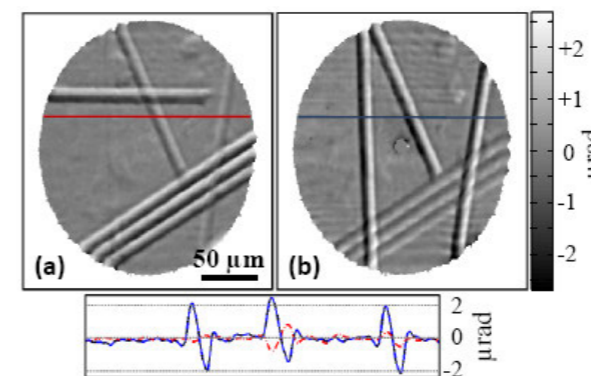


Figure 3: Calculated deflection angle in μrad (a) vertical gradient, (b) horizontal gradient. The lower image shows a horizontal line profile through the two images, which clearly shows that the gradient map is lost in one direction because of the insensitivity of the device to objects oriented parallel to the lines of the grating.

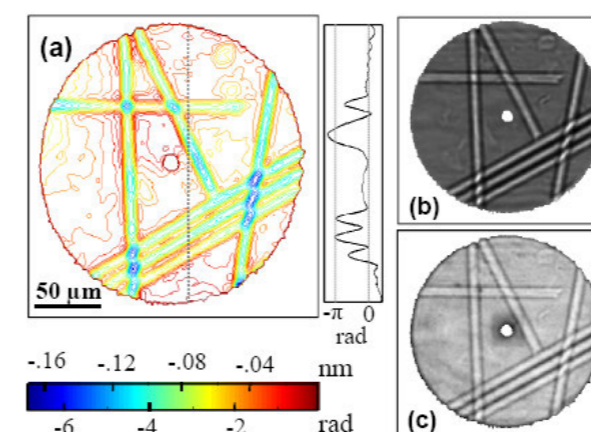


Figure 4: (a) Wavefront reconstruction from the two directional gradient and (bottom) the corresponding wavefront phase shift. The line-profile shown on the right corresponds to a section of the image at the dashed line location, (b) Absorption image, and (c) Darkfield image.

correlation algorithms, and offers a pixel size resolution, providing a 2D wavefront gradient. This technique has a low sensitivity to mechanical vibrations and the requirements on transverse and longitudinal coherence are also low.

The setup is quite simple, requiring only the random phase object and a 2D detector to resolve the high-spatial frequency features contained in the object. A solid membrane, easy to align and with low sensitivity to vibrations, produces a random intensity speckle pattern that is static. The simplicity of the setup of the XST technique also avoids any tedious calibrations. By recording this random pattern two times in planes located at two different distances from the membrane (Fig. 5) or in the same plane at two different time intervals, the ray paths or their evolution can be tracked using a digital image correlations algorithm capable of sub-pixel accuracy.

The XST method can be understood as a high spatial frequency intensity modulation of the wavefront using motionless speckle to trace the geometrical path of the light passing through each pixel of the detector. To demonstrate the application of the XST technique, a 2D parabolic, rotationally symmetric compound refractive lens (CRL) has been characterised. The reconstructed wavefront influence function of the CRL is shown in Fig. 6. The corresponding aberrations of the lens can then be retrieved from the wavefront profile, which are otherwise difficult to measure.

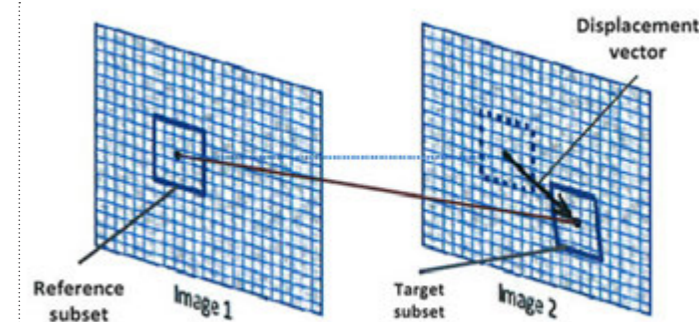


Figure 5: Digital image correlation principle in the X-ray speckle tracking technique. The position of a speckle subset of a few pixels is tracked from one image to the next using a cross correlation criterion.

Summary and Outlook

The grating interferometer and the X-ray speckle tracking technique have both been established and commissioned on B16, and user-friendly software has been developed on the IDL platform for complete data analysis. Both techniques are compact, robust and have low requirements on longitudinal and transverse coherence. The representative examples given above show that sub-microradian accuracy in determining the wavefront gradient is achieved. These at-wavelength metrology methods will enable determination of the wavefront distortions caused by the various beamline components like mirrors, monochromators, Be windows, refractive lenses, Fresnel Zone Plate, KB mirrors etc.

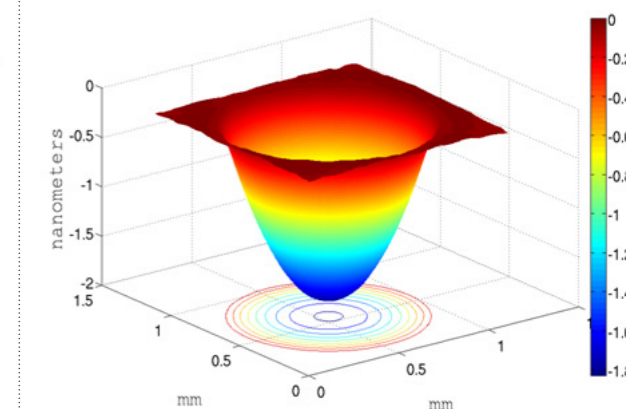
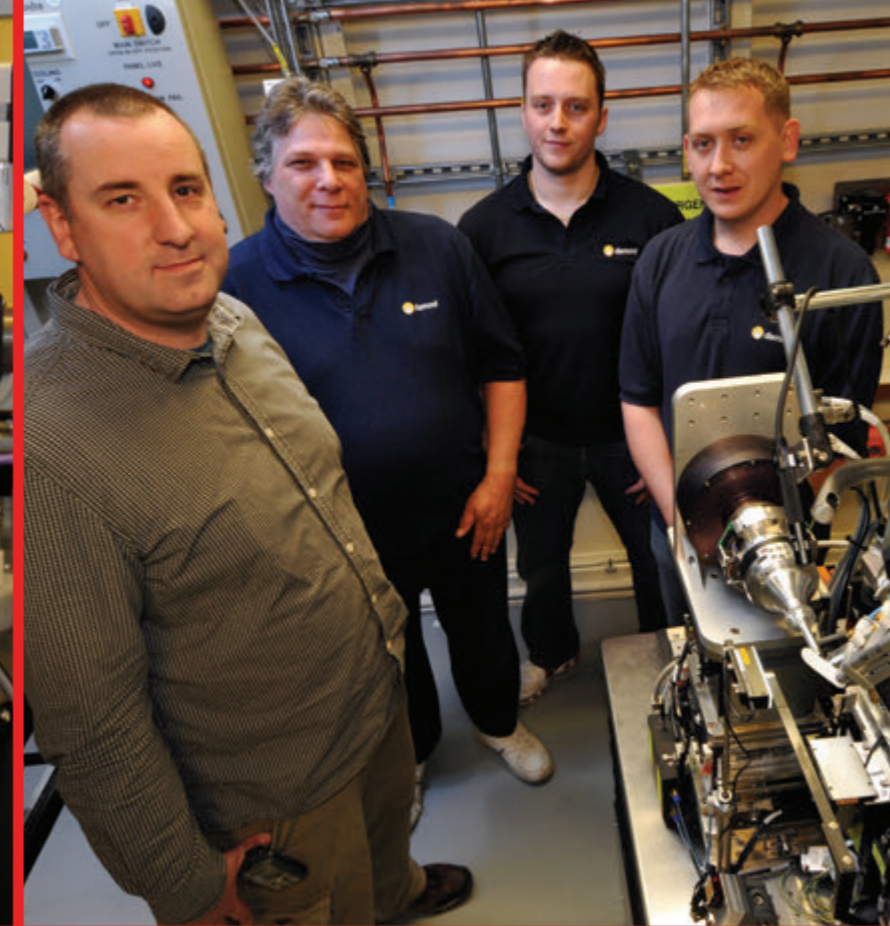
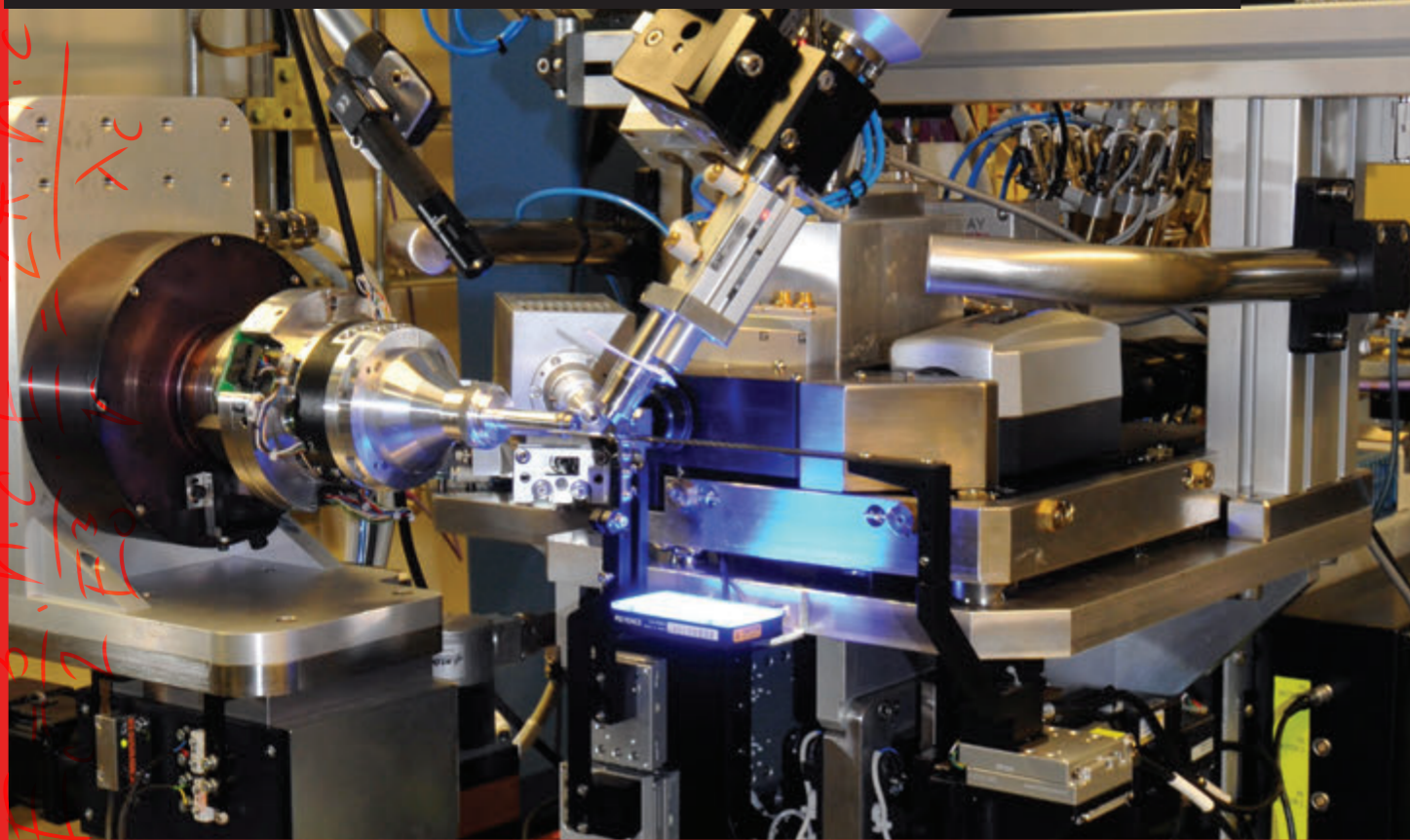


Figure 6: The reconstructed wavefront from a parabolic compound refractive lens using the X-ray speckle tracking technique on B16.

References

1. Wang, H., Sawhney, K., Bérubon, S., Ziegler, E., Rutishauser, S. and David, C. X-ray wavefront characterization using a rotating shearing interferometer technique. *Optics Express*. **19**, 16550 (2011).
2. Bérubon, S., Wang, H., Pape, I., Sawhney, K., Rutishauser, S. and David, C. X-ray sub-micron phase contrast imaging with a Fresnel Zone Plate and a two dimensional grating interferometer. *Optics Letters* **37** (10), (2012).
3. Bérubon, S., Ziegler, E., Cerbino, R. and Peverini, L. Two-dimensional X-ray beam phase sensing, *Phys. Rev. Lett.* **108**, 158102 (2012).



Macromolecular Crystallography Village

Gwynndaf Evans, Village Coordinator

2011 has been a year of intense development in the MX Village, in particular it has seen the completion of a two year project to design, manufacture and install new end-stations for three beamlines; the beginning of an upgrade program of mirror motor systems and the mirrors themselves for beamlines I02, I03 and I04; the upgrade of motion stages in I24's microfocusing mirror assembly; and the completion of an upgrade to I04-1 and I24's sample changer. These developments have been keenly balanced against minimising downtime and allowing the high impact science detailed below to be delivered by our user community. Since the last report at least another 300 structures have been added to the Protein Data Bank.

Looking to the future it is a pleasure to report that the final beamline to be approved for construction in Diamond's Phase III program is the versatile microfocus and *in situ* beamline proposal (VMX) that was submitted on the behalf of the MX community by Dave Brown et al. The VMX beamline will consist of a submicron tuneable end-station and a dedicated *in situ* data collection end-station. The beamline and its two end-stations will bring the final count of MX Village end-stations to seven by 2017 and enable a broad range of unique capabilities while maintaining its core ability of satisfying the UK user demand for high quality and high throughput structure solution.

In September 2011 the Village hosted the 2nd MX user workshop at the Diamond Synchrotron Users meeting. The workshop had about 50 attendees and comprised sessions on 'Spectroscopy', 'Crystal dehydration and room temperature data collection', 'Using microbeams' and 'Getting the most out of your beamtime'. Each session saw one staff and two user presentations where experiences of using beamlines and equipment effectively for science were shared.

New end-stations for I02, I03 and I04

In the past year a team of Diamond beamline scientists, engineers and technicians led by Dave Hall (pictured) has been delivering new end-stations to beamlines I02, I03 and I04. The new end-stations incorporate the best of the previous sample environments whilst providing a versatile chassis for adding new features which have been in parallel development within the

MX Village. Several novel features are already available to users, including microfocus beams (on I04), minibeam apertures, improved sample viewing and positioning, easy switching between cryogenic to room temperature or humidity controlled environments and *in situ* data collection. Current developments that will be rolled out for routine use in 2012 include the integration of microspectrophotometry, mini-kappa geometry and further improvements to microfocus capabilities and variable beam sizes. This platform is now the bedrock on which the MX team at Diamond can develop and deliver new functionality to our users. The new end-stations are now in routine use on beamlines I02, I03 and I04 and are supporting the user programme with aplomb.

Mirror polishing to achieve improved beam quality and beam size versatility on I02 and I03

A programme of work to refurbish the horizontally and vertically focusing bimorph mirrors on I02, I03 and I04 has been running and towards the end of 2011 the repolished mirrors were reinstalled on I02 and I03. Beam sizes at the sample down to $17 \mu\text{m}$ (v) \times $70 \mu\text{m}$ (h) are now routinely delivered with fluxes in excess of 1.2×10^{12} ph/s. The high quality of the polish is illustrated in Figure 1 and this results in the ability to defocus the beam away from the sample plane thereby increasing the vertical beam size up to $80 \mu\text{m}$ while preserving the near-perfect Gaussian profile of the beam. This ability to vary the beam size while preserving its quality is vitally important to users for optimising signal to noise in their diffraction data and will be

the subject of ongoing collaboration with the Optics Group at Diamond throughout 2012. The final set of mirrors for I04 are now being repolished and will be reinstalled later in 2012 making the three Phase I MX beamlines an immensely competitive set of instruments. The important capability of flexible beam size has been a key factor in the success of I24 to date and has also been recently introduced to I04-1 through the use of defining apertures ranging in size from $10 - 70 \mu\text{m}$.

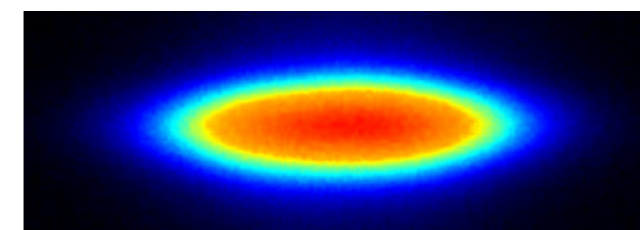
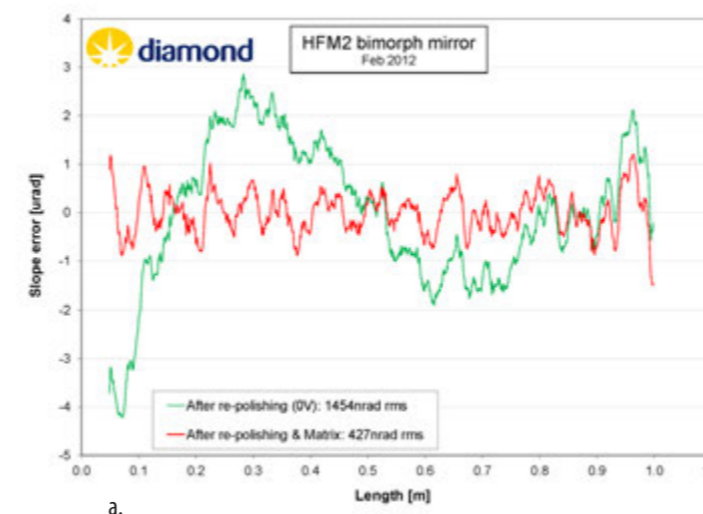


Figure 1. (a) After formal acceptance testing of the mirrors, the Diamond-NOM was used in the Metrology lab to find the optimal voltages to be applied to the piezos to correct the optical polishing errors and achieve the best beamline performance. (b) False coloured image of a 90 by 20 micrometer beam captured at the sample position.

Microfocusing on I04 using CRLs (Compound Refractive Lenses)

Since July 2011 I04 has been delivering beam focused using compound refractive lenses rather than the more conventional mirror set-up. The mirror systems are currently undergoing repolishing to provide improved beam profile and flux and are expected to return later in 2012. By using a carefully selected CRL setup I04 has continued to operate a highly successful user programme in the absence of mirrors and has been able to deliver beams down to $2 \mu\text{m}$ (v) \times $8 \mu\text{m}$ (h) in size at two specific energies. Intuitive beamline software has enabled users to select which beam size they would like to use and have the beamline set itself up accordingly. The use of CRLs in combination with focusing mirrors is currently under investigation on I02 and I03 with a view to delivering a highly versatile focusing arrangement on I02, I03 and I04 towards the end of 2012.

Faster sample changers for I04-1 and I24

The end-effectors for the CATS sample changer systems on I04-1 and I24 were upgraded during 2011 and now deliver exchange times of 45 seconds for the users. This upgrade follows a similar upgrade to the ACTOR sample changers on I02, I03 and I04 from the previous year and now ensures that all beamlines can operate robustly to the highest levels of throughput. On average the combination of fast exchange sample changers and high frame rate Pilatus 6M and 2M detectors can double the data throughput of users.

I23 team begins assembly of beamline components

The lead hutches of the long-wavelength MX beamline I23 started to appear in the experimental hall during summer 2011, with the cabins following before the end of the year. In parallel, all contracts for the major beamline components were signed, with the semi-cylindrical Pilatus 12M being the most outstanding one. Design of the I23 in-vacuum end station will have priority in the coming months, while the components for the optics hutch will be assembled and installed to receive first light in autumn 2012. So far all milestones have been met and the beamline is on track for first users in autumn 2013.

How DNA is kinked by ruthenium complexes and by dehydration

Hall, J.P., O'Sullivan, K., Naseer, A., Smith, J.A., Kelly, J.M., and Cardin, C.J. Structure determination of an intercalating ruthenium complex which kinks DNA by semiintercalation of a tetraazaphenanthrene ligand. *Proc. Natl. Acad. Sci. USA*. **108**, 17610-17614 (2011)

Ruthenium is a rare element, a heavier analogue of iron, and a key sensitiser in some solar energy conversion systems. This rarity may prove to be a handicap in that application, but is less so in the more value-added applications of DNA sensing and photodynamic therapy. Both applications make use of the valuable photochemistry and synthetic versatility of ruthenium complexes, which, unlike iron, keep their enantiomeric purity in solution. Although ruthenium polypyridyl complexes have been known to bind to DNA since the 1980s, most famously giving the so-called 'light switch' effect (fluorescence on binding), there has been no crystallographic evidence for any of the suggested binding models¹. Recently we were successful in obtaining crystals of two ruthenium complexes, one of which is photooxidising, bound to several DNA decamer sequences. Unexpectedly, the structures show intercalation by one ligand of the complex into one DNA duplex, though shallowly enough to permit a second ligand to kink a second duplex, a mode of binding known as semiintercalation. The net result is that two duplexes are noncovalently crosslinked. In a second structure, we see three binding modes, the new one being a classical symmetrical perpendicular intercalation from the minor groove. All three modes of binding appear to be DNA sequence-specific, and involve the recognition of a specific basepair step. The kinking of DNA² by small molecules turns out to be a rather unusual phenomenon, though well known in the area of transcriptional regulation by regulator proteins. By controlling crystal humidity at room temperature, we have shown the reversible dehydration of this crystal, which is accompanied by further kinking of the DNA.

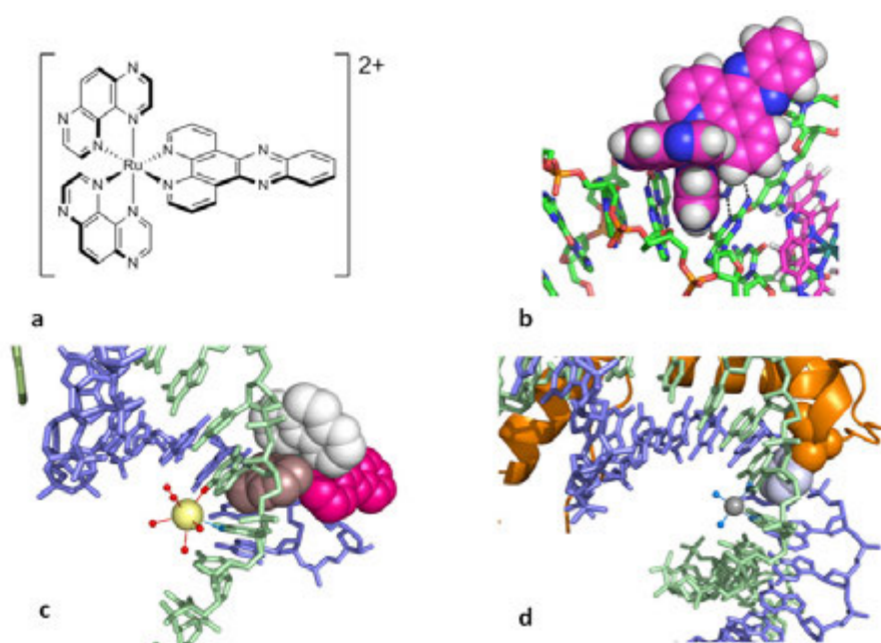


Figure 1: Kinking of DNA duplexes: a) The photooxidising 'light-switch' ruthenium complex Λ -[Ru(tetraazaphenanthrene)₂(dipyridophenazine)]²⁺; b) One of the tetraazaphenanthrene (TAP) ligands semiintercalated at the GG step of the d(TCGGCGCCGA)₂ duplex; c) the same structure, in a different orientation and with the two TAP ligands distinguished by colour, with the dipyridophenazine (dppz) ligand in pink, also showing (yellow sphere) the coordinated and hydrated barium ion important in obtaining crystals; d) the overall similarity to the [Pt(NH₃)₂]²⁺ covalent complexing of platinum at a GG step, which facilitates the binding of an HMG protein (pdb :1CKT).

Despite the enormous amount of work on DNA and its binding by small molecules, there are comparatively few atomic resolution structure determinations showing distinct binding modes. 'Classical' intercalation is well documented, for example by daunomycin, which intercalates from the minor groove. Such structures have illuminated the field of anticancer drug design for many years. The binding of the platinum anticancer drugs to DNA, when such a complex was eventually crystallised, showed covalent linkage between platinum and two adjacent guanine residues in the major groove, resulting in a 50° kinking of the duplex at that site, constricting the major groove and expanding the minor groove. Subsequent studies showed that the therapeutic effect of platinum arose from its effect on proteins which could then bind in the expanded minor groove. Such an arrangement is strongly reminiscent of the effect of the planar aromatic ligands of ruthenium polypyridyl complexes on DNA, first demonstrated by our recent key paper. In both cases, the kinking is seen specifically at a GG step in a duplex (Fig. 1).

Although what we thought we were looking for was a definitive characterisation of the intercalation mode of these complexes (major vs minor groove, parallel vs perpendicular vs some other orientation), this very rare characterisation of semiintercalation may yet turn out to be the key finding.³ Our work suggests that there may be therapeutic applications, which, as with platinum, could be connected to a facilitation of, or blocking of, a transcriptional regulator. Unlike platinum, some of these complexes are readily visualised in cells, thanks to the 'light switch' property of the complex fluorescing when intercalated between DNA basepairs, and several groups are working to locate the binding in the cell nucleus.

Kinking of DNA and intercalation into DNA can be distinguished in solution⁴, e.g. by hydrodynamic methods which detect overall changes in shape, but our work is the first to establish both binding modes unambiguously, and to the same ruthenium complex (Fig. 2). The flipped-out adenine at the end of the chain means that the intercalation is not

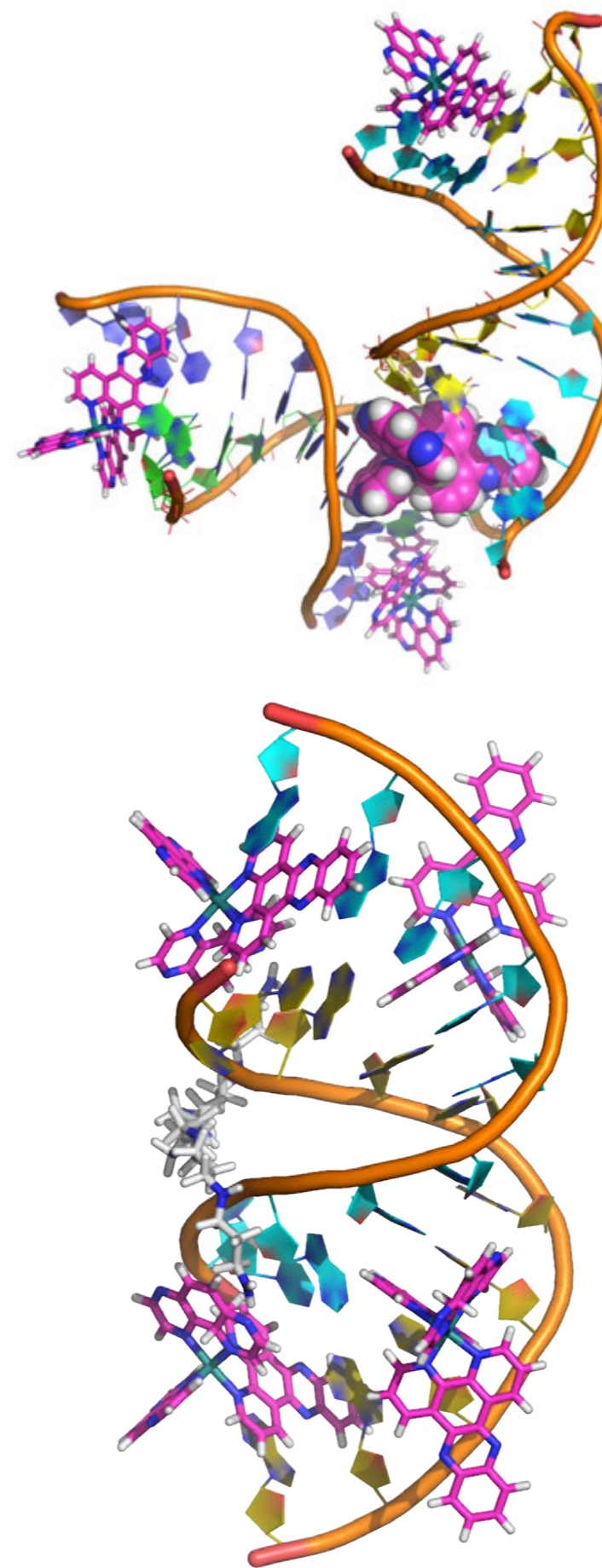


Figure 2: The linking of two duplexes of the DNA decamer d(TCGGCGCCGA)₂ by a single ruthenium complex. Some of the semiintercalated ruthenium complexes are omitted for clarity, compare Fig. 3. The complex is the lambda enantiomer of [Ru(TAP)₂dppz]²⁺. All the DNA strands and all the ruthenium complexes are actually symmetry equivalents of each other. Note that the intercalation of the dppz cannot really be described as classical, due to the adenine flipping, which gives a reverse Watson-Crick basepair at the end.

'classical', because it is a symmetry-related adenine which stacks onto the dipyridophenazine (dppz) chromophore.

This work has opened many scientific doors. The photoactivation of some of the complexes is a property we are still exploring, and is very relevant to questions of DNA damage mechanisms, and possible applications in photodynamic therapy. Analysis of the sequence-specificity of the binding, and the extension to other compounds, will clearly occupy us for some time to come. We have already shown that classical intercalation can indeed be seen, by making small changes to the decamer sequence. More unexpectedly, the crystal in Fig. 2 can be reversibly dehydrated at room temperature, using Diamond Light Source's own controlled humidity device⁵, giving a second crystal form. In this second form, the reversible movement of water in and out of the solvent channel in the crystal means that we can observe an increased bending of the DNA towards the major groove, in the form of an additional 53° kink. Remarkably, the adenine flipping at the end of the duplex is also reversible, so that in the dehydrated form the intercalated dppz chromophore is tightly sandwiched between two purine bases from the same DNA strand, rather than between two symmetry related strands, as shown in Fig. 3.

This result is a tribute to the power of stacking interactions, and to the stabilising and stiffening effect of the ruthenium complex on our famously flexible friend, the DNA duplex.

References

- McKinley, A.W., Lincoln, P. & Tuite, E.M., Environmental effects on the photophysics of transition metal complexes with dipyrido[2,3-a:3',2'-c]phenazine (dppz) and related ligands. *Coord. Chem. Revs.* **255**, 2676-2692 (2011).
- Crick, F.H.C. and Klug, A. Kinky Helix. *Nature*. **255**, 530-533 (1975).
- Turro, C. To intercalate or semiintercalate or both? *Proc. Natl. Acad. Sci. USA*. **108**, 17573-17574, (2011).
- Lincoln, P. and Norden, B. DNA binding geometries of ruthenium(II) complexes with 1,10-phenanthroline and 2,2'-bipyridine ligands studied with linear dichroism spectroscopy. *J Phys Chem B*. **102**, 9583-9594 (1998).
- Sanchez-Weatherby, J. *et al.* Improving diffraction by humidity control: a novel device compatible with X-ray beamlines. *Acta Crystallogr D Biol Crystallogr*. **65**, 1237-46 (2009).

Funding Acknowledgements

James Hall is supported by a Studentship from Diamond Light Source. The collaboration with Professor John Kelly in Trinity College, Dublin was possible thanks to a Royal Society/Royal Irish Academy International Joint project grant.

DOI 10.1073/pnas.1108685108

Figure 3: A single duplex of the dehydrated form of the complex shown in Fig. 2, obtained by reversible controlled dehydration to 79% humidity using the Diamond controlled humidity device. Both the intercalated and semiintercalated ruthenium cations are shown. The duplex is kinked by 53° at the central step. A spermine molecule (white sticks) can be seen in the compressed major groove (left of figure) which is not visible in the form shown in Fig. 2, even at 1.1 Å resolution, as it must be disordered in the solvent space. More than 100 water molecules per duplex can be located, even in this dehydrated form at room temperature, not shown for clarity.

Mechanisms of up-regulating a tumourigenic lipid kinase

Hon, W.-C., Berndt, A. & Williams, R. L. Regulation of lipid binding underlies the activation mechanism of class IA PI3-kinases. *Oncogene*, (online 28 November 2011) in press

The phosphoinositide 3-kinases (PI3Ks) are a family of lipid kinases, which can be found in animals. These enzymes have a key role in various cell functions. They transduce growth factor signalling by phosphorylating the lipid substrate phosphatidylinositol 4,5-bisphosphate (PtdIns(4,5)P₂) to produce PtdIns(3,4,5)P₃ on the plasma membrane. The produced lipids act as docking sites and activation platforms for cytosolic signalling molecules, such as PDK1 and AKT/PKB, which orchestrate downstream signalling cascades promoting cell growth and proliferation. Cellular levels of PtdIns(3,4,5)P₃ are tightly controlled. Up-regulation of this pathway commonly occurs in human cancers. Uniquely, among variants of class I PI3K catalytic subunits, p110 α is frequently mutated in human tumours. Activating cancer-linked mutations have also been found in p85 α , a variant of the regulatory subunits which complex with p110, suppressing its basal activity through inter-molecular inhibitory contacts. These cancer-linked mutations are diverse in chemical nature and structural context. Most studies focus on two hotspot mutations - E545K and H1047R, which recently have been shown to confer different biological outcomes. Our functional studies reveal that membrane binding underlies the activation mechanism for both wild-type (WT) and a representative set of oncogenic mutant complexes of p110 α /p85 α . The maximal activities of these mutants do not correlate with their frequency of occurrence, but do depend on activation by receptor tyrosine kinase (RTK) phosphopeptides. Our crystal structure of WT p110 α /p85 α co-crystallised with the ATP-competitive inhibitor PIK-108 represents an alternative view of an activated form of p110 α /p85 α . We observe a serendipitous, second inhibitor binding site that could pose a potential for development of novel inhibitors for p110 α .

The kinase domain of p110 adopts a protein kinase fold. Its so-called 'activation loop' does not play a phosphorylation-dependent regulatory role, but instead is highly basic and binds the lipid substrate headgroup. Full-length p110 forms a high-affinity heterodimer with p85, principally via interactions with the p85 inter-SH2 (iSH2) domain. For p110 α , the p85 N-terminal SH2 (nSH2) domain plays a dominant regulatory role, forming an inhibitory contact with the helical and the C2 domains of p110 α ^{1,2}. Binding of an RTK phosphopeptide bearing a pYXXM motif to nSH2 competes with this contact, resulting in elevated lipid kinase activity. This auto-inhibitory contact can also be disrupted by the hotspot E545K cancer mutation in the helical domain². Some other p110 α and p85 α cancer-linked mutations, both frequent and rare, map to the intermolecular contact sites¹. Relieving p85 inhibition appears to be one mechanism of activation. However, there are others not in this category. Some confer positive charges to the enzyme, such as the p110 α C420R (in C2 domain) and H1047R (in kinase domain). These have been suggested to enhance membrane binding, presumably due to increased electrostatic interactions with lipid headgroups. However, this conjecture leaves other activating mutations unexplained, such as M1043I and H1047L.

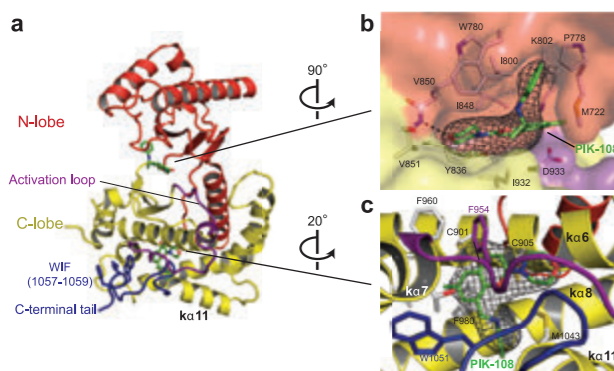


Figure 1: Structure of the kinase domain in WT p110 α /p85 α -iSH2 complexed with the inhibitor PIK-108. (a) A global view highlighting the activation loop, the C-terminal tail and the WIF motif. (b,c) PIK-108 in the ATP-binding pocket (b), and in a novel site in the kinase C-lobe (c). The σ_v -weighted $F_v - F_c$ electron density maps are contoured at 3.5 σ . The WIF motif and the PIK-108 interacting residues (≤ 3.8 Å inter-atomic distances) are shown as stick models.

We co-crystallised WT p110 α with a p85 α -nSH2 fragment and the inhibitor PIK-108. The structure was determined to 3.5 Å resolution, and was phased by molecular replacement using the model of an apo form of WT p110 α /p85 α -iSH2 complex³. Electron density for p85 α nSH2 is missing, the high salt concentration in the crystallisation cocktail could have competed off nSH2 binding to p110 α . Our structure therefore represents an alternative view of activated p110 α /p85 α . PIK-108 is a p110 β /p110 δ -selective, ATP-competitive inhibitor. A broad panel of p110-selective inhibitors, including ones more selective for p110 α , were screened for crystallisation. PIK-108 co-crystals diffracted the best, while most other compounds did not yield any crystal even in similar crystal growth conditions. There is clear density for the propeller-shaped compound in the kinase domain ATP-binding pocket (Fig. 1a, b). Towards the late stage of refinement, complete density for an unexpected, second PIK-108 became apparent (Fig. 1a, c). It snuggles in a hydrophobic pocket in the kinase C-lobe, surrounded by lipid-binding elements including the activation loop and the C-terminal tail (Fig. 1c). All current PI3K-selective inhibitors are ATP-competitive and many of these are in clinical trials for treatment of cancers or inflammation. This activation-loop pocket for PIK-108 poses the possibility of developing inhibitors that could interfere with p110 α binding to the membrane.

Other notable features in the kinase domain include the complete tracing of the activation loop, and an extended conformation of the C-terminal tail (residues 1045-1061) (Fig. 1a). Although our structure is for WT p110 α , its C-terminal tail conformation resembles that of the p110 α /p85 α -nSH2 complexes bearing the H1047R cancer mutation¹. In current published structures, this region persistently forms extensive crystal contacts with the Ras-binding domain from a neighbouring p110 α molecule. Details of crystal contacts differ among the various crystal forms, in terms of the degrees of order and the conformations of the activation loop and the C-terminal tail. This implies flexibility in these membrane-binding structural elements. There are regions within the C-terminal tail resembling distorted helical turns, such as the WIF motif (Fig. 1a). Thus, the C-terminal tail of p110 α could also be helical in solution, similar to helix K α 12 in other PI3K structures. Residue H1047 is surface exposed in our WT p110 α structure; the H1047R mutation likely does not cause gross conformational change as seen in the crystal structure of the mutant complex.

The class IA PI3Ks phosphorylate the lipid substrate PtdIns(4,5)P₂ in membrane bilayers (made from long-chain lipids) or in micelles (from diC8-PtdIns(4,5)P₂) and are inactive towards soluble substrate with very short acyl chains (e.g. diC4-PtdIns(4,5)P₂). This limits a crystallographic approach to delineating the membrane-binding site via co-crystallisation with lipid substrates. We investigated the premise that enhanced membrane-binding forms a general mechanism for p110 activation, by performing functional analyses using liposomes of defined compositions mimicking those of generic plasma membranes. We find that lipid kinase activities strongly correlate with lipid binding levels for both the WT enzyme and cancer mutants (Fig. 2). An activation loop charge-reversal mutant, and an AAA mutant of the conserved WIF motif have no lipid kinase activity, indicating that hydrophobicity and electrostatics are important parameters governing membrane interactions.

A striking pattern emerges from our survey of seven representative cancer-linked mutations of diverse chemical nature and structural context. It appears that they can be classified into two basic types: (I) those that relieve p85-mediated inhibition (e.g. E545K) and (II) those that lead to additional lipid-binding capability (e.g. H1047R) (Fig. 3). Type I mutations

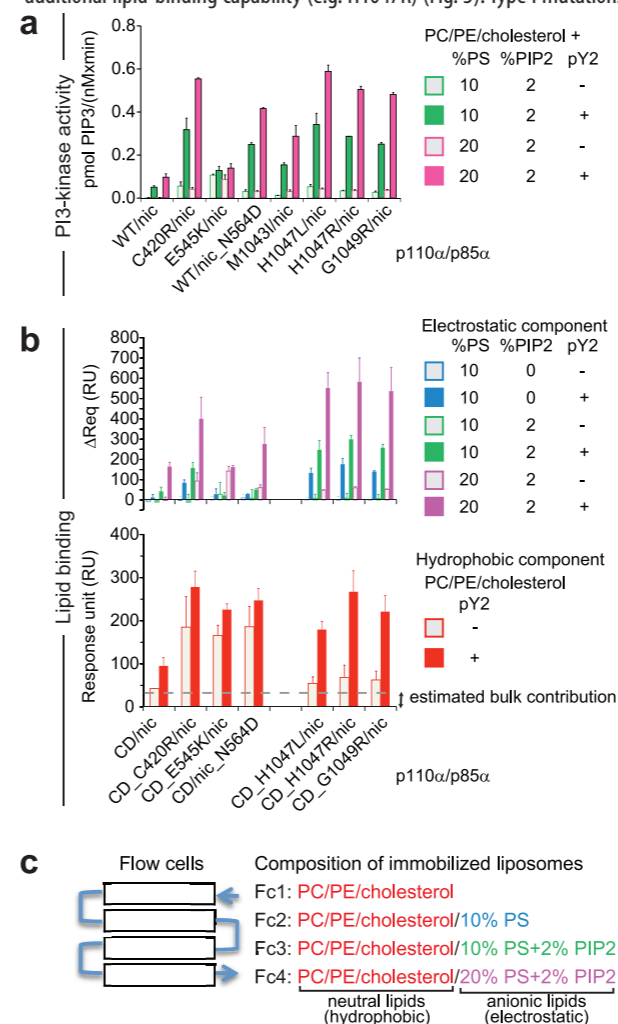


Figure 2: Lipid kinase and lipid binding activities of WT and cancer-linked mutants of p110 α /p85 α complexes. (a) Lipid kinase activities. The initial rates of PtdIns(3,4,5)P₃ production were measured with fixed substrate concentration (50 μ M PtdIns(4,5)P₂ and 100 μ M ATP) using liposomes of the indicated compositions. (b) Lipid binding measured by surface plasmon resonance (SPR). Binding levels were compared at protein concentration of 500 nM. Data represent the mean \pm s.d. of two to three independent experiments. (c) Schematics of the SPR experiment. (Abbreviations: PC, phosphatidylcholine; PE, phosphatidylethanolamine; PS, phosphatidylserine; PIP2, PtdIns(4,5)P₂; PIP3, PtdIns(3,4,5)P₃; nic, n-i-cSH2 fragment of p85 α ; CD, catalytically-dead mutant D915N; pY2, phosphopeptide bearing two pYXXM motifs from platelet-derived growth factor receptor- β).

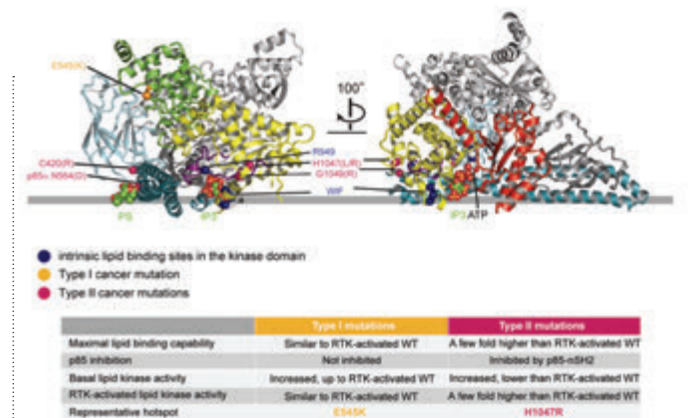


Figure 3: Summary and modelling of membrane binding for the p110 α /p85 α -iSH2 complex. The grey line approximates the putative membrane surface and is drawn collinear with the phosphate in PS and the P1 atom in Ins(1,4,5)P₃ (IP3, headgroup of PtdIns(4,5)P₂). Positions of PS, IP3 and ATP are derived by structural comparisons with the following structures: 1DSY, 1W2C and 1E8X. The C-terminal tail, the last two helices on which H1047, G1049 and the WIF motif reside, is from 1E8X. The C α atoms of the labelled residues are represented in spheres. For clarity, the kinase domain N-lobe is coloured red in the right panel only, and the helical domain is coloured green on the left panel only. Docking of PS is solely for the purpose of approximating the lipid-binding site in the p110 α C2 domain, and does not imply that this domain binds PS specifically.

unmask the intrinsic lipid-binding capability of WT p110 α /p85 α , and have basal activities similar to that of the activated WT enzyme. Binding of RTK phosphopeptide does not significantly further enhance their activities. Type II mutations are found in the p110 α C2 and kinase domains, as well as in the p85 α iSH2 domain. Their locations demarcate the putative membrane binding surface on p110 α /p85 α (Fig. 3). They do not interfere with nSH2 inhibition, although their basal activities are higher than that of WT enzyme. In contrast to type I mutants, the maximal activities of type II mutants exceed that of activated WT enzyme by three- to seven-fold upon RTK phosphopeptide binding in our experimental setup.

Our *in vitro* results imply that the biological outputs of type II mutants can be greatly enhanced by growth factor/RTK signalling. This notion concurs with *in vivo* experiments comparing the E545K and the H1047R mutants in the backgrounds of RTK amplification or hyper-activation. Moreover, the ability to initiate tumour formation in engineered mouse models of cancers has thus far only been demonstrated for the H1047R, but not yet for the E545K mutants. The roles of the different PI3K mutations in cancer initiation, progression and maintenance are yet unclear. We hypothesise that type I mutations could be critical to stages where growth factor independence, which is also a hallmark of cancer cells, is important.

References

- Mandelker, D. *et al.* A frequent kinase domain mutation that changes the interaction between PI3K α and the membrane. *Proc Natl Acad Sci U S A.* **106**, 16996-17001 (2009).
- Miled, N. *et al.* Mechanism of two classes of cancer mutations in the phosphoinositide 3-kinase catalytic subunit. *Science.* **317**, 239-242 (2007).
- Huang, C. H. *et al.* The structure of a human p110 α /p85 α complex elucidates the effects of oncogenic PI3K α mutations. *Science.* **318**, 1744-1748 (2007).

Funding Acknowledgements

This work was supported by the Medical Research Council, UK.

Research was carried out at Diamond Light Source on I02 and I03 and at the ESRF on ID 23-2.

DOI 10.1038/ncr.2011.532

Crystal structure of a cell surface cytochrome involved in metal and mineral respiration

Clarke, T.A., Edwards, M.J., Gates, A.J., Hall, A., White, G.F., Bradley, J., Reardon, C.L., Shi, L., Beliaev, A.S., Marshall, M.J., Wang, Z., Watmough, N.J., Fredrickson, J.K., Zachara, J.M., Butt, J.N. & Richardson, D.J. Structure of a bacterial cell surface decahaem electron conduit. *Proceedings of the National Academy of Sciences U S A*. **108**, 9384-9 (2011)

While many organisms require oxygen to breathe, bacteria are more versatile and use alternative chemicals such as nitrate, sulphate, or even solid iron or manganese minerals. One example of these mineral breathing bacteria is the organism *Shewanella oneidensis*. These bacteria generate energy by breaking down organic molecules, releasing electricity inside the cell that is conducted through biological wires to the outside surface of the cell where it is discharged into the mineral. To do this the surfaces of these bacteria are covered in red iron-containing proteins known as cytochromes that act as the surface electrode terminals and are at the centre of the interface between microbe and mineral. This year, we solved the crystal structure of one of these cell surface cytochromes. The protein was shaped roughly like a disc, with ten iron atoms arranged in a staggered cross through the disc. Each iron is bound in an organic cofactor called a haem. The iron chain forms an electrical wire that can conduct electrons through the protein to one of three conductive terminals. The disc-like structure could provide support for the wire, enabling it to stand upright on the surface of the cell allowing the tip of the structure to make direct contact with a mineral surface. This is a significant advance in the understanding of microbe-to-electrode electron transfer processes that will see a step change in the research field of a much studied area of low-carbon fuel technology.

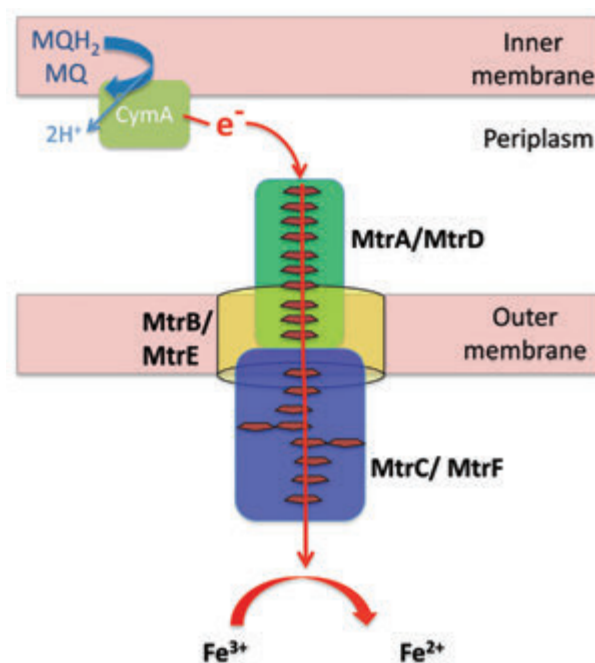


Figure 1: Mineral respiring electron transport chain of *Shewanella oneidensis*. Electrons from the quinol pool are transported to the porin-cytochrome complexes MtrCAB or MtrFED that ultimately reduce soluble metals species and insoluble minerals.

While most organisms require soluble electron acceptors such as oxygen, nitrate or sulfate for respiration, some bacteria are able to utilise insoluble minerals in the form of iron and manganese hydroxides as respiratory electron acceptors¹. In the model organism *Shewanella oneidensis*, this requires a range of multi-haem cytochromes that function as electron carriers through the entire cell. Initially, the cytochrome CymA obtains electrons from the quinol pool in the cytoplasmic membrane. These electrons are transported across the periplasm by a variety of multihaem cytochromes and then passed through the insulative outer cell membrane

via dedicated porin-cytochrome complexes that function as molecular wires² (Fig. 1).

The porin-cytochrome complexes consist of a transmembrane β -barrel porin (MtrB or MtrE), a small periplasmic decahaem cytochrome (MtrA or MtrD) that inserts into the porin and a larger decahaem cytochrome (MtrC or MtrF) that is inserted into the outer side of the porin. Both MtrA/D and MtrC/F insert far enough into the MtrB/E porin to bring respective haem groups close enough to allow efficient electron transfer from the periplasmic side of the outer membrane to the cell surface (Fig. 1). Once electrons arrive on the cell surface they can be transported to insoluble minerals. However, the mechanism by which the electrons move across the microbe-mineral interface is the source of much debate in recent literature. There is evidence for direct electron transfer between MtrC/F and the insoluble mineral surface, mediated electron transfer by catalysing electron exchange with flavin electron shuttles or participation in extracellular inter-cytochrome electron exchange along filamentous 'nanowire' appendages.³

A significant advancement has been our recent discovery of the structure of one of the outer membrane cytochromes. In 2008, crystals of purified MtrF protein were obtained (Fig. 2A). These crystals were over 85% solvent

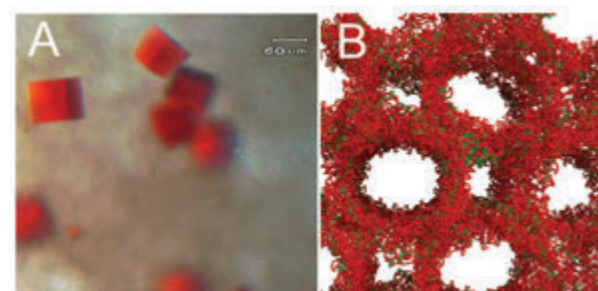


Figure 2: (A) Cubic crystals of MtrF protein diffracted to a final resolution of 3.2 Å. (B) Crystals were >85% solvent: due to large channels in the crystal lattice.

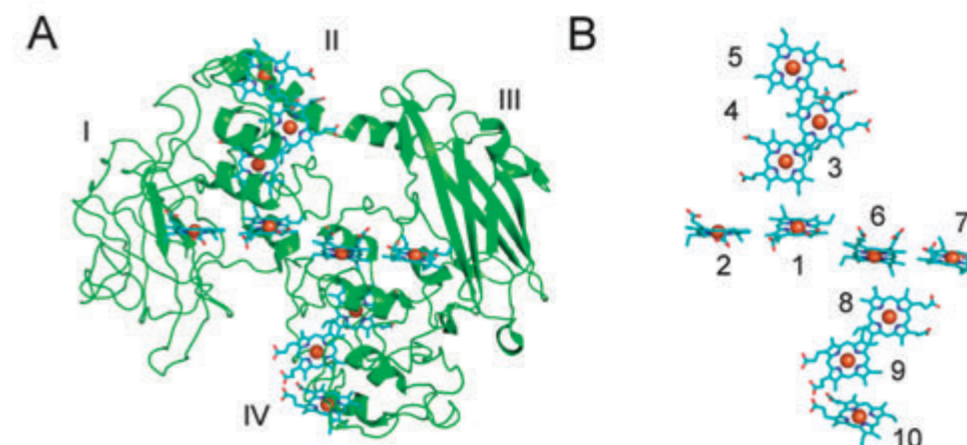


Figure 3: (A) Crystal structure of MtrF showing the ten hemes (blue) arranged within the four domains of the polypeptide chain (green). (B) Haem arrangement of MtrF. The numbers indicate the position of the c-type hemes in the amino acid sequence. Haems 5 and 10 represent likely electron entry/exit sites for interacting with MtrD or insoluble minerals, while 2 and 7 could transfer electrons to soluble electron shuttles.

and consequently very delicate, making them difficult to manipulate and acquire interpretable data from (Fig. 2B). However, in 2009 we obtained a phased map based on Single-wavelength anomalous diffraction data that we were able to use to identify the positions of all 10 haem groups and build a low resolution polyaniline chain. A final model was obtained in 2010 at a resolution of 3.2 Å that contained 10 c-type haems and 90% of the polypeptide chain.⁴

The structure revealed that MtrF was roughly ellipsoid in shape and comprised of four domains; a N-terminal β -barrel domain (I); a penta-haem domain (II); a second β -barrel domain (III) and a C-terminal penta-haem domain (IV) (Fig. 3A). The four domains fold together so that the two penta-haem domains make contact in the centre of the structure and are flanked by the β -barrel domains. This gives the structure rigidity and could allow the cytochrome to stand perpendicular to the cell surface. The ten haems are organized across the four domains in a unique crossed conformation in which a 6.5 nm octa-haem chain transects the length of the protein and is bisected by a planar 4.5 nm tetra-haem chain (Fig. 3B). The haems are all within 0.7 nm of each other meaning that electrons can rapidly pass through the chain. Surprisingly there are not two sites for electron entry/exit, as would be expected for a simple wire, but four. Two sites are positioned at the ends of the penta-haem domains, while the other two extend from the tetra-haem chain towards the β -barrel domains.

While one of these four sites will accept electrons from the MtrD-MtrE complex, the other three could serve as electron egress sites. The most likely site for electron ingress is either heme 5 or heme 10, at the opposite edges of the pentaheme domains, leaving the opposing heme to be potentially available for direct electron transfer to the surface of a mineral. The other two sites are unlikely to be involved in direct electron transfer, but the β -barrel domains could potentially serve as association sites for flavins and soluble electron acceptors. MtrF was shown to be able to serve as an electron donor to a variety of iron chelates and flavin acceptors. The discovery of the MtrF structure has provided a rationale for previous studies that show *S. oneidensis* is able to use multiple routes of electron egress,

and has for the first time given biochemists and molecular modellers the opportunity to understand and predict how minerals can associate with the surface of an outer membrane cytochrome.

References

- Shi L., Squier T. C., Zachara, J. M. & Fredrickson, J. K. Respiration of metal (hydr)oxides by *Shewanella* and *Geobacter*: a key role for multiheme c-type cytochromes. *Mol. Microbiol.* **65**, 12-20 (2007).
- Hartshorne, R.S., Reardon, C.L., Ross, D., Nuester, J., Clarke, T.A., Gates, A.J., Mills, P.C., Fredrickson, J.K., Zachara, J.M., Shi, L., Beliaev, A.S., Marshall, M.A., Tien, M., Brantley, S., Butt, J.N. & Richardson, D.J. Characterization of an electron conduit between bacteria and the extracellular environment. *Proc. Nat. Acad. Sci. USA*. **106**, 22169-74 (2009).
- Brutinel, E.D. & Gralnick, J.A. Shuttling happens: soluble flavin mediators of extracellular electron transfer in *Shewanella*. *Appl. Microbiol. Biotechnol.* **93**, 41-8 (2012).
- Clarke, T.A., Edwards, M.J., Gates, A.J., Hall, A., White, G.F., Bradley, J., Reardon, C.L., Shi, L., Beliaev, A.S., Marshall, M.J., Wang, Z., Watmough, N.J., Fredrickson, J.K., Zachara, J.M., Butt, J.N. & Richardson, D.J. Structure of a bacterial cell surface decahaem electron conduit. *Proc. Nat. Acad. Sci. USA*. **108**, 9384-9389 (2011).

Funding Acknowledgements

This research was supported by the Biotechnology and Biological Sciences Research Council (H007288/1) and the EMSL Scientific Grand Challenge project at the W. R. Wiley Environmental Molecular Sciences Laboratory, a national scientific user facility sponsored by the U.S. Department of Energy.

PMID 21606337

A neutralizing antibody that binds to all influenza A haemagglutinins

Corti, D., Voss, J., Gamblin, S.J., Codoni, G., Macagno, A., Jarrossay, D., Vachieri, S.G., Pinna, D., Minola, A., Vanzetta, F., Silacci, C., Fernandez-Rodriguez, B.M., Agatic, G., Bianchi, S., Giacchetto-Sasselli, I., Calder, L., Sallusto, F., Collins, P., Haire, L.F., Temperton, N., Langedijk, J.P., Skehel, J.J. & Lanzavecchia, A. A neutralizing antibody selected from plasma cells that binds to group 1 and group 2 influenza A haemagglutinins. *Science*. **333**, 850-6 (2011)

Antibodies that neutralise influenza virus infectivity bind to the haemagglutinin virus membrane glycoprotein (HA), recognising in particular its virus membrane-distal, sialic acid receptor binding subdomain. The majority of antibodies characterised are strain specific, and the antigenic variants that they select are able to re-infect individuals previously infected even with related viruses. As a consequence, this variation requires influenza vaccines to be frequently updated so that they contain HAs closely related to those of viruses in current circulation. Due to this, and because there is a continuous threat of influenza viruses being introduced into humans from avian species that serve as reservoirs for viruses containing all sixteen subtypes of HA, attempts have been made to obtain antibodies that would block virus infection irrespective of strain and subtype variation.

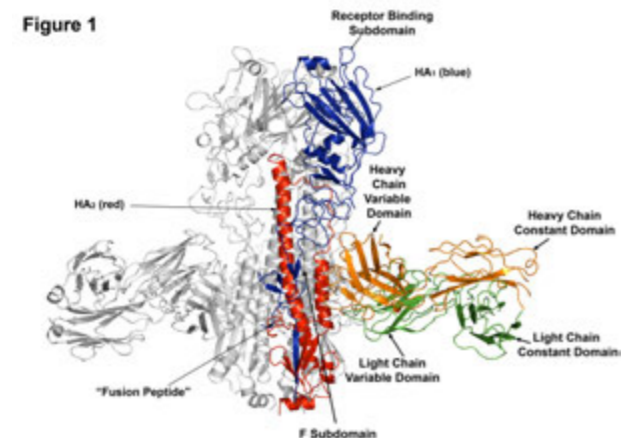


Figure 1: 3 Fabs from F6 human monoclonal antibody bind to the F subdomain of the H3 HA trimer (pdb 3ZTJ) represented in Ribbons. One HA monomer is coloured blue for HA1 and red for HA2; the other two monomers are coloured grey.

With these objectives, Corti *et al.* cultured plasma cells donated by a vaccinee¹ and selected rare monoclonal antibodies that bound to HAs of a range of subtypes. The antibody F6 that we studied in collaboration at Diamond Light Source, binds to all 16 subtypes and neutralises infection by viruses and pseudoviruses representative of the two Groups that the 16 subtypes form². X-ray crystallography of F6 Fab (fragments antigen binding) complexes with H1 and H3 subtype HAs, from Group 1 and Group 2 respectively, shows that each monomer of the HA trimers binds one Fab, at a site about 30Å from the virus membrane (Fig. 1) The HCDR3 loop of the

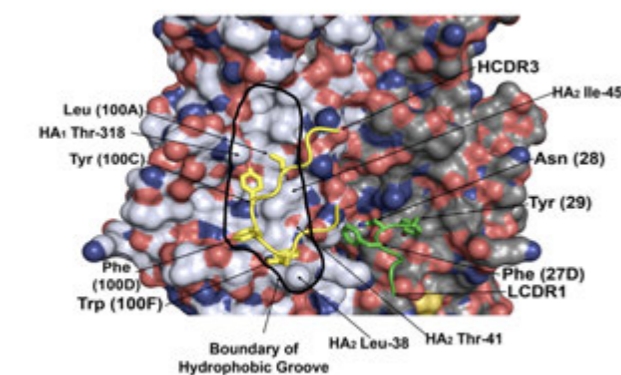


Figure 2: A surface representation of the F subdomain of H3 HA coloured according to atom type: carbon, grey; oxygen, red; nitrogen, blue; and sulphur, yellow. The HCDR3 and LCDR1 loops of the F6 antibody are coloured yellow and green respectively. The boundary of the hydrophobic groove of the F6 binding site is outlined.

Fab binds into a shallow groove in the F subdomain of HA (Fig. 2), the sides of which are formed by residues from helix A of HA2 and from two strands of HA1 (residues 38-42 and 318-320) and the base of which is formed by the HA2 turn containing residues 18-21 of the 'Fusion Peptide'. The HCDR3 loop crosses helix A at an angle of about 45°, enabling Leu-100A, Tyr-100C, Phe-100D, and Trp-100F to make hydrophobic contacts with residues in the groove. Tyr-100C and Trp-100F potentially also make hydrogen bonds with the side chain of Thr-318 of HA1 and the main-chain carbonyl of residue 19 of HA1, respectively. Two additional polar interactions are formed by main-chain carbonyls at residues 98 and 99 of HCDR3 with Asn-53 and Thr-49 of helix A. Overall, the interactions F6 makes with the hydrophobic groove in H1 and H3 HAs, are remarkably similar. The LCDR1 loop of F6 makes two contacts with the side of helix A, opposite to the side that contributes to the hydrophobic groove. Phe27D makes hydrophobic contact with the aliphatic part of Lys-39, and Asn-28 hydrogen bonds to Asn-43.

Two differences between the F6-H3 and F6-H1 complexes are notable. The first is that H3 HA is glycosylated at HA1 Asn-38, but H1 HA, in common with all Group 1 HAs, is not. In the unbound structure of H3 HA, the carbohydrate side-chain projects towards helix A of HA2 of the same subunit, overlapping the site of F6 binding. However, F6 binding to H3 HA is made possible by reorientation of the carbohydrate side-chain that involves its rotation through about 80°, away from the surface of HA (Fig. 3).

The second difference involves the Group-specific environment and orientation of HA2 Trp-21. In Group 1 HAs, Trp-21 is approximately parallel to the surface of the F subdomain, but in Group 2 HAs, it is roughly perpendicular to the surface³ (Fig. 4). Phe-100D of F6 contacts Trp-21 in both Group1 and Group2 orientations as a result of rearrangements in the HCDR3 loop that position Phe-100D approximately 2Å deeper in the hydrophobic groove in the H1 HA complex than in the H3 HA complex, maintaining a similar contact distance between Trp-21 and Phe-100D in both cases. In previously published structures of complexes formed by Group-1 specific antibodies^{4,5} it appears that there is less flexibility than in F6 complexes for the contact residues to move in the hydrophobic groove to accommodate the Group2 orientation of HA2 Trp-21.

Attempts to derive information on the mechanism of infectivity neutralisation by F6 by selecting resistant antigenic variants from cells infected *in vitro* in the presence of antibody or from lungs of antibody-treated, infected mice, were not successful. However, from consideration of the structures of the antibody complexes, a number of suggestions can be made. In the first stages of infection, bound influenza viruses are taken into endosomes from where the virus genome-transcriptase complex is released

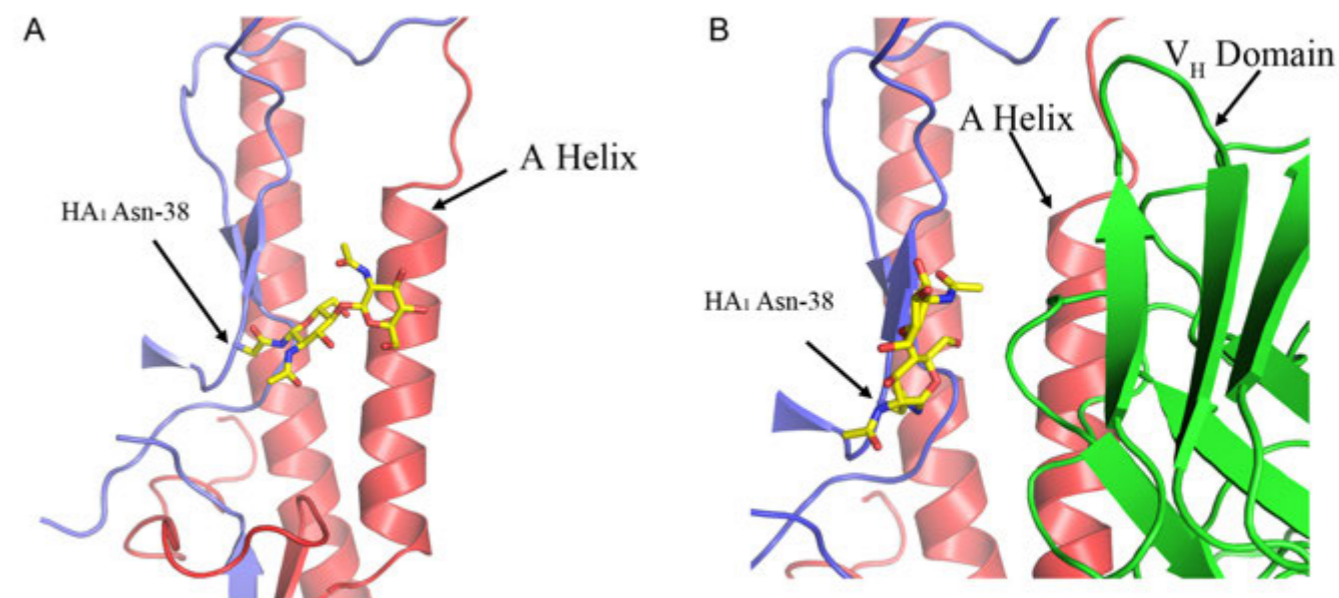


Figure 3: Different orientations of the carbohydrate side-chain attached to HA1 Asn-38 of H3 HA. (A) The apo structure, the F6-bound structure. (B) The HA1 and HA2 chains are coloured blue and red respectively; the VH domain of F6 is coloured green.

into the cell as a result of low pH-activated, HA-mediated fusion of virus and endosomal membranes. Assuming that F6-virus complexes are taken into endosomes, it is possible that F6 could block the mechanism of membrane fusion, through HCDR3 interactions with the 'Fusion Peptide' and LCDR1 interacting with the C-terminal residues of HA1 from the neighbouring subunit, to crosslink the HA trimer and prevent the conformational changes in HA required for fusion. Membrane fusion might also be blocked by bound antibodies restricting the formation of complexes of activated HAs that have been proposed to be involved in the fusion process.

The efficiency of these mechanisms of neutralisation would obviously be influenced by the affinity of F6 for HAs on viruses and this would depend on the accessibility of the binding site. Accessibility is presumably related to the spacing of HAs on the virus surface relative to the size of the antibody molecule. Estimates of between 20% and 50% of virus surface coverage

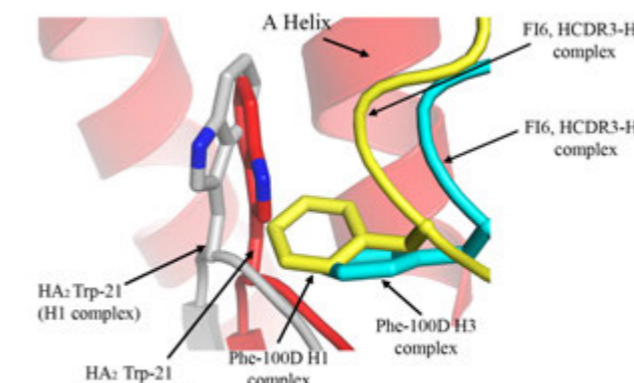


Figure 4: The Group-specific different orientations of HA2 Trp-21, a conserved residue of the 'Fusion Peptide', and the Group-specific differences in interaction with F6.

by HA have been made from different measurements, and at either level, access of F6 to its binding site at the membrane proximal region of HA is likely to be comparatively restricted.

It is also likely that HA is a target for infection-blocking antibodies in the final stages of infection at the surfaces of infected cells, where the interaction of F6 with newly-made HA is less likely to be restricted by spacing considerations. At this site, HA-bound antibody might prevent virus assembly by crosslinking HAs or by more specifically blocking functions or associations in assembly which have not as yet been defined. In addition, infected-cell lysis as a result of F6-HA complex recognition at the cell surface by Fc-receptor-bearing cells may, as our negative results with mutant F6 antibodies that do not bind Fc-receptors indicate, represent an important mechanism for blocking the progress of infection.

The main incentives for our studies of cross-reactive antibodies are the unpredictability of the occurrence of influenza epidemics, the wide range of antigenically novel viruses that might cause them, and the need for new anti-viral agents for treatment of severe influenza infections. The results of prophylaxis and therapy experiments that we report with these studies of F6 antibody structure, provide justification for adding F6 to the arsenal of monoclonal antibodies that is accumulating for potential use against influenza. Among the antibodies available to date, F6, because of its pan-influenza cross-reactivity, would have an obvious advantage.

References

1. Corti, D., Suguitan, A.L.Jr., Pinna, D., Silacci, C., Fernandez-Rodriguez, B.M., Vanzetta, F., Santos, C., Luke, C.J., Torres-Velez, F.J., Temperton, N.J., Weiss, R.A., Sallusto, F., Subbarao, K. & Lanzavecchia, A. Heterosubtypic neutralizing antibodies are produced by individuals immunized with a seasonal influenza vaccine. *J Clin Invest*. **12**, 1663-73 (2010).
2. Gamblin, S.J. & Skehel, J.J. Influenza haemagglutinin and neuraminidase membrane glycoproteins. *J Biol Chem*. **285**, 28403-9 (2010).
3. Russell, R.J., Gamblin, S.J., Haire, L.F., Stevens, D.J., Xiao, B., Ha, Y. & Skehel, J.J. H1 and H7 influenza haemagglutinin structures extend a structural classification of haemagglutinin subtypes. *Virology*. **325**, 287-96 (2004).
4. Ekiert, D.C., Friesen, R.H., Bhabha, G., Kwaks, T., Jongeneelen, M., Yu, W., Ophorst, C., Cox, F., Korse, H.J., Brandenburg, B., Vogels, R., Brakenhoff, J.P., Kompier, R., Koldijk, M.H., Cornelissen, L.A., Poon, L.L., Peiris, M., Koudstaal, W., Wilson, I.A. & Goudsmit, J. A highly conserved neutralizing epitope on group 2 influenza A viruses. *Science*. **333**, 843-50 (2011).
5. Sui, J., Hwang, W.C., Perez, S., Wei, G., Aird, D., Chen, L.M., Santelli, E., Stec, B., Cadwell, G., Ali, M., Wan, H., Murakami, A., Yammanuru, A., Han, T., Cox, N.J., Bankston, L.A., Donis, R.O., Liddington, R.C. & Marasco, W.A. Structural and functional bases for broad-spectrum neutralization of avian and human influenza A viruses. *Nat Struct Mol Biol*. **16**, 265-73 (2009).

PMID 21798894

Helping to lower cholesterol levels - the crystal structure of a bacterial homologue of the bile acid sodium symporter ASBT

Hu, N.J., Iwata, S., Cameron, A.D. & Drew, D. Crystal structure of a bacterial homologue of the bile acid sodium symporter ASBT. *Nature* **478**, 408-411 (2011)

Although cholesterol is an essential component of the plasma membrane, excessively high cholesterol levels greatly increase the risk of heart disease. Approximately half of the daily amount of cholesterol that is eliminated from the body is through its conversion to bile acids. Bile acids are secreted into the intestine where they help emulsify dietary lipids. Rather than being excreted from the intestine and so eliminated from the body 95% of the bile acids are reabsorbed and taken back to the liver. The Apical Sodium-dependent Bile acid Transporter (ASBT) actively transports bile acids across the apical membrane of the ileum using an inwardly-directed sodium gradient. As this is the rate-limiting step for bile acid reabsorption, ASBT is a target for drugs aimed at lowering cholesterol levels with some success in animal models. To further understand the molecular basis for bile acid transport and to aid drug discovery we have determined the structure of an ASBT bacterial homologue in complex with sodium ions and bile acid at 2.2Å resolution. The structure should aid the rational-based design of new inhibitors against ASBT, with the goal of treating hypercholesterolaemia.

ASBT is a secondary transporter that uses the energy stored in the sodium motive force to drive the uphill transport of bile acids across the apical membrane of the ileum. It is a member of the SLC10 family of secondary transporters, with several members identified to date¹. Very little structural information has been available for this family and there has been some disagreement in the proposed topology. As ASBT is a pharmaceutical target for drugs aimed at lowering cholesterol, the structure of the bile acid binding-site would be beneficial to drug discovery. Using fluorescence

based screening methods we identified a bacterial homologue of ASBT that was tractable to crystallography². More specifically, the protein is stable in short chain detergents, which is important to obtaining well-ordered crystals, especially for membrane proteins with short loops like ASBT. ASBT_{NM} from *N. meningitidis* is 26% identical to human ASBT with many of the residues known to be critical for function conserved. Through transport assays we were able to confirm that ASBT_{NM} is a sodium-dependent bile acid transporter.

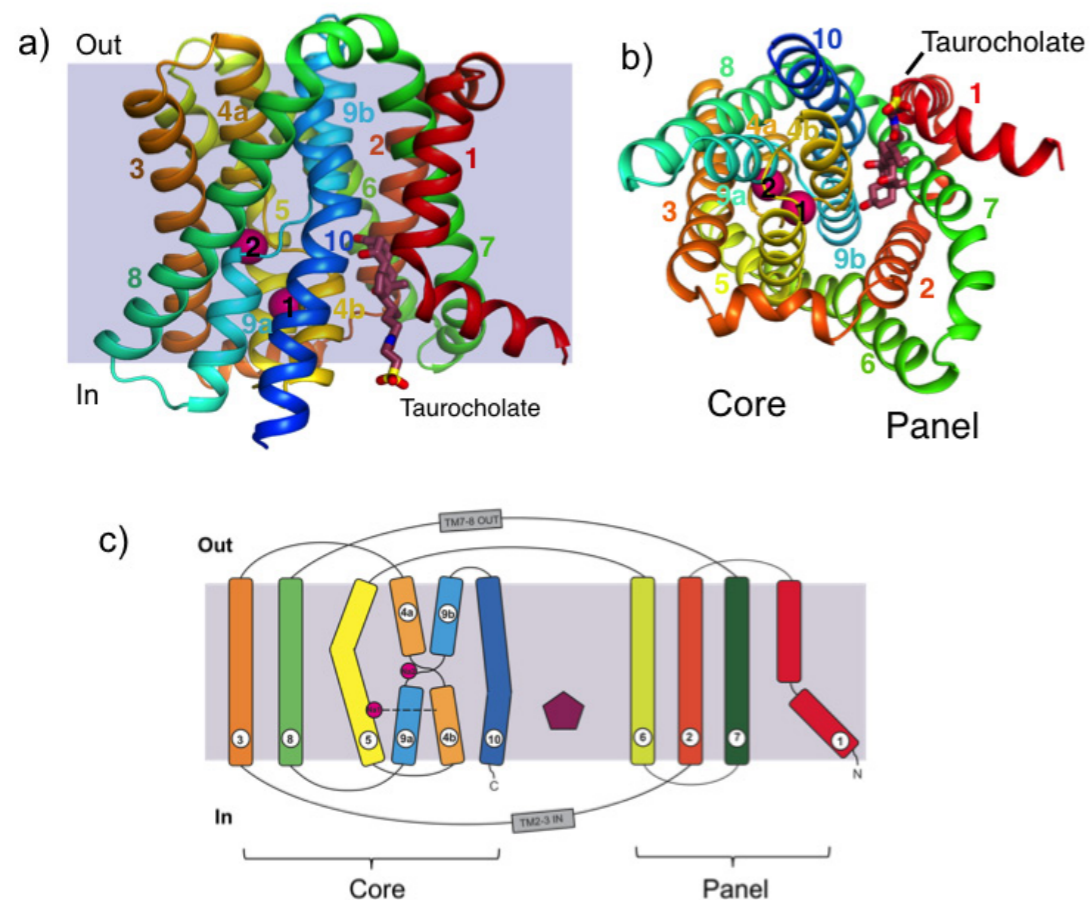


Figure 1: ASBT_{NM} structure. a) Ribbon representation of ASBT_{NM} as viewed in the plane of the membrane: sodium ions (pink spheres), taurocholate stick model (wine red). The helices have been coloured from red at the N-terminus to blue at the C-terminus. The position of the membrane is depicted in grey. b) ASBT_{NM} structure as viewed from the intracellular side as a ribbon representation. c) ASBT_{NM} topology: coloured rods depict TMs 1 to 10, pink circles sodium sites, Na1/Na2, and the wine-red pentagon taurocholate.

We solved the structure ASBT_{NM} by SAD from a mercury derivatised crystal using data collected on I02 and I03 beamlines. The structure was refined at a resolution of 2.2Å to an R-factor of 19.7% and an R-free of 22.9%. Important to obtaining high resolution data for this membrane protein was the use of dehydration. Controlled dehydration of the crystals was carried out using the HC1³ device at Diamond Light Source.

The structure of ASBT_{NM} is shown in Fig. 1. The key features of the 10 transmembrane helix TM structure are: 1.) It is made of two 5-TM segments that are structural repeats related by a pseudo 2-fold axis running through the centre of the membrane; 2.) The fourth TM in each domain is discontinuous, a helix-break-helix (TM 4, TM 9); 3.) The two 5 TM repeats intertwine to form two domains, a core domain (TMs 3-5 and 8-10) and a panel domain (TMs 1-2 and 6-7), and 4.) The discontinuous helices cross over to create two pseudo-helices formed from the amino-terminal and the carboxy-terminal halves of these helices respectively (Fig. 1c).

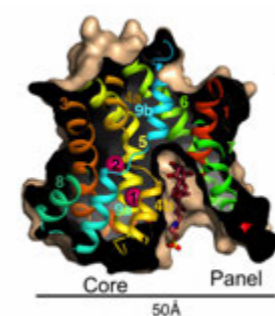


Figure 2: Surface representation showing the location of the taurocholate-bound intracellular cavity as a section through the protein.

with bile acid in ASBT_{NM} versus small ions in NhaA.

The transport of bile acid against its concentration gradient is energised by the downhill flow of sodium into the cell. In ASBT, two sodium ions are transported for every bile acid and consistent with this requirement we observe two sodium ions in the structure, defined by the coordination geometry. The first of these sodium ions lies in the centre of the protein between the two C-terminal halves of the discontinuous helices (Na2). Presumably the sodium in this position serves to stabilise the negative dipoles of the broken helices. The second sodium site is located 10Å from the cytoplasmic side of the protein between the C-terminal half of one of the discontinuous helices (TM4b) and the adjoining helix. The residues that make up the sodium binding sites are completely conserved and mutations in these residues reduce transport.

A large cavity extending into the centre of the protein lies between the core and panel domains on the cytoplasmic face of the protein (Fig. 2). Its walls are mainly hydrophobic but there are a number of polar residues and water molecules at the bottom. Bound in the cavity is the bile acid taurocholate, which was co-crystallised with the protein. However this relatively large molecule does not completely fill the cavity. The size of the cavity may explain why a wide variety of ligands are known inhibitors of ASBT. A 150-fold difference in inhibition of the mouse and human forms of ASBT by benzothiazepines has been ascribed to sequence differences corresponding to Ser291 at the bottom of the cavity.

Secondary transporters work by the alternating access mechanism in which conformational changes to the protein enable the substrate-binding

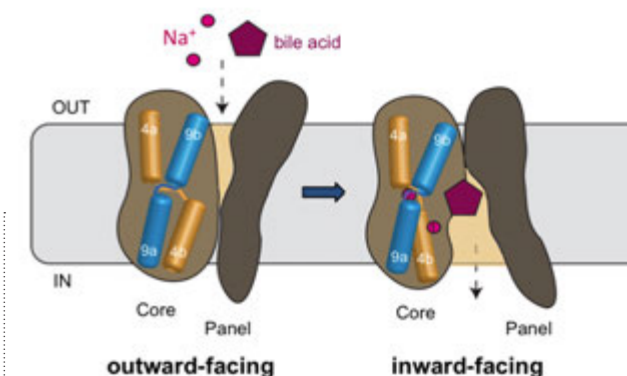


Figure 3: Schematic of proposed mechanism illustrating the movement of the Panel against the Core domain to transport sodium and bile acid.

site to alternately face the outside or inside of the cell. In this way the substrate is transported across the membrane. For transporters with inverted repeats it has been shown that by exploiting the subtle differences in the conformations of the N and C-terminal domains a model of the outward-facing state can be generated from the inward-facing state and vice versa⁵. By applying this methodology we generated a plausible model of ASBT_{NM} in an outward-facing state and observe that the largest conformational change between this model and our inward-facing structure is the movement of the panel against the core domain. We propose that sodium binding at critical locations in ASBT_{NM} controls the conformation of the core domain, which in turn drives the movement of the panel domain (Fig. 3). This large conformational change of the panel domain relative to the core domain is required to alter the accessibility of the substrate-binding pocket.

References

- Hagenbuch, B. & Dawson, P. The sodium bile salt cotransport family SLC10. *Pflugers Arch.* **447**, 566-570 (2004).
- Sonoda, Y. *et al.* Benchmarking membrane protein detergent stability for improving throughput of high-resolution X-ray structures. *Structure.* **19**, 17-25 (2011).
- Sanchez-Weatherby, J. *et al.* Improving diffraction by humidity control: a novel device compatible with X-ray beamlines. *Acta Crystallogr. D.* **65**, 1237-1246 (2009).
- Hunte, C. *et al.* Structure of a Na⁺/H⁺ antiporter and insights into mechanism of action and regulation by pH. *Nature.* **435**, 1197-1202 (2005).
- Forrest, L. R. *et al.* Mechanism for alternating access in neurotransmitter transporters. *Proc. Natl. Acad. Sci. USA.* **105**, 10338-10343 (2008).

Funding Acknowledgements

This work was funded by the European Union (EMeP grant, LSHG-CT-2004-504601), and the Medical Research Council (MRC grant, LDAD_P25504). The authors are grateful for the use of the Membrane Protein Laboratory funded by the Wellcome Trust (grant 062164/Z/00/Z) at the Diamond Light Source. D. Drew acknowledges the support from The Royal Society through the University Research Fellow scheme. A part of this work was also supported by a grant from the ERATO IWATA Human Receptor Crystallography Project from the Japan Science and Technology Agency.

Research was carried out at Diamond Light Source on beamline I02 and I03 and at the ESRF.

DOI 10.1038/nature10450

Keep CALM and carry on endocytosing

Miller, S.E., Sahlender, D.A., Graham, S.C., Höning, S., Robinson, M.S., Peden, A.A. & Owen, D.J. The molecular basis for the endocytosis of small R-SNAREs by the clathrin adaptor CALM. *Cell*. **147**, 1118-31 (2011)

All eukaryotic cells, from yeast through to humans, are characterised by their compartmentalisation: membrane-bound organelles separate the distinct chemical environments within the cell that sustain its various biological functions. Small membrane-bound transport vesicles transfer components between these intracellular organelles and to/from the extracellular milieu in a highly directed manner. Components are delivered when a cargo-containing vesicle that budded off one organelle, or the plasma membrane at the cell surface, fuses with another organelle into which its contents mix. Much of the energy and specificity involved in the fusion of transport vesicles with their target organelles in eukaryotic cells is provided by a large family of proteins termed SNAREs (soluble N-ethylmaleimide-sensitive factor attachment protein receptor). These small membrane-anchored proteins have distinct steady state organelle localisations, although the individual SNARE proteins are constantly in motion as they bud off from, or fuse with, source/target organelles. Three Q-SNAREs from one membrane form a complex with one R-SNARE from the other membrane, their 16-turn helical SNARE motifs wrap around each other and thus provide the energy to pull the two membranes together to facilitate their fusion. Previous studies have shown that only limited combinations of the 38 SNARE proteins present in mammalian cells form complexes, conferring specificity to vesicle:organelle and organelle:organelle membrane fusion events. However, the mechanisms by which the correct SNAREs are selected for incorporation into forming vesicles remain poorly understood. Data collected on beamlines I03 and I04 demonstrate that the endocytic clathrin-coated vesicle (CCV) component CALM (Clathrin Assembly Lymphoid Myeloid-leukemia protein) binds directly to the R-SNARE VAMP8, selecting this SNARE for incorporation into endocytic vesicles and thereby ensuring their ability to fuse with the correct target organelle.

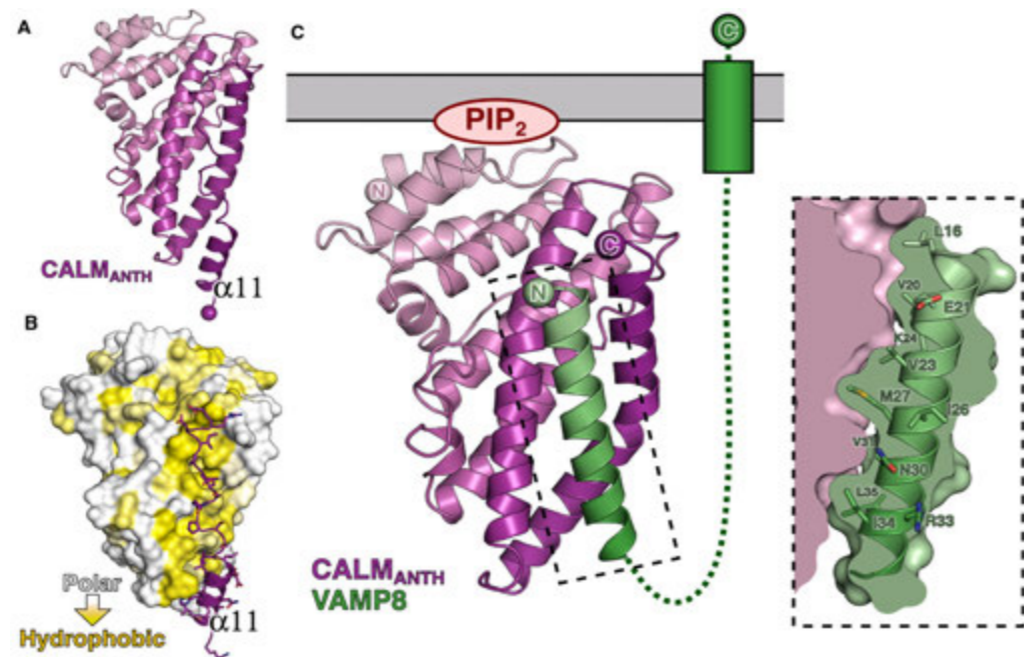


Figure 1: The SNARE helix of VAMP8 binds a hydrophobic patch on the CALM ANTH domain. (A) Structure of the CALM ANTH domain in isolation. (B) Surface of this domain, calculated excluding the poorly-ordered helix $\alpha 11$, colored by hydrophobicity (C) Structure of the CALM ANTH domain in complex with the VAMP8 SNARE helix. Inset (view is rotated 90° around the vertical axis) shows the surface complementarities of the interaction.

The process of clathrin-mediated endocytosis from the plasma membrane is the main mechanism by which the complement of transmembrane proteins on the surface of the cell is regulated and as such plays a critical role in a vast array of processes including; cell/cell and cell/substratum recognition, transduction of external signals, and the uptake of nutrients and other small molecules. It is also the route by which many pathogens gain entry into cells. Endocytic CCVs are surrounded by a polyhedral clathrin scaffold, which is linked to the membrane by a group of architecturally similar proteins termed clathrin adaptors. These bind directly to both clathrin through a natively unstructured region and to the plasma-membrane enriched phospholipid PtdIns4,5P₂ via a folded domain. A subset of clathrin adaptors are responsible for selecting the cargo that is

to be incorporated into CCVs through their binding to a variety of specific determinants on the cargos' cytoplasmic regions¹. In addition to its general transmembrane protein cargo, an endocytic CCV must also contain the R-SNAREs that will allow it to fuse with its target organelle, the early endosome. In mammalian cells these R-SNAREs are either VAMP8, VAMP3 or the neuronal specific VAMP2. How these R-SNAREs are sorted into endocytic CCVs was unknown, however, studies in *D. melanogaster*², *C. elegans*³ and *S. cerevisiae*⁴ suggested that these organisms' single ANTH domain containing clathrin adaptor was somehow involved.

Biochemical studies allowed us to show that the ANTH domain of ubiquitously-expressed mammalian clathrin adaptor CALM bound directly to

the SNARE motifs of VAMP8, VAMP3 and VAMP2 with a K_d of around 20 μM. Extensive attempts to crystallise CALM's ANTH domain in the presence of VAMP8 yielded only structures of the unliganded ANTH domain. However, inspection of these structures revealed that the final helix of this domain, helix $\alpha 11$ (Fig 1), was often poorly ordered and assumed different positions on top of helices $\alpha 9$ and $\alpha 10$ which form a hydrophobic trough (Fig 1). As this was a potential binding site for the long amphipathic SNARE motif of VAMPs, helix $\alpha 11$ was deleted. Surprisingly, rather than potentiating VAMP binding, deletion of helix $\alpha 11$ blocked VAMP binding completely. Structure determination and MALS analysis showed that truncated ANTH domains lacking helix $\alpha 11$ form tight dimers, the buried dimer interface being the proposed VAMP binding site. However, point mutations of hydrophobic residues lining the potential SNARE-binding trough of the full-length ANTH domain resulted in strong inhibition of VAMP binding in biochemical assays without affecting the fold of the ANTH domain. A chimeric construct was thus created in which the SNARE motif of VAMP8 was appended to the end of helix $\alpha 10$ of the CALM ANTH domain. The crystal structure of this chimeric

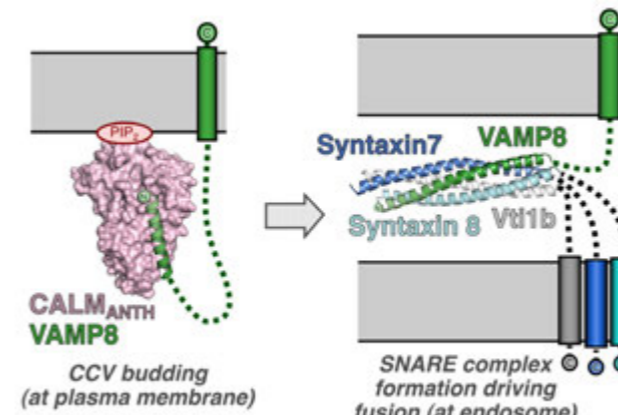


Figure 2: The binding of VAMP8 to the CALM ANTH domain is mutually exclusive with its participation in SNARE complexes. CALM thus promotes incorporation of fusion-ready SNAREs into nascent vesicles.

protein showed that VAMP8 does indeed bind in the hydrophobic trough between helices $\alpha 9$ and $\alpha 10$ of the CALM ANTH domain with excellent spatial and chemical compatibility (Fig. 1). We therefore propose that helix $\alpha 11$ binds loosely to the CALM ANTH domain to protect the hydrophobic interface from the polar solvent until it encounters a SNARE. The residues which form the interaction between VAMP8 and CALM are well conserved in VAMP2 and VAMP3, allowing us to conclude that these other R-SNAREs will bind the CALM ANTH domain in an identical manner. The CALM-binding region of VAMP8 adopts a helical conformation and its interaction with the CALM ANTH domain is reminiscent of its participation in an assembled SNARE complex (Fig. 2). While binding of VAMP8 to CALM is mutually exclusive with SNARE complex formation, since the same binding interface is utilised for both interactions, pre-assembly of the CALM-binding region of VAMP8 into helix is compatible with its identification as the 'trigger' region of the R-SNARE that potentiates SNARE complex formation (Fig. 2). CALM thus incorporates fusion-ready R-SNAREs into nascent vesicles. Point mutations of key residues in the interface of either partner as indicated by the chimeric structure abolished the interaction between CALM ANTH and VAMP8 in vitro and, when transferred into the genes in vivo, blocked endocytosis of VAMP8 without significantly affecting the endocytosis of standard cargo (Fig. 3).

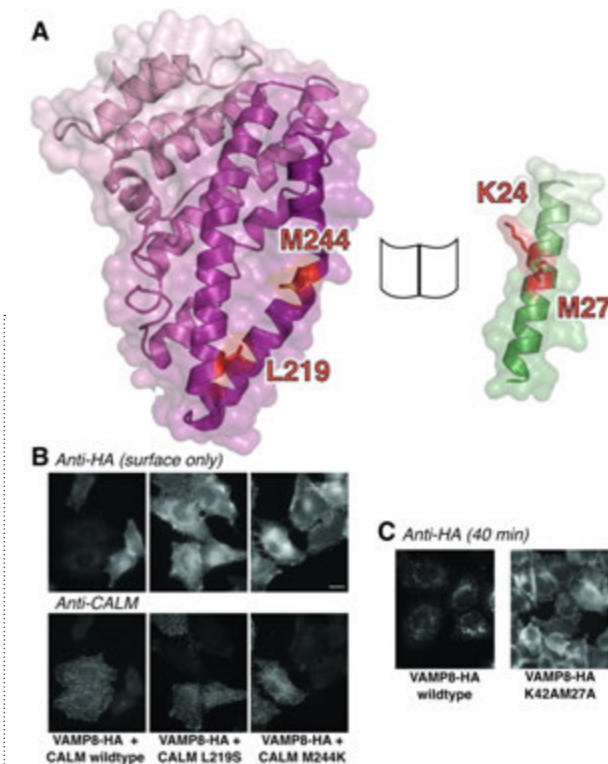


Figure 3: Mutations at the CALM/VAMP8 binding interface disrupt their interaction in vivo. (A) CALM ANTH domain and VAMP8 SNARE helix from the complex structure, peeled apart (like opening a book) to show some of the interacting residues that were mutated coloured red. (B) Immunofluorescence of cells expressing VAMP8-HA in combination with either wild-type or mutant (L219S or M244K) small interfering (si)RNA resistant CALM were mixed and then depleted of endogenous CALM by siRNA treatment. Scale bar represents 20 μm. (C) Localisation of anti-HA in cells expressing wild-type or mutant (K24AM27A) VAMP8 that were incubated with the antibody for 40 min before washing, fixing and visualisation.

Nonsense mutations in CALM are responsible for hematopoietic and iron metabolism abnormalities, growth retardation and shortened life span in mice. The CALM gene has also been directly implicated in alterations in cognitive function with increasing age and in risk of developing Alzheimer's disease⁵. These pathophysiological effects could, until now, only be explained by the role of CALM in linking clathrin to the PtdIns4,5P₂-containing membrane during endocytosis, a role replicated by all clathrin adaptors. Our study suggests that such effects result instead from CALM's unique ability to directly drive the endocytosis of the SNAREs VAMP8, VAMP3 and VAMP2.

References

- Kelly, B. T. & Owen, D. J. Endocytic sorting of transmembrane protein cargo. *Curr Opin Cell Biol*. **23**, 404-412, (2011).
- Bao, H. *et al.* AP180 maintains the distribution of synaptic and vesicle proteins in the nerve terminal and indirectly regulates the efficacy of Ca²⁺-triggered exocytosis. *J Neurophysiol*. **94**, 1888-1903, (2005).
- Nonet, M. L. *et al.* UNC-11, a Caenorhabditis elegans AP180 homologue, regulates the size and protein composition of synaptic vesicles. *Mol Biol Cell*. **10**, 2343-2360 (1999).
- Burston, H. E. *et al.* Regulators of yeast endocytosis identified by systematic quantitative analysis. *J Cell Biol*. **185**, 1097-1110, (2009).
- Harold, D. *et al.* Genome-wide association study identifies variants at CLU and PICCALM associated with Alzheimer's disease. *Nat Genet*. **41**, 1088-1093, (2009).

Funding Acknowledgements

The Wellcome Trust, the UK Medical Research Council, the Royal Commission for the Exhibition of 1851 and the German Science Foundation.

PMID 22118466

Polynucleotide Kinase 3' Phosphatase: revealing the molecular details of substrate and co-factor recognition

Garces, F., Pearl, L.H. & Oliver, A.W. The structural basis for substrate recognition by mammalian Polynucleotide Kinase 3' Phosphatase. *Molecular Cell*. **44**, 1-12 (2011)

Genetic material, within each cell of the human body, is under attack from a seemingly continuous barrage of DNA-damaging agents, arising from a wide range of both internal and external sources. One of the most commonly occurring forms of damage to DNA are single-strand breaks (SSBs) where one strand of the DNA duplex is interrupted or broken; appearing with a frequency of around 1000, per cell, per day. If these breaks are not quickly resolved, they can be converted to the potentially more harmful double-strand breaks (DSBs) during the process of DNA replication, leading to genetic instability and even to the onset of cancer. Additionally, the damage processes that generate SSBs often do not leave free 3' hydroxyls or 5' phosphates at the margins of the gap, both of which are essential for subsequent template-directed repair. Polynucleotide Kinase 3' Phosphatase (PNK)¹ is an unusual dual function enzyme, which can restore DNA ends, by the removal of 3' phosphate blocking lesions and/or by phosphorylating 5' hydroxyls, thereby facilitating the subsequent gap-filling and ligation steps through the respective actions of DNA polymerase β and DNA ligase III α . Previous structural studies had defined the overall architecture of PNK² but provided little insight into how the enzyme actually recognises its different DNA substrates. With diffraction data principally collected on beamlines I02 and I03, we were able to determine structures of the catalytic region of PNK in complex with DNA, bound to the active sites of both the 3'-phosphatase and 5'-kinase domains, thereby providing a comprehensive picture of DNA end recognition by this enzyme.

With an *E.coli* expression construct encoding a truncated form of the murine protein (PNK Δ FHA), we were able to produce initial crystals of the ligand-free (or *apo*) form of the enzyme. Diffraction data were collected on beamline I03 to a resolution of 1.65 Å, and a molecular replacement solution obtained with PDB: 1YJ5 as a search model.

Subsequent crystals with single-stranded DNA (ssDNA), engaged with the phosphatase domain, were obtained by incubation of PNK Δ FHA with a synthetic oligonucleotide in the presence of a 10-fold excess of Mg²⁺-ATP. Crystals only appeared from screens after several weeks at 4 °C. Examination of initial difference maps obtained from a 2.0 Å dataset collected in-house, revealed that ssDNA was indeed bound to the phosphatase domain, but at only relatively low occupancy. Additional soaking of the crystals before

cryoprotection, in precipitant supplemented with 0.5 mM of the same oligonucleotide, was sufficient to resolve the issue.

The ssDNA was found to sit in a narrow channel traversing the surface of the phosphatase domain. In close proximity to the DNA, was a well-ordered magnesium ion coordinated by the side-chains of amino acids Asp170 and Asp288, as well as the backbone carbonyl of Asp172 (Fig. 1A). The location and coordination of the ion identified it as the essential cofactor required for the phosphatase activity of the enzyme. Of the five bases comprising the co-crystallised ssDNA (5'-GTCAC-3'), only three were clearly resolved in maps. The bases of C3 and A4 are stacked against each other, and are themselves sandwiched between the side-chains of Lys225 and Phe184 (Fig. 1B). The terminal base C5 is however rotated with respect to the other bases, sitting between the side-chains of Phe184 and Phe30; imposing conformational restrictions on the phosphate group connecting bases A4 and C5 and preventing productive engagement with the active site. *A bona fide*

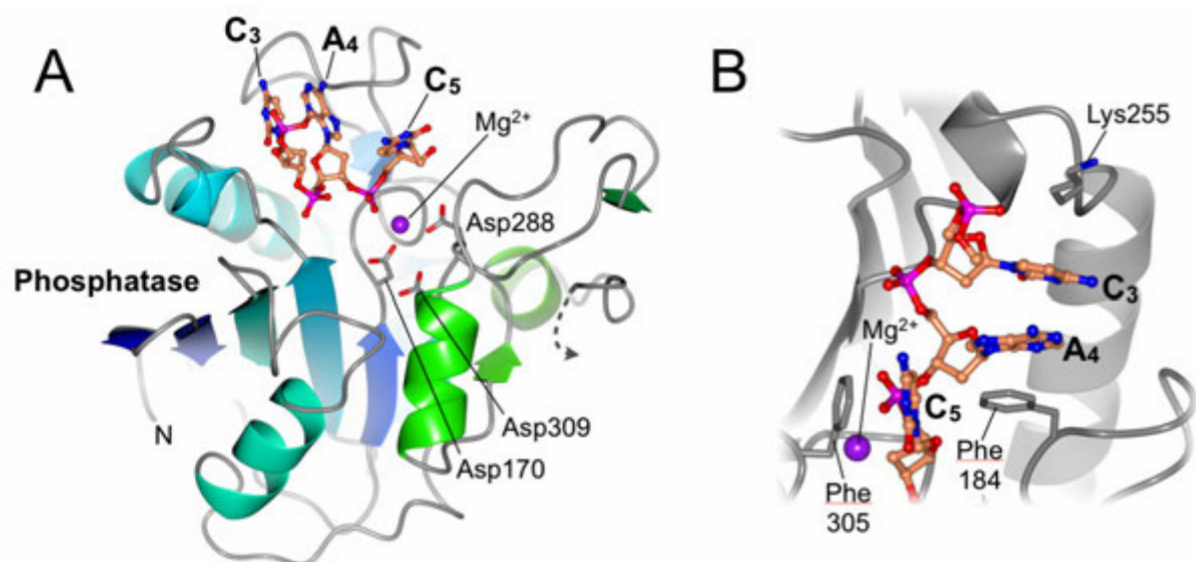


Figure 1: (A) Secondary structure cartoon representation of the phosphatase domain in complex with a short single-stranded oligonucleotide (PNK-DNA1). Key amino acids involved in coordinating the essential magnesium co-factor are also shown. (B) Molecular details of the base-stacking interactions made by the bound oligonucleotide.

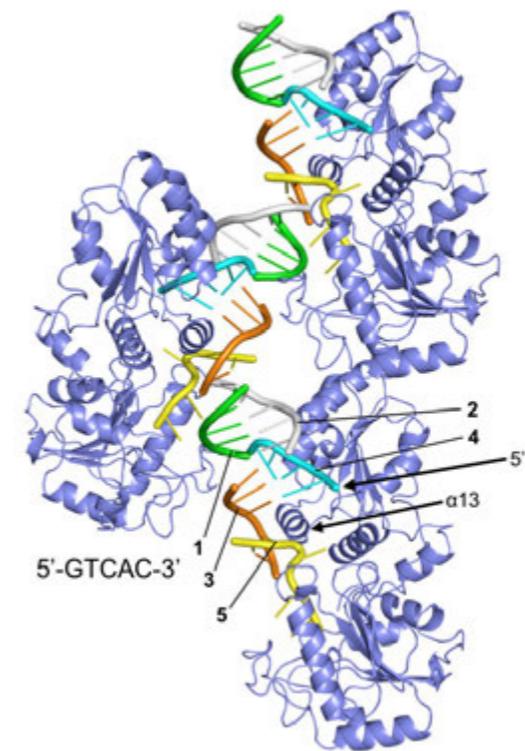


Figure 2: A pseudo-continuous nicked DNA duplex, formed by five separate copies of the 5'-GTCAC-3' oligonucleotide in the asymmetric unit, builds the crystal lattice in the PNK-DNA2 complex.

3'-terminal phosphate would, however, be unencumbered, and readily hydrolysed. The dimensions of the DNA binding channel would also preclude binding of duplex DNA, therefore providing an explanation for the *in vitro* observations that PNK preferentially dephosphorylates either ss- or dsDNA with at least a 3 nucleotide 3' overhang¹.

Despite exhaustive trials with the wild-type protein and conventional nicked or gapped double-stranded DNA substrates (i.e. those generated by annealing of three separate oligonucleotides), we were unable to obtain crystals with DNA bound to the kinase domain. We therefore tried a number of alternative strategies, with success ultimately resulting from incubation of a phosphatase-inactive version of the enzyme (D170N) with Mn²⁺-ATP and a 10-fold excess of ssDNA. Diffraction data for this crystal form were collected on beamline I02, to a resolution of 2.15 Å.

Interestingly, the asymmetric unit of these crystals contains a single copy of PNK, associated with five copies of the 5'-GTCAC-3' oligonucleotide that are annealed to each other to form a pseudo-continuous nicked DNA duplex, which then builds the crystal lattice (Fig. 2). From examination of experimental maps, it was also evident that the enzyme had turned over during crystallogensis, as the 5' ends of each oligonucleotide were phosphorylated, and a residual molecule of ADP was bound to the active site.

The nick or discontinuity in the DNA backbone is recognised through

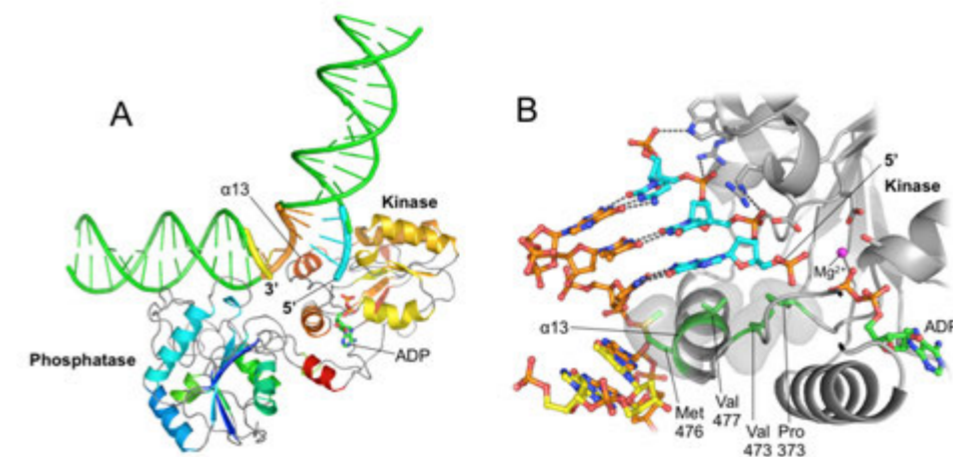


Figure 3: (A) Molecular model for binding of an extended nicked DNA substrate to PNK, productively engaged with the kinase domain. The extended DNA is bent by ~70° by its interaction with PNK and through insertion of helix 13 into the path of the bound duplex. (B) A hydrophobic 'wedge', which assists access to the internal 5' DNA end, is formed from amino acids Pro373, Val473, Val477 and Met476.

insertion of a helix from the kinase domain (α 13) into the path of the DNA duplex, causing a substantial bend (~70°), which provides access to the incoming substrate 5' hydroxyl (Fig. 3A). The side-chains of Met476 and Val477 from helix 13 form part of a hydrophobic surface or wedge, upon which the base pairs both 5' and 3' to the nick can stack (Fig. 3B).

Our crystal structures therefore provide a definitive view of the interaction of PNK with both of its known substrates and fully explains the distinctive and individual specificities of both the phosphatase and kinase functions. With clinical interest now growing in PNK as a therapeutic target^{3,4} for the treatment of cancer, our methodologies and data also provide the molecular framework for development of small molecule inhibitors, targeting either or both enzymatic activities.

The coordinates for each of the structures, PNK-APO, PNK-DNA1 and PNK-DNA2 have been deposited in the Protein Data Bank, under accession codes 3zv1, 3zvm and 3zvn, respectively.

References

- Jilani, A., Ramotar, D., Slack, C., Ong, C., Yang, X.M., Scherer, S.W., and Lasko, D.D., Molecular Cloning of the Human Gene, *PNKP*, Encoding a Polynucleotide Kinase 3'-Phosphatase and Evidence for Its Role in Repair of DNA Strand Breaks Caused by Oxidative Damage, *J Biol Chem*. **274**, 24176-24186 (1999).
- Bernstein, N.K. *et al.*, The Molecular Architecture of the Mammalian DNA Repair Enzyme, Polynucleotide Kinase, *Molecular Cell*. **17**, 657-670 (2005).
- Allinson, S.L., DNA end-processing enzyme polynucleotide kinase as a potential target in the treatment of cancer, *Future Oncol*. **6**, 1031-1042 (2010).
- Freschauf, G.K. *et al.*, Identification of a Small Molecule Inhibitor of the Human DNA Repair Enzyme Polynucleotide Kinase/Phosphatase, *Cancer Res*. **69**, 7739-7746 (2009).

Funding Acknowledgements

This work was supported by a Cancer Research UK programme grant C302/A8265 and Infrastructure Support Grant C302/A7803.

DOI 10.1016/j.molcel.2011.08.036

Understanding HIV cellular defence mechanism by determining the structure of deoxynucleotide triphosphate triphosphohydrolase SAMHD1

Goldstone, D.C., Ennis-Adeniran, V., Hedden, J.J., Groom, H.C., Rice, G.I., Christodoulou, E., Walker, P.A., Kelly, G., Haire, L.F., Yap, M.W., Carvalho, L.P., Stoye, J.P., Crow, Y.J., Taylor, I.A., Webb, M., HIV-1 restriction factor SAMHD1 is a deoxynucleoside triphosphate triphosphohydrolase. *Nature* **480**, 379-382 (2011)

Lentiviruses are associated with chronic disease states in a variety of mammals. In humans the HIV-1 lentivirus is the aetiological agent of AIDS, a disease that affects 34 million people worldwide and is responsible for 1.8 million annual deaths. In order to combat lentiviruses and other retroviruses, cells have evolved restriction factors that in some cases are able to inhibit infection. SAMHD1 is a protein originally associated with the human infantile disease Aicardi-Goutières syndrome (AGS). Additionally, it is the latest of the human restriction factors to be discovered and is responsible for the inhibition of HIV-1 infection of myeloid derived dendritic cells (MDDCs) and macrophages (MDMs). Using the tuneable beamline I04, we determined the structure of the catalytic core of SAMHD1 and in complementary biochemical studies demonstrated that SAMHD1 is a dGTP-activated enzyme that catalyses the hydrolysis of deoxyribonucleoside triphosphates to the component nucleoside and inorganic triphosphate. Based on these data and previous virological studies we have proposed that this activity acts to reduce the level of the cellular dNTP pool and is responsible for the inhibition of HIV-1 replication observed in MDDCs and MDMs by preventing productive reverse transcription.

SAMHD1 was originally identified in a human dendritic cell cDNA library as an orthologue of the mouse IFN- γ -induced gene *Mg11* and is highly expressed in dendritic cells and other cells of the myeloid lineage^{1,2}. Mutations in SAMHD1 are associated with AGS; a severe genetic infantile encephalopathy characterised by chronic cerebrospinal fluid lymphocytosis, elevated levels of α -interferon and likened to congenital viral infection³. More recently, SAMHD1 has been identified as an HIV-1 restriction factor that inhibits early stage viral replication in MDDCs and MDMs^{1,2}. In addition, it has been demonstrated that the lentiviral accessory protein Vpx is able to relieve SAMHD1 mediated inhibition of HIV-1 by transferring SAMHD1 to the DDB1/CUL4A/DCAF1 E3 ubiquitin ligase complex for proteasome-dependent degradation^{1,2}. SAMHD1 is a multidomain protein, containing a unique arrangement of a sterile alpha motif (SAM) domain and a phosphohydrolase HD domain. SAM domains are found in many diverse signalling molecules and serve as protein interaction modules that can bind to other SAM domains and also to non-SAM containing proteins⁴. The HD domain is characterised by two catalytic histidine and aspartic acid residues and defines a superfamily of metal-dependent phosphohydrolases⁵. The fact that other proteins associated with AGS have known nucleic acid metabolising functions^{6,7}, combined with the potential phosphohydrolase activity associated with the HD motif, prompted us to analyse the hydrolytic activity and substrate specificity of SAMHD1⁸. A variety of nucleotides, deoxynucleotides and nucleic acid substrates were assessed. No activity against nucleoside triphosphate or polymeric nucleic acids was observed. However, in the presence of dGTP, SAMHD1 rapidly hydrolysed deoxynucleoside triphosphates (dATP, TTP, dCTP and dGTP) to constituent deoxynucleoside and inorganic triphosphate. Thus, SAMHD1 is an allosterically activated dGTP dependent deoxynucleoside triphosphate triphosphohydrolase, an activity that is unprecedented in eukaryotes.

In order to learn more about SAMHD1 activity and its function in restriction of HIV-1, we next determined the structure of the catalytic core of the enzyme (residues 120-626; SAMHD1cc) using SAD methods at beamline I04 at Diamond Light Source. The structure of a SAMHD1cc dimer is shown in Fig. 1.

In the crystal, SAMHD1cc forms a dimer where each molecule comprises nineteen α -helices (α 1- α 19) and nine β -strands (β 1- β 9) arranged in a

mixed α/β fold. Within each monomer the secondary structure elements pack into a large domain (residues 120-451) containing a major and minor lobe, together with a smaller C-terminal region (residues 455-583). The homodimer interface buries approximately 2000 \AA^2 of surface and, consistent

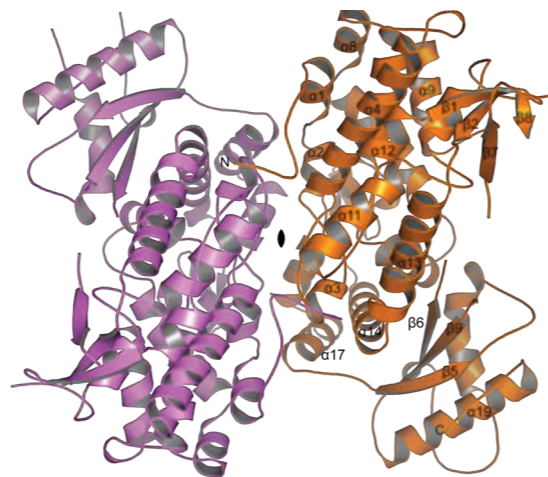


Figure 1: Crystal structure of the catalytic core of SAMHD1. A ribbon representation of the SAMHD1cc dimer viewed down the two-fold dimer axis. Each monomer is coloured separately and the secondary structure elements are labelled sequentially from the N- to C-terminus on a single chain.

with the crystal structure, solution hydrodynamic data demonstrate that SAMHD1 is dimeric in solution ($K_d \sim 5 \mu\text{M}$). The active site of the molecule is located in a deep cavity between the major and minor lobe. It is marked by the presence of a phosphate ion and comprises residues from helices α 4, α 5, α 6, α 7 and α 11 that include the conserved HD motifs, together with other surrounding aspartate, histidine and arginine side-chains that co-ordinate the phosphate and a tightly bound zinc ion (Fig. 2A).

The phosphate ion was fortuitously included in the crystallisation condition, but its close association with the zinc ion, and its proximity to the HD catalytic motif helps to define the active site serving as a marker for the likely position of a substrate α -nucleotidyl phosphate. The zinc ion is at the centre of the active site and is coordinated by the side chains of His206 and Asp207, a phosphate oxygen and the side chains of His167 and Asp311. The side chains of the two zinc-coordinating aspartate residues, 207 and 311, also form hydrogen bonds with other phosphate oxygens,

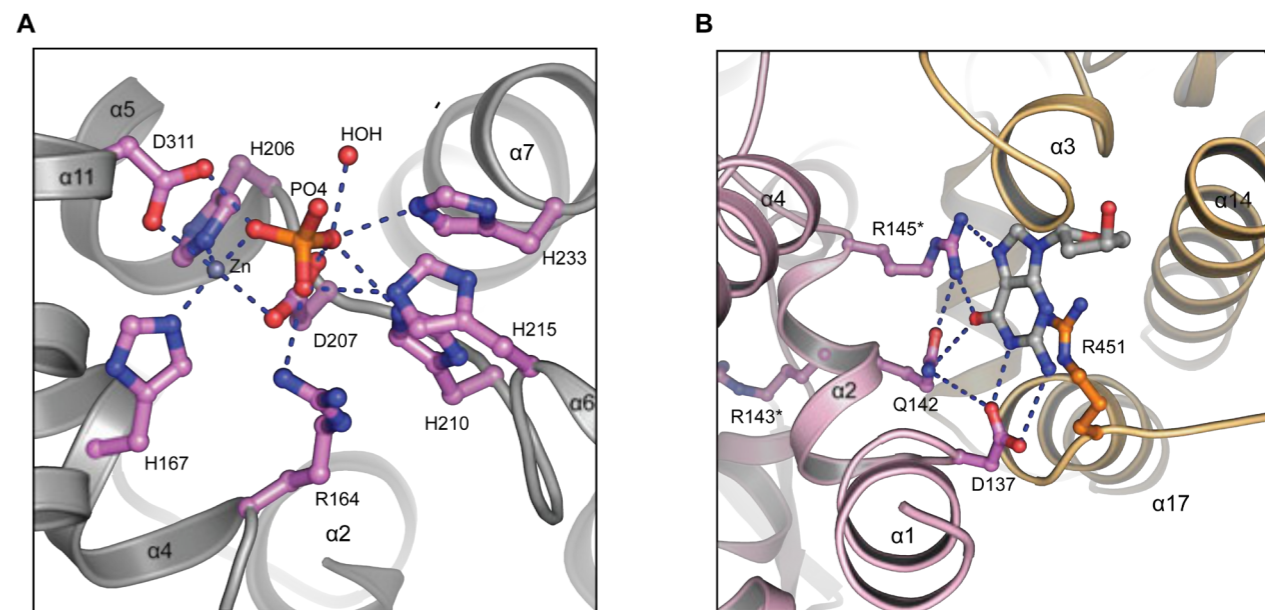


Figure 2: SAMHD1 active and allosteric sites. (A) The active site of SAMHD1 is located at the intersection of helices α 4, α 5, α 7 and α 11 in a deep cavity and contains tightly bound zinc and phosphate ions. The histidine, aspartate and arginine residues that line the cavity and coordinate the zinc and phosphate are shown in stick representation. Hydrogen bonding interactions are displayed as dashed lines. (B) The allosteric site is located at the dimer interface and contains residues mainly from helix α 2. Hydrogen bonds from the side-chains of Asp137, Gln142 and Arg145, located on α 2, to the functional groups on the guanine base are shown as dashed lines. Arg143 is located on the opposite face of α 2 with the guanidinium side chain protruding into the back of the active site. Residues highlighted with asterisks are those where mutations are found in AGS patients.

extending the linkage between the zinc and phosphate ions. Further salt bridges between the phosphate and the side chains of four basic residues adjacent to the active site, Arg164 and His210, 215 and 233, are also apparent completing this network of active site interactions. The importance of these phosphate and zinc co-ordinating residues is clear as, although an exact mechanism for SAMHD1 mediated triphosphate hydrolysis is still to be determined, amino acid substitution of any of these residues results in catalytically deficient or inactive SAMHD1⁸.

A clue to the mechanism of allosteric activation of SAMHD1 by dGTP comes from a comparison of the SAMHD1cc structure with a related HD protein from *Aquifex aeolicus* (PDB code; 2HEK). At the dimer interface of the 2HEK structure two nucleotide-binding sites are present, each containing GDP. Examination of the residues that interact with the guanine base in 2HEK reveals that they are conserved in SAMHD1 and equate to residues Asp137, Gln142, Arg145 and Arg451. This analysis strongly suggests the location of the allosteric nucleotide binding sites in SAMHD1 and enables us to model guanine-nucleotides into the SAMHD1 structure. In the resulting model (Fig.2B), Asp137, Gln142 and Arg145 are positioned to recognise the base edge accounting for guanine selectivity at the allosteric sites of SAMHD1, whilst Arg451 from the other monomer makes a stabilising stacking interaction. Asp137 is located in the helix α 1- α 2 loop whilst Gln142 and Arg145 are on the same face of helix α 2. Arg143 neighbours both Gln142 and Arg145 but is located on the opposing face of the α 2 helix where its guanidinium side chain protrudes into the back of the active site making hydrogen-bonds to the main-chain carbonyls of Leu208 and His210. In this way the presence of bound dGTP in the allosteric site can be sensed and Arg143 is likely to be key to allosteric activation occupying the pivotal position linking the active and allosteric sites facilitating communication between residues that recognise the bound base and those involved in catalysis. Importantly, several AGS mutations also cluster around the allosteric site (Arg145-Gln, Arg143C-Cys, Arg143-His and Gly209-Ser) and likely cause loss of SAMHD1 function in AGS patients by interfering with the allosteric activation mechanism.

In terms of restriction, in order to successfully replicate, HIV-1 has to efficiently reverse transcribe its genome and this is critically dependent on the abundance of dNTPs available to the virus. Analysis of the expression pattern of SAMHD1 reveals that although basal levels are found in most tissues, much higher SAMHD1 expression is found in the myeloid cells that are refractive to HIV-1. Additionally, the concentration of the dNTP pool in non-permissive MDDCs and MDMs is significantly lower compared to

permissive T-cells. Our structural and biochemical studies have now defined a potent SAMHD1 dNTP triphosphohydrolase activity that links strongly with these *in vivo* observations. In combination these data now provide the basis of a mechanism for SAMHD1 restriction where the enzyme acts to reduce the cellular dNTP pool preventing reverse transcription and replication of HIV-1.

References

1. Laguette, N. *et al.* SAMHD1 is the dendritic- and myeloid-cell-specific HIV-1 restriction factor counteracted by Vpx. *Nature* **474**, 654-657 (2011).
2. Hrecka, K. *et al.* Vpx relieves inhibition of HIV-1 infection of macrophages mediated by the SAMHD1 protein. *Nature* **474**, 658-661 (2011).
3. Rice, G.I. *et al.* Mutations involved in Aicardi-Goutieres syndrome implicate SAMHD1 as regulator of the innate immune response. *Nat Genet.* **41**, 829-832 (2009).
4. Kim, C.A. & Bowie, J.U. SAM domains: uniform structure, diversity of function. *Trends Biochem Sci.* **28**, 625-628 (2003).
5. Aravind, L. & Koonin, E.V. The HD domain defines a new superfamily of metal-dependent phosphohydrolases. *Trends Biochem Sci.* **23**, 469-472 (1998).
6. Lindahl, T., Barnes, D. E., Yang, Y. G. & Robins, P. Biochemical properties of mammalian TREX1 and its association with DNA replication and inherited inflammatory disease. *Biochem Soc Trans.* **37**, 535-538 (2009).
7. Rydberg, B. & Game, J. Excision of misincorporated ribonucleotides in DNA by RNase H (type 2) and FEN-1 in cell-free extracts. *Proc Natl Acad Sci U S A* **99**, 16654-16659 (2002).
8. Goldstone, D.C. *et al.* HIV-1 restriction factor SAMHD1 is a deoxynucleoside triphosphate triphosphohydrolase. *Nature* **480**, 379-382 (2011).

Funding Acknowledgements

This work was funded by the Medical Research Council, UK.

DOI 10.1038/nature10623

Structural and mechanistic insights into PAR hydrolysis by the PARG enzyme poly(ADP-ribose) glycohydrolase

Slade, D., Dunstan, M.S., Barkauskaite, E., Weston, R., Lafite, P., Dixon, N., Ahel, M., Leys, D. & Ahel, I. The structure and catalytic mechanism of a poly(ADP-ribose) glycohydrolase. *Nature* **477**(7366), 616-20 (2011)

A key role in many critical cellular pathways, from DNA repair and chromatin stability to mitotic progression and caspase-independent cell death¹, plays poly(ADP-Ribosyl)ation, which is a reversible protein post-translational modification. While poly(ADP-ribose)polymerases (PARPs) are responsible for catalysing poly ADP-ribosylation using NAD as a substrate, poly(ADP-ribose) glycohydrolase (PARG) reverses the modification through hydrolysis of the unique ribose-ribose PAR bond to produce free ADP-ribose. These enzymes are vital for many biological processes – the absence of PARG activity leads to the accumulation of PAR and ultimately cell death². We were able to solve the first crystal structure of a PARG enzyme, revealing it is a distant member of the ubiquitous ADP-ribose-binding macro domain family³. PARG structures complexed with ADP-ribose have allowed us to propose a detailed model for PAR binding and catalysis by PARG. These structural insights provide a framework for understanding PARG activity in reversible protein poly(ADP-ribosyl)ation and for further study and therapeutic intervention.

The failure to maintain a stable genome has been linked to many disease states including cancer, neurodegeneration, immunological disorders and numerous developmental syndromes⁴. The poly (ADP-ribosyl)ation of proteins is an early step in the initiation of DNA damage repair in cells. The activation of nuclear poly(ADP-Ribosyl)ation enzymes such as poly(ADP-ribose) polymerase (PARPs) and poly(ADP-ribose) glycohydrolase (PARG) mediates the formation and degradation of the poly-ADP-ribose (PAR) modification. PARPs signal the presence of DNA damage and facilitate DNA repair. While PARP catalyses the addition of ADP-ribose units to DNA, histones, and various DNA repair enzymes, PARG is the key enzyme involved in the specific and efficient hydrolysis of the PAR ribose-ribose bond. Given the link between DNA repair and cancer, targeting poly(ADP-ribosyl)ation has attracted considerable attention in recent years and PARP inhibitors have already been shown to exhibit striking efficacy against hereditary breast and ovarian cancers⁵. PARG plays a key role in DNA repair and appears to possess a protective role within the cell, as the build up of PAR leads to apoptotic cell death. Moreover, increased PARG activity has been linked to uncontrolled cell proliferation and differentiation in glioma tumor dividing cells suggesting that PARG regulation may also have a crucial role in cancer⁶. Although the first PARG enzyme was discovered more than 40 years ago, until now there has been no structural data available for any PARG enzyme, hindering development of effective PARG specific inhibitors.

To address this, we solved a bacterial PARG crystal structure (from *Thermomonospora curvata*) both with and without ADP-ribose. The PARG structures reveal a core ADP-ribose-binding macrodomain fold with an additional ~50 amino acid N-terminal extension (Fig.1a). The diphosphate-binding loop that flanks one side of the ADP-ribose-binding cavity is highly conserved between PARG and other macrodomain structures, with ADP-ribose bound in a similar manner. In contrast, the opposite side of the PARG ADP-ribose-binding cavity is lined by a stretch of amino acids containing the PARG-specific GGG-X₆₋₈-QEE signature sequence (Fig.1a). The introduction of this 'PARG-specific loop' would seem the reason why only PARGs, and not other macrodomain proteins, are catalytically active. We speculate that the PARG-specific loop has been introduced into the macrodomain fold to position the Glu115 side chain into the PARG active site to catalyse hydrolysis (Fig.1b).

To provide further insight into PAR binding, an $\alpha(1'' \rightarrow 2')$ O-glycosidic linkage with an additional ADP-ribose group was modelled into the PARG active site (with P. Lafite, Université d'Orléans, Orleans), creating a model of PARG in complex with di(ADP-ribose). Our models suggest that the

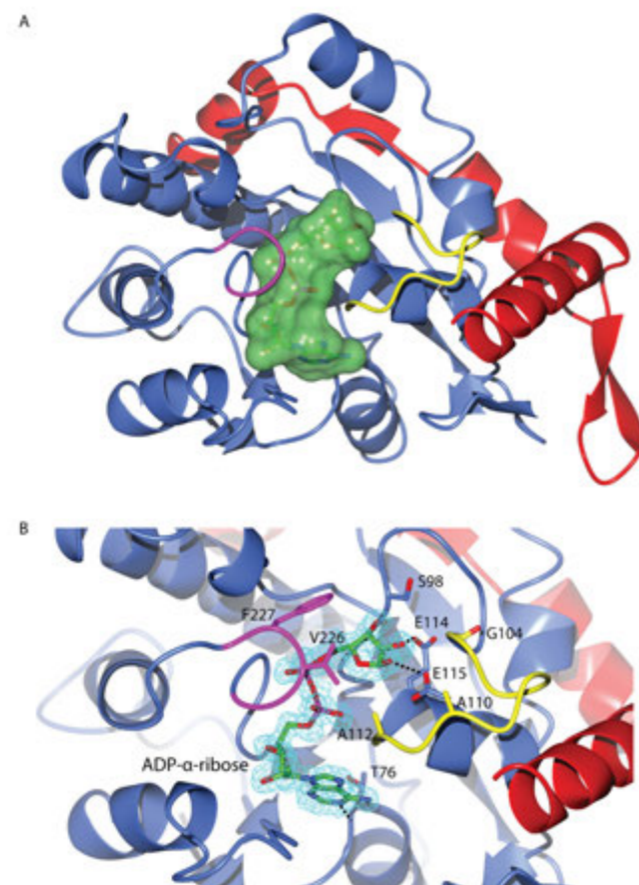


Figure 1: (a) Overall fold of PARG with the core macro domain depicted in blue, and the additional N-terminal extension in red. The bound ADP-ribose is shown in green van der Waals surface. The PARG-specific catalytic loop is shown in yellow, and the diphosphate-binding loop in magenta. (b) Detailed view of ADP-ribose bound in the PARG active site coloured as in (a). ADP-ribose is shown with the corresponding $2F_o - 2F_c$ (omit map) density contoured at 1.2σ in cyan. Key active site residues are represented in sticks with hydrogen bonds indicated by black dotted lines.

additional adenine moiety is partially enclosed by Ala 110, Ala 112 and Val 226 while the additional ribose' is in close contact with Ser 98 and Gly 104. Obvious binding sites for the additional phosphate and ribose' moieties could not be identified, suggesting that (bacterial) PARG is unlikely to make specific interactions with additional PAR elements. The bacterial PARG

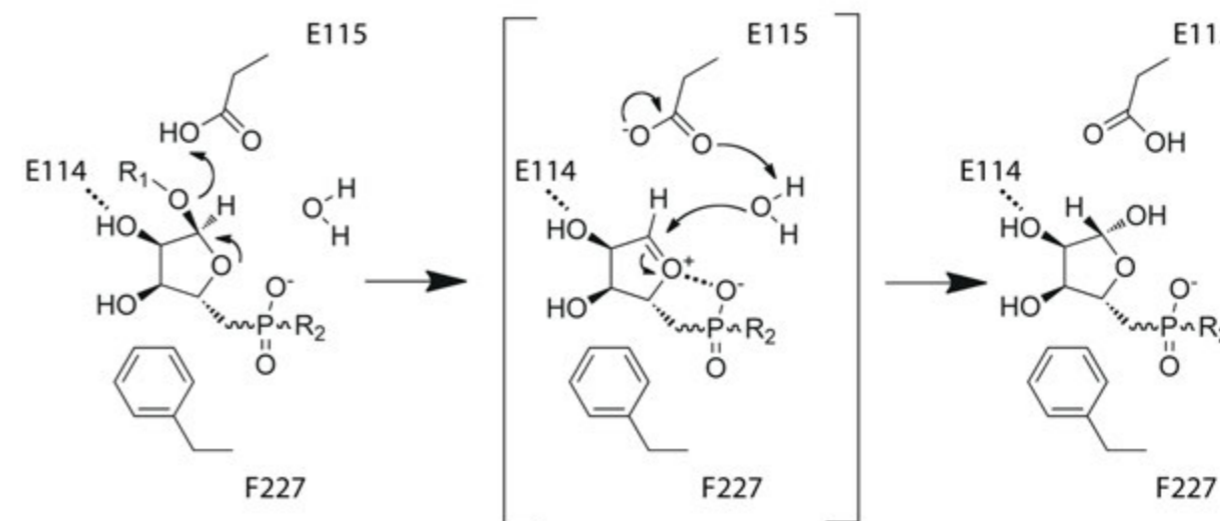


Figure 2: Proposed mechanism for PAR glycohydrolysis. R1 and R2 represent (n-1) PAR and terminal adenosine moieties respectively.

structure also reveals this enzyme is likely to be an exohydrolyse, as the protein structure does not provide sufficient space for any substituent on the bound ADP-ribose 2'-OH group.

The *T. curvata* PARG complex with ADP-ribose and the corresponding PAR-PARG model allow us to propose a mechanism for PARG catalysis. The key ribose-ribose PAR O-glycosidic linkage is in direct hydrogen-bonding contact with Glu 115. This supports the formation of a putative positively charged oxocarbenium intermediate concomitant with protonation of the (n-1) PAR ribose' 2'-OH leaving group by Glu 115. The barrier to oxocarbenium formation is lowered by electrostatic interaction with the diphosphate group (a contact enforced by the conserved Phe227). A water molecule present in the active site is ideally positioned to attack the oxocarbenium intermediate, activated through concomitant deprotonation by Glu 115, leading to the release of ADP-β-ribose' and (n-1) PAR (Fig. 2).

We tested our proposed mechanism by analysing the properties of PARG active site mutants (with I. Ahel, Patterson Institute, Manchester). Both Glu114Ala and Glu115Ala mutants were inactive, and binding studies revealed Glu115Ala had no effect on ligand binding, while Glu114Ala led to an approximate tenfold decrease in binding affinity. Mutations of Phe 227 implicated in positioning the terminal ribose' also render the enzyme inactive. Mutations of Ser 98 and Val 226, implicated by our model in binding the (n-1) ADP-ribose, greatly diminish *T. curvata* PARG activity. Importantly, mutations of the corresponding catalytic residues in human PARG (a more complex enzyme) have a very similar effect on the enzymatic activity, suggesting a universal structural and catalytic mechanism for bacterial and mammalian PARGs.

Our recent findings offer the first detailed structural and mechanistic insights into this intriguing protein family. These findings should help lay the

framework to unraveling the biochemical strategies regulating reversible poly(ADP-ribosyl)ation. We believe that our findings will provide the necessary tools for future studies that might ultimately lead to the development of small, cell-permeable PARG inhibitors and the potential to manipulate the physiology of health and disease by interfering with PAR metabolism.

References

- Hakme, A. *et al.* The expanding field of poly(ADP-ribosyl)ation reactions. *EMBO Rep.* **9**(11), 1094-1100 (2008).
- Koh, D.W. *et al.* Failure to degrade poly(ADP-ribose) causes increased sensitivity to cytotoxicity and early embryonic lethality. *Proceedings of the National Academy of Sciences of the United States of America.* **101**(51), 17699-17704 (2004).
- Karras, G.I. *et al.* The macro domain is an ADP-ribose binding module. *Embo Journal.* **24**(11), 1911-1920 (2005).
- McKinnon, P.J. DNA repair deficiency and neurological disease. *Nat Rev Neurosci.* **10**(2), 100-112 (2009).
- Fong, P.C. *et al.* Inhibition of Poly(ADP-Ribose) Polymerase in Tumors from BRCA Mutation Carriers. *New England Journal of Medicine.* **361**(2), 123-134 (2009).
- Seigny, M.B. *et al.* Expression and activity of poly(ADP-ribose) glycohydrolase in cultured astrocytes, neurons, and C6 glioma cells. *Brain research. Molecular brain research.* **117**(2), 213-20 (2003).

DOI 10.1038/nature10404

The structure of the protein BLF1: understanding the mechanism of the Vietnam time bomb

Cruz-Migoni, A., Hautbergue, G. M., Artymiuk, P. J., Baker, P. J., Bokori-Brown, M., Chang, C.-T., Dickman, M. J., Essex-Lopresti, A., Harding, S. V., Mahadi, N. M., Marshall, L. E., Mobbs, G. W., Mohamed, R., Nathan, S., Ngugi, S. A., Ong, C., Ooi, W. F., Partridge, L. J., Phillips, H. L., Raih, M. F., Ruzheinikov, S., Sarkar-Tyson, M., Sedelnikova, S. E., Smither, S. J., Tan, P., Titball, R. W., Wilson, S. A. & Rice, D. W. A *Burkholderia pseudomallei* Toxin Inhibits Helicase Activity of Translation Factor eIF4A. *Science*. **334**. 821-824 (2011)

The structure of BPSL1549, a protein of unknown function from *Burkholderia pseudomallei*, was determined to high resolution to reveal a striking similarity to the *E. coli* cytotoxic necrotising factor. This strongly suggested that it might function as a site specific glutamine deamidase inactivating a critical component of the cell responsible for viability and therefore be an important weapon in the armoury of this pathogen, which is the causative agent of the disease, melioidosis. Subsequent work confirmed that BPSL1549 acted as a potent cytotoxin against eukaryotic cells and was lethal when administered to mice. Biochemical studies established that BPSL1549 promotes deamidation of Gln³³⁹ of the translation initiation factor eIF4A, abolishing its helicase activity and inhibiting translation. With the identification of its function BPSL1549 was renamed *Burkholderia* Lethal Factor 1 (BLF1).

Exactly one hundred years ago, the causative agent of the disease melioidosis, a bacterium that today goes under the name *Burkholderia pseudomallei*, was first described by Alfred Whitmore, a British pathologist working in Burma¹. For the next fifty years, until the Vietnam War, when the American military realised that troops fighting in the conflict were prone to this infection, the disease languished in virtual obscurity. Nevertheless, along with HIV and tuberculosis, melioidosis is currently one of the top three causes of death by infectious disease in parts of Southeast Asia. Today, with the bacterium recognised as being multi-drug resistant and leading to mortality rates as high as 40% amongst individuals with acute forms of the disease and with the classification of this particular pathogen as a potential biological weapon, the pace of research has accelerated.²

One finding that has emerged from this increased attention is that in some regions of Southeast Asia, where the bacterium flourishes in moist soil and stagnant water, up to 80% of people have antibodies against *B. pseudomallei* by the age of 4 years.³ Whilst, for reasons that are not fully understood, most of these individuals are apparently asymptomatic, the discovery of the remarkable ability of the bacterium to remain latent in an infected individual for decades before symptoms emerge has given rise to considerable concerns. Indeed, the realisation that more than 250,000 troops serving in Vietnam were serologically positive resulted in the pathogen acquiring a new, chilling nickname: the 'Vietnam Time Bomb'.² Infection by the bacterium can occur through contact of wounds with contaminated soil or water, but the most important route is thought to be by inhalation of airborne soil particles. This provides an explanation as to why, in the Vietnam War, it was the helicopter crews who were first identified as belonging to a particular risk group. Despite the widespread distribution and the severity of the disease, one area where understanding was particularly lacking was the absence of any identifiable mechanism whereby the bacterium killed its host. Working with partners at the Malaysia Genome Institute and Universiti Kebangsaan Malaysia we sought to address this gap in understanding through a programme of structure determination on proteins of unknown function from *B. pseudomallei*.

One of the first structures to emerge from this programme was that of the protein encoded by the gene *bpsl1549*. This 23 kDa protein of unknown function had been identified as being heavily expressed in pathogenic, but not in non-pathogenic, strains of *Burkholderia*. Whilst homologues of BPSL1549 could readily be identified in different strains of *Burkholderia*, bioinformatic analysis failed to identify a homologue in any other species hampering the assignment of a function to this protein and suggesting

that it was an orphan. The determination of the structure of BPSL1549 thus became a high priority.

Crystals of BPSL1549 were obtained and found to diffract to atomic resolution on synchrotron sources. Using data collected to 1.04 Å, the structure was solved by exploiting the anomalous signal from the selenium atoms of a selenomethionine derivatised sample of the protein. This led to the production of an extremely high quality electron density map from which a model of the structure was readily constructed. The fold of the protein was unremarkable and was seen to consist of a sandwich of two curved mixed beta sheets decorated on the outside by alpha helices and loops (Fig. 1A). Unfortunately, the identification of the function of the protein from its structure was initially hampered by the fact that, with the only recognisable homologues being from other strains of *Burkholderia* with virtually identical sequences, clusters of conserved residues that might have represented the active site could not be recognised.

Crucially, comparison of the fold of BPSL1549 showed that it was similar to that of the catalytic domain of an *E. coli* toxin, the cytotoxic necrotising factor 1 (CNF1-C). Whilst eleven strands of the beta sandwich of these two proteins shared identical sequence order and direction, on the peripheries of the structures there were major differences in both the extensions to the β-strands and the helices and loops, with only one helix in common. The structure comparison also showed that, despite the absence of any recognisable sequence similarity, six residues, which were known to be important in the activity of CNF1-C, were spatially conserved in BPSL1549 (Fig. 1B) including a critical cysteine whose mutation had been shown to lead to the total loss of biological activity of the *E. coli* toxin.

CNF1-C inactivates Rho GTPases by deamidation of a glutamine necessary for GTPase hydrolysis, thereby affecting actin cytoskeleton assembly. The conservation of the fold and key catalytic residues with CNF1-C immediately suggested BPSL1549 might also be cytotoxic via a glutamine deamidase activity. However, given that the molecular surface around the BPSL1549 active site cavity (Fig. 1C) was broader and shallower than that of CNF1-C (Fig. 1D), this suggested that its molecular target was different. With colleagues in Sheffield, Exeter and DSTL, functional studies quickly showed that BPSL1549 was toxic and that, as with CNF1-C, the toxic activity could be abolished by mutagenesis of the structurally equivalent cysteine residue. Subsequent studies showed that the deletion of the gene encoding BPSL1549 from the *Burkholderia* genome led to significant attenuation of the pathogenicity of the mutant strain indicating that this toxin was an

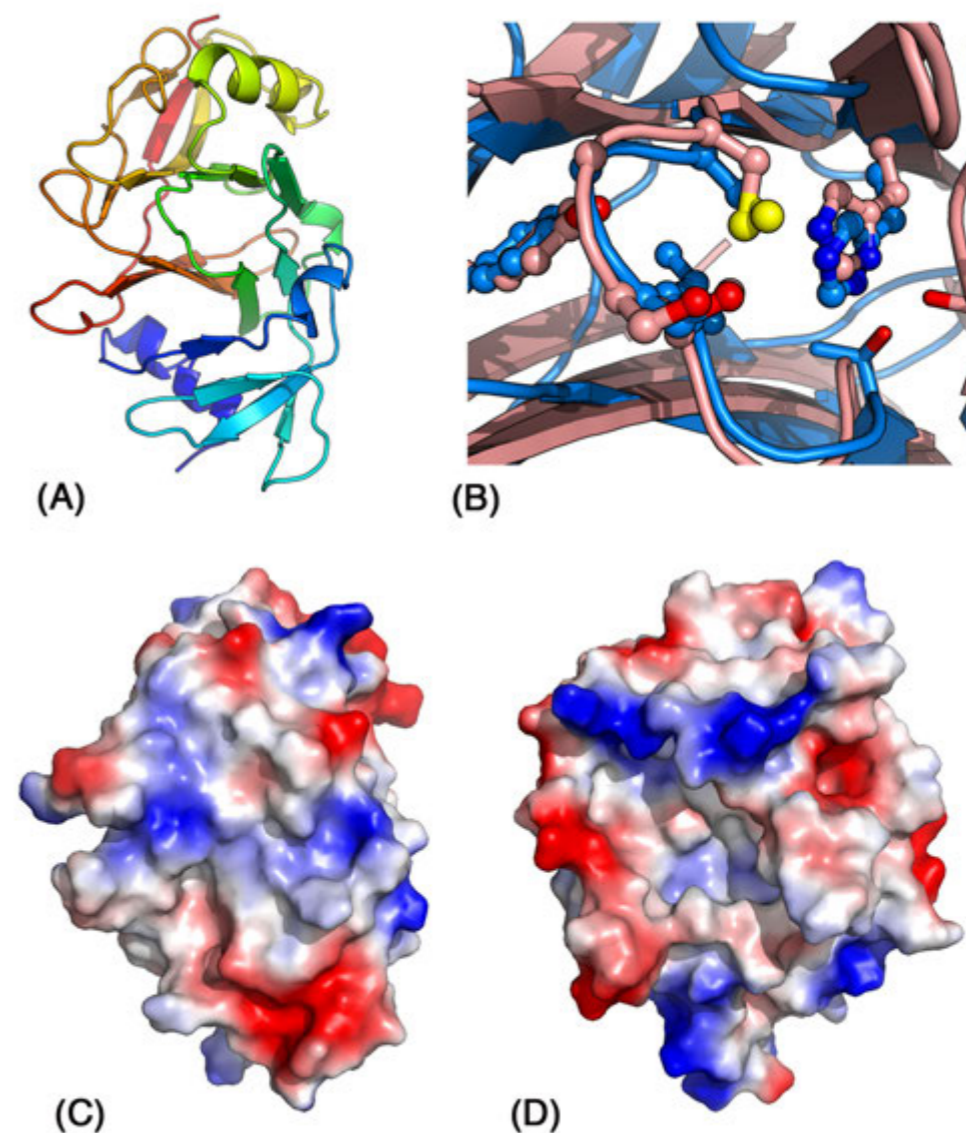


Figure 1: Structural analysis of BPSL1549, now renamed BLF1. (A) Cartoon representation of BPSL1549 with rainbow colours (N-terminus blue, C-terminus red). (B) Superposition of BLF1 (pale blue) and CNF1-C (pale red) around their active sites with residues strongly conserved between the two toxins, including the critical cysteine (centre, yellow sulphur) and histidine (centre right), highlighted. (C) View of electrostatic surface of BLF1 with active site at centre; and (D) equivalent view of CNF1, showing the differences in shape and character of the surfaces around their respective active sites.

important weapon in the armoury of this bacterium, leading us to rename the protein, *Burkholderia* Lethal Factor 1 (BLF1).

With colleagues in Sheffield, BLF1 binding-partners were purified from human cell extracts. This led to the identification of an interaction between BLF1 and the eukaryotic initiation factor 4A (eIF4A), a RNA helicase that serves as a critical component of the human protein translational machinery. This strongly suggested that BLF1 might inhibit translation. Further studies confirmed this hypothesis and showed that translation was stalled upon exposure to cells with the toxin. Subsequently, mass spectrometry revealed that BLF1 catalyses the deamidation of Gln 339 of eIF4A to glutamate, a modification that was confirmed to lead to the abolition of its RNA helicase activity and to block protein synthesis.

The insights provided by the structure determination of BLF1 were pivotal in uncovering its biological role and have opened the door to the possible design of inhibitors that might, in the future, be useful in ameliorating the effects of the disease while other treatments seek to kill the bacteria. However, the research into this obscure bacterium could well have another important consequence in that it might be possible to harness the toxicity of BLF1 in killing rapidly dividing cancer cells. Work on this is now underway.

References

- Whitmore, A. & Krishnaswami, C.S. An account of the discovery of a hitherto undescribed infective disease occurring among the population of Rangoon. *Indian Med Gaz.* **92**, 262–267 (1912).
- Stone, R. Racing to Defuse a Bacterial Time Bomb. *Science*. **317**, 1022–1024 (2007).
- Wiersinga, W. J., van der Poll, T., White, N. J., Day, N. P. & Peacock, S. J. *Nat. Rev. Microbiol.* **4**, 272–282 (2006).

Funding Acknowledgements

We thank the Biotechnology and Biological Sciences Research Council UK; the Ministry of Science, Technology and Innovation, Government of Malaysia; and the British Council PMI-2 Initiative for financial support.

Research carried out at Diamond Light Source on beamline I04 and at the ESRF on ID29.

DOI 10.1126/science.1211915

Structural insight into the attachment of anionic polymers to the Gram positive cell wall

Kawai, Y., Marles-Wright, J., Cleverley, R.M., Emmins, R., Ishikawa, S., Kuwano, M., Heinz, N., Bui, N.K., Hoyland, C.N., Ogasawara, N., Lewis, R.J., Vollmer, W., Daniel, R.A. & Errington, J. A widespread family of bacterial cell wall assembly proteins. *EMBO J.* **30**, 4931-41 (2011)

The bacterial cell wall maintains the structural integrity of the cell and enables bacteria to survive in a wide range of environments. The Gram-positive bacteria include many important human pathogens, including *Streptococcus pneumoniae*, the causative agent of invasive pneumococcal diseases. In these bacteria, the cell wall contains two major components: peptidoglycan, the target of many successful antibiotics and anionic cell wall polymers, which are attached to the peptidoglycan. These polymers include wall teichoic acids (WTAs) and acidic capsular polysaccharides which play a wide range of roles within the cell, including the control of autolytic activity, antigenicity and innate immune recognition, and the resistance to antibiotics. The addition of WTAs to peptidoglycan is vital to cell wall architecture and function. We identified the widespread LytR-Cps2A-Psr (LCP) protein family as the most likely candidates for the enzymes required for anionic polymer attachment. In order to gain insight into the function of this enzyme class, we determined the crystal structure of *S. pneumoniae* Cps2A. This structure, along with functional data, confirms that this family of proteins attach anionic polymers to peptidoglycan. The knowledge gained of this protein family provides a foundation for the exploration of these enzymes as novel targets for antibiotic development.

The cell wall is crucial for the maintenance of the structural integrity and the characteristic shape of bacterial cells. In Gram-positive bacteria, the cell wall has two major components: peptidoglycan (PG), whose synthesis is the target for the highly successful β -lactam and glycopeptide antibiotics and the PG-attached anionic cell wall polymers (APs), which include wall teichoic acids (WTAs) and acidic polysaccharides. The WTAs and their lipid-linked variant, the lipoteichoic acids, have a wide range of important roles in the cell, including the control of autolytic activity, antigenicity and innate immune recognition, pathogenicity, cation homeostasis, and cell elongation and division¹. Most of the steps involved in the synthesis of WTA are known²; the polymer is synthesised in the cytoplasm and then translocated across the membrane by an ABC transporter³ before covalent attachment to the PG outside the cell by a phosphotransferase enzyme⁴. The physical connection to the cell wall is essential for the proper function of the WTA, but the enzyme catalysing this final step has thus far not been identified.

Deletion of different components of the gene cluster responsible for WTA synthesis in the Gram-positive model organism, *Bacillus subtilis*, has

various effects, from severe growth defects to lethality. A number of genes encoding the poorly characterised LytR-Cps2A-Psr (LCP) family of proteins were identified within the WTA locus in *B. subtilis*, with homologues widely distributed across Gram-positive bacterial phyla. These proteins possess an N-terminal trans-membrane (TM) region of one to three TM helices and a major C-terminal catalytic domain. To gain insight into the role the LCP protein family plays in WTA synthesis, we determined the structure of the soluble portion of the Cps2A protein from *S. pneumoniae* by selenomethionine SAD using diffraction data⁶ collected on beamline I02.

The structure of Cps2A comprises two distinct domains: domain 1, the accessory domain; and domain 2, the LCP domain (Fig. 1). The accessory domain has a three-layered α - β - α fold that has weak secondary structure homology with a large variety of other proteins, including the mono-nucleoside triphosphate hydrolases and phospho-receiver domains of response regulators. This domain is not conserved in the wider family of LCP proteins and is found only in the sequences of streptococcal LCP-like proteins. Its distribution and lack of significant homology to other known proteins precludes functional assignment based on the structure. It is possible that this domain mediates interactions with the capsule, cell wall, or other molecules involved in cell wall homeostasis.

The conserved LCP domain also has an α - β - α architecture, with a central five-stranded β -sheet. It has no significant homology to any other protein family. Interestingly, a polyisoprenoid lipid was found in a pocket formed between the central β -sheet and the α -helices on one face of the protein (Fig. 2). This lipid was presumably incorporated into the protein during expression in the heterologous *Escherichia coli* host used for protein production. The structure of this lipid, modelled as mono-*trans*, octa-*cis* decaprenyl-phosphate, is consistent with this protein binding a lipid-linked capsule precursor. We subsequently determined the structure of this protein with an octaprenyl-pyrophosphate molecule in the lipid-binding site; again, this molecule was incorporated in the expression host. These lipids are intermediates in the synthesis of isoprenoid carrier lipids and are structurally equivalent to the undecaprenyl phosphate carrier lipid that the WTA is attached to during its synthesis. Indeed, we have recently determined by mass spectrometry that the recombinant form of the LCP homologue, YwfF from *Bacillus subtilis*, can be purified from *E. coli* with undecaprenyl phosphate bound⁷.

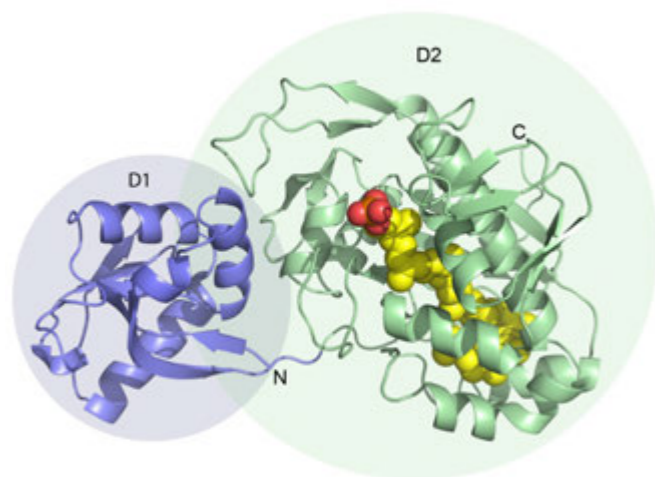


Figure 1: The structure of Cps2A from *S. pneumoniae*. Cartoon representation showing the domain architecture of the protein and the bound lipid ligand. The accessory domain (D1) is coloured blue, and the LCP domain (D2) is coloured green. The mono-*trans*, octa-*cis*-decaprenyl-phosphate lipid is shown as spheres, with yellow carbon atoms, orange phosphorous and red oxygens.

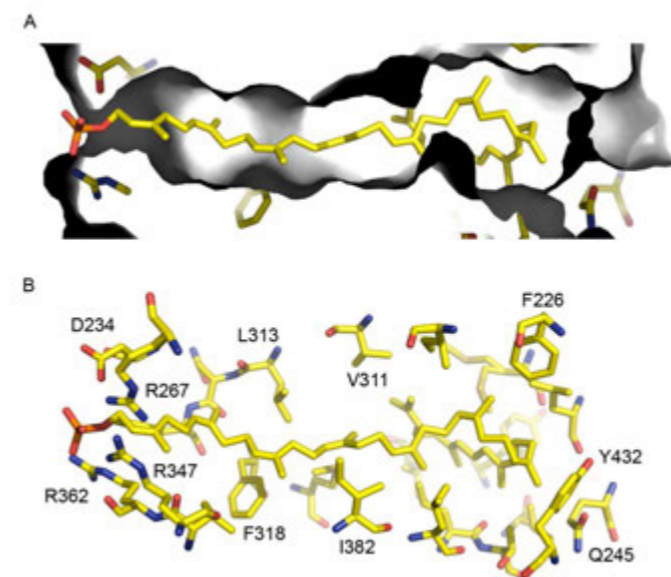


Figure 2: The Cps2A lipid binding site (A) View of the mono-*trans*, octa-*cis*-decaprenyl-phosphate lipid in the hydrophobic cleft of Cps2A, with the surface shown in grey and ligand and protein residues shown as coloured sticks. (B) The lipid binding pocket is lined with hydrophobic residues, with charged amino acids co-ordinating the phosphate group, which is solvent exposed.

The presence of the lipid within a conserved hydrophobic pocket in the core of the protein allowed the identification of the active site, rich in charged residues that are also maintained throughout the entire LCP family. This region of the protein places the phosphate groups, which would be covalently linked to the mature WTA chain, in position for phosphotransfer to the PG acceptor. Although we were unable to demonstrate WTA transfer to PG with these recombinant proteins, the failure of the assay can be rationalised because the proteins used are pre-loaded, in the *E. coli* expression host, with lipids that cannot be removed without denaturation. We were, however, able to demonstrate that Cps2A acts as a phosphatase, capable of catalysing the magnesium dependent release of phosphate from the pyrophosphate-lipid bound to Cps2A. Two conserved aspartic acid residues responsible for metal ion coordination are essential for this catalytic activity (Fig. 3), consistent with the observation that mutation of these aspartates to alanine in the LCP homologue, TagU, is lethal to *B. subtilis*⁶. Moreover, the introduction of phenylalanines into the hydrophobic pocket blocks lipid binding and also causes a lethal phenotype⁶.

The sequence conservation in this phosphate binding region and the crystallisation of Cps2A in the presence of mono- and pyro-phosphate lipids, close mimics of the expected reaction product and substrate, support strongly the notion that the LCP family of proteins are the phosphotransferases that catalyse the final linkage of anionic polymers to PG.

In summary, the structural and functional characterisation of the LCP family has identified the proteins responsible for the final step in the anionic polymer synthesis pathway. The identification of its active site and its catalytic mechanism will allow directed drug discovery, particularly because the active site of this transferase is outside the cytoplasmic membrane; any inhibitor will not have to pass across the cytoplasmic membrane thus rendering the LCP family an excellent target for the development of much needed novel antibiotics.

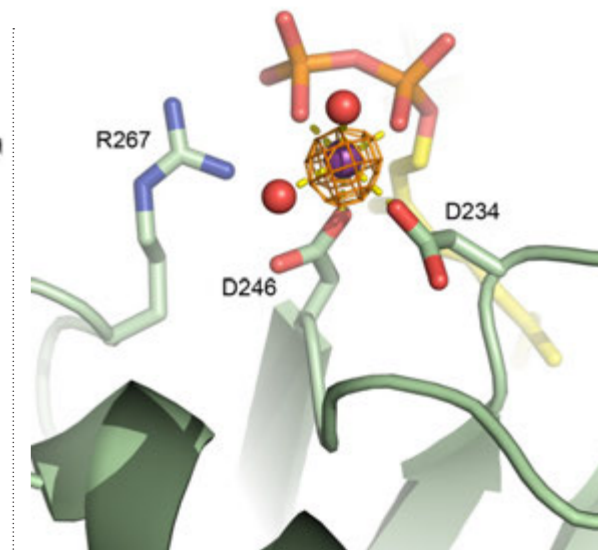


Figure 3: The Cps2A metal binding site. In the active site of the structure of Cps2A, determined with octaprenyl-pyrophosphate a manganese ion (purple sphere) is visible coordinated by protein (cartoon and sticks), ligand (sticks) and solvent atoms (red spheres). A peak is present in an anomalous difference map calculated at the manganese K-edge, shown as an orange mesh contoured at 5 σ .

References

- Weidenmaier, C. & Peschel, A. Teichoic acids and related cell-wall glycopolymers in Gram-positive physiology and host interactions. *Nat Rev Microbiol* **6**, 276-287 (2008).
- Brown, S., Zhang, Y. H. & Walker, S. A revised pathway proposed for *Staphylococcus aureus* wall teichoic acid biosynthesis based on *in vitro* reconstitution of the intracellular steps. *Chem Biol* **15**, 12-21 (2008).
- Schirner, K., Stone, L. K. & Walker, S. ABC transporters required for export of wall teichoic acids do not discriminate between different main chain polymers. *ACS Chem Biol* **6**, 407-412 (2011).
- Yokoyama, K., Mizuguchi, H., Araki, Y., Kaya, S. & Ito, E. Biosynthesis of linkage units for teichoic acids in gram-positive bacteria: distribution of related enzymes and their specificities for UDP-sugars and lipid-linked intermediates. *J Bacteriol* **171**, 940-946 (1989).
- D'Elia, M. A., Millar, K. E., Beveridge, T. J. & Brown, E. D. Wall teichoic acid polymers are dispensable for cell viability in *Bacillus subtilis*. *J Bacteriol* **188**, 8313-8316 (2006).
- Kawai, Y., Marles-Wright, J., Cleverley, R.M., Emmins, R., Ishikawa, S., Kuwano, M., Heinz, N., Bui, N.K., Hoyland, C.N., Ogasawara, N., Lewis, R.J., Vollmer, W., Daniel, R.A., Errington, J. A widespread family of bacterial cell wall assembly proteins. *EMBO J* **30**, 4931-41 (2011).
- Eberhardt, A., Hoyland, C.N., Vollmer, D., Bisle, S., Cleverley, R.M., Johnsborg, O., Håvarstein, L.S., Lewis, R.J. & Vollmer, W. Attachment of capsular polysaccharide to the cell wall in *Streptococcus pneumoniae*. *Microbial Drug Resistance In press* (2012).

Funding Acknowledgements

This work was funded by the BBSRC grant BB/G015902/1.

DOI 10.1038/emboj.2011.358

Dotting the 'i' in complement: the crystal structure of human complement factor I

Roversi, P., Johnson, S., Caesar, J.J., McLean, F., Leath, K.J., Tsiftoglou, S.A., Morgan, B.P., Harris, C.L., Sim, R.B. & Lea, S.M. Structural basis for complement factor I control and its disease-associated sequence polymorphisms. *Proc Natl Acad Sci U S A.* **108**(31), 12839-44 (2011)

Diffraction data enabled us to determine the crystal structure of the 88 KDa serine protease human complement Factor I (fI), a key regulator of the complement system, which is a part of the immune system. The project was hampered by the combined effects of sample heterogeneity, intrinsic conformational plasticity of the serine protease domain, lack of reactivity of the enzyme to small molecule inhibitors, and by tetrahedral twinning. The fI crystal structure, together with mapping of fI and cofactors' point mutations with altered C3b/C4b proteolytic activity, supports the idea that only upon encountering cofactor and substrate does the serine protease domain fold into its fully active conformation. The structure also reveals that in the native enzyme, the fI heavy chain behaves as a non-competitive inhibitor of the serine protease domain. Disruption of the fI heavy-chain:light-chain interface, either effected by the physiological binding of fI to the cofactor:substrate complex, or by mutations of interface residues, releases the inhibition.

Many biological processes involve amplification loops, which in turn need to be controlled. By using diffraction data from beamlines I02 and I03, we determined the crystal structure of a protein essential to keep one such biological amplification loop in check: the 88 KDa serine protease complement Factor I, a key regulator of the complement system¹. This 500 million years old arm of innate immunity is conserved throughout evolution in the plasma of vertebrates, and has evolved to function as a quick-acting machinery to target foreign tissues for destruction if they come into contact with the plasma. After surveillance, complement molecules make initial contact with the enemy, a sequence of proteolytic events is triggered, converging onto proteins C3b and C4b. These molecules enter complexes ('C3-convertases') amplifying the cascade, generating many more copies of C3b on the targeted cellular surfaces and in the plasma fluid phase. By cleaving C3b and C4b, fI offers the only means of keeping complement activation in check in the plasma fluid phase; on cell surfaces, fI-mediated inactivation of C4b/C3b provides extra complement control, in addition to the C3-convertase decay acceleration warranted by other self-cell anchored regulators. When complement regulators go wrong, self-tissues are harmed, and a number of auto-immune conditions ensue. Some of the naturally occurring fI polymorphisms are associated with diseases ranging from renal pathologies to arthritis-like syndromes. We undertook the fI structural determination with the aim of gaining insight on the molecular basis for fI function and its disease-associated polymorphisms.

Factor I is secreted by the liver in mature form as a disulphide linked heavy-chain (51 KDa, 4 domains) and light-chain (37 KDa, a single serine protease (SP) domain). Eukaryotic cell-expression systems produce insufficient amounts of human fI for crystallography, but a ten days purification of the protein from expired plasma yields 15 mg of pure fI², as judged by SDS-page gels. Perhaps not unexpectedly, given the several known single nucleotide polymorphisms in the human fI gene, when

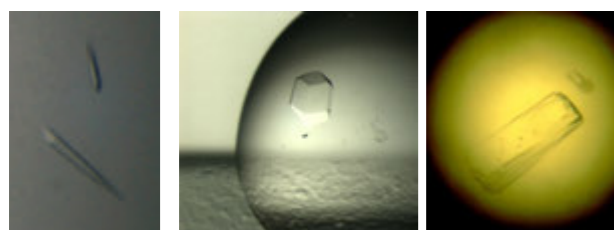


Figure 1: Three different crystal forms of human fI. A.) Space group $P3_2$, diffracting to 3.7 Å resolution, 2 molecules/asu, 70% solvent content, tetrahedrally twinned. B.) Space group $I2_3$, diffracting to 6.5 Å resolution, 2 molecules/asu, 90% solvent content. C.) Space group $P1$, diffracting to 2.4 Å resolution, 4 molecules/asu, 42% solvent content, tetrahedrally twinned.

isoelectric focusing is applied to a purified fI sample, even after enzymatic removal of the 6 Asn-linked glycans, a few distinct species are apparent. Despite this sample heterogeneity, over the course of 7 years, we managed to obtain diffracting human fI crystals in three different crystal forms (Fig. 1).

The human fI structure determination required about 300 96-well crystallisation plates, diffraction measurements from about a hundred crystals, and thousands of data-processing and phase-determination computing jobs. The project was plagued by the combined effects of sample heterogeneity, intrinsic conformational plasticity of the serine protease domain, partial reactivity to inhibitors, and by a relatively rare and not trivial to detect/overcome type of crystal twinning³.

With hindsight, and in the light of the structure (Fig. 2), a few of the difficulties mentioned above resided in properties of the fI molecule that are essential for its function. For example, the active site of native fI in our crystals turns out to be partially disordered, a property fI shares with many plasma serine proteases, which circulate in zymogen form until a transition to the enzymatically competent form takes place. Thus, the fI structure, together with mapping of fI and cofactors' point mutations showing altered C3b/C4b proteolytic activity, supports the idea that only upon encountering cofactor and substrate does the serine protease domain become fully active. Structures of inhibitor-bound fI and/or of fI with substrate and cofactor (e.g. a C3b:fI ternary complex) will be needed to fully appreciate the details of this zymogen-to-enzyme conformational transition.

It is also possible that our early attempts at rigidifying/ordering the SP domain by reacting it with covalent and non covalent inhibitors of serine proteases (e.g. PEFABLOC, benzamidine) created a mixture of inhibitor-bound and inhibitor-free molecules, perhaps explaining the initial failure to reproducibly grow large, well-ordered crystals. Indeed, human fI was demonstrated to be fully inactivated by the covalent serine protease inhibitor DFP only when treated in presence of one of its cofactors⁴. As soon as serine protease inhibitors were omitted, we obtained crystals in which the SP domain formed most of the contacts, ordering itself well enough for the crystals to grow. The same crystal contacts may unfortunately have originated twinning: the SP A:B and C:D interfaces are slightly different, and yet similar enough that a twin-domain boundary may be formed whenever either of molecules B,C or D substitutes for A³.

The fI SP domain was shown to possess weak activity for small molecule substrates even in absence of cofactors, and kinetic measurements on several point mutants of fI gave values of V_{max} significantly higher than the native⁵. Our structure reveals that the fI mutations that give increased

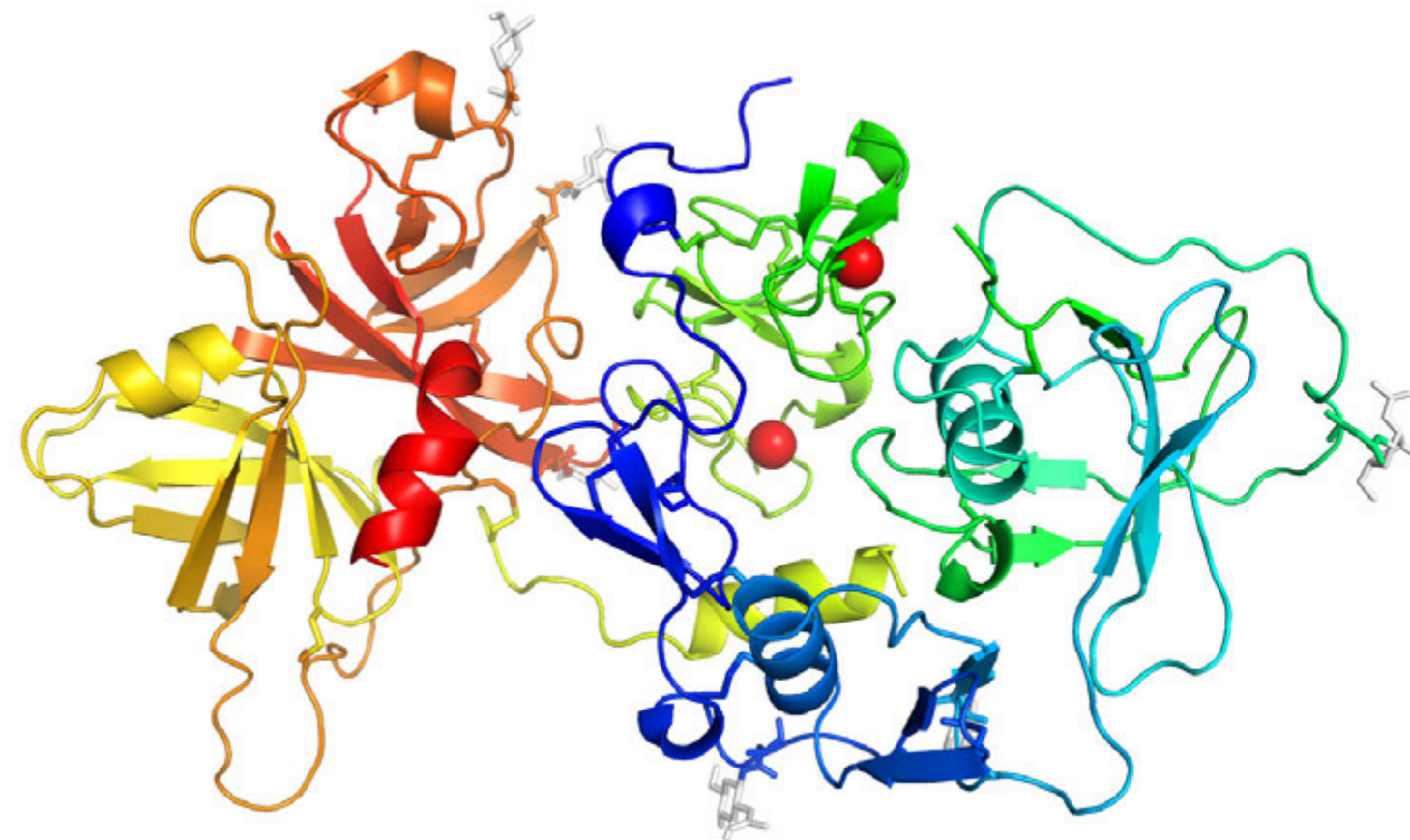


Figure 2: The crystal structure of human factor I. On the left hand side, the light chain (SP domain), painted yellow to red. On the right hand side, the heavy chain, painted blue to light green. Disulphide bonds and Asn-linked glycosylation sites in sticks. Red spheres: two Ca^{++} ions bound to the LDLRA domains.

catalytic activity, all map to the interface between the heavy chain and the SP domain. We therefore propose that in the native enzyme, the heavy chain behaves as a non-competitive inhibitor of the SP domain (Fig. 3). Disruption of that interface, either effected by the physiological binding of fI to the cofactor:substrate complex, or by the known point mutations to the heavy-chain:light-chain interface residues, allosterically releases the inhibition.

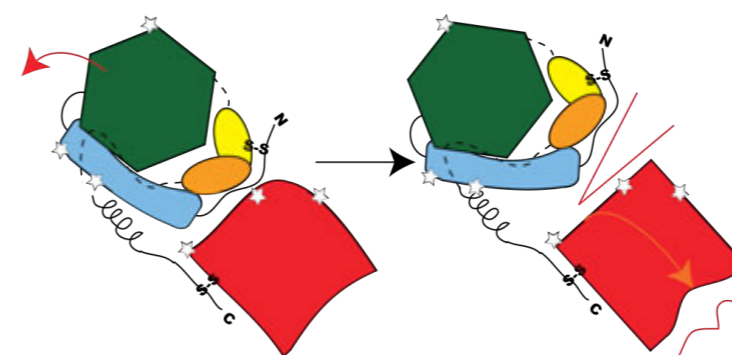


Figure 3: The heavy-chain acts as an allosteric inhibitor of human fI SP domain. The cartoon illustrates the proposed opening (red arrows) of the interface between the heavy-chain (blue, green, orange and yellow domains) and the light-chain (dark red domain), leading to allosteric activation of the SP domain (wiggly red line). White stars: glycosylation sites.

References

1. Nicol, P.A. & Lachmann, P.J. The alternative pathway of complement activation. The role of C3 and its inactivator (KAF). *Immunology*. **24**(2),259-75 (1973).
2. Roversi, P., Blanc, E., Johnson, S. & Lea, S.M. Tetrahedral twinning can happen to you too. Accepted for publication in *Acta Crystallographica D* **68** (2012).
3. Sim, R.B., Day, A.J., Moffatt, B.E. & Fontaine, M. Complement factor I and cofactors in control of complement system convertase enzymes. *Methods Enzymol.* **223**, 13–35 (1993).
4. Ekdahl, K.N., Nilsson, U.R. & Nilsson, B. Inhibition of factor I by diisopropyl- fluorophosphate. Evidence of conformational changes in factor I induced by C3b and additional studies on the specificity of factor I. *J. Immunol.* **144**, 4269–4274 (1990).
5. Nilsson, S.C., Nita, I., Månsson, L., Groeneveld, T.W., Trouw, L.A., Villoutreix, B.O. & Blom, A.M. Analysis of binding sites on complement factor I that are required for its activity. *J. Biol. Chem.* **285**(9), 6235–45 (2010).

Funding Acknowledgements

P. Roversi was supported by Medical Research Council Project Grant G0400775 and S. Johnson was funded by Grant 083599 from the Wellcome Trust.

DOI 10.1073/PNAS.1102167108

Structural basis for the killing of human beta cells by CD8+ T-cells in type 1 diabetes

Bulek, A.M., Cole, D.K., Skowera, A., Dolton, G., Gras, S., Madura, F., Fuller, A., Miles, J.J., Gostick, E., Price, D.A., Drijfhout, J.W., Knight, R.R., Huang, G.C., Lissin, N., Molloy, P.E., Wooldridge, L., Jakobsen, B.K., Rossjohn, J., Peakman, M., Rizkallah, P.J. & Sewell, A.K. Structural basis for the killing of human beta cells by CD8+ T cells in type 1 diabetes. *Nature Immunology Advance Online Publication*. **13**(3), 283-9(2012)

Type 1 diabetes can occur as a result of the body's own immune system attacking and destroying the cells in the pancreas that manufacture the hormone insulin. Insulin controls blood sugar levels and a lack of insulin is fatal if untreated. The mechanism by which the body attacks its own insulin producing cells in the pancreas is not fully understood. Our findings show how killer T-cells might play an important role in autoimmune diseases - like diabetes - and we have caught the first ever glimpse of the mechanism by which killer T-cells can attack our own body's cells to cause disease. This first sight of how killer T-cells make contact with the cells that make insulin is very enlightening, and increases our understanding of how Type 1 diabetes may arise. This knowledge will be used in the future to help us predict who might get the disease and also to develop new approaches to prevent it. Our aim is to catch the disease early before too many insulin-producing cells have been damaged. The team now hope that by gaining a deeper insight in this process it will put them in a much stronger position to devise new ways to prevent or even halt the disease.

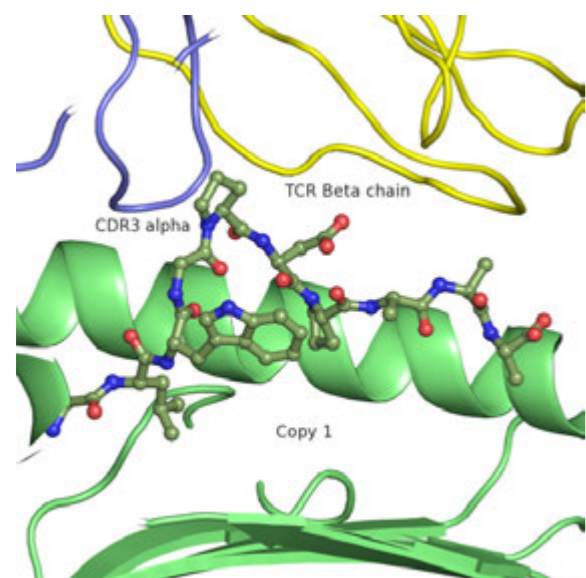


Figure 1: View of the TCR/pMHC interface. The peptide is shown as sticks. The central residues of the peptide are bulged out to make contact with the TCR.

T-cells are part of the adaptive immune system and mediate responses to disorders, infections and diseases. In order to perform this role, T-cells have a polymorphic receptor on their surface, the T-cell receptor (TCR), that can bind to disease markers, usually peptide oligomers, bound by the major histocompatibility complex (pMHC) on the surface of Antigen Presenting Cells (APCs). The initial recognition event triggers a cascade of secondary interactions, resulting in direct killing of the APC, or recruiting other immune cells to effect programmed cell death or apoptosis. The genome can produce up to 100 million TCRs, but the disease marker peptides, 9 residues or longer, may have $>10^{15}$ (thousand trillion) possible sequences. The gap is bridged, somewhat, by the TCRs' ability to each recognise many thousands of sequences, a property known as degeneracy or cross-reactivity.

The thymus is a small organ, which regulates TCR specificity by negatively selecting, or eliminating, TCRs that recognise self motifs with an affinity above a certain threshold. The twilight zone around the threshold is not well defined. This 'twilight zone' results in some T-cells exhibiting unwanted auto-reactivity, i.e. they target signals that are present on healthy cells. Type 1 diabetes is an example of this and it has recently been shown that some

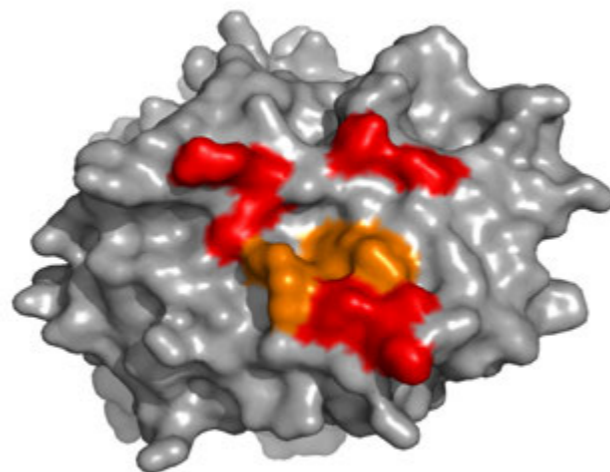


Figure 2: Footprint of contacts between TCR and pMHC.

T-cells can target the cells that make insulin (beta cells) in the pancreas. As a result of this interaction, pancreatic beta cells can be destroyed reducing or eliminating insulin production – a condition that, without medical intervention, is life threatening. In order to examine the role of T-cells during type 1 diabetes, we recently isolated a T-cell clone (1E6) from the pancreas of a type 1 diabetes patient. The 1E6 T-cell clone was shown to have the ability to recognise and kill beta cells, strongly implicating 1E6-like T-cells in disease progression. We isolated the TCR from this clone using molecular techniques for structural and biophysical experiments. Biophysical analysis, using surface plasmon resonance, showed that the 1E6 TCR had an affinity much lower than has been previously observed, for a peptide arising from the pre-pro-insulin signal sequence, PPI (ALWGDPAAAA) - produced by the Islet of Langerhans cells in the pancreas. Our findings indicate that a loose short-term association between 1E6 and MHC, allows the 1E6-like T-cells to escape the attentions of the thymus.

The research conducted involved collecting diffraction data of crystals of the 1E6 TCR, the MHC carrying the PPI marker, and complexes of the two. The experiments were conducted on the various beamlines of the

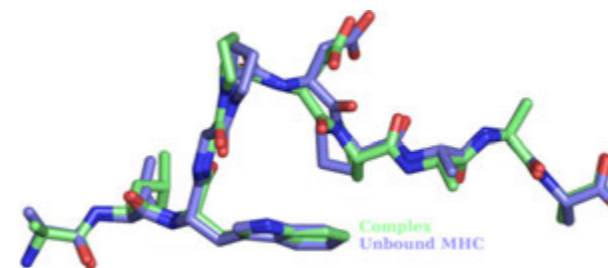


Figure 3: The superposed peptides in the Complex and in the unbound MHC. Very little differences are observed.

Macromolecular Crystallography village. Initial experiments were partially successful, as the crystals gave diffraction to only 3Å resolution, just enough to solve the structure. It quickly transpired that of the two copies in the asymmetric unit, one was disordered in comparison with the other and refinement stalled. After crystal optimisation, improved resolution allowed us a handle on the structure solution, leading to straightforward refinement. The automated systems at the MX beamlines were of prime importance in completing many of the routine tasks involved. So we were able to study many samples while computer software and hardware analysed the emerging data seamlessly in the background, enabling us to move on to the structure solution and refinement quickly.

The picture that emerged showed a classical presentation of a 'bulged out' peptide marker (Fig. 1), offering the central GDP residues for interaction with the TCR. The main contact interface utilised by the TCR occurred at the highly variable complementarity determining regions 3 of both the alpha and beta chains of 1E6 (CDR3α & CDR3β). What was different about this complex, when compared with complexes of TCR with pathogen or virus markers presented by MHC, was that the 1E6 TCR had very few contacts with the MHC, using only the CDR3s for binding to the peptide bulge, while unusually, the CDR1s and CDR2s were almost completely uninvolved in the interface, in contrast to the other complexes, as shown by the contact footprint (Fig. 2). Consequently, the buried surface area between the TCR and the pMHC is the smallest for this kind of complex.

Comparing the peptide conformation inside the MHC groove, in the presence and absence of the TCR, very little change was apparent (Fig. 3). Thus, almost no change in the conformation of the CDR loops in the TCR was required (Fig. 4). This was substantially different from the large shifts in the CDR loops observed with other TCR/pMHC complexes, where induced fit seems to be the norm.

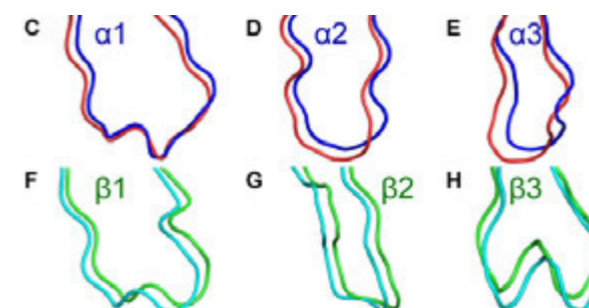


Figure 4: The superposed CDRs in the complex and in the unbound TCR show small changes, in contrast to the large movements observed in other cases, e.g. NYESO.

The arms-length interaction between the two sides of this immune synapse appears to be the underlying cause of the weak interaction. This was quantified by measuring the affinity between the two components using surface plasmon resonance, SPR. A dilution series at set temperatures (Fig. 5) indicated an affinity in the region of 280 nM, some 10 to 30 times weaker than affinities recorded between TCRs and MHCs carrying pathogen or virus markers. This weak affinity, which was explained by the minimal contact footprint of the TCR, could allow 1E6-like T-cells to escape thymic selection and recognise and destroy insulin producing beta cells in the pancreas.

This work has enabled a better understanding of how T-cells are seeing insulin-producing beta cells, and therefore why they are destroying them. Furthermore, using the structural information, it will be possible to generate diagnostic molecules that can be used to detect 1E6-like T-cells in patient blood. This important advance could serve as an early warning system for

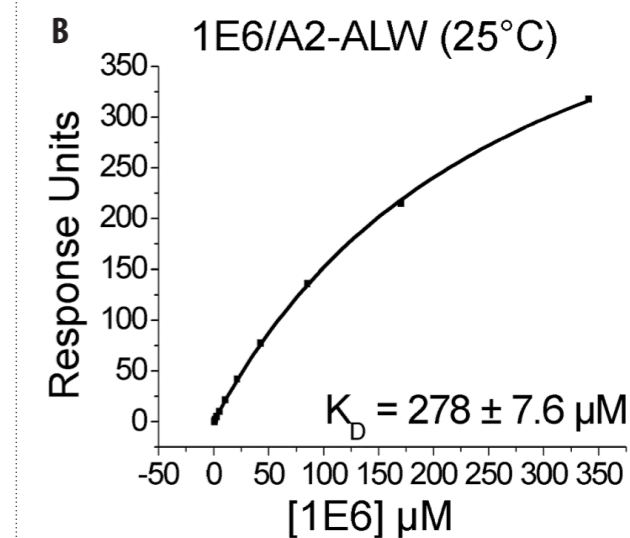


Figure 5: The SPR dilution series at 25°C, showing the calculated affinity falling in the range usually observed for weak interactions.

individuals at risk of developing type 1 diabetes and could lead to preventive therapies to try and slow, or halt the onset of the disease.

Funding Acknowledgements

Supported by the Biotechnology and Biological Sciences Research Council (BB/H001085/1), the Wellcome Trust (WT086716; WT079848; WT095767), the Juvenile Diabetes Research Foundation (7-2005-877 and 1-2007-1803; 17-2009-806), the European Union Seventh Framework Programme (241447 NAIMIT), the National Institute for Health Research Comprehensive Biomedical Research Center at Guy's & St. Thomas' National Health Service Foundation Trust and King's College London, Research Councils UK, the National Health and Medical Research Council, the Welsh Office of Research and Development and the Medical Research Council.

DOI 10.1038/ni.2206

Structure of a novel single-stranded DNA binding protein

Paytubi.S., McMahon, S.A., Graham, S., Liu, H., Botting, C.H., Makarova, K.S., Koonin, E.V., Naismith, J.H. & White, M.F. Displacement of the canonical single-stranded DNA-binding protein in the Thermoproteales. *Proc. Natl. Acad. Sci. USA*. **109**(7), E398-405 (2011)

Biology requires a single-stranded DNA (ssDNA) binding protein and all organisms from humans to bacteria have one. Yet despite this, the archaeal organism *Thermoproteus tenax*, who can live under extreme conditions such as high temperatures, lacked the consensus sequence for ssDNA binding. Bioinformatics had identified a candidate and the structure and biochemistry of this protein was evaluated. The structure determined revealed a novel fold and a new member of the ssDNA binding superfamily. This has important implications for the evolution of life.

The oligonucleotide-binding (OB) fold¹ is the hall mark of ssDNA binding proteins (SSB). In fact the OB fold plays a wider role and is found in proteins which bind other biopolymers. The amino acid sequence homology varies enormously amongst the OB superfamily but modern bioinformatics tools are able to detect OB fold-containing proteins in all living organisms, with one exception, the Thermoproteales, a member of the Crenarchaea family of organisms. The puzzle is that all forms of life that we know of, require to replicate and repair DNA. Thus all forms of life must have an SSB protein, and it follows they should have an OB fold.

As bioinformatics failed to identify a candidate gene for the SSB function, *T. tenax* cell extracts were prepared and passed over affinity columns. This led to the identification of two new proteins, Ttx2090 and Ttx1576, both of which were candidates for the role of SSB. Ttx2090 did not express in a soluble form, is similar to proteins from other SSB containing organisms and appears to belong to a different family, which left Ttx1567. Biochemical assays showed the expressed protein did indeed bind to ssDNA and biophysical quantitation showed this was a strong and specific binding. However, the full length protein did not yield consistently reproducible crystals. Using a technique of incubating with a protease during crystallisation²

did indeed give good quality reproducible native crystals (denoted cTtx1756). Using beamline I03 we collected a native data set to 2.9 Å. As the protein was predicted to contain a new fold, we resorted to SeMet and anomalous phasing. Crystals were once again grown with protease present in the well.

A number of these crystals were screened at the beamline and all diffracted poorly, with a lower resolution limit and higher mosaic spread than native. The crystal we collected, judged by us to be the 'best' based on diffraction resolution, spot shape and mosaic spread, processed with a very high R-merge of 22%.

We have not established whether differences between native and SeMet crystal were systematic or simply reflected batch to batch variability.

	TtX 1-148	cTtx1576	cTtx1576 SeMet
Resolution (Å)	50 - 2.0	50 - 2.9	50 - 3.4
Space group & Cell dimensions	P2 ₁ a = 39.8 b = 103.7 c = 39.8 β=118	I2 ₁ 3 a = b = c = 105.7	I2 ₁ 3 a = b = c = 106.6
Completeness (%)	92	100	100
Redundancy	5.5	21	20
Rmerge	9.0	7.2	22.4
Rwork/Rfree	20.4/25.6		
PDB	3TEK		

Table 1.

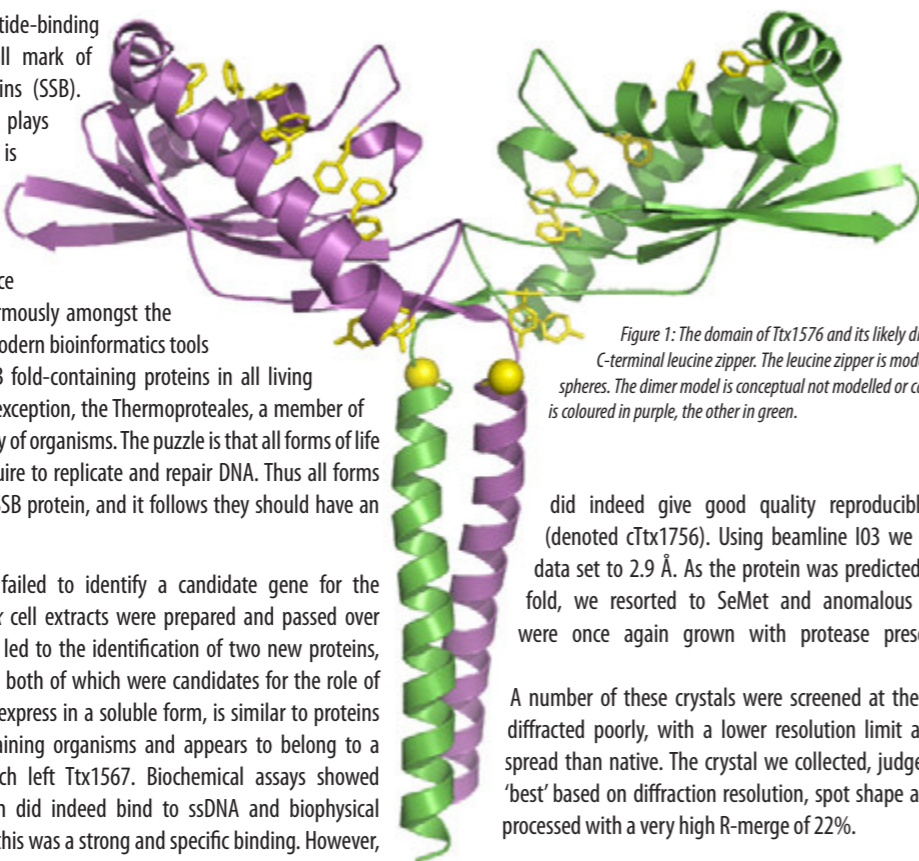


Figure 1: The domain of Ttx1576 and its likely dimerization by the C-terminal leucine zipper. The leucine zipper is modelled after the yellow spheres. The dimer model is conceptual not modelled or calculated. One monomer is coloured in purple, the other in green.

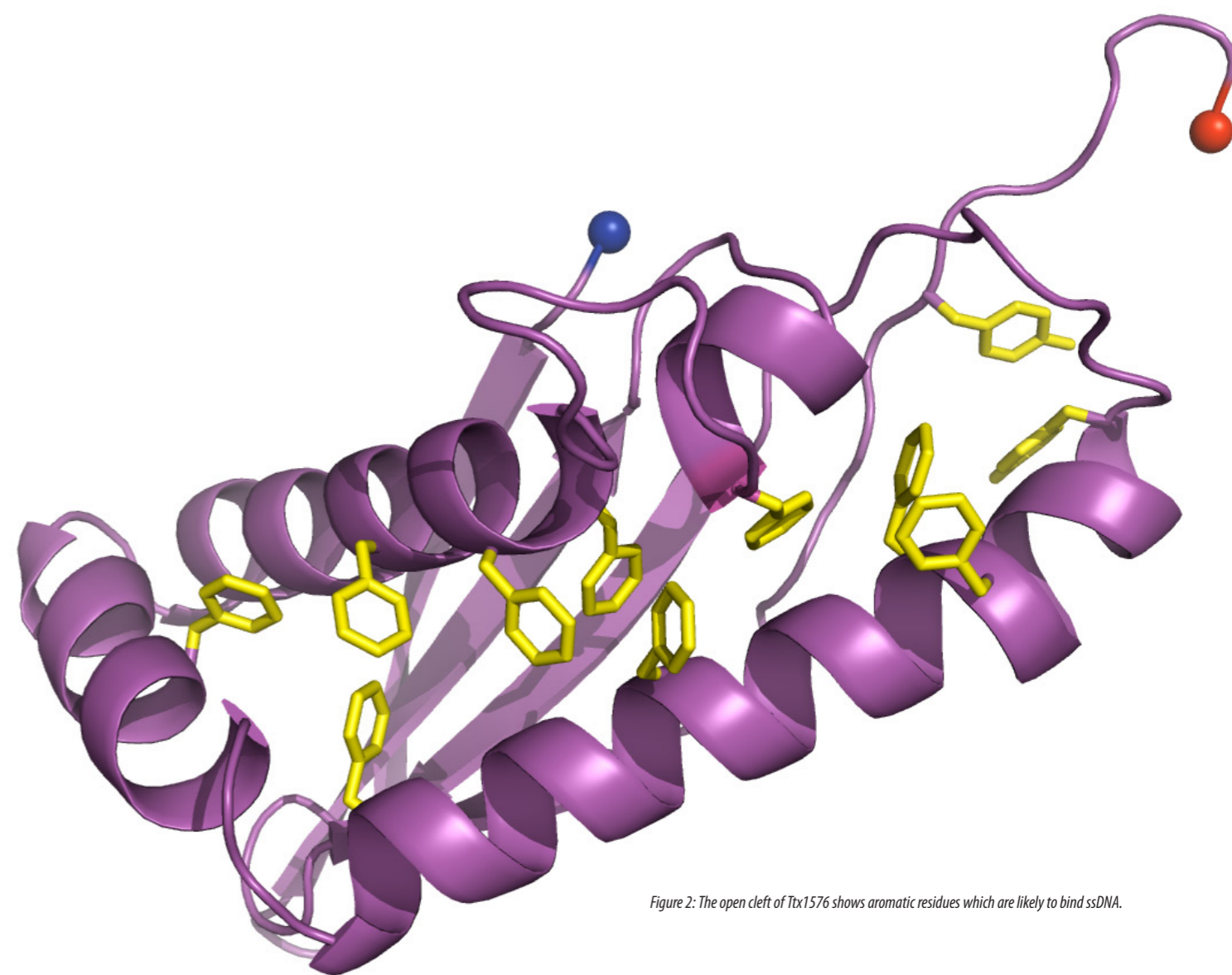


Figure 2: The open cleft of Ttx1576 shows aromatic residues which are likely to bind ssDNA.

Despite the apparent low quality of the data which would normally be expected to preclude solution, we were able to identify selenium positions and proceed with phasing in a relatively straightforward manner. The highly redundant data (20) may have been responsible for our success. We traced amino acids 24–139 and identified a compact folded domain. We did not know, since mass spectrometry on the crystals was inconclusive, whether the missing residues (amino acids 1–23 and 140–196) were disordered or as we suspected cleaved off - at least in part - during crystallisation.

Using the compact folded domain as a guide and bioinformatics, we delineated the native protein into two domains, the C-terminal region (148 to 196), which we identified as a dimerisation helix (leucine zipper), and the new SSB domain. We cloned, crystallised and collected data on I04 on this construct. The final structure is shown in Figure 1. These new data were of high quality.

The structure shows a clear large central cleft lined with aromatic residues (Fig. 2). The spacing around 4 Å of these residues is a match for DNA base binding. The electrostatics of the surrounding protein surface are consistent with ssDNA binding.

Crystallography at Diamond Light Source has been used to define a new fold and match it to well known function. The work has established that

for even a core, competence (binding ssDNA) biology has evolved multiple solutions. In this case high redundancy may have compensated for poor quality data.

References

1. Murzin, A.G. OB(oligonucleotide/oligosaccharide binding)-fold: Common structural and functional solution for non-homologous sequences. *EMBO J* **12**, 861–867 (1993).
2. Wernimont, A. & Edwards, A. In situ proteolysis to generate crystals for structure determination: An update. *PLoS ONE*. **4**, e5094 (2009).

Funding Acknowledgements

Funded by Biotechnology and Biological Sciences Research Council Grant BB/S/B14450. K.S. Makarova and E.V. Koonin are supported by intramural funds of the US Department of Health and Human Services to the National Library of Medicine, National Institutes of Health. Mass spectrometry which was used in the work is supported by the Wellcome Trust.

DOI 10.1073/pnas.1113277108

Small bacterial haemprotein reveals a novel mechanism of protection against CO toxicity

Antonyuk, S.V., Rustage, N., Petersen, C.A., Arnst, J.L., Heyes, D. J., Sharma, R., Berry, N.G., Scrutton, N.S., Eady, R.R., Andrew, C.R., and Hasnain, S.S. Carbon monoxide poisoning is prevented by the energy costs of conformational changes in gas-binding haemproteins. *PNAS*. **108**, 38, 15780-15785 (2011)

Haem is one of the most versatile protein cofactors with involvements in gas transport, electron transfer, catalysis and signaling. Preventing the irreversible binding of Carbon monoxide (CO) to haem is a critical aspect of its biological functionality. CO binding to hemoglobin can lead to eventual death in environments with excess CO, and more general poisoning of haemproteins by CO can have fatal consequences for cellular function and metabolism. CO is a normal metabolic product and is now recognized as having a variety of physiological functions in immune regulation and antioxidant defence mechanisms. The toxicity of CO results from its very high affinity for haem. Competing hypotheses have sought to explain why myoglobin (Mb) is able to lower the ratio of CO to O₂ affinity to ~25 as compared to ~20,000 in bare haem. Because of the inherent geometric preferences of Fe-C-O (linear) and Fe-O-O (bent) moieties it was initially proposed that Mb discriminated against CO due to distal pocket steric hindrance, which created a significant energetic cost for bending the Fe-C-O unit. This hypothesis has since been downplayed for Mb in favour of preferential H-bonding to haem-bound O₂. Variations in haem conformation and propionate interactions have also been suggested as key factors that modulate haem reactivity with diatomic gases. Using single amino acid mutations, reaction kinetics, Raman spectroscopy, X-ray crystallography and energy measurements and calculations, we provide a paradigm shift in our understanding of how CO poisoning is prevented in haem proteins due to the energy costs associated with conformational changes.

In biology, substrates have distinctive sizes, shapes, and charge distributions that are specifically recognised by their target biological partner proteins. The discrimination between the gases O₂, NO and CO by haem proteins is a remarkable example of biological specificity because these molecules are apolar and of very similar size. Molecular recognition of these gases is essential for respiration, cell-signaling, aero/chemotaxis, and regulation of gene expression¹. Cytochrome *c'* belongs to a family of pentacoordinate (5c) haem proteins that discriminate between these diatomic gases efficiently helping protect bacteria from nitrosoative stress and/or NO shuttling during denitrification²⁻³. The best characterized CYTc is from the denitrifying bacterium *Alcaligenes xylosoxidans* (Ax)^{4,5}, which does not form a stable complex with O₂, binds CO weakly as a distal six-coordinate (6c) haem-carbonyl (6c-CO), and reacts with NO to form a unique proximal 5c haem-nitrosyl (5c-NO) via a distal 6c haem-nitrosyl (6c-NO) intermediate. This utilisation of both faces of the haem in ligand binding is unprecedented. The crowded distal haem pockets of all CYTc proteins contain a non-polar residue (Leu, Phe, or Met) close to the Fe, which enforces selectivity in exogenous ligand binding. The binding of CO to AxCYTc is 2-3 orders of magnitude slower than to Mb.

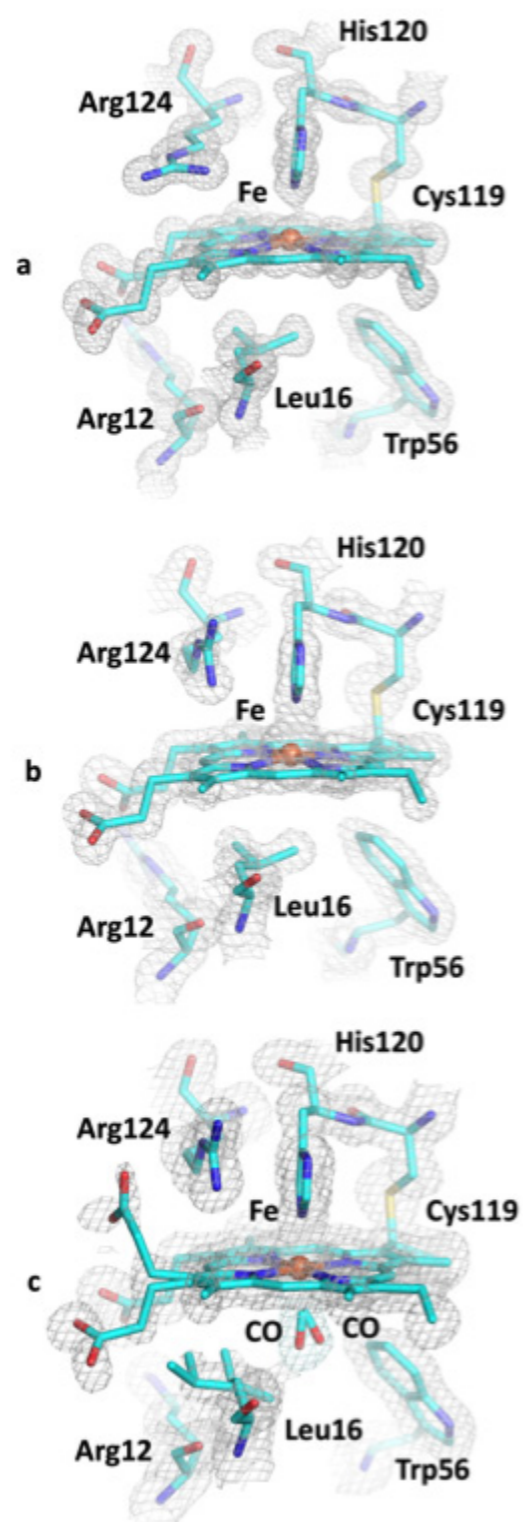


Figure 1: Structural comparison of the haem sites of (a) ferric AxCYTc at 0.84 Å resolution, (b) ferrous AxCYTc at 1.45 Å resolution, and (c) AxCYTc-CO at 1.25 Å resolution. Fe atoms are shown as orange spheres. 2Fo-Fc electron density maps, contoured at 1 σ .

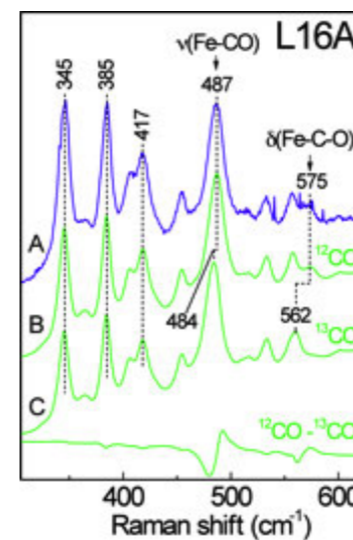


Fig. 2. Identification of CO as the distal haem ligand of 'as-isolated' L16A from the equivalence of RR vibrations with preformed L16A-CO. Correspondence of the low-frequency room-temperature RR spectrum of as-isolated L16A AxCYTc (a) with that of its carbonyl complex prepared with ¹²C¹⁸O (b). Substitution of the carbonyl complex with ¹³C¹⁸O (c) identifies vibrations of the Fe-CO moiety from the ¹²C¹⁸O-¹³C¹⁸O difference spectrum. The match of the as-isolated L16A AxCYTc spectra to the carbonyl complex, in particular the 487-cm⁻¹ RR vibration attributable to ν(Fe-CO), confirm that CO is the distal ligand.

of Leu-16, which in turn induced a shift of the haem propionate from the distal to the proximal face. In the bent conformation, a smaller shift in the position of Leu16 was accompanied by a comparably smaller shift in the propionate, which remained on the distal haem face. Resonance Raman (RR) spectroscopy confirmed the presence of both conformations at cryogenic temperatures, but only the linear conformation was detected at room temperature. Typical RR spectroscopic data for L16A are shown in Fig. 2.

Mutation of Leu16 to Gly or Ala resulted in a linear CO binding conformation that did not require movement of the haem propionate fig.3 A, B respectively. The affinity of the L16A and L16G mutants for CO was increased by 8 orders of magnitude when compared to that of the wild-type (WT) protein. The K_d's of the mutants for CO, in the range of 10⁻¹¹ to 10⁻¹², were among the highest reported for any haem protein. Both mutant proteins were isolated in complex with CO.

Redox titration of WT AxCYTc led to release of CO to yield the free ferrous protein at -200 to 0 mV, followed by oxidation to the ferric protein at 0 to 200 mV. In contrast, the L16A protein released CO concomitant with oxidation to the ferric state at 300 to 600 mV. Thus, the requirement for movement of Leu16 and the haem propionate upon CO binding reduces the potential of the haem-CO adduct of WT AxCYTc by 600 mV or 58 kJ/mol, allowing reversibility of CO binding. Energy calculations using Density Functional Theory (DFT) approach provided consistent values to these measured values. We propose that these new findings, coupling the energetic of structural change with gas release, may have broad implications for the functioning of a wide variety of haem systems including haem-based sensors.

Crystallographic data collected on I02, X06SA (SLS), SRS Daresbury and a home source Rigaku FRE+ (Barkla Laboratory at the University of Liverpool) revealed that the structures of the haem binding sites of the ferric and ferrous AxCYTc proteins were nearly identical except for the conformation of Arg-124 (see Fig. 1 a and b, respectively). In as-isolated ferric AxCYTc at 0.84 Å resolution, Arg124 is parallel to the haem plane, while in ferrous AxCYTc at 1.45 Å resolution Arg124 is perpendicular to the haem plane. In AxCYTc-CO structure, CO bound to the ferrous protein in two conformations (Fig. 1c). In the linear conformation, CO was aligned perpendicular to the plane of the haem, necessitating a movement

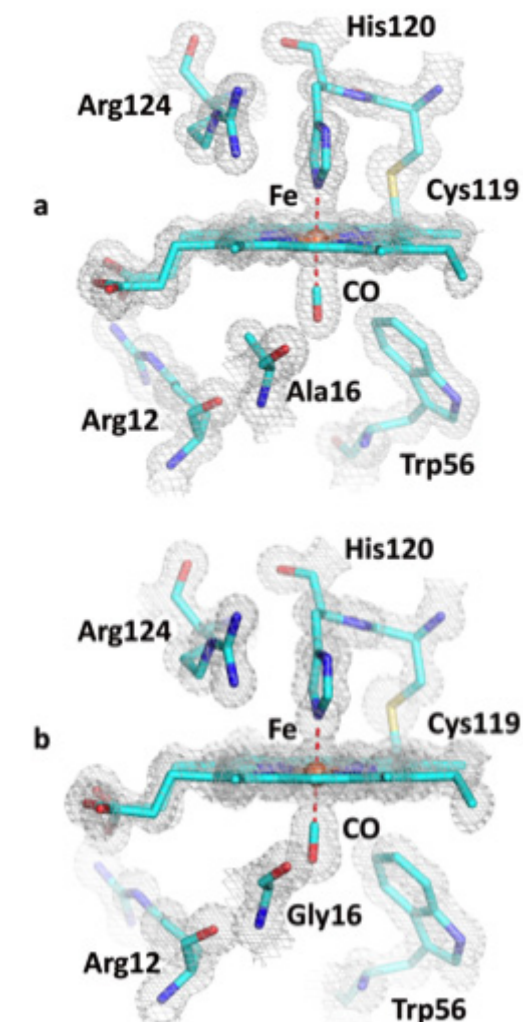


Figure 3. 2Fo-Fc electron density maps, contoured at 1 σ around models of the haem sites of the CO adducts of (a) L16A and (b) L16G variants of AxCYTc at 1.03 and 1.04 Å resolution respectively.

References:

- Gilles-Gonzalez, M.-A. & Gonzalez, G. Haem-based sensors: defining characteristics, recent developments, and regulatory hypotheses. *J Inorg Biochem.* **99**, 1-22 (2005).
- Choi, P.S., Grigoryants, V.M., Abruna, H.D., Scholes, C.P. & Shapleigh, J.P. Regulation and function of cytochrome *c'* in *Rhodobacter sphaeroides* 2.4.3. *J Bacteriol* **187**, 4077-4805 (2005).
- Ramão, M.J. & Archer, M. Handbook of metalloproteins. Wiley, Chichester pp 44-54 (2001).
- Lawson, D.M., Stevenson, C.E.M., Andrew, C.R. & Eady, R.R. Unprecedented proximal binding of nitric oxide to haem: implications for guanylate cyclase. *EMBO J.* **19**, 5661-5671 (2000).
- Hough, M. A., Antonyuk, S. V., Barbieri, S., Rustage, N., McKay, A. L., Servid, A. E., Eady, R. R., Andrew, C. R., Hasnain, S. S. Distal-to-Proximal NO Conversion in Hemoproteins: The Role of the Proximal Pocket. *J. Mol. Biol.* **405**, 395-409 (2011).

Funding Acknowledgements

Research carried out at Diamond Light Source on beamlines I02-I04, at the SLS on X06SA, and at the SRS Daresbury and in the Barkla Laboratory at the University of Liverpool.

DOI 10.1073/pnas.1109051108

Insights in the regulation of cell-to-cell interactions - structural and functional analysis of the LDL-receptor-related protein 6 (LRP6)

Chen, S., Bubeck, D., MacDonald, B.T., Liang, W.-X., Mao, J.-H., Malinauskas, T., Llorca, O., Aricescu, A.R., Siebold, C., He, X. and Jones, E.Y. Structural and Functional Studies of LRP6 Ectodomain Reveal a Platform for Wnt Signaling. *Dev. Cell.* **21**, 848–861 (2011)

Within a multi cellular organism, whether fly, fish, mouse or human, gradients in concentration of secreted signalling molecules, termed morphogens, provide one of the fundamental mechanisms determining the development of the basic body plan. The Wingless-Type MMTV Integration Site Family (Wnts) form one of the major morphogen families. As well as playing a central role during embryogenesis, the development process that enables the formation of a multicellular organism from an egg cell, Wnts are involved in many aspects of adult physiology and aberrant Wnt signalling is profoundly implicated in cancer biology. Classically, Wnts trigger their signalling pathway within a cell by binding to two types of receptors on its surface. The first type is the signalling receptor, and, according to the specificity of the Wnt molecule, is one of ten members of the rather evocatively named Frizzled (Fz) family. The second type is one or other of two members of the LDL-receptor-related protein (LRP) family, either LRP5 or LRP6. The extracellular region of LRP5/6, which protrudes from the cell surface to bind Wnts, was predicted to contain four repeated units, each a six-bladed β -propeller plus epidermal growth factor (EGF)-like module, together they form the PE repeat. We used X-ray diffraction data collected on beamline I24 to determine the crystal structure of a Wnt-binding portion of the LRP6 extracellular region comprising the third and fourth PE repeats. Guided by this detailed structural information we were then able to use electron microscopy, cellular and binding assays to build up a model in which LRP5/6 functions as platform structure supporting an interplay of ligands through multiple interaction sites.

Wnts have a central role in control of embryonic development and adult tissue homeostasis. Conversely, Wnt signalling is implicated in a broad range of human diseases including cancer and osteoporosis. Therefore, there is considerable biomedical interest in this mechanism of Wnt signalling and its inhibition. Several physiological inhibitors have been identified, including Dickkopf 1 (Dkk1), a secreted protein which acts through binding to the co-receptor for Wnt signalling, LRP5/6. In mammals LRP5 and LRP6 can have overlapping roles, but in general LRP6 takes the dominant role in development. LRP5/6 is a type 1 transmembrane protein (i.e. with N-terminal extracellular region preceding a single plasma membrane spanning helix). Sequence homologies with the low-density lipoprotein receptor (LDLR) suggest that the extracellular region of LRP5/6 contains four YWTD β -propeller-EGF-like domain (PE) repeats (P1E1–P4E4) in tandem followed by three LDLR type A domains (L1–L3). Prior data from a number of laboratories indicated that P3E3 plus P4E4 (i.e. P3E3P4E4) acts as a single functional unit and provides the primary binding site for Wnt3a. We therefore set out to determine the structure of this basic building block of the Wnt signalling system.

In order to produce soluble LRP6_{P3E3P4E4} for structural and functional studies we needed to use a eukaryotic (mammalian) cell-based expression system. Human LRP6_{P3E3P4E4} (residues 629–1244) was transiently expressed in HEK293 cell derivatives HEK293S GnT1⁻ (for crystallisation) or HEK293T (for functional analyses). A specialised chaperone, Mesd (Mesoderm development), is known to be important for LRP6 biogenesis and so we co-expressed our LRP6_{P3E3P4E4} construct with human Mesd to boost the levels of secreted protein. The purified LRP6_{P3E3P4E4} crystallised at 21 °C in 20% (w/v) polyethylene glycol (PEG) 3350, 0.2 M calcium chloride and, after optimisation, yielded thin, long plate-like crystals. Initial X-ray diffraction characterisation and data collection used the microfocus beam on beamline ID23-2 at the European Synchrotron Radiation Facility. X-ray diffraction data of sufficient quality for a high resolution structure determination were collected on beamline I24 of the Diamond Light Source. The optimal data set was achieved by collecting at 100 K in wedges of 30° from multiple positions along a single crystal using the Pilatus 6M detector. These data allowed us to

refine the crystal structure of LRP6_{P3E3P4E4} at a resolution of 1.9 Å (R_{work} 18.1%, R_{free} 21.1%).

The structure reveals the detailed architecture of the tandem P3E3P4E4 arrangement, defining the domain interfaces and the surfaces exposed for potential Wnt-binding (Fig. 1). The β -propellers (P3 and P4) are classic examples of the six bladed YWTD class with main chain topologies that superpose well on the crystal structures of β -propeller domains from LDLR and nidogen (each propeller to propeller superposition giving root mean square deviations in the range 1.13–1.35 Å for some 200–220 Ca pairs). As expected E3 and E4 have the standard EGF-like fold and form apparently rigid interfaces with their respective β -propeller domains. The two repeat units, P3E3 and P4E4, abut side by side forming an extensive and tight interface. When viewed in the orientation shown in Fig. 1, upper panel, the EGF-like domains can be described as packing against the bases of the two β -propellers while the tops of the β -propellers form a continuous, curved surface. Guided by this structural information we used site directed mutagenesis in combination with cellular and binding assays to locate the Wnt3a binding site on the 'top' surface of, primarily, β -propeller P3. We used similar assays to demonstrate overlap between this Wnt binding site and the binding site of a protein, Dickkopf 1 (Dkk1), known to inhibit Wnt signalling (Fig. 2). Gratifyingly, we published our results simultaneously with structural reports from two other laboratories (those of Prof Wenqing Xu, University of Washington, and Prof Bill Weis, Stanford University) that confirmed this footprint for Dkk1 binding.

In order to provide some structural insight into the overall architecture of the LRP6 extracellular region we also produced a secreted form of the full LRP6 ectodomain. We could only generate rather low yields of protein but these were sufficient for us to carry out negative stain electron microscopy (EM). This allowed us to produce a low resolution (25 Å) single-particle EM reconstruction of the LRP6 ectodomain which revealed a relatively compact horseshoe-like structure. This observation combined with our crystallographic and functional analyses, led us to propose that the LRP5/6 forms a tray-like platform at the cell surface. Data from ourselves and others

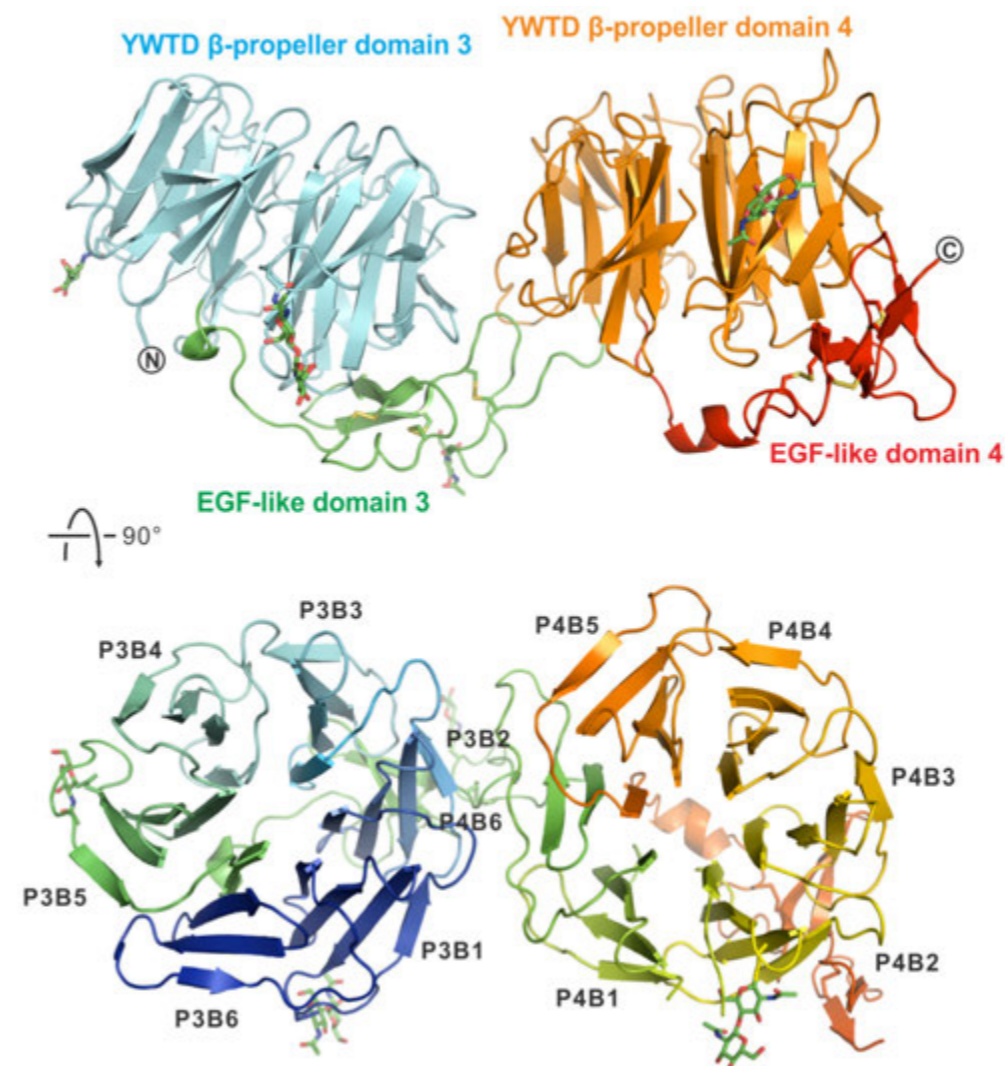


Figure 1: The crystal structure of LRP6_{P3E3P4E4}. In the upper panel the β -propeller and EGF-like domains are indicated (P3, cyan; E3, green; P4, orange; E4, red). In the lower panel the structure is coloured as rainbow from N (blue) to C (red) terminus, and the 4-stranded blades of the β -propellers are labelled (P3B1, propeller 3 blade 1, etc).

suggest that the various members of the Wnt family may vary as to which PE unit they use as their primary binding site. A platform structure would allow a variety of Wnt-LRP6 complexes to have similar spatial relationships to the plasma membrane and to the Frizzled signaling receptors. Furthermore, this platform construction could support a relatively complex interplay of interactions between LRP6 and its agonists or antagonists. These insights can now be taken forward into further structural and functional studies.

References

- Logan, C.Y. & Nusse, R. The Wnt signaling pathway in development and disease. *Annu. Rev. Cell Dev. Biol.* **20**, 781–810 (2004).
- MacDonald, B.T., Tamai, K. & He, X. Wnt/beta-catenin signaling: components, mechanisms, and diseases. *Dev. Cell.* **17**, 9–26 (2009).
- Aricescu, A. R., Lu, W. & Jones, E. Y. A time- and cost-efficient system for high-level protein production in mammalian cells. *Acta Crystallogr. D* **62**, 1243–1250 (2006).
- Cheng, Z., Biechele, T., Wei, Z., Morrone, S., Moon R.T., Wang, L. & Xu, W. Crystal structures of the extracellular domain of LRP6 and its complex with DKK1. *Nature Struct. & Mol. Biol.* **18**, 1204–1210 (2011).
- Ahn, V.E., Chu, M.L., Choi, H.J., Tran, D., Abo, A. & Weis, W.I. Structural basis of Wnt signaling inhibition by Dickkopf binding to LRP5/6. *Dev. Cell.* **21**, 862–873 (2011).

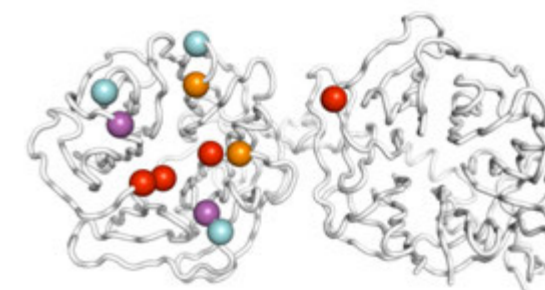


Figure 2: Main chain representation of LRP6_{P3E3P4E4} with spheres for the Ca atoms of residues important for the activity and binding of both Wnt3a and Dkk1 (red), of Wnt3a only (magenta), of Dkk1 only (orange) and of neither (cyan). The view is as for the lower panel of Fig. 1.

Funding Acknowledgements

Cancer Research UK, the UK Medical Research Council, the Spanish Ministry of Science and Innovation, the 'Red Temática de Investigación Cooperativa en Cáncer', the NIH, EMBO, the Chinese Ministry of Education–University of Oxford scholarship fund, the Leukemia and Lymphoma Society and the Wellcome Trust.

Research carried out at Diamond Light Source on beamline I24 and at the ESRF on ID23-2.

DOI 10.1016/j.devcel.2011.09.007

Structure-function relationship of the human Histamine H₁ receptor in complex with the first generation antihistamine Doxepin

Shimamura, T., Shiroishi, M., Weyand, S., Tsujimoto, H., Winter, G., Katritch, V., Abagyan, R., Cherezov, V., Liu, W., Han, G.W., Kobayashi, T., Stevens, R.C. and Iwata, S. Structure of the human histamine H₁ receptor complex with doxepin. *Nature*. **475** (7354), 65–70 (2011)

Allergies are widespread amongst human beings. Allergic reactions occur to usually harmless environmental substances such as dust, pollen, animal hair or food. Treatments for allergies include the use of antihistamines, which bind to the respective receptor. The human Histamine receptor H₁ belongs to the family of G-protein-coupled receptors (GPCRs). Activation of this receptor increases vascular permeability causing fluid to escape from capillaries into the tissues, which leads to the common symptoms of allergic reactions. Antihistamines are inverse agonists (inhibitors) of the Histamine H₁ receptor. They suppress the histamine-induced response by blocking the binding of Histamine to this receptor. Although antihistamines are commonly used safely, they have some side effects including: sedation, drowsiness or even more major symptoms such as arrhythmia, which are caused by non-specific binding to various other receptors in the body. Therefore, the high resolution structure of the human Histamine H₁ receptor with a commercially available antihistamine bound in the active site, helps to understand the ligand binding and activation mechanisms of this important membrane protein. Although there are more than 1,000 GPCRs in the human body, which are major drug targets, only about a handful of drug-binding GPCR structures have been known so far. The structure of the Histamine H₁ receptor also provides invaluable information for GPCR studies and more rational drug discovery.

Allergic reactions are widespread and have increased over the last decades amongst human beings. This reaction of our immune system occurs in response to usually harmless antigens such as dust, pollen, animal hair or food. Treatments for allergies include the use of antihistamine drugs. Over the years the pharmaceutical industry have developed a wide range of different antihistamine compounds, but a common problem of these drugs is their strong side effects, which are mainly due to the low selectivity of the receptor and the penetration across the blood brain barrier. Improved drugs significantly reduce brain permeability, although residual central nervous system effects are still reported. The groups of Prof So Iwata and Prof Ray Stevens collaborated and determined the high resolution crystal structure of the human Histamine H₁ receptor in complex with a 1st generation antihistamine bound to it by using the beamline I24. This work was carried out across 3 continents. The H₁ receptor protein was cloned and overexpressed recombinantly using *Pichia pastoris* cells at the University of Kyoto (Japan). The cell material was shipped to the Scripps Institute in San Diego, where the receptor protein was crystallized in the Lipidic Cubic Phase. The optimised crystals were flash frozen in liquid nitrogen and shipped to the Membrane Protein laboratory at Diamond Light Source and screened at the microfocus beamline I24. One special feature of these very small microcrystals (in average 10 x 10 x 3 microns) is that although visible under the microscope, they became transparent after mounting and flash freezing to 100 K. For this reason we had the great advantage of a diffraction grid scanning each of the more than 700 loops in order to rapidly locate and centre the protein crystals (Fig. 1). We then collected data with a microbeam (10 x 10) and because of the radiation sensitivity of the crystals and also due to their small size, several wedges of data with typical 12 – 15 degrees oscillation each were collected and combined. The I24 robotics, but also the grid scan and availability of the processing program Xia2 with microcrystal options, made this tedious process much more efficient and crystal screening could be carried out in a high throughput manner. Rapid access to I24 dramatically sped up this procedure so that we could determine, validate and analyse the structure within a short time.

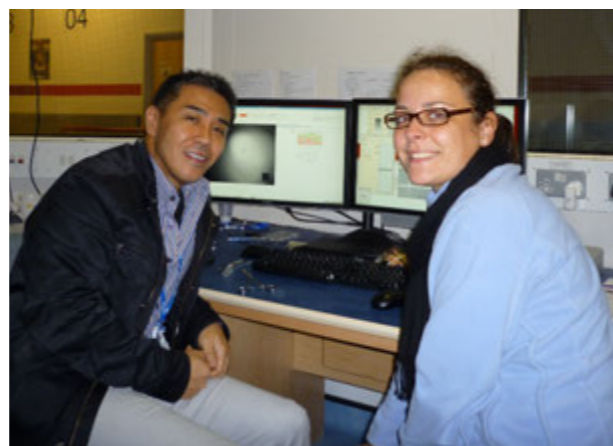


Figure 1: Data collection of the human Histamine H₁ receptor at the microfocus beamline I24 (So Iwata (left) and Simone Weyand).

The human Histamine H₁ receptor belongs to the family of GPCRs which share a common feature of 7 helices spanning the membrane (Fig. 2). The well-conserved pocket of mostly hydrophobic nature contributes to low selectivity of the first-generation drugs. This pocket is associated with an anion-binding region occupied by a phosphate ion and the docking of various second-generation H₁R-antagonists have shown that the unique carboxyl-group present in this class of compounds interacts with two lysines, both of which form part of the anion-binding region. This region is not conserved in other aminergic receptors, defining how minor differences in receptor lead to major selectivity differences with small molecules. H₁R-antagonists act as highly effective inverse agonists of the protein, reduce basal activity of the receptor and therefore are expected to interfere with the key molecular switches involved in the GPCR activation mechanism. Interestingly, in the H₁R structure, like in inactive rhodopsin, the H₁R-antagonist doxepin makes extensive hydrophobic interactions with Trp rings, which is unique among the known non-rhodopsin GPCR structures and could stabilize the

hydrophobic packing around helix VI. It has been shown that the second-generation H₁R-antagonists are much more specific, with lower affinity to other aminergic receptors. Antagonist specificity has been previously analysed using homology models based on rhodopsin crystal structures in combination with the H₁R antagonist, pharmacophore models, as well as mutational studies and some residues important for selectivity have been successfully determined. Our receptor structure with the extracellular loops should significantly improve the understanding of the H₁R-antagonist selectivity. Doxepin binds in the pocket mainly defined by the side chains of helices III, V and VI. Asp107, which is strictly conserved in aminergic receptors, forms an anchor salt bridge with the amine of the ligand. This interaction is essential for the binding of H₁R-antagonists and agonists by mutational studies.

The ligand is primarily surrounded by highly conserved residues among aminergic receptors, which make the major interactions with the protein. A novel feature of our complex structure is the existence of an anion-binding site at the entrance to the binding pocket. A phosphate ion, which is part of the crystallisation buffer, is placed into the observed strong density in the site. The presence of phosphate at this position is likely because a phosphate ion affects the binding of some ligands and also the stability of the receptor. The ionic interaction between the phosphate ion and the ligand Doxepin suggest that a phosphate ion may serve as a positive modulator of ligand binding. This has been supported by comparing thermostability and ligand affinity with and without phosphate present. The detailed analysis of the structure gives depth insights into the protein-drug relationship of this protein for the first time and enables a much more rational drug design.

References

1. Shimamura, T., Shiroishi, M., Weyand, S., Tsujimoto, H., Winter, G., Katritch, V., Abagyan, R., Cherezov, V., Liu, W., Han, G.W., Kobayashi,

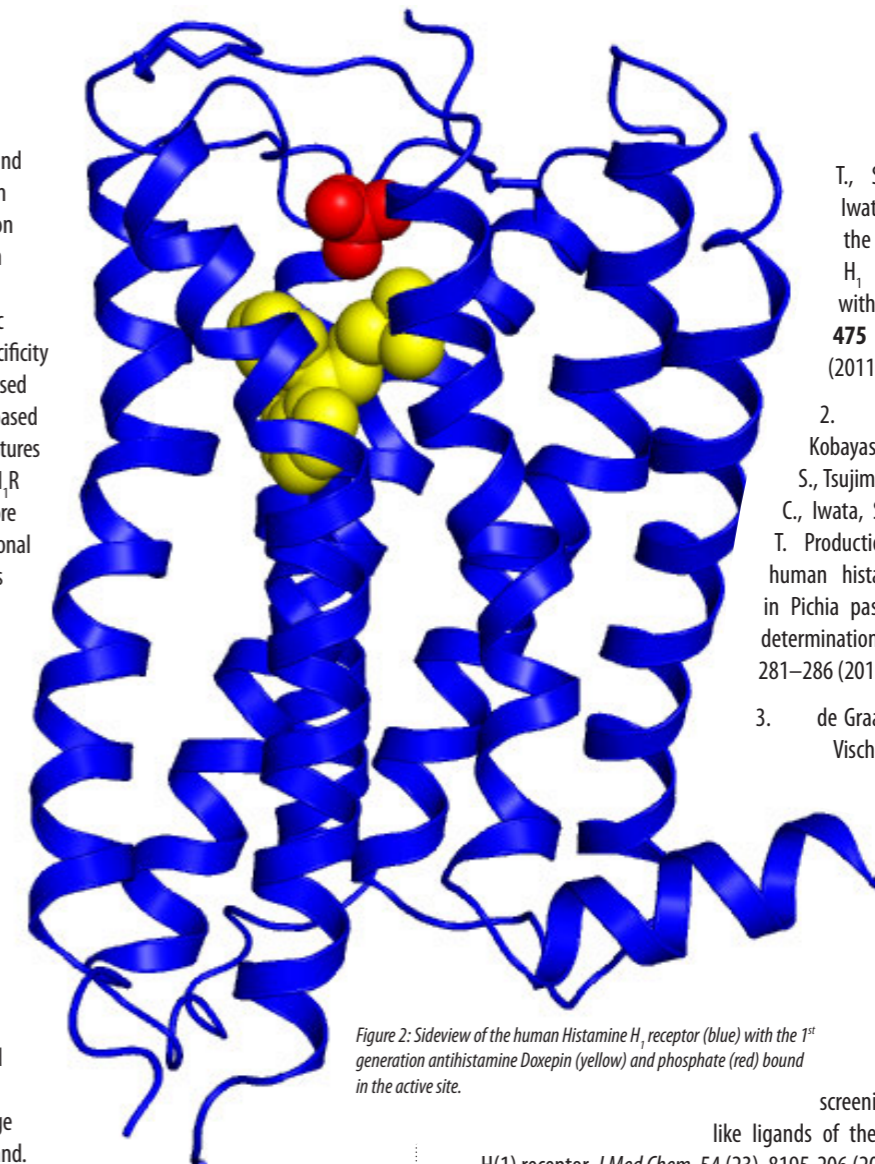


Figure 2: Sideview of the human Histamine H₁ receptor (blue) with the 1st generation antihistamine Doxepin (yellow) and phosphate (red) bound in the active site.

T., Stevens, R.C. and Iwata, S. Structure of the human histamine H₁ receptor complex with doxepin. *Nature*. **475** (7354), 65–70 (2011).

2. Shiroishi, M., Kobayashi, T., Ogasawara, S., Tsujimoto, H., Ikeda-Suno, C., Iwata, S. and Shimamura, T. Production of the stable human histamine H₁ receptor in *Pichia pastoris* for structural determination. *Methods*. **55** (4), 281–286 (2011).

3. de Graaf, C., Kooistra, A.J., Vischer, H.F., Katritch, V., Kuijjer, M., Shiroishi, M., Iwata, S., Shimamura, T., Stevens, R.C., de Esch, I.J. and Leurs, R. Crystal structure-based virtual screening for fragment-like ligands of the human histamine H(1) receptor. *J Med Chem*. **54** (23), 8195–206 (2011).

Funding Acknowledgements

This work was supported by the ERATO Human Receptor Crystallography Project from the Japan Science and Technology Agency and by the Targeted Proteins Research Program of MEXT (S.I.), Japan; NIH Common Fund grant P50 GM073197 for technology development (R.C.S.) and NIH PSI:Biolog grant U54 GM094618 (R.C.S, V.C., V.K. and R.A.); R.A. was also partly funded by NIH R01 GM071872. The work was also partly funded by the Biotechnology and Biological Sciences Research Council (BBSRC) BB/G023425/1 (S.I.), Grant-in-Aid for challenging Exploratory Research (T.S.), the Mochida Memorial Foundation for Medical and Pharmaceutical Research (T.S. and T.K.), Takeda Scientific Foundation (M.S.) and the Sumitomo Foundation (T.K.). A part of the work was performed in the Membrane Protein Laboratory funded by the Wellcome Trust (grant 062164/Z/00/Z) and at The Scripps Research Institute, Y. Zheng (The Ohio State University) and M. Caffrey, Trinity College (Dublin, Ireland), for the generous loan of the in meso robot.

DOI 10.1038/nature10236

Intermolecular 'glue' – the role of inositol tetrakisphosphate in the HDAC3 co-repressor complex

Watson, P.J., Fairall, L., Santos, G.M. & Schwabe, J.W.R. Structure of HDAC3 bound to co-repressor and inositol tetrakisphosphate. *Nature*. **481**, 335-340, (2012)

Histone deacetylase complexes play a central role in the regulation of gene expression through the regulation of the acetylation state of histones and hence chromatin structure. The enzymes 'class 1 histone deacetylases' (HDACs) are recruited to chromatin, by repressive transcription factors, as complexes with cognate co-repressor proteins. These complexes are essential for cell viability and are particularly important for determination of cell fate and lineage commitment during development. They are particularly important for determination of cell fate and lineage commitment during development. Importantly, most of the class 1 HDACs are only enzymatically active when recruited to their respective large multi-subunit co-repressor complexes. To understand the structural and functional basis for this activation, we determined the structure of HDAC3, in complex with the interacting portion of the SMRT co-repressor. This is the first structure of an HDAC:co-repressor complex and it reveals the molecular basis for the specificity of assembly and provides clues as to the activation mechanism. Most surprisingly a small molecule, inositol-(1,4,5,6)-tetrakisphosphate (IP4), was observed at the interface between HDAC3 and the SMRT co-repressor. The IP4 appears to act as an 'intermolecular glue' between the two proteins. Functional studies show that the IP4 is essential for both co-repressor interaction and for HDAC3 activation. HDAC's are emerging cancer drug targets, and these results offer potential new therapeutic opportunities.

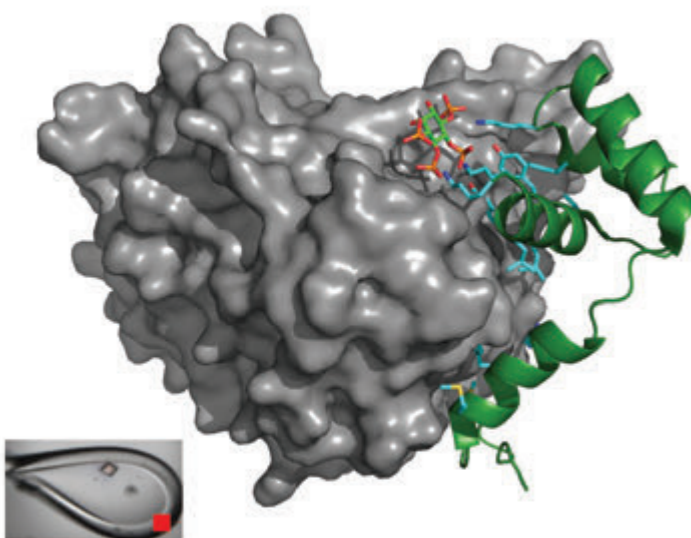


Figure 1: Structure of the HDAC3:SMRT-DAD complex, HDAC3 is shown as a grey surface, SMRT-DAD as a green cartoon, and the Ins(1,4,5,6)P₄ in a stick representation. Side chains which are important for the interaction of the SMRT-DAD with HDAC3 and Ins(1,4,5,6)P₄ are shown as cyan sticks. Insert panel – 15 μm crystal in loop.

We sought to understand the mechanism through which HDAC3 is activated on binding to the deacetylase activation domain of the SMRT co-repressor (SMRT-DAD)¹. However, early attempts to prepare complex from proteins expressed in bacteria were unsuccessful since the two proteins failed to interact even when co-expressed. This was in line with the finding of others. However, we were able to express and purify the isolated SMRT-DAD for structure determination by NMR spectroscopy. This structure revealed that the SMRT-DAD is a variant SANT domain in which an additional amino-terminal helix interacts with the canonical 3 helix bundle of the SANT domain². Site directed mutagenesis identified surface residues on this domain that impaired both interaction with and activation of HDAC3.

To overcome the failure of bacterially expressed proteins to form a complex, we expressed proteins in insect cells using baculovirus vectors. This methodology enabled purification of an HDAC3:SMRT-DAD complex,

but in our hands, the expression was highly variable and could not be scaled to give yields sufficient for structural biology. However, when we used transient transfection methods to express the complex in suspension grown HEK293 cells, we were able to routinely obtain good yields of pure complex (c. 0.5mg/l). Crystallisation trials yielded small crystals, 15 μm in maximum dimension (Fig. 1), that diffracted to 2 Å using the microfocus beamline I24 and the structure was solved by molecular replacement techniques using the structure of HDAC8 as a model (Fig. 2). The SMRT-DAD was readily identified and all but a few residues could be modelled.

The structure of HDAC3 in the complex is very similar to previously determined structures of class 1 HDACs, which consist of an eight-stranded parallel beta-sheet surrounded by a number of alpha-helices. The SMRT-DAD undergoes a significant structural re-arrangement on binding to HDAC3. The amino terminal helix no longer interacts with the canonical SANT domain, but instead lies along the surface of the HDAC3 making multiple interactions that contribute to the overall interface (Fig. 1). Amino-terminal to this

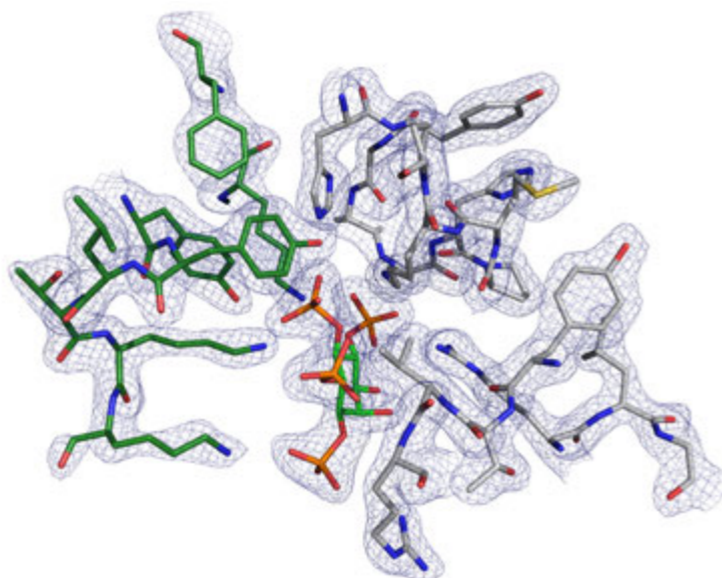


Figure 2: Electron density map (2Fo-Fc, contoured at 1.6σ) around the Ins(1,4,5,6)P₄ binding site. Residues in HDAC3 and SMRT-DAD are coloured grey and dark green respectively.

helix is a structured loop - unstructured in the NMR structure - which also contributes to the interface as well as making a packing interaction in the crystal lattice such that a methionine side chain is located in the active site tunnel of an adjacent HDAC3. This, together with a bound acetate molecule, mimics the product complex of the enzyme.

The most surprising finding from the structure was the presence of an unexpected small molecule bound in a highly basic pocket at the interface between the HDAC3 and SMRT-DAD, which had co-purified with the proteins from the mammalian cells. The small molecule was first identified in the early stages of refinement and the high quality of the electron density map meant that it could be unambiguously assigned as D-myo-inositol-1,4,5,6-tetrakisphosphate, based on the axial orientation of the hydroxyl group on carbon 2 (Fig2). The Ins(1,4,5,6)P₄ is coordinated by ten residues, five each from HDAC3 and SMRT-DAD (Fig. 3). If the Ins(1,4,5,6)P₄ were not present then the many basic residues on either side of the pocket would repel each other electrostatically and likely prevent complex formation. The fact that the Ins(1,4,5,6)P₄ remained tightly bound through out purification suggests that the Ins(1,4,5,6)P₄ is essential for complex formation and acts as an 'intermolecular glue' holding the complex together. The presence of Ins(1,4,5,6)P₄ in the structure also provides an explanation as to why proteins expressed in bacteria do not interact, since bacteria probably do not contain sufficient Ins(1,4,5,6)P₄ to support complex formation.

Mutation of residues on either the SMRT-DAD or on HDAC3 that are involved in Ins(1,4,5,6)P₄ binding resulted in the loss of both HDAC3:SMRT-DAD interaction and HDAC3 activity. This suggests that both the SMRT-DAD and the Ins(1,4,5,6)P₄ are required for activation of HDAC3. To test this, we established an *in vitro* reconstitution assay in which bacterially expressed SMRT-DAD was able to activate mammalian expressed HDAC3 in the presence of Ins(1,4,5,6)P₄. Other inositol phosphates (Ins(1,4,5)P₃ and Ins(1,2,3,4,5,6)P₆) were able to support reconstitution but only at 10 fold higher concentrations than that observed with Ins(1,4,5,6)P₄, thus confirming that Ins(1,4,5,6)P₄ is the physiologically relevant ligand. Of course this was expected, since both IP6 and IP5 are much more abundant in cells than IP4, yet the complex selected and co-purified with the tetraphosphate.

The role of inositol phosphate in HDAC:co-repressor interaction/activation appears to be common feature with other HDAC:co-repressor complexes since the residues which mediate Ins(1,4,5,6)P₄ binding on HDAC3 and the SMRT-DAD are conserved in HDAC1 and 2 and their co-repressor partners (MTA(1-3) and CoREST(1-3)). This conservation extends to the yeast HDAC Rpd3, and the Snt1 co-repressor, suggesting that the mechanism is conserved through evolution.

The structure of the HDAC3:SMRT-DAD complex also provides insights in to the mechanism of activation of HDAC3 upon binding SMRT-DAD. The binding of the SMRT-DAD and Ins(1,4,5,6)P₄ to HDAC3 probably stabilise a number of loops and helices which contribute to one side of the active site tunnel. As such, we propose that changes in both conformation and dynamics occur when the SMRT-DAD and Ins(1,4,5,6)P₄ bind to HDAC3 and that these facilitate substrate access to the active site resulting in enhanced enzyme activity.

The presence of Ins(1,4,5,6)P₄ at the interface of the HDAC3:SMRT-DAD complex raises the question of whether it is simply an essential structural co-factor or whether it has a regulatory role. Previous studies have linked

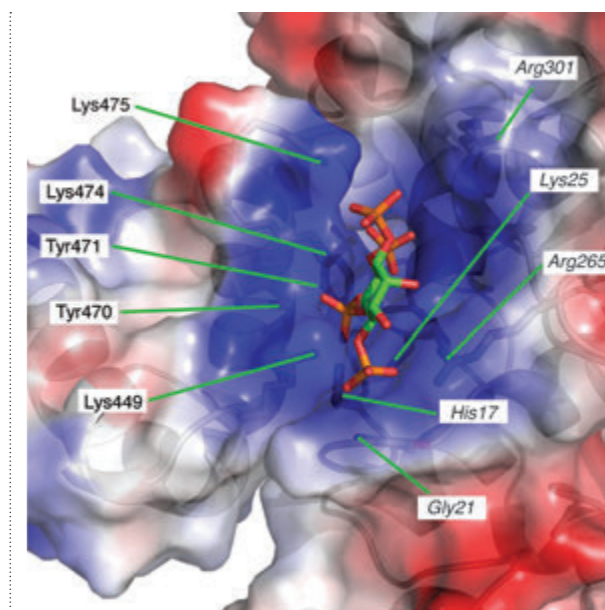


Figure 3: Electrostatic surface of HDAC3 and SMRT-DAD, showing the Ins(1,4,5,6)P₄ (sticks) binding in a basic pocket formed at the interface of the two proteins. Residues which coordinate the Ins(1,4,5,6)P₄ are labelled (italic text for HDAC3 and normal text for SMRT-DAD).

phosphoinositols and their kinases with transcriptional regulation, suggesting that Ins(1,4,5,6)P₄ probably plays a regulatory role. The yeast protein Arg82, which is an inositol phosphate kinase that converts Ins(1,4,5)P₃ to Ins(1,4,5,6)P₄, has been shown to be required for chromatin remodelling, and mutation of this protein resulted in changes in the regulation of many genes. Ins(1,4,5,6)P₄ itself has been shown to modulate the activity of ATP-dependent chromatin remodelling complexes and consequently stimulate nucleosome mobilisation.

The HDAC3:SMRT-DAD structure is the first structure of a HDAC with its co-repressor partner. This structure has provided insights into the activation of HDAC3 by the DAD domain of SMRT and revealed an unexpected small molecule Ins(1,4,5,6)P₄ which bridges the interface between HDAC3 and the SMRT-DAD. The requirement of a phosphoinositol for complex assembly and activation is likely to be conserved to other HDAC:co-repressor complexes, and presents a novel opportunity to target HDACs for anti-cancer and other therapies.

References:

1. Watson, P. J., Fairall, L. & Schwabe, J. W. R. Nuclear hormone receptor co-repressors: Structure and function. *Mol. Cell. Endocrinol.* (2012).
2. Codina, A. *et al.* Structural insights into the interaction and activation of histone deacetylase 3 by nuclear receptor corepressors. *Proc Natl Acad Sci USA*. **102**, 6009–6014 (2005).

Funding Acknowledgements

The Wellcome Trust (grant WT085408).

DOI 10.1038/nature10728.

Structure determination and crystal characterisation in situ

Danny Axford, Robin Owen, Alice Douangamath, Jose Brandao-Neto, Katherine McAuley, Dave Stuart, Gwyndaf Evans

X-ray data collection from protein crystals within crystallisation plates - in situ data collection - is quickly growing in popularity at Diamond owing to the ease with which crystals can be characterised for their diffraction properties in a 'non-invasive' way and the efficiency with which data can be accumulated from multiple crystals to yield novel structures. Three beamlines, I24, I04-1 and I03 within the MX Village, now offer this powerful analysis technique to users.

I24 was the first beamline at Diamond to introduce in situ macromolecular crystallography and utilizes an adaptation of standard goniometry to hold crystallisation trays (Figure 1a). Development of the method on beamline I24 has culminated in the solution and publication of six virus structures¹, in addition to a publication detailing the new methodology² in which the determination of two other human protein structures is described.

The ability to obtain information on the diffraction quality of crystallisation hits is particularly valuable in the challenging task of membrane protein crystallisation. In situ characterisation on I24 has become a routine part of the crystallisation optimisation operations of the Diamond Membrane Protein Laboratory. This method of data collection reduces the risk of false negatives and offers a faster and more sensitive way to compare different crystallisation conditions.

For virus crystallography the virtue of in situ data collection is the elimination of sample handling, allowing a safe working environment for pathogenic samples and removing the potentially destructive effects of cryogenic cooling. To this end I24 can now operate at biological containment level 2, moderate risk to personnel and the environment, thereby broadening the range of virus samples that can be analysed at the beamline. This work has shown how it is possible to collect enough data to solve a virus structure in situ from crystals no larger than 50 µm using only a few hours of beamtime (Figure 2).

During 2011 the availability of in situ data collection and crystal screening has now been extended with I03 and I04-1 also offering the capability. Beamline I03 will provide a wholly unique twist however by offering category level 3 containment (CL3) together with in situ diffraction analysis

making it the only facility of its type worldwide. The I03 system uses the Rigaku ACTOR sample changer to automatically mount plates kept in a rack (see Figure 1b) onto the sample goniometer. This system allows analysis of many plates under CL3 conditions without users or staff having to enter the experimental hutch. To facilitate this, plates are supported in a metal frame prior to mounting in the rack.

I04-1 provides users with a four position plate hotel and utilises the existing CATS sample changer system to position the crystallisation plates in the X-ray beam (Figure 1c). The system permits the screening of 30 crystallisation conditions per hour and has to date allowed the determination of four novel structures (to be published).

The Generic Data Acquisition (GDA) beamline control software has now been developed on each beamline to allow users to navigate around the plate so that each crystallisation drop can be easily aligned to the beam (Figure 3). The evolution of in situ methods and software will continue at Diamond in the coming years as the beamline teams and software developers offer closer integration between the crystallisation facilities and the beamline. Together with the installation of plate hotels and plate mounting systems this will allow for the automation and full remote control of in situ crystal characterisation and data collection.

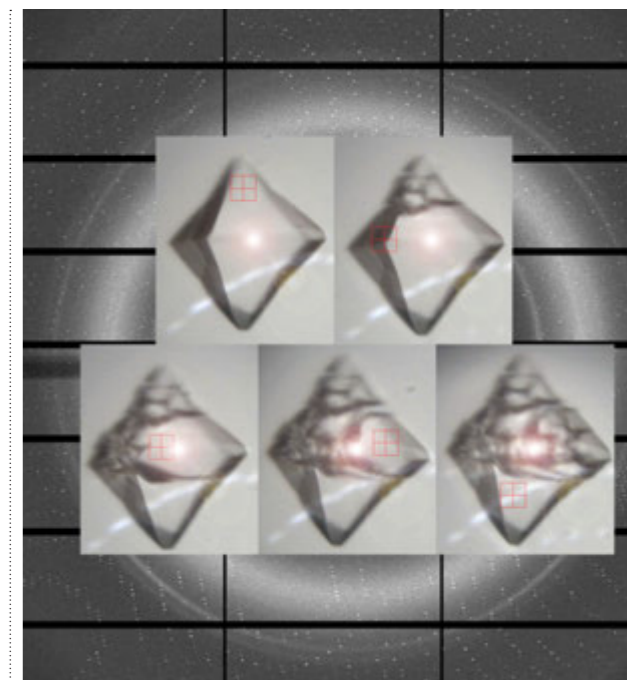


Figure 2: Sequence of images of a virus crystal as viewed on the beamline within a crystallisation drop. After exposure to the X-ray beam the crystal is destroyed locally but multiple positions of each crystal may be used for data collection. Typically many crystals are used to form a complete data set.

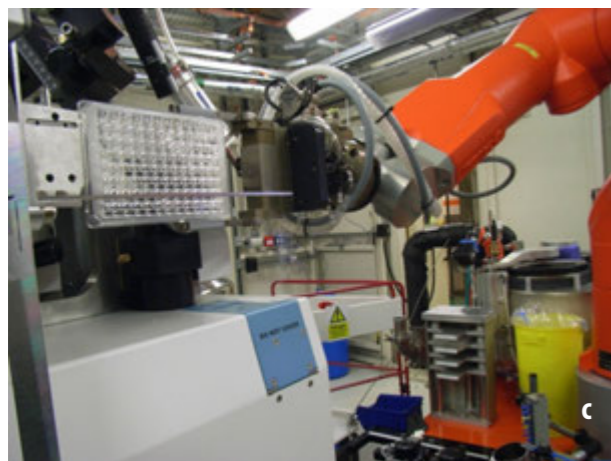
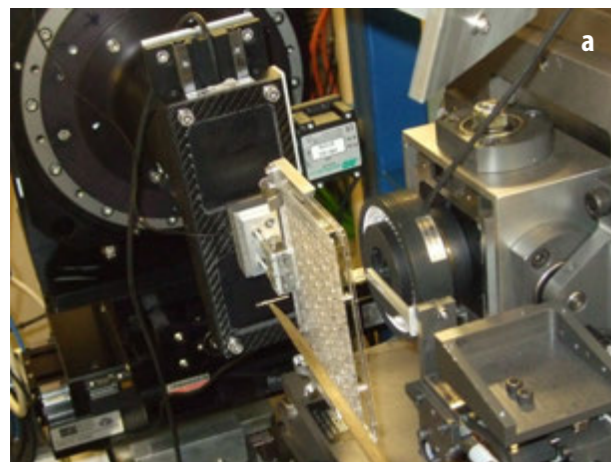


Figure 1: a) In situ set up on the I24 microfocus beamline. The plate is positioned into the beam using a modified goniometer system. b) Rack from which the I03 ACTOR sample changer picks up crystallisation plates and mounts them to the goniometer. c) In situ set up on I04-1 using the CATS sample changer to position plates in the X-ray beam.

References

1. Wang, X. et al. A sensor-adaptor mechanism for enterovirus uncoating from structures of EV71. *Nature Structural & Molecular Biology* **19**, 424–429 (2012).
2. Axford, D. et al. In situ macromolecular crystallography using microbeams. *Acta Crystallographica Section D* **68**, 592–600, (2012).

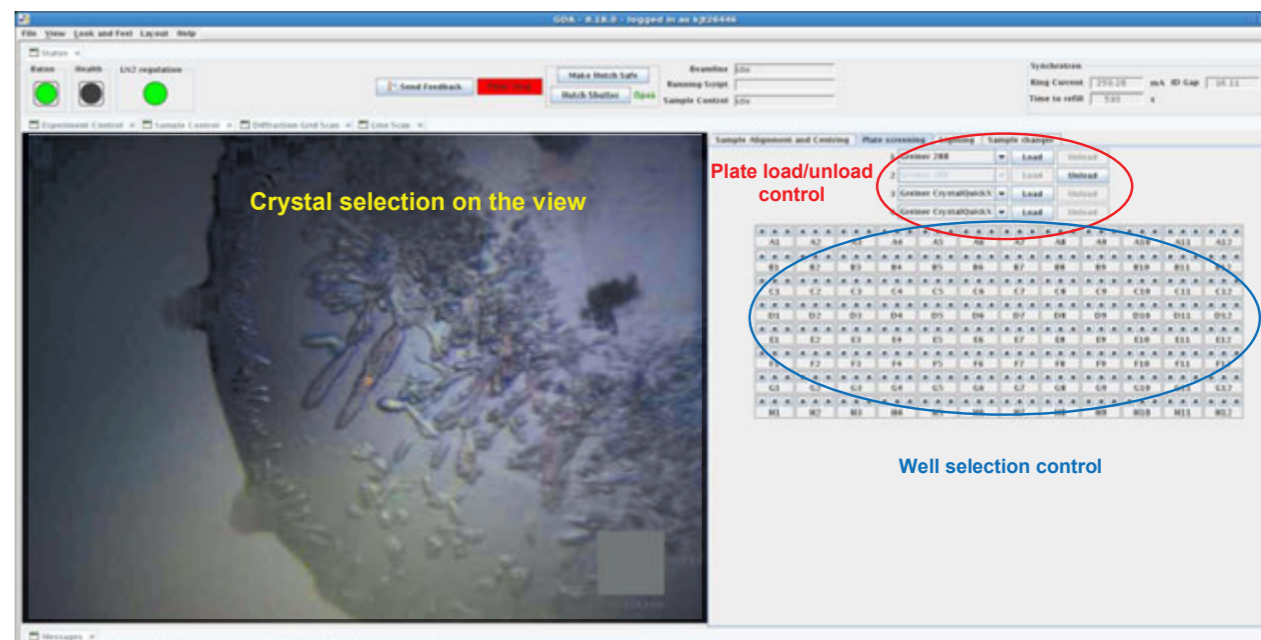


Figure 3: GUI panel within the GDA beamline software allowing navigation across a crystallisation plate to select a drop of interest. The use of SBS format 96 well plates is typical for all three beamlines.

Machine Operations

Richard Walker, Technical Director

In our 5th year of operation (2011/2012) we saw an increase both in scheduled beam delivery and reliability. A total of 211 days, which corresponds to 5064 hours, were scheduled for users, the majority being either in standard multibunch mode (900 bunch train) or hybrid mode (686 bunch train and single bunch) with top-up operation.

Because of the lack of a spare RF cavity, a cautious approach has been taken to increasing the beam current, which was raised to 225 mA in May 2011 and 250 mA in July 2011. In addition, there were two periods of four days of 'Special Beam Conditions' in September 2011 and February 2012, when the machine was operated in low-alpha mode to produce short bunches (3.5 ps rms) for both time-resolved experiments and coherent THz radiation. The uptime, which is the beam delivered as a percentage of scheduled standard user mode hours, was 97.7%. This is a slight increase when compared to the previous year (97.5%), however the mean time between failures increased significantly from 28.5 hours last year to 55.4 hours. In July 2011 we also achieved our longest period of beam delivery without a trip, 12.6 days, interrupted only by scheduled weekly Machine Development periods.

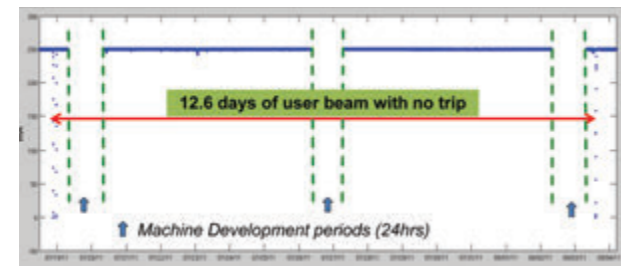


Figure 1: 12.6 days of user beam time with no beam trip in July 2011.

Further problems have unfortunately been experienced with the superconducting cavity that was sent back to the supplier for repair following its removal from the storage ring in January 2010. The cavity was returned to Diamond in June 2011, but subsequently failed during cool-down, which then required a further lengthy repair. The cavity has just been returned to Diamond in March 2012 and testing and conditioning is about to start. Meanwhile, to ensure the long-term operability of the RF cavities, the go-ahead has been given for the purchase of a fourth cavity, which is due to be delivered at the end of 2013.

Another restriction on increasing beam current in the past was the excessive helium consumption of the two superconducting wigglers which supply beamlines I12 and I15. This was resolved following an intervention during the March/April 2011 shutdown to install a new liner in the I15 device, with reduced aperture to improve its thermal isolation, while improved helium condensers were fitted in the I12 device. The cooling of the RF tapers which connect the liners to the outer room temperature flanges were also improved in both wigglers. The result was a significant drop in liner temperature and a dramatic reduction in helium consumption, even at increased beam current, as shown in Table 1.

Helium consumption	Before (200 mA)	After (200 mA)	After (250 mA)
I15 (3.5T)	1 l/h	<0.01 l/h	<0.01 l/h
I12 (4.2T)	0.33 l/h	<0.01 l/h	<0.01 l/h
Liner Temperature			
I15 (3.5T)	22 K	10.4 K	10.9 K
I12 (4.2T)	12.7 K	9.7 K	9.9 K

Table 1: Liner temperatures and helium consumption in the I12 and I15 superconducting wigglers before and after the improvements made in March/April 2011.

Phase II & III Beamlines

It was another busy year in carrying out installations and modifications to the Storage Ring for the remaining Phase II and initial Phase III beamlines. Front-ends were installed for beamlines I09, B21 and I23 and insertion devices were installed for I10 (second APPLE-II undulator), I13 (in-vacuum undulator) and I09 (APPLE-II undulator). In addition, extensive changes have been made to the storage ring itself.

In March/April 2011 a major modification of the Storage Ring was carried out for the I09 beamline, similar to that carried out for I13 described in last year's Annual Report. This involved swapping two of the main girders, one on either side of the insertion device straight section, with modified ones containing an extra quadrupole magnet. In addition, a short girder with two extra quadrupoles was installed in the middle of the straight. The additional quadrupoles allow the machine optics to be altered to produce two minima of the beam envelope in the vertical plane, allowing the installation of two narrow-gap undulators. Commissioning of the I13 optics in late 2010, with a shift of vertical tune from 12.36 to 12.86, proved to be more difficult than expected; however, the second modification for I09 allowed the vertical tune to be increased to 13.36, which, because it differs by a whole integer from the original value, results in very similar beam dynamics performance. As a result, commissioning the new I09/I13 optics took only a few days and was in regular use by the end of April 2011.

Further significant changes have also taken place for the implementation of the second phase of operation of the I10 beamline, namely in 'polarisation switching' mode, see Fig. 2. This involved, in August 2011, swapping the two adjacent girder units with modified ones, which would later allow the required kickermagnets to be installed. The new kicker magnets themselves were installed in January 2012.

The five kicker magnets allow the polarisation of the light received by the beamline to be switched, using the scheme illustrated in Fig. 3. The upper part of the diagram shows the situation when the electron beam is made to travel at an angle through the upstream undulator (B) so that the beamline only receives radiation from the downstream undulator (A). The lower part shows the reverse situation when the beamline only receives radiation from the upstream undulator (B). This switching from one undulator to the other takes place at a frequency of 10 Hz or every 100 msec. Thus, if the undulators are set to opposite polarisation (e.g. right-circular and left-circular) the light that the beamline receives is switched between these two states, so allowing experiments which measure small effects due to differences in polarisation to be carried out.

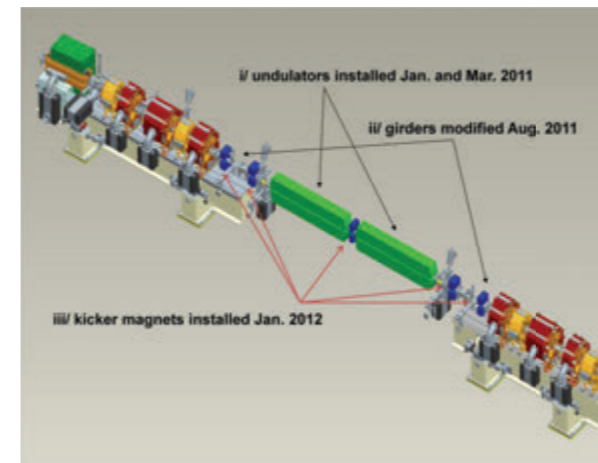


Figure 2: Machine modifications for the I10 beamline polarisation switching mode.

The challenge for this new mode of operation is to make it invisible to users on other beamlines, which means cancelling out any orbit disturbances elsewhere in the Storage Ring - during switching-on, cycling, and switching-off. Good progress has been made towards achieving this, and so being able to operate polarisation switching during normal user operation from April 2012 onwards. The main disturbance was removed by correction of the waveforms that are applied to the kickers while a combination of harmonic correction (10Hz and its harmonics), and the global fast orbit feedback system take care of the remainder, resulting in negligible disturbance of the beam orbit stability.

Accelerator Physics Studies

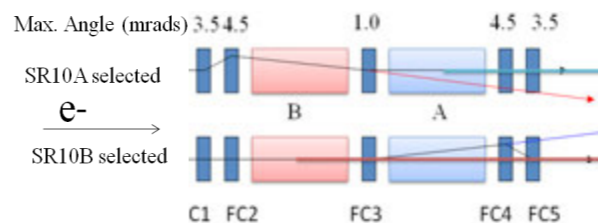


Figure 3: Illustration of the I10 beamline polarization switching scheme.

As well as underpinning the current operation of the machine and the developments that are needed for future beamlines, some of which are described above, a vigorous programme of accelerator physics studies has been carried out, aimed at achieving a better understanding of the machine behaviour which might lead to performance improvements in the future. These include: studies of non-linear beam dynamics (affecting dynamic aperture and lifetime), collective effects and instability behaviour, and operation at a reduced vertical emittance etc. At the same time, improved diagnostics are also being developed to permit different beam characteristics to be measured.

One example of recent work has been the successful absolute measurement of the machine energy using a technique called 'resonant spin depolarisation'. This measurement has proved very elusive in previous attempts, and success was only achieved after improving the electron loss rate measurement. The successful measurement shown in Fig. 4 reveals that the true machine energy is 3.0147 GeV. As well as being of interest in itself, such measurements have also allowed other basic machine parameters, e.g. chromaticity and the momentum compaction factor, to be determined and compared with the machine model.

A second example is the measurement of microbunching, as evidenced by bursts of emission of coherent mm-waves. Early measurements were reported in the 2009/10 Annual Report using a Schottky barrier diode installed on the output port originally developed for visible light extraction. During the last year a dedicated extraction port has been installed which has resulted in significantly greater sensitivity, and enabling finer features to be

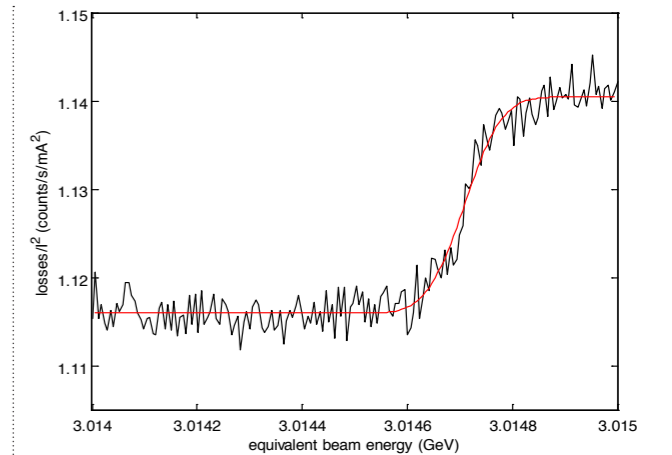


Figure 4: Measurement of the absolute energy of Diamond using resonant spin depolarization.

observed. Figure 5, for example, shows the bursts of mm-wave emission in low-alpha mode at two different RF voltages. The higher voltage produces a shorter bunch which shows regular bursts of mm-wave emission and a lower overall threshold for bursting, shown by the white dashed lines. Such measurements are useful to compare with the predictions of instability theory and detailed particle tracking simulations, allowing a deeper understanding of the complex interaction of the beam with its environment via the ring 'impedance' and with itself via coherent synchrotron radiation emission.

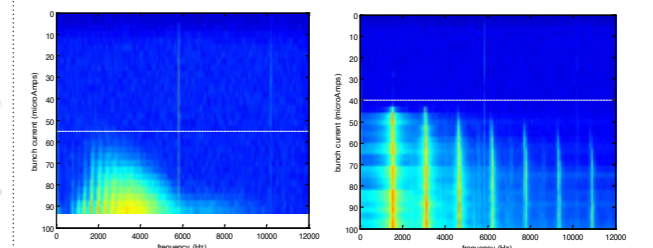


Figure 5: Fourier analysis of mm-wave emission in low-alpha ($\alpha_1 = -1.4 \cdot 10^{-5}$) mode as a function of bunch current at two different RF voltages, 1.5 MV (left) and 4.0 MV (right).

Efficiency Saving Measures

The Installation and Facilities Management group has been progressively introducing various utility saving measures over the past few years (see Table 2). Areas of particular focus related to savings on electrical and liquid nitrogen consumptions. Electrical savings were achieved mainly by modifications to the lighting system (i.e. installing light sensors, removing unnecessary fittings etc.), a reduction in the number of Air Handling Units in operation, as well as the installation of variable speed drives on a number of pumps. A programme of reconditioning the whole liquid nitrogen system started in June 2010. By restoring the vacuum insulation, the nitrogen losses were reduced while at the same time the quality of the liquid nitrogen supply to the end users was also improved.

Further savings have been achieved following the decision in 2011 to bring in-house the maintenance activities. A review indicated that reducing the frequency of certain maintenance tasks and re-arranging the team structure, could bring about a significant reduction in maintenance costs.

Area of Saving	Predicted Annual Savings for 2012
Electrical	£403k
Liquid Nitrogen	£41k
Maintenance	£163k
Total Savings	£607k

Table 2: Predicted overall savings for utilities and maintenance in 2012.

Optics and Metrology Group

Kawal Sawhney, Optics Group Leader

The Optics and Metrology Group support all of Diamond's beamlines in a number of key areas including: optical simulation and design, specification and procurement, acceptance testing and optimisation of beamline optics and mechanics. To extend Diamond's capability and achieve world leading performance, the group is also actively involved in a range of diverse research projects including development of next-generation optics, instrumentation, and techniques¹⁻⁵.

Over the past year, the Optics and Metrology group have moved beyond simple acceptance testing of synchrotron optics, and progressed to investigate routinely and optimise complete optical systems in a configuration which closely replicates beamline conditions (Fig. 1). Industrial scale mechanics have been developed to manipulate and test large (>1.5 m) and heavy (>100 kg) optical assemblies in the metrology cleanroom laboratory. Using feedback from the metrology instruments, the Diamond Nanometre Optical Metrology - known as the Diamond-NOM - and the Fizeau interferometer, the metrology and beamline teams are able to adjust interactively the clamping configuration, or physically modify the mechanics, until an acceptable compromise is achieved between mechanical stability, cooling rates, and optical performance. This improved procedure gives a much clearer understanding of how optics will ultimately perform on Diamond's beamlines.

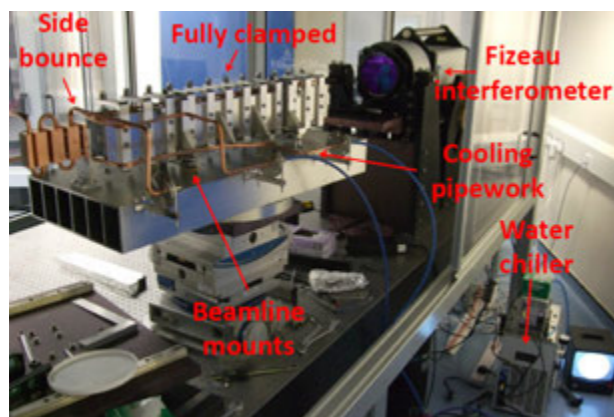


Figure 1: An example of optimisation of a complete optical system in the Metrology lab: I13 Coherence branchline mirror investigated using the Fizeau interferometer. Before optimisation, it was found that the clamping and cooling pipework were significantly distorting the mirror surface. Characterisation in the metrology cleanroom, prior to beamline installation, can save significant amounts of X-ray commissioning time.

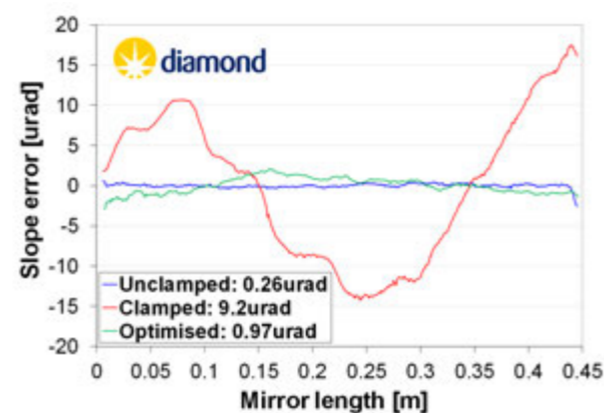
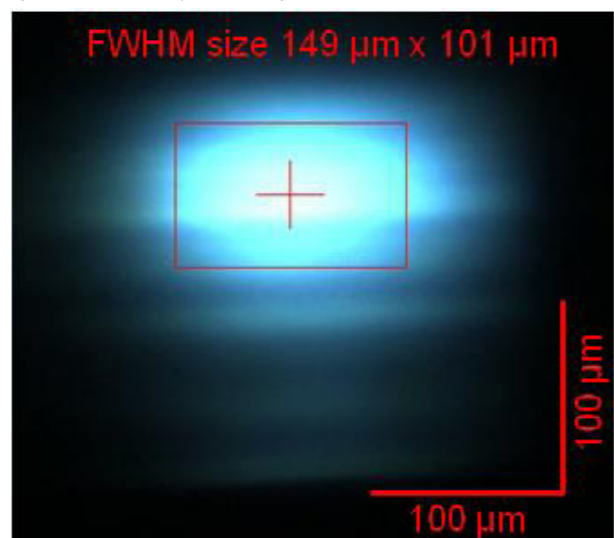


Figure 2: Prior to clamping, a Diamond-NOM slope error scan (blue curve) showed that the mirror for the I09 plane grating monochromator was of exceptional quality. However, after initial clamping, the slope error of the mirror was degraded significantly (red curve). Using feedback from the Diamond-NOM, the clamps were iteratively adjusted to minimise mechanical strain (green curve) and provide good optical performance.

Recent investigations have provided several alarming examples of how clamping, or attaching water cooling manifolds, can seriously deform the optical surface, which dramatically distorts the reflected or diffracted X-ray beam. In one case, a state-of-the-art mirror for the Surface and Interface Structural Analysis (I09) beamline was significantly degraded. Using the Diamond-NOM, the mirror mechanics and clamps were iteratively adjusted to an acceptable level (Fig. 2). Without this insight, this mirror, and other such optics, would have been installed on the beamlines in a distorted state causing debilitating problems. Currently, the major limiting factor for synchrotron optics is not the quality of optical substrates, but how the optics are mechanically clamped. In collaboration with the engineers and optics suppliers, it is hoped that metrology data can be used to help design and implement improved mechanics for synchrotron optics, resulting in world class performance and scientific output for Diamond's beamlines.

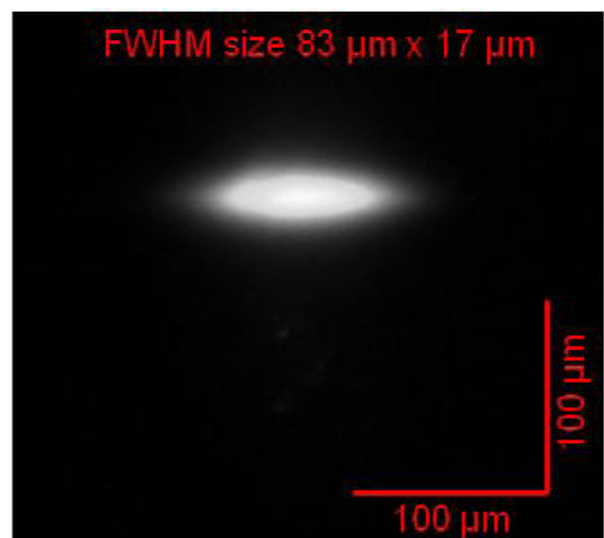


Figure 3: The focussed beam profile before (left) and after (right) re-polishing a pair of bimorph mirrors on an MX beamline. The improved surface quality has significantly improved the size and shape of the X-ray beam profile.

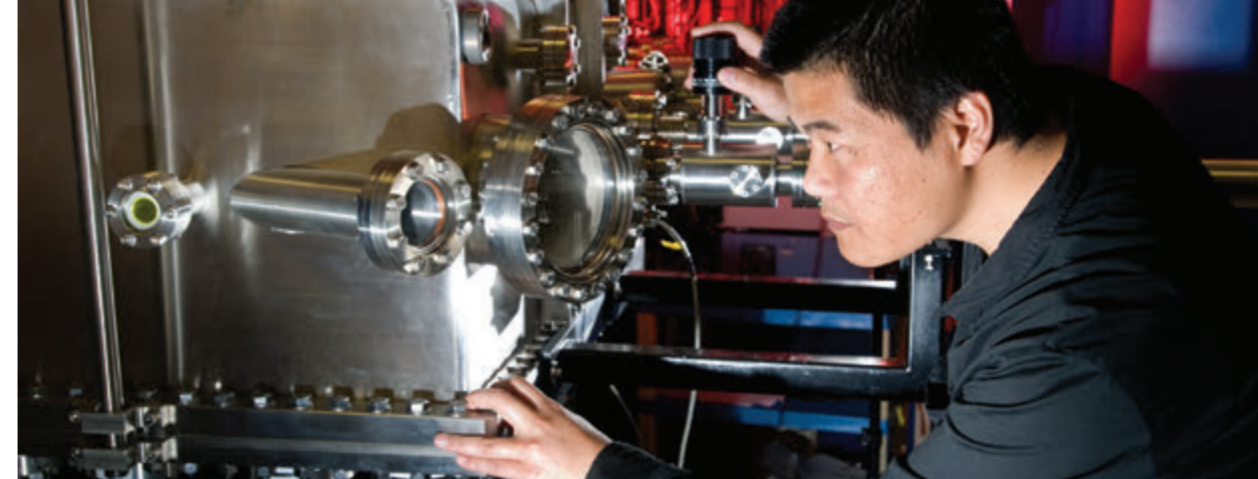


Figure 5: Optics Scientist Hongchang Wang inspects the high-precision soft X-ray Polarimeter.

A series of X-ray and ex-situ metrology tests revealed surface defects on several bimorph mirrors at Diamond, which were degrading the beamline performance. To investigate and correct these issues, the optics group worked together with teams from I02, I03 and I04. Four bimorph mirrors were removed from the beamlines and returned to the manufacturer. After successful repolishing at SESO (Société Européenne de Systèmes Optiques), and optimisation in the Metrology lab using the Diamond-NOM and Fizeau interferometer, the mirrors were safely reinstalled on their beamlines. X-ray tests have recently shown that the re-polished, high quality mirrors have significantly improved the size and shape of the focal X-ray beam (Fig. 3), extending the impact of science performed on the beamlines.

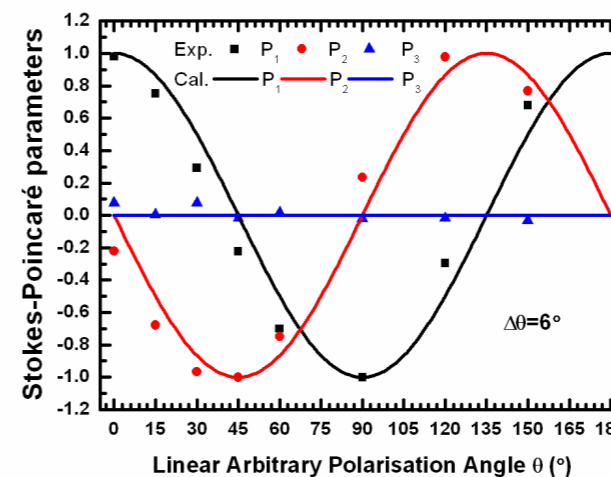


Figure 4: Stokes-Poincaré parameters (P1, P2 and P3) of the polarised light on I10 beamline from one insertion device, as a function of the linear arbitrary polarisation angle.

Modern undulators in the soft X-ray regime provide a range of polarisation states including left- and right-circular and variable linear polarised light. Knowledge of the degree of polarisation is essential, not only for improving beamline performance, but also for precise analysis of dichroic and chiral samples. To perform a polarisation characterisation of soft X-ray beams, a versatile, multi-purpose Polarimeter has been designed and built by Diamond scientists and colleagues from STFC. This high-precision, seven-axis device is ultra high vacuum compatible and employs reflection/transmission multilayers as phase retarders/analysers. Several sets of multilayers installed in the UHV chamber can be exchanged in-situ. This stand-alone instrument can be operated via an independent control system, and easily transported between different beamlines and synchrotron facilities. Following X-ray commissioning on the Nanoscience I06 beamline with Sarnjeet Dhesi and his team, the Polarimeter has measured the polarisation characteristics of X-rays from the variable polarisation, APPLE-type undulators installed on the I06 and I10 beamlines. Fig. 4 shows the polarisation states of the I10 undulator in linear arbitrary

mode. Data were recorded for the first harmonic at 712 eV, and used to correct a misalignment of $\sim 6^\circ$ in the angle of the linear-polarisation. The capabilities of the Polarimeter have been extended by using crystal analysers to perform polarisation characterisation in the difficult >1 keV range. The combination of multilayer phase retarders and crystal analysers should open up a new field of soft X-ray polarisation analysis in the energy range of 1 to 2 keV. The Polarimeter can also be employed as a versatile reflectometer/ellipsometer for determining the polarisation properties of optical elements including multilayers. In the near future, the Polarimeter will be used at several other soft X-ray and VUV beamlines, including I09, I05 and I08.

Hard X-ray nano-beams are highly beneficial for studying complex, inhomogeneous and disordered materials as they are able to probe individual nano-scale structures within samples. Consequently, nanoprobe techniques have found numerous applications in a range of disciplines, including: microelectronics, material science, biology, geology, cultural heritage and environmental and earth sciences. Several solutions exist for delivering highly focussed, nanometre sized beams to samples using refractive or refractive-diffractive optics, which include zone-plates, planar compound refractive lenses, kinoform lenses, and multilayer-Laué lenses. To minimise the time and expense of investigating such optics on beamlines, a nano-focusing optical bench has been designed and fabricated. Four independent, multi-axis, mini-stations can be arranged in a variety of combinations to provide a flexible and robust setup for testing nano-focusing optics. Using this apparatus and commercial Fresnel zone plates, sub-100nm foci have recently been achieved for the first time at Diamond on the Microfocus Spectroscopy beamline I18. Further trials are planned to provide such beams routinely to Diamond users.

References

1. Wang, H., Dhesi, S. S., Maccherozzi, F., Cavill, S., Shepherd, E., Yuan, F., Deshmukh, R., Scott, S., van der Laan, G. and Sawhney, K. J. S. High-precision soft x-ray polarimeter at Diamond Light Source. *Rev. Sci. Instrum.* **82**, 123301 (2011).
2. Alianelli, L., Sawhney, K.J.S., Barrett, R., Pape, I., Malik, A. and Wilson, M. C. High efficiency nano-focusing kinoform optics for synchrotron radiation. *Optics Express*. **19**, 11120 (2011).
3. Wang, H., Sawhney, K., Berujon, S., Ziegler, E., Rutishauser, S. and David, C. X-ray wavefront characterization using a rotating shearing interferometer technique. *Optics Express*. **19**, 16550 (2011).
4. Sutter, J.P., Alcock, S.G. & Sawhney, K.J.S. Automated in-situ optimization of bimorph mirrors at Diamond Light Source. *Proc-SPIE* **8139**, 813906 (2011).
5. Sutter, J.P., Alcock, S.G. & Sawhney, K.J.S. X-ray wavefront modelling of Bragg diffraction from crystals, *Proc-SPIE* **8141**, 8141, 81410V (2011).

Detector Group

Nicola Tartoni, Senior Scientist

In the past year, the detector group of Diamond has contributed to a number of projects in collaboration with STFC and other institutions. The detector group was a partner of the EU funded joint research activity HiZPAD where it contributed to the characterisation beam tests of the hybrid CdTe detector assemblies produced by other partners. The detector group collaborated with the Daresbury Laboratory of STFC in the development of a germanium strip detector for dispersive EXAFS, and with Rutherford Appleton Laboratory (RAL) in the development of a detector for high energy diffraction based on CMOS sensors previously developed at RAL. These two detectors will be delivered in 2012 to Diamond.

Diamond is a member of the CERN-led MEDIPIX3 consortium, and through the detector group contributes very actively to the characterisation, development, and scientific exploitation of the MEDIPIX3 ASIC. A contract with the University of Manchester was recently agreed to develop a beam profile diagnostic based on MEDIPIX3 technology.

The majority of the work of the detector group in detector development has been devoted to two development projects: EXCALIBUR and MERLIN.

EXCALIBUR detector development

The EXCALIBUR project has its origin in the survey on future detector needs undertaken in 2008¹. From this, it emerged that the major detector need for the beamlines of Diamond was a photon counting area detector with a pixel size of 50 micron. The detector group then promoted the use of the MEDIPIX3 ASIC to build a first prototype of large area detector with photon counting characteristics.

The detailed specifications that came from beamline I13 - which had been chosen as the test case - were for a matrix of 3 million pixels, with at least 2000 pixels with no dead areas in one direction. The detector should

be capable of storing data continuously at a speed of 100 frames per second or to local memory at a speed of 1,000 frames per second for a few seconds. The plan was then to build the detector from three monolithic silicon sensors with a matrix of 2048 x 512 pixels each. Each sensor is hybridised to 16 MEDIPIX3 ASICs leading to a total of 48 ASICs for the entire detector. These specifications were a big challenge, pushing the boundaries of the production technology of hybrids and of the data acquisition electronics. The sensors are the longest monolithic sensors built for this kind of applications and the largest wafers available from the manufacturer had to be used to produce them. A big challenge for the manufacturer was to keep the wafer bow over the entire wafer to acceptable levels. Similarly the frame rate stipulated in the specifications, required the ASICs to operate in full parallel read out mode, leading to an extremely high density of electronics tracks in the interconnections boards and a huge data volume to be managed by the back-end of the detector.

The EXCALIBUR project was pursued in the framework of an organic collaboration with STFC. The team took the responsibility for the development and production of hybrid assemblies, including the design

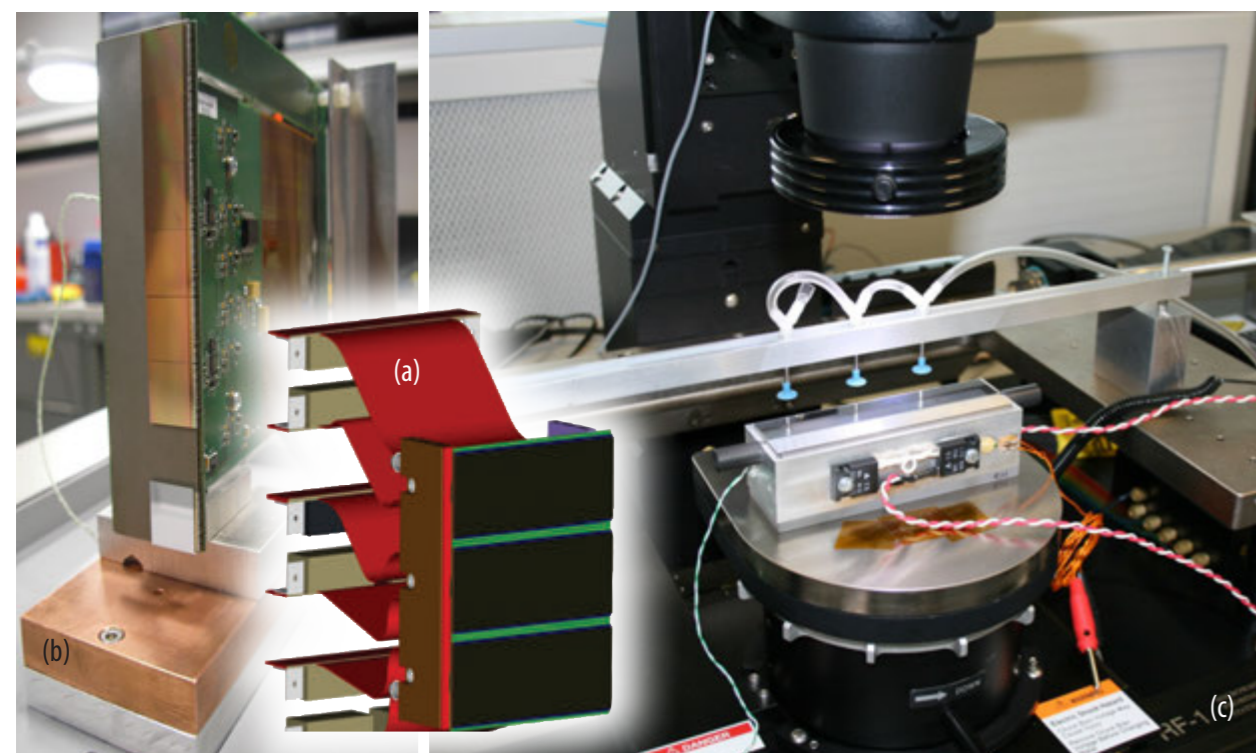


Figure 1: (a) CAD drawing of the EXCALIBUR detector front-end showing 3 hybrid pixel detector modules assembled onto a heat-sink. (b) Test assembly consisting of several MEDIPIX3 read-out ASICs (6 MEDIPIX3 ASICs without sensor and 1 MEDIPIX3 ASIC with sensor) wire-bonded onto EXCALIBUR electronic boards. This test assembly is currently used to develop the firmware of the read-out FPGA boards to be used for the read-out EXCALIBUR detector modules. (c) Photograph of the set-up used to align and bond an EXCALIBUR hybrid pixel detector onto a cold finger. This hybrid pixel detector consists of a 1M-pixel silicon sensor bump-bonded to an array of 8x2 MEDIPIX3 chips.

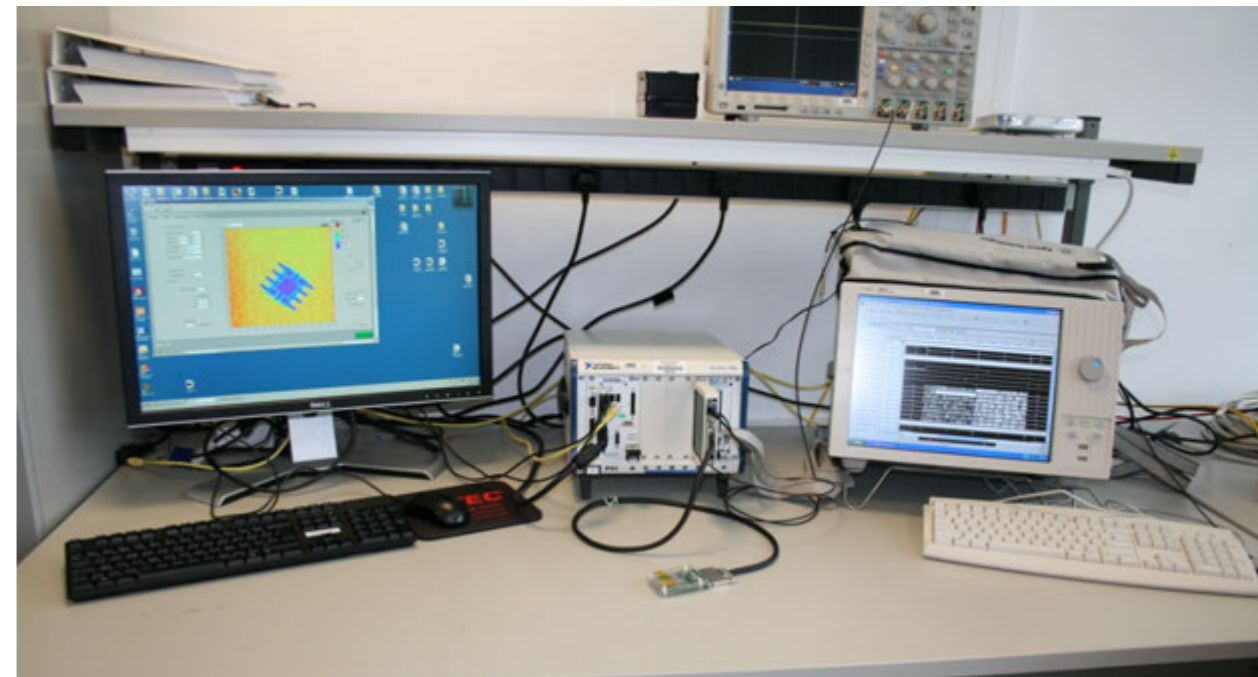


Figure 2: The MERLIN system during testing on the bench. The system is on the centre of the picture with the ASIC carrier board connected with a cable to a National Instruments PXI crate through an adapter board. A logic analyzer (right) is used to monitor the data sent to and received from the ASIC. The PC screen on the left shows the user interface of the software that drives MERLIN.

and production of carrier and interconnection boards. We coordinated the design and hybridisation of the silicon sensors by liaising actively with the developers of the read-out chips as well as the manufacturers of silicon sensors and hybrid assemblies. A class-10,000 clean tent was set-up in our laboratories to provide a clean environment for the test and bonding facility which was developed for assembly and quality control of EXCALIBUR modules. This facility includes a probe station to test, electrically and with radioactive sources, the hybrids before they are bonded to the carrier board, assembly jigs to bond the hybrid to the cold-finger and the carrier board (Fig.1(c)), visual inspection instruments for alignment and documentation. At the same time, we carried out the design of carrier and flexi-rigid interconnection boards needed to interface MEDIPIX3 ASICs to the read-out FPGA boards developed by STFC. The design was sent to manufacturers and the boards were used to produce test-assemblies such as the one shown in Fig.1(b). These test assemblies were delivered to STFC, where they are used to develop the firmware of the read-out FPGA boards.

The work on EXCALIBUR is ongoing - initial results with the first hybrid produced are encouraging, and no show stoppers emerged with the interconnection boards and the module assembly procedures developed by the detector group. The EXCALIBUR detector will be delivered to I13 in 2012 and we look forward to seeing our detector in operation.

MERLIN detector project

The MERLIN project is carried out entirely at Diamond and consists of the development of a single MEDIPIX3 ASIC read-out system. The ASIC is driven by a National Instruments FPGA board through an adapter board designed by us and a 1 m to 10 m long cable that connects the adapter board to the ASIC.

The origin of this project is in the pilot read-out system that the detector group built to understand the challenges related to driving the MEDIPIX3 ASIC². It was then realised that this system could be a very compact and high performance detector operating a single MEDIPIX3 ASIC, which could be easily located in places such as a diffractometer arm. A project was then started to develop and build two systems for I16 and B16, consolidating and expanding the capabilities of our pilot system (Fig.2). The MERLIN project is carried out with the support of a contractor for the National Instruments card programming.

The MERLIN project will deliver detectors to B16 and I16 in 2012 and will become the major development, test, and evaluation platform of the detector group for MEDIPIX3 ASICs. This system is presently the fastest available data acquisition single ASIC system within the MEDIPIX3 consortium and we will offer it to the other members when a high performance system is required.

References

1. Marchal, J., Tartoni, N. and Nave, C. Synchrotron applications of pixel and strip detectors at Diamond Light Source. *Nucl. Instr. Meth. Phys. Res. A*. **604**, 123-126 (2009).
2. Horswell, I., Gimenez, E.N., Marchal, J. and Tartoni, N. A Medipix3 readout system based on the National Instruments FlexRIO card and using the LabVIEW programming environment. *JINST*. **6** C01028 (2011).

Data Acquisition and Scientific Computing

Bill Pulford, Head of Data Acquisition and Scientific Computing

The Data Acquisition and Scientific Computing group provides a number of software tools namely the Generic Data Acquisition (GDA) for customised data acquisition and the Scientific Data Analysis workbench (SDA) for data analysis. In combination with highly evolved software workflows, customised parallelised applications and powerful underlying architecture of processing systems and networks, some of the most advanced acquisition and analysis systems are now available for scientists.

The efficient storage of all data resulting from experiments at the beamlines is an important task of the computing group. In the year 2011, a total of 1726 experimental visits took place. Together with preceding years, the measured data volumes sum up to ~ 228Tb and 95,000,000 files on the ICAT data archive.

There have been many advances during the past year, highlights include the full use of I12 for tomography and imaging within the standard user interface, a common user interface and scripting system for all spectroscopy beamlines, implementation of the MX end station upgrades with full fast integration of Pilatus detectors up to 6M and the implementation of ptychography on the I13 coherence beamline.

The GDA and SDA technology

GDA and SDA are written in JAVA within the Eclipse Rich Client Platform. The common underlying architecture virtually eliminates duplication of software by using common plug-ins that are highly configurable within an industry standard framework. Moreover the architecture facilitates beamline customised configurations and allows specific scientific analyses to be built as plug-ins while encouraging collaboration in their implementation.

The GDA highly evolved powerful python based scripting interface and associated Graphics User Interfaces are used for the acquisition part of the underlying EPICS software control system or for systems such as TANGO (Taco Next Generation Objects) or even bespoke controllers; e.g. the Medipix2 detector on the I13 Coherence beamline is TANGO interfaced. It is important also to note that GDA includes native support for the continuous scanning mode which is faster and more capable than stepping mode further enabling advanced experimentation. GDA is an open-source framework (link: www.opengda.org).

The SDA has an integrated Python and Jython scripting interface for these programming languages, to enable both simple and complex data evaluation and analysis. Additional options include support for ICAT, Nexus browsing, remote data download and interfaces with tools such as EDNA, a framework for developing plugin-based applications, and Passarelle a

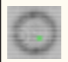




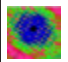
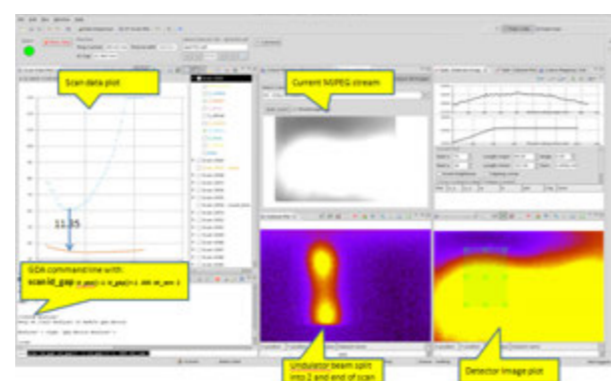
MX Macromolecular Crystallography	DIVA/MX tools diffraction image analysis	
I06 Nanostructures	PEEMA Photo Emission Electron Microscopy Analysis tool	
I07 Surfaces	Python scripting for re-processing image data	
I12 Tomography and Imaging	DExplore NeXus Data Visualisation and Detector Calibration and Python/Jython scripting	
I16 Materials and Magnetism	Python Scripting and scan and image analysis	
I22 Non Crystalline Diffraction	Non Crystalline Diffraction Data Reduction and Calibration	

Table 1: Example of beamlines where SDA is in use at Diamond.

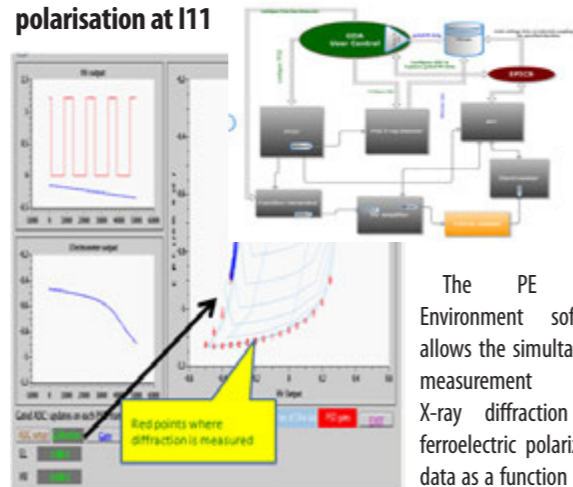
workflow tool. Mechanisms can be provided for the complex workflows necessary for automating data analysis or even for defining interspersed acquisition scans with complex analysis. The SDA is available on all Diamond beamlines, however it can also have science specific plug-ins that are specialised for certain beamlines and are in routine use, see table 1.

GDA – used a powerful and flexible beamline alignment tool



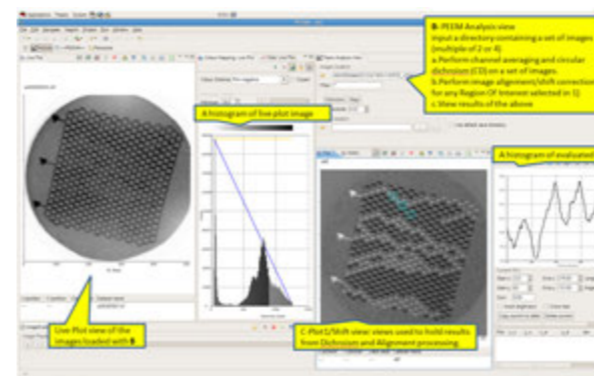
In configuring a beamline for user services it is usually necessary to optimize the X-ray insertion device in order to optimize the photon flux and the cross-sectional area of the beam. The extraordinary flexibility of GDA scanning allows this hitherto laborious or sometimes near impossible, procedure to be performed accurately and easily in minutes. In the case of the I13 undulator, for instance, this was done in less than two minutes and all with just one scripting command that even enabled the user to view every step graphically.

GDA enabling the PE Loop Environment - a new tool for measurement of X-ray diffraction and ferroelectric polarisation at I11



The PE Loop Environment software allows the simultaneous measurement of X-ray diffraction and ferroelectric polarization data as a function of the applied electric field. The goal was to investigate the electric polarization of polycrystalline materials

Examples for the SDA - Graphical sample analysis for Nanostructures (I06)



SDA Integrating detailed sample viewing and analysis in a consistent and coordinated view for I06 – Nanostructures.

as a function of frequency in order to determine the microstructural origin of the piezoelectric effects within these materials by probing their dynamic ferroelectric response. Stroboscopic and real time data can be collected by using the time frame generator (TFG) with a continuous display of collected data.

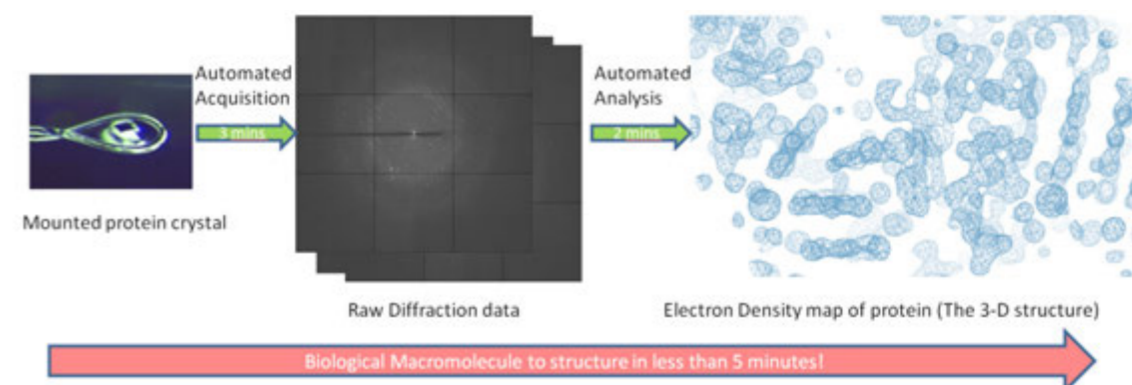
GDA Diffcalc – an improvement for diffractometry at Diamond

The enhanced Diffcalc II program includes a new calculation engine that offers hundreds of ways to constrain the extra degrees of freedom provided by many diffractometers and their geometries. The application allows a much wider range of experiments to be performed at Diamond using several different diffractometer types. In addition the new functionality offered supports the full range of features for conventional step scans, but also extends them to continuous or trajectory scans in any mix on the command line.

Diamond's Materials and Magnetism beamline I16 exploits this new functionality and can now continuously scan its 6-circle diffractometer through reciprocal lattice space while collecting and processing images from a Pilatus 2M detector at 10 Hz. Acquiring 2d data while the sample and detector are moved continuously rather than stepped from image to image allows data to be collected orders of magnitude faster and in some cases captures information that step scanning cannot. Diffcalc II is currently available and is being used on the following beamlines, each with different hardware and scientific disciplines to support: I06 (Nanoscience), I07 (Surfaces), I10 (Advanced Dichroism), I13 (Imaging/Coherence), B16 (Testing) and I16 (Materials and Magnetism).

High Speed automated data processing for MX

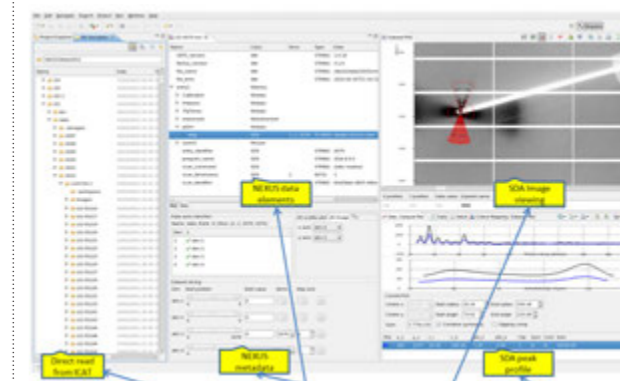
Raw diffraction data can be recorded in less than three minutes on Diamond MX beamline I02, as part of ongoing research into DNA/ligand structures. The automatically calculated map, derived purely from



experimental information, requires a search over a number of parameters. This automated analysis enables scientists to get the results less than two minutes after data collection, a step which would once have taken hours. The whole process from data acquisition to an electron density map of the sample was performed in less than five minutes.

Further activities

Examples for the SDA - Integrating detailed sample viewing, evaluation and archiving for I22



SDA Integrating archived data, descriptive metadata, image views and analysis in a consistent and coordinated view for the Non Crystalline Diffraction beamline I22.

There are further on-going activities including:

- Active participation in the European funded projects PANData and BioXhit on the implementation of a federated data infrastructure, in particular on software and data catalogues, user identities and authentication systems or optimized data analysis methods.
- Collaboration has been set up with a number of European light sources called 'DAWNscience' to provide advanced data analysis software packages mainly based on the Eclipse RCP plug-in architecture. The version 1.0 of the DAWNscience should be made available in the second quarter of 2012. A very significant component of this will be provided by the SDA.

References

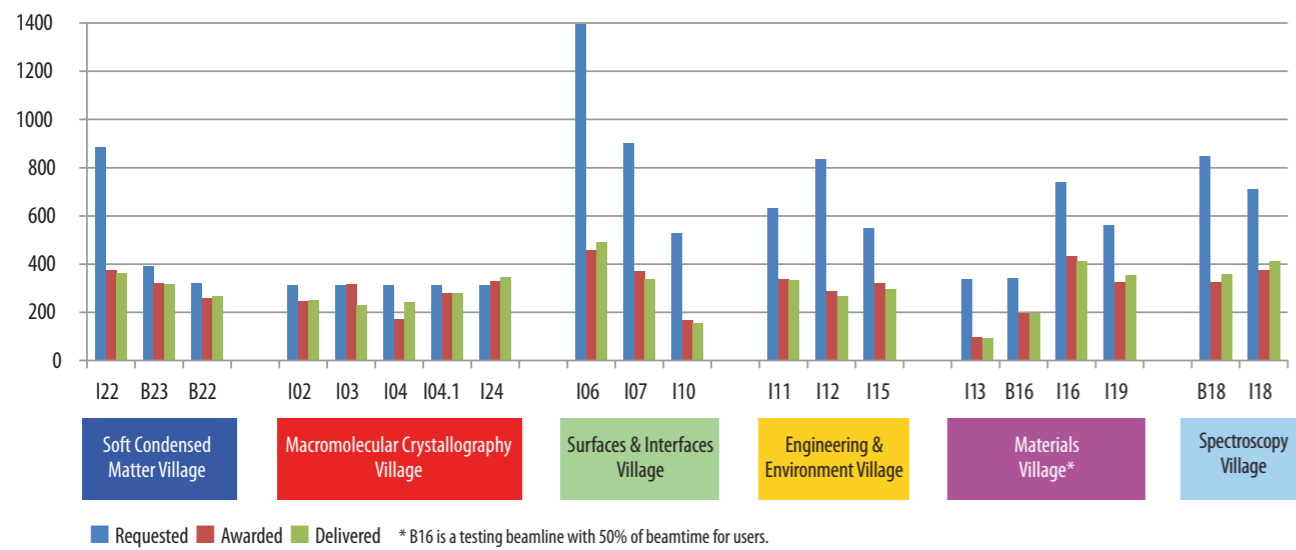
- Woolliscroft, R.J. et al., Quick EXAFS Experiments Using a New GDA Eclipse RCP GUI with EPICS Hardware Control, *Proceedings of ICALPECS 2011*, Grenoble, France (2011).
- McAuley K.E, Automated data collection for macromolecular crystallography Graeme Winter. *Methods in Structural Proteomics*. **55**, 1, 81–93 (2011).
- Shimamura, T. et al. Structure of the human histamine H1 receptor complex with doxepin *Nature*. **475**, 65–70 (2011).

Key Facts and Figures

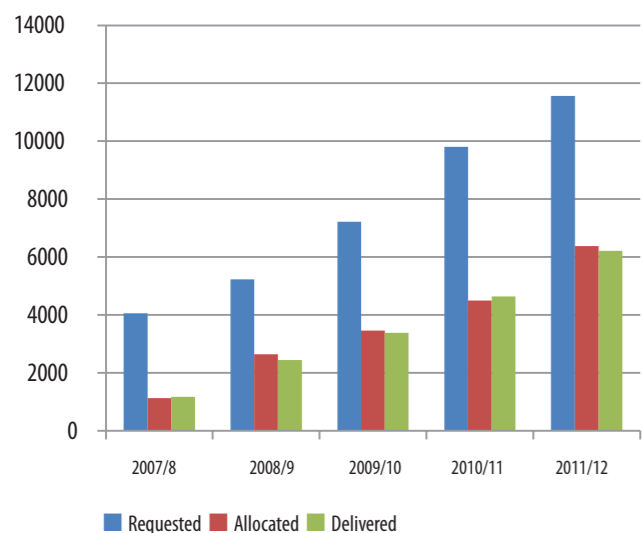
Facility usage

In our fifth year of operations (April 2011 to end of March 2012), we received 881 proposals for experiments, which requested a total of 11,568 shifts. After peer-review, 475 proposals were awarded beamtime. This resulted in 6,349 experimental shifts being allocated, spread across 20 beamlines. We welcomed 4851 user visits throughout the year.

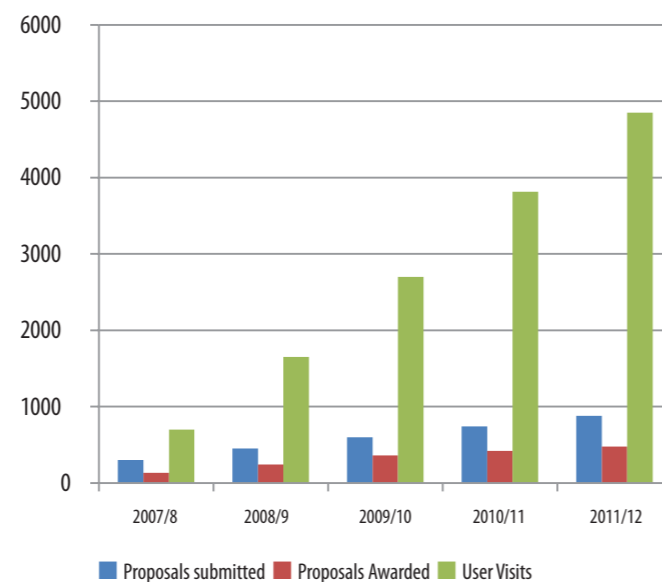
User shifts requested, awarded and delivered by village and beamline 2011/12



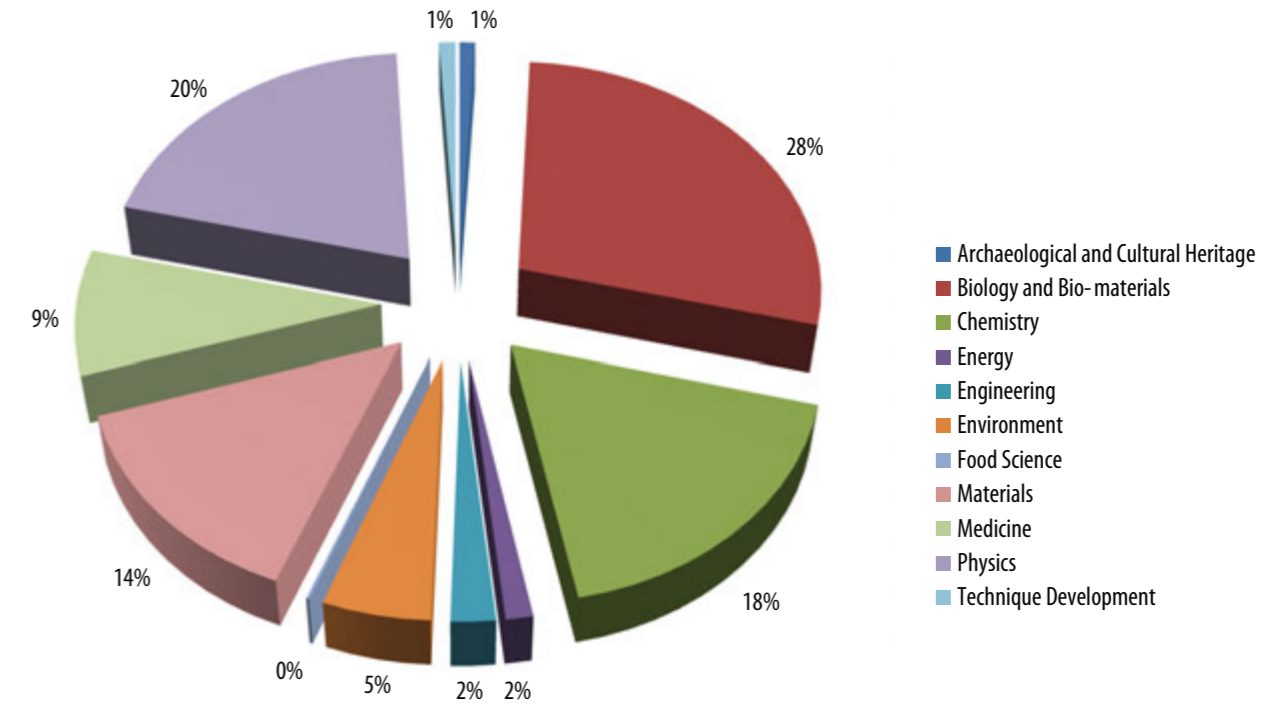
Total user shifts requested, allocated and delivered



Total numbers of proposals and users per year



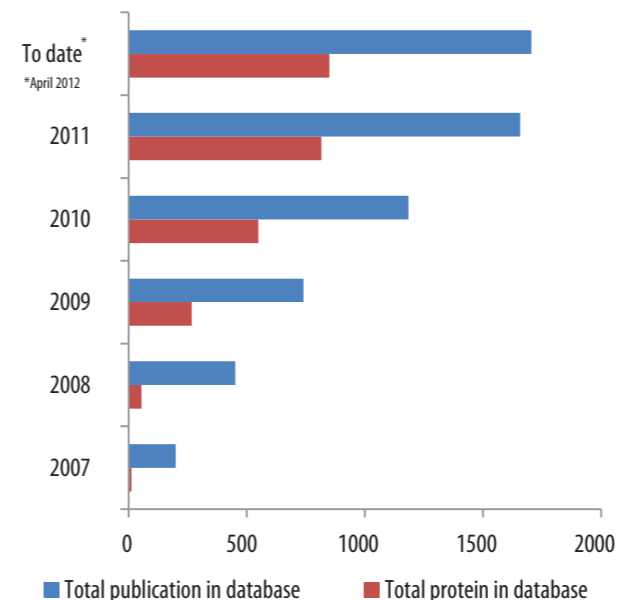
Experimental shifts awarded by Diamond by main subject area for 2011/12



Research outputs

The Diamond publications database contains all user publications based on synchrotron data gathered wholly or in part at Diamond Light Source and scientific papers published by our staff. Further improvements have been made to simplify the submission of publications. Another key indicator of our performance is the number of protein structures solved on the Macromolecular Crystallography beamlines and deposited in the Protein Data Bank.

Cumulative number of publications by our scientists and users and cumulative number of protein structures solved



Machine performance

	2007/8	2008/9	2009/10	2010/11	2011/12
Total no. operational beamlines by end FY	9	13	17	19	20
Scheduled hours of machine operation	4944	5640	5712	5808	6000
Scheduled hours of user operation	3495	4305	4728	4728	5064
Machine uptime %	93.7	95.0	97.0	97.5	97.7
Mean time between failures (hours)	11.2	15.3	26.2	28.5	55.4

The Industrial Diamond

Elizabeth Shotton, Industrial Liaison Manager

With over 50 companies participating in experiments across 17 beamlines, industrial research and development activities continues to be of great importance throughout the facility. The Industrial Liaison Office has developed a flexible approach to working with industrial partners, recognising that providing a tailored research solution may require varying levels of support at different stages of the project. Diamond offers a wide variety of access mechanisms ranging from: collaboration and full data collection and analysis services, through to mail-in data collection, remote access, and beamtime only access for experienced users who prefer to perform their own experiments.

With industrial partners from across the globe and just around the corner, from large organisations through to SMEs and small start ups, the range of types of companies that use Diamond is often surprising. Heptares, a Herfordshire-based biotechnology SME, have solved the structure of a protein involved in Parkinson's disease and other neurological disorders. The team used the microfocus macromolecular crystallography beamline I24 to reveal the complex structure of the adenosine A2A receptor and show how xanthine-based drugs such as caffeine bind to their target. Their findings, published in the journal *Structure*, could pave the way for a new generation of targeted drug treatments. Dr Fiona Marshall, Chief Scientific Officer at Heptares, explains "these co-structures of xanthines in complex with the adenosine A2A receptor advance our understanding of what is happening at the molecular level when the drug binds to its target and blocks the receptor's response. Along with novel chemotypes discovered by our team, the structural data we collected at Diamond is enabling us to develop highly optimised next-generation drug candidates for Parkinson's disease and other neurological disorders."

BioFocus, a Cambridge based drug discovery provider, is working with CHDI Foundation, Inc., a biomedical research organisation exclusively focused on developing disease-modifying therapies for Huntington's Disease; a dominantly-inherited neuropsychiatric disorder. It has been

known since 1993 that the disease is due to mutation of a single gene coding for huntingtin (HTT) that extends the poly-glutamine (poly-Q) repeats in the protein. Inhibiting the enzyme responsible for the cleavage of mutant HTT - thereby reducing the generation of the poly-Q fragments - could be one way of preventing neurodegeneration. Caspase-6 has been suggested to be this processing enzyme, but, while structures of other caspase enzymes have been solved, caspase-6 had proven resistant to structural studies, with only the crystal structure of the apo-enzyme in a pH-inactivated state solved. BioFocus identified crystallisation conditions for apo-caspase-6 in the active state, in complex with the reversible inhibitor as well as in complex with the irreversible inhibitor. They found that, surprisingly unlike the reversible inhibitor, the irreversible inhibitor binds to caspase-6 in the inactivated conformational state, and in a binding mode not previously observed for any other caspase-inhibitor complex. "The rapid access to the MX stations at the Diamond synchrotron helps us to deliver final structures to our clients within a few weeks of obtaining the first crystals." said Dr Ilka Müller, Senior Scientist at BioFocus.

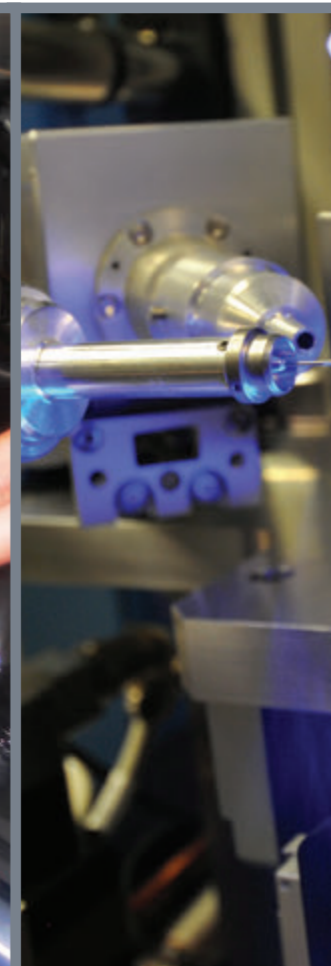
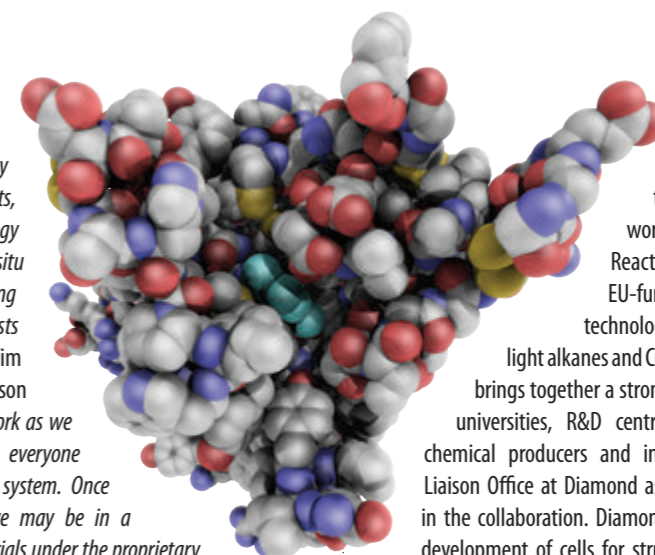
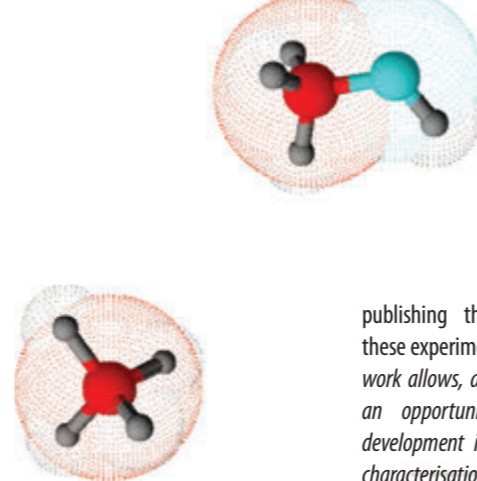
Johnson Matthey is a speciality Chemicals Company with key research areas focusing on catalysis, precious metals, fine chemicals and process technology. They access our facilities via the proprietary route and also apply for peer-reviewed beamtime in collaboration with leading UK academics,

publishing their findings from these experiments. "Non proprietary work allows, amongst other aspects, an opportunity for methodology development in the areas of in situ characterisation while working with academically relevant catalysts and materials," explains Dr Tim Hyde, Principal Scientist at Johnson Matthey. "This is a great way to work as we help to develop techniques that everyone can use through the peer review system. Once these techniques are available we may be in a position to apply them to our materials under the proprietary arrangement for industry."

Large scale research challenges facing an entire industry sometimes require a large scale collaborative approach. In the past decade, the world has experienced a widening gap between the predicted demand for oil and known reserves, fuelled particularly by the growth of new economies like China and India. High oil price may particularly affect the competitiveness of the chemical industry in Europe, relying on imported oil for more than 70% of supplies. In a global environment, with the higher cost of naphtha from crude oil and the higher cost of CO₂, the chemical industry may need to turn to novel feeds such as natural gas, coal and biomass to stay competitive. Technologies that are able to use light alkanes (C1 - C4) and CO₂ as feedstocks are needed. However, light alkanes and CO₂, in contrast to long-chain hydrocarbons from oil, are stable molecules that are difficult to activate and transform directly and selectively to added value products. Radical scientific and technological improvements are thus required to

enable efficient and competitive routes for their use. In June 2011, the Industrial Liaison Office started work on the CARENA project (Catalytic Reactors based on New materials), a large EU-funded collaborative project to create technologies enabling efficient conversion of light alkanes and CO₂ into higher value chemicals. CARENA brings together a strong European consortium with top level universities, R&D centres, industrial technology providers, chemical producers and innovative SMEs, with the Industrial Liaison Office at Diamond as one of the British partners involved in the collaboration. Diamond's role in the project focuses on the development of cells for structural properties studies of catalysts under operating conditions. Additionally, spectroscopic and diffraction techniques will be exploited to characterise the novel catalytic materials, membranes, metal organic framework materials and proton conductors prepared by the other members of the consortium. Collaboration in the CARENA project will allow Diamond to continue to develop its capabilities as a centre of excellence for catalysis research and in providing additional support for Diamond's industry and academic users.

In the past year three new members joined the team: Dr Alexandre Dias and Dr Jitka Waterman, experienced structural biologists, work closely with our industrial partners to provide research solutions to the pharmaceutical and biotechnology industries, and Dr Leigh Connor takes responsibility for industrial engineering and diffraction experiments at Diamond. To find out more about the work done by all members of the team and ways in which we may be able to help a wide range of industries solve their research problems, please visit our webpages at www.diamond.ac.uk/industry.



Public Engagement

Communications and Public Engagement Team

Engagement remains part of Diamond's vision to inspire the public especially youngsters. The facility welcomed over 5,100 visitors over the past financial year. We also continued our commitment to developing new and innovative projects to connect the facility to wider society, utilising social media and taking our science and technology off-site to festivals and events around the country.

Engaging the public

We aim to engage the public both on and off our site, and to work with organisations around the country to underline our role as a national facility. In addition to visiting science festivals in London, Bradford, Oxford and Cheltenham, we have launched new engagement projects aimed at the online community.

Light Reading was a short story writing competition, which produced works of fiction across all genres, inspired by our science and technology. Following promotion through social media, the competition attracted over 70 entries, which were judged by Jenny Rohn, founder of LabLit, and Anjana Ahuja, freelance science journalist. The entries demonstrated deep engagement with the science and technology of Diamond, the writers produced stories of incredibly high quality both in a scientific and literary sense. The project continued our long standing relationship with the arts, which will continue into 2012 through collaborations with Oxford Inspires. We intend to extend the project in 2012 to local schools, creating a new cross curricular project linking science with the arts in the classroom, and in the process, have become partners in the bid for Oxford to be the UNESCO 2014 World Book Capital.

We also produced a new series of films focussing on applications in engineering, environment, health and structural biology. These are available to everyone, and have been created to promote the breadth of science being undertaken at Diamond. In the coming year, we will promote these resources for teaching in schools and to undergraduates. We also worked with STFC on their 'Backstage Science' programme aimed at a younger audience, with contributions from Diamond scientists and engineers.

Inside Diamond was as popular as ever, with the four Saturday events in the past year being full to capacity, which means in total almost 1,000 people got the chance to visit through these sessions. Being able to talk directly with our scientists and engineers about the work being carried out here is incredibly important, and is inspiring for our staff and visitors alike.

Away from Diamond, the past year saw us visiting the Big Bang Fair, Cheltenham Science Festival, the British Science Festival and the Oxfordshire Science Festival, meeting members of the public and encouraging engagement with our science and technology. Festivals are an important means of engagement, and we will continue to take our science on the road throughout 2012, starting with the Edinburgh Science Festival in April. The Oxfordshire Science Festival also hosted a celebration exhibition of images from our construction and operations at Oxford Castle complex throughout the duration of the festival.

Engaging schools

Our series of events for A-level students, based on the format for Inside Diamond continued to grow in 2011-2012, welcoming 720 students. In addition, we continued our successful partnership with STFC to deliver expanded Particle Physics Master classes and the Engineering your Future event by welcoming 420 pupils to the facility to joint events.

We carried out our first continuing professional development for teachers event in collaboration with the examinations body OCR (Oxford Cambridge and RSA Examinations), and we will continue to develop resources for A-level teaching throughout the coming year, delivering training for teachers in schools around the region. For teachers, we have also continued to host celebration events with STEMnet, bringing together our STEM ambassadors with local teachers to encourage collaborative working.

Engaging through our scientific user community

Our role in supporting the user community in engagement is growing, and we are committed to providing opportunities for engagement, resources and training for users.

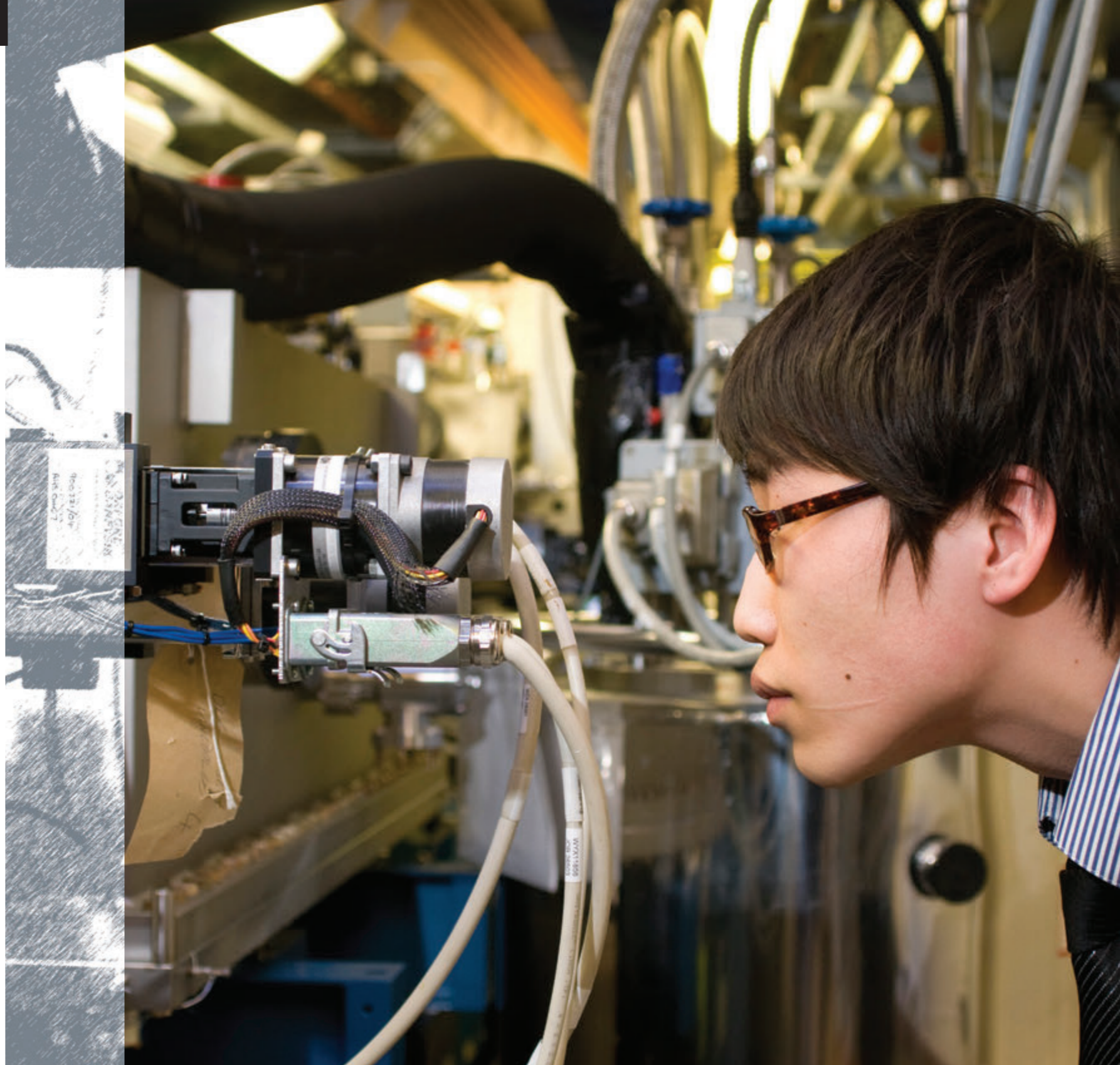
In the past year, we hosted our first dedicated student event as part of the user meeting, bringing 30 PhD students together for training in communication skills and public engagement. The student workshop will become a regular event, linked to the user meeting, and we will implement a coordinated training scheme for all PhD students linked to Diamond.

We introduced a new scheme - the Young Investigators Award - launched at the user meeting 2011. The first winner of the award will be invited to speak at the 2012 meeting, and we hope that the competition will become an important means of recognising achievements made by our younger users.

We welcomed over 1,000 scientists through our programme of workshops and scientific conferences.

Some of the highlights include CD2011 which saw 150 members of the circular dichroism community come together for a successful conference hosted at the Said Business School, Oxford. We also hosted international meetings for the optics community (ACTOP), and in radiation damage (RD7).

The 2011 user meeting welcomed Nobel Prize winner and Diamond user Venki Ramakrishnan as a key note speaker, with over 200 delegates attending. The user meeting continues to grow in its new format, with the 2012 meeting celebrating our 10th anniversary.



Governance and Management

Diamond Light Source Ltd was established in 2002 as a joint venture limited company funded by the UK Government via the Science and Technology Facilities Council (STFC) and by the Wellcome Trust, owning 86% and 14% of the shares respectively. Diamond now employs over 400 scientists, engineers, technicians and support staff from over 40 countries worldwide. The Chief Executive and Directors are advised by committees representing key stakeholder groups, including the Science Advisory Committee, Diamond Users' Committee, and Diamond Industrial Science Committee (DISCO).

Diamond is free at the point of access for researchers, provided the results are in the public domain. Allocation of beam time is via a peer-review process to select proposals on the basis of scientific merit. Six peer-review panels meet twice a year to assess the proposals submitted for each six-month allocation period. Diamond also welcomes industrial researchers through a range of access modes including proprietary research.

Board of Directors

Lord Alec Broers (Chairman)

House of Lords Science & Technology Select Committee

Prof Gerhard Materlik

Chief Executive Officer, Diamond Light Source

Andy Akerman

Director Finance & Corporate Services, Diamond Light Source

Prof Jim Naismith, FRSE

Professor of Chemical Biology, University of St Andrews

Marshall Davies

Business Advisor, Science and Technology Facilities Council

Simon Jeffreys

Chief Operating Officer, Wellcome Trust

Prof Tony Ryan

Pro Vice Chancellor, University of Sheffield

Prof Richard Wade

Chief Operating Officer, Science and Technology Facilities Council

Company Secretary

John Comfort, Head of Finance and Procurement, Diamond Light Source

Executive



Prof Gerhard Materlik FRS, CBE, FInstP was appointed CEO of Diamond Light Source in 2001. He was previously Director of the Hamburg Synchrotron Radiation Laboratory and a member of the Scientific Directorate of the German Electron Synchrotron DESY, and also Professor of Physics at Hamburg University.



Prof Trevor Rayment joined Diamond as Director of Physical Sciences in 2008. He is also Professor of Physical Chemistry at the University of Birmingham, where his research focuses on development of novel techniques for studying interfaces and their application in nanoscience, solid-liquid interface of electrodes and biomolecular interactions at interfaces.



Prof David Stuart FRS is MRC Professor of Structural Biology at the University of Oxford, and Head of the Division of Structural Biology at the Department of Clinical Medicine. He was appointed Director of Life Sciences at Diamond in 2008. His principal research interests include the structure of viruses and viral proteins as well as cellular proteins, especially those that interact with viruses.



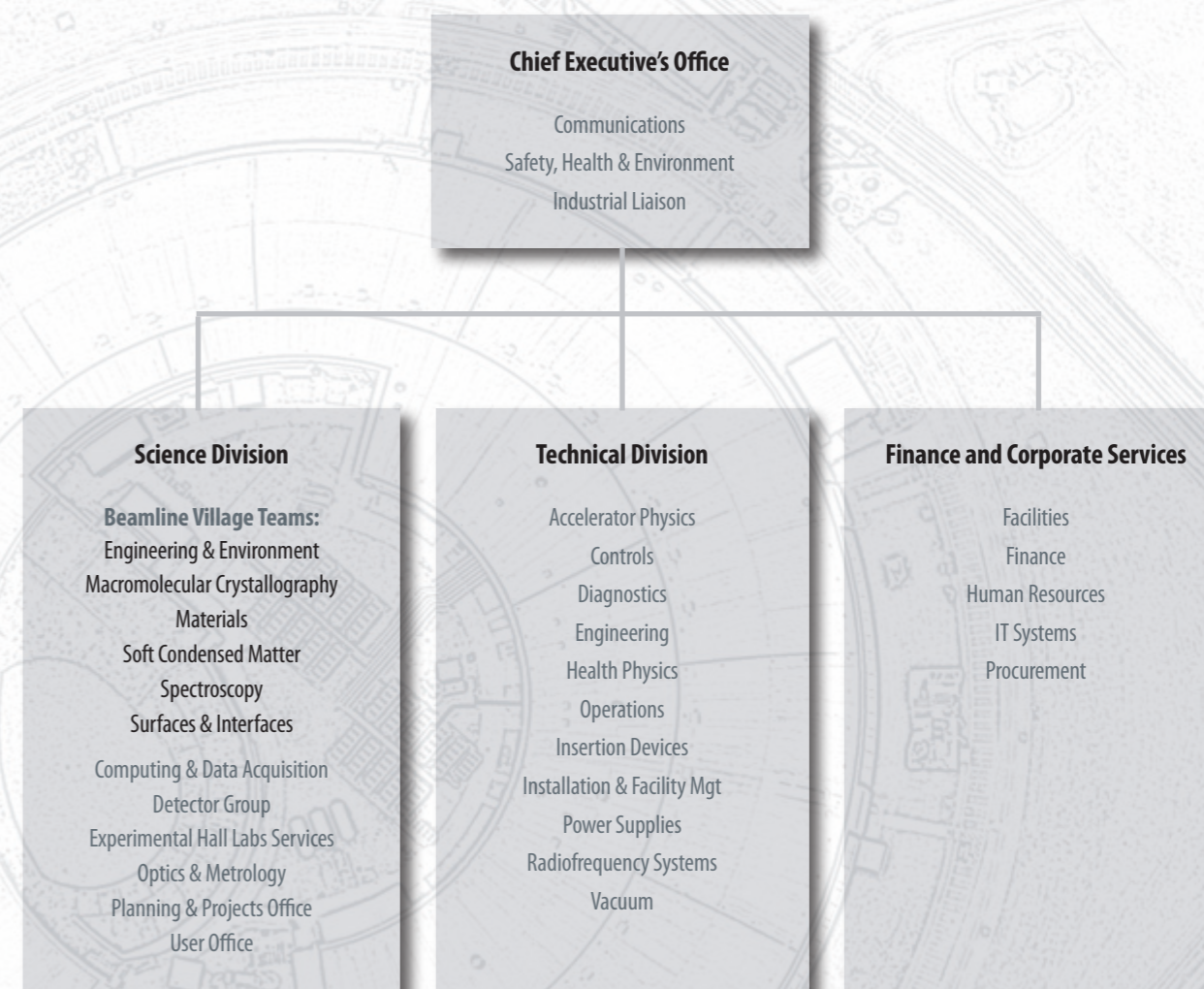
Prof Richard Walker joined Diamond Light Source as Technical Director in January 2002. He was previously Director of the Light Sources Division at Sincrotrone Trieste in Italy, and prior to that he was a key member of the Daresbury Laboratory SRS team. He is a visiting Professor of Physics at the University of Oxford.



Andy Akerman joined Diamond as Director of Finance and Corporate Services in 2009. With over 30 years experience in financial management, he was most recently Finance Director of the Defence Aviation Repair Agency.

Staffing and Financial Information

Outline Organisational Chart



Summary of Financial Data

	2007/08	2008/09	2009/10	2010/11	2011/12
Near Cash Operating Costs £m	23.5	28.4	30.5	33.5	36.5
Total Staff (Year End)	326	369	401	419	438
Capital Expenditure – Operations £m	1.0	4.5	5.7	8.6	5.1
Phase II £m	24.5	25.5	22.0	16.2	9.9
Phase III £m	0	0.1	0.3	3.0	10.3

Committee Membership

The Scientific Advisory Committee (SAC) advises the CEO and the Science Directors on the scientific and technical questions impacting on the specification, design, commissioning and operation; experimental and user support facilities, and opportunities for scientific exploitation.

Prof Alexander Korsunsky (Chair)
University of Oxford (UK)

Prof Paul Freemont (Vice Chair)
Imperial College London (UK)

Prof Jesper Andersen
University of Lund (Sweden)

Dr John Barker
Evotec (UK) (DISCo Representative)

Prof Anthony Cheetham
University of Cambridge (UK)

Prof Chi-Chang Kao
SSRL (USA)

Prof Giacomo Ghiringhelli
Politecnico di Milano (Italy)

Prof Chris Jacobsen
Argonne National Lab (USA)

Prof Sean Langridge
ISIS, STFC (UK)

Dr Andrew Leslie
MRC Laboratory of Molecular Biology
Cambridge (UK)

Prof Des McMorrow
UCL (UK)

Prof Richard Patrick
University of Manchester (UK)

Prof Rasmita Raval
Univ. of Liverpool (UK)

Prof Janet Smith
University of Michigan (USA)

Prof Mark Spearing
University of Southampton (UK)

The Diamond Industrial Science Committee (DISCo) advises the CEO and Directors on opportunities for industry to be engaged in research at Diamond, industrial research priorities that will help shape operational strategy, including the best way to exploit the current suite of beamlines and to develop the case for investment in future beamlines, and to develop best practice for industrial engagement.

Dr Malcolm Skingle (Chairman)
GlaxoSmithKline

Dr Peter Ash
Johnson Matthey

Dr John Barker
Evotec

Prof David Brown
Cangenix Ltd

Dr Rob Cooke
Heptares Therapeutics

Dr Jonathan Hyde
National Nuclear Laboratory (NNL)

Dr Matthew Johnson
GlaxoSmithKline

Dr Anne Kavanagh
AstraZeneca

Dr Ken Lewtas
Infineum

Prof Dave Rugg
Rolls-Royce

Emily Nott
Technology Strategy Board

The Diamond User Committee (DUC) has been set as a platform for discussion between Diamond and the user community of matters relating to the operation and strategy of Diamond.

Prof Bill Clegg (Chair)
University of Newcastle

Dr Joanna Collingwood
University of Warwick

Dr David Dye
Imperial College London

Prof Peter Lee
University of Manchester

Dr Karen Edler
University of Bath

Dr Karen Hudson-Edwards
Birkbeck, University of London

Dr David Lawson
John Innes Centre

Prof Malcolm McMahon
University of Edinburgh

Prof Keith Meek
University of Cardiff

Dr Peter Moody
University of Leicester

Prof Pagona Papakonstantinou
University of Ulster

Dr Josep Sulé-Suso
Keele University







Diamond Light Source Ltd
Harwell Science & Innovation Campus
Didcot, Oxfordshire OX11 0DE
Tel: +44 (0)1235 778 639
Fax: +44 (0)1235 778 499
www.diamond.ac.uk

Acknowledgement:

We would like to thank the authors and all colleagues who contributed to this publication.

The authors of each of the science papers are responsible for the contents, and all figures, images and graphs are reproduced with permission of the copyright holders.



Printed on Forest Stewardship Council (FSC) accredited paper stock. All materials used in this publication are biodegradable.

Published May 2012